Intercellular Coordination in Epithelial Morphogenesis

Dissertation

for the award of the degree
"Doctor rerum naturalium"

Division of Mathematics and Natural Sciences of the Georg August University Göttingen within the doctoral program GGNB of the Georg August University School of Science (GAUSS)

submitted by

Matthias Andreas Häring
from Salzgitter, Germany

Göttingen 2021

Thesis committee:

- Prof. Dr. Fred Wolf (Thesis supervisor and 1st reviewer)
  Göttingen Campus Institute for Dynamics of Biological Networks
- Prof. Dr. Jörg Großhans (Thesis cosupervisor and 2nd reviewer)
  Department of Biology, Philipps University Marburg
- Prof. Dr. Ulrich Parlitz (Thesis cosupervisor)
  Biomedical Physics, Max Planck Institute for Dynamics and Self-Organization, Göttingen

Further members of the examination board:

- Prof. Dr. Martin Göpfert
  Cellular Neurobiology, University of Göttingen
- Prof. Dr. Stefan Luther
  Biomedical Physics, Max-Planck-Institut for Dynamics and Selforganization, Göttingen
- Dr. Andreas Neef
  Göttingen Campus Institute for Dynamics of Biological Networks

Date of oral examination: July 30th, 2021

meinen Eltern,
Martina und Hans

Contents

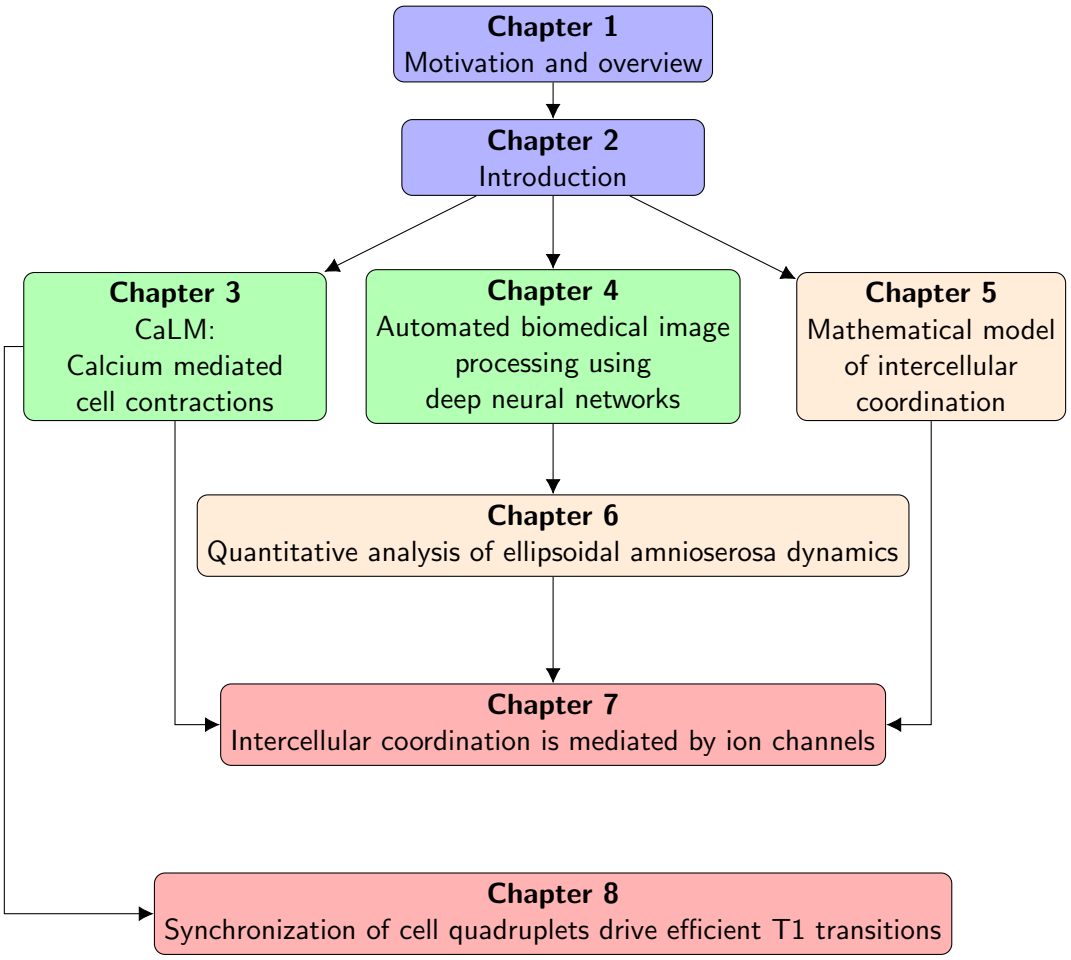

Dependency graph of thesis: **Blue** are introduction chapters. **Green** indicates methods, arrows point to chapters where these methods are directly applied. **Orange** denotes independent investigations where arrows point to chapters where the results are applied and compiled into new studies. **Red** are studies reporting new findings about the biology during *Drosophila* morphogenesis. Chapters 3-8 are either published, submitted or in preparation for publication respectively.

Chapter 1

Motivation and overview

> "Once again I had to put myself in a vulnerable position in order to become stronger."
>
> Cedric Villani

This chapter provides a motivation of the research questions and brief overview of the key results in this thesis. In the last section, the content of each chapter is summarized.

1.1 Physics in developmental biology - a systemic approach to study morphogenesis

Morphogenesis, literally "the generation of form", is a biological process during which a fertilized egg acquires its characteristic morphology and ultimately results in a living organism. Here we consider a model organism: a common fruit fly, under the scientific name of *Drosophila melanogaster*. Its development begins with a single nucleus that divides 13 times, eventually filling the surface of the ellipsoidal embryo and forming a monolayered epithelium. Major tissue rearrangements during gastrulation then completely reshape the embryo and from the originally homogeneous layer of cells an organism with muscles, organs, head and tail emerges.

How does this work, how do cells know their purpose and how is their activity concerted to robustly evolve towards a complex organism? The high reproducibility of developmental systems suggests that some form of information must be available to orchestrate the behavior of up to billions of cells in a directed manner.

One part of the answer is genetics, which has been extensively studied for over a century [225]. The discovery of the interactions between genetics and biochemical signaling constitutes a major breakthrough [239]. So-called morphogen patterning determines cell fate in a spatially and temporally specified manner. For example the morphogen *bicoid* is maternally placed mRNA at one end of the embryo. It diffuses through the system, resulting in a protein concentration gradient along the head-tail axis of the embryo. Cells express certain proteins according to the spatial concentration read off, which effectively breaks the head-tail symmetry of the embryo and establishes polarity. In this way cells 'know' if they are at the head or the tail of the organism. Such morphogen based information is one major part of microscopic organization during development.

However, the assumption that organization solely arises from microscopic preprogrammed regulation has been challenged by both biologists and physicists in the latter half of the 20th

century. One of the earliest examples, from the 50s, is the Turing instability in morphogenesis [322]. A chemical reaction-diffusion system with short range activation and long range inhibition can produce patterns that are resembling fur of animals like zebras, tigers, leopards, or the skin of the giant pufferfish. Those patterns are an emergent phenomenon that arise by an instability in the dynamical system from simple components and a homogeneous initial state. No gene is encoding how the stripes of the tiger are spatially distributed.

Self-organization is a general concept in physics, involving simple components, microscopic homogeneity or randomness, and instabilities or spontaneous symmetry breaking to yield emergent phenomena. However, the situation in developmental biology is arguably much different. Here we have information on microscopic scales, microscopic machines and preprogrammed dynamics. Both concepts represent extreme views from either side of a spectrum, while in reality both play a greater or lesser role depending on the process. Understanding the interplay between genetics and self-organization is one of the main challenges in developmental biology right now.

From an evolutionary perspective, the success of an organism in the long run is tightly linked to the efficiency and robustness of the developmental processes. Morphogenesis has to be resilient enough to withstand external perturbations, for instance of mechanical or genetic kind, and has to overcome fluctuations which are dominant for small scale systems. During morphogenesis, the main sources of noise are thermal fluctuations and a property of biological systems that is called 'active', which means that they constantly convert chemical energy into directed motion and heat. This drives the system out of equilibrium and results in mechanical fluctuations. In addition, embryo by embryo variations are also introduced by variability in the boundary conditions, caused by heterogeneity of biological parameters such as for example egg size.

Preprogrammed dynamics through genetic regulation provides uni-directional information, which is therefore not flexible enough to react to external perturbations. On the other hand, self-organization provides multi-directional information via feedback between biochemistry, geometry and, very importantly for this thesis, mechanics. Epithelial tissue dynamics is mainly governed by a few local cellular processes, including e.g. cell junction remodeling and shape changes among others. Those processes depend on active stresses that drive shape changes by exerting directionally and temporally organized contractile forces. Collectively, many of these local processes drive the rearrangement of tissues on the global scale.

Feedback between mechanics and biochemistry for the regulation of forces during morphogenesis is a main reason for the robustness of epithelial dynamics [226]. It has been shown that cells can adjust their mechanical activity in response to environmental stimuli. One of countless examples are cells in the amnioserosa, an epithelium that will be extensively studied in this thesis, which exhibit surface area oscillations. If one cell is wounded, its neighbors react with an arrest of the oscillations and contract in order to stabilize the tissue.

It remains elusive to this day how active cell mechanics is controlled and coordinated on the tissue level. How can cells sense their neighbors states and react to it? How do cells coordinate?

This question is the main subject of this thesis. To this end, we assume a systemic view: instead of focusing on a single cellular process, we take the intercellular interactions in a network of cells into account and record data from dozens of embryos which enables us to study thousands of cell interactions in an ensemble. Such a large scale approach is necessary to detect deterministic laws despite the sample by sample variation due to extrinsic noise sources. Previous studies have mostly focused on a few examples, spatially restricted regions of interest and processes on the cellular level.

It is not enough just to study collective dynamics of cells descriptively. We must put cell interactions into context of molecular mechanisms that may mediate coordination. One hypothesis

of such a molecular coordination mechanism is that mechanosensitive ion channels are behaving as molecular switches to transduce mechanical into chemical signals [141]. In this way, mechanical stimuli could directly influence biochemical regulation in neighboring cells. We already know such a mechanism from the auditory system: cochlea hair cells, where mechanosensitive ion channels are responsible for the transduction of mechanical vibrations into Ca^{2+} influx. Another mechanism concerns the mechanical connections of cells directly by investigating proteins that participate in the adhesion and mechanical signaling at the cell-cell junction [33]. Without those mechanisms we expect to observe loss in efficiency of epithelial processes, higher susceptibility to perturbations and even a failure of function if the coordination mechanism is fundamental enough.

Setting up such a novel large scale study is a challenging task that requires new experimental, quantitative and theoretical tools. First, we need high throughput and high accuracy methods to automatically analyze time lapse movies of epithelial tissues. If years are spent only to acquire the data, the project would not be feasible. Secondly, careful quantitative analysis approaches and statistical tools have to be applied to faithfully represent the biology and to uncover hidden laws in an ensemble of thousands of trajectories. Thirdly, while treading on new grounds, mathematical theories are indispensable tools that enable us to think thoroughly about the system, build expectations and formulate well defined hypothesis. Only then we can test our hypothesis experimentally, which requires tools to probe the tissue we are investigating. Finally, the puzzle pieces obtained from these studies have to be set together to answer our question: how do cells coordinate?

1.2 Thesis summary

Drosophila tissue morphogenesis is driven by complex but highly robust and coordinated cell rearrangements, shape changes and cell proliferation. Work over the past half century has established that local physical forces are required for tissue-shaping. However, how cell mechanics is coordinated and regulated spatio-temporally while performing collective movement is not yet well understood.

In order to understand cell coordination during development on the systemic level, novel experimental and quantitative methods are needed. The first results in this dissertation contribute in this regard.

A novel experimental technique, called CaLM (**Ca**lcium mediated **l**ight activation of **m**yosin), is proposed to induce contractions, with single cell and high temporal resolution, *in vivo*. Thereby Ca^{2+} cages are injected into the embryo and via laser light Ca^{2+} is released, which in turn activates myosin II, a main force producer in epithelial tissues. By inducing contractions in selected target cells, the tissue is mechanically probed and reactions of neighbors can be studied in the living embryo during development. The temporal resolution is high enough to allow simultaneous uncaging in several cells at once and thus to study local processes that are known to require coordination by inducing or disrupting them on the fly.

Large scale whole-tissue analysis of the data requires automated algorithms with high accuracy that take time-lapse movies of epithelial tissues, segment the images by separating background information from the relevant cell borders and parse data of interesting observables e.g. cell surface area or junction lengths. We have developed such a novel data acquisition and analysis pipeline based on deep neural networks. At the core of this architecture, generative adversarial networks (GANs) are used to perform the segmentation. This approach outperforms traditional rule-based algorithms significantly. Roughly speaking, the time to segment a full

movie came down from weeks to days. Compared to other machine learning methods our architecture can be trained even in absence of annotated image-mask pairs, which omits the need to create paired ground truth datasets by hand.

Equipped with these methods, the coordination of cells during *Drosophila* morphogenesis is studied. We hypothesize that a possible molecular mechanism that could mediate intercellular coordination are mechanosensitive ion channels. We study cell oscillations in the amnioserosa, a squamous epithelium that contributes to close the back of the fly embryo in a process called dorsal closure by generating internal forces. These forces have to be coordinated on the tissue level to yield non-zero net forces on the edge of the tissue in direction towards the midline. Before dorsal closure, the epithelium is in a statistically stationary state which allows us to record relatively long trajectories of cell surface oscillations and investigate their interplay.

We first develop a mathematical theory to understand how a molecular mechano-transduction mechanism based on mechanosensitive ion channels could work. The model consists of one-dimensional single cell units that are capable of oscillations due to cell area dependent turnover of myosin, a compartment of force producing molecules. Cell units are arranged on a triangular lattice coupled via direct negative mechanical interactions and the mechano-chemical coupling mechanism. Neighboring cell contractions induce Ca^{2+} influx, which is coupled to the myosin dynamics and thus may lead to synchronized contractions if the coupling is strong enough, also depending on the parameter regime. Simulations are compared to experiments to find optimal parameters for the model. Results indicate that mechanical interactions promote anti-synchronized oscillations and a mechano-transduction coupling is necessary to achieve similar synchronization as in the experiment. Simulations of the above described Ca^{2+} uncaging experiment predict that without a strong Ca^{2+} coupling mechanism, neighboring cells would not respond significantly to the contraction of a target cell.

The analysis of the experimental data reveals morphological and dynamical differences between wild type embryos and the two mutants *xit* and *Tmc* . *xit* mutants display a different distribution of E-Cadherin at the adhrens junction at the cell-cell interface and therefore directly interfere with mechanical signal transmission [355]. *Tmc* stands for transmembrane channel like and is a mechanosensitive ion channel that has been shown to directly affect Ca^{2+} dynamics in *Drosophila* [113, 180].

Both mutants affect the efficiency of the so-called ellipsoidal phase of the amnioserosa, beginning shortly after germband retraction and lasting until dorsal closure onset. The ellipsoidal phase is prolonged in the mutants and cells, in both cases, do not assume isotropic cell shapes as wild type cells do. Using junction cut experiments it is shown that tension in the lateral direction is increased in the mutants while wild type embryos are able to isotropically distribute tension. In addition, *Tmc* cell pairs show a drastic reduction in synchronized cell area oscillations as well as a different spatial organization of synchronized cell hubs. *xit* mutants loose synchronization as well but retain parts of the spatial structure observed in the wild type. Only via our large scale approach the ensemble averaged analysis was able to detect these differences, which otherwise would have remained hidden in the sample by sample variation.

Uncaging experiments confirm the theory's prediction that neighboring cells react to the contraction of a target cell in wild type while in the mutants no significant simultaneous contraction can be detected. Challenging the tissue via wounding directly shows that Ca^{2+} signaling at neighboring junctions of the wounded cell is dramatically reduced in both mutants. Together, our results suggest that the mechanosensitive ion channel *Tmc* is necessary for intercellular synchronization and for the maintenance of morphology. *xit* is required for synchronization as well but the differences to *Tmc* , especially in the spatial organization of synchronized cell pairs,

point to distinct mechanisms.

The role of *xit* is further investigated by studying T1 processes in the germband of *Drosophila*. These processes are directed neighbor exchanges that are crucial for driving the convergent extension of the germband. Using Ca^{2+} uncaging it is shown that those processes can be induced via simultaneous, synchronized, contraction of two neighbors. Our statistical analysis reveals that *xit* affects the efficiency of T1 transitions. First, those transitions are stochastic and exhibit an exponential, *xit* dependent, exit rate. Furthermore, it is possible that a T1 transition is being reversed. *xit* mutants increase the occurrence of those reversal events. Comparing time resolved correlation analysis from the participating cells with a theoretical model shows that the coordination is time dependent and that cells in *xit* mutants loose their clear synchronization. Therefore, *xit* could be necessary for mechanical signal transmission needed to coordinate cell dynamics during topological transitions.

In this dissertation, we demonstrate dynamical intercellular synchronization in active epithelia during development. This was possible due to a systemic large scale analysis of up to 10 embryos per genotype. Molecular components, such as loss of *Tmc* and *xit* , that disrupt synchronization also negatively impact efficiency and increase volatility, are unable to isotropically distribute forces across the tissue and display clear morphological changes. We therefore directly confirm, for the first time, a function of mechanosensitive ion channels for mediation of intercellular synchronization in epithelia during morphogenesis. Furthermore, it is shown that E-Cadherin is necessary for synchronization of cells during directed local mechanical processes. Our results indicate that regulation of active cell mechanics through feedback may be crucial for the efficiency and robustness of developmental processes in epithelia.

This work has been done in the group of Fred Wolf at the Max Planck Institute for Dynamics and Selforganization (MPI DS) and the Campus Institute for Dynamics of Biological Networks (CIDBN) in Göttingen and in collaboration with the lab of Jörg Großhans at University Medicine Göttingen and now University of Marburg. Prachi Richa, who is now Postdoc at Cambridge University and Deqing Kong who is a Postdoc in the Großhans lab, took over the experimental side of the work. The machine learning segmentation project was done together with Stephan Eule at the MPI DS.

1.3 Chapter content

This thesis consists of six main chapters, as well as an introduction and conclusion chapter. A brief description of chapter contents is given here. Chapters 3 and 4 contain published manuscripts that are both available online. Chapters 5 and 6 are currently prepared with the aim for publication. Chapters 7 and 8 contain prepared manuscripts that are close to submission for peer review.

Chapter 2 serves as introduction to the topics of this thesis and lays out the biological foundations needed to understand the research. Furthermore, through knowledge of the context and state of the art of the field, motivations for the scientific questions of this thesis will become clear.

In **Chapter 3**, a novel experimental technique for inducing cell contractions *in vivo* using Ca^{2+} mediated activation of myosin-II, is introduced. The Ca^{2+} is released, with single cell resolution, by photo-cleaving cage molecules that have been previously injected into the embryo. This method can be used to study the response of tissues to the exerted contraction with high

spatial and temporal resolution.

Chapter 4 presents a novel framework for automated analysis of biomedical microscopy images of epithelial tissues. Using methods from deep learning, namely cycle-consistent generative adversarial networks, it is shown that segmentation tasks can be performed with high accuracy, even despite challenging source data, and greatly outperform conventional rule based methods. An advantage of the here presented method is that the network does not have to be trained with annotated ground truth image-mask pairs.

In **Chapter 5** a mathematical theory of epithelial dynamics is developed. The model that is presented allows to study the impact of a molecular Ca^{2+} coupling mechanism leading to local synchronization of cell neighbors. We make concrete predictions, which are successfully tested in later chapters experimentally, and show that the experimentally observed degree of coordination within the tissue can only be achieved by a deliberate mechanism.

Chapter 6 presents quantitative findings from analysis of amnioserosa dynamics in wild type *Drosophila* embryos and two mutants, *Tmc* and *xit* . This data is the first of its kind because it was build on 100% segmented movies from the amnioserosa, which was possible through the novel segmentation pipeline presented in Chapter 4. Morphological differences, as well as differences in cell dynamics are described for wild type embryos and *xit* and *Tmc* mutants. The ensemble and statistical analysis approach reveals that intercellular synchronization is affected by the mutants.

Chapter 7 investigates the function of mechanosensitive ion channels as signal transducers and their role for nearest neighbor synchronization in the amnioserosa. Quantitative findings are supplemented by concrete experiments which shows that *Tmc* mutants experience an anisotropic force distribution across the tissue. In addition, synchronization is described quantitatively as well as confirmed via uncaging experiments. Wounding of the tissue shows that Ca^{2+} signaling is affected. This suggests a role of *Tmc* for intercellular coordination.

Chapter 8 investigates coordination of cell quadruplets during T1 transitions during germband extension in *Drosophila* embryos. Key findings are that T1 transitions require coordination between the participating cells, and that *xit* affects the efficiency of transitions as well as time dependent synchronization of participating cells.

Chapter 9 summarizes the main results and puts them into context of each other and published literature. In addition we give an outlook on possible continuations of the research and discuss some open questions.

Chapter 2

Introduction

> "I immediately loved working with flies. They fascinated me and followed me around in my dreams."
>
> Christiane Nüsslein-Volhard

In this chapter, I lay out the biological and physical basics which are needed to understand the investigations in all following chapters.

2.1 Open questions in morphogenesis - how do cells coordinate?

The human body consists of 10^{14} individual cells [266]. In order for us to perform tasks, for example walk, prepare dinner or read a PhD thesis, it is necessary that these cells are acting collectively and are carefully organized during their development.

The process that ensures the emergence of such an organism from a fertilized egg is called morphogenesis [322]. Epithelial tissues, mono-layered cell networks consisting of hundreds, up to billions, of cells, play a central role in the morphogenesis of many species. As a characteristic feature, epithelial cells are mechanically linked by adherens junctions, which provide a fast mode of signaling in addition to chemical signaling [204]. Tissue deformations are controlled by the concerted activity of many cells that internally produce active stresses, which have to be coordinated on the tissue level [106, 112, 130, 164]. The robustness of developmental processes and their resilience against external perturbations suggests that spatial and temporal information must be available at all times to direct these forces.

"*Thus, the primary role of the morphogenetic information is to orchestrate cellular mechanics.*" (Collinet, Lecuit 2021 [57])

The main question in this dissertation is: How do cells coordinate? How is this abstract notion of information that orchestrates the behavior of many cells realized? What molecular components are necessary for coordination? Is coordination completely predetermined by genetics and cells simply execute molecular programs? Or is self-organization and dynamical regulation the key to concerted cellular activity?

Two different views have historically dominated the developmental biology field. The first is a deterministic view of preprogrammed cells and molecular machines. In 1888 W. Roux published a paper where he stated that after cutting a frog embryo in half at stage 4, only half

of the organism develops [282]. He concluded that cells must have a predetermined fate, and that their behavior must be programmed, which is now known as the mosaic theory of development.

In the 20th century the discovery of genetics played a major role in supporting this view [262, 331], especially due to the discovery of morphogens: molecules that report information in spatially organized manner [100]. For example the morphogen gradient of the mRNA bicoid (see section 2.3) results in the spatially dependent expression of proteins which is mediated by its scalar concentration field [68]. This causes cells to differentiate differently according to the local field.

There is a complex interplay of several morphogen dynamics, such that genetics distributes information on the microscopic scales of scalar, vectorial and tensorial quality. An example for vectorial information is planar cell polarity, which provides information e.g. for the directed elongation of the germband in *Drosophila* [62].

Spatial information through biochemical signals is thought to be organized by a cascade of morphogenes which provides increasingly refined spatial information at the different patterning stages of Drosophila development [343]. However, using mathematical concepts based on information theory, this view has been contrasted as it could be shown that spatially precise information about cell fate can already be reliably predicted from genetic information from the very early stages [257, 320].

Genes and biochemistry, in this programmed view, result in deterministic protocols that uni-directionally control cellular activity together with geometrical constraints imposed by the shape of the environment, see Figure 2.1.

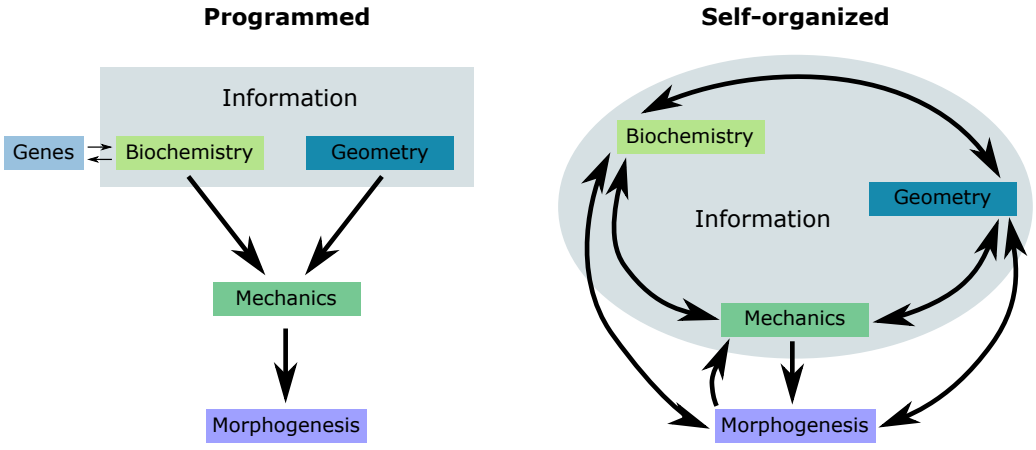

Figure 2.1: Programmed and self-organized information both organize morphogenesis. The depicted principles of uni-directional information flow, to the left, and regulation through self-organization, to the right, are extreme views. Information for the coordination of cellular processes is provided by both programmed and self-organized principles to a different extent, depending on the specific process. Adapted from [57].

The second view considers the interplay of mechanics, biochemistry and geometry to achieve regulation and organization through feedback. An early example is the research of Hans Driesch in 1891 who separated two blastomeres in sea urchin which as a result both yield a complete organism, therefore showing that cells react to perturbations from the environment and alter their fate accordingly [67].

Considering a second example from *Drosophila* development, dorsal closure (DC) is a key process, where the dorsal side of the embryo is closed after gastrulation [37]. DC is of great relevance for this thesis, as we are investigating the amnisoerosa, the main epithelium involved in the process, shortly before DC onset. An orchestra of forces is providing directed stresses from

multiple sources which makes the process surprisingly resilient [166]. Perturbations of genetic or mechanical kind can be quite substantial and dorsal closure still completes. For instance the amnioserosa can be depleted of myosin II, molecules providing contractile forces together with F-actin (see section 2.7), and DC still manages to complete [252]. The reason for this is regulation of multiple force components. If one force producing component is experiencing failure, the others react and are up-regulated to still complete this essential developmental process [166]. How this coordination is achieved remains elusive to this day, but it has been shown that Ca^{2+} signaling is involved [141].

From a physics perspective morphogenetic information can emerge self-organized due to non-linear interactions between simple components and instabilities in the dynamical system. A prominent example are Turing patterns in morphogenesis [322]. An organism that utilizes self-organization also constitutes an evolutionary advantage because information storage must be associated with providing capacity and thus consumes energy. Self-organization therefore can also serve as an evolutionary optimization principle, which has been demonstrated for instance in the organization of neurons in the brain [160, 341].

However, during development both aspects of morphogenetic information are crucial. Cells have predetermined deterministic fates, but also react to stimuli from their environment which makes development very resilient and robust. A full picture of morphogenesis must therefore take both viewpoints into account. Developing a better molecular understanding of cell coordination and contributing to understand the interplay of biochemistry and mechanics are two of the main aims of this dissertation.

The mechanics of tissues for single cellular processes as well as collective cell dynamics has been extensively studied, see e.g. [4, 84, 176, 299]. Researchers have described collective rheological, elastic and viscous properties of tissues and epithelia have been studied in context of active matter, systems that are constantly driven out of equilibrium due to internal dissipation of energy. Biophysical models have been devised to reproduce and understand the mechanics of tissues, see e.g. [64, 287]. Further information can be found in section 2.15. Possible mechanisms of intercellular coordination, however, have been less studied.

Biological dynamics is complex, meaning that global behavior is an emergent phenomenon arising from the interplay of simple components that would not have been expected only by studying those components individually. In addition they are noisy due to thermal fluctuations and constant dissipation of energy. Separating intrinsic and extrinsic noise from the deterministic dynamics is a challenging task that requires precise quantitative methods and incorporation of stochastic thought into mathematical modeling [133, 189]. This is not only true in the self-organization view, also programmed information has to overcome noise induced limits [319].

In order to detect the deterministic protocols, hidden within these variations, large scale ensemble analysis, known from statistical physics, can be employed. Well defined ensembles of certain observables can be constructed by exploiting that biology is mostly evolving towards functionally important target states [188]. Because evolution favors energetically optimized systems, we can assume that most processes in biology have a clearly defined function and lead towards a specific goal. In the above noted example of dorsal closure, such a target state would be the onset of dorsal closure or the completion when the back of the fly embryo is fully closed. Another example for target states are the 4x vertex points of cell quadruplets during T1 transitions [172].

The basic idea is to align single realizations from several experiments to these target states. Statistical analysis of such a well defined ensemble can then reveal subtle deterministic laws which drive the system towards these states and would otherwise remain hidden in the sample

by sample variation.

Large scale approaches are nowadays possible due to revolutions in the imaging and data acquisition technology, reviewed in section 2.13. We are able to record massive amounts of data and via novel tools, like neural networks, it has become feasible to analyze large datasets, see section 2.14.

In this thesis we want to understand whether and how cells dynamically synchronize in epithelial morphogenesis. Can we detect cell-cell coordination during important developmental processes? If yes, is it possible to identify molecular mechanisms for intercellular coordination? What is the specific function of the observed synchronization? Two specific processes during *Drosophila* morphogenesis are investigated in this thesis:

In chapter 7 we hypothesize that a mechanosensitive ion channel, called *Tmc* , may mediate intercellular coordination, which leads to synchronization of neighboring cell oscillations in the amnioserosa. Ion channels, such as *Tmc* , may provide a molecular mechanism for coordination by mechanotransduction of tension into chemical Ca^{2+} signaling.

In chapter 8 we study a prototypical process during germband elongation, called T1 process. Cells are exchanging neighbors due to topological transitions, which ultimately drive tissue extension. It is investigated how the coordination of participating cells drives these neighbor exchanges.

In the remaining chapter we will introduce the model system, *Drosophila*, used in this thesis to study intercellular coordination during morphogenesis. We briefly review important components and processes of this system and afterwards introduce the data acquisition state of the art and mathematical models.

2.2 *Drosophila melanogaster* as a model system

The model used in this thesis to study morphogenesis is *Drosophila melanogaster*, commonly referred to as the fruit fly. It is one of the dominating model systems in developmental biology. Other animal models used to study development have in common to be relatively simple, for example zebrafish [115] or *C.elegans* [330]. Other higher organisms like mice [44] or *xenopus* [337] are also studied but due its unique features *Drosophila* is one of the best understood systems today [342].

Drosophila has been extensively used to study developmental processes for over a hundred years [225] and possesses several key advantages as a model system.

On a practical level, *Drosophila* is a cost-efficient model as they are cheap, easy to breed, feed and keep. Lab space and organizational effort are relatively little [26].

Because of its small size, tissue dynamics in *Drosophila* can be easily imaged in the living organism using modern techniques like for example spinning disc confocal [246] or lattice light sheet microscopy [45]. See section 2.13 for details on the microscopy methods. Spatial resolution and recording time are of a quality to allow observations for hours with single cell resolution [73, 148, 163, 167]. Even complete 3D recordings for several hours with single cell resolution are possible [178, 309]. This revolution in the imaging technology makes large scale datasets comparably easily available.

The same is true for image segmentation and data visualization. Open source tools like Image-J [292, 293] or Fiji [291], including many community developed packages, provide digital representation of the microscopy data and help with automated data analysis and visualization. The large research community has a direct impact on innovation in the field.

Another aspect are the available tools to manipulate the system *in vivo* and make it possible to perform specific experiments. Biophysical methods are mostly used to mechanically interfere with epithelial tissue by for example laser probing and ablation or simple mechanical probing [150, 167, 298, 306]. In addition, pharmacological tools can be used for example via microinjection [149].

Last but not least, the long history in Drosophila research has led to a wealth of genetic methods. Advantageous here is the comparably compact genome, yet containing roughly 15.000 genes [166]. This includes the possibility to control and manipulate protein function and gene expression[39, 252].

The large amount of publications on morphogenetic processes, like tissue rearrangements, makes morphogenesis research highly accessible and thereby qualifies *Drosophila* an ideal model to study development.

2.3 Morphogen patterning sets the body plan

A key principle in *Drosophila* development is morphogen expression. These are biochemical signaling molecules that establish the body-plan of the fly and determine cell fate in a position dependent manner. Alan Turing predicted a chemical basis for biological patterns already in 1952 [322]. Only decades later could this be demonstrated in a living organism.

The mRNA bicoid is a maternally placed gene at the anterior end of the fly egg. It is translated into *Bcd* protein at the anterior pole, which is free to diffuse in the egg but has a half-time of ∼30 min. The local production, differentiation and half-live establishes a concentration gradient, which leads to position dependent transcription of different proteins. In this way the polarity of the embryo results from a spatially specified chemical signal along the anterior-posterior axis [239].

There is a whole cascade of morphogen patterns following bicoid downstream. For example it activates the transcription of anterior gap genes including hunchback, orthodenticle, and buttonhead, further leading to even-skipped which establishes the embryonal segments [100].

The A-P patterning system also plays a role during tissue rearrangements [255]. It is connected to planar cell polarity during germband elongation, which sets the direction of the tissue extending processes [351]. In general, morphogens transmit information by enhancing or inhibiting the transcription of certain proteins or genes.

In epithelial morphogenesis, the interplay between morphogen mediated genetic information, self-organization and intercellular coordination remains largely unclear to this day.

2.4 Overview of *Drosophila* development

The expression of morphogenes contributes to define the whole life cycle of *Drosophila* from egg/embryo via larval and pupal stage to the adult fly. This cycle takes about 10-12 days (Figure 2.2). Here, I only focus on the development of the embryo starting from a fertilized egg. The other stages are not relevant for this thesis.

The different stages of *Drosophila* embryogenesis are described in detail in [37]. The developmental process begins with the fertilized egg and successive cell division which slows down at midblastula transition. At this stage the whole embryo is uniformly covered on the surface by a mono-layer of cells and the plasma membrane between nuclei are forming. This process is therefore also called cellularization, see Figure 2.3 (stage 1-5).

Afterwards, during a process called gastrulation, mesoderm, ectoderm and endoderm are separating [63, 171]. Ectodermal cells are migrating towards the midline and form the germband, which is a key study system for tissue rearrangements, see Figure 2.3 (stage 8).

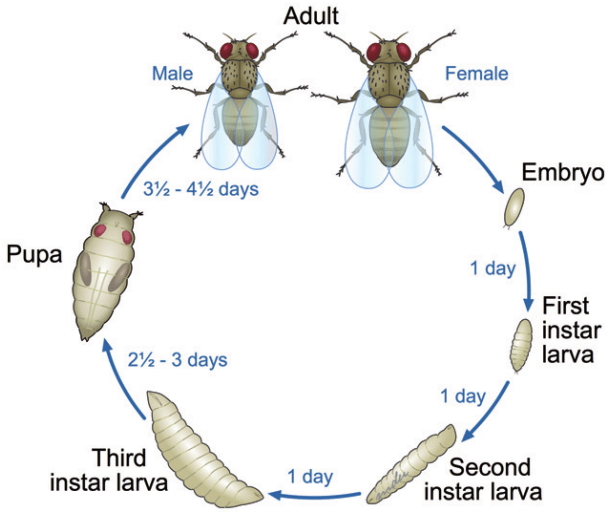

Figure 2.2: Lifecycle of *Drosophila melanogaster*. Scheme taken from [244].

Next, during the germband extension, the tissue is stretching in posterior direction to wrap around the dorsal surface, Figure 2.3 (stage 9) [37]. Interestingly, this process is driven by topological transitions of cells within the tissue, leading to convergent extension in an orchestrated manner. In Chapter 8 we investigate coordination of cells that participate in these topological T1 transitions.

The embryo afterwards begins with segmentation, the germband retracts again and the second important epithelial tissue for this thesis, the amnioserosa (AS), fills the gap [122, 129]. AS cells begin to oscillate followed by dorsal closure, where the AS contracts to close the back of the fly. We will study AS oscillations and their coordination extensively in this thesis for example in Chapters 6 and 7. After dorsal closure embryogenesis continues, Figure 2.3 (stage 12-17).

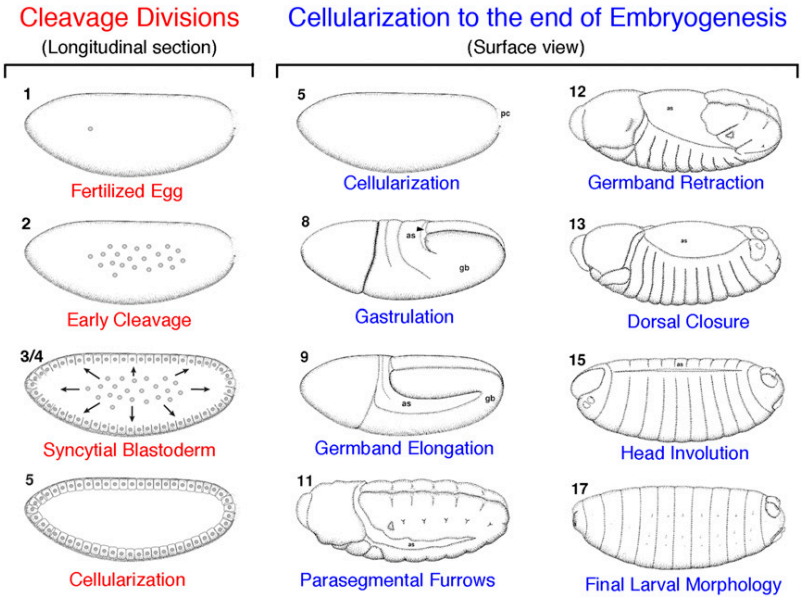

Figure 2.3: Stages of *Drosophila melanogaster* embryogenesis. Investigations in this thesis, focus on stages 9, 12 and 13. Scheme taken from [117].

Epithelial tissue rearrangements which happen during embryogenesis are largely a consequence of regulated and coordinated dynamics of groups of cells. Epithelial cells are mechanically coupled to their neighbors and are able to react to mechanical stimuli by for example contracting, expanding and even proliferation [15, 72, 105]. However, the mechanisms of mechano-sensing, their coupling to other bio-chemical signaling pathways and their function remain for the most part unknown.

It has been shown that tissue rearrangements are driven by local processes [350]. Because these rearrangements happen in a very robust and directed manner local cell dynamics have to be orchestrated. They are therefore well suited model systems to study intercellular coordination. In my project, I considered two prominent morphogenetic processes which are germband extension and dorsal closure. Both involve tissue scale reshaping processes, fulfill important functions during development and are thought to be mainly driven by local processes.

2.5 Germband extension

Germband extension takes roughly two and a half hours and during this period stretches by a factor of 2 around the posterior end of the embryo. It is a prime example of convergent extension, a process happening during development in many organisms, where local neighbor exchanges drive the extension of the tissue. Because of this generality local neighbor exchanges are thought to be one of the main tissue rearranging mechanisms [137].

Germband extension is driven by the autonomous local dynamics of single cell hubs. These local processes are either comprised of a cell that crawls in between two neighbors or are induced by junction shrinkage between two cells and perpendicular junction extension [297]. The second possibility is called T1 transition, which are nontrivial topological transitions where cells change their neighbors either in quadruplets or with rosette formation prior to junction elongation (Figure 2.4) [62]. The collective effect of many of these neighbor exchanges effectively causes the elongation of the whole tissue [172]. In *Drosophila* germband extension the main form of neighbor exchanges are cell quadruplet T1 transitions [297]. Other effects, for example external forces from posterior midgut invagination, can assist in the elongation but are not sufficient [173].

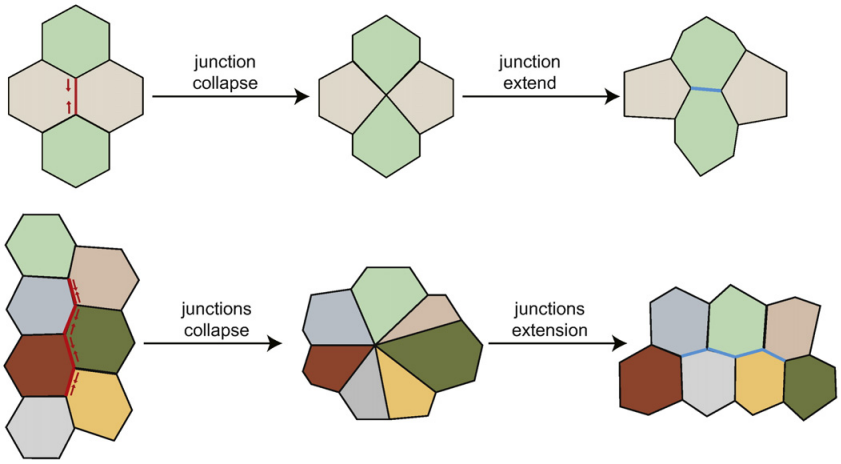

Figure 2.4: Two modes of T1 transitions: Top row depicts junction collapse and subsequent junction extension in a cell quadruplet. The bottom row shows the rosette formation if more than four cells are involved in the transition. Scheme taken from [172].

T1 transitions seem to be a simple concept, but they show surprisingly rich and complex

behavior. For example, the mechanisms that drive junction remodeling during collapse and elongation are highly debated. In Chapter 8 we show that T1 transitions are stochastic processes, which means that large scale ensemble analysis is needed to faithfully describe their dynamics, e.g. in [188].

Oriented cell intercalation is possible on the molecular level because relevant cell compartments are spatially organized in the anterior-posterior and dorsal-ventral directions. This molecular organization is called planar cell polarity (PCP), which is itself connected to the morphogen based AP patterning system [351]. Crucial for this organization are the interactions of the morphogen eve and runt with the Toll receptor family. However, the full pathway that establishes PCP and how PCP interacts in detail with cell intercalation has remained unclear [172].

2.6 Dorsal closure

Another prominent example for morphological reshaping during *Drosophila* development is dorsal closure (DC). DC is the process is the process in which the amnioserosa, a squamous epithelium at the dorsal side of the embryo, closes the back of the fly by contracting and connecting the lateral epidermis on both sides. The process has many similarities to wound healing and is therefore often studied as a model in this context [119, 166]. DC starts 8-12 hours after fertilization and lasts 2.5-3h (at 25°C) [37, 166]. Kiehart divides DC into four phases: "preclosure" beginning with germband retraction, "onset of closure" defined by collective leading edge displacement towards the midline, "bulk of closure" where the canthi drastically shrink and "endgame of closure" where the dorsal hole closes and ingressing AS cells undergo apoptosis [166], depicted in Figure 2.5. There is no consensus for the names of the phases. For example in [147] they are called "initiation", "epithelial sweeping", "zippering" and "termination" phases.

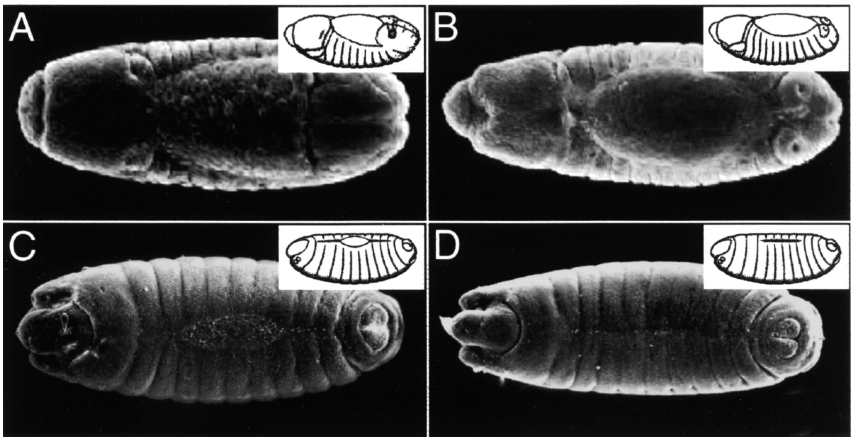

Figure 2.5: Dorsal closure can be divided into 4 phases. A) preclosure. B) onset of closure. C) bulk of closure. D) endgame of closure. There is no consensus in the literature about exact timing and naming of the phases. Scheme taken from [147] who adapted it from [121].

In this thesis we are interested in the phase that is leading up to the onset of dorsal closure and happens directly after germband retraction, which is what we call ellipsoidal AS phase because of its tissue geometry. Since the function of AS cell dynamics is closely related to dorsal closure we will take a closer look into it in the following.

Preclosure onset is not clearly defined but begins during germband retraction. Amnioserosa cells, which have been specified during the cellularization stage of embryogenesis, fill the gap

left behind by the germband [122]. The tissue takes an ellipsoidal shape, cells become morphologically isotropic and begin with oscillations [182].

The formation of the canthi is marking the onset of dorsal closure. The dorsal-most epidermal cells surrounding the amnioserosa, the so called leading edge, is displaced towards the midline. At the same time the purse string, an actin cable forming in the cells at the leading edge, is maturing [123, 142, 167]. While the whole amnioserosa takes an eye shape, it is not completely symmetric. The anterior canthi is shaped by the edges that run to a point while the posterior end is noticeably more rounded [166].

The most important process during the bulk of the closure is zipping, where the edges from the lateral epidermis are pulled together at the canthi, therefore shrinking the amnioserosa with roughly constant speed [107, 254, 255]. The zipping is probably not driven, as one could expect, by contractions of the purse string or the lateral epidermis. Forces provided from actomyosin dynamics in the AS bulk cells contribute to dorsal closure [70, 195, 252, 305]. These cells are continuously oscillating during the bulk of closure, even when undergoing apoptosis [150, 306]. A complex orchestra of forces and signals ensures that single cell dynamics collectively drive closure [105].

In the endgame of closure the zipping completes the joining of both sides from the lateral epidermis [142]. Remaining AS cells ingress and undergo apoptosis. Other residual components, for example remnants of the purse strings, disappear as well. Afterwards, a seamless dorsal epithelium is left and embryogenesis continues [166].

Success of dorsal closure and germband extension, and with it further development of the embryo, depends on active stresses generated by the involved cells. In the following section I will explain in more detail how forces can be generated and regulated in the tissue.

2.7 How epithelial cells generate forces: apical contractions

We have already established that local cell behavior can drive embryogenetic events (see section 2.4). To this end, cells have to be able to generate forces and react to the movements of their neighbors. Apical contractility is an important mechanism how cells establish these forces [185].

Apical contractility means that most of the molecular processes that generate forces happen at the upper part of the three dimensional cell, the side which forms the surface of the tissue [31, 61, 155, 199, 200, 213, 286]. This fact is one of the main justifications in mathematical modeling for describing epithelial tissues as 2-dimensional cell sheets despite their 3 dimensional geometry. The basal part of the cell often is only dragged along by the dynamics of the surface part.

The most important subcellular force generation mechanism is actomyosin contractility [314]. Non-muscle myosin II motors thereby form complexes with F-actin fibers building a network across the cell. The actual forces are created due to ATP hydrolysis, which provides free energy for conformational changes of the myosin II motors. These are equipped with several head domains that can be attached onto the F-actin fibers (see Figure 2.6). Conformational changes, caused by the phosphorylation of the regulatory light chain, result in myosin II motors walking along the actin [327]. If a myosin motor is thereby connected to two actin fibers on both ends at the same time, walking results in a force that pulls separate actin fibers together. The actomyosin network is connected to the junction, as we will explain later in more detail, which results in the whole cell contraction if enough myosin is collectively activated [213].

On the tissue level, spatially organized force generation drives morphogenetic events. For example tissue folding is associated with apical accumulation of myosin II, depending on the distance to the ventral midline and resulting in a tissue scale myosin II gradient [127, 185].

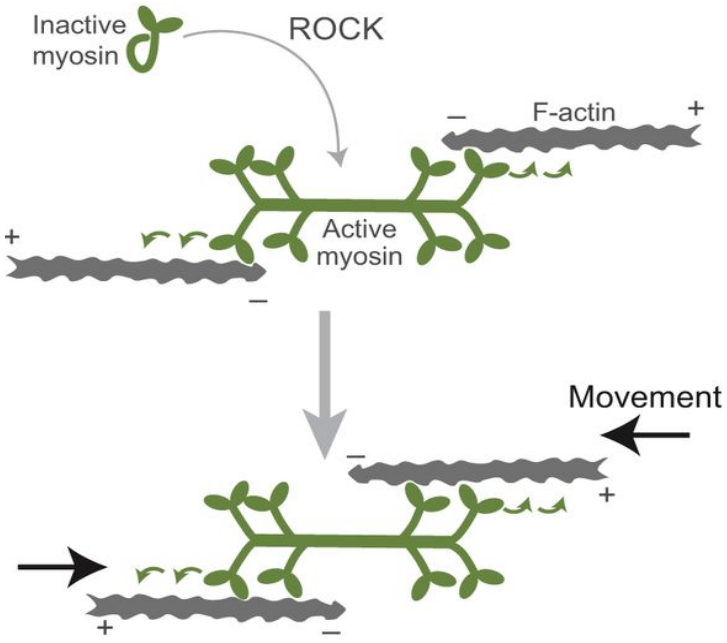

Figure 2.6: Actomyosin provides contractile forces during morphogenesis. Activated myosin II minifilaments associate on F-actin and can walk along it by conformational changes. Energy is provided by ATP. Myosin connected to two F-actin effectively pulls them closer due to the walking. Scheme adapted from [127]

The orchestration of many-cell force generation towards directed rearrangements remain poorly understood. To make it possible for single cells to effectively participate in global processes, their properties and dynamics have to be precisely altered and timed. For example, changes in cell-cell adhesion, regulation of tension along junctions or polarized contractions along certain junctions may play a role [61, 155, 213]. During germband extension, planar cell polarity results in an enrichment of actomyosin along vertical junctions, which leads to tissue-wide elongation perpendicular to this direction [86, 92, 155, 167, 236]. It is hypothesized that the enrichment along these junction only serves as stabilization while medial myosin pulses towards these junctions are the actual driving forces [274].

The main regulator for non-muscle myosin II is the Rho-Rok pathway which can activate myosin to allow it to bind to actin filaments [161, 230]. As shown in Figure 2.7, in this pathway extracellular ligands, like Fog, bind to G-protein coupled receptors whose intracellular sub-units can then bind to DRhoGEF2, a GTP exchange factor which is located at the proximity to the plasma membrane and has previously been shown to be a regulator of apical constriction [15, 18, 114]. DRhoGEF2 in turn activates Rho1, which acts on actin filaments in two major ways, among others. First, it enhances actin polymerization using the cytoskeletal regulator diaphanous (dia) and the actin binding protein Chic [2, 227]. Second, Rho activates the Rho-associated protein kinase Rok which phosphorylates the regulatory light chain of non-muscle myosin. This causes a conformational change in myosin which facilitates binding to F-actin [127, 326]. The phosphorylation of myosin and thereby myosin activity need to be precisely coordinated in several neighboring cells to allow movement on the tissue level [29, 89].

Epithelial processes in which cells generate local forces and contribute to global deformations are therefore excellent candidates to investigate their coordination, sensing and force transmission.

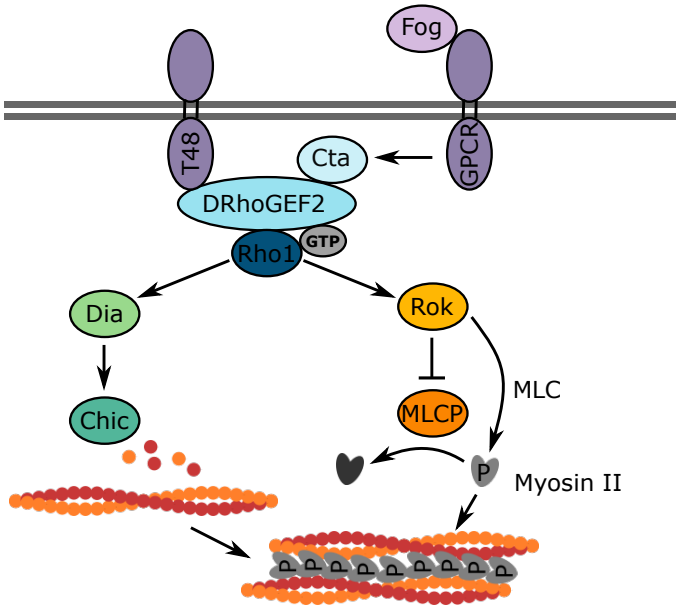

Figure 2.7: Regulation of non-muscle myosin II by the Rho-Rok pathway. The left pathway shows the regulation of actin polymerization via Dia and Chic. Scheme adapted from [227].

2.8 The ellipsoidal amnioserosa and its function

The amnioserosa is a squamous epithelium that plays a key role during dorsal closure. It develops from the ∼200 dorsal-most cells during the cellularization phase of *Drosophila* embryogenesis [122]. Its formation depends on the gradient expression of Decapentaplegic (dpp) and zerknüllt (zen) [97, 251]. During DC it comprises roughly 180 cells and has an ellipsoidal shape [182]. It fills the hole left from germband retraction at the dorsal side of the embryo. Because of its involvement in force generation during dorsal closure it is an often studied model system. After the germband retraction cells assume an isotropic shape and begin with apical area oscillations [306]. Studies show that at this stage, tension is isotropically distributed across the tissue [194].

There are 5 different cell types that are involved in dorsal closure and therefore also play a role for the dynamics of the whole amnioserosa [166]: 1) The yolk that separates the amnioserosa from the underlying embryo when the germband retracts but also forms adhesion sites via integrins. 2) The AS is completely surrounded by the lateral epidermis, which exerts external tension. 3) Dorsal-most epidermal (DME) cells which together with 4) peripheral-most amnioserosa (PAS) cells form the leading edge of the amnioserosa. 5) Last, there are the bulk AS cells which comprise the largest part of the amnioserosa.

These cell types are involved in the generation of contraction forces that drive dorsal closure. Biomechanical processes that contribute to dorsal closure are the oscillations of AS bulk cells [306], ingression of AS bulk cells [305], tension generated from the actomyosin purse string at the AS leading edge [142], zipping at the canthi [255] and contractile as well as elastic forces from the lateral epidermis [167] as summarized in Figure 2.8. Efficient closure requires coordination of these different processes, but also internal orchestration for example of the single AS cell oscillations [30, 105, 129]. From a physical point of view a smooth contraction can only happen if local processes are coordinated to yield a non-zero net force on outer DME cells in direction to the midline.

Although the different contributions are not negligible and partly redundant [166], there is a

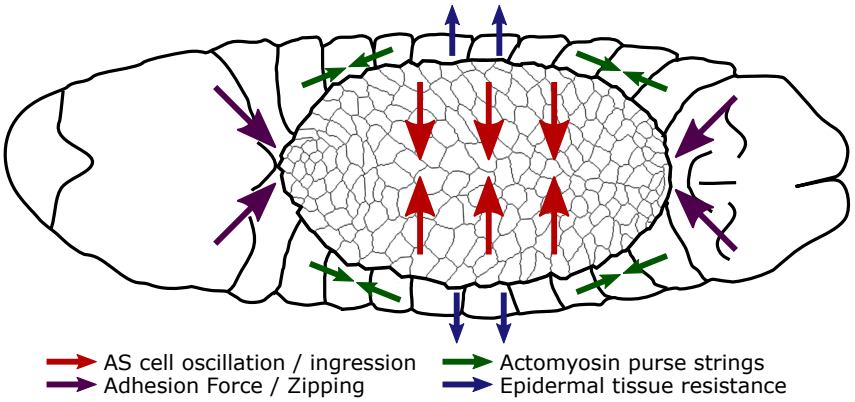

Figure 2.8: Major force contributions during dorsal closure. Several redundant forces are contracting the amnioserosa during DC and close the dorsal side of the embryo. In case of failure of a force contribution, other forces can be upregulated. Scheme adapted from [110].

large consensus that apical constrictions and ingression of bulk AS cell comprise the main driver for dorsal closure [31, 69, 70, 92, 142, 167, 252, 305, 306].

Mechanical properties of the tissue are governed by the actomysoin dynamics [89]. Laser ablation experiments demonstrate that during closure a stiffening of the epithelium is occurring, as shown by a decrease in recoil power law exponents [198]. Both junctional and medio-apical actomyosin are contributing to the stiffening while the medial tension is roughly double the junctional tension [200]. Forces are transmitted among cells via adhesion complexes at the cell-cell junction, which are also crucial for the zipping process [107]. Details on the function of adherens junctions are reviewed in section 2.10. Force transmission via adherens junctions regulates apical contractions in the AS bulk cells by stabilizing actomyosin and E-Cadherin at the junction and has an impact on area oscillations, closure rate and purse string formation [155].

Cell ingression is essential for dorsal closure as well. Inhibiting the ingression process leads to failure of closure [228, 305, 321]. In this thesis, however, since we only focus on the ellipsoidal amnioserosa until dorsal closure onset, ingression does not play a role for us.

I already mentioned that different force contributions are redundant for successful dorsal closure. This is demonstrated by interfering *in vivo* by perturbing the biomechanical process which still results in completed closure [167, 280, 339]. Closure even completes despite crucial genetic perturbations for example by the removal of myosin at the purse string [252] or blocking the myosin activation of AS cell oscillations [72]. The collective dynamics of many directed mechanisms and their interplay therefore dramatically increases the robustness and resilience of this important morphogenetic process.

While practically all of these processes can be inhibited without disrupting closure, some combinations are required. The components of the epithelia have to sense that other components are not functioning and upregulate their own force to counterbalance the missing contribution. How this coordination is working is not understood. So far there was only speculation that mechanosensitive membrane proteins might be involved [141, 155]. In Chapters 7 and 8 we uncover some of the molecular mechanisms involved in mechano-sensing in epithelial tissues.

2.9 Amnioserosa cell surface oscillations

Bulk cells in the amnioserosa begin to oscillate shortly after germband retraction. In the last section, we have emphasized the importance of those oscillations for force generation in the amnioserosa that drive dorsal closure. How do these oscillations originate? Let us take a look.

Actomyosin driven oscillations seem to be a fundamental property because the phenomena can be observed in many systems. Examples from other *Drosophila* tissue rearrangements are from invagination, sealing, or remodeling of organ shape [28, 105]. They are more prominent in the AS because the bulk cells are very flat. In other models this behavior appears during convergent extension in vertebrates [304] or during compaction in the early mouse embryo [205].

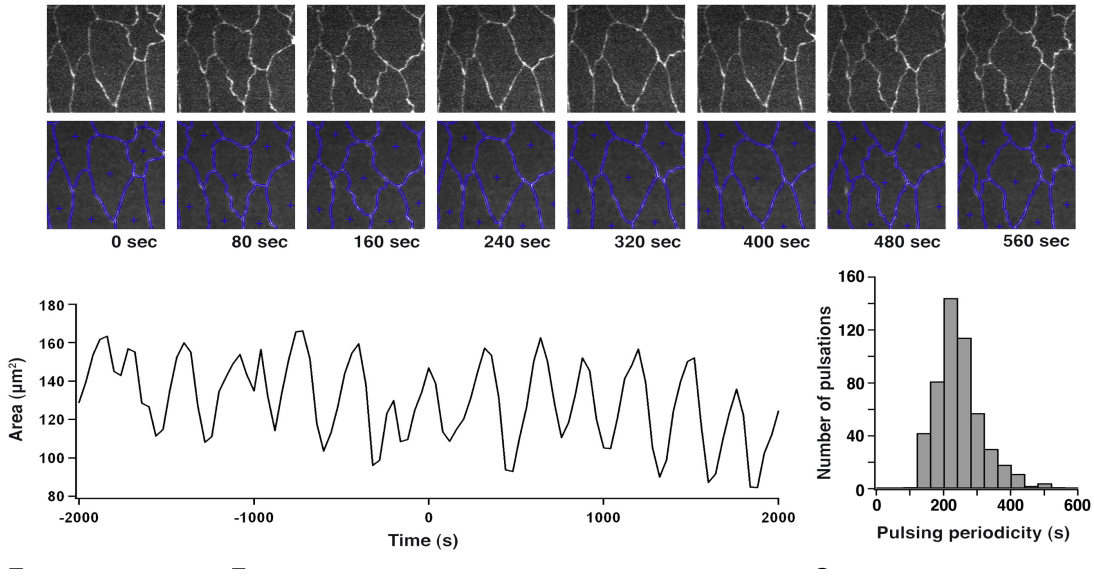

Figure 2.9: Amnioserosa cells exhibit surface area oscillations. (top) live cell imaging of surface area pulsations of an amnioserosa cell expressing GFP with segmented image below. (bottom left) Measurement of cell surface area over time. (bottom right) Period distribution of measured oscillations. Scheme adapted from [306].

As shown in Figure 2.9 amnioserosa cell surface areas continuously oscillate with a period of $230 \pm 76s$ [306]. Their origin probably are cycles of assembly and disassembly of actomyosin networks. To this end cycles of phosphorylation and dephosphorylation are necessary [72, 89]. Therefore, myosin II motors localize at junctions, forming a cortical ring around the cell, and in apico-medial regions.

It is not clear yet whether these oscillations are autonomous or arise due to interactions with their neighbors. While some research points toward a non-autonomous mechanism [306] other studies have pointed out the strong anti-correlation of internal actomyosin levels and cell area, suggesting that contractions are autonomously driven [106]. For the expansion phase, if an oscillating cell is separated from its neighbors by laser microsurgery it continues to oscillate despite the contact loss [150]. The mechanism we uncover in Chapter 7 suggests that it may be a combination of an autonomous internal process that is coupled to neighboring cells.

Several models about the origin of actomyosin oscillations have been suggested and there is no consensus yet. Mathematical models have shown that in principle there is no need of a biochemical upstream regulator. The oscillations arise "self-organized" from mechano-chemical feedback alone. In more detail, myosin contraction working against elasticity of the actin network, leads to more recruitment of myosin to the network. This is counterbalanced by load-dependent de-

tachment of myosin. Cycles of myosin association and dissociation then lead to oscillations [64]. Underlying chemical oscillations alone are operating on timescales that are too fast to regulate myosin dynamics [177].

There are also models that involve regulation pathways, that can have a connection to mechanics. For amnioserosa cell oscillations a model has been proposed that links an upstream signaling molecule, which degrades depending on myosin, and load dependent dissociation [333]. In follicular epithelial cells it has been proposed that external tension may lead to the activation of Rho GTPase, which via Rho-associated kinase activates myosin, leading to contractions that oppose the external tension. This can lead to oscillations in the biochemical network because of a delay between chemical and mechanical response [174].

All of these models, with and without regulation pathways, have yet to be validated experimentally [105].

Oscillations react to the dynamics of their neighbors. Their coupling has been shown to be distinctly either in-phase or anti-phase [306]. Direct interference, for example by UV laser wounding, shows that oscillations around the wounded cell arrest and the tissue increases in stiffness to support the tissue [150]. Geometrical constraints also play a role because in the amnioserosa the overall area is roughly preserved during this phase. A contracting cell therefore has to be balanced by an expansion occurring somewhere in the tissue, promoting anti-phase coupling between neighbors. Studies have also observed that simultaneous contractions of neighbors are boosting the contraction efficiency of single cells [346]. Therefore promoting simultaneous contractions can be advantageous for many epithelial processes. In summary, these indications of coordinated neighbor dynamics imply some form of mechano-transduction at the cell-cell interface.

2.10 Adherens junctions - signal transmitters during morphogenesis

Any kind of dynamical regulation requires some form of feedback. A mechanism that reads out information and acts in dependence of the output. The most essential part of any coordination mechanism is therefore the ability to sense and process stimuli in the first place.

Epithelial cells are connected to their neighbors via transmembrane proteins in so-called adherens junctions. Their most obvious function is the mediation of cell-cell adhesion which gives an epithelium its structure [234]. Otherwise cells would be independently floating through the tissue. However, mechanical signals can also be transmitted via protein complexes that connect to the actin cytoskeleton of individual cells. An important example is E-Cadherin which provide a mechanical link between cell neighbors [33, 204]. A third function is stability provided by resisting mechanical pull and thus regulating tension at the junction. This is especially important during junction remodeling processes [258].

Mechanical stimuli can even be translated into biochemical signals which is called mechanotransduction [43, 247]. Prominent molecular components of mechanotransduction mechanisms are mechanosensitive ion channels, integrins, cadherins, actomyosin networks, vinculin, catenins and many more. We only begin to understand the variety of modes of signal transduction that cells are using and their importance for epithelial morphogenesis [112]. Other forms of cellular sensing involve direct exchange of chemical signals through ligands or electrical stimuli as used most prominently by neurons [266] but in this thesis I will focus on the role of mechanotransduction for tissue organization.

E-Cadherin binds to the actomyosin network of the cells via adaptor proteins such as α-catenin, β-catenin or vinculin, which together form adhesion complexes [40]. Mechanical stimuli are received at and transmitted via these complexes. As shown in Figure 2.10, β-catenin binds

to the intracellular domain of E-Cadherin and α-catenin dynamically binds to β-catenin to serve as link to the actomyosin network. α-catenin then undergoes force dependent conformational changes, which promotes the recruitment of vinculin, which in turn binds to F-actin. However, α-catenin can also bind to F-actin directly. This suggests that α-catenin has an important function for force transmission by regulating actin dynamics. Forces transmitted to F-actin promote the recruitment of myosin II minifilaments and forces have also been shown to directly affect actin polymerization [43, 185].

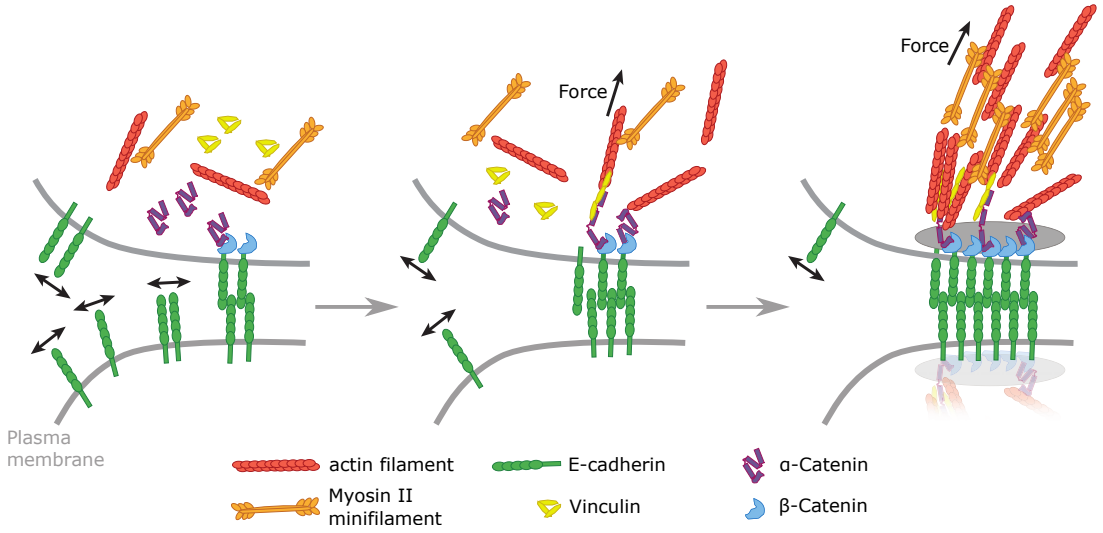

Figure 2.10: E-Cadherin dependent adherens junction formation. Scheme depicts different components important for mechanical signal transmission. E-Cadherin connects the cytoskeleton of neighboring cells. Adapted from [185].

Another possible mechanism for signal transduction capability is the clustering of E-Cadherin in adherens junctions, which is dependent on N-glycolization. This is partly encoded by the glucosyltransferase Xiantuan (*xit*), whereas embryos that are depleted of *xit* show no change in frequency of E-Cadherin but strongly affected spatial distribution, which is more uniform [355]. Those *xit* mutants experience impaired germband elongation, which is driven by local neighbor transitions that probably require cell-to-cell force transmission for coordination. In Chapter 8 we further investigate this hypothesis.

Promising candidates for the conversion of mechanical stimuli into bio-chemical signals are mechanosensitive ion channels [128, 141, 187]. Caused by tension, ion channels undergo conformational changes which leads to opening of the channel allowing for example influx of extracellular Ca^{2+} into the cell. Ca^{2+} can then serve as upstream regulator of actomyosin dynamics [212, 315]. To this end ion channels have to interact with the plasma membrane to receive mechanical signals from actomyosin networks which are linked to the plasma membrane. The ion channel could thereby directly react to tension tangent to the plasma membrane or alternatively respond to conformational changes in secondary proteins (tethers) that relay received tension [51, 353].

Mechanotransduction provides an important link between mechanical dynamics and biochemical signaling pathways. It is therefore a promising candidate for a "grand unification theory" of chemical signaling, for example due to morphogens, and dynamical organization guided by physical principles. This connection between chemical regulation and force-driven self-organized embryogenesis is considered one of the most pressing frontiers in developmental biology [60]. This work directly contributes to this question by studying the role of mechanosensitive ion channels (Chapter 7) and E-Cadherin (Chapter 8) for coordination.

2.11 Mechanosensitive ion channels

Ion channels are known to influence actomyosin dynamics through gating and subsequent Ca^{2+} influx [12, 55, 65]. An example is TRP ion channel activity in *Drosophila* photoreceptor cells, where they dynamically reshape the actin cytoskeleton [175]. Mechanosensitive ion channels play a role in sensory neuroscience, for example in the auditory system. Their task is mainly to translate mechanical stimuli into electrical signals [58, 74, 128, 156, 191].

In this thesis, we are investigating the hypothesis that ion channels also play a role in tissue dynamics. They are hypothesized to be mechano-transducers that mediate intercellular coordination in epithelial tissues [141, 173, 212]. So far, nobody has provided a detailed study on their role during epithelial morphogenesis.

There are several candidates for ion channels that might be involved in cell-cell coordination during development. Three channels that deserve a closer look because of their function in different organisms and processes are *Tmc* , *nompC* and *Piezo* .

Tmc (transmembrane channel-like) is an evolutionary conserved ion channel that has so far mostly been studied in auditory sensing in cochlea hair cells [162, 168, 179, 180]. *Tmc* interacts with the extracellular tip links that are thought to mediate mechanical tension, see also Figure 2.11 [24, 181, 202]. In 2020 it has been reported that TMC1 and TMC2 indeed are pore-forming subunits of mechanosensitive ion channels [151]. It is clear, however, that TMC1 and TMC2 are necessary for the mechanosensory currents in hair cells [249, 250]. *Tmc* is present in many organisms, for example *xenopus*, *C.elegans*, *Drosophila* or *Danio rerio* [82, 113, 317]. In *Drosophila* there is only one *Tmc* gene found (CG46121). *Tmc* is expressed in *Drosophila* sensory system and *Tmc* mutant larvae show locomotion defects [113, 279], indicating their mechanosensory role.

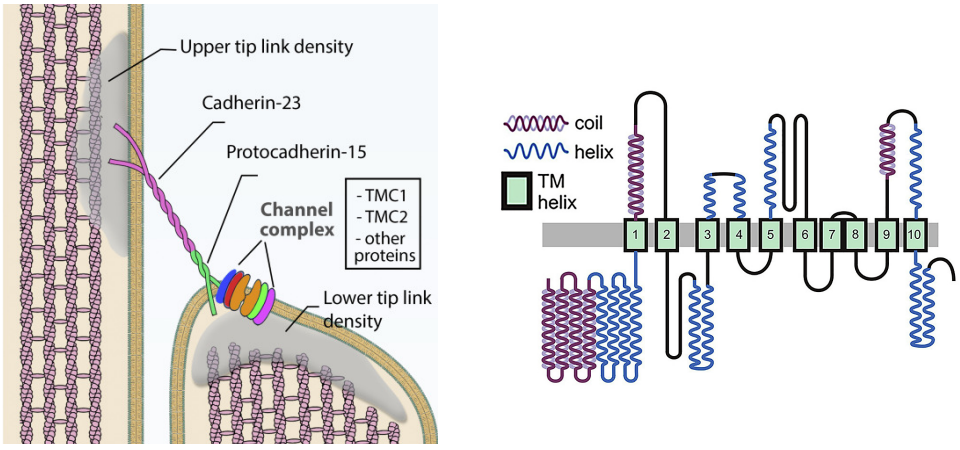

Figure 2.11: *Tmc* at inner hair cells. (left) Schematic of inner hair cell stereocilia showing possible localization of TMC1 and 2. (right) Predicted transmembrane structure of *Tmc* . Adapted from [181] and [249].

We already mentioned TRP ion channels as an example for interaction with the actin cytoskeleton. *nompC* (no mechanoreceptor potential c) belongs to this class of channels and is activated by the tether mechanism. *nompC* has been shown to be essential for mechanosensory transduction [332] *Drosophila nompC* mutants show several impairments, most noticeably in hearing and locomotion but also touch sensation [50, 104, 156, 348].

As the last example there is *Piezo* , which is activated directly by plasmamembrane tension [190]. *Piezo* is widely expressed among many organisms and cell types that have a mechanosens-

ing function. For example, *Piezo* knock out mice experience loss in touch sensation and it is associated with deficiencies in vascular remodeling [203, 271, 278]. It has also been shown that *Piezo* is involved in epithelial sheet homeostasis [79]. One of the greatest advantages of *Piezo* is that it has been well studied. Its structure has been resolved using cryo-electron microscopy and it is considered evolutionary conserved [98, 289]. In *Drosophila*, two *Piezo* genes are present. It is involved in midgut homeostasis in adult flies, which can be rescued via Ca^{2+} level manipulation, suggesting a role in Ca^{2+} signaling [125].

In Chapter 7 the role of *Tmc* as signal transducer during morphogenesis is closely examined. Studies regarding *nompC* are in preparation and currently in a preliminary state, but are not included in this thesis.

2.12 Calcium signaling during development

Ca^{2+} is an important signaling molecule, that also plays a role in many morphogenetic processes. The main focus in this thesis is on the function of Ca^{2+} as upstream activator of non-muscle myosin II. However, it is not clear yet how Ca^{2+} can regulate actomyosin dynamics apart from muscle cells. In mechano-transduction processes mechanical stimuli open mechano-gated ion channels, which leads to Ca^{2+} influx [65, 187, 247].

The presence of Ca^{2+} is necessary for many processes in morphogenesis. For example for neural tube formation in *Xenopus* or for epithelial cell contractility [187]. Most importantly for this thesis, it has been shown that Ca^{2+} is essential for efficient dorsal closure in the amnioserosa in *Drosophila* [141]. In detail, Hunter *et al.* [141] have shown that optochemical Ca^{2+} release induces contractility in amnioserosa cells, the chelation of Ca^{2+} slows closure and blocking ion channels impairs force generation and regulation. Ca^{2+} triggers cell contraction in other epithelial, like the germband, as well [173]. Another example is from *Drosophila* oogenesis where Ca^{2+} controls myosin II dependent contractions in egg chamber elongation. [126]

However, the detailed activation pathway is only known in muscle cells. Here, Ca^{2+} activates a myosin light chain kinase (MLCK) which activate the regulatory light chain of myosin II motors [224, 313]. A direct activation of myosin II also seems possible [20, 32].

An interesting process where Ca^{2+} dynamics plays an essential role is epithelial wounding. There are some similarities between epithelial wounding and dorsal closure, for example both form a purse string around the wound (the amnioserosa) and they both require the coordination of local forces from cells in the participating tissue [119, 166]. The wounding process is associated with drastic rise in cytosolic Ca^{2+} concentration in the wounded cell, but also in neighbors [9, 296]. It is hypothesized that the sudden change in epithelial tension after the wounding leads to mechanical activation of gated ion channels to signal the wound to neighboring cells and initiate wound closure [344].

In summary, many studies suggest a role for Ca^{2+} dynamics in the regulation of epithelial forces, especially during morphogenesis. However, details regarding the connection of Ca^{2+} dynamics, mechanosensitive ion channels and its impact on actomyosin network dynamics remain elusive to this day.

2.13 Live cell imaging in Drosophila

An important tool to help us understand these processes in more detail is the continuous improvement of imaging techniques and data analysis methods. Compared to the early days where biologists could only study dynamics of a few cells under very controlled conditions, nowadays

3 dimensional whole embryo *in vivo* recordings are possible.

To observe the dynamics of tissues one has to make cellular compartments, for example the cell walls, visible. Continuous development and improvement of different tools have made it possible to attach fluorescent labels to proteins, molecules as well as DNA or RNA and thereby mark specific cell components [192, 308, 335]. When these tags are excited by the corresponding laser light, they emit light which can be observed in a microscope and recorded with a camera.

A prime example is GFP (green fluorescent protein) which can for example be used to tag E-Cadherin in cell junctions and thus make cell outlines visible under the microscope [144]. Other examples include GFP-moesin used to image the cytoskeleton [73] and live cell imaging of GFP-tagged actin during *drosophila* development [148].

However, GFP has the important disadvantage that its fluorescence bleaches over time, which means that the intensity of the emitted light decreases with excitation duration. Therefore, early time-lapse recordings suffered from a low signal duration. Another problem is that the excitation light also excites fluorophores next to, below or above regions of interest. This approach, which is called widefield microscopy, therefore records a lot of background noise which compromises the quality of the actual signal of interest [6, 71].

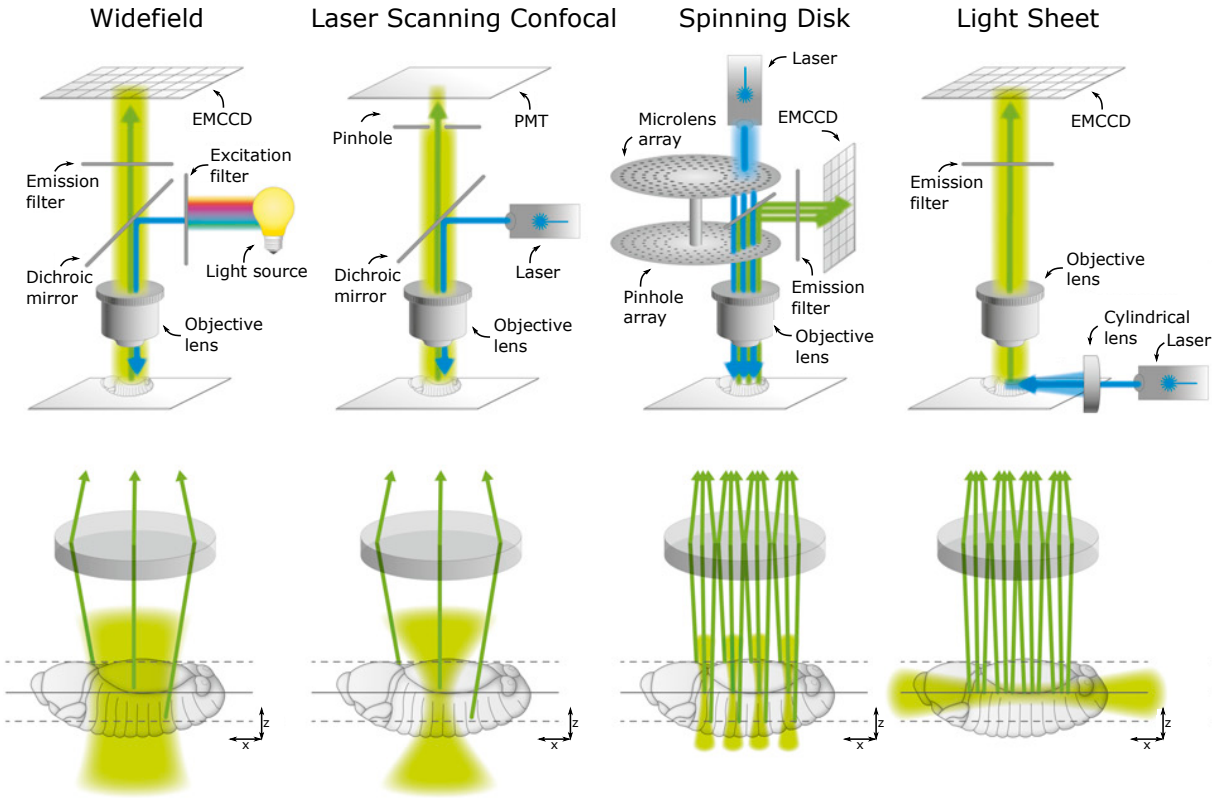

Figure 2.12: Overview of different fluorescence microscopy techniques depicting the light exposure on a *Drosophila* embryo. From left to right the principles of widefield microscopy, confocal laser scanning microscopy, spinning disk microscopy and light sheet microscopy are shown. Adapted from [71].

Innovation in the microscopy technology mitigated these problems over time [310]. Some of the most important techniques are summarized in Figure 2.12. Instead of wide field illumination, confocal microscopes only excite fluorophores in a certain spot in the focal plain. This is done by using a pinhole to block light that would otherwise illumine out of focus regions.

So-called confocal laser scanning microscopes (LSM) scan the specimen and respectively excite only the fluorophores in the current raster position. Photo-bleaching and background noise are both mitigated, increasing spatial resolution and recording length, however especially bleaching over longer time periods is still a problem [6, 248].

The microscopy technique that was also used in this thesis to record time-lapse movies is called confocal spinning disc microscopy [108]. The most relevant improvement compared to LSM is that the illumination intensity can be significantly reduced and thus control photo-bleaching enough to yield long time-lapse movies with sufficient signal to noise ratio [71, 310].

The single pinhole of the LSM is replaced by a spinning disc with several pinholes (depending on the design roughly a thousand) [108]. This makes it possible to illuminate several positions at the same time, but still preserve the high spatial resolution. Because of this, the scanning time is drastically shortened, which makes higher frame rates possible. Due to the shorter scanning time, single spots can be illuminated longer with reduced intensity which overall reduces photo-bleaching effects.

As the previous examples demonstrated, the general theme to yield high resolution and control photo-bleaching is to specifically illuminate the regions of interest with high precision. Another technique following this principle is using light sheets that narrowly illuminate only the focus plane [139, 140, 301, 329]. Hereby the optical recording axis is normal to the light sheet plane.

Since the emitted photons can only originate from the focus plane there is no need for additional technical solutions for high precision plane focusing like the pinhole techniques from confocal or spinning disc microscopes [71, 310]. Advantages are that the whole plane can be recorded simultaneously and the resulting high temporal resolution can be used to illuminate several planes of the specimen to generate 3D recordings [139, 140, 163]. Recording with two combined perpendicular planes yields equal spatial resolution in all directions for 3D specimen. This method is called selective plane imaging microscopy (SPIM) [139], an example of images obtained by this method is shown in Figure 2.13.

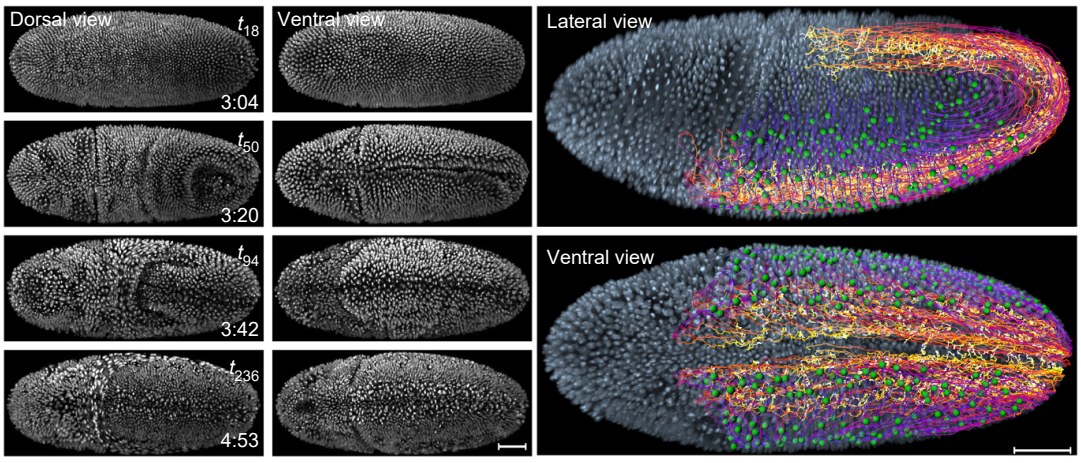

Figure 2.13: Selective plane imaging microscopy (SPIM) allows for recording of developing *Drosophila* embryos with single cell resolution. (left) Maximum-intensity projections of dorsal and ventral view taken from time-lapse recordings. (right) Imaris rendition of time point t50 to visualize cell-lineage reconstruction. Green represents position of progenitor cells and the lines track the migration of the cells between 2.9h (purple) - 5.4h (yellow) after egg laying. Adapted from [8].

Further improving on this technique is lattice light sheet microscopy which even allows super resolution in 3D for a whole *Drosophila* embryo with high temporal solution and long recording times [45]. This is possible by using interference of many single bessel-beams on a lattice to yield a highly controllable light sheet.

This setup offers extensive advantages for developmental biologists because for the first time it is possible to observe long term development of an embryo in 3D with single cell resolution and high frame rate. Currently, data acquisition is the bottleneck for researchers because the resulting large datasets need automated segmentation and analysis tools. Manual analysis is unfeasible for these big data sets.

Large scale data investigation is one of the drivers of this thesis. Studying ensembles instead of examples allows to infer complex stochastic models [188] and generally to apply techniques from statistical physics and stochastic dynamics that need a high amount of data.

2.14 Segmentation: data acquisition from microscopy recordings

Imaging technology also includes the advances in data acquisition, meaning the generation of analyzable quantitative data from the raw microscopy images. The process of separating an image into meaningful regions is called segmentation [152]. A simple example from epithelial tissues is the segmentation into background and cell outlines. The technology in this field received a substantial boost first through the digital revolution, accelerating data acquisition through rule-based algorithms and making handling of larger data sets feasible. Recently, another revolution happened through the advances in machine learning (ML) [302]. This thesis contributes to this development by applying so-called generative adversarial networks to the segmentation task, meaning that cell junctions are recognized by the artificial intelligence and separated from the background that does not contain meaningful information. More on that can be found in Chapter 4.

Early methods are largely rule based and for instance use filters for edge detection. An example for this is the canny algorithm [38]. Arguably one of the most simple methods is thresholding, where all pixels in the image that exceed a certain grayscale value are set to 1 and all below the threshold to 0. This separates the background from the features of interest, but require microscopy images with very high signal to noise ratio and only including objects that should be segmented [152]. Several methods can also be combined, for example a typical prefiltering step is to set low and highpass filters to remove noise and large-scale structures not belonging to the features of interest. Although new methods from the machine learning field are generally outperforming rule-based methods, it can still help to pre-process images using these methods, going for a combined approach. Rule-based methods are also still being developed, for example [241] used a phase-congruency tensor to detect curvilinear structures in microscopy images.

One of the most widely used rule-based segmentation tools is the watershed algorithm [338]. It is a core component of one of the most popular segmentation tools for epithelial cells, called Tissue Analyzer [3]. The basic idea comes from geology, where watershed means the separation between water basins. Inspired by this, the watershed algorithm virtually puts water into the minima of the image topography set by grayscale values for example. Then the water level is being raised. At those points where the water level is meeting water from a different basin, the boundary is set. This procedure works very well for the segmentation of cells and has been one of the dominant methods.

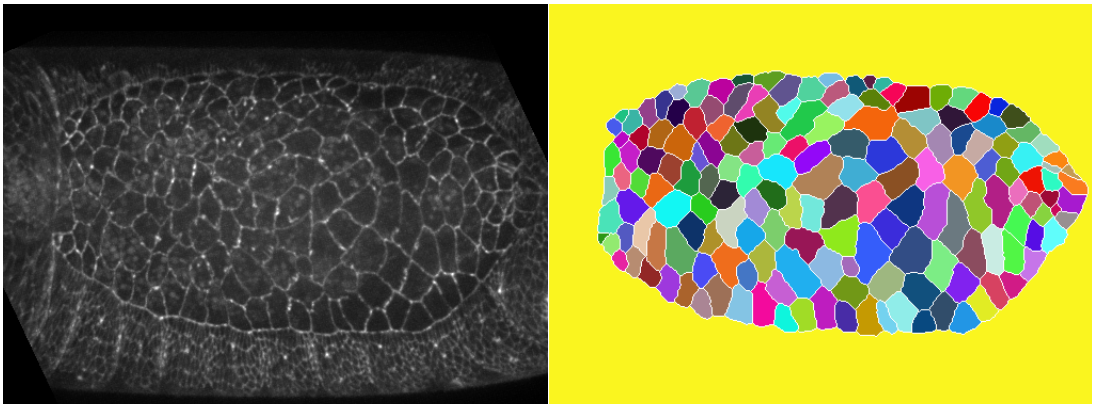

Figure 2.14: Example of an amnioserosa recording with corresponding segmented cells. The color of the cells is uniquely labeling them. The data shown here is analyzed in chapter 6.

Machine learning tools have entered by using them as pixel by pixel classifiers. The neural network is trained to output a probability for a pixel to belong into predetermined classes and the pixel in the image is labeled accordingly. A prominent example is the U-Net classifier [281]. Since then, numerous network architectures for segmentation have been proposed [5, 34, 53, 85, 132, 221, 309, 312]. This includes tools that specifically specialize on the segmentation of cells and tissues [5, 312].

It is important to note that rule-based methods are usually more computationally taxing than machine learning, because the prediction process of neural networks is very fast (usually a single matrix operation) [284]. Only the training procedure takes a lot of time. This is another advantage of ML architectures. Disadvantages are the time consuming training, which often requires powerful graphics cards that are usually not available on every computer. In addition, until very recently they require expert knowledge in computer science [196, 324]. Only now, developers started to provide software with graphical user interfaces (GUI) to make them more accessible to researchers without training in coding.

The most widely used open source platform for biomedical image analysis probably is ImageJ [292, 293], and its derivative Fiji [291], which is exactly the same platform but is shipped with more scientific packages that are typically needed. It includes a lot of community developed tools and provides high usability because of its GUI. Another often utilized open tool is Ilastik [307]. There are also several proprietary software solutions that include both rule-based and machine learning tools. An example for this is IMARIS (Bitplane). The community has declared their intent to strive toward open source solutions to make them widely available [5, 34, 41, 196].

To provide some intuitive understanding of these advances it is instructional to look at the time researchers need to spend on the acquisition of data from the raw microscopy images. 20 years ago a researchers needed years to record, segment and analyze tissue dynamics which was often restricted to certain regions in the tissue. Later it was possible to analyze data from several embryos in the same time [231, 316]. Now, the complete amnioserosa can be segmented and analyzed in dozens of embryos in a matter of a month, which includes manual correction for the few segmentation errors of the AI. At the moment researchers are working on full 3-dimensional segmentation of all cells in the complete embryo [34]. The data is recorded via lattice light sheet microscopy and then analyzed by machine learning algorithms. This will open a new era in developmental biology having access to the complete dynamics of the complete embryo.

2.15 Biophysical models of epithelial tissues

Investigations of biological systems can benefit from mathematical formalizations of biological and physical properties in order to better understand and predict their interplay.

Modeling epithelial tissue is not a trivial task because of the biological complexity laid out in this chapter. They consist of heterogeneous, visco-elastic, three dimensional, fluctuating cells that may have a polarity or can be otherwise distinguished. On top of that epithelia are, what physicists call "active matter", a state far from thermodynamic equilibrium [211]. Living organisms often operate far from equilibrium because molecular components constantly dissipate energy in the form of ATP into directed motion. This continuous conversion of chemical energy into heat, and thus into mechanical energy, leads to the system being constantly out of equilibrium [101, 211].

Nonetheless, many mathematical models of epithelial dynamics have been attempted using approaches ranging from discrete to continuum theories.

Large-scale continuum models do not play a huge role in this thesis. They are mainly used to describe tissue surfaces according to internal and external stresses to describe coarse-grained deformations and material properties such as viscosity or elasticity, or rheological properties. The theory of active gels plays a huge role describing large scale properties of viscoelastic matter driven out of equilibrium [176, 265]. Following classic hydrodynamic theories, forces and torques acting on a surface are introduced and their balance equations derived. The innovation here lies in the incorporation of active terms [46, 270] that extend previous passive theories [131]. Due to local, internally produced forces epithelial morphogenesis involves in-plane tension and torques that arise from differential stresses, which were not included in the theory. Recently, [287] successfully incorporated these effects in a theory of active surfaces. Other continuum models involve for example foams [56], visco-elastic solids [207] or visco-elastic-plastic solids [264]. A significant drawback of continuum models is that they can not describe the microscopic properties of cell-cell interactions by construction, for example cell heterogeneity or subcellular processes, [90] and also have trouble with some typical tissue processes like plasticity. Plasticity here means that tissues undergoing shape changes due to stresses must not return to the reference state in the absence of these stresses [269]. On the other hand they stand on a very strong mathematical foundation and typically involve few parameters [90].

In this thesis we focus on the dynamics of single cells and their interplay. Cell-based models are able to describe the dynamics of tissues beginning with microscopic dynamics and then inferring emergent tissue properties from simulations.

More simple approaches model cells as spheres or even point particles to model tumor growth [27, 66] or as cell pairs [272], whereby interactions are modeled by distance dependent potentials. Simulations rely on a variety of methods ranging from Langevin dynamics [94], or dissipative particle dynamics [19] to the Metropolis algorithms [35].

Then there are vertex models, which are one of the most popular approaches to describe epithelial dynamics. Instead of directly describing the surface area, the dynamics of the cell vertices are modeled such that cells are comprised of the polygons spanned by the vertices and their connections [7, 90, 91]. To this end one can write down an energy function [84, 138]

$$E(r_i) = \sum_{\alpha} \frac{K_\alpha}{2}(A_\alpha - A_\alpha^0)^2 + \sum_{(i,j)} \gamma_{ij} L_{ij} + \sum_{\alpha} \frac{\Gamma_\alpha}{2} P_\alpha^2 \tag{2.1}$$

including the vertices at positions r_i, connected by line segments L_{ij} pointing from vertex i to vertex j, with cells α and the corresponding area A_α. The terms, from left to right, describe

the surface elasticity K_α, the line tension γ_{ij} and contractility Γ_α of the perimeter P_α. The equations of motion then take the following form

$$\eta \frac{\mathrm{d}r_i}{\mathrm{d}t} = -\frac{\partial}{\partial r_i} E(r_i) \tag{2.2}$$

Models with varying degrees of complexity include more effects, altered energy functions or include different topologies for example instead of line segments use curvi-linear segments [237, 311]. The here presented basic model is quasi-static as it relaxes toward equilibrium junction lengths when the energy is minimized. Due to the lack of inertial effects, the described dynamics will inevitably come to a halt and thus explicit time-dependence must be introduced by including for example orientation dependent tension coefficients [275], time-dependent protocols [81] or chemical coupling regulating force production [300]. Vertex models have been applied to virtually every conceivable situation in epithelial morphogenesis including studies about topology [84], growth control [138], anisotropic growth [210] or planar cell polarity [288]. There exist extensions for the three dimensional case as well [243]. One of the greatest advantages of vertex models is their ability to explicitly incorporate neighbor interactions and that they have physically convincing descriptions of adhesion and rearrangement processes. In turn they typically neglect cell-matrix adhesion and their 2 dimensional nature neglects medial contractility [90].

A last class of models that play a particular role for the modeling of cell surface oscillations, are visco-elastic models. These are based on visco-elastic contractile materials, and thus on the Kelvin-Voigt or Maxwell dashpot model [242]. They provide 1 dimensional descriptions of the dynamics of elements in tissues, for example actin filaments, single cell junctions or cell surface areas. Because of their simplicity they are comparably easy to study and partially analytically tractable [90]. It is also straight forward to couple the dynamics to other compartments, which can for instance model regulation pathways or mechanosensitive interactions [64]. The change in the effective coordinate is then directly modeled such as

$$\mu \frac{\mathrm{d}L}{\mathrm{d}t} = T - T(m) \tag{2.3}$$

where L is the length of the element, μ the damping constant, T is an external tension and T(m) an internal tension, which depends on a second compartment, modeling the corresponding myosin dynamics.

Several mathematical models concerning actomyosin oscillations and surface area oscillations in epithelial tissues have been proposed. Earlier models explaining myosin oscillations are roughly 25 years old [153, 154] and are based on myosin groups that are elastically coupled to their environment. An elastic contractile material with turnover was used to model area oscillations in the amnioserosa [64]. Here, the myosin turnover is dependent on the concentration along the contractile element, which introduces feedback between myosin and length compartments. The model is able to produce oscillatory behavior, resulting from a Hopf bifurcation. Before the bifurcation the dynamics is stable. If certain parameters exceed a threshold, the dynamics collapse because of diverging myosin concentration causing a diverging tension. Other models of the same type can be found in [199, 294]. A second model that uses very similar basic assumptions, but derives the single cell behavior from the microscopic actin filament dynamics, is [193]. Using percolation theory, the authors arrive at the same effective dynamics as presented in [64] for the area dynamics. In addition, they can faithfully represent the collapse phase in a mathematically well defined manner, which is important to model cell ingression during dorsal closure.

In Chapter 5 I also use a visco-elastic model as basis to study intercellular coordination in the amnioserosa.

In addition, there has been a proposal for a mechano-chemical model for calcium signaling in embryonic epithelial cells [158]. The activation dynamics of Ca^{2+} is thereby taken from experimentally validated calcium dynamics. Ca^{2+} concentration saturates according to a hill function and is coupled with a linear, visco-elastic representation of a cell.

Chapter 3

CaLM: A novel optochemical tool to induce cell contractions in vivo

"What we observe is not nature itself, but nature exposed to our method of questioning."

Werner Heisenberg

3.1 Content

In this chapter, it is demonstrated how Ca^{2+}-uncaging can be employed to induce cell contractility in epithelial cells during tissue morphogenesis. Our method works with high spatial and temporal precision, meaning that it is possible to induce contraction with single cell resolution and with timescales of the same order as physiologically observed cell dynamics. This allows the experimentalist to precisely control cell behavior during complex tissue dynamics in vivo. As a side effect, the functioning of this method provides direct evidence for a role of intracellular Ca^{2+} to activate non-muscle myosin II and its recruitment to the actomyosin cortex.

Versatile tools to optically control cell behavior are in high demand among researchers studying tissue morphogenesis but also among cell biologists in general. Several optogenetic strategies by activating GEF proteins acting upstream of Rho have been reported, for instance [240, 325]. Despite their great promise, optogenetic approaches based on activation of Rho signaling come with intrinsic problems concerning the genetics, the use of visible light for activation and the required amount/duration of light exposure. An inherent problem with Rho signaling is that multiple targets are activated, such as Dia and actin polymerization beside myosin, as reviewed in section 2.7.

Because our approach is based on Ca^{2+}-uncaging, it does not rely on transgenes, uses short pulses of UV light and is in principle applicable to many species. Cell contraction is induced by Ca^{2+} bursts similar to the established applications in the field of neurobiology. The innovation of our study lies in the transfer of a method from neurobiology to the mechanobiology of epithelial cells.

In later chapters 7 and 8, we use this method to study coordination in epithelia. In chapter 7, we find that the reaction of neighbors in response to the uncaging is dependent on *xit* and *Tmc* which therefore mediate mechanical signaling. In chapter 8, simultaneous Ca^{2+} uncaging can be used to induce T1 transitions and promote the formation of a new junction between two cells. A key result is that efficiency of T1 transitions depends on the coordination of participating cells.

3.2 In vivo optochemical control of cell contractility at singe-cell resolution

Original contribution

Deqing Kong conducted the experiments and analyzed the data. Zhiyi Lv generated the VinculinD1-GFP transgenic fly and analyzed the VinculinD1-GFP data. **Matthias Häring** analyzed data and obtained Figs 2E, 3E-G, 4E, and 5G. Benjamin Lin generated the Rho sensor transgenic fly. Deqing Kong, Fred Wolf, and Jörg Großhans conceived the study and wrote the manuscript. Fred Wolf and Jörg Großhans supervised the study.

DOI

https://doi.org/10.15252/embr.201947755

Report

TRANSPARENT PROCESS OPEN ACCESS

EMBO reports

In vivo optochemical control of cell contractility at single-cell resolution

Deqing Kong[1,2,3,*], Zhiyi Lv[1], Matthias Häring[3,4,5,6,7], Benjamin Lin[8], Fred Wolf[3,4,5,6,7,†] & Jörg Großhans[1,2,†]

Abstract

The spatial and temporal dynamics of cell contractility plays a key role in tissue morphogenesis, wound healing, and cancer invasion. Here, we report a simple optochemical method to induce cell contractions *in vivo* during *Drosophila* morphogenesis at single-cell resolution. We employed the photolabile Ca^{2+} chelator *o*-nitrophenyl EGTA to induce bursts of intracellular free Ca^{2+} by laser photolysis in the epithelial tissue. Ca^{2+} bursts appear within seconds and are restricted to individual target cells. Cell contraction reliably followed within a minute, causing an approximately 50% drop in the cross-sectional area. Increased Ca^{2+} levels are reversible, and the target cells further participated in tissue morphogenesis. Depending on Rho kinase (ROCK) activity but not RhoGEF2, cell contractions are paralleled with non-muscle myosin II accumulation in the apico-medial cortex, indicating that Ca^{2+} bursts trigger non-muscle myosin II activation. Our approach can be, in principle, adapted to many experimental systems and species, as no specific genetic elements are required.

Keywords actomyosin; Ca^{2+} uncaging; cell contractility; morphogenesis; optochemical

Subject Categories Cell Adhesion, Polarity & Cytoskeleton; Methods & Resources

DOI 10.15252/embr.201947755 | Received 19 January 2019 | Revised 14 September 2019 | Accepted 2 October 2019 | Published online 30 October 2019

EMBO Reports (2019) 20: e47755

Introduction

Contractility underlies manifold processes in cell and tissue morphogenesis, including cell migration, cell shape changes, or junction collapse [1–4]. In epithelial tissues, cell contractions impact neighboring cells by exerting forces on adherens junctions. This mechanical linkage may elicit specific responses and could thus positively or negatively affect contractility and cytoskeletal organization in neighboring cells, i.e., mediate non-autonomous mechanical behaviors [5]. Within a tissue, cellular contraction and cell–cell interactions based on such force transduction can contribute to emergent tissue behavior, such as the formation of folds and furrows. The function of mutual cell–cell interactions, however, is difficult to study by classical genetic approaches. What is needed are methods for acute noninvasive interventions with high temporal and spatial resolution, ideally on the scale of seconds and of single cells.

For controlling cell contractility, optogenetic approaches have recently been developed. Cell contractility can be inhibited by optically induced membrane recruitment of $PI(4,5)P_2$ leading to interference with phosphoinositol metabolism and subsequent suppression of cortical actin polymerization [6]. Optical activation of contractility has been achieved by light-induced activation of the Rho-ROCK (Rho kinase) pathway, which controls myosin II-based contractility [7,8]. While functionally effective, such optogenetic methods require multiple transgenes driving the expression of modified proteins such as light-sensitive dimerization domains, which restrict the application to genetically tractable organisms. In addition, chromophores used in optogenetic effectors are activated by light in the visible spectrum, which limits the choice of labels and reporters for concurrent cell imaging.

Optochemical methods represent an alternative to genetically encoded sensor and effector proteins [9]. Intracellular calcium ions (Ca^{2+}) are known to be an important regulator of contractility in many cell types. Ca^{2+} plays a central role not only in muscle contraction, but also in cultured epithelial cells [10], in amnioserosa cells during dorsal closure [11], during neural tube closure [12,13], and in the folding morphogenesis of the neural plate [14]. In *Drosophila* oogenesis, tissue-wide increase in intracellular Ca^{2+} activates myosin II and impairs egg chamber elongation [15]. In *Xenopus*, a transient increase in Ca^{2+} concentration induces apical constriction

1 Institute for Developmental Biochemistry, Georg-August-Universität Göttingen, Göttingen, Germany
2 Faculty of Biology, Philipps-Universität Marburg, Marburg, Germany
3 Bernstein Center for Computational Neuroscience, Göttingen, Germany
4 Max Planck Institute for Dynamics and Self-Organization, Göttingen, Germany
5 Institute for Nonlinear Dynamics, Georg-August-Universität Göttingen, Göttingen, Germany
6 Campus Institute for Dynamics of Biological Networks, Göttingen, Germany
7 Max Planck Institute for Experimental Medicine, Göttingen, Germany
8 Department of Cell Biology, HHMI and Kimmel Center for Biology and Medicine of the Skirball Institute, New York University School of Medicine, New York, NY, USA
*Corresponding author. Tel: +49 551 39 68273; E-mail: deqing.kong@med.uni-goettingen.de
†These author contributed equally to this work as co-senior authors

in cells of the neural tube [16]. Although the detailed mechanism of Ca^{2+}-induced contraction in non-muscle cells remains to be resolved, it conceivably offers a simple and temporally precise way to interfere with and control contractile activity. In neuroscience, optochemical methods for the release of intracellular Ca^{2+} have been well established and widely employed [17,18]. Here, we report an optochemical method to control epithelial cell contractility via Ca^{2+}-mediated light activation of myosin (CaLM) on the scale of seconds and at single-cell resolution during tissue morphogenesis in *Drosophila* embryos. Optochemical control of contractility by Ca^{2+} uncaging has minimal spectral overlap with fluorescent protein reporters and optogenetic activators. Our results provide evidence for a ROCK-dependent effect of increased intracellular Ca^{2+} on activating non-muscle myosin II and its recruitment to the actomyosin cortex.

Results

Uncaging induces a rapid Ca^{2+} burst in epithelial cells in *Drosophila* embryos

Photolysis of the Ca^{2+} chelator *o*-nitrophenyl EGTA (NP-EGTA) [19] (Fig 1A) is widely used in neurobiology for the modulation of intracellular Ca^{2+} concentration [18,20]. Here, we employed the membrane-permeant acetoxymethyl (AM) ester derivative, which complexes Ca^{2+} once the AM moiety is cleaved off by intracellular esterase. The *o*-nitrophenyl EGTA-Ca^{2+} complex cannot get out again because the AM moiety has been cleaved off by intracellular esterase. Following microinjection into staged embryos, uncaging was induced in the focal volume with a diameter of 2–3 μm and thus an area of 5 μm^2 of a pulsed 355-nm laser beam (Fig 1B). To allow for concomitant uncaging and imaging, we used a setup, in which the light paths of the UV laser for uncaging and the excitation laser for confocal imaging in the visible spectrum were controlled independently. We conducted experiments in the lateral epidermis of *Drosophila* embryos during germband extension (stage 7). The epidermis during this stage constitutes a columnar epithelium with a cell diameter in the range of about 8 μm and cell height of about 25 μm (Fig 2A).

We recorded changes in intracellular Ca^{2+} concentration induced by uncaging using a genetically encoded Ca^{2+} sensor protein, GCaMP6s. Embryos expressing a membrane-bound, myristoylated variant of GCaMP6s [21] were injected with NP-EGTA-AM and subjected to uncaging. We observed a transient increase in GCaMP6 fluorescence within a second specifically in cells targeted by a UV light pulse (Fig 1C, Movie EV1). Quantification of GCaMP fluorescence ($\Delta F/F_0$) showed a fourfold increase within 2-s. Afterward, GCaMP6s fluorescence gradually decreased to near initial levels within a few minutes (Fig 1E). As GCaMP6s has a decay time constant in the range of seconds, this indicates that Ca^{2+} clearance and extrusion mechanisms in the epithelial cells operate on an effective time scale of minutes. We did not detect an increase in GCaMP6s fluorescence after UV exposure in control embryos injected with buffer only (Fig 1D and E).

The increase in the Ca^{2+} sensor signal was restricted to the individual target cell (Fig 1C, Movie EV1). The Ca^{2+} sensor signal in the next and next–next neighbors of the target cell was temporally constant and comparable to control embryos (Fig 1F). In summary, our experiments show that Ca^{2+} uncaging with single-cell precision can be conducted in epithelial tissue in *Drosophila* embryos. Uncaging leads to a reversible, second-scale increase in intracellular Ca^{2+} concentration that is restored by cell-intrinsic mechanisms on a minute scale. The magnitude of the Ca^{2+} increase was similar to what was previously reported for neuronal cells [22].

Ca^{2+} bursts induce cell contraction

We next investigated the consequence of Ca^{2+} bursts on cell shape. We conducted uncaging in embryos expressing E-Cad-GFP, which labels adherens junctions near the apical surface of the epithelium (Fig 2A). We detected a contraction of the target cell in the lateral epidermis to about half of the apical cross-sectional area following uncaging (Figs 2B and EV1A, Movies EV2 and EV3). Target cells in control embryos injected with buffer remained largely unaffected (Fig 2C). Quantification revealed a reduction by half of the cross-sectional area within 1–2 min in the target cell but not in controls (Figs 2D, and EV1A and B). The constriction rate reached the maximum in 0.5 min (Fig 2E). Most cells remained contracted during the following 15 min, whereas a minority of cells reexpanded to the original cross-sectional area (Fig 2F and G). We did not observe that the exposure to UV laser and Ca^{2+} uncaging noticeably affected the further behavior of the target cells and surrounding tissue (Fig 2F and G). We did not observe that target cells were extruded or got lost from epithelial tissue. This behavior indicates that the Ca^{2+} uncaging is compatible with ongoing tissue morphogenesis. We conducted Ca^{2+} uncaging in the head and dorsal region at stage 7 embryos, where these cells do not display apical myosin and do not display obvious changes in cross-sectional area. Cell contraction event was detected in these cells following Ca^{2+} uncaging (Fig EV1C and D).

Induced cell contraction in a squamous epithelium

Next, we applied Ca^{2+} uncaging to a different tissue in *Drosophila* embryos. The amnioserosa represents a squamous epithelium on the dorsal side of the embryo with cells about 15 μm in diameter and only 3 μm in height (Fig 3A–C). As in the lateral epidermis, we employed E-Cadherin-GFP to label the apical cell outlines (Fig 3B). Ca^{2+} uncaging led to contraction of the target cells but not in the control cells (Fig 3D, Movie EV4). The cells that are from the same recording but not the next-neighboring of target cell were used as control (Fig 3D). Quantification of the apical cross-sectional areas revealed specific uncaging-induced contraction within a minute, and the peak constriction rate was observed about 30 s after uncaging (Fig 3E). The amnioserosa cells are naturally contracting overtime (Fig 3F). We calculated the maximum constriction rate from 12 control cells over 5 min and detected a statistically significant difference when comparing the maxima in the constriction rates between the target and control cells (Fig 3G). We next conducted three uncaging experiments in amnioserosa cells with recording over 30 min. Two cells contracted irreversibly, one cell relaxed after 10 min as in the lateral epidermis (Fig EV2B and C). We did not observe that the exposure to UV laser and Ca^{2+} uncaging noticeably affected the further behavior of the target cells and surrounding

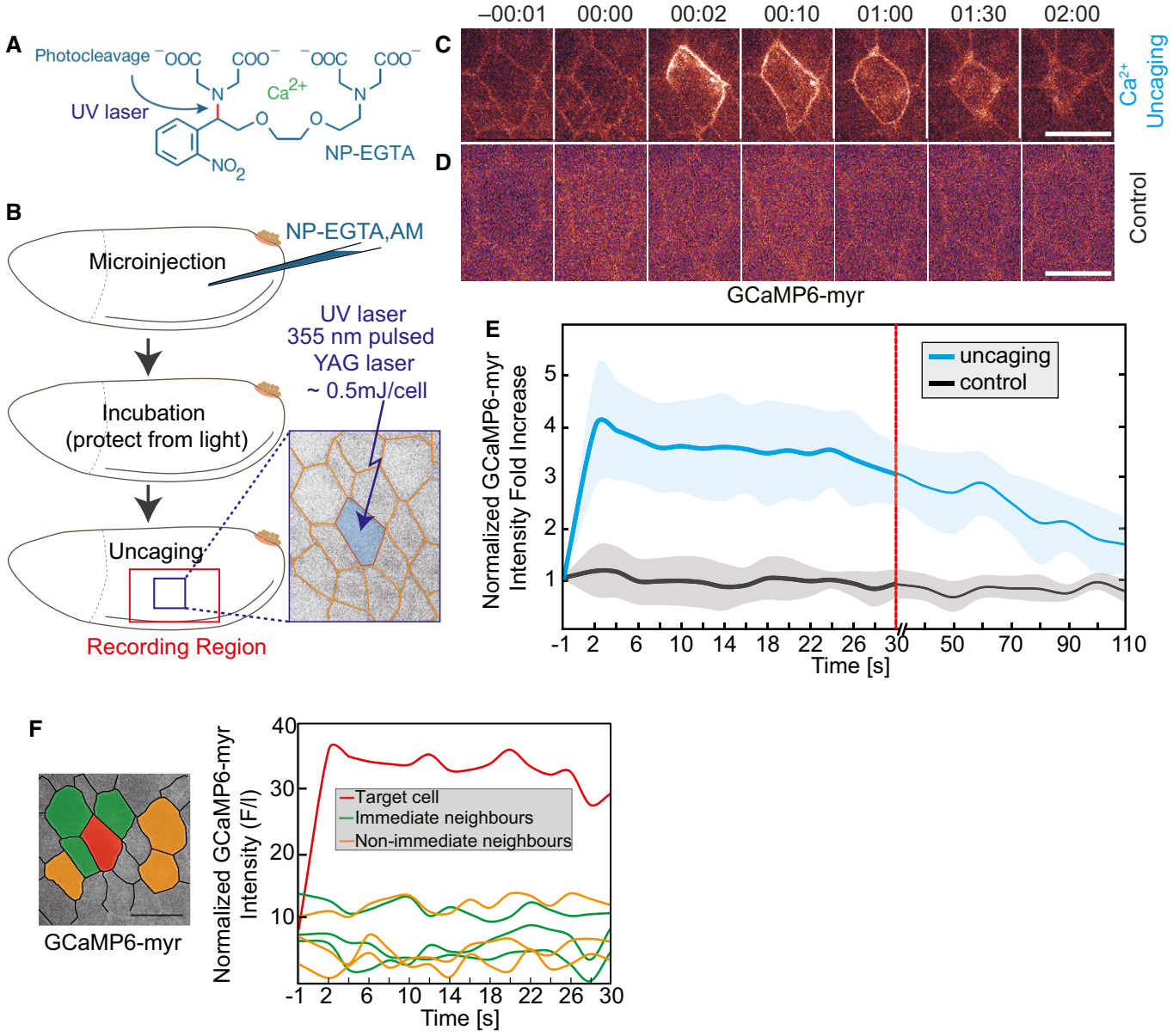

Figure 1. CaLM induces a rapid increase in intracellular Ca^{2+} concentration in epithelial cells.

A Structure of the cage NP-EGTA. UV illumination cleaves the bond in red and releases Ca^{2+}.

B Experimental scheme for Ca^{2+} uncaging in *Drosophila* embryos. NP-EGTA, AM was injected into the staged embryos. Followed by a short incubation, a target cell (blue) was exposed to a UV laser flash.

C, D Images from time-lapse recording of embryos (stage 7, lateral epidermis) expressing a membrane-bound Ca^{2+} sensor (GCaMP6-myr) and injected with (C) 2 mM NP-EGTA, AM or (D) with buffer (control). Time in min:s.

E Normalized fluorescence intensity of GCaMP-myr in the target cell. Mean (bold line, six cells in six embryos) with standard deviation of the mean (ribbon band).

F Normalized fluorescence intensity of GCaMP sensor in target cell (red), three next neighbors (green), and three non-immediate neighbors (orange).

Data information: scale bars: 10 μm in (C, D, F).

tissue. Furthermore, in order to rule out that UV laser induced cell apoptosis during uncaging, we employed a reporter of apoptosis [23,24] in the amnioserosa, where we can demonstrate the functionality of the reporter due to the normal presence of apoptotic cells during dorsal closure (Fig EV2A). We detected reporter signal in apoptotic cells but not in target cells subject to uncaging. In summary, our experiments show that Ca^{2+} uncaging can be employed as a noninvasive method to induce contractions in selected single cells in different cell types and tissues.

We next ask whether further contraction in the target cell can be generated by repeating the UV pulse in the same cell. We therefore exposed a selected cell in the amnioserosa three times with a UV pulse (0, 2.5, and 5 min). We observed the typical contraction after the first pulse but no further obvious contractions after the second

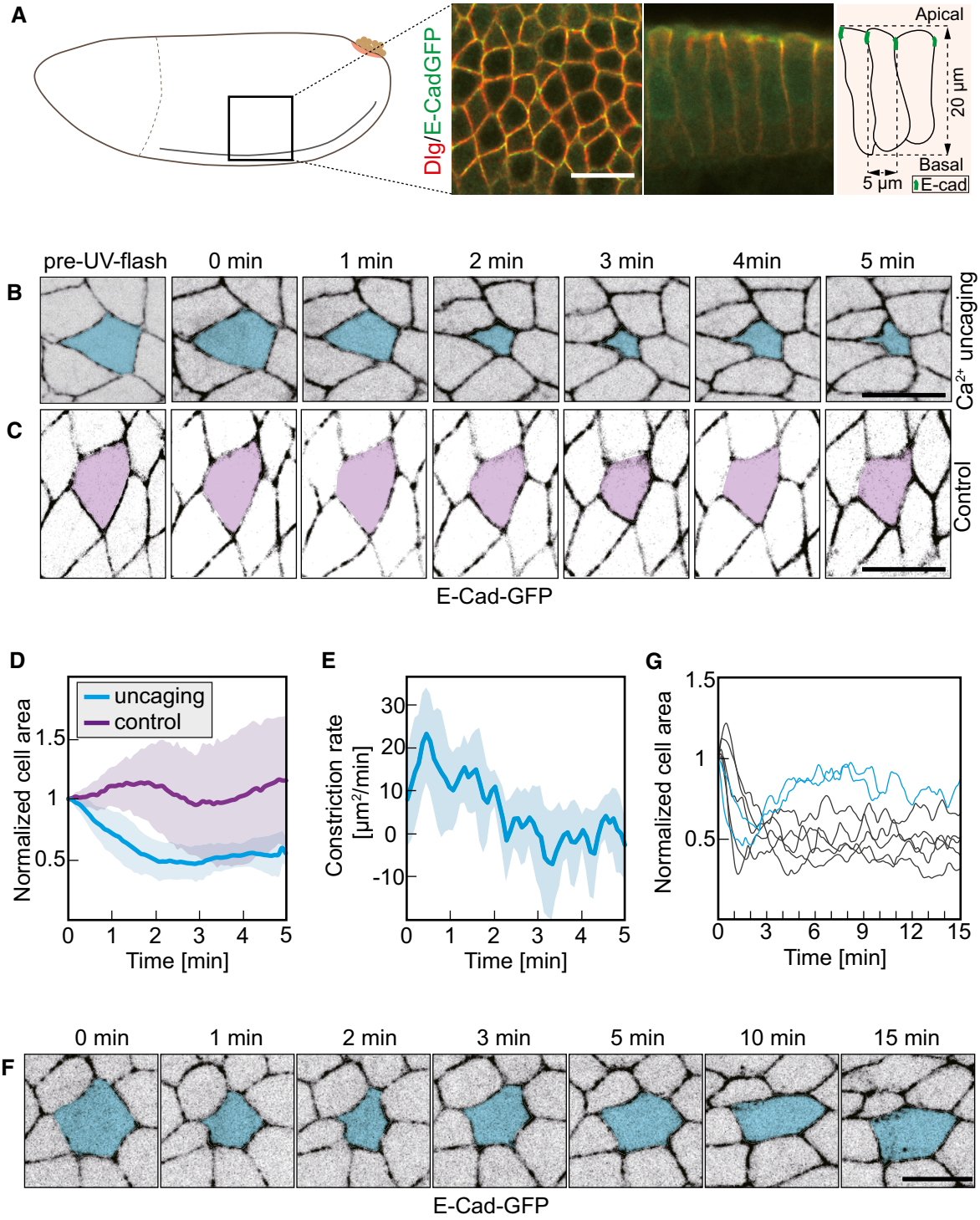

Figure 2. CaLM triggers apical constriction in a columnar epithelium.

A Schematic drawing and morphology of columnar epithelium in the lateral epidermis in stage 7 *Drosophila* embryos.

B, C Images from a time-lapse recording embryos expressing E-Cad-GFP and injected with (B) 2 mM NP-EGTA, AM or (C) buffer and exposed to the UV laser. Target cells are labeled in blue or purple.

D Cross-sectional area of target cells over time. Cell areas were normalized to their initial size (the first frame of recording after uncaging). Mean (bold line) with standard deviation of the mean (ribbon band). Uncaging (blue), eight cells in eight embryos. Control (purple), five cells in five embryos.

E Apical constriction rate over time in target cells in (D) (n = 8 cells in eight embryos). Mean (bold line) with standard deviation of the mean (ribbon bands).

F Images from time-lapse recording showing long-term behavior after CaLM. Target cell is marked in blue.

G Cross-sectional area of target cells over 15 min after Ca^{2+} uncaging. Cell contraction was reversible in two out of seven target cells (blue lines).

Data information: scale bars: 10 µm in (A, B, C, F).

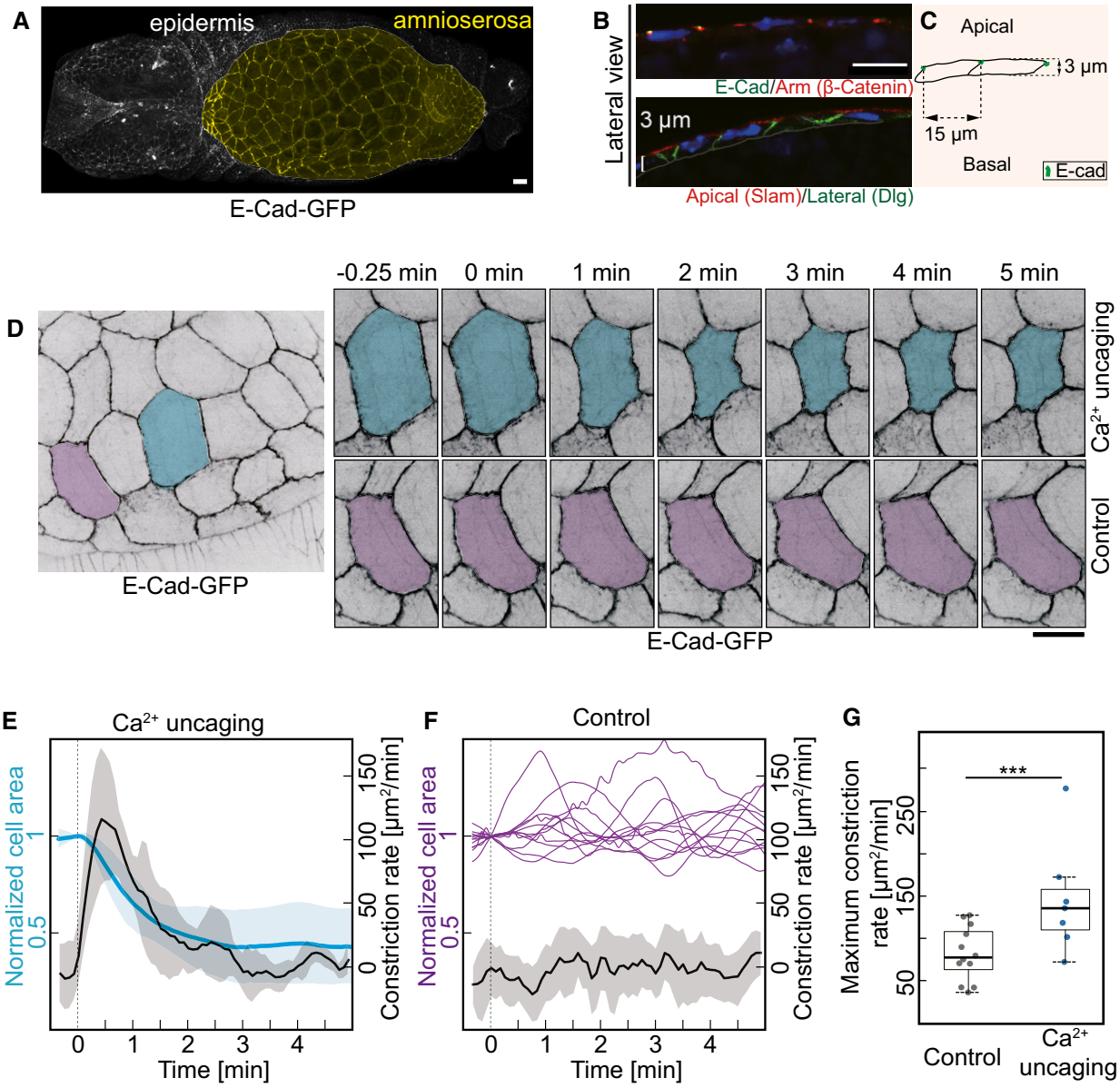

Figure 3. CaLM triggers apical constriction in a squamous epithelium.

A–C Amnioserosa (yellow in A) represents a squamous epithelium. Confocal image of *Drosophila* embryo expressing E-Cadherin-GFP. Sagittal sections of amnioserosa cells. Confocal images (B) and schematic drawing (C).

D Images from a time-lapse recording in embryos (stage 14) expressing E-Cad-GFP and injected with 1 mM NP-EGTA, AM. The target cell is highlighted in blue. The control cell (next–next neighbor of target cells) highlighted in purple was not exposed to UV light.

E Cross-sectional area (blue) and apical constriction rate (black) of target cells normalized to initial size (the first frame of recording after uncaging). Mean (bold line) with standard deviation of the mean (ribbon band) (n = 7 cells in seven embryos).

F Cross-sectional area traces (purple) of 12 individual control cells. Mean of apical constriction rate of control cells is indicated with black bold line (n = 12 cells in seven embryos) with standard deviation of the mean (ribbon band).

G Boxplot shows the maximum apical constriction rate from target and control cells. Bold horizontal line, mean. Box, second and third quartile. Black horizontal dash line with whisker, 95% bootstrap confidence intervals. ***P = 0.00004949 (two-tailed unpaired t-test).

Data information: Scale bars: 10 µm in (A, B, D).

and third UV pulses (Fig EV3A and B). Next, we induced contraction by uncaging in a row of four cells in the amnioserosa (Fig EV3C). An axial projection after 5 min shows a small groove in the tissue. Importance of this study is that we demonstrate the induced contraction of a row of cells. Having the method in hand to induce cell contraction in a selected patch of cells will allow us to test the contribution of contraction of morphogenetic movements such as furrow formation and invagination in future experiments.

Role of myosin II in Ca^{2+}-induced cell contraction

Multiple mechanisms are conceivable for Ca^{2+}-induced cell contraction. Given their time scale in the minute range, it is unlikely that slow transcriptional or translational processes are involved. It is also unlikely that Ca^{2+} directly activates contraction similar to its role in muscle cells due to the distinct organization of cortical actomyosin and indicated by the substantial time lag between Ca^{2+} increase and cell contraction. Ca^{2+} may activate myosin II, similar to what has been reported for the *Drosophila* egg chamber [15]. Such a specific myosin II activation may be mediated via Rho-ROCK signaling or via Ca^{2+}-dependent protein kinases or phosphatases, such as myosin light-chain kinase (MLK) [25].

As a first step toward identifying the mechanism of Ca^{2+}-induced cell contraction, we imaged myosin II dynamics following uncaging in embryos expressing E-Cad-GFP to label cell–cell contacts and sqh-mCherry (spaghetti squash, myosin regulatory light chain). sqh-mCherry fluorescence is a direct indicator of active myosin II mini filaments, which are visible as clusters. Myosin II is found associated with adherens junctions (junctional pool) and at the apical cortex (medial pool), where it is responsible for apical constriction [26]. We focused on the medial pool of myosin II. We observed an

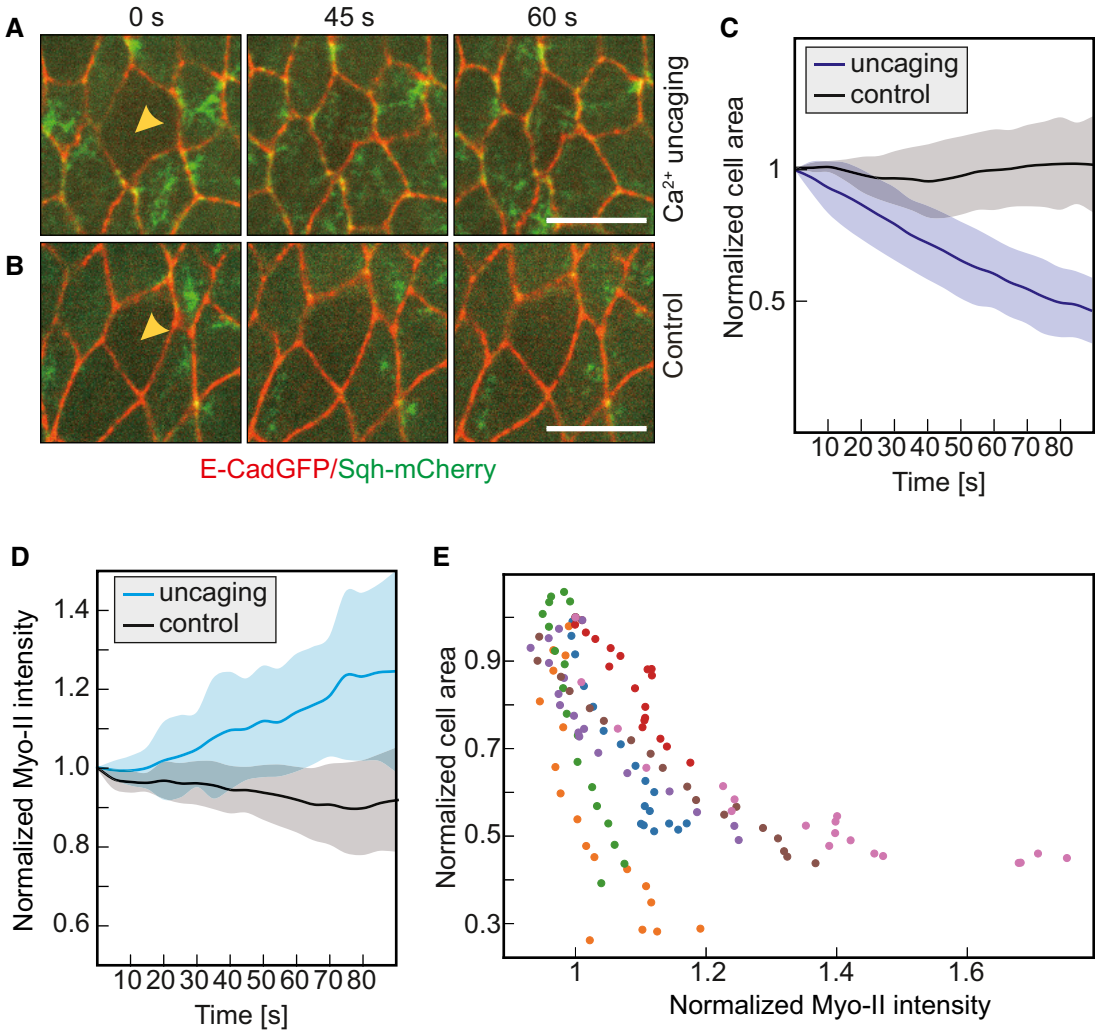

Figure 4. CaLM induces myosin II.

A, B Embryos expressing Sqh-mCherry (green) and E-Cadherin-GFP (red) were injected with 2 mM NP-EGTA, AM (A) or buffer (B). Images from a time-lapse recording in the cells of the lateral epidermis (stage 7) and exposed to the UV laser (yellow arrowheads).

C Cross-sectional area of target cells and control cells normalized to the initial area (the first frame of recording after uncaging or UV laser illumination). Mean (bold line) with standard deviation of the mean (ribbon band) (n = 7 cells in seven embryos).

D Medio-apical Sqh-mCherry fluorescence in target (blue) and control (black) cells normalized to the initial fluorescence intensities (the first frame of recording after uncaging or UV laser illumination). Mean (bold line) with standard deviation of the mean (ribbon band) (n = 7 cells in seven embryos), P = 0.013 at 45 s (CE50), P = 0.011 at 90 s (two-tailed unpaired t-test).

E Scatter plot of normalized medio-apical myosin II (the first frame of recording after uncaging is normalized to 1) with normalized cross-sectional area (the first frame of recording after uncaging is normalized to 1) in target cells. Different colors indicate the individual cells.

Data information: Scale bars: 10 μm in (A, B).

increase in sqh-mCherry fluorescence after about 0.5–1 min specifically in target cells (Fig 4A and B). Quantification of the medial myosin II revealed specific uncaging induced a 20% increase in target cells within 1.5 min after uncaging (Fig 3D). However, medial myosin II intensity dropped a bit in the control cells following UV exposure from the embryos injected with buffer without NP-EGTA,

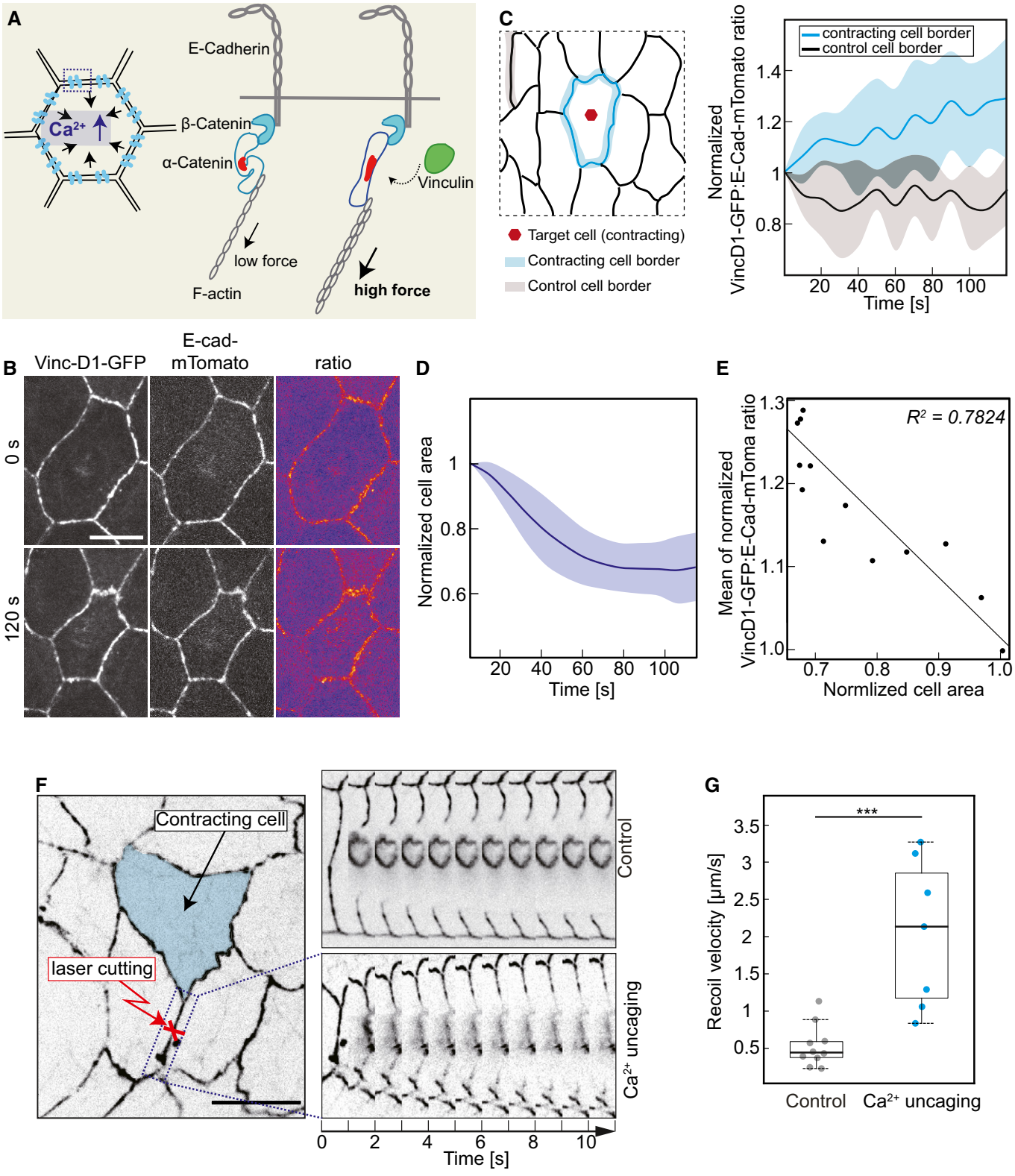

Figure 5.

Figure 5. CaLM induces cortical tension.

A Schematic drawing of force-dependent Vinculin association to adherens junctions and principle of the Vinculin reporter.

B Images from time-lapse recording of an amnioserosa cell after CaLM in embryos (stage 14) expressing E-Cad-mTomato and VinculinD1-GFP.

C Ratio of VinculinD1-GFP and E-Cadherin-mTomato fluorescence at the junctions of the target contracting cells (blue) and control cells (black) The ratio was normalized to initial ratio (the first frame of recording after uncaging). Mean (bold line) with standard deviation of the mean (ribbon band) (n = 6 constricting cells and nine inactive cell borders in six embryos), P = 0.033 at 60 s (CE50), P = 0.011 at 120 s (two-tailed unpaired t-test).

D Cross-sectional area in target cells normalized to initial size (the first frame of recording after uncaging). Mean (bold line) with standard deviation of the mean (ribbon band) (n = 6 cells in six embryos).

E Scatter plot of normalized area of target cells with the mean of VinculinD1/E-Cadherin ratio at the cell junctions (n = 6 cells in six embryos).

F The schematic of amnioserosa shows the first neighbor junction of CaLM target cells (indicated by red cross). Kymographs show recoil after junction ablation. Control ablations were conducted in the embryos injected with buffer without NP-EGTA, AM, and the junctions were selected randomly.

G Boxplot shows the initial recoil velocity after laser ablation. Bold horizontal line, mean. Box, second and third quartile. Black horizontal dash line with whisker, 95% bootstrap confidence intervals. ***P = 0.00035151 (two-tailed unpaired t-test). Dots indicate the individual recoil velocity. Control, n = 10 junctions in four embryos. Ca^{2+} uncaging, n = 7 junctions in seven embryos.

Data information: Scale bars: 10 μm in (B, F).

AM (Fig 4C and D). The cross-sectional area of these control cells remained largely unaffected (Fig 4C and D). To establish a link between the increase in myosin II and the reduced cell area, we correlated both parameters with each other (Fig 4C and E). Indeed, we detect a strong correlation that the smaller the cell area is the higher the myosin II activity.

Contracting cell induces cortical tension

One expects that a contracting cell applies a force on the junctional complexes linking it to its neighbors within the epithelium (Fig 5A). To assess this action, we employed a reporter for tension across adherens junctions, based on the force-dependent conformational state of α-Catenin [27–30]. α-Catenin exhibits a force-dependent switch between two stable conformations. In the closed state, α-Catenin is bound to the Cadherin complex but does not bind to the D1 domain of Vinculin, because the central mechanosensitive modulatory (M) domain is inaccessible. In contrast, the central mechanosensitive modulatory (M) domain is exposed, when a force is applied to the molecule. α-Catenin bridges the Cadherin complex with the actin cytoskeleton and can thus sense and transduce forces acting on the adherens junctions. We thus introduced a GFP reporter based on the D1 domain of Vinculin (Fig EV4A) together with E-Cadherin-tomato inserted at the endogenous locus (Fig 5B and Movie EV5). We quantified the dynamics of VinD1-GFP fluorescence during an uncaging experiment (Fig EV4B). We detected a significant increase in the range of 10% of reporter fluorescence at the junctions next to the contracting target cell in the time scale of a minute. We did not detect such an increase at distant junctions, which served as a control in this experiment. As the time scale in response to uncaging by area change and VincD1 reporter fluorescence was comparable, we quantified their relationship and found a strong correlation between VincD1 reporter fluorescence and cell area (Fig EV4C).

The Vinc/E-cad ratio has been reported to correlate with junctional tension in *Drosophila* embryos [31]. We therefore quantified the dynamics of VincD1/E-cad fluorescence ratio in the CaLM-activated contracting cells (Fig 5B–E). We detect a 25% increase in VincD1/E-cad fluorescence ratio at the junctions next to the contracting target cell that appeared on a time minute scale. We did not detect such an increase at distant junctions, which served as a control in this experiment (Fig 5C). As the time scale in response to uncaging by area change (Fig 5D) and VincD1/E-cad fluorescence ratio was comparable, we quantified their relationship. We plotted the mean of Vinc/E-cad ratio against the mean of cell area from six contracting cells and found a strong correlation between Vinc/E-cad ratio and cell area (Fig 5E). Furthermore, we assume that the CaLM-activated contracting cell applies a force to its neighbors within the epithelium. Following Ca^{2+} uncaging, we therefore performed laser ablation on the first neighboring junctions of the CaLM-activated contracting cell (Fig 5F). The control ablation was performed on randomly selected junctions from the embryos injected with buffer (Fig 5F). We observed faster and greater recoil in Ca^{2+} uncaging embryos compared within the control embryos (Fig 5F). The initial recoil velocity within 2-s after ablation is statistically significantly larger in Ca^{2+} uncaging embryos than control embryos (Fig 5G). In summary, our experiments show that Ca^{2+} uncaging induces cortical tension and CaLM-activated contracting cell applies a force on the junctional complexes linking it to its neighbors within the epithelium.

Mechanism of Ca^{2+}-induced cell contraction

Although we have observed that medio-apical myosin II accumulates in response to uncaging and that it correlates with the degree of cell contraction (Fig 4), the mechanism of how Ca^{2+} induces contraction is unclear. At least two different mechanisms are conceivable. Firstly, Ca^{2+} may activate myosin II activity via the generic pathway involving Rho kinase and phosphorylation of the regulatory light chain. Secondly, Ca^{2+} may activate the myosin light-chain kinase or directly engage at the actomyosin filaments. We first tested whether the Ca^{2+}-induced contraction depended on Rho kinase by employing its specific inhibitor Y-27632 [32]. sqh-mCherry fluorescence is reduced obviously in Y-27632-injected embryos compared with water-injected embryos (Fig 6A and B). Following Ca^{2+} uncaging, we did not detect any cell contraction in embryos treated with the Rho kinase inhibitor indicating that Ca^{2+}-induced contraction depends on Rho kinase (Fig 6E and I, EV4D, Movie EV7). Ca^{2+} uncaging was functional in these embryos (Fig 6C and D, Movie EV6) as Ca^{2+} fluorescence in Y-27632-treated embryos was comparable in timing and magnitude to wild-type embryos (Fig 6D). The dependence on Rho kinase strongly supports the model that the Ca^{2+} signal acts via myosin II activation.

Rho kinase is activated by Rho signaling. RhoGEF2 is a major activator of Rho1 in the epidermal tissue during gastrulation, for example. We tested the dependence of the Ca^{2+}-induced cell contraction on RhoGEF2 by conducting the uncaging in embryos lacking RhoGEF2. The embryos from the female of *RhoGEF2* null mutation germline clones show multinucleated cell phenotype

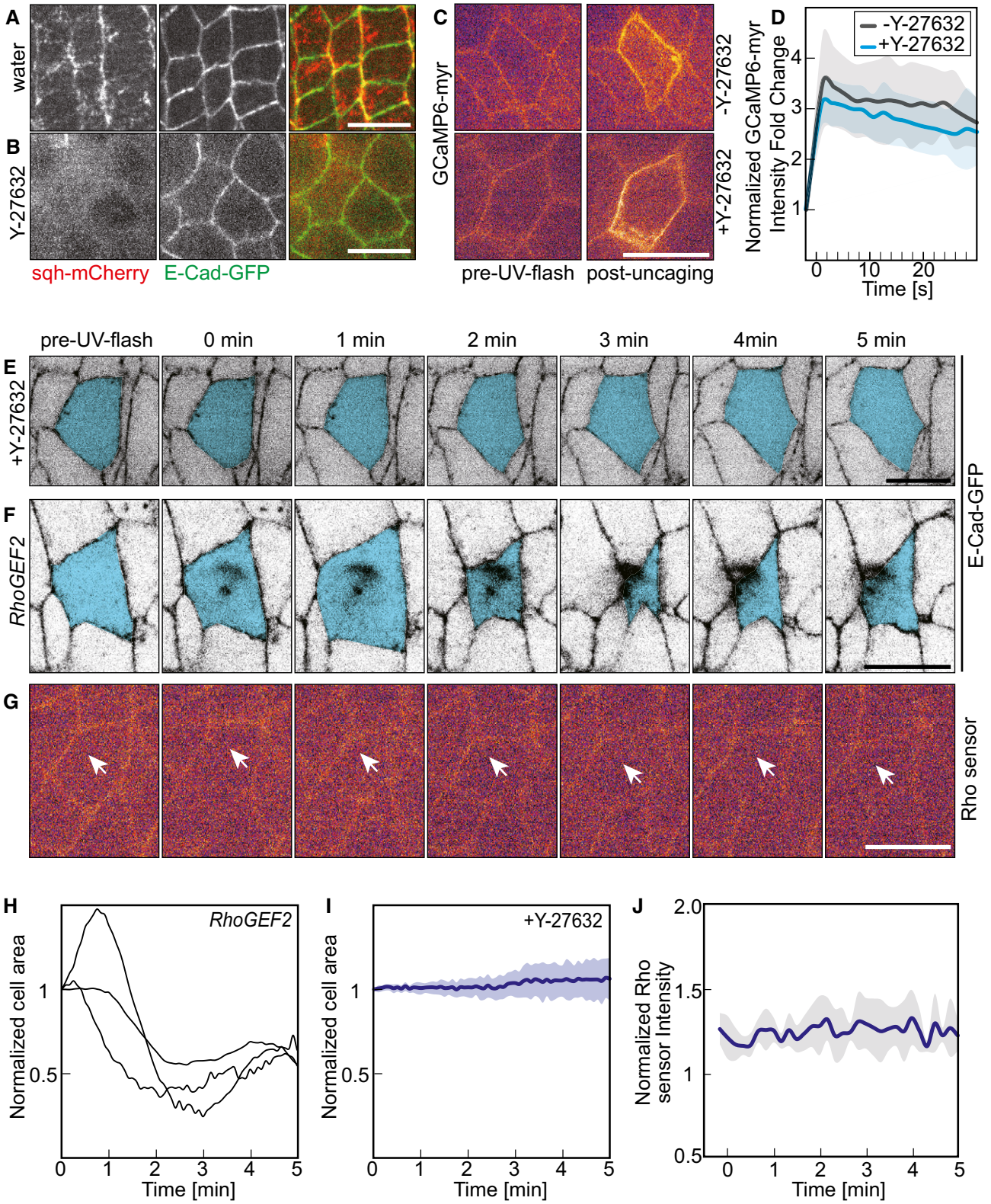

Figure 6.

Figure 6. CaLM requires ROCK but not RhoGEF2.

A, B Confocal images of embryos expressing sqh-mCherry and E-Cadherin-GFP injected with Y-27632 (ROCK inhibitor, 10 mM) or water.

C, D CaLM in embryos (stage 7, lateral epidermis) expressing a membrane-bound Ca^{2+} sensor (GCaMP6-myr) and injected with NP-EGTA, AM and Y-27632 as indicated. Images from time-lapse recording. (D) Fluorescence intensity of GCaMP-myr in the target cell with (black, the same data with Fig 1E) or without (blue) Y-27632. Mean (bold line) with standard deviation of the mean (ribbon band, six cells in six embryos).

E–G Images from time-lapse recordings following CaLM (lateral epidermis, stage 7). Target cells marked in blue. (E) Co-injection of Rho kinase inhibitor Y-27632. (F) Embryos from *RhoGEF2* germline clones. (G) Embryo expressing a Rho sensor, and white arrows indicate the target cell.

H Cross-sectional area traces of target cells normalized to initial size (the first frame of recording after uncaging) in embryos from *RhoGEF2* germline clone female following CaLM.

I Cross-sectional area of target cells normalized to initial size (the first frame of recording after uncaging) in embryos injected with 10 mM Y-27632 (n = 8 cells in five embryos) following Ca^{2+} uncaging. Mean (bold line) with standard deviation of the mean (ribbon band).

J Rho sensor fluorescence in target cells (n = 6 cells in six embryos) following Ca^{2+} uncaging. Mean (bold line) with standard deviation of the mean (ribbon band).

Data information: Scale bars: 10 μm in (A, C, E, F, G).

during cellularization as previous report (Fig EV4E) [33]. Quantification of the area dynamics of target cells revealed a behavior comparable in magnitude and timing to that in wild-type embryos (Fig 6F and H, Movie EV8). Lastly, we tested whether Rho1 was involved in mediating the Ca^{2+} signal to Rho kinase by visualizing Rho1 activation with a sensor protein. The Rho sensor was functional, since we detected activation in cells undergoing cellularization (Fig EV4F) and cytokinesis (Fig EV4G). In contrast, we did not detect a change in Rho sensor fluorescence in response to Ca^{2+} uncaging (Fig 6G and J, Movie EV9). In summary, we propose a mechanism linking Ca^{2+} with myosin activation via Rho kinase but independent of Rho signaling via RhoGEF2.

Discussion

We developed and validated a new method, which we designate CaLM to induce cell contraction in epithelial tissues with precise temporal and spatial control. The approach applies Ca^{2+} uncaging, which has been well established in neurobiology, for example, to epithelial cell and developmental biology. By inducing Ca^{2+} bursts in single or multiple cells, CaLM enabled us to induce contraction in selected cells to about half of the cross-sectional area within a minute. The induced contraction did not damage cells or perturb tissue integrity. To our best knowledge, this is the first report for optically controlled cell contraction on the minute scale and at single-cell resolution *in vivo* during epithelial tissue morphogenesis.

CaLM is based on UV laser-induced photolysis of a Ca^{2+} chelator that has been widely employed [18]. The caged compound "NP-EGTA, AM" is membrane-permeant and thus allows convenient application on the tissue scale. The 355-nm pulsed UV laser, which we employ in this study, is compatible with modern objectives and can be conveniently mounted on standard live imaging microscopes via the epiport, for example. The dose of UV light depends on factors such as light scattering by the tissue and thickness of the sample. The actual dose of light at the target site can only be estimated and needs to be carefully titrated for the specific experimental system. We employed a genetically encoded Ca^{2+} sensor protein for setting up the experimental conditions and testing the scale and time course of the Ca^{2+} burst. Alternatively, Ca^{2+} indicator dyes may be applied, depending on the sample. Besides the 355-nm pulsed UV laser, we tested the suitability of a continuous wave laser at 405 nm, which is often installed at standard confocal microscopes. Using point scan illumination similar to FRAP protocols, we did not detect any increased signal of the GCaMP reporter (Fig EV5). The inefficiency of the 405-nm laser is consistent with the absence of significant absorbance of NP-EGTA at wavelengths longer than 400 nm [19]. Since our focus is to use CaLM to control contractility at single-cell resolution during tissue morphogenesis. In order to make the approach easy of handling, we only used 100× objective in all experiments. To stimulate contractility in multiple cells simultaneously, we applied CaLM in four amnioserosa cells (Fig EV3). Technically, CaLM should be applicable also to even more cells (e.g., 15–20 cells). Such experimental schemes will be tested in future investigations.

The detailed mechanism for the induced Ca^{2+} burst and profile remains unclear. At this point, we do not know the origin and fate of Ca^{2+} ions measured by the GCaMP sensor protein. A proportion of the Ca^{2+} ions will be released from the photolyzed cage. It is conceivable, that in addition to this, intra- or extracellular Ca^{2+} reservoirs are opened by Ca^{2+}-gated Ca^{2+} channels, comparable to SERCA in muscle cells [34]. As the Ca^{2+} levels return to low levels within minutes after uncaging, calcium ions may be exported from the cytoplasm to internal reservoirs such as ER or to the outside by Ca^{2+} transporters.

The detailed mechanism of how Ca^{2+} is functionally linked to contractile actomyosin also remains unclear, although there is no doubt that Ca^{2+} is involved in regulation of contractility in many cell types [10–14,16]. It is clear that Ca^{2+} does not directly act on actomyosin similar to the contractile system involving troponin C, given the time lag between Ca^{2+} burst and contractility in the range of many seconds. The delayed response may indicate an indirect link via a signaling cascade.

In non-muscle cells, contractility is mediated by non-muscle myosin II, which is largely controlled by Rho-ROCK pathway [4]. In the cells we tested, we find that Ca^{2+} is linked to this pathway at the position of ROCK. CaLM induces contractility by activating the medial pool of non-muscle myosin II, at least. Whether other pools of myosin II, such as junctional or basal myosin, are also activated remains unclear.

An expected consequence of a contracting cell within an epithelial tissue is a mechanical pull on its neighbors, which should be mediated by junctional complexes. This is an important issue, because an immediate application of CaLM is in tissue

morphogenesis with one of its central questions of how the temporal–spatial distribution of forces leads to changes in visible morphology. We tested the potential mechanical pull of target cells on its neighbors in two ways. Firstly, we applied a Vinculin-derived reporter, which preferentially binds to the open conformation of α-Catenin. α-Catenin undergoes a force-dependent conformational change, which opens a Vinculin binding site under mechanical pull [27–30]. Secondly, we directly assayed junctional tension in neighboring cells by measuring the initial recoil velocity after ablation. This experiment nicely shows the versatility of CaLM. The pulsed UV laser is employed for two tasks: firstly, the controlled uncaging in a single-target cell and secondly, shortly afterward the precise ablation of a single junction, all recorded in a movie of the tissue. CaLM will be, in principle, useful in many types of experiments concerning tissue morphogenesis. For example, intercellular coupling between neighboring cells poses a challenge to experimental design in studies of tissue morphogenesis. Here, cause and consequence cannot be easily distinguished without targeted activation of cellular contractility and precise external control of cellular behaviors. Thus, acute interference is mandatory for dissecting causal functional dependencies.

Taken together, CaLM allows us to control rapid cell contractility and generates forces within the tissue during morphogenesis. CaLM can be applied to a wide range of processes and organisms and should greatly improve our ability to study the causality of cell contractility in tissue mechanics and mechanotransduction *in vivo*. Importantly, CaLM does not require any genetically encoded protein and can be readily applied to any stock and genetic background. The independence from genetic constitution should vastly accelerate analysis and enable screening of mechanobiological cellular pathways and components, e.g., by comparing wide arrays of mutants to wild-type behavior. In addition, Ca^{2+} uncaging is likely to open applications in manifold experimental systems with low genetic tractability. Importantly, UV-induced Ca^{2+} uncaging leaves the entire visible spectrum available for optical interfacing with florescent protein indicators and opsin-based effectors. This in particular increases the options for simultaneously recording of cell and tissue behavior with the large palette of available fluorescent protein tags from CFP to RFP.

Materials and Methods

Drosophila strains and genetics

Fly stocks were obtained from the Bloomington Drosophila Stock Center, if not otherwise noted and genetic markers and annotations are described in FlyBase [35]. Following transgenes were used: UAS-GCaMP6-myr [21], E-Cadherin-GFP [36], E-Cadherin-mTomato [36], ubiquitin-E-Cadherin-GFP, Sqh-mCherry [26,37], UAS-GC3Ai, UAS-α-Catenin-TagRFP [23], Mat-Gal4-67,15 (D. St. Johnston, Cambridge/UK), and amnioserosa-Gal4 (Bloomington).

The allele *RhoGEF2*^{04291} [33] together with FRT$^{2R,\ G13}$ was recombined with ubiquitin-E-Cadherin-GFP. *RhoGEF2* germline clones were generated and selected with *ovo*^{D}. First- and second-instar larvae were heat-shocked twice for 60 min at 37°C.

Drosophila genotypes	Figures
w; +/+; pUAS-GCaMP6-myr;	Figs 1C, D, 6C, and EV5, Movies EV1 and EV6
w; ubiquitin-E-Cadherin::GFP; +/+;	Figs 2B, C, F, and EV1D, E, Movies EV2 and EV3
w; E-Cadherin::GFP; +/+;	Figs 2A, 3A–D, 5F, and EV2B, EV3, Movie EV4 and EV7
sqh^{AX3}*; ubiquitin-E-Cadherin::GFP, Sqh::mCherry; +/+;*	Figs 4, and 6A and B
w; pUAS-VinculinD1::GFP E-Cadherin::mTomato; +/+;	Fig 5B, Movie EV5
w; ubiquitin-E-Cadherin::GFP RhoGEF2$^{[04291]}$*, FRT*$^{[2R,\ G13]}$*; +/+*	Figs 6E and EV4E, Movie EV8
w; pUAS-α-Catenin::TagRFP; pUAS-GC3Ai;	Fig EV2A
w; Nanos-Anillin-RBD::tdTomato; +/+;	Figs 6G, and EV4F and G, Movie EV9

Cloning

VinculinD1 domain (aa6–257) (HindIII-Xho1) and eGFP (EcoR1-Xho1) were inserted between the EcoR1-Xho1 sites of a pUASt with attB sequence. PCR cloning was verified by sequencing of the fragments. pUASt-attB-VinculinD1-eGFP was inserted in chromosome II and recombined with E-Cad-mTomato. Homozygous lines were healthy and fertile.

The Rho sensor is a bicistronic cassette that contains tdTomato fused to the Rho-binding domain (RBD) from Anillin (aa748–1,239) followed by a P2A peptide and membrane marker, tdKatushka2, fused to the CAAX box from human KRAS. The utility of the Anillin-RBD for detecting regions of active Rho has been validated previously [38–40]. The Rho sensor was constructed by infusion cloning of three fragments into a Nanos cassette (Nanos promoter/5′utr and Nanos 3′utr) placed within P{valium22-(1)} tdTomato (Addgene—54653), (2) Anillin-RBD (DGRC-LD2793), and (3) p2a-tdKatushka2-caax (Addgene—56041). P2A and CAAX sequences were appended via primers. Transgenic lines were created by PhiC31 integrase-mediated transgenesis provided by BestGene at the following sites—attP2 and attP40. Homozygous lines were healthy and fertile.

Embryo preparation and injections

Embryos were prepared as previously described [41]. Briefly, embryos (2–2.5 h at 25°C in Figs 1, 2, 4A–E and 5, and 15–17 h at 20°C in Figs 3 and 4F–K) were collected and dechorionated with 50% bleach (hypochloride) for 90 s, dried in a desiccation chamber for ~ 10 min, covered with halocarbon oil, and injected dorsally into the vitelline space in the dark at room temperature (~ 22°C). After injection, the embryos were incubated at room temperature in the dark for about 10 min prior to uncaging.

NP-EGTA, AM (Invitrogen) was prepared in 1× injection solution [180 mM NaCl, 10 mM HEPES, 5 mM KCl, 1 mM $MgCl_2$ (pH 7.2)] [11]. 2 mM NP-EGTA, AM was injected for Ca^{2+} uncaging in epidermal cells, and 1 mM NP-EGTA, AM was injected for Ca^{2+} uncaging in amnioserosa cells. To inhibit Rock activity, 10 mM Y-27632 (Sigma) in water was injected.

Ca^{2+} uncaging and imaging

We employed a pulsed 355-nm YAG laser (DPSL-355/14, Rapp OptoElectonic) mounted on the epiport. We illuminated under the "Click and Fire" Mode on the "REO-SysCon-Zen" platform (Rapp OptoElectonic), while a movie was recorded via a spinning disk mounted on the side port (Zeiss ObserverZ1, 100×/oil, NA1.4, AxioCam MRm). For the images in Figs 2, 4, 5B, and EV2, EV3, the movies were recorded with an emCCD camera (Photometrics, Evolve 512) and the recording started about 20 s after Ca^{2+} uncaging. The intensity of the UV laser was adjusted so that no morphological changes were induced in 1× injection solution-injected embryos. The laser was applied for 1.5 s (around 300 pulses) per cell with 2.5% laser power (~ 0.5 mJ/cell).

The Ca^{2+} sensor GCaMP6-myr was maternally expressed with Mat-Gal4-67, 15 (Figs 1 and 6C). The cross-sectional images were recorded in GFP channel with a frame rate of 1/s. Ca^{2+} uncaging was applied during recording. Control experiments were conducted in embryos injected without NP-EGTA, AM but exposure to a similar UV laser pulse. To test Ca^{2+} uncaging with a 405-nm cw laser, the cross-sectional images were recorded in GFP channel with a frame rate of 0.2/s from the stage 7 embryo injected with NP-EGTA, AM and point scan illumination similar to FRAP bleaching was used for Ca^{2+} uncaging (Fig EV5).

E-Cad-GFP was the membrane marker for analysis of the cell dynamics after Ca^{2+} uncaging in epithelium. For the images in Figs 2, and EV2B and EV3, after uncaging, axial stacks of 3–4 images with 0.5 μm step size were recording in the GFP channel with frame rates of 0.2/s (Fig 2B–E) or 0.1/s (Figs 2F and G, and EV2B and EV3) with an emCCD camera (Photometrics, Evolve 512). The recording started about 20 s after Ca^{2+} uncaging. For the images in Figs 3, 6E, F, and EV1D, E, EV3A, B, the cross-sectional images were recorded in the GFP channel with a frame rate of 0.2/s. Ca^{2+} uncaging was applied during recording.

To analyze myosin dynamics after Ca^{2+} uncaging (Fig 4A and B), the GFP and mCherry channels were recorded simultaneously with a frame rate of 0.1/s for E-Cad-GFP and Sqh-mCherry. After uncaging, axial stacks of 3–4 images with 1 μm step size were recorded with an emCCD camera (Photometrics, Evolve 512). The recording started about 20 s after Ca^{2+} uncaging. Control experiments were conducted in embryos injected without NP-EGTA, AM but exposed with a comparable UV pulse.

VinculinD1-GFP was expressed under control of the AS-Gal4 driver in amnioserosa tissue. To analyze VinculinD1-GFP dynamics after Ca^{2+} uncaging (Fig 5A–E), GFP and mTomato channels were recorded simultaneously with a frame rate of 0.1/s with an emCCD camera (Photometrics, Evolve 512). The apical side of the amnioserosa tissue was acquired with four axial sections of 0.5 μm. The recording started about 20 s after Ca^{2+} uncaging.

α-Catenin-RFP and apoptosensor were expressed under control of the driver AS-Gal4 in the amnioserosa (Fig EV3A). Stage 14 embryos were collected and injected with 1 mM NP-EGTA. The Ca^{2+} uncaging was conducted in embryos expressing both α-Catenin-RFP and apoptosensor. After uncaging, axial stacks (10 images, 1 μm step size, GFP, and RFP channels) were recorded with a frame rate of 0.1/s on a spinning disk microscope (100×/oil, NA1.4) with an emCCD camera (Photometrics, Evolve 512). The recording started about 20 s after Ca^{2+} uncaging.

The Rho sensor was recorded in the GFP channel with a frame rate of 0.2/s (Fig 6G and J). Ca^{2+} uncaging was applied during recording. In Fig EV4F, axial stacks of 11 images with 0.5 μm step size were recording from an embryo undergoing cellularization with an emCCD camera (Photometrics, Evolve 512). In Fig EV4G, the cross-sectional images were recorded in the GFP channel with a frame rate of 0.2/s from a stage 8 embryo with an emCCD camera (Photometrics, Evolve 512).

In Fig 5A and B, embryos expressing sqh-mCherry and E-Cad-GFP were injected with water or 10 mM Y-27632, GFP, and mCherry channels were recorded simultaneously on a spinning disk microscope (Zeiss, 100×/oil, NA1.4) with an emCCD camera (Photometrics, Evolve 512). The apical planes of the embryo with four axial sections of 0.5 μm were acquired.

Histology

Embryos were fixed, stained, and mounted as previously described [42]. Antibodies against the following antigens were used: Dlg (mouse, 0.4 μg/ml) [43], Arm (mouse M7A1, 0.4 μg/ml) [44], and Slam (rabbit, 1:5,000) [45]. Secondary antibodies were labeled with Alexa dyes (Invitrogen, 0.4 μg/ml). GFP booster labeled with ATTO488 (ChromoTek, 1:500) was used for E-Cad-GFP.

Laser ablation

Stage 14 embryos expressing E-Cad-GFP were injected with 1 mM NP-EGTA, AM. Cross-sectional images were recorded in the GFP channel with a frame rate of 1/s from amnioserosa on a spinning disk microscope (100×/oil, NA1.4) with a CCD camera. Ca^{2+} uncaging was applied during recording. After the target cell started to contract, the 1st neighboring junction was ablated with the 10% of laser power, and 200 ms (around 40 pulses) exposure time during the recording mode (100× oil, NA 1.4) (Fig 5F). The control ablation was performed in the embryos injected with buffer without NP-EGTA, AM but exposed to the uncaging laser pulse. The junctions were selected randomly for ablation. The recoil velocity was calculated from the displacement of both ends of ablated junctions during the first 2 s.

Image processing and analysis

The fluorescence intensity of GCaMP6-myr (Figs 1 and 6D) was measured manually with ImageJ/Fiji [46]. The integrated density (a.u.) was measured along the cell membrane and divided by the cell membrane length (μm) to get the mean fluorescence intensity I_t. The background I_b was determined from the integrated density (a.u.), which was measured from the cytoplasm and divided by the measurement length (μm). The normalized GCaMP6-myr intensity fold increase was calculated as follows:

$$F/F_0 = (I_t - I_b)/(I_{-1} - I_{-1b})$$

where I_t is the mean intensity at time t, I_b is the mean intensity of the background at time t, I_{-1} is the mean intensity at 1-s before UV illumination, and I_{-1b} is the mean intensity of the background at 1 s before UV illumination.

To analyze cell dynamics after Ca^{2+} uncaging, image stacks were projected by the "Max Intensity" option. The projected and cross-sectional images were segmented and tracked with "Tissue Analyzer" [47] in ImageJ/Fiji. Cell area measurements were carried out with ImageJ/Fiji. In Movie EV3, the Z-projected images were stabilized with "Image Stabilizer" [48].

To analyze myosin dynamics after Ca^{2+} uncaging (Fig 4), the image stacks from sqh-mCherry embryos were projected with the "Max Intensity" option. Mean medio-apical Sqh-mCherry fluorescence intensity was measured manually with ImageJ and normalized with the initial fluorescence ($t = 0$).

To analyze Rho sensor dynamics, the fluorescence intensity of Rho sensor (Fig 6J) was measured manually with ImageJ/Fiji. The integrated intensity (a.u.) was measured along the cell membrane and divided by the cell membrane length (μm) to get the mean fluorescence intensity I_t. The background I_{bt} represents the averaged fluorescence intensity (a.u.) within the cytoplasm. The normalized Rho sensor intensity was calculated as follows: $I = I_t/I_{bt}$.

The ratio of VincuinD1-GFP/E-cadherin-mTomato (Fig 5C) was generated by plugin "Ratio plus" in ImageJ/Fiji. The fluorescence intensity was measured along cell junctions and normalized to the initial fluorescence ($t = 0$). To analyze VinculinD1 and E-Cadherin dynamics, the fluorescence intensity of VinculinD1-GFP (in Fig EV4B) at cell junctions was measured manually with ImageJ/Fiji. The fluorescence intensity was measured along cell junctions and normalized to the initial fluorescence ($t = 0$).

Expanded View for this article is available online.

Acknowledgements
We are grateful to Marion Silies, Stefan Luschnig, Adam Martin, Daniel St Johnston, and Magali Suzanne for materials. Stocks obtained from the Bloomington Drosophila Stock Center (NIH P40OD018537) were used in this study. BL is a New York Stem Cell Foundation—Druckenmiller Fellow. This work was in part supported by the Göttingen Centre for Molecular Biology (funds for equipment repair) and the Deutsche Forschungsgemeinschaft (DFG, FOR1756 GR1945/6-1/2, SFB937/TP10, and equipment grant INST1525/16-1 FUGG).

Author contributions
DK conducted the experiments and analyzed the data. ZL generated the VinculinD1-GFP transgenic fly and analyzed the VinculinD1-GFP data. MH analyzed data and obtained in Figs 2E, 3E–G, 4E, and 5G. BL generated the Rho sensor transgenic fly. DK, FW, and JG conceived the study and wrote the manuscript. FW and JG supervised the study.

Conflict of interest
The authors declare that they have no conflict of interest.

References

1. Bertet C, Sulak L, Lecuit T (2004) Myosin-dependent junction remodelling controls planar cell intercalation and axis elongation. *Nature* 429: 667 – 671
2. Blankenship JT, Backovic ST, Sanny JSP, Weitz O, Zallen JA (2006) Multicellular rosette formation links planar cell polarity to tissue morphogenesis. *Dev Cell* 11: 459 – 470
3. Heisenberg C-P, Bellache Y (2013) Forces in tissue morphogenesis and patterning. *Cell* 153: 948 – 962
4. Martin AC, Goldstein B (2014) Apical constriction: themes and variations on a cellular mechanism driving morphogenesis. *Development* 141: 1987 – 1998
5. Hoffman BD, Yap AS (2015) Towards a dynamic understanding of cadherin-based mechanobiology. *Trends Cell Biol* 25: 803 – 814
6. Guglielmi G, Barry JD, Huber W, De Renzis S (2015) An optogenetic method to modulate cell contractility during tissue morphogenesis. *Dev Cell* 35: 646 – 660
7. Valon L, Marín-Llauradó A, Wyatt T, Charras G, Trepat X (2017) Optogenetic control of cellular forces and mechanotransduction. *Nat Commun* 8: 14396
8. Oakes PW, Wagner E, Brand CA, Probst D, Linke M, Schwarz US, Glotzer M, Gardel ML (2017) Optogenetic control of RhoA reveals zyxin-mediated elasticity of stress fibres. *Nat Commun* 8: 15817
9. Fehrentz T, Schönberger M, Trauner D (2011) Optochemical genetics. *Angew Chem Int Ed* 50: 12156 – 12182
10. Lee HC, Auersperg N (1980) Calcium in epithelial cell contraction. *J Cell Biol* 85: 325 – 336
11. Hunter GL, Crawford JM, Genkins JZ, Kiehart DP (2014) Ion channels contribute to the regulation of cell sheet forces during *Drosophila* dorsal closure. *Development* 141: 325 – 334
12. Lee H, Nagele RG (1986) Toxic and teratologic effects of verapamil on early chick embryos: evidence for the involvement of calcium in neural tube closure. *Teratology* 33: 203 – 211
13. Smedley MJ, Stanisstreet M (1986) Calcium and neurulation in mammalian embryos. II. Effects of cytoskeletal inhibitors and calcium antagonists on the neural folds of rat embryos. *J Embryol Exp Morphol* 93: 167 – 178
14. Ferreira MC, Hilfer SR (1993) Calcium regulation of neural fold formation: visualization of the actin cytoskeleton in living chick embryos. *Dev Biol* 159: 427 – 440
15. He L, Wang X, Tang HL, Montell DJ (2010) Tissue elongation requires oscillating contractions of a basal actomyosin network. *Nat Cell Biol* 12: 1133 – 1142
16. Suzuki M, Sato M, Koyama H, Hara Y, Hayashi K, Yasue N, Imamura H, Fujimori T, Nagai T, Campbell RE *et al* (2017) Distinct intracellular Ca (2+) dynamics regulate apical constriction and differentially contribute to neural tube closure. *Development* 144: 1307 – 1316
17. Heinemann C, Chow RH, Neher E, Zucker RS (1994) Kinetics of the secretory response in bovine chromaffin cells following flash photolysis of caged Ca^{2+}. *Biophys J* 67: 2546 – 2557
18. Ellis-Davies GCR (2008) Neurobiology with caged calcium. *Chem Rev* 108: 1603 – 1613
19. Ellis-Davies GC, Kaplan JH (1994) Nitrophenyl-EGTA, a photolabile chelator that selectively binds Ca^{2+} with high affinity and releases it rapidly upon photolysis. *Proc Natl Acad Sci USA* 91: 187 – 191
20. Schneggenburger R, Neher E (2000) Intracellular calcium dependence of transmitter release rates at a fast central synapse. *Nature* 406: 889 – 893
21. Chen T-W, Wardill TJ, Sun Y, Pulver SR, Renninger SL, Baohan A, Schreiter ER, Kerr RA, Orger MB, Jayaraman V *et al* (2013) Ultrasensitive fluorescent proteins for imaging neuronal activity. *Nature* 499: 295 – 300
22. Delaney KR, Shahrezaei V (2013) Uncaging calcium in neurons. *Cold Spring Harb Protoc* 2013: 1115 – 1124
23. Schott S, Ambrosini A, Barbaste A, Benassayag C, Gracia M, Proag A, Rayer M, Monier B, Suzanne M (2017) A fluorescent toolkit for

spatiotemporal tracking of apoptotic cells in living *Drosophila* tissues. *Development* 144: 3840 – 3846

24. Gracia M, Theis S, Proag A, Gay G, Benassayag C, Suzanne M (2019) Mechanical impact of epithelial-mesenchymal transition on epithelial morphogenesis in *Drosophila*. *Nat Commun* 10: 2951
25. Vicente-Manzanares M, Ma X, Adelstein RS, Horwitz AR (2009) Non-muscle myosin II takes centre stage in cell adhesion and migration. *Nat Rev Mol Cell Biol* 10: 778 – 790
26. Martin AC, Kaschube M, Wieschaus EF (2009) Pulsed contractions of an actin-myosin network drive apical constriction. *Nature* 457: 495 – 499
27. Choi H-J, Pokutta S, Cadwell GW, Bobkov AA, Bankston LA, Liddington RC, Weis WI (2012) αE-catenin is an autoinhibited molecule that coactivates vinculin. *Proc Natl Acad Sci USA* 109: 8576 – 8581
28. Rangarajan ES, Izard T (2012) The cytoskeletal protein α-catenin unfurls upon binding to vinculin. *J Biol Chem* 287: 18492 – 18499
29. Yao M, Qiu W, Liu R, Efremov AK, Cong P, Seddiki R, Payre M, Lim CT, Ladoux B, Mège R-M *et al* (2014) Force-dependent conformational switch of α-catenin controls vinculin binding. *Nat Commun* 5: 4525
30. Ishiyama N, Sarpal R, Wood MN, Barrick SK, Nishikawa T, Hayashi H, Kobb AB, Flozak AS, Yemelyanov A, Fernandez-Gonzalez R *et al* (2018) Force-dependent allostery of the α-catenin actin-binding domain controls adherens junction dynamics and functions. *Nat Commun* 9: 5121
31. Kale GR, Yang X, Philippe J-M, Mani M, Lenne P-F, Lecuit T (2018) Distinct contributions of tensile and shear stress on E-cadherin levels during morphogenesis. *Nat Commun* 9: 5021
32. Uehata M, Ishizaki T, Satoh H, Ono T, Kawahara T, Morishita T, Tamakawa H, Yamagami K, Inui J, Maekawa M *et al* (1997) Calcium sensitization of smooth muscle mediated by a Rho-associated protein kinase in hypertension. *Nature* 389: 990 – 994
33. Großhans J, Wenzl C, Herz H-M, Bartoszewski S, Schnorrer F, Vogt N, Schwarz H, Müller HA (2005) RhoGEF2 and the formin Dia control the formation of the furrow canal by directed actin assembly during *Drosophila* cellularisation. *Development* 132: 1009 – 1020
34. Somlyo AP, Somlyo AV (2003) Ca^{2+} sensitivity of smooth muscle and nonmuscle myosin II: modulated by G proteins, kinases, and myosin phosphatase. *Physiol Rev* 83: 1325 – 1358
35. Gramates LS, Marygold SJ, Santos GD, Urbano J-M, Antonazzo G, Matthews BB, Rey AJ, Tabone CJ, Crosby MA, Emmert DB *et al* (2017) FlyBase at 25: looking to the future. *Nucleic Acids Res* 45: D663 – D671
36. Huang J, Zhou W, Dong W, Watson AM, Hong Y (2009) Directed, efficient, and versatile modifications of the *Drosophila* genome by genomic engineering. *Proc Natl Acad Sci USA* 106: 8284 – 8289
37. Oda H, Tsukita S (2001) Real-time imaging of cell-cell adherens junctions reveals that *Drosophila* mesoderm invagination begins with two phases of apical constriction of cells. *J Cell Sci* 114: 493 – 501
38. Piekny AJ, Glotzer M (2008) Anillin is a scaffold protein that links RhoA, actin, and myosin during cytokinesis. *Curr Biol* 18: 30 – 36
39. Munjal A, Philippe J-M, Munro E, Lecuit T (2015) A self-organized biomechanical network drives shape changes during tissue morphogenesis. *Nature* 524: 351 – 355
40. Priya R, Gomez GA, Budnar S, Verma S, Cox HL, Hamilton NA, Yap AS (2015) Feedback regulation through myosin II confers robustness on RhoA signalling at E-cadherin junctions. *Nat Cell Biol* 17: 1282 – 1293
41. Kanesaki T, Edwards CM, Schwarz US, Großhans J (2011) Dynamic ordering of nuclei in syncytial embryos: a quantitative analysis of the role of cytoskeletal networks. *Integr Biol (Camb)* 3: 1112 – 1119
42. Zhang Y, Kong D, Reichl L, Vogt N, Wolf F, Großhans J (2014) The glucosyltransferase Xiantuan of the endoplasmic reticulum specifically affects E-Cadherin expression and is required for gastrulation movements in *Drosophila*. *Dev Biol* 390: 208 – 220
43. Parnas D, Haghighi AP, Fetter RD, Kim SW, Goodman CS (2001) Regulation of postsynaptic structure and protein localization by the Rho-type guanine nucleotide exchange factor dPix. *Neuron* 32: 415 – 424
44. Riggleman B, Schedl P, Wieschaus E (1990) Spatial expression of the *Drosophila* segment polarity gene armadillo is posttranscriptionally regulated by wingless. *Cell* 63: 549 – 560
45. Yan S, Acharya S, Gröning S, Großhans J (2017) Slam protein dictates subcellular localization and translation of its own mRNA. *PLoS Biol* 15: e2003315
46. Schindelin J, Arganda-Carreras I, Frise E, Kaynig V, Longair M, Pietzsch T, Preibisch S, Rueden C, Saalfeld S, Schmid B *et al* (2012) Fiji: an open-source platform for biological-image analysis. *Nat Methods* 9: 676 – 682
47. Aigouy B, Umetsu D, Eaton S (2016) Segmentation and quantitative analysis of epithelial tissues. *Methods Mol Biol* 1478: 227 – 239
48. Li K (2008) The image stabilizer plugin for ImageJ. http://www.cs.cmu.edu/~kangli/code/Image_Stabilizer.html

Expanded View Figures

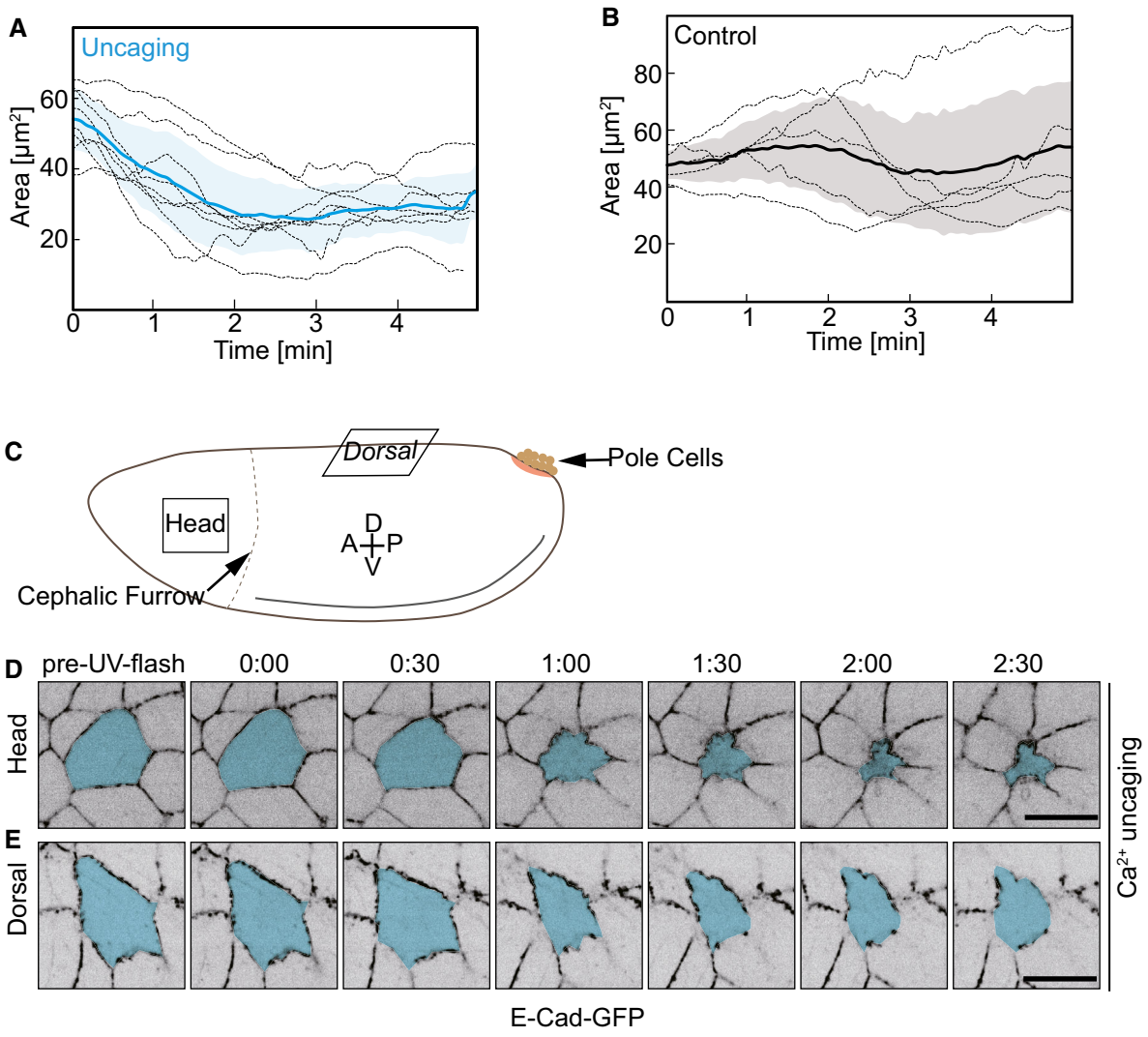

Figure EV1. Cell contraction following CaLM in epithelium.

A, B Cross-sectional cell areas of individual target cells (dashed lines) following a UV laser pulse. (A) Embryos injected with 2 mM NP-EGTA, AM (n = 8 cells in eight embryos). (B) Embryos injected with buffer (n = 5 cells in five embryos). Mean (bold line) with standard deviation of the mean (ribbon).

C Schematic drawing of an embryo shows the head and dorsal region where CaLM was performed.

D, E Images from a time-lapse recording embryos expressing E-Cad-GFP and injected with 2 mM NP-EGTA, AM following with Ca^{2+} uncaging in head (B) or dorsal (C) region. Target cells are labeled in blue.

Data information: Scale bars: 10 µm in (D, E).

Figure EV2. CaLM does not induce apoptosis.

A Images from embryos express α-Catenin-RFP and apoptosensor. Two blue dotted boxes indicate the apoptotic cells. A yellow dotted box indicates the selected cell where CaLM was performed in the same embryos.

B Images of amnioserosa cells from two time-lapse recordings in embryos (stage 14) expressing E-Cad-GFP and injected with 1 mM NP-EGTA, AM followed by UV illumination showing long-term behavior after uncaging. The target cells for CaLM are highlighted in magenta.

C Cross-sectional area of target cells over 30 min after Ca^{2+} uncaging. Cell contraction in 1 out of 3 target cells was reversible in 10 min.

Data information: Scale bars: 10 µm in (A, B).

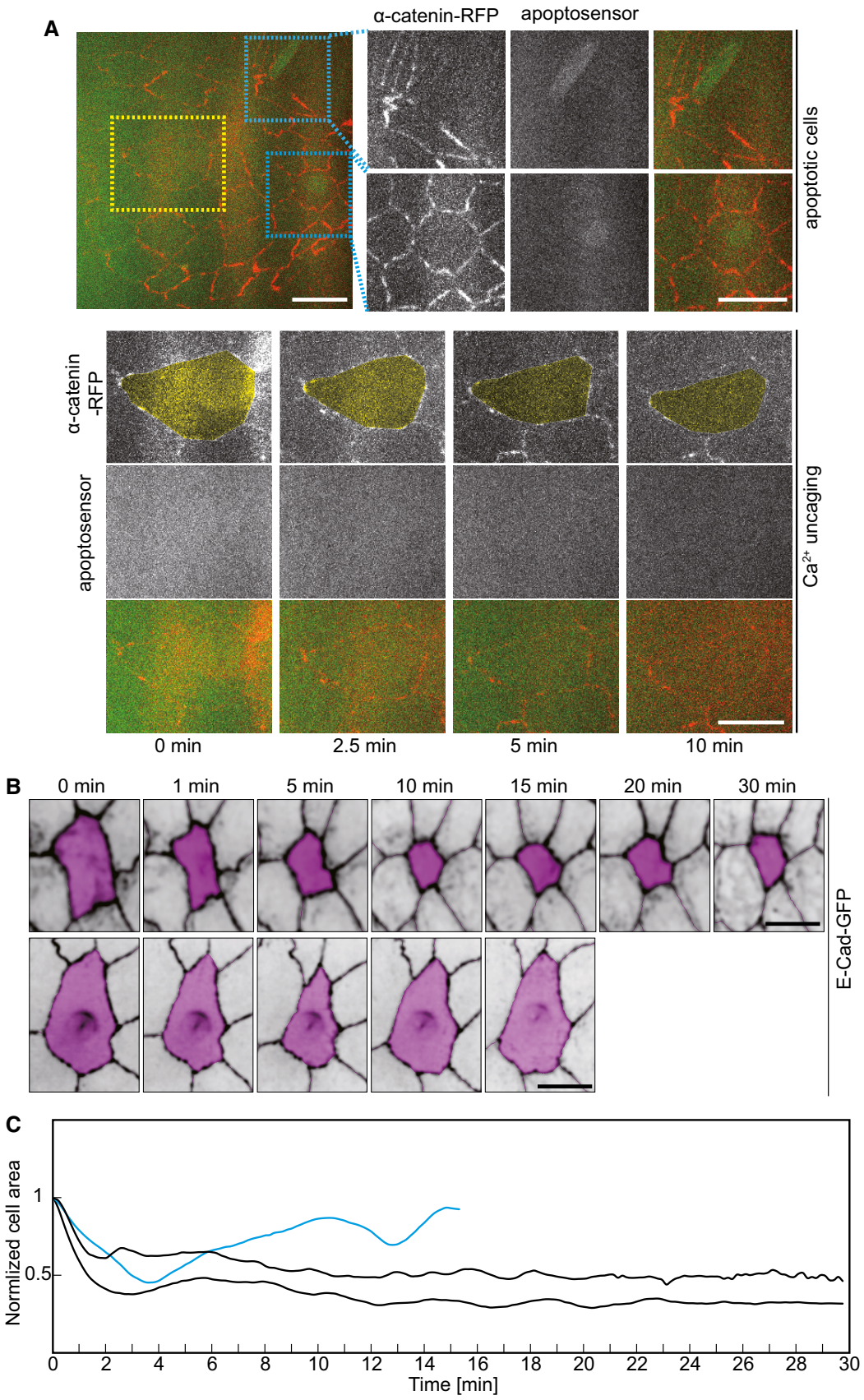

Figure EV2.

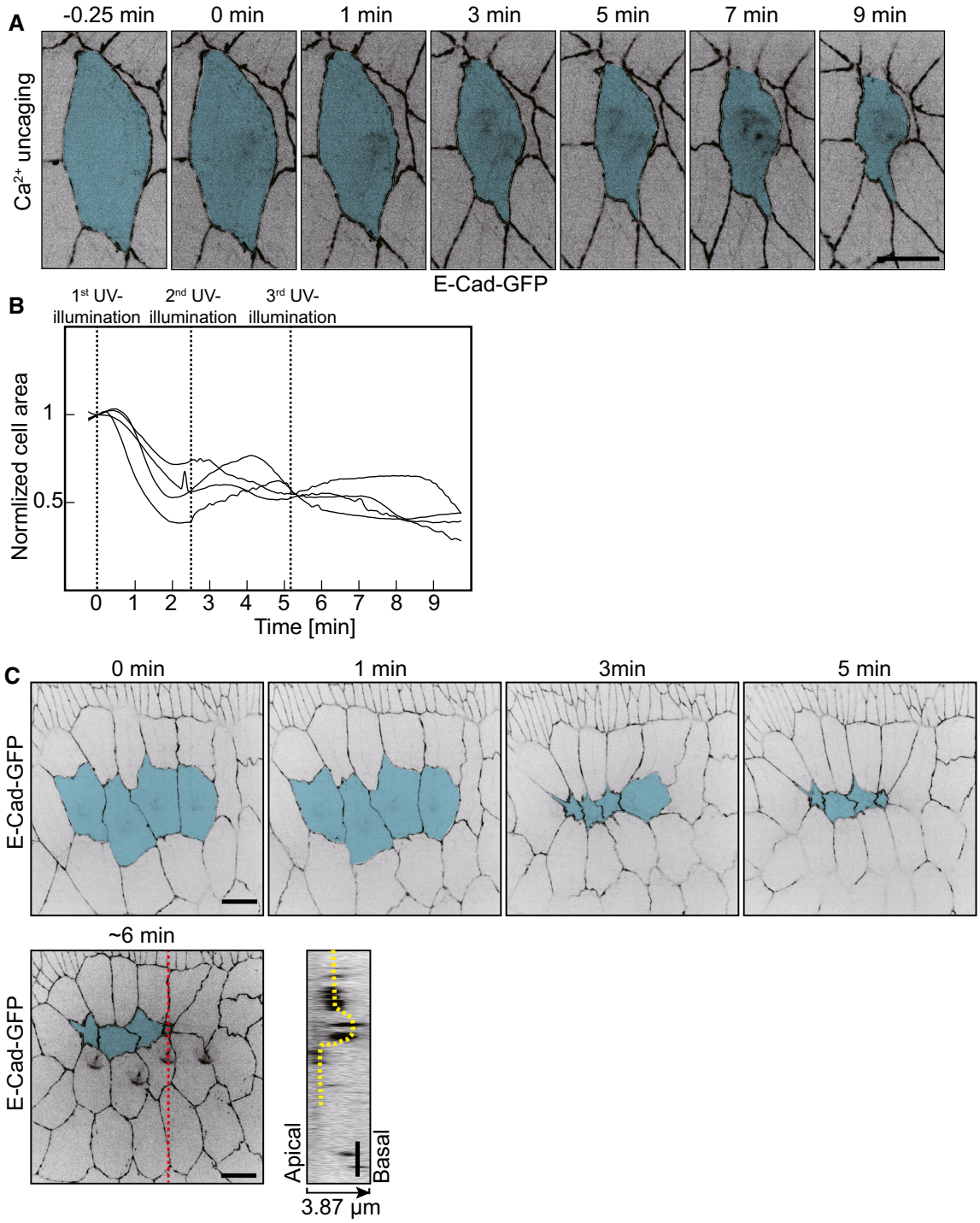

Figure EV3. Cell contraction following CaLM in amnioserosa.

A Images of amnioserosa from time-lapse recording in embryos (stage 14) expressing E-Cad-GFP and injected with 1 mM NP-EGTA, AM following with three times UV illumination (0, 2.5 and 5 min). Target cell is highlighted in blue.

B Cross-sectional cell areas of four individual target amnioserosa cells from the embryos injected with 1 mM NP-EGTA, AM following three times UV laser pulses. Cell area was normalized with the initial size (the first frame of recording after 1st UV illumination). The time points of UV laser pulses are indicated.

C CaLM triggers multiple cell constriction simultaneously in amnioserosa. Images of amnioserosa from a time-lapse recording in embryos (stage 14) expressing E-Cad-GFP and injected with 1 mM NP-EGTA, AM following with UV illumination. The target cells are highlighted in blue. An orthogonal view shows an invagination (yellow dash line) is induced by Ca^{2+} uncaging triggered contraction. The red dash line indicates the region of orthogonal view.

Data information: Scale bars: 10 μm in (A, C).

Figure EV4. VinculinD1 reporter, Rock inhibitor, *RhoGEF2* mutant, and Rho sensor.

A Scheme of the domain structure of Vinculin. Numbers indicate position of amino acid residues. Transgenic construct with the D1 domain (blue) fused to GFP and expressed under GAL4/UAS control.

B VinculinD1-GFP fluorescence on cell junctions of target and control cells (n = 6 target cells and 6 control cell borders). Mean (bold line) with standard deviation of the mean (ribbon band).

C Scatter plot of normalized cross-sectional area with normalized VinculinD1-GFP intensity in target cells.

D The Rock inhibitor inhibits Ca^{2+}-induced constriction. Cross-sectional areas of eight individual target cells following CaLM in Y-27632 co-injected embryos.

E A confocal cross-sectional image from a *RhoGEF2* germline clone embryo expressing E-Cadherin-GFP shows the characteristic phenotype of multinucleated cells during cellularization. The red asterisks indicate multinucleated cells.

F Axial image stack of an embryo during cellularization showing the functionality of the Rho sensor.

G Images from time-lapse recording of an embryos expressing the Rho sensor. Cells in cytokinesis. Stage 8. Lateral epidermis.

Data information: Scale bar: 10 μm in (B, E, F, G).

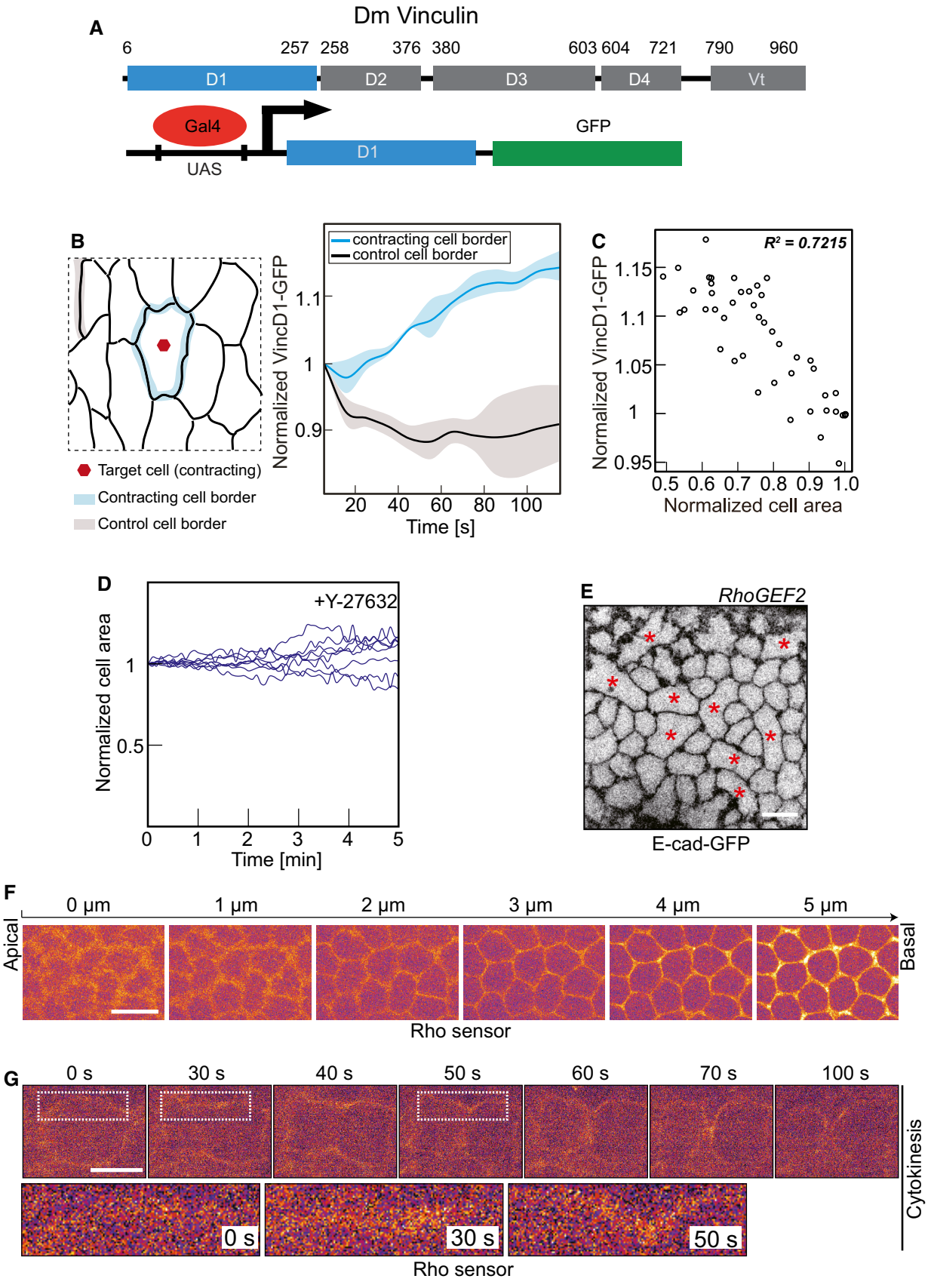

Figure EV4.

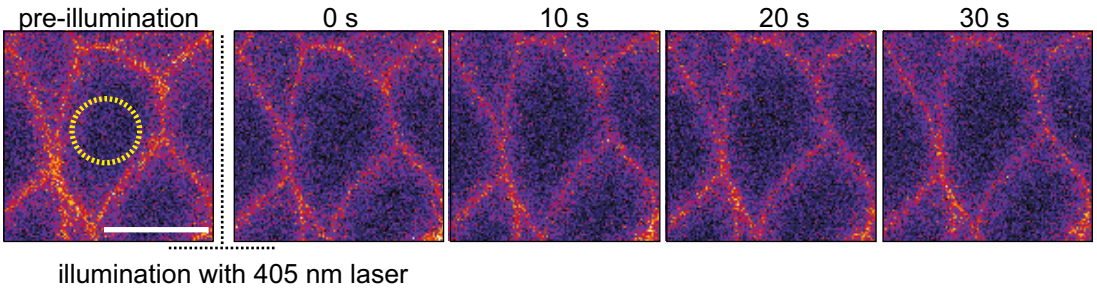

Figure EV5. No increased signal of the GCaMP reporter after illumination by 405-nm laser in single individual cells.
Images from time-lapse recording of embryos (stage 7, lateral epidermis) expressing a membrane-bound Ca^{2+} sensor (GCaMP6-myr) and injected with 2 mM NP-EGTA, AM. Target cells were exposed to a 405-nm cw laser.

Data information: Scale bars: 10 μm.

Chapter 4

Automated biomedical image processing using deep neural networks

"A method is more important than a discovery, since the right method will lead to new and even more important discoveries."

Lev Landau

4.1 Content

Biomedical image processing nowadays is one of the bottlenecks for data generation in biology and medical research. In this regard, it has replaced technological limitations in the microscopy field which are able to provide 3D time-lapse movies of *Drosophila* embryos with single cell resolution. For such huge datasets manual data acquisition is not feasible. Therefore there is a great need for automated tools that accurately and efficiently perform segmentation and analysis tasks.

I contribute to this field by applying deep learning methods, concretely generative adversarial networks, to the segmentation of epithelial tissues. Our method can be trained even in absence of labeled ground truth training data, which constitutes an important bottleneck in the training of neural networks.

The deep learning method is embedded in an automated segmentation pipeline, which also allows to manually correct segmentation errors. Data from the segmented tissue is parsed to SQL tables and the data is further analyzed by custom Python scripts. In principle, this technique is able to perform segmentation in real time and could therefore be applied in real time experimental setups to analyze data on the fly or automate secondary experimental procedures.

The innovation of this study lies in the transfer of deep neural network methods to the biomedical image processing field. The possibility to use unpaired training data makes this method widely applicable and easier to generalize compared to direct competitors that mainly use supervised discriminative architectures, which require paired ground truth training data. For the actual task at hand, the segmentation of epithelial cell borders, there is no significant difference in segmentation accuracy between our method and a standard classification network, the U-Net [281], that requires paired training data and has been designed for the purpose of biomedical image segmentation.

Basics of biomedical image segmentation have been reviewed in the introduction section 2.14. The results of this chapter are applied in chapters 6 and 7 to segment and analyze recordings of epithelial tissue.

4.2 Deep learning in a nutshell

This section is contains a brief overview of deep learning core concepts. The interested reader may find more information in the literature, for example in the fantastic "Deep learning book" by Goodfellow, Bengio and Courville [143].

Deep learning takes inspiration from biological neuronal dynamics. Single units, the neurons, are receiving input from one or many sources, do a computation and produce an output which is submitted to neurons in the next layer. Figure 4.1 illustrates the concept.

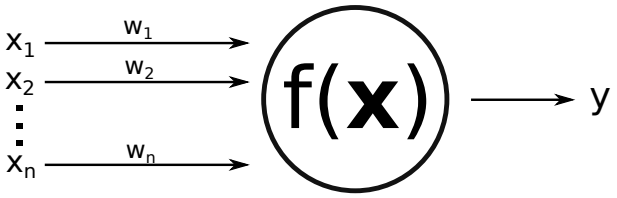

Figure 4.1: Scheme of neuron computation principle. Inputs are weighted and summed to yield an outcome y. Usually, regularization functions are additionally applied e.g. to confine the output to positive values.

The inputs x_i of each neuron are weighted according to weights w_i and usually summed up. In order to produce an output y of the same order as other neurons in the previous layer, a regularization is used, which is also called activation function, inspired by neuroscience. Often utilized examples are sigmoid, or ReLU (rectified linear) functions. Using a sigmoid activation, the output y would then be

$$y = \frac{1}{1 + e^{-z}} \tag{4.1}$$

$$z = \sum_{i=1}^{N} w_i \, x_i \tag{4.2}$$

where N is the total number of inputs to the neuron.

Single units are then combined into a network, where the presence of more than one hidden layer defines the term "deep" neural networks. Generalizing this idea of an isolated neuron, and considering the jth neuron in the kth layer of a graph, we obtain

$$y_j^{(k)} = f\left(\sum_{(i,j)} w_{ij}^{(k)} \, x_{ij}^{(k)} + b_j^{(k)} \right) \tag{4.3}$$

whereas $y_j^{(k)}$ denotes the output and i is the index of a neuron in the $(k-1)$th layer. The sum runs over all tuples (i, j). $b_j^{(k)}$ is a bias, however since it is only additive, it is also possible to extend each layer by a single bias neuron which summarizes all individual biases.

Free parameters in this network are the weights $w_{ij}^{(k)}$ and the bias $b_j^{(k)}$. During learning, these parameters are optimized.

The great advantage of deep learning, and machine learning in general, is that no specific algorithm has to be programmed but instead the network is able to "learn" a certain task.

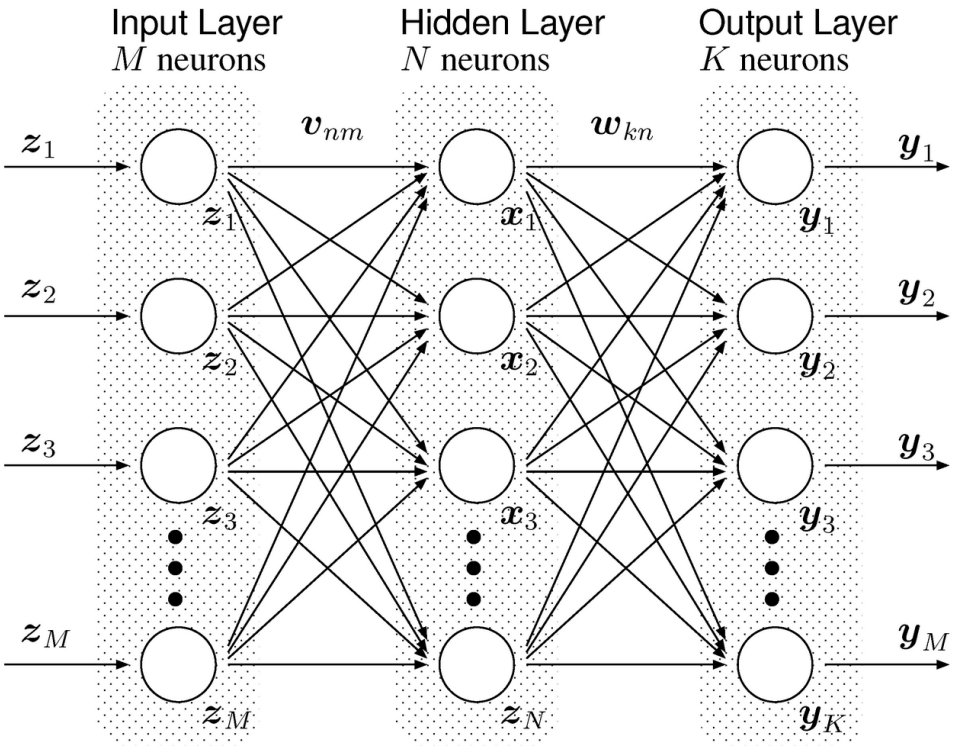

Figure 4.2: Scheme of multilayered network. Single units of the network, called neurons, are connected in between layers by weights v_{nm} and w_{kn}. Each layer can have a different amount of neurons. Figure taken from [145].

Learning means that the free parameters of the networks, mainly the weights, are adjusted such that a specific output is yielded. To this end a cost, or objective function, has to be defined. A simple example would be a binary classifier. The output of the network is a number 0 or 1, for example the task could be to detect whether a human is in an image or not. The image is fed into the network and an output is produced. If there is no human in the picture but the network had 1 as output, all the weights are adjusted. This is done via backpropagation.

A simple error function would be

$$E = \frac{1}{2}\sum_n (T^n - y^n)^2 \tag{4.4}$$

where T^n denotes the nth sample from the training set, which is compared with the output y of the network.

To figure out in which direction the weights have to be changed to minimize the error, the gradient of the error has to be calculated.

$$\frac{\partial E}{\partial w_i} = \sum_n \frac{\partial E}{\partial y^n}\frac{\partial y^n}{\partial w_i} \tag{4.5}$$

According to the gradient the weights at each layer can be adjusted step by step, which is called backpropagation. If the gradient can be calculated analytically the numerical costs of training for neural networks is quite low because they can be reduced to simple matrix operations. This allows the construction of networks with millions of weights that can be adjusted during training.

There are many possible optimization procedures for the learning. Among the most popular are stochastic gradient descent [283] and ADAM [170]. For different types of networks different

Figure 4.3: Demonstration of style transfer. Left is the original image and to the right it is in painting style generated by a deep neural network. The inset shows the original painting where the style was taken from. Scheme adapted from [96].

optimization protocols may be advantageous. For example in the case of generative adversarial networks (GAN) consensus optimization has be demonstrated to have robust convergence for multimodal problems where other algorithms may fail [222].

4.3 Idea: style transfer instead of classification

Segmentation is the task to separate an image into distinct labels for features of interest. The aim of this chapter is to create a segmentation pipeline for the automated segmentation of epithelial tissues. Therefore, the background information has to be separated from the labels of cell borders. If the cell borders are clearly segmented, other quantities, for example cell area, can be computed easily.

If deep learning methods are used for segmentation, people often refer to classification algorithms [281]. The output is a feature map of the different labels, for example a binary image which include the label 1 at the pixels of the borders and 0 for background. This approach works well but often has to be trained with corresponding ground truth data.

An alternative to classification can be the use of so-called style transfer. It has been shown that deep neural networks can separate the image information from the style information. If this is possible, then the network can take the image information and apply a different style. For example Figure 4.3 shows an image of several houses which are translated into the style of several artists [96].

The segmentation of an image can also be understood in terms of style transfer. The segmentation style is the label corresponding to the objects in the original image. In the following sections I lay out the approach we used, which is based on cycle-consistent generative adversarial networks.

4.4 Generative adversarial networks

A generative adversarial network (GAN) [102] is a deep learning architecture designed to estimate generative models, a class of models that estimates the probability distribution $p(x)$ from available data x. Many generative models, like variational autoencoders [220], are explicit density models, which means that they use maximum likelihood estimation via an explicit definition

of the density function and hence require some form of, possibly uninformative, prior knowledge. GANs on the other hand belong to the class of implicit density models [103]. The GAN principle is shown in Figure 4.4.

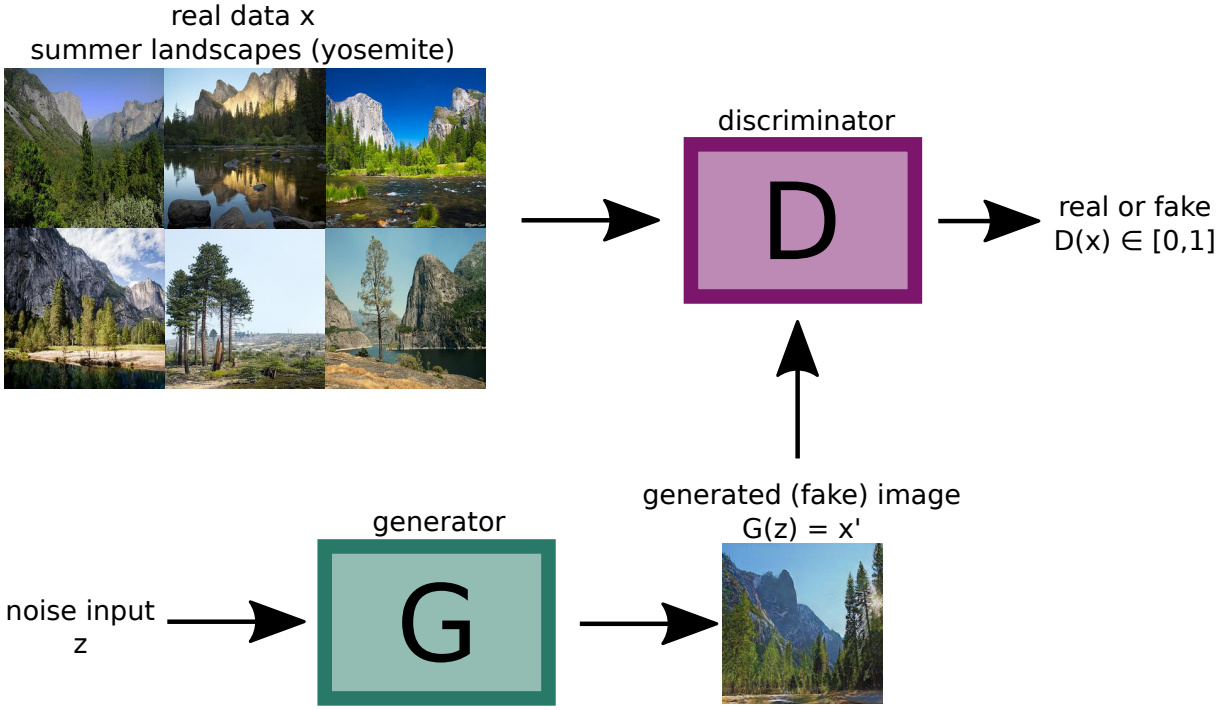

Figure 4.4: GAN principle: Two neural networks are set up in a minimax game against each other. The generator tries to create faithful samples that could come from the training data distribution. The discriminator is learning to find out if an image comes from the real data set or is a fake that was generated. Now the generator tries to fool the discriminator into believing that the generated images are real, while the generator is trying to detect the fakes.

The innovation lies in the way the objective function is formulated as a minimax game between two networks. The first network, called generator G, estimates the probability distribution from the data and the second network, the discriminator D, is learning to estimate the probability that a sample is coming from the training data rather than G. These networks are setup in an adversarial game. Hereby the generator tries to fool the discriminator into believing that its generated fake sample comes from the training data. The discriminator is optimized to recognize real samples from training data and fake samples from the generator. In a game theoretic sense, the game is designed such that in the Nash equilibrium [233], the generator recovers the probability distribution of the training data.

GANs are among the most popular deep learning architectures and many variants exist. They are thought to produce highly believable samples of very complex probability distributions, for example human faces. Compared to other popular generative models, like variational autoencoders, samples look generally more believable but the drawback is that GANs are theoretically less understood and have problems with mode collapse and overfitting. In addition, it is not clear how learning can be interpreted.

The objective function (cost function) of GANs reads

$$\min_G \max_D V(D,G) = \mathbb{E}_{x\sim p_{data}(x)}[\log D(x)] + \mathbb{E}_{z\sim p_z(z)}[\log(1 - D(G(z)))] \tag{4.6}$$

Here, x is coming from the training data and z is a latent random vector with distribution $p_z(z)$. $D(x)$ is the probability that the sample comes from the training data, hence $D : x \to [0, 1]$.

If G is fixed, the optimal discriminator is given by

$$D_G^*(x) = \frac{p_{data}(x)}{p_{data}(x) + p_g(x)} \tag{4.7}$$

which can be seen by maximizing (4.6). First we write out the expectation and use the generator distribution $p_g(x)$ explicitly.

$$V(D, G) = \int_x p_{data}(x) \log D(x) \mathrm{d}x + \int_z p_z(z) \log(1 - D(g(z))) \mathrm{d}z \tag{4.8}$$

$$= \int_x p_{data}(x) \log D(x) + p_g(x) \log(1 - D(x)) \mathrm{d}x \tag{4.9}$$

Then the function

$$f(y) = a \log(y) + b \log(1 - y) \tag{4.10}$$

has its maximum in $[0, 1]$ at $\frac{a}{a+b}$ □ [102].

It can be seen that the objective function of GANs is connected to maximizing the log-likelihood. Therefore we rewrite the minimax game, using the optimal discriminator $D_G^*(x)$ for fixed G

$$C(G) = \max_D V(D, G) \tag{4.11}$$

$$= \mathbb{E}_{x \sim p_{data}}[\log D_G^*(x)] + \mathbb{E}_{z \sim p_z}[\log(1 - D_G^*(G(z)))] \tag{4.12}$$

$$= \mathbb{E}_{x \sim p_{data}}[\log D_G^*(x)] + \mathbb{E}_{x \sim p_g}[\log(1 - D_G^*(x))] \tag{4.13}$$

$$= \mathbb{E}_{x \sim p_{data}}\left[\log \frac{p_{data}(x)}{\frac{1}{2}(p_{data}(x) + p_g(x))}\right] + \mathbb{E}_{x \sim p_g}\left[\log \frac{p_{data}(x)}{\frac{1}{2}(p_{data}(x) + p_g(x))}\right] - 2 \log 2 \tag{4.14}$$

$$= KL(p_{data} || \frac{p_{data} + p_g}{2}) + KL(p_g || \frac{p_{data} + p_g}{2}) - 2 \log 2 \tag{4.15}$$

$$= 2JS(p_{data} || p_g) - 2 \log 2 \tag{4.16}$$

where the Kullback-Leibler divergence and Jensen-Shannon divergence are defined as follows

$$KL(p||q) = \int p(x) \log \frac{p(x)}{q(x)} \mathrm{d}x \tag{4.17}$$

$$JS(p||q) = \frac{1}{2} KL(p||\frac{p+q}{2}) + \frac{1}{2} KL(q||\frac{p+q}{2}) \tag{4.18}$$

which are distance metrics between the distributions $p(x)$ and $q(x)$. They are not well-defined metrics in the mathematical sense. For example the KL-divergence is not symmetric.

Because the Jensen-Shannon divergence is zero when both distributions are equal and it can never be negative, this is proof that the global minimum of $C(G)$ is $-\log 4$ and that this minimum is reached if $p_g = p_{data}$. Therefore we have shown that the GAN objective formulation as minimax game yields that the generator distribution recovers the data distribution after optimization [102].

A problem of the original GAN objective is that the gradient for the generator cost vanishes, or is at least not sufficient, if the discriminator is "too good" and rejects samples with high

confidence. This means that $\log(1 - D(G(z)))$ saturates when $D \to 0$. To mitigate this problem in such a non-saturating game setting the objective function can be altered slightly. The cost for the generator is hereby replaced by

$$J^{(G)} = \mathbb{E}_{z \sim p_z(z)}[-\log D(G(z))] \tag{4.19}$$
$$= \mathbb{E}_{x \sim p_g}[-\log D(x)] \tag{4.20}$$

which provides larger gradients, especially early in learning, but still leads to the same fixed points of the dynamics [111].

Drawbacks of this version are that there is no theoretical justification for the loss, only following heuristics. In addition, gradients are much lower if the generator is learning faster than the generator and $D \to 0$. The game however, is not zero-sum anymore and can not by described be a single value function [103].

Many models are applying the maximum likelihood principle, which minimizes the KL-divergence between the data and the model.

$$\Theta^* = \arg\min_{\Theta} KL(p_{data}(x) \,||\, p_{model}(x; \Theta)) \tag{4.21}$$

To be able to also perform maximum likelihood optimization on GANs, it is possible to approximate (4.21) with a GAN objective. Under the assumption that the discriminator is optimal the following cost function for the generator is used.

$$J^{(G)} = \mathbb{E}_{z \sim p_z(z)}[-\exp\left(\sigma^{-1}(D(G(z)))\right)] \tag{4.22}$$
$$= \mathbb{E}_{z \sim p_z(z)}[-D(G(z))/(1 - D(G(z)))] \tag{4.23}$$

σ is the logistic sigmoid function [111].

Figure 4.5 shows a comparison of the three different optimization procedures. It can be seen that the non-saturating game provides a larger gradient for very optimized discriminator. Both minimax and maximum likelihood game have problems providing a significant gradient in this regime. On the other hand the maximum likelihood gradient is pretty much dominated by the right end of the curve. This results in over-representation of a relatively small number of samples during batch training [103].

Convergence of GAN training is a difficult problem. Theoretically it is less understood than other networks, like variational autoencoders, that have a clearer mathematical structure. GANs suffer more from problems with mode collapse or overfitting than other architectures. The paper of Mescheder et al. gives a good overview on related problems and attempts a basic theoretical solution of the optimization procedure [222].

GANs are among the most popular deep learning techniques. Thousands of extensions of the framework exist, but the unifying principle always remains the two player minimax game between generator and discriminator. Among the most known architectures are InfoGAN [49], conditionalGAN [223], CycleGAN [357], f-GAN [238], WassersteinGAN [11], DCGAN [268], StyleGAN [159], pixelRNN [245] and DiscoGAN [169]. Almost every day there are more GAN architectures becoming available.

4.5 Conditional GAN

If the generative model should be constrained or produce output according to external information we need a model that can be conditioned to some data y, which can in practice be

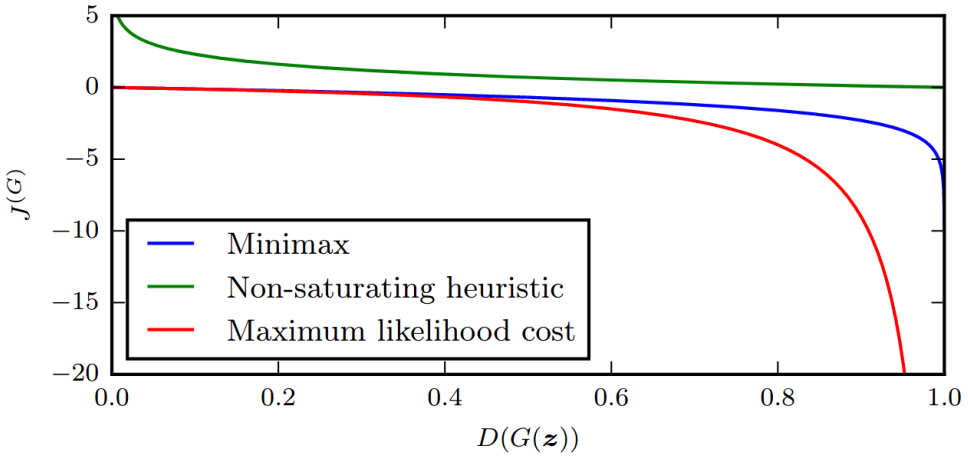

Figure 4.5: Comparison of cost functions for the generator plotted over discriminator output. Compared are the vanilla GAN objective (4.6), the non-saturating game (4.19) and the maximum-likelihood game (4.21). Scheme taken from [103].

anything, for example class labels or images. Conditional GANs (cGAN) are providing this extension [223]. The objective function of GANs (4.6) is extended as follows.

$$\min_G \max_D V(D,G) = \mathbb{E}_{x\sim p_{data}(x)}[\log D(x|y)] + \mathbb{E}_{z\sim p_z(z)}[\log(1 - D(G(z|y)))] \tag{4.24}$$

In practice, the auxiliary data y can be easily fed into G and D as an additional input layer.

An important special case is the architecture called *pix2pix* [146], which is shown schematically in Figure 4.6. Instead of using noise as latent vector z with prior distribution $p_z(z)$ as input, *pix2pix* learns a mapping from an input image x to an output image $G(x)$. Examples are ranging from mappings from horses to zebras, winter landscapes to summer landscapes or grayscale to colored images. This process is called image to image translation.

The loss function for *pix2pix* is hereby slightly altered, compared to (4.24). It is comprised of two losses: an adversarial loss $\mathcal{L}_{cGAN}$ and a L1 loss $\mathcal{L}_{L1}$. The adversarial loss reads

$$\min_G \max_D \mathcal{L}_{cGAN}(D,G) = \mathbb{E}_{x,y}[\log D(x,y)] + \mathbb{E}_{x,z}[\log(1 - D(x,G(x,z)))] \tag{4.25}$$

Here, x denotes an observed image, z a latent random vector and y an output image such that the mapping $G : \{x,z\} \to y$ is learned.

The adversarial loss is augmented by an additional term comprised of a L1 norm

$$\mathcal{L}_{L1}(G) = \mathbb{E}_{x,y,z}[||y - G(x,z)||_1] \tag{4.26}$$

This is mainly an empirical result, that GANs can benefit from a second, more traditional, loss function to improve convergence. Therefore, in addition to the task that the generator must produce faithful samples to fool the discriminator network, it should also produce samples that are close to the ground truth in an L1 distance sense. Traditionally a L2 distance is used for this [253], but in case of generated images, the L1 distance introduces less blurring [146].

The final objective function then reads

$$G^* = \arg\min_G \max_D = \mathcal{L}_{cGAN}(D,G) + \lambda\,\mathcal{L}_{L1}(G) \tag{4.27}$$

where λ is a free parameter. It weights the contributions of adversarial loss and L1 loss.

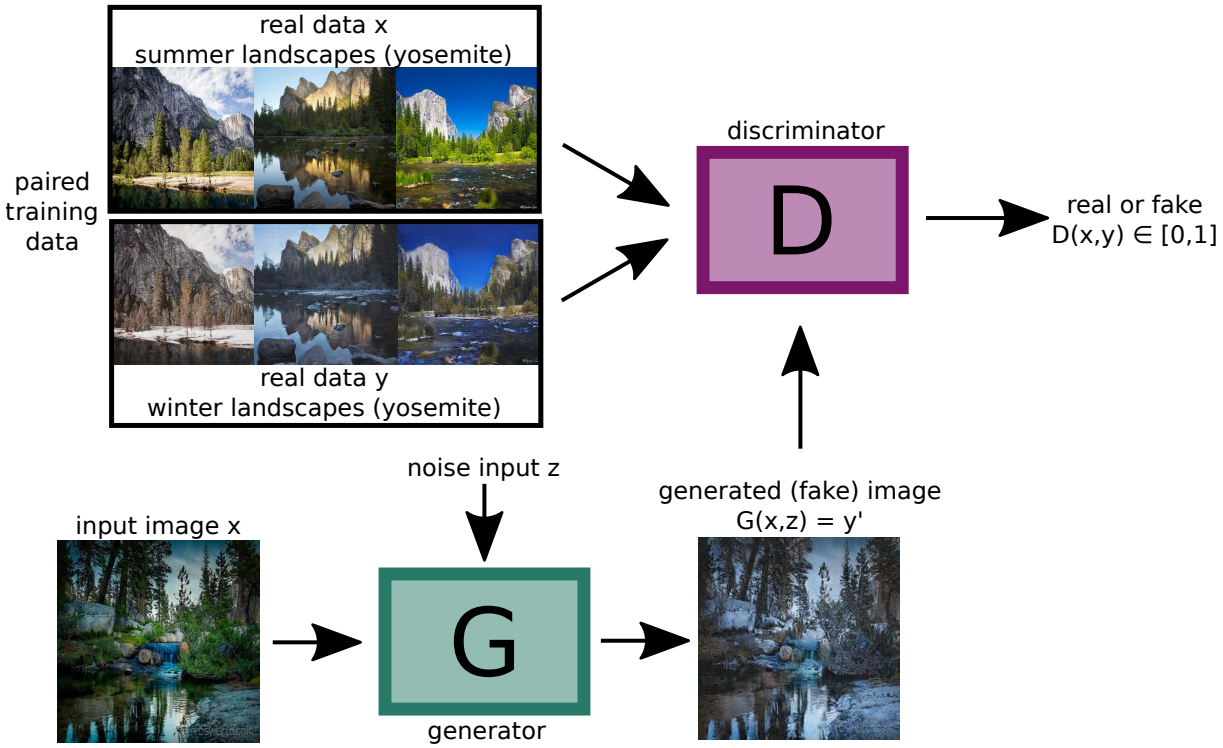

Figure 4.6: Principle of pix2pix, a conditional GAN that performs image to image translation tasks. The example here is to take a summer landscape and translate it into a winter landscape. The GAN principle stays the same, but in addition the generator gets an image as input. The discriminator also has knowledge of both the original image x and the result from domain y, thus in each case being handed two images: a summer image and its actual winter version, or a summer image and a fake winter version of it. This is why the translation can only be learned via paired ground truth training data.

Without noise the mapping would be deterministic and it has been shown that the networks learn to ignore noise if provided as input [216]. The noise therefore is put in as dropouts in several layers. However, even then the resulting volatility of the output is low, which points to a narrow learned probability distribution.

4.6 Cycle GAN

One of the main problems for cGANs in image to image translation tasks is that paired training data has to be available. The discriminator needs to "see" the output of the generator and the target ground truth to compare them. This problem has been mitigated in cycle-consistent GANs (CycleGAN), which work with unpaired training data [357]. The great advantage is that images can be translated into domains where only samples from the respective domain are available, but no corresponding ground truth to an input image. An example is the translation from a photograph into the style of a famous artist, like Van Gogh. For paired training, an army of artists would have to create corresponding pictures in the style of said artist. CycleGAN instead is trained by presenting several images of Van Gogh and the network is able to separate the image information from the style information and create a mapping from one style to the other [357].

To this end, a cGAN architecture is combined with a second backward cGAN into a loop such that the image from the backward cycle can be compared with the original input image. The objective function then is extended by this cycle-consistency loss. This is depicted in Figure 4.7. Without cycle-consistency loss the generator would only learn to create samples from the respective domains X or Y, but the generated images do not have to fit the input image. This restraint is only imposed by the additional loss function which therefore enables image to image translation capability without paired training data.

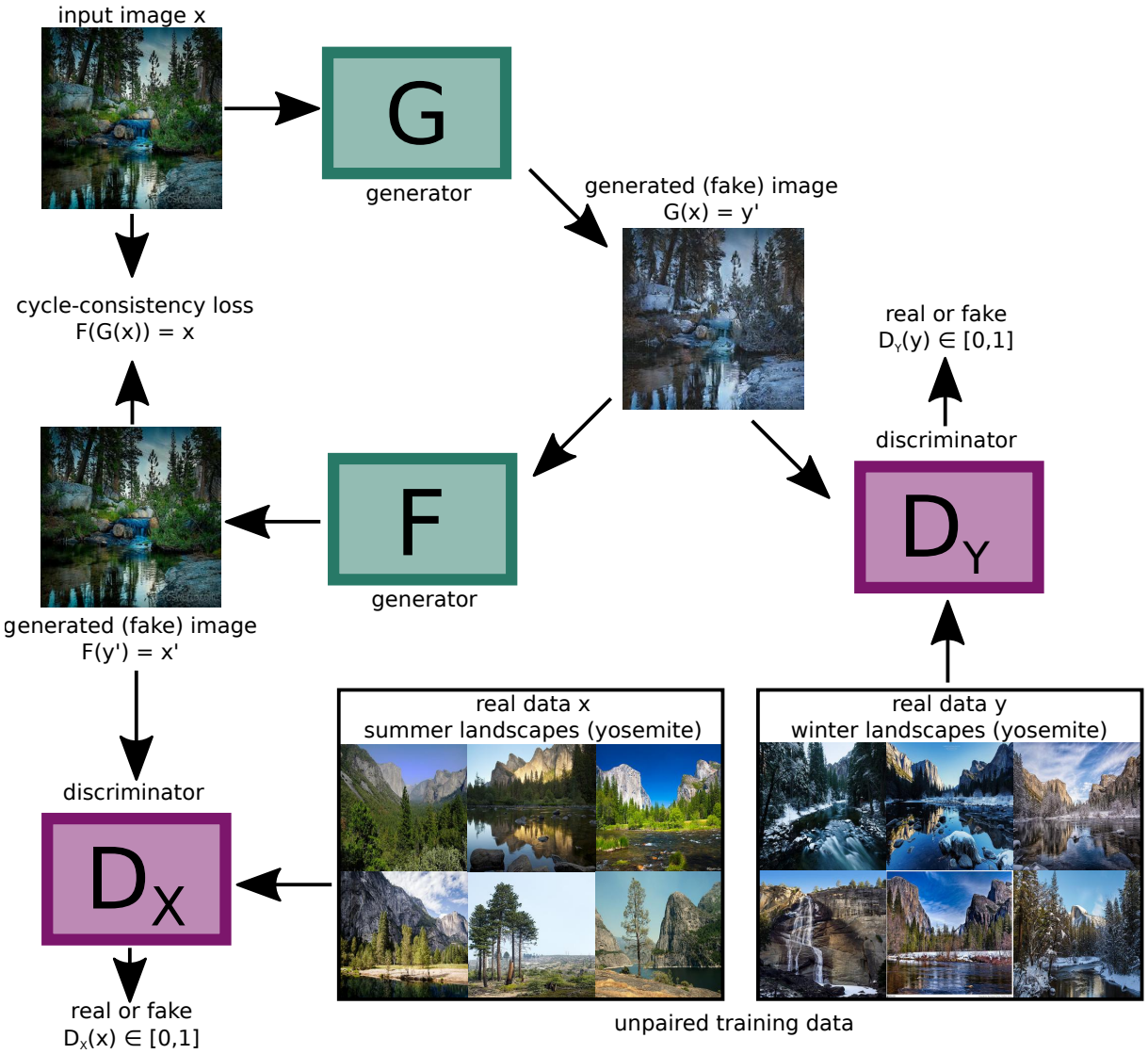

Figure 4.7: Cycle GAN principle: two generators and discriminators learn the mapping from domain X to domain Y and back. Only depicts one loop for simplicity. Each generator does the mapping in one direction and plays against a respective discriminator. To obtain the conditional translation from one image to the other, a cycle-consistency loss is introduced which punishes deviations of the original input image from the result after one cycle. Otherwise the generator would just learn to create any example from the target domain, but not to fit the conditional information into the output. This trick makes it possible to train the networks without paired ground truth data. The full scheme, including backward cycle, is also depicted in Section 4.9, Figure 2.

The objective function in the CycleGAN architecture consists of adversarial loss in forward direction, another adversarial loss in backward direction and the cycle-consistency loss. The adversarial loss is

$$\mathcal{L}_{GAN}(G, D_Y, X, Y) = \mathbb{E}_{y \sim p_{data}(y)}[\log D_Y(y)] + \mathbb{E}_{x \sim p_{data}(x)}[\log(1 - D_Y(G(x)))] \tag{4.28}$$

For the cycle-consistency loss the L1 norm is used

$$\mathcal{L}_{cyc}(G, F) = \mathbb{E}_{x \sim p_{data}(x)}[||F(G(X)) - x||_1] + \mathbb{E}_{y \sim p_{data}(y)}[||G(F(Y)) - y||_1] \tag{4.29}$$

This is combined to the full objective function as follows

$$\mathcal{L}(G, F, D_X, D_Y) = \mathcal{L}_{GAN}(G, D_Y, X, Y) + \mathcal{L}_{GAN}(F, D_X, Y, X) + \lambda \mathcal{L}_{cyc}(G, F) \tag{4.30}$$

λ is a free parameter to weight both objectives against each other. The optimizing procedure yields

$$G^*, F^* = \arg \min_{G,F} \max_{D_X, D_Y} \mathcal{L}(G, F, D_X, D_Y) \tag{4.31}$$

This procedure can be related to autoencoder architecture because mathematically the objective is similar to learning two autoencoders together [134]. Namely $G \circ F : X \to X$ and $F \circ G : Y \to Y$. There exists a unification of GANs and variational autoencoders, which is called adversarial variational Bayes [222].

In the end, this procedure thus yields two generating functions, one for each direction. In the example from Figure 4.7, one generator translates summer images to winter images and the other winter images to summer images. We use the cycleGAN architecture to create segmentation labels for microscopy images of epithelial cells. The first domain are the microscopy images and the second domain the segmentation, consisting of a binary image of white cell junctions and black background. Later, only the translation from microscopy data to segmentation is needed.

4.7 U-Net

For the comparison of cycleGAN performance with other state of the art deep learning segmentation methods we now introduce the U-Net as one of the most widely used DL segmentation architectures, specifically designed for biomedical images [281]. It takes an image as input and classifies each pixel according to labels that have been predetermined by ground truth. As an example, for the segmentation of epithelial cells there is one label for the cell border and one label for the background. After the U-Net segmentation all noise is removed from the original microscopy image and cells are easily identified and tracked.

The name comes from the u-shape of its architecture, consisting of a contracting path and an expanding path, which are interconnected via skip-connections, see Figure 4.8. The general idea is to learn the global features in the contracting path and then re-introduce local features in the expansion procedure. This way, the classifier can take global information into account but still basis its decision on local information.

In more detail the contracting path consists of convolutional layers and max-pooling operations. In the expanding path the pooling operation is suspended for an up-convolution. The resulting feature map output is compared to a ground truth and weights are adjusted according to the difference, therefore the U-Net is a supervised architecture and needs paired training data.

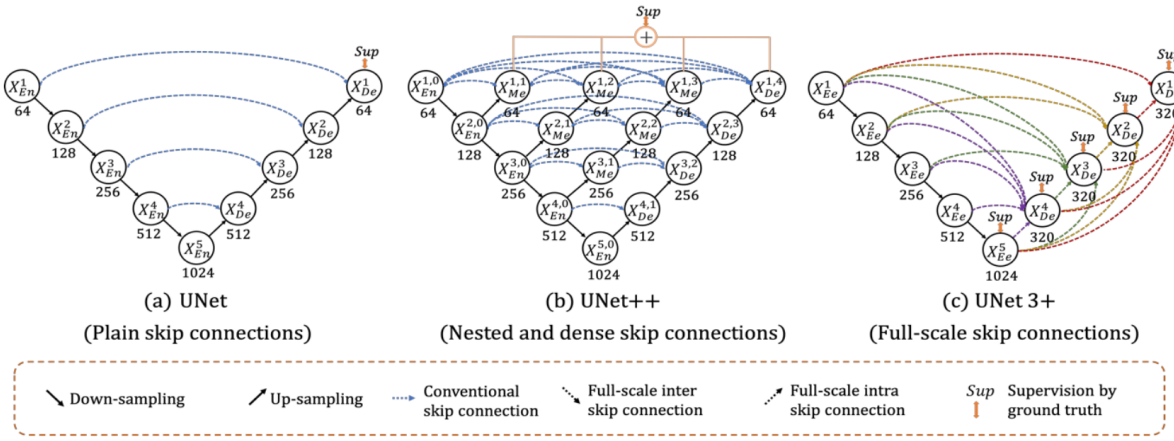

Figure 4.8: Scheme of U-Net architectures. The U-Net consists of a contracting path and an expanding path. Layers are connected via skip connections that can be realized in different ways, as shown in (a), (b), (c). Scheme taken from [135].

Before the loss is computed, a softmax regularization is used to set the probability of the feature channel with the highest activation near 1 and all other features near 0. The softmax function is

$$p_k(\mathbf{x}) = \frac{\exp(a_k(\mathbf{x}))}{\sum_{k'=1}^{K} \exp(a_{k'}(\mathbf{x}))} \tag{4.32}$$

$a_k(\mathbf{x})$ is the activation of feature k for pixel $\mathbf{x}$, K denotes the number of feature channels, and $p_k(\mathbf{x})$ is the approximated maximum function.

The objective function then is the pixelwise cross entropy of the regularized featuremap compared with the ground truth

$$E = \sum_{\mathbf{x}\in\Omega} \omega(\mathbf{x})\, p_{l(\mathbf{x})}(\mathbf{x}) \tag{4.33}$$

with $l : \Omega \to \{1, ...K\}$ being the ground truth label for each pixel $\mathbf{x}$. Therefore the deviation of $p_{l(\mathbf{x})}(\mathbf{x})$ from 1 is penalized. $\omega(\mathbf{x})$ denotes a weight matrix, that can shift the importance of different pixels. This can be useful if for example one label is very dominant which would without weighting result in optimization for this one label while the others are neglected. The weight map is precomputed from the ground truth images [281].

Nowadays, improved architectures U-net 2 [356] and U-Net 3 [135] are available, which expand on the idea by using more layers between skip connection or feeding multiple contracting layers via skip-connection into expanding layers (Figure 4.8). Both approaches have been shown to further improve the segmentation accuracy.

4.8 Performance metrics for tissue segmentation

In this chapter we use several measures to quantify segmentation algorithm performance. A principle problem here is that for proper evaluation, the segmentation has to be compared to a ground truth, which is almost always based on manual segmentation where labels are created by a human. It is possible to test segmentation methods on artificial data, where exact labels are available but the ultimate test is real data. In case of biomedical image segmentation these

are microscopy images where the final ground truth labels can only be manually created. This bounds accuracy measures by human precision.

Our application are cells in epithelial tissues. We want to separate background information and other unwanted features from the cell walls, which we can then use to calculate all other quantities of interest, for example cell area using Leibniz' rule, cell anisotropies and more. Ultimately, we need fully segmented tissue, which we can reach via manual correction of the computer generated segmentation. To this end the segmentation from the algorithm must be as good as possible.

One of the simpler measures we use is related to counting the assigning errors and successes. There are different classes: true positives (TP) are correctly identified objects, false positives (FP) are identified objects that are not in the ground truth and false negatives (FN) are missing objects in the segmentation map. Note that these only denote the whole object and does not measure how well the segmentation fits in a pixelwise manner. An object is classified as true positive if there is a $> 50\%$ pixelwise overlap of the ground truth object with the segmentation object.

Just displaying the counts gives some information about the success of the segmentation, but these can be combined in high level metrics. First, there are precision and recall, which are defined as [261]

$$\text{precision} = \frac{TP}{TP + FP} \tag{4.34}$$

$$\text{recall} = \frac{TP}{TP + FN} \tag{4.35}$$

Thereby the precision gives the ratio of true positives and all positives. If the method segments all objects from the ground truth but also creates many artificial objects this is punished by the measure. The recall measures how many objects of the total number of available objects in the ground truth were segmented.

From precision and recall one can define a combined metric, called F1 score [290], which is defined as the harmonic mean between precision and recall

$$F1 = 2\frac{\text{precision} \cdot \text{recall}}{\text{precision} + \text{recall}} = \frac{TP}{TP + \frac{1}{2}(FP + FN)} \tag{4.36}$$

The F1 score produces a number between 0 and 1, whereas 1 can only be reached with perfect segmentation accuracy.

As we have already stated, a TP is assigned by $> 50\%$ pixelwise overlap of ground truth and segmentation object. The sole counts of TP, FP and FN is therefore not enough to determine the full accuracy. In addition, we use the pixelwise dice coefficient which measures how much overlap two objects in the ground truth and the segmentation output have.

Mathematically, the dice coefficient is actually the same as the F1 coefficient. The difference here is that we apply the measure to pixels in one object.

$$\text{dice}(A_G^i, A_S^i) = 2\frac{|A_G^i \cap A_S^i|}{A_G^i + A_S^i} \tag{4.37}$$

where $A_G^i = \#\text{px} \in i\text{th object}$. G denotes ground truth and S segmentation. To assign the index i to the same object in ground truth and segmentation, the $> 50\%$ overlap rule is used, thus there can be no conflict in assigning more than one segmentation object to one ground truth object. To have a clear notation in later chapters we will always refer to the dice coefficient when

we mean to evaluate pixelwise overlap and to the F1 score if we want to measure the fraction of successfully segmented objects.

There are several ways to compute an ensemble value for the dice coefficient. We simply average the single dice coefficients and weigh them according to the number of pixels in the object. This gives a consistent overall dice value for all objects. The dice coefficient also outputs a number between 0 and 1. Figure 4.9 shows an example of the principles F1 and dice score are based on.

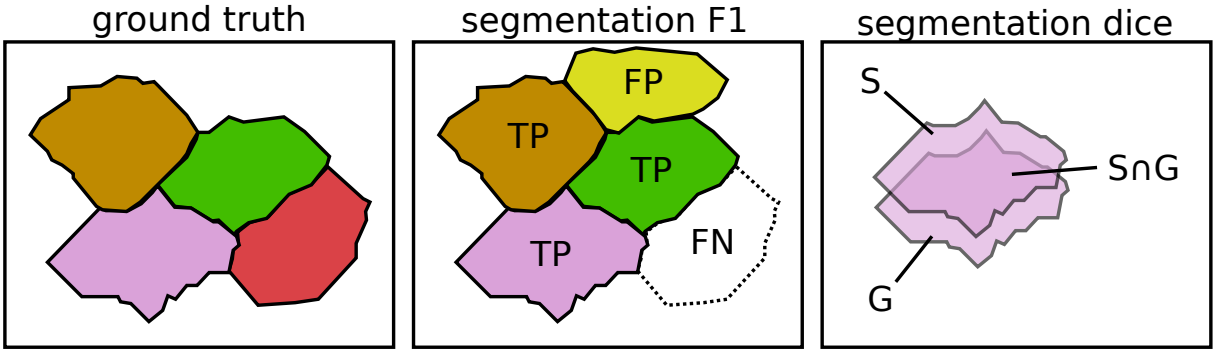

Figure 4.9: F1 score and dice score are used to evaluate segmentation accuracy. To the left is the ground truth segmentation. In the middle it is evaluated which cells have been identified and have been correctly labeled true positive (TP), a cell was additionally segmented that is not in the ground truth and therefore labeled false positive (FP), and finally a missing cell that is labeled false negative (FN). To the right the overlap of ground truth and segmentation object is shown. The higher the overlap, the higher the dice score.

Consider a movie: A time-ordered set of images, to each of which the segmentation procedure is applied individually. It is possible that an object (e.g. a cell) is correctly identified in one frame, but not in the consecutive one. Thus, a natural measure for segmentation consistency of a movie is that a cell is tracked throughout the entire movie. The number of successfully tracked cells over time is therefore used as a last metric.

More generally applicable and metrics, such as [218, 336], are available in literature. Since we have a specific application in mind, however, their advantages are not of interest here, and it is actually more advantageous to use metrics well-suited specifically for our needs. Our dataset is well defined and we have clear criteria what the segmentation must do in order for us to explore the biological research questions in later chapters. In particular, we care for as many true positives as possible to keep the manual correction to a minimum. These TPs should have a high pixelwise overlap with the ground truth, which is quantified by the dice coefficient. Furthermore, we want consistent segmentation over many frames as our data consists of time-lapse microscopy movies. This is quantified by the number of successfully tracked cells.

4.9 Automated Segmentation of Epithelial Tissue Using Cycle-Consistent Generative Adversarial Networks

Original contribution

Stephan Eule, **Matthias Häring** and Fred Wolf conceptualized the research. Stephan Eule trained the networks. **MH** did additional training, generated the training data, analyzed the results and wrote the manuscript. FW supervised the research. All authors discussed the results. Microscopy data was provided from the lab of Jörg Großhans by Prachi Richa and Deqing Kong.

DOI

https://doi.org/10.1101/311373

Automated Segmentation of Epithelial Tissue Using Cycle-Consistent Generative Adversarial Networks

Matthias Häring[1], **Jörg Großhans**[2], **Fred Wolf**[1] **and Stephan Eule**[1,3]
[1]Max-Planck-Institute for Dynamics and Self-Organization
[2]Department of Developmental Biochemistry, University of Göttingen
[3]German Primate Center, Göttingen

Abstract

A central problem in biomedical imaging is the automated segmentation of images for further quantitative analysis. Recently, fully convolutional neural networks, such as the U-Net, were applied successfully in a variety of segmentation tasks. A downside of this approach is the requirement for a large amount of well-prepared training samples, consisting of image - ground truth mask pairs. Since training data must be created by hand for each experiment, this task can be very costly and time-consuming. Here, we present a segmentation method based on cycle consistent generative adversarial networks, which can be trained even in absence of prepared image - mask pairs. We show that it successfully performs image segmentation tasks on samples with substantial defects and even generalizes well to different tissue types.

1 Introduction

Mechanically active tissues, force generating and proliferating cell groups, and topological tissue rearrangement play a critical role for a wide range of biomedical research challenges. Analyzing such dynamical tissues is of central importance to advancing regenerative medicine and stem cell technologies, to understand cancer progression and treatment and for fundamental research into organogenesis and embryo development. Over the past decade, the rapid advancement of photonic imaging technologies has made it relatively easy to collect time lapse imaging data sets of massive size, recording tissue dynamics and rearrangement in vivo over extended periods of time. A prominent bottleneck in the computational analysis of such large-scale imaging datasets is the automated segmentation of cell shapes to quantify tissue topology, geometry and dynamics. Especially the segmentation of images with lower quality remains challenging.

Recently, deep convolutional neural networks were applied successfully in a vast variety of visual recognition tasks, including automatic biomedical image segmentation. In general, their performance is equal or superior to sophisticated rule-based methods [1], [2]. One drawback of these models, however, is the necessity to prepare a well-suited dataset on which the network can be trained. Generating hand-labeled datasets of image - ground truth mask pairs is time-consuming and thus represents an expensive bottleneck. Due to this training bottleneck many practitioners still use rule-based methods instead of machine learning techniques. Moreover, even if extensive training data is available, the performance of these systems degrades significantly when they are applied to test data that differ from the training data, for example, due to variations in experimental protocols. Furthermore, pixel by pixel classifiers based on deep convolutional architectures can perform poorly on image data with substantial defects that have been labeled incompletely due to bleaching and label failure.

Here, we focus on the segmentation of epithelial tissue from *Drosophila Melanogaster* embryos (see figure 1). Drosophila is a common model system due to its simplicity, availability of well explored

*Correspondence to `eule@nld.ds.mpg.de` and `matthias.haering@ds.mpg.de`

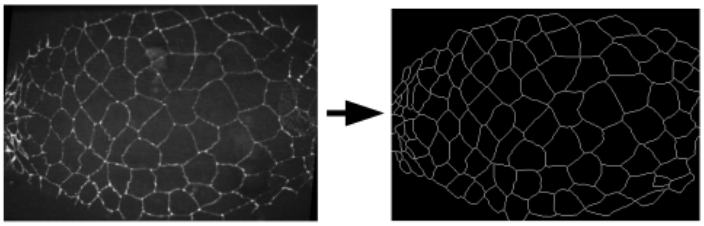

Figure 1: Segmentation of Amnioserosa tissue from Drosophila embryos. For further quantitative analysis a skeletonized version of the microscopy image has to be created such that it contains only cell outlines in a binary representation. From this segmented image, quantities like cell area or cell junction length can be easily extracted.

genetic tools, economic advantages and short life cycles [3]. Furthermore, the size of the organism allows recording of cell tissue in the living, developing embryo. Research in morphogenesis often relies on observations in this model system and in particular the analysis of dynamic processes during morphogenetic phases, like gastrulation, can give important insights about embryonic development [4]. As these processes typically are highly active and involve remodeling and reshaping of cell tissues, a well functioning data acquisition pipeline is crucial to obtain good statistics for quantifying complex dynamics such as coordinated cell oscillations [5], [6], [7]. Generating segmentations of cell tissues in sufficient quantities for such studies is very time-consuming and, depending on the scope of the project, can take months. Therefore, it is highly desirable to automate the segmentation process.

We propose to employ an automated segmentation pipeline based on cycle-consistent generative adversarial networks (Cycle-GANs [8]). The advantage of this approach is that Cycle-GANs can be trained even in absence of prepared image - mask pairs. We show that this model performs competitively on standard segmentation tasks even when trained on just a few target samples. In addition, our model generalizes well to test data differing from the training data and successfully performs image segmentation tasks on samples with substantial defects. We test this framework on Amnioserosa, an oval shaped tissue that appears at the end of gastrulation in Drosophila morphogenesis.

This paper is structured in the following way: first we briefly review some state of the art methods for cell segmentation, then we introduce our approach based on generative adversarial networks, and finally compare and evaluate the accuracy obtained by our Cycle-GAN approach, a fully convolutional neural network approach (U-Net) and the Tissue Analyzer software, which is commonly used in the field.

2 State of the Art Cell Segmentation

We first briefly introduce two state of the art methods, which are commonly used in image segmentation tasks of cell tissues. These methods will then serve as benchmarks for our approach.

2.1 Rule-based Methods

To extract cell features from microscopy recordings, practitioners typically employ segmentation methods based on the watershed algorithm, which is e.g. implemented as a plugin in *ImageJ* as the *Tissue Analyzer* [9]. In this plugin, the user can vary the parameters of the algorithm to meet differences in the recording e.g. due to contrast, cell type or bleaching. In addition, segmentation errors can be corrected by redrawing cell contacts by hand, deleting wrongly assigned cell contacts or completely segment the image by hand. If the recording quality is not sufficient for accurate watershed based contour detection, correcting the image by hand can take up to several days for a single movie of 150 frames. The main disadvantage of this method is therefore the time-consuming manual correction of low-quality cell tissue recordings that do not allow for an accurate watershed segmentation. Thanks to the many useful tools for analysis or visualization implemented in the Tissue Analyzer, it is a very popular segmentation program for cell tissues in biology, e.g. [10], [11], [12].

2.2 Machine Learning

Machine learning and in particular deep learning approaches are applied in a variety of visual recognition tasks. Especially for biomedical image segmentation they have been shown to be very successful in terms of accuracy and robustness, e.g. [13], [14], [15], [16], [17]. By now there are many competing architectures that yield fast performance and high accuracy. One widely used example is the U-Net, which employs a fully convolutional network architecture with pixel by pixel classification, see [18] for more information. Pixel by pixel classification networks take global information into account but final classification decisions are made based on local information. Therefore, when looking at cell segmentation tasks, errors may happen if recordings are distorted by bleaching effects or gaps in cell contours due to discontinuous labeling. In this study, we take a different approach using so-called *generative networks*, which will be described in the following section.

3 Methods

3.1 Generative Networks

In contrast to pixel by pixel classifiers, *generative networks* learn general global features of a certain class of images, encoded as a very high dimensional probability distribution [19]. Drawing one sample from this learned distribution corresponds to the creation of a specific image. Since we do not just want to generate a realistically looking segmentation but transform a microscopy recording into its corresponding segmentation (image to image translation) it is necessary to condition the output image on an input. After the network has learned how segmentation images are generated from input images, the network can take a microscopy image as input and generate the corresponding segmentation. The idea of this approach is that the quality of microscopy recordings affects contour detection to a lesser extent since the general shape of target images is already known. Furthermore, we utilize the Cycle-GAN framework as it allows for unpaired training and thus does not require the preparation of dedicated image - ground truth training pairs. Details of these frameworks are described in the following section.

3.2 Generative Adversarial Networks

Generative Adversarial Networks [20] (GANs) have proven to be one of the most successful methods in image generation and image manipulation tasks [19]. Originally solely developed for image generation, GANs have recently also been applied to conditional image processing like pix2pix [21], text2image [22], image impainting [23], movies [24] or 3D data analysis [25].

The idea behind GANs is the cunning training procedure, incorporating a so-called *adversarial loss*, meaning that two networks are set up in a game against each other. The first network, called *generator*, is trying to generate realistic images to fool a second network, called *discriminator*, which tries to distinguish between real and fake images. This can mathematically be formulated as a minimax game, given the adversarial loss

$$J^{(D)}\left(\theta^D, \theta^G\right) = -\frac{1}{2}\mathbb{E}_{x\sim p_{\text{data}}}\log D(x) - \frac{1}{2}\mathbb{E}_z \log(1 - D(G(z))) \tag{1}$$

$$J^{(G)}\left(\theta^D, \theta^G\right) = -J^{(D)} \tag{2}$$

with $J^{(D)}$ and $J^{(G)}$ denoting the respective cost functions of discriminator and generator, whereas θ^D and θ^G represent the parameters of both networks to be optimized. Hereby, $D : x \rightarrow [0, 1]$ represents the discriminator network, mapping from an image to the probability of this image being real and $G : z \rightarrow x$ the generator network, whereas z is a latent random variable and $x \sim p_{data}$ a sample from the target distribution. Both networks minimize their respective cost function during training. Therefore, the Nash-equilibrium of this game is reached when the discriminator can not decide anymore if the generated image is real or fake, $D(G(z)) = 0.5$. It can be shown that in this case the probability distribution of the training data is fully recovered [20].

The key aspect is that training happens in a semi-supervised manner, meaning that the discriminator part of the architecture is presented with examples from the generator and the real world and is afterwards informed about its decision being right or wrong. Note that up to this point image to image translation has not entered yet, the generator converts random input into target images, and

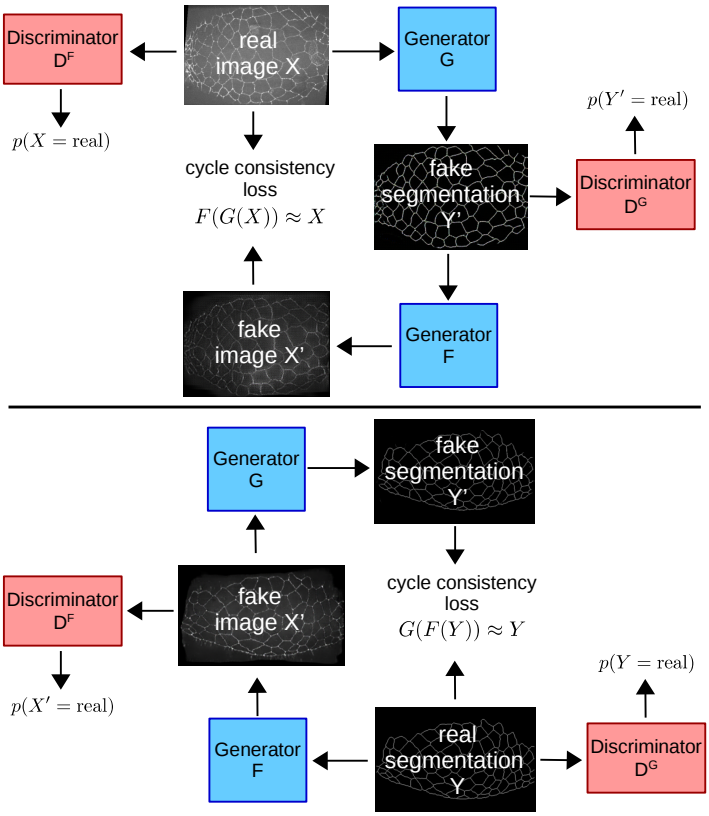

Figure 2: Simplified Cycle-GAN framework. By incorporating a second generator that translates from the segmentation to the microscopy image domain and a cycle-consistent loss that punishes deviations of this outcome from the original microscopy image, the need of dedicated image-ground truth training pairs can be omitted.

thus can create images that look like segmentation images but it can not create the corresponding segmentation to a specific tissue recording.

Isola et al. have extended this principle into a unifying framework for image to image translation tasks called conditional generative adversarial networks (cGANs) [21]. Hereby, the generator gets an image as input instead of random variables. Furthermore, decisions of the discriminator now also take the input image into account $D(G(\text{image})|\text{image})$. At this point, we still need microscopy recording - ground truth segmentation pairs to train the network since the discriminator must be aware of both the correct input and output images. If we omit the necessity of presenting the discriminator with the correct corresponding segmentation it will declare any faithful looking image as being correct. Then it is not guaranteed that the generator learns to create fitting segmentations, it will most likely just convert the input image into random segmentations that look faithful but do not fit the input.

3.3 Cycle-GAN

To lift the necessity of microscopy recording - ground truth segmentation pairs in biomedical image processing, we use the Cycle-GAN architecture introduced by Zhu et al. [8]. A simplified sketch of the Cycle-GAN framework is shown in figure 2.

The idea behind Cycle-GAN is to enforce a relationship between input domain and target domain by introducing a second generator F that translates the generated image of the first generator G back into the input domain. Original input image and the target image of the second generator are then compared for similarity. This *cycle-consistency loss* ensures that the target image of the first

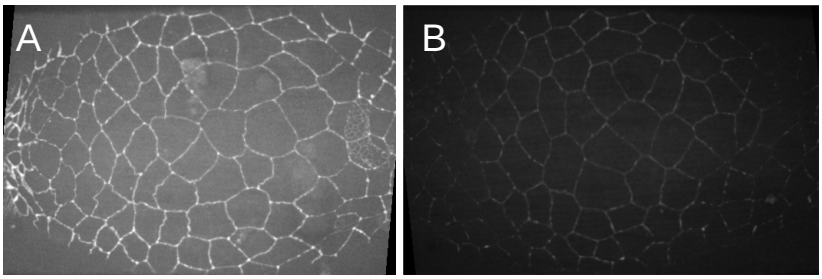

Figure 3: Two movies of Amnioserosa tissue are prepared to test the segmentation accuracy of Cycle-GAN, U-Net and Tissue Analyzer. **A)** Movie of high quality: cell outlines are clearly visible. **B)** Movie of low quality: low contrast makes junctions hard to infer.

generator fits to the specific input whereas the adversarial loss ensures that the generator hits the target distribution in the first place.

For the purpose of simplicity we are content with giving an intuitive explanation of the Cycle-GAN framework and refer the interested reader to the literature for a rigorous explanation and further details [8].

We mainly use the original architecture introduced by Zhu et al. with minor changes. For the specific task of image segmentation of epithelial tissues a generator with six Resnet blocks proved to be most successful. We also used a U-Net architecture for the generator with seven down- and upsampling layers, which however showed a slightly worse performance. Although images and and segmentation are grey-scale, we found that the results significantly improved when three colour channels were used. For implementation details we refer to the original paper of Zhu et al. [8].

3.4 Training Procedure

The training set for the Cycle-GAN framework consisted of 112 unpaired images of Amnioserosa tissue and ground truth segmentation images, respectively, which were downscaled to a size of 256 x 256 pixels. The images were randomly drawn from a pool of ten, roughly 150 frames long Amnioserosa movies. For evaluation purposes two movies were excluded from the training data: one movie of rather high quality with good contrast and high signal to noise ratio and a second movie with low contrast and discontinuously labeled cell contacts, see figure 3. The low quality movie was picked specifically as a challenging example where watershed might come to its limitations. Depending on the specific setup of the network the training took between 2 - 6 hours on a Titan Xp GPU based on the PyTorch implementation and the hyper-parameters proposed by Zhu et al [8]. After the training, generation of new segmentation images is done at roughly 30fps.

3.5 Evaluation

Two test sets of Amnioserosa movies were used to compare the performance of three segmentation methods: Tissue Analyzer, U-Net and Cycle-GAN approach.

For the Tissue Analyzer, we choose parameter settings that yield the best possible watershed segmentation. There is no hand correction applied, such that the resulting segmentation will reflect the accuracy of a state of the art watershed algorithm.

For all three methods, the output is a skeletonized version of the input microscopy recording, meaning that the output is a greyscale image with white cell contours and black background. Each method is compared with manually prepared ground truth segmentation images. A fundamental limit to the accuracy tests is therefore the human manual segmentation accuracy.

Segmentation accuracy is measured by the number of correctly identified cells in each frame. Each segmented cell is classified into one of three classes: true positives, cells that are correctly segmented, and false positives, cells that have been segmented although there is no corresponding cell in the ground truth. This can happen if the segmentation method infers additional cell contours for example

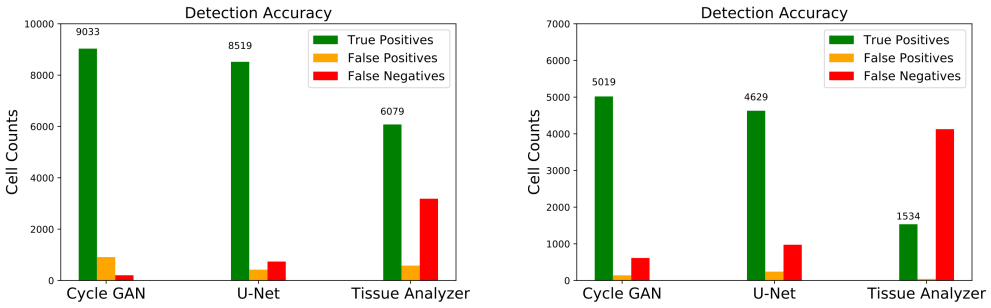

high quality movie low quality movie

Figure 4: Segmentation accuracy of Cyle-GAN, U-Net and Tissue Analyzer tested with Amnioserosa tissue. Both machine learning methods outperform the rule-based method (without manual correction), whereas Cycle-GAN and U-Net approach achieve comparable accuracy. In the challenging low quality movie case it can be seen that the watershed algorithm reaches its limits, while Cylce-GAN and U-Net correctly detect most of the cells.

due to noise or other objects in the recording that are no cell contacts. In addition, cells that appear in the ground truth but not in the segmentation are counted as false negatives.

The comparison between ground truth images and segmentation images of the three methods happens on a pixel by pixel basis. We identify all pixels belonging to a cell in the ground truth and check if these pixels correspond to cells in the output segmentation. Whenever we have an overlap of more than 50% with the ground truth, a cell in the output segmentation is identified as a true positive.

4 Results

For the evaluation, we compare the performances of Cycle-GAN, Tissue Analyzer and U-Net. While results show that both machine learning approaches outperform the rule-based approach, it is noteworthy that the accuracy of the Cycle-GAN is at least comparable to the U-Net, which has to be trained on image-mask pairs (figure 4). Even in the challenging case of the lower quality movie, most of the cells are successfully recovered by both machine learning techniques while the watershed method shows a significantly higher failure rate.

From this example we can conclude that the Cycle-GAN framework performs competitively well when compared to the U-Net. It also shows that the Cycle-GAN framework achieves higher accuracies compared to the watershed algorithm.

4.1 Domain adaptation

To show the domain adaptation capabilities of the Cycle-GAN framework, we have tested its segmentation performance on different tissue types that are qualitatively different from the tissue on which the network was trained, see figure 5. One of these tissues is a *TMC* mutant, an ion channel knockout, that shows larger cells and often displays yolk granules in the focus plane, which makes segmentation with traditional methods very challenging. The second tissue is called *xit*, presenting elongated cells with wavy cell borders. As a last example, we take tissue from the *germband*, another tissue type that is playing an important role during gastrulation in Drosophila embryos. This tissue is heavily remodeled during the process and therefore more dynamic than Amnioserosa.

We can see that the overall performance is still very good, but at the same time limitations of this method become clear. In the case of the TMC mutant, it is impressive how accurate the segmentation is despite the original image being highly distorted by yolk granules that moved into focus. There are however a number of wrongly assigned cell contacts where the network identified the outline of a yolk granule as cell outline. The Xit mutant is accurately segmented as well, but the network fails to show accuracy on small scale details of the cell junctions, in particular the wavyness of some cell borders is lost. This effect is due to the training on Amnioserosa wild type tissue where cell contacts

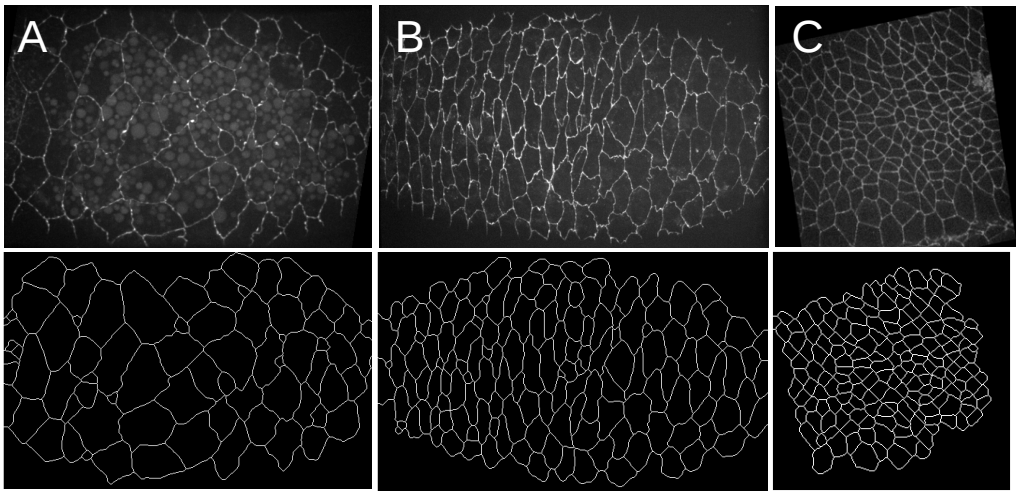

Figure 5: Further examples of Cycle-GAN segmentation in different tissues, trained on the same Amnioserosa data. This comparison shows how well the Cycle-GAN approach is able to generalize from a specific type of training data to similar but qualitatively different tissues. **A)** TMC Amnioserosa mutant: cells are bigger and yolk granules have wandered into focus which makes segmentation very challenging. **B)** Xit Amnioserosa mutant: shows a different phenotype with longer stretched cells and wavy borders. **C)** Epithelial tissue from the germband in Drosophila during gastrulation: continuously reshaping tissue type that consists of smaller cells.

are exclusively smooth and thus while being able to identify the overall cell shapes the microscopic structure is lost. Interestingly, in the third case of germband tissue we obtain very high accuracy without visible errors. The main difference to the Amnioserosa tissue is that cells are much smaller and more dynamic in time, whereas the overall shape of the cells is similar.

These examples show that the Cycle-GAN framework is very robust and shows high performance on the specific tasks it was trained for. It can however not adapt to identify qualitatively different shapes as seen in the case of wavy cell borders. On the other hand, if the general shape of cells is similar to the training data, like in the TMC case, then high accuracy can be achieved despite distortion of the image by yolk granules.

5 Conclusions

In this paper we showed that the problem of ground truth creation for training of deep convolutional networks can be circumvented using a Cycle-GAN framework. Our results indicate comparable performance to other deep learning methods and advantages over traditional rule-based methods. In addition, Cycle-GANs shows high potential on cell tissues that differ from the training set.

Future work has to explore generalization to different segmentation tasks as this study is limited to the segmentation of epithelial cell tissue.

References

[1] Lei Ma, Manchun Li, Xiaoxue Ma, Liang Cheng, Peijun Du, and Yongxue Liu. A review of supervised object-based land-cover image classification. *ISPRS Journal of Photogrammetry and Remote Sensing*, 130:277 – 293, 2017.

[2] Ulman et al. An objective comparison of cell-tracking algorithms. *Nature Methods*, 14:1141–1152, 2017.

[3] Karen G. Hales, Christopher A. Korey, Amanda M. Larracuente, and David M. Roberts. Genetics on the fly: A primer on the drosophila model system. *Genetics*, 201(3):815–842, 2015.

[4] Deqing Kong, Fred Wolf, and Jörg Großhans. Forces directing germ-band extension in drosophila embryos. *Mechanisms of Development*, 144:11 – 22, 2017. Roles of physical forces in development.

[5] J Solon, A. Kaya-Copur, J. Colombelli, and D. Brunner. Pulsed Forces Timed by a Ratchet-like Mechanism Drive Directed Tissue Movement during Dorsal Closure. *Cell*, 137(7):1331–1342,, June 2009.

[6] A. Jayasinghe, S. Crews, D. Mashburn, and S. Hutson. Apical Oscillations in Amnioserosa Cells: Basolateral Coupling and Mechanical Autonomy. *Biophysical Journal*, 105(1):255–265,, July 2013.

[7] A. Sokolow, Y. Toyama, D. Kiehart, and G. Edwards. Cell Ingression and Apical Shape Oscillations during Dorsal Closure in Drosophila. *Biophysical Journal*, 102(5):969–979,, March 2012.

[8] J.-Y. Zhu, T. Park, P. Isola, and A. A. Efros. Unpaired Image-to-Image Translation using Cycle-Consistent Adversarial Networks. *ArXiv e-prints*, March 2017.

[9] Benoît Aigouy, Reza Farhadifar, Douglas B. Staple, Andreas Sagner, Jens-Christian Röper, Frank Jülicher, and Suzanne Eaton. Cell flow reorients the axis of planar polarity in the wing epithelium of drosophila. *Cell*, 142(5):773 – 786, 2010.

[10] Gabriel L. Galea, Oleksandr Nychyk, Matteo A. Mole, Dale Moulding, Dawn Savery, Evanthia Nikolopoulou, Deborah J. Henderson, Nicholas D. E. Greene, and Andrew J. Copp. Vangl2 disruption alters the biomechanics of late spinal neurulation leading to spina bifida in mouse embryos. *Disease Models & Mechanisms*, 11(3), 2018.

[11] Elizabeth Carroll Driver, Amy Northrop, and Matthew W. Kelley. Cell migration, intercalation and growth regulate mammalian cochlear extension. *Development*, 144(20):3766–3776, 2017.

[12] M. Williams, A. Sawada, T. Budine, C. Yin, P. Gontarz, and L. Solnica-Krezel. Gon4l regulates notochord boundary formation and cell polarity underlying axis extension by repressing adhesion genes. *Nature Communications*, (9):1319, 2018.

[13] X. Li, H. Chen, X. Qi, Q. Dou, C.-W. Fu, and P. A. Heng. H-DenseUNet: Hybrid Densely Connected UNet for Liver and Liver Tumor Segmentation from CT Volumes. *ArXiv e-prints*, September 2017.

[14] Y. Xue, T. Xu, H. Zhang, R. Long, and X. Huang. SegAN: Adversarial Network with Multi-scale L_1 Loss for Medical Image Segmentation. *ArXiv e-prints*, June 2017.

[15] D. Yang, D. Xu, S. K. Zhou, B. Georgescu, M. Chen, S. Grbic, D. Metaxas, and D. Comaniciu. Automatic Liver Segmentation Using an Adversarial Image-to-Image Network. *ArXiv e-prints*, July 2017.

[16] A. Mortazi, J. Burt, and U. Bagci. Multi-Planar Deep Segmentation Networks for Cardiac Substructures from MRI and CT. *ArXiv e-prints*, August 2017.

[17] Y. Zhou and O. Tuzel. VoxelNet: End-to-End Learning for Point Cloud Based 3D Object Detection. *ArXiv e-prints*, November 2017.

[18] O. Ronneberger, P. Fischer, and T. Brox. U-Net: Convolutional Networks for Biomedical Image Segmentation. *ArXiv e-prints*, May 2015.

[19] I. Goodfellow. NIPS 2016 Tutorial: Generative Adversarial Networks. *ArXiv e-prints*, December 2017.

[20] I. J. Goodfellow, J. Pouget-Abadie, M. Mirza, B. Xu, D. Warde-Farley, S. Ozair, A. Courville, and Y. Bengio. Generative Adversarial Networks. *ArXiv e-prints*, June 2014.

[21] P. Isola, J.-Y. Zhu, T. Zhou, and A. A. Efros. Image-to-Image Translation with Conditional Adversarial Networks. *ArXiv e-prints*, November 2016.

[22] S. Reed, Z. Akata, X. Yan, L. Logeswaran, B. Schiele, and H. Lee. Generative Adversarial Text to Image Synthesis. *ArXiv e-prints*, May 2016.

[23] Deepak Pathak, Philipp Krähenbühl, Jeff Donahue, Trevor Darrell, and Alexei Efros. Context encoders: Feature learning by inpainting. *CVPR*, 2016.

[24] H. Pirsiavash C. Vondrick and A. Torralba. Generating videos with scene dynamics. *NIPS*, page 613–621, 2016.

[25] T. Xue B. Freeman J. Wu, C. Zhang and J. Tenenbaum. Learning a probabilistic latent space of object shapes via 3d generative-adversarial modeling. *NIPS*, pages 82–90, 2016.

4.10 Additional results

Evaluation procedure

We evaluate the success of the machine learning segmentation according to 3 datasets. The first dataset is consisting of randomly selected images from a variety of movies of amnioserosa tissue. These movies were recorded using a 40x magnification, using a spinning disc microscope with CCD. The time resolution is $10s$/frame. The spatial resolution is $0.3333 \cdot 0.3333 \cdot 1\,\mu m^3 = 1$voxel.

In addition, we selected two full movies of oscillating amnioserosa cells, one with very high quality, already yielding good watershed segmentation accuracy, and one example of lower quality due to low signal to noise and background signal from the yolk. Figure 4.10 shows example frames from the test movies.

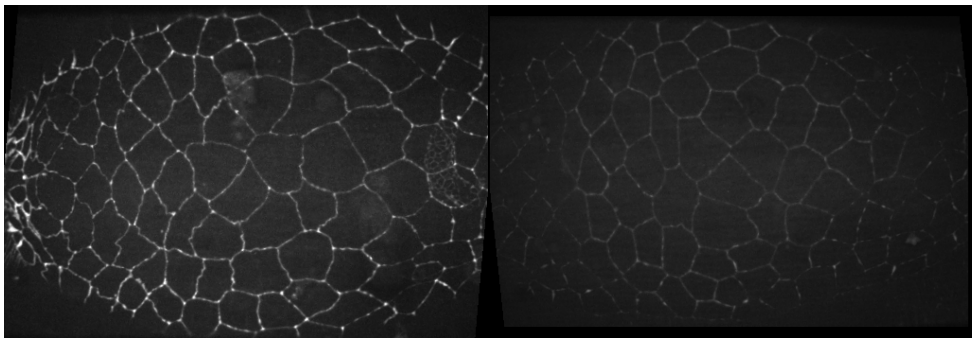

Figure 4.10: Recording quality affects segmentation accuracy. Shown are two example frames from movies used for segmentation evaluation. To the left an example with higher quality is shown that displays clearly visible fluorescent label at the cell borders. To the right the label has lower signal to noise ratio, therefore many cells are not as visible. Microscopy images recorded by Prachi Richa.

Using these three datasets we compute true positive, false positive and false negative rates. The F1 score and the pixelwise dice coefficient are calculated as well. To compare architectures we trained cycleGAN, pix2pix and U-Net architectures. Hereby pix2pix and U-Net are supervised, while cycleGAN is shown unpaired training data. The ground truth for evaluation and training using the Tissue Analyzer [3]. was manually created. For comparison, we also show results from the watershed based Tissue Analyzer.

The training is described in section 4.9. In addition, we tried a variety of architectures. For the cycleGAN we compared ResNet [124] and U-Net architectures for the generator. In case of the ResNet the number in the key denotes the number of blocks, for example CG_Res6 is a cycleGAN architecture with ResNet generator that has 6 blocks. The principle here is that the higher number (ResNet9, Unet256) has basically a bigger receptive field and is able to process larger images at once without cropping. This means that a ResNet9 may learn the relationship between features in the image that are larger apart compared to a ResNet6. The same principle applies to U-Net generators that are tried in the versions 128 and 256, which makes it possible to feed a 128x128px image directly into the U-Net without cropping. The hyperparameters were taken from the optimized versions available on Github by their authors and we did not alter these. However, since at least the U-Net greatly benefits by augmentation, we used a heavily augmented dataset with scaling, shearing, noise and rotation operations. The parameters of the Tissue Analyzer were carefully tested to find the most optimal parameters possible for the watershed. Because we generated the ground with the Tissue Analyzer, there is some experience with this.

Results

We made the general observation that cells in the epithelium that are correctly identified as true positive, usually also have excellent pixelwise overlap with the ground truth. If the networks place a label to denote a cell border, its accuracy is empirically higher than human precision on average. This is because the network identifies features according to which it places the label, while humans might lack concentration over a 3 hour long manual correction session and generally have small deviations due to suboptimal hand-mouse coordination skills.

In figure 4.11 the results for the random test set is shown.

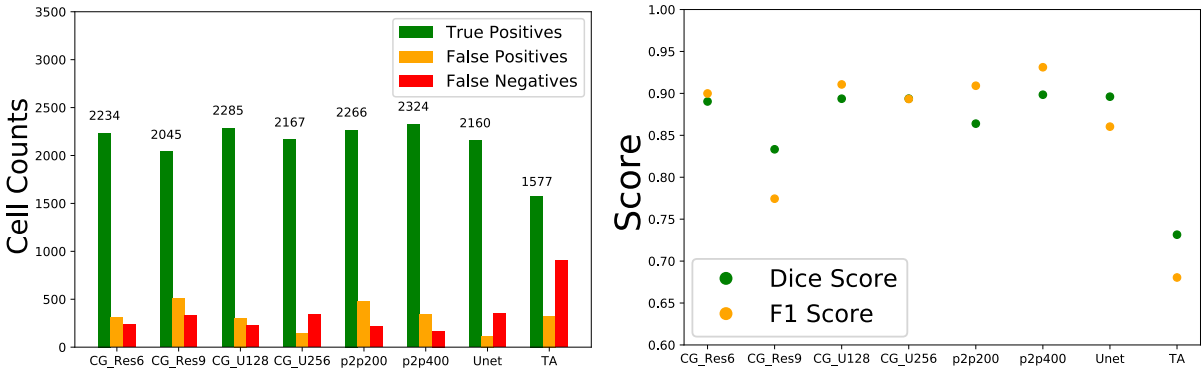

Figure 4.11: Deep learning networks outperform rule-based algorithms in randomly selected microscopy images. Evaluation data was excluded from training data. On the left side TP, FP, and FN are displayed for a number of architectures. The prefix CG is the cycleGAN, p2p stands for pix2pix, Unet is the U-Net architecture and TA is the Tissue Analyzer, which uses watershed based segmentation. To the right there are the corresponding F1 and dice metrics.

The data shows generally high performance across the deep learning frameworks, while the watershed method falls short. This is confirmed by both looking at the total number of successes and errors, as well as the coarse grained F1 score. The pixelwise dice coefficient certifies similar accuracy as the F1 score, which confirms our impression that networks place the label of the cell borders very accurately. In the random data set microscopy images of relatively high quality were overrepresented, which explains some of the similarities with the high quality movie set shown in Figure 4.12. For this dataset the results are even better than for the random set and very high scores are achieved. The watershed technique still underperforms by only finding two thirds of the cells in the tissue.

The results for the last dataset, the movie with low signal quality, is shown in Figure 4.13.

Here, the differences become more pronounced. The Tissue Analyzer, based on watershed, is greatly outperformed by the deep learning solutions. It almost only segments a fourth of the cells in the ground truth. There are also greater differences in the deep learning methods compared to the other datasets. CycleGAN with ResNet9 generator, pix2pix400 and the U-Net show very good performance with relatively low need for manual correction, depending on the required final accuracy. The architectures with the U-Net generator are less successful than with ResNet architectures.

Across all datasets it can be said that the cycleGAN performs with at least comparable accuracy then the supervised pix2pix and U-Net architectures, despite unpaired training. The watershed method is generally outperformed. For the higher quality samples, simpler architectures seem to perform better, namely CG_Res6 and CG_U128. This can probably be explained

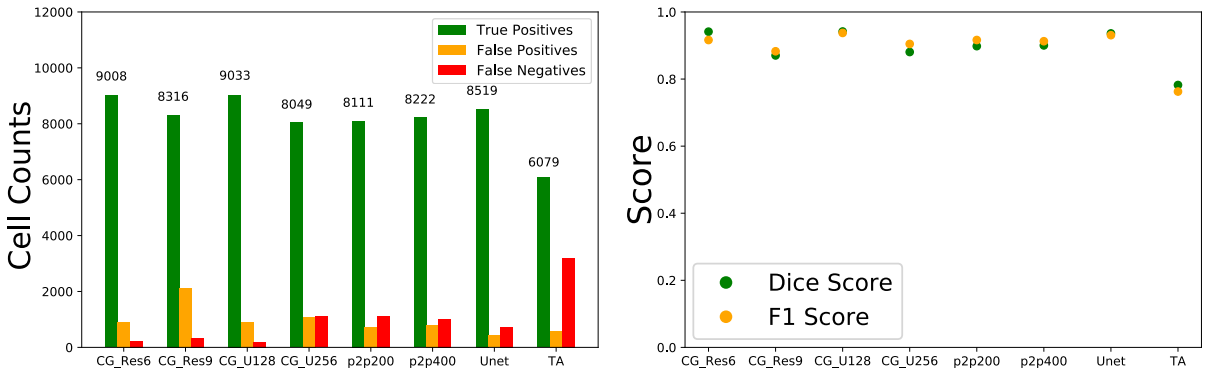

Figure 4.12: Deep learning networks outperform rule-based algorithms in high quality movies. Evaluation data was excluded from training data. On the left side TP, FP, and FN are displayed for a number of architectures. The prefix CG is the cycleGAN, p2p stands for pix2pix, Unet is the U-Net architecture and TA is the Tissue Analyzer, which uses watershed based segmentation. To the right there are the corresponding F1 and dice metrics.

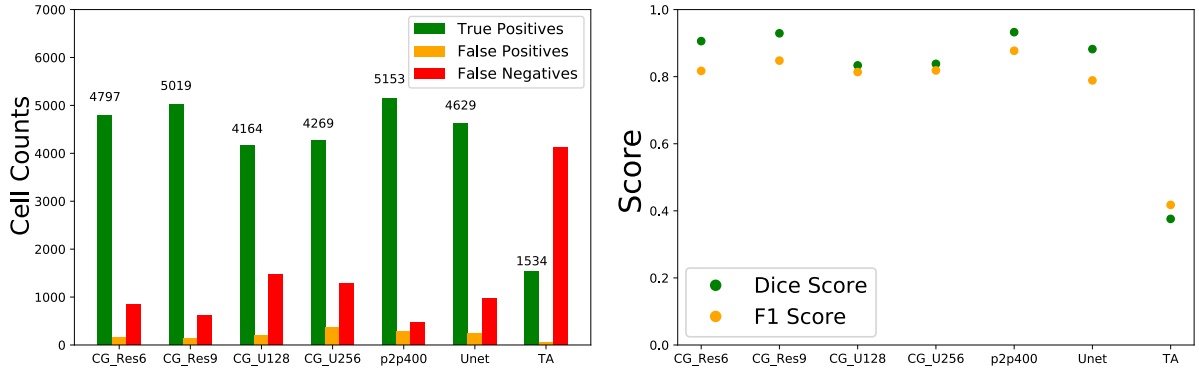

Figure 4.13: Deep learning networks considerably outperform rule-based algorithms in low quality movies. Evaluation data was excluded from training data. On the left side TP, FP, and FN are displayed for a number of architectures. The prefix CG is the cycleGAN, p2p stands for pix2pix, Unet is the U-Net architecture and TA is the Tissue Analyzer, which uses watershed based segmentation. To the right there are the corresponding F1 and dice metrics.

by the narrower receptive field of these generators. If local structures are clearly identifiable, it is better to emphasize local information in the decision making process. If the quality is worse, however, it might be advantageous to take global information into account.

On the movie datasets we also tested the tracking capabilities, which is an important metric for the analysis of time lapse movies. Since all used segmentation methods perform frame by frame, consistency across the whole movie is key. All frames in the movie were segmented and afterwards tracked via a subroutine in the Tissue Analyzer. The method was set to dynamic tissue. If a cell is substantially different at the next frame, for example a frequently occurring error is to place an additional cell border in the cell, then the cell is not tracked anymore but instead a new label is created. Interrupted cell tracking therefore is a measure for the consistency of the segmentation. If the same cells in each frame are always correctly recognized the track will persist across the movie. In Figure 4.14, we compare the best performing cycleGAN with the watershed algorithm form the Tissue Analyzer.

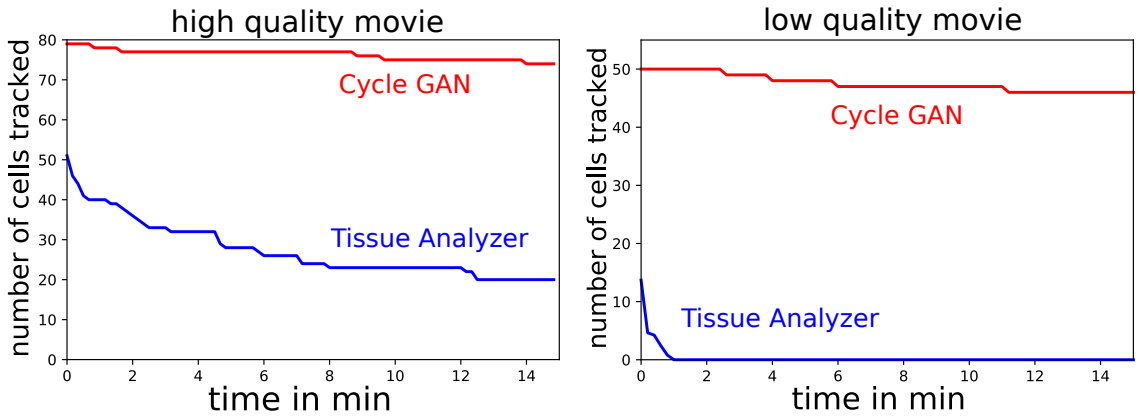

Figure 4.14: CycleGAN segmentation allows to track cells over the course of whole movie. The graph shows how many cells from the first frame still can be tracked in subsequent frames. To the left data from a movie of high quality and signal to noise ratio is shown. To the right data from a movie of low quality is shown.

It can be seen that in both cases, the cycleGAN segmentation performs very consistently, only losing a few cells during the tracking. The Tissue Analyzer, on the other hand, already begins with fewer segmented cells, but also does not find the segmented cells again in the consecutive frame. This shows, that the cycleGAN can perform consistently on a whole movie, even without additional temporal losses that exist in TecoGAN [52] or vid2vid [334] architectures.

Therefore it is now possible to segment large datasets, as we have used in this dissertation, e.g. in chapters 6 and 7. With the here presented method it was possible to segment the data within weeks, including all manual corrections to achieve 100% accuracy which would have been unfeasible before.

4.11 Data acquisition and analysis pipeline

In order to analyze an ensemble of epithelial cells from *Drosophila* embryos a fully automated data acquisition pipeline is built upon the deep learning segmentation framework. In practice, several steps may need manual supervision or correction to achieve the desired outcome.

Pipeline

The pipeline was conceived with the goal in mind to allow integration into other existing workflows. In the community there a strong bias to use FIJI [291] as the platform to process microscopy data. For segmentation, tracking and rudimentary data parsing there is the *Tissue Analyzer* [3]. Tools like this should remain usable, which is why the pipeline is build in a modularized way such that single processing steps can be substituted. The processing stages in the pipeline are

1. preprocessing
2. segmentation
3. cell detection and tracking
4. data parsing

Afterwards the data is analyzed using custom written software in Python. Especially the segmentation and tracking step can be supplemented with manual corrections.

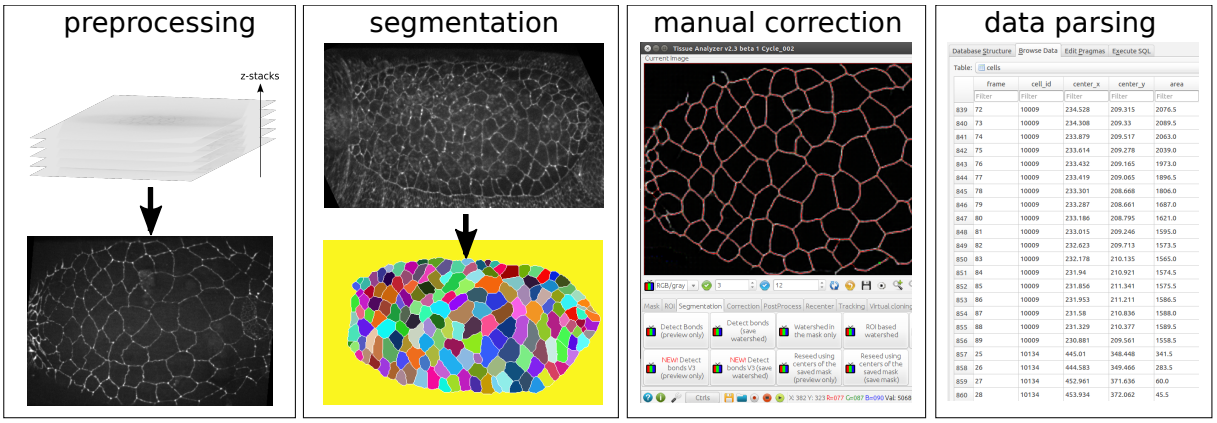

Figure 4.15: Data acquisition pipeline consisting of preprocessing, segmentation, manual correction and data parsing. In the first step microscopy image stacks are projected and images are put into correct format. The neural network produces a prediction map for the segmentation label. Using the Tissue Analyzer cell labels are created and errors are manually corrected. Finally the data is parsed from the finalized segmentation.

The first stage is preparing the raw images for further processing. This includes the conversion of the file format, rescaling the image and saving the images in the correct folders for the segmentation.

The segmentation takes the preprocessed images and creates prediction maps of the images. The pixels of the cell border and the background are labeled.

After segmentation watershed is used to obtain skeletonized versions of the cell borders that have only 1 pixel width. Beforehand a Gaussian filter is used on the prediction map, which can help to close small gaps in the labeled cell borders. The Tissue Analyzer then creates cell labels and tracks cells across the whole movie. In this step, we can use the existing UI of the Tissue Analyzer to manually correct the remaining segmentation errors.

To parse the data, the Tissue Miner [221] is used, which uses the segmentation data created by the tissue analyzer and calculates cell area, anisotropy and more. The data is saved in SQL tables. From there, the data can be further processed in Python or any other evaluation software.

4.12 Summary

In this chapter, we built a data acquisition pipeline based on generative adversarial networks. The networks can be trained even in absence of paired ground truth training data and show similar performance in comparison to the U-Net. Rule-based methods are significantly outperformed.

We use this pipeline to generate data from time-lapse movies of the amnioserosa in *Drosophila*. An example for such a segmentation is shown in Figure 4.16.

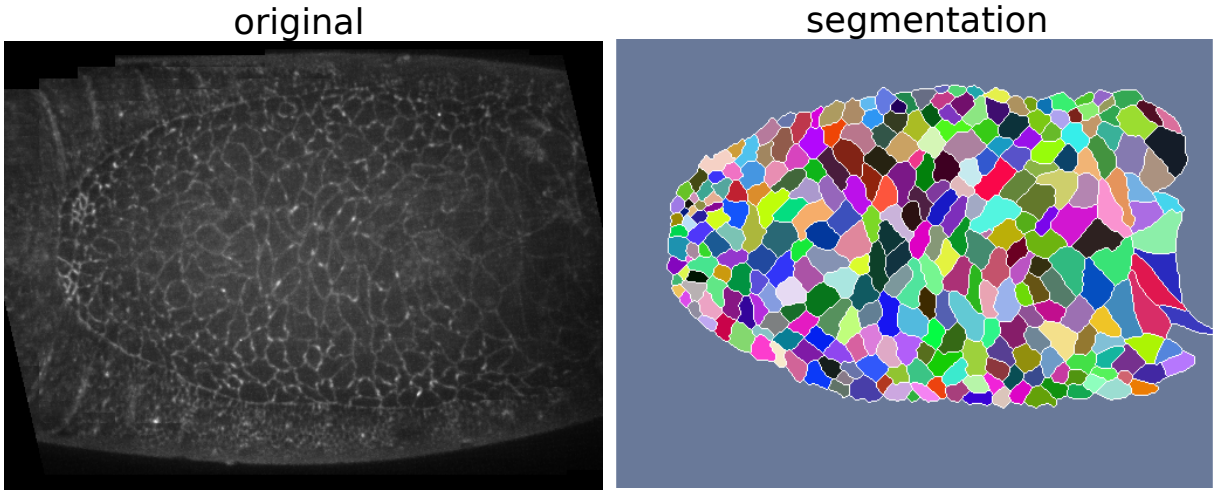

Figure 4.16: Segmentation example of *Drosophila* amnioserosa tissue from *Tmc* mutant using cycleGAN. (left) Maximum projection of a frame from the original timelapse movie. (right) The completed segmentation. Colors of each cell uniquely labels them.

Such a time-lapse movie typically consists of several hundred frames that all have to be segmented. Because our research requires complete segmentation of the whole tissue manual correction is needed to correct the errors of the neural network prediction. The time needed for the correction depends on the number of frames but also on the quality of the original image. For movies with very high signal to noise ratio, the network prediction is already close to 100% and almost needs no correction. In those cases several full movies can now be segmented in a day. Previously this would have been a task lasting several weeks, despite the good quality of the source material. However, especially autofluorescence of secondary features, like the underlying yolk, can increase the time to perform the manual correction because cell borders are hardly visible even for human eyes. In those cases the processing can take a day or even several days. Via rule-based methods the manual correction would have taken several weeks.

We have preliminary data suggesting that some further improvements of the accuracy can be achieved if another loss is added to punish temporal deviations of the segmentation when comparing frames. Unpaired temporally consistent GANs already exist [52] and have shown to improve the accuracy for video to video translation tasks.

The methods described in this chapter are directly applied in chapters 6 and 7.

Chapter 5

Mathematical modeling of epithelial cell dynamics

"Never make a calculation until you know the answer. "

J. A. Wheeler

5.1 Content

In this chapter, a mathematical theory for the dynamics of amnioserosa tissue is constructed. The model consists of single one dimensional cell units operating on a hexagonal lattice. Cell units are capable of area oscillations and are coupled to their neighbors via mechanical and chemical interactions. The approach is to utilize a simple model to study how emergent tissue scale coordination, which is observed in experiments (see Chapter 6), can arise from local cell dynamics and coupling.

A scheme of the most important model parts is shown in Figure 5.1. Each cell is following the model introduced by Dierkes et al. [64], consisting of dynamical equations for the cell surface area and its actomyosin dynamics. In their model, the cell area is described by a one dimensional effective coordinate coupled to an underlying chemical reservoir of force producing molecules (myosin). Due to interactions of area dynamics and myosin turnover, the system yields area oscillations, resulting from a Hopf-bifurcation in the dynamical system for critical parameter values.

We devise extensions to this model: adding Gaussian noise to the cell area dynamics, solving the dynamics of N cell units on a 2-dimensional hexagonal lattice with ellipsoidal topology and adding interactions between neighboring cells.

The first of these interactions introduces a negative coupling between two cells to model mechanical interactions. If a cell expands, its neighbors have to decrease in area to give way to the expansion of their neighbor due to geometrical constraints. The whole tissue has an ellipsoidal topology, resembling the amnioserosa shape, surrounded by border cells with high stiffness which are preserving the total area of the tissue.

For the second interaction, we introduce another dynamical compartment which is modeling Ca^{2+} dynamics. Due to contraction in a neighbor cell, tension is exerted at the cell-cell border between two cells. The pulling of the neighbor cell opens an ion channel which leads to Ca^{2+} increases in the cell that is subject to the tension. Myosin dynamics is coupled to the Ca^{2+} compartment, leading to an increase of the myosin concentration, which in turn induces area contraction. This mechanism provides a positive coupling between contracting neighboring cells.

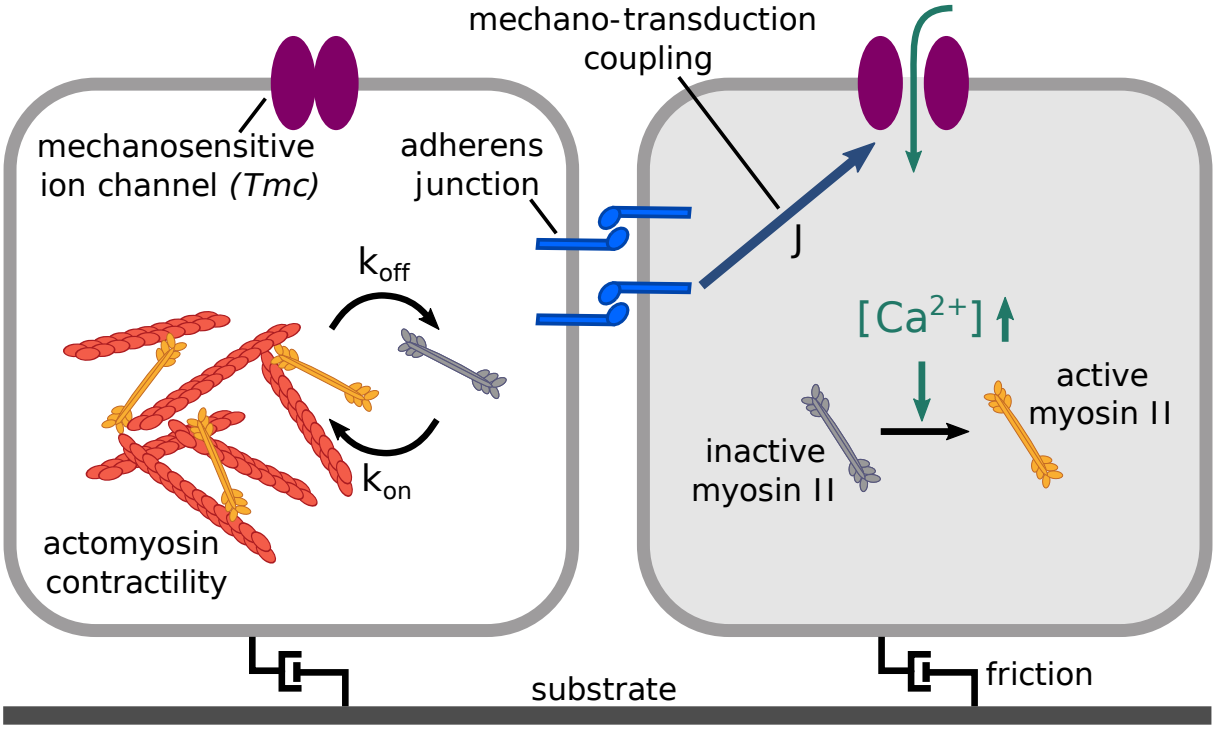

Figure 5.1: Basic principle of the model of intercellular coordination created in this chapter. Each cell has a surface area that is modeled as one dimensional contractile element which is coupled to actomyosin dynamics. Actomyosin dynamics is governed by the force producing compartment myosin and its association and dissociation rates. The interplay between area dynamics and myosin turnover gives rise to oscillations in a certain parameter regime. Neighboring cells are mechanically coupled to each other. The innovation lies in the mechano-chemical coupling of neighboring cells. Contractions from one cell result in mechanical activation of Ca^{2+} dynamics, which serves as upstream regulator of myosin. Ca^{2+} mediated, myosin induced, area contraction leads to synchronization of neighboring area dynamics. Epithelial cells are also subject to the three dimensional geometry of the embryo and may be coupled to underlying substrates, which is explicitly modeled as additional friction.

We show that this Ca^{2+} coupling mechanism leads to synchronization of the oscillations between neighboring cells. We perform simulations for a case of only two coupled cells as well as for the full 2D tissue.

In order to compare the model to the experiments, the distribution of correlation coefficients is calculated from several simulation runs of the full 2D simulation. The Jensen-divergence serves as distance metric between model outcome and experiment. We fixed all parameters except for the coupling strength J and the fraction of coupled neighbors, which is expressed by the occupation probability p. J determines the strength of the mechano-transduction coupling, effectively determining how strongly the Ca^{2+} inflow is in response to the mechanical stimulus, and p the heterogeneity of cell junctions by adding the Ca^{2+} coupling only to random junctions with uniformly distributed probability p.

Simulations are compared to wild type amnioserosa tissue and a mutant called *Tmc* , which is a ion channel knockout. The sloppiness of the model in the occupation probability parameter is greater compared to the real *Tmc* distribution, which means that more parameter combination can produce close matches to the experiment, while in WT optimal parameters are clearly biased

toward a homogeneous distribution of channels and a fixed coupling strength. This suggests that a distribution of correlation coefficients which is skewed towards anticorrelated values, like in *Tmc* , is much easier to obtain. In contrast, the parameter landscape for WT is unimodal and has a sharp peak. Therefore, a distinct mechanism is necessary to find the comparably high synchronization we see in the wild type. Antisynchronized cell oscillations are the natural state of mechanically coupled oscillators which explains why *Tmc* mutants reduce overall coordination if it simply switches off the coupling mechanism.

Using these parameters, we conduct simulations where Ca^{2+} is suddenly increased in a random cell that does not lie at the border of the tissue. We find that with stronger coupling, the neighbors of this cell are following the contraction induced by the increase in Ca^{2+} and decrease in area as well. In case of weak coupling, neighboring cells react to the contraction of their neighbor by expanding. This prediction of the model is experimentally tested, and confirmed, in chapter 7.

5.2 Viscoelastic models

The aim in this chapter is to model a biological system simplified as coupled oscillators. Epithelial tissue is falling into the category of soft matter where some of the basic assumptions from solid matter physics can not be applied. Most importantly, tissue and cell dynamics is dissipative and shows time dependent strain response when stress is exerted: a phenomenon commonly referred to as viscoelasticity. Other types of models that are not used here have been discussed in section 2.15.

Elastic materials deform when subjected to stresses and return to the reference configuration in absence of said stress. Viscous materials resist deformations linearly with time if stresses are applied. Viscoelastic material have both properties, thus resulting in time dependent strain in response to applied stresses. The most important distinction is that for elastic materials the stress-strain curve is the same for forward and backward process, showing no hysteresis, and that the stress does not depend on strain history, only on the momentary configuration [17].

The basis of the eventual tissue model is a linear viscoelastic model. By linear we mean that the strain tensor is linearly related to the stress tensor. In addition, linear combinations of stresses must result in the same strain response as if those contributions would be applied separately and afterwards linear combinations of the strain are formed [17].

The canonical equations of elastic and viscous materials are Hooke's law

$$\sigma(t) = E\epsilon(t) \tag{5.1}$$

for instance modeling a spring, and Stokes' law

$$\sigma(t) = \eta\frac{\mathrm{d}\epsilon(t)}{\mathrm{d}t} \tag{5.2}$$

which describes the dynamics of a dashpod and models dissipation. The symbols denote the stress $\sigma(t)$, the strain $\epsilon(t)$ with the elastic modulus E and the viscosity η.

These basic elements can be combined in different ways which yields the basic viscoelastic models, depicted in Figure 5.2. The *Maxwell body* [242] has a serial connection between spring and dashpod yielding

$$\frac{\mathrm{d}\epsilon(t)}{\mathrm{d}t} = \eta^{-1}\,\sigma(t) + E^{-1}\,\frac{\mathrm{d}\sigma(t)}{\mathrm{d}t} \tag{5.3}$$

Connecting the elements in parallel results in the *Kelvin-Voigt (KV) model* [242], which will be used in later sections

$$\sigma(t) = E\epsilon(t) + \eta\frac{\mathrm{d}\epsilon(t)}{\mathrm{d}t} \tag{5.4}$$

Both can be solved analytically [90]. The KV model is widely used to model polymers and also actin dynamics which is important for this study. Many studies have been able to accurately predict actin dynamics using a KV type model [64, 193]. Further extensions can be applied for instance by including plasticity [358] (not returning to the reference configuration) or nonlinear terms [17]. However, we will only use the basic linear viscoelastic version.

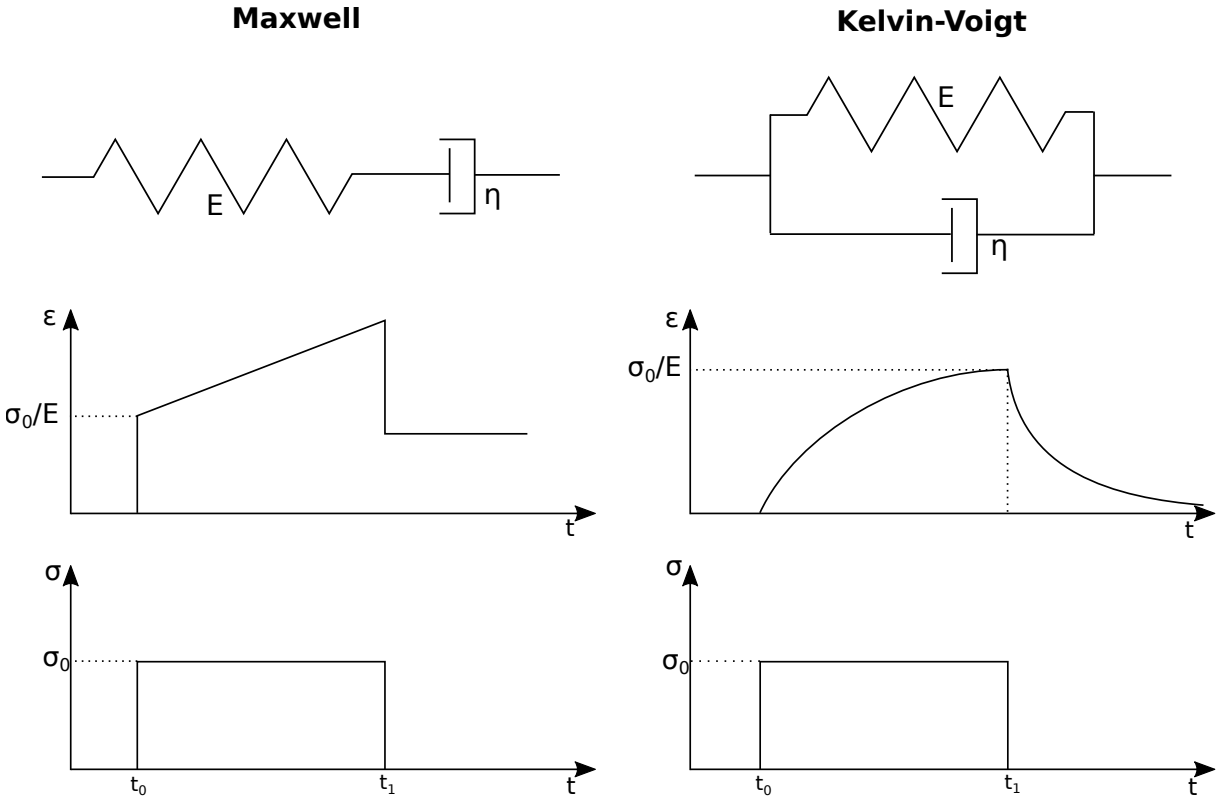

Figure 5.2: Viscoelastic models consist of the two elements spring and dissipative dashpot. The here depicted Maxwell and Kelvin-Voigt models are the most simple ways to connect both elements to yield a linear viscoelastic element. (top) Configuration of spring and dashpod. (middle) Response curve when element is subjected to tension. (bottom) Tension that is applied to the element.

5.3 Single cell model and the linear chain

As basis for the full tissue model we are first discussing how to model a single cell unit from mechanical and chemical principles. The resulting system of differential equations combines viscoelastic dynamics with a coupling to a reservoir of force producing molecules.

Contributions

Section 5.3 is reviewing results of Dierkes et al. [64] and Lo et al. [193]. Symbols may have been changed to keep the notation consistent throughout the thesis. Compared

to the original publications this text puts a different focus on certain subjects with the aim to lay the ground work for subsequent sections. To this end, additional calculations and discussions have been added that do not have to reflect opinions of the original authors.

Viscoelastic material with turnover

In order to mathematically describe cell oscillations in *Drosophila*, Dierkes et al. [64] have applied the Kelvin-Voigt model with an added active force-generating compartment. The model consists of a spring with parallel dashpod and a dynamical compartment with feedback between the size of the element and a contracting force. Figure 5.3 shows a basic scheme of this model.

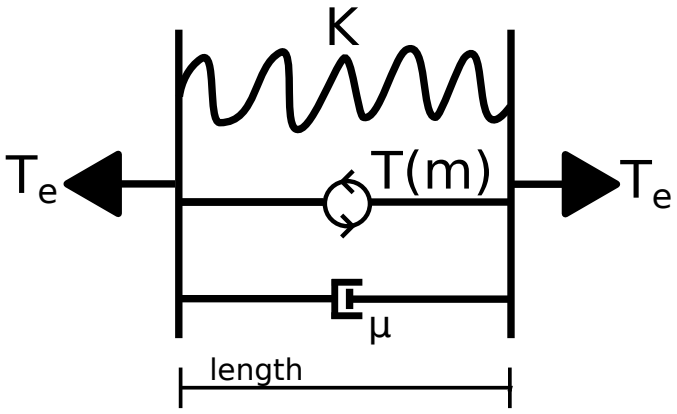

Figure 5.3: Dierkes' viscoelastic contractile material with turnover. Similar to the Kelvin-Voigt model we have a parallel configuration of spring and dashpod, yielding a viscoelastic material. In addition, myosin turnover is added, which produces tension exerted on the contractile element $T(m)$. In the steady state, this tension is balanced by an external tension T_e.

The dynamical system reads

$$\mu \frac{\mathrm{d}l}{\mathrm{d}t} = T_e - T(m) - K(l) \tag{5.5}$$

$$\frac{\mathrm{d}m}{\mathrm{d}t} = -\frac{1}{\tau_m}(m - m_0) - \frac{m}{l}\frac{\mathrm{d}l}{\mathrm{d}t} \tag{5.6}$$

Here, l denotes the length of the contractile element, m the myosin concentration, μ the damping coefficient and τ_m the timescale of myosin turnover.

Equation (5.5) is a direct application of a Kelvin-Voigt model with an additional force term $T(m)$ which we call the myosin induced tension. $K(l)$ describes the Hooke spring response and T_e denotes the equilibrium tension at (m_0, l_0).

$$T(m) = T(m_0) + t_1(m - m_0) \tag{5.7}$$

$$K(l) = K(l_0) + k_1(l - l_0) + k_3(l - l_0)^3 \tag{5.8}$$

$$T_e = T(m_0) + K(l_0) \tag{5.9}$$

The myosin tension causes a linear contraction of the element. The spring response is expanded until third order because we want the system to exhibit oscillations and the nonlinearity drives the system into a Hopf-bifurcation for critical values of k_3. The second order term must be omitted to keep the solution antisymmetric.

For the myosin dynamics, two effects are considered: (i) conservation of mass and (ii) turnover according to constant rate dynamics. Considering the density of myosin ρ along the contractile element of length l we begin by writing down the continuity equation

$$\partial_t \rho + \partial_x(\rho v_x) = k_{on} - k_{off}\rho \tag{5.10}$$

Here, x denotes the length and v_x the velocity of element length change. Now, we integrate both sides

$$\int_{x=0}^{x=l} \partial_t \rho + \partial_x(\rho v_x)\,\mathrm{d}x = \int_{x=0}^{x=l} k_{on} - k_{off}\rho\,\mathrm{d}x \tag{5.11}$$

which yields

$$\partial_t \int_{x=0}^{x=l} \rho\,\mathrm{d}x + \int_{x=0}^{x=l} \partial_x(\rho v_x)\,\mathrm{d}x = k_{on}l - k_{off}\int_{x=0}^{x=l} \rho\,\mathrm{d}x \tag{5.12}$$

Dividing by l on both sides and identifying the integral over ρ with the myosin concentration $m = \frac{1}{l}\int_{x=0}^{x=l} \rho\,\mathrm{d}x$ yields

$$\frac{\mathrm{d}m}{\mathrm{d}t} = k_{on} - k_{off}m - \frac{m}{l}\frac{\mathrm{d}l}{\mathrm{d}t} \tag{5.13}$$

Assuming that the rates are constant and follow the timescale τ_m we can write $k_{on} = m_0/\tau_m$ and $k_{off} = 1/\tau_m$ which results in equation (5.6).

The equations for the 1-dimensional contractile element can be extended to a 1-dimensional area description

$$\tilde{\mu}\frac{\mathrm{d}A}{\mathrm{d}t} = T_e - T(m) - \tilde{K}(A) \tag{5.14}$$

$$\frac{\mathrm{d}m}{\mathrm{d}t} = -\frac{1}{\tau_m}(m - m_0) - \frac{m}{A}\frac{\mathrm{d}A}{\mathrm{d}t} \tag{5.15}$$

To this end, equations (5.5) and (5.6) can simply be multiplied with a fixed width l_0.

$$\tilde{\mu}l_0\frac{\mathrm{d}l}{\mathrm{d}t} = T_e - T(m) - \tilde{K}(l\,l_0) \tag{5.16}$$

$$\frac{\mathrm{d}m}{\mathrm{d}t} = -\frac{1}{\tau_m}(m - m_0) - \frac{l_0}{l_0}\frac{m}{l}\frac{\mathrm{d}l}{\mathrm{d}t} \tag{5.17}$$

We will use this 1-dimensional description of the cell area dynamics in the following sections. Whether such an effective description is valid is discussed later in this section.

Linear stability

The viscoelastic contractile model with turnover, as described in this section, is able to produce oscillations due to a Hopf bifurcation in the dynamical system. A full discussion on linear stability of this model can be found in [64] and [193]. We here only state the result for the oscillatory transition.

Linearization of the dynamical system yields two eigenvalues $r \pm i\omega$, with

$$r = \frac{\bar{t}_1\bar{\tau}_m - 1 - \bar{\tau}_m}{2\bar{\tau}_m} \tag{5.18}$$

$$\omega = \frac{\sqrt{4\bar{\tau}_m - (1 + \bar{\tau}_m - \bar{t}_1\bar{\tau}_m)^2}}{2\bar{\tau}_m} \tag{5.19}$$

where $\bar{\tau}_m = \frac{\tau_m k_1}{\mu}$ and $\bar{t}_1 = \frac{t_1 m_0}{k_1 A_0}$. The Hopf bifurcation transition is therefore at $\bar{t}_1 = 1 + \frac{1}{\bar{\tau}_m}$. At that point the angular frequency is given by $\omega = \frac{1}{\sqrt{\bar{\tau}_m}}$.

Further investigation shows that the transition is supercritical for

$$3\frac{k_3 l_0^2}{k_1}\left(\frac{\mu}{\tau_m k_1}+1\right) > 2\left(\frac{\mu}{\tau_m k_1}\right)^2 + 6\frac{\mu}{\tau_m k_1} + 4 \tag{5.20}$$

In this case, the amplitude of the oscillation is mainly determined by the parameter k_3. Figure 5.4 shows a phase diagram for this system.

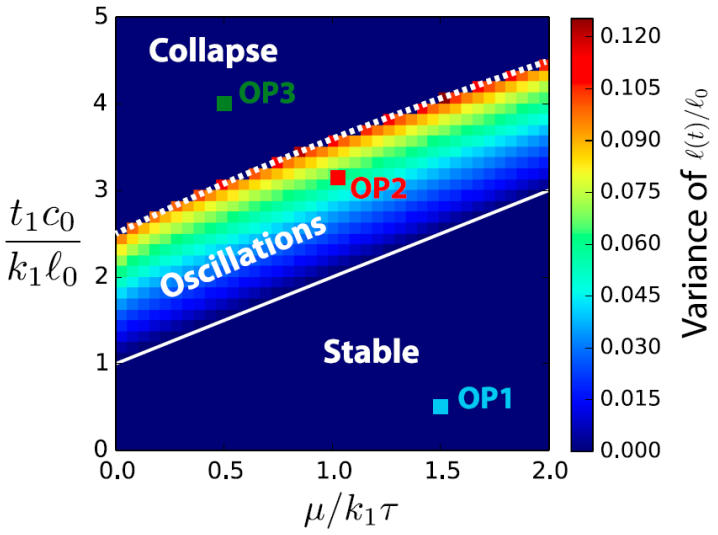

Figure 5.4: Effective myosin induced contractile tension and effective internal friction determine the emergence of oscillations. Shown is the phase diagram for the elastic contractile material with turnover. The notation in this section slightly deviates from the notation used as the x and y label. In particular it is $\tau = \tau_m$ and $c_0 = m_0$. The diagram shows that the oscillatory transition due to the Hopf bifurcation is controlled by the effective myosin strength on the y axis and the effective internal damping on the x axis. Figure taken from [64].

Oscillations arise because of the interplay of myosin turnover and contractile element size. Consider an element in equilibrium for both l and m. Now we perturb the system by pulling and thus increasing its size. the myosin concentration drops because the number of molecules stays the same, which results in myosin association. The tension exerted by the myosin increases until the equilibrium concentration m_0 is reached. Meanwhile the myosin tension and the elastic response of the spring have begun to counteract the imposed elongation and the element contracts. Because of the myosin turnover timescale and the nonlinear damping there is no instantaneous reaction and the concentration overshoots before myosin dissociates when its concentration is above the equilibrium. This causes the element to contract further than it would have because of the increased myosin. A backward cycle begins which follows exactly the same reasoning only in the other direction.

Crucial for the stability of the oscillation is the correct ratio of myosin produced force t_1 and spring elasticity k_1 on the one hand, and the ratio of internal damping μ and myosin turnover rate τ_m on the other. Damping and turnover timescale cause a delay in the myosin association and dissociation which accelerates the contractile element just enough in the opposite direction, which causes the cycle. However this only works if the strength of the myosin is high enough in comparison to the elastic constant of the spring. Internal damping dissipates energy from the system and thus requires more energy/myosin tension to keep the limit cycle going.

The phase diagram in addition shows that another possible solution of the system is to run into a fixed point, and therefore display stable dynamics for subcritical parameter values. For higher effective myosin strength $\bar{t}_1$ the system displays a collapse phase which means that the myosin compartment is diverging, driving the contractile element to shrink to zero. This happens when the myosin turnover rate, determined by τ_m, can not keep up with the shrinking element. The concentration rises faster than the off rates can dissociate myosin from the element, thus leading to diverging tension.

The authors argue that this collapse solution of the model could reflect the ingression and following apoptosis of amnioserosa cells during dorsal closure. Cells have to make room when the amnioserosa is contracting to close the dorsal side of the fly embryo therefore decrease to zero. This interpretation is debated [193]. Authors in [193] point out that, at the diverging critical point, the numerical stability of the simulation can no longer be trusted. They have devised an alternative description that includes ingression without singularities in the solution.

Later, we will extend the model of Dierkes et al. to investigate intercellular synchronization. To this end, parameter regions are chosen that show oscillatory behavior and the collapse is not of interest. The singularity, causing the diverging solution, therefore plays no role for us. In addition, for those parameters the revised model of Lo et al. [193] is mathematically equivalent to the model of Dierkes et al.

Validity of effective low dimensional representation

Whether we are permitted to use a low dimensional effective description of cell area dynamics is not immediately clear. A real biological cell in a tissue is a three dimensional object and can generally not be considered a one dimensional viscoelastic element. The cellular compartments are soft, usually subject to anisotropic tension and can react with local plastic deformations of the cytoskeleton instead of global oscillations.

Nonetheless, fitting the effective viscoelastic model to data shows good agreement [64] and makes it clear that, depending on task and scientific question behind the modeling, such an effective description can be successful despite the above-mentioned drawbacks. The most important argument why this works is that the actomyosin dynamics causing cellular deformations is mostly happening at the apical surface of the cell. A two dimensional cross-sectional description of cell area dynamics is thus actually not far from the true dynamics because the rest of the three dimensional cell is simply following the dynamics of the apical part. Even more convincingly, in the case of the amnioserosa, we are presented with a squamous epithelium that is very flat. In comparison to the germband where cells have an average depth of 15-20μm, amnioserosa cells only have a depth of 4-5μm while having an average area of 180μm^2.

Secondly, it has to be taken into consideration that the actomyosin dynamics is local and comprised of the dynamics of many actin filaments, interacting with myosin II. It is therefore not clear whether an effective one-dimensional description of the whole area must faithfully represent the actual microscopic dynamics. Local processes might give rise to anisotropic dynamics within a single cell.

Instead of making the top down assumption that we can describe cell area dynamics by an effective reaction coordinate, Lo et al. [193] have developed a unified biophysical mechanism for cell-shape oscillations by beginning with the modeling from the dynamics of single actomyosin contractile elements. The full discussion will not be repeated here and the interested reader is referred to the study.

In a nutshell, Lo et al. treat single actin filaments as viscoelastic elements, described by the same visco-elastic equations as the ones of Dierkes et al. Using percolation theory they derive the full area dynamics as emerging effect from the microscopic acto-myosin dynamics. In addition, the microscopic treatment shows that it is necessary to incorporate a duty ratio into

the equations that describes the time a myosin II motor is bound to an actin filament during the mechanoenzymatic cycle. The force that myosin can exert locally onto the crosslinked actomyosin network depends on the duty ratio and the number of myosin heads that can bind to actin.

Via nondimensionalization and linear stability analysis Lo et al. show that they arrive at the same effective description as Dierkes et al. only deviating by the additional terms for the duty ratio. The duty ratio makes it possible to faithfully describe the ingression of cells, which were given in the Dierkes model only via numerically instable solutions due to a singularity. For the oscillation solution their equations are mathematically equivalent.

The consistency between the models of Dierkes et al. and Lo et al. for the oscillatory dynamics shows that an effective one dimensional description can suffice for a simple representation of amnioserosa bulk cell dynamics. The trajectories fit to experimental data [64] and the effective mathematical form emerges from detailed modeling of microscopic dynamics.

Viscoelastic chain model

We start by considering a linear chain of viscoelastic springs of total length L and want to derive an equation of motion for the nth border between two springs. A scheme of the linear chain is depicted in Figure 5.5

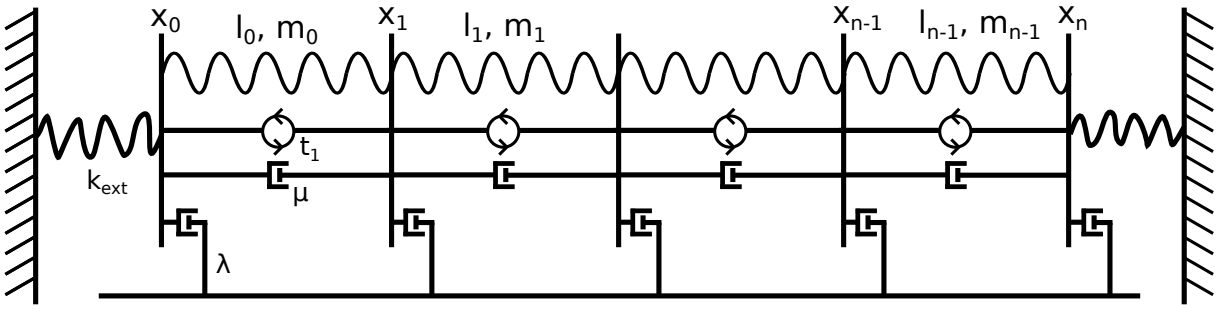

Figure 5.5: Chain of viscoelastic contractile elements with turnover. Each element length l_i is determined by the positions of the borders x_i and x_{i+1} and the myosin concentration on the element is m_i. Spring, dashpod and myosin turnover determine the stress that is exerted on each border. The chain is connected to walls via external springs k_{ext}. Each border is subjected to an additional substrate friction λ.

If the position of a cell border is denoted by x, its equation of motion, according to Newton's law, reads

$$M\frac{\mathrm{d}^2x}{\mathrm{d}t^2} = -\lambda\frac{\mathrm{d}x}{\mathrm{d}t} + \sum_i F_i \tag{5.21}$$

where F_i denotes forces acting on that border, M is the mass and λ a friction coefficient. As a first approximation we consider the overdamped regime which means that we can neglect inertial forces, which reduces the equation to

$$\lambda\frac{\mathrm{d}x}{\mathrm{d}t} = \sum_i F_i \tag{5.22}$$

The sum of the forces on the right hand side consists of the forces from the springs on either end. Here the equation for the force results from the assumption that that viscoelastic springs follow

a Kelvin-Voigt model as described in section 5.2. In the KV-model the spring is in parallel with a dashpod which results in following balance

$$\sigma = E\epsilon + \eta\frac{\mathrm{d}\epsilon}{\mathrm{d}t} \tag{5.23}$$

where σ denotes the stress, ϵ the strain, E the elastic modulus and η the damping. Each position in the linear chain is connected to 2 viscoelastic elements acting in opposite directions. For the nth border we therefore obtain

$$\lambda\frac{\mathrm{d}x_n}{\mathrm{d}t} = f_n - f_{n-1} \tag{5.24}$$

$$f_n = T(m_n) + K(l_n) + \mu\frac{\mathrm{d}l_n}{\mathrm{d}t} \tag{5.25}$$

using Dierkes extension with the myosin compartment for the myosin induced tension $T(m)$ as additional force contribution. $T(m)$ and $K(l_n)$ assume the same form as in equations (5.7) and (5.8), where the length of a contractile element is defined as

$$l_n = x_{n+1} - x_n \tag{5.26}$$

The myosin dynamics then follows the known equation (5.6). The linear chain can be realized with periodic boundary conditions. Otherwise, the boundary is included via external springs with spring constant k_{ext} as depicted in Figure 5.5.

5.4 Special case: 2 cells

In order to investigate how our extensions, which will be introduced in later sections, alter the basic behavior of the model we will run simulations of only two cells that interact with each other. Figure 5.6 shows the basic structure of the 2 cell model.

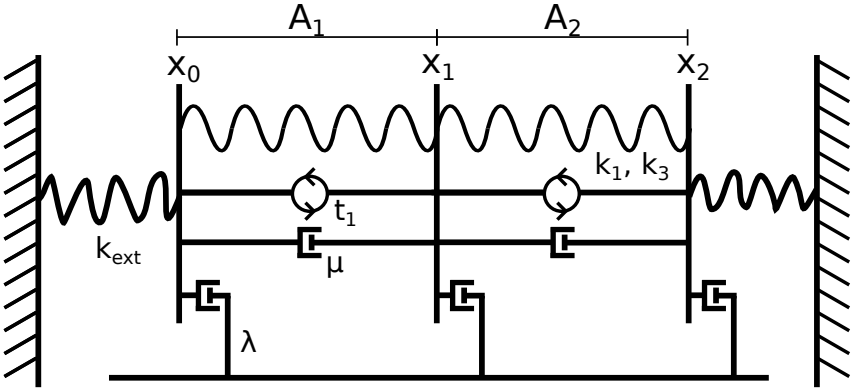

Figure 5.6: Scheme of the two cell system. In addition to the known interactions from the basic model [64], we will later add mechano-chemical coupling between the two cells and stochasticity.

From the equations for the linear chain (5.24) and (5.25) we deduce the following system for

a chain of two elements

$$\lambda\frac{\mathrm{d}x_0}{\mathrm{d}t} = T(m_1) + K(A_1) - k_{ext}(x_0 - x_0^0) + \mu\frac{\mathrm{d}(x_1 - 2x_0)}{\mathrm{d}t} \tag{5.27}$$

$$\lambda\frac{\mathrm{d}x_1}{\mathrm{d}t} = T(m_2) + K(A_2) - T(m_1) - K(A_1) + \mu\frac{\mathrm{d}(x_2 - 2x_1 + x_0)}{\mathrm{d}t} \tag{5.28}$$

$$\lambda\frac{\mathrm{d}x_2}{\mathrm{d}t} = -T(m_2) - K(A_1) - k_{ext}(x_2 - x_2^0) + \mu\frac{\mathrm{d}(-2x_2 + x_1)}{\mathrm{d}t} \tag{5.29}$$

$$\tag{5.30}$$

Myosin dynamics is omitted here since it is independent of the topology of the model and always follows equation (5.6). We see that we can write this system in terms of a mass-matrix on the left hand side and the sum of forces on the right hand side since x appears only linearly on both sides

$$M\vec{\dot{x}} = \vec{F}(\vec{x}) \tag{5.31}$$

where

$$M = \begin{pmatrix} \lambda + 2\mu & -\mu & 0 \\ -\mu & \lambda + 2\mu & -\mu \\ 0 & -\mu & \lambda + 2\mu \end{pmatrix} \tag{5.32}$$

and

$$\vec{F}(\vec{x}) = \begin{pmatrix} T(m_1) + K(A_1) - k_{ext}(x_0 - x_0^0) \\ T(m_2) + K(A_2) - T(m_1) - K(A_1) \\ -T(m_2) - K(A_1) - k_{ext}(x_2 - x_2^0) \end{pmatrix} \tag{5.33}$$

In the following sections we extend this to arbitrary length and number of elements as well as different topologies like the hexagonal lattice.

5.5 The tissue model

The amnioserosa epithelium will be modeled as single cell units which follow the dynamics described in the previous sections and are arranged on a triangular lattice. We are not modeling the hexagonal configuration with tight packing where all vertices are moving freely. Rather the model is comprised of one dimensional limit-cycle oscillators on a grid, with connections determined by an interaction matrix. To understand how the mechanical interactions are realized on the lattice it is instructive to take a look at the linear chain first and develop an understanding from there.

From border to length dynamics

We take another look at the linear chain and ask the question how the dynamics of the length of the contractile elements is determined by the dynamics of the borders. Borders (of 0 width) experience dissipation mediated by the friction coefficient λ and at the ends of the chain are springs with external spring constant k_{ext} that are connected to non-moving walls, which is displayed in Figure 5.5.

We start with the force balance for the nth position of a cell border as described in section 5.3.

$$\lambda\frac{\mathrm{d}x_n}{\mathrm{d}t} = f_n - f_{n-1} \tag{5.34}$$

$$f_n = T(m_n) + K(l_n) + \mu\frac{\mathrm{d}l_n}{\mathrm{d}t} \tag{5.35}$$

To obtain the dynamical equation for change of length, it has to be expressed in terms of the position of its borders. Then (5.35) is inserted

$$\begin{aligned}
\lambda\frac{\mathrm{d}l_n}{\mathrm{d}t} = \lambda\frac{\mathrm{d}x_{n+1}}{\mathrm{d}t} - \lambda\frac{\mathrm{d}x_n}{\mathrm{d}t} &= f_{n+1} - f_n - f_n + f_{n-1} && (5.36)\\
&= -2f_n + f_{n+1} + f_{n-1} && (5.37)\\
&= -2\left[T(m_n) + K(l_n) + \mu\frac{\mathrm{d}l_n}{\mathrm{d}t}\right] && (5.38)\\
&\quad + T(m_{n+1}) + K(l_{n+1}) + \mu\frac{\mathrm{d}l_{n+1}}{\mathrm{d}t}\\
&\quad + T(m_{n-1}) + K(l_{n-1}) + \mu\frac{\mathrm{d}l_{n-1}}{\mathrm{d}t}
\end{aligned}$$

It follows that

$$\begin{aligned}
\left(\frac{\lambda}{2} + \mu\right)\frac{\mathrm{d}l_n}{\mathrm{d}t} &= -T(m_n) - K(l_n) && (5.39)\\
&\quad + \frac{1}{2}\left[T(m_{n+1}) + K(l_{n+1}) + \mu\frac{\mathrm{d}l_{n+1}}{\mathrm{d}t} + T(m_{n-1}) + K(l_{n-1}) + \mu\frac{\mathrm{d}l_{n-1}}{\mathrm{d}t}\right]\\
&= -T(m_n) - K(l_n) + \frac{1}{2}\left[f_{n+1} + f_{n-1}\right] && (5.40)
\end{aligned}$$

Therefore the change in length of one contractile element is given by the difference of internal forces, trying to contract the cell, and external forces from its neighbors which try to extend it. Sorting all derivatives to the left hand side yields

$$\begin{aligned}
\left(\frac{\lambda}{2} + \mu\right)\frac{\mathrm{d}l_n}{\mathrm{d}t} - \frac{\mu}{2}\frac{\mathrm{d}l_{n+1}}{\mathrm{d}t} - \frac{\mu}{2}\frac{\mathrm{d}l_{n-1}}{\mathrm{d}t} &= -T(m_n) - K(l_n) && (5.41)\\
&\quad + \frac{1}{2}\left[T(m_{n+1}) + K(l_{n+1}) + T(m_{n-1}) + K(l_{n-1})\right]
\end{aligned}$$

Which shows that we can write the ODE system (for the l-dynamics) in matrix notation

$$M\dot{\vec{l}} = -\vec{F} + W\vec{F} \tag{5.42}$$

hereby M denotes the mass matrix

$$M = \begin{pmatrix}
\ddots & \vdots & & \\
& \lambda/2+\mu & -\mu/2 & 0 & \\
& -\mu/2 & \lambda/2+\mu & -\mu/2 & \\
& 0 & -\mu/2 & \lambda/2+\mu & \\
& & \vdots & & \ddots
\end{pmatrix} \tag{5.43}$$

$\vec{F}$ denotes the vector of internal stresses and W is the interaction matrix

$$\vec{F} = \begin{pmatrix}
\vdots \\
T(m_{n-1}) + K(l_{n-1}) \\
T(m_n) + K(l_n) \\
T(m_{n+1}) + K(l_{n+1}) \\
\vdots
\end{pmatrix}, \qquad W = \begin{pmatrix}
\ddots & \vdots & & \\
& 0 & 1/2 & 0 & \\
& 1/2 & 0 & 1/2 & \\
& 0 & 1/2 & 0 & \\
& & \vdots & & \ddots
\end{pmatrix} \tag{5.44}$$

Therefore with $Q = W - \mathbb{I}$, where $\mathbb{I}$ is the identity, and assuming that M is invertible we find

$$M\dot{\vec{l}} = -\vec{F} + W\vec{F} \tag{5.45}$$

$$\Leftrightarrow \dot{\vec{l}} = M^{-1}Q\vec{F} \tag{5.46}$$

$$\Leftrightarrow \dot{\vec{l}} = P\vec{F} \tag{5.47}$$

whereas $M^{-1}Q = P$.

We have seen that in the linear chain the length dynamics can be constructed from the dynamics of the borders. As could be expected, the change in length of one element is given by the linear combination of external forces of direct neighbors and internal forces. The substrate friction λ enters on the diagonal of the mass matrix, which disrupts the symmetry between the internal damping μ on the off diagonal elements with the diagonal element.

Below, this result is used as analogue, where we take linear combinations of external forces to define the mechanical nearest neighbor interactions of limit cycle oscillators on a triangular lattice with substrate friction.

Hexagonal configuration

For simulating amnioserosa cell oscillations the hexagonal configuration is of special interest because it is the closest regular lattice representation, in the Bravais sense, of the actual neighbor distribution in a tissue. We show the neighbor distribution from data of epithelial packing in several organisms [99] and own data from the bulk amnioserosa cells in Figure 5.7.

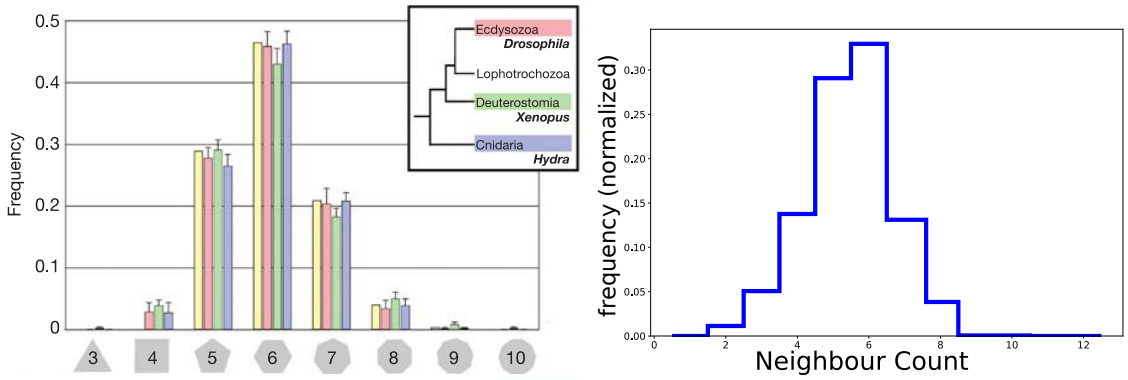

Figure 5.7: Hexagonal packing is the most frequent configuration among epithelial model systems. (left) Histograms of epithelial cell packing from different organisms. Yellow bars are results from vertex model simulations. The histogram is taken from [99]. (right) Measured neighbor distribution from amnioserosa wild type data. The dataset is discussed in chapter 6.

Both distributions show that hexagonal packing is the most frequent one, but configurations with five neighbors appear often as well. Other packings appear less frequently. Additional data from the literature determines that a Gaussian distribution of cell neighbor count around 6 neighbors is the prototypical configuration also in wingdisc cells in *Drosophila* and underpins it with theoretical calculations [84].

Triangular lattice

A hexagonal packing of cells mathematically corresponds to a triangular lattice. Single cell units are operating on the grid points, each following the above described dynamics of Dierkes' model [64]. We explicitly chose not to pursue a vertex representation of the amnioserosa dynamics, which would be another popular choice for a biophysical model, see section 2.15 for more details. Our modeling philosophy is to construct a model with the least complexity as possible to investigate a concrete research question: We want to understand how a mechano-transduction coupling would lead to intercellular synchronization in a hexagonal configuration. To this end, a model of limit-cycle oscillators coupled via nearest neighbor interactions already shows rich dynamics which can be compared to experimental data. The additional complexity of a vertex model can only be justified if we want to answer questions that can not be investigated in the lattice model. However, the model could be extended to a vertex model in the future to investigate for instance the influence of finer grained neighbor distribution which can be directly implemented in a vertex model.

Biologically, interactions between cells are mechanical and are transmitted via the adherens junctions connecting the cytoskeleton of two cells. Our interaction matrix therefore also only concerns nearest neighbors. We have shown in section 5.3 that a switch in notation to the area A instead of contractile element length l is straight forward and from now on use the cell area A as variable.

The above noted principle of the linear chain is now used to motivate how the mechanical nearest neighbor interactions are constructed. Because external forces that pull on a cell are the same forces that act internally, the total force acting on a cell unit is comprised of linear combinations of that internal force. In a hexagonal cell arrangement, cells have six neighbors. Thus, instead of two, there are now six interactions that determine the area change of a cell. Interactions still have to be negative because of geometrical constraints. An increasing area exerts a force which pushes on its neighbors.

It is convenient to introduce two indices $j, k \in \mathbb{N}$ denoting the lattice sites. The base vectors are given by

$$\vec{e}_1 = \frac{1}{2}\begin{pmatrix} -1 \\ \sqrt{3} \end{pmatrix}, \qquad \vec{e}_2 = \frac{1}{2}\begin{pmatrix} 1 \\ \sqrt{3} \end{pmatrix} \tag{5.48}$$

Then each lattice site is determined via $\vec{R}_n = j\vec{e}_1 + k\vec{e}_2$ where n is the cell label and a bijective map exists such that $n \to (j, k)$. The cell area dynamics at each lattice site is conceptually given by the internal dynamics and external interactions with the neighboring sites.

$$\begin{aligned} \frac{\mathrm{d}A_{j,k}}{\mathrm{d}t} &= f_{int}(A_{j,k}) + f_{ext}(A_{j+1,k}) + f_{ext}(A_{j-1,k}) \\ &\quad + f_{ext}(A_{j,k+1}) + f_{ext}(A_{j,k-1}) + f_{ext}(A_{j-1,k+1}) + f_{ext}(A_{j+1,k-1}) \end{aligned} \tag{5.49}$$

As in preceding sections, the stress each site exerts is given by an extended Kelvin-Voigt model, which reads

$$\sigma_{j,k} = \mu\frac{\mathrm{d}A_{j,k}}{\mathrm{d}t} + T(m_{j,k}) + K(A_{j,k}) \tag{5.50}$$

In the linear chain, we saw that this stress is distributed equally across the neighbors. We approximate the actual stress distribution by using the assumption of isotropic force distribution and to simplify the mechanical interactions.

Using indexing via n for simplicity, the resulting equation governing a single cell unit now reads

$$\left(\frac{\lambda}{N}+\mu\right)\frac{\mathrm{d}A^{(n)}}{\mathrm{d}t} = -T(m^{(n)}) - K(A^{(n)}) + \frac{1}{N}\sum_{\text{neighbors}} f_{ext}(A^{(i)}) \qquad , i \in [1, N] \tag{5.51}$$

With N, the number of direct neighbors and $f_{ext}(A_i)$ the stress exerted by neighbor i. We assume that internal forces are isotropically affecting all six neighbors. In addition, the substrate friction λ would also be affected by the number of neighbors but this is only a technicality and N can be absorbed into the parameter $\tilde{\lambda} = \lambda/N$ if the neighbor distribution is constant. That neighboring force contributions can be averaged assumes isotropic interactions.

Our approach is an approximation since each external force results in an isotropic response of a cell. Therefore in the exact two dimensional representation, the tiling in the plane is not complete. The exact tiling can only be solved using a description of the vertices, which requires a different model that focuses on the energetics of the vertices instead of the cell-cell borders. In the linear chain, this approach is exact, as we have shown that the dynamics of contractile elements arises directly from the border dynamics using simple algebra. From the linear chain we also know that the substrate friction, which dissipates energy when a border is moving, simply enters on the diagonal of the mass matrix for the dynamics of the contractile elements.

Boundary and topology

Since the amnioserosa features an ellipsoidal shape we also employ such a topology. Fully unconstrained cell units are arranged on a hexagonal lattice and are surrounded with border cells. We choose an ellipse with ratio of the half axes a/b = 1/2 such that we have roughly 150 cells in the tissue (approximate cell count from the experiments) and find the optimal number such that the a/b ratio is fulfilled.

We choose border cells to exhibit a different dynamics, realized as simple relaxators consisting only of contractile elements with spring constants k_{ext}. They are only mechanically coupled to the cells from the tissue and are perturbed by the direct neighbor forces.

$$\left(\frac{\lambda}{N}+\mu\right)\frac{\mathrm{d}A_{boundary}}{\mathrm{d}t} = -K_{ext}(A_{boundary}) + \frac{1}{N}\sum_{\text{neighbors}} f_i \qquad , i \in [1, N] \tag{5.52}$$

$$K_{ext}(A_{boundary}) = k_{ext}(A_{boundary} - A_0) \tag{5.53}$$

There is no myosin compartment. By making k_{ext} larger we can tune the tissue dynamics between a freely oscillating tissue and a tissue where the overall area must be preserved. In the simulations we fix k_{ext} to an intermediate value constraining the tissue dynamics but not making it too rigid. This resembles the amnioserosa dynamics from the experiments as we observe displacement of the leading edge of the tissue. The amnioserosa is more constrained towards later stages shortly before the onset of dorsal closure when the actin cable around it has fully formed.

5.6 Mechano-chemical interactions and noise

In the amnioserosa of Drosophila we observe synchronization of neighboring cell oscillations in wild type embryos. Mutants that are depleted of *Tmc* , a mechanosensitive ion channel, show a drastic loss in the number of synchronized cell pairs and different spatial organization. To investigate the possible effects of a microscopic mechano-transduction coupling mechanism, based on Ca^{2+} dynamics, we devise extensions to the model discussed above. To this end, a

third compartment for calcium dynamics is added. In addition, a noise term, and therefore stochasticity, is added to the dynamical system. Experimental trajectories are stochastic and fluctuate around the average deterministic behavior. Investigations of synchronization must take these fluctuations into account because noise has a decorrelating effect against which any coupling mechanism must compete.

Conceptual model

The equations that govern the dynamics of a single cell unit are realized by a system of three coupled differential equations for the cell area A, the myosin concentration m and amount of Ca^{2+}-ions c. We consider a single cell here, using a placeholder external tension T_e instead of neighbor tension and also only considering a single placeholder cell neighbor n for the Ca^{2+} coupling. Terms that denote extensions of Dierkes' model are colored. The system of differential equations reads

$$\begin{aligned}
\mu\frac{\mathrm{d}A}{\mathrm{d}t} &= T_e - T(m) - K(A) + \xi(t) \\
\frac{\mathrm{d}m}{\mathrm{d}t} &= -\frac{1}{\tau_m}(m - m_0) - \frac{m}{A}\frac{\mathrm{d}A}{\mathrm{d}t} + \alpha\,\frac{c}{A} \\
\frac{\mathrm{d}c}{\mathrm{d}t} &= J\;\Theta(\dot{A}^{(n)})\;\Theta(\dot{A}^{(n)} + \dot{A}) - c/\tau_c
\end{aligned} \tag{5.54}$$

With the abbreviations:

$$T(m) = T(m_0) + t_1(m - m_0) \tag{5.55}$$

$$K(A) = K(A_0) + k_1(A - A_0) + k_3(A - A_0)^3 \tag{5.56}$$

$$T_e = T(m_0) + K(A_0) \tag{5.57}$$

$$\Theta(x) = \frac{1}{1 + \exp(\beta x)} \qquad , \beta \gg 1 \tag{5.58}$$

where $T(m)$ is the myosin induced contractile force, T_e the equilibrium tension and $K(A)$ the intrinsic spring force, which have the same form compared to Dierkes' model. The noise $\xi(t)$ is a Gaussian random force with

$$\langle \xi(t) \rangle = 0 \tag{5.59}$$

$$\langle \xi(t)\xi(t') \rangle = 2D\,\delta(t - t') \tag{5.60}$$

$\Theta(x)$ is a Fermi function which is being used as activation function to keep the expression analytic and also enable smooth activation characteristics. Thereby the activation of Ca^{2+} reads

$$\frac{\mathrm{d}c}{\mathrm{d}t} = J\;\Theta(\dot{A}^{(n)})\;\Theta(\dot{A}^{(n)} + \dot{A}) - c/\tau_c \tag{5.61}$$

The second term is a decay of the number of Ca^{2+} molecules characterized by the time constant τ_c. The first term determines the influx of Ca^{2+} into the cell according to the coupling strength parameter J. The higher J the more Ca^{2+} increases if tension is exerted on the cell.

Determining the tension on the cell is done via the activation functions $\Theta(x)$. For the opening of an ion channel, due to mechanical force, a non-zero net force has to be applied to the junction between the two cells. To keep the notation simple we choose the area derivative as argument and not the actual tension. This is equivalent because the sum of all forces acting on a cell determines its area change. The first Fermi-function is causing an activation if the neighbor cell $\Theta(\dot{A}^{(n)})$ decreases in area, thus exerting tension. It determines the direction of the coupling,

which is only activated if the stress is exerted from the neighbor. Otherwise cells would increase their Ca^{2+} concentration each time they contract. The second Fermi function $\Theta(\dot{A}^{(n)} + \dot{A})$ only yields an activation if the area of the actual cell is not increasing more than the neighbor is decreasing. If the area increases with the same rate as the neighbor shrinks no net force will be applied at the junction and therefore no ion channel will open.

Two-dimensional model on triangular lattice

For a full model of the amnioserosa dynamics in 2D we compute the dynamics of single cell units on a triangular lattice. Compared to (5.54), we replace the external tension T_e with mechanical interactions between neighboring cells, which also includes the friction term, counteracting the movement of single cell units across an underlying substrate. See Figure 5.1 for a graphical representation. The full equations in the 2D case now read

$$\left(\frac{\lambda}{N} + \mu\right)\frac{\mathrm{d}A^{(i)}}{\mathrm{d}t} = F^{(\text{internal})} + F^{(\text{external})} + F^{(noise)} \tag{5.62}$$

$$= -T(m^{(i)}) - K(A^{(i)}) - \frac{1}{N}\sum_{n=1}^{N}\left[\mu\frac{\mathrm{d}A^{(n)}}{\mathrm{d}t} + T(m^{(n)}) + K(A^{(n)}) - \xi^{(n)}\right] + \xi^{(i)} \tag{5.63}$$

$$\frac{\mathrm{d}m^{(i)}}{\mathrm{d}t} = -\frac{1}{\tau_m}(m^{(i)} - m_0) - \frac{m^{(i)}}{A^{(i)}}\frac{\mathrm{d}A^{(i)}}{\mathrm{d}t} + \alpha\frac{c^{(i)}}{A^{(i)}} \tag{5.64}$$

$$\frac{\mathrm{d}c^{(i)}}{\mathrm{d}t} = \sum_{n=1}^{N}\left[J^{(n)}\,\Theta(\dot{A}^{(n)})\,\Theta(\dot{A}^{(n)} + \dot{A}^{(i)})\right] - \frac{1}{\tau_c}c^{(i)} \tag{5.65}$$

The index i denotes cells on the lattice sites, n runs over the N neighbors (N=6 for hexagonal configuration). Myosin and Ca^{2+} dynamics remain mostly unchanged except for summing all contributions from neighboring cells to obtain the total calcium influx.

External mechanical forces $F^{(\text{external})}$ are comprised of the total internal force acting inside neighboring cells. We simplify by assuming that the force is distributed isotropically among all 6 neighboring cells and thus the external force component acting on cell i from cell j is $F_{ji}^{(internal)}/6$ in case of a hexagonal lattice.

The substrate friction λ is causes dissipation as cells move across a substrate. Biologically, this is motivated by the amnioserosa lying above the yolk of the developing embryo. It remains unclear how the tissue exactly connects to the underlying substrate and how this connection influences the cell dynamics. During the ellipsoidal amnioserosa phase connections adhesion to the substrate can be mediated via integrin complexes. This adhesion might play a role during dorsal closure [166, 232, 276].

Origin of fluctuations and where to put the noise term

Why did we choose the area equation as the appropriate place to add noise to the system? After all, it could also be the myosin molecules that show substantial volatility and therefore introduce noise to the system.

The first answer is that noise in experimental data is always comprised of two contributions: measurement noise and intrinsic noise

$$\xi(t) = \xi_{\text{measurement}} + \xi_{\text{intrinsic}} \tag{5.66}$$

The measurement noise can only be found in the area time series since this is the only observable we have in our experiments. But this is no argument from a theoretical point of view.

To investigate what would happen if noise was introduced into the myosin compartment we do a quick back of the envelope calculation. We assume that the number of myosin molecules is constant on short timescales (conservation of mass was one basic assumption in the derivation of the model).

$$\frac{\mathrm{d}N_m}{\mathrm{d}t} = 0 \qquad \rightarrow \frac{\mathrm{d}(mA)}{\mathrm{d}t} = 0 \tag{5.67}$$

Then it follows

$$\frac{\mathrm{d}(mA)}{\mathrm{d}t} = A\dot{m} + m\dot{A} = 0 \tag{5.68}$$

$$\Leftrightarrow \dot{A} = \frac{\dot{m}}{m}A \tag{5.69}$$

Now let us imagine we introduced noise to the myosin turnover dynamics

$$\dot{m} = k_{on} - k_{off}m + \xi(t) \tag{5.70}$$

Inserting this into equation (5.69) for the area yields

$$\dot{A} = \frac{k_{on}}{m}A - k_{off}A + \frac{\xi(t)}{m}A \tag{5.71}$$

What is important here is that we obtain multiplicative noise in the last term of the area dynamics. Multiplicative noise introduces correlations in the noise we should be able detect in the experiments. It is a known result from statistical physics that separation of timescales leads to multiplicative noise if there is not one single effective reaction coordinate [21]. In broader terms this is also understood within the Mori-Zwanzig projection formalism of statistical mechanics [359]. In the appendix, section 5.12, we present data from experiments showing that there are no correlations in the area trajectories.

5.7 Implementation

Parameters

To nondimensionalize the system (5.54), we introduce the following dimensionless parameters:

$$\bar{\tau}_m = \frac{\tau_m k_1}{\mu} \tag{5.72}$$

$$\bar{t}_1 = \frac{t_1 m_0}{k_1 A_0} \tag{5.73}$$

$$\bar{k}_3 = \frac{k_3 l_0^2}{k_1} \tag{5.74}$$

$$\bar{\lambda} = \frac{\lambda}{\mu} \tag{5.75}$$

$$\bar{J} = J\,\alpha\,\tau_c \tag{5.76}$$

$$\bar{k}_{ext} = k_{ext} \tag{5.77}$$

$$\bar{D} = D \tag{5.78}$$

The dynamics therefore depends on 7 free parameters and the dimensionless time $\bar{t} = \frac{k_1 t}{\mu}$. We always choose $\bar{k}_3$ such that the Hopf bifurcation is supercritical to yield limit cycle dynamics at the transition.

Basic dynamics of the single cell units is then determined by the effective contractile myosin strength $\bar{t}_1$ and the effective internal friction $1/\bar{\tau}_m$. Compare the phase diagram in Figure 5.4. The interplay of myosin strength and friction determines if the system can oscillate. If the friction is too strong, energy is dissipated too quickly and the system will approach the fixed point. In a balanced state between the two, the system can oscillate, but if the myosin strength is too high in comparison to the friction, the system is being driven into collapse as the energy can not be dissipated and tension diverges. $\bar{k}_3$ determines the amplitude of the oscillations.

$\bar{k}_{ext}$ is kept fixed at an intermediate value for the here described analysis. It introduces global coupling by providing a geometrical constraint to the area dynamics. $\bar{\lambda}$ promotes local interactions. For higher values of $\bar{\lambda}$ more energy will be dissipated at the borders between the cells. Therefore tension can not travel without limit through the whole network. In case of no friction, the effect of one cell contraction could be instantaneously affect the whole network. Both $\bar{k}_{ext}$ and $\bar{\lambda}$ are therefore important for the global coupling of the system and determine strength of geometrical constraint and propagation of stress.

Ca^{2+} coupling strength $\bar{J}$ determines how strongly the amount of Ca^{2+} increases in response to mechanical stimuli and how much additional myosin is recruited. It therefore provides a mechanical coupling between the dynamics of the neighbors and the internal contractile forces. We will see that increasing this parameter leads to synchronization of area oscillations because a cell contraction induces contractile forces in the neighbors. The noise strength $\bar{D}$ determines the fluctuations in the area variable. It decorrelates the system and constantly perturbs it.

In addition, another parameter p is introduced, which denotes the occupation probability of the ion channels. In simple words, it specifies the fraction of cell pairs that are coupled by the Ca^{2+} mechanism. p is drawn from a uniform distribution on $[0, 1]$, 0 meaning that no pairs exhibit Ca^{2+} coupling and 1 that all pairs have the mechanism. This is done to investigate the influence of heterogeneous spatial coupling in the tissue.

In total we thus have 8 parameters determining the behavior of the system. However, for the investigation we focus only on 5, while the others remain fixed: effective contractile myosin strength $\bar{t}_1$ and the effective internal friction $1/\bar{\tau}_m$ determine the phase transition towards oscillations and $\bar{J}$ and p determine the Ca^{2+} coupling, and therefore synchronization, last is the noise strength $\bar{D}$.

Below we use the original parameter values, not the nondimensionalized version. We keep parameters fixed except for t_1, μ, J, p and D. In the next section we mention prototypical parameter values.

Simulations

The model is implemented and optimized in Julia (v1.4.0). A single simulation of the 2D model with 150 cells (450 coupled DEs + noise) completes in 2-3 minutes on a single core of a 8 year old laptop with an Intel i5 2.50 GHz processor. For parameter searches, nested sampling and repeated simulations the code is parallelized. For 800 full length realizations, parallelized on a 20 core Intel E5-2670 v2 2.50 GHz node, it takes 6-12 hours depending on the parameter regime. For more unstable parameter combinations, the adaptive solver takes smaller timesteps to maintain convergence.

Integration of the system of stochastic differential equations is done via the Julia package "DifferentialEquations.jl" [267]. As solver for the SDEs, the high order adaptive algorithm "SKenCarp" [273] is used, which is optimized for stiff stochastic problems. A set of other

solvers, for instance an implicit Euler-Mayurama method, have been used to compare different solvers, but SkenCarp showed empirically the best performance and stability.

If not specified differently, parameter values are fixed at certain typical values $k_3 = 6$, $k_1 = 1$, $\tau_m = 1$, $\tau_c = 1$, $A_0 = 1$, $m_0 = 1$, $k_{ext} = 0.001$, $D = 0.001$, $\lambda = 0.5$. The internal damping constant μ and myosin strength t_1 are used to tune the system towards oscillating/stable regimes. Coupling strength J and occupation probability p influence the synchronization, but usually $p = 1$ is fixed.

Initial conditions are equilibrium values ($A^{(i)}(0) = 1$, $c^{(i)}(0) = 0$, $\forall i$) with small randomized deviations for the myosin concentration m of the order 10^{-4} to get the system out of the initial fixed point. Border cells are starting in the equilibrium point $A^{(border)}(0) = 1$. Before the collection of data for later analysis is started, simulation runs are given sufficient time to let transients induced by the initial conditions decay.

5.8 Simulations of 2 coupled cells

We perform simulations of two cells to investigate effects of the extensions, namely the Ca^{2+} coupling mechanism and the noise which were both not present in previous studies. The basic setup was described in section 5.4.

Basic model behavior

First, let us see whether we can find the same phases, namely stable fixed point, limit cycle and collapse despite the noise, which should be the case. Coupling between the 2 cells is turned off for the time being, i.e. $J = 0$. Figure 5.8 shows example trajectories.

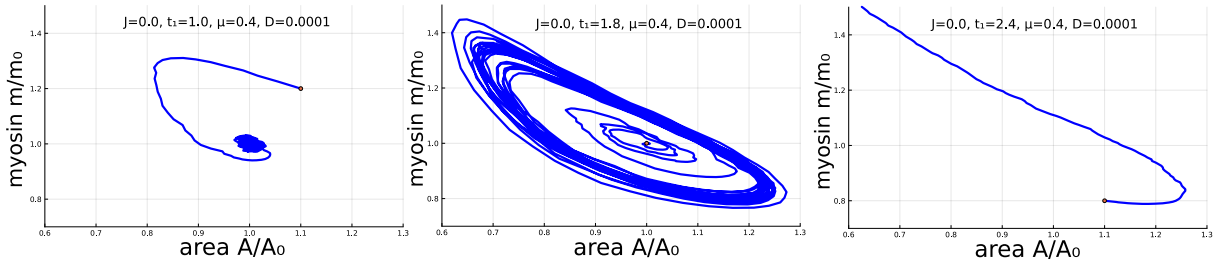

Figure 5.8: Three phases of dynamical behavior, stable dynamics, limit cycle and collapse, were reproduced in the two cell system. Examples for each phase are shown from left to right. The trajectories are beginning at the initial condition denoted by the orange dot. In addition to Dierkes' model noise is applied. The left panel shows stable dynamics, the middle displays a limit cycle and to the right the dynamics is going into collapse. Noise is causing fluctuations around the stable fixed point and the stable orbit of the limit cycle.

The myosin concentration is plotted against the area. All three phases, dynamics running into 1) a fixed point, 2) stable limit cycle, and 3) collapse dynamics can be reproduced. In the here shown example we tuned the myosin strength t_1 and kept other parameters fixed. Only different initial conditions were chosen such that the behavior is representative.

Figure 5.4 showed the original phase diagram of the Dierkes model. From that it is clear that increasing the myosin strength t_1 drives the system from stable phase into oscillations into collapse. The same seems to be possible for our model, which is intuitively clear because the underlying deterministic dynamics has not changed. Noise is consistently perturbing the system, such that the resulting trajectories fluctuate around stable fixed point and stable orbit, which

shows that the orbit and fixed point are indeed stable as otherwise the system would eventually diverge.

Below, a more detailed investigation of the phases is undertaken. But first we want to get an intuition about the second important addition to the model: the Ca^{2+} coupling. Figure 5.9 displays two example trajectories, one for synchronized and one for anti-synchronized oscillations depending on the coupling strength J.

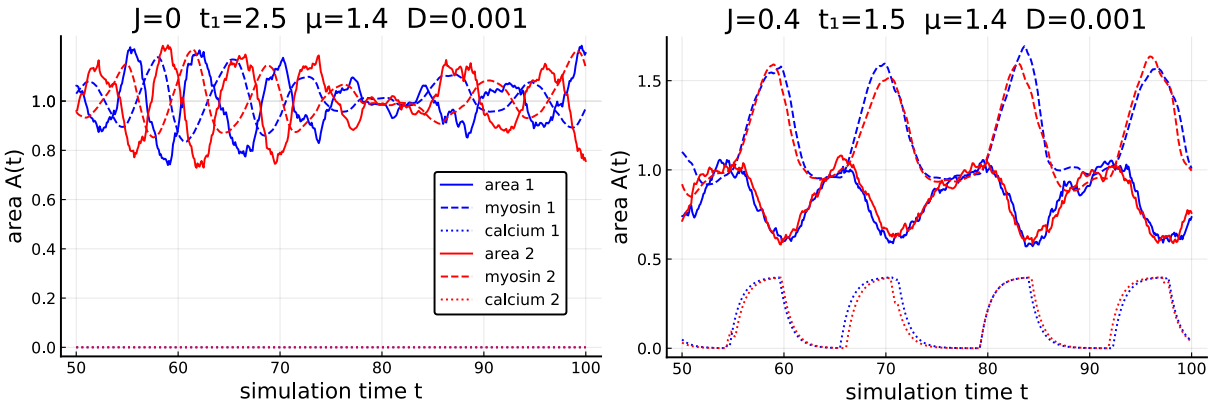

Figure 5.9: Coupling strength J determines if cell neighbors show anti-synchronized or synchronized oscillations. Solid lines are the areas of the two cells. The two types of dashed lines denote myosin and Ca^{2+} compartments respectively. Myosin shows anticorrelated dynamics with the area. Ca^{2+} is usually zero and activated by the mechano-chemical coupling. To the left, no coupling is present and the two cells behave anti-synchronized which is due to the geometrical constraints of the two cell chain. To the right, cell areas oscillate in synchrony.

Parameters were chosen such that cells exhibit oscillations. The dynamics of the myosin concentration is anticorrelated with the area, which could already be seen in Figure 5.9 because of the limit cycle. Ca^{2+} is obviously zero for the system without coupling where neighboring cell area trajectories are anti-synchronized. This is due to the global coupling introduced by the external border springs k_{ext}. One cell growing, while the other is shrinking is thus following the geometrical constraints in the chain. The substrate friction λ is enhancing this anti-synchronized behavior because it disrupts the instantaneous whole system coupling. This does not matter in the two cell model, but for long linear chains and the lattice model λ results in perturbations traveling to their neighbors first and influencing them the most. Without any dissipation the whole system can be described by a single mode, because all perturbations are instantaneously distributed along all elements of the chain. An example would be to induce a contraction ΔA_i in a cell i of a chain containing 50 elements. Without friction all other cells would increase by the amount $\Delta A/49$. With friction the neighbors will increase the most, next-neighbors substantially less and so on.

If the coupling strength is high enough, the neighboring cell oscillations synchronize. Later, we show that there must not always be a synchronized phase for certain parameters because the simulation is directly driven into collapse from the anti-synchronized state. By construction, Ca^{2+} increases when the cells contract and then decay when the cells increase. Myosin dynamics is still anticorrelated to the area dynamics, as expected, since it is the main pacemaker of the oscillations. Due to Ca^{2+} mediated additional recruitment of myosin, the average tension is increased which decreases the equilibrium area. Compare the anti-synchronized trajectories where A fluctuates around $A_0 = 1$. Interestingly, in the experiment we observe smaller cell areas in the wild type bulk cells compared to an ion channel knock out mutant, called *Tmc* (see

Figure 6.5). Wild type cells are also showing a higher degree of synchronization (e.g. Figure 6.26).

Coupling strength J is working against the external springs k_{ext}, the substrate friction λ and the noise D which all counteract synchronization. This makes it clear that a distinct mechanism is necessary for synchronized oscillations. Naturally, anti-synchronized neighbor oscillations is the energetically favorable state of the system. This is important from the view of biology because the organism has to gain something from investing that energy. Otherwise such mechanisms would not have survived evolution if the same organism could be developed with less energy spending. If a mutant embryo is depleted of mechanosensitive ion channels, like in the *Tmc* mutant, which comprises the hypothesized microscopic synchronization mechanism, the degree of synchronization is expected to drop.

Phase diagrams

To determine the degree of synchronization between the two cells correlation coefficients between the area trajectories are calculated from the simulation. In order to classify system behavior, parameter combinations with positive correlation coefficients are labeled "synchronized" and parameter combinations with negative correlation coefficients are labeled "anti-synchronized". In addition, parameter regions without oscillations are assigned the labels "stable" and "collapse". Examples for coupling strengths $J = 0$ and $J = 0.01$ are shown in Figure 5.10. Noise is turned off, i.e. $D = 0$. The original phase diagram of the Dierkes model, for comparison, was shown in Figure 5.4.

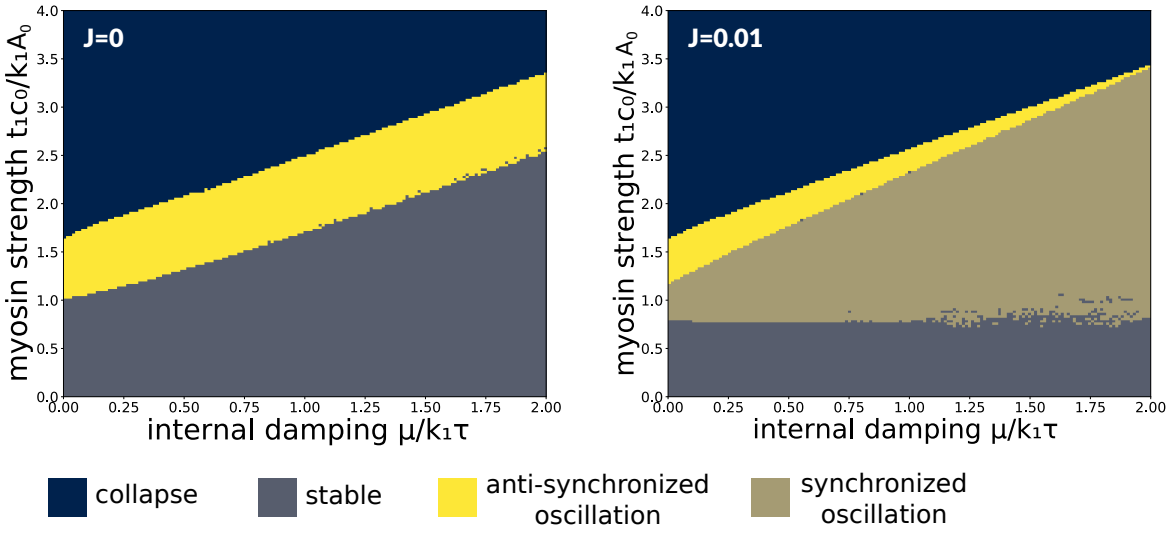

Figure 5.10: Ca^{2+} coupling is required to allow synchronized oscillations. Phase diagrams for coupling strength $J = 0$ (left) and $J = 0.01$ (right) indicate that synchronized oscillations only appear when Ca^{2+} coupling is turned on. Both conditions produce stable and collapsing cells as well as anti-synchronized oscillation.

It can be seen that the case without Ca^{2+} coupling reproduces the phase diagram of the Dierkes model. A band of parameters which show oscillations is visible. In addition, we find parameter regions where the cell dynamics collapses due to diverging myosin concentration along the cells and stable regions where cell areas approach a fixed point. Slight deviations stem from the fact that here the two cell system with substrate friction is shown, whereas Dierkes plotted the single cell phase diagram. This deviation is for instance responsible for the narrowing

oscillating region for $\mu \to 0$. Small deviations at the border of phase regions are due to computer precision in the simulation.

When Ca^{2+} coupling is turned on, a fourth phase with synchronized oscillations appears. The phase of anti-synchronized oscillations does not vanish, it is still present, except for very high coupling strength where the system goes from synchronized oscillations directly to collapse. A side effect of the Ca^{2+} coupling is that the parameter region that is displaying oscillations of any kind is greatly extended.

Noise adds another layer of complexity to the model. Since noise has a decorrelating effect, the coupling strength J has to be increased for the model to display synchronized oscillations. We now take a look at the exact correlation coefficient for the same set of parameters, which yields a finer grained picture how noise influences the dynamics. Results are shown in Figure 5.11.

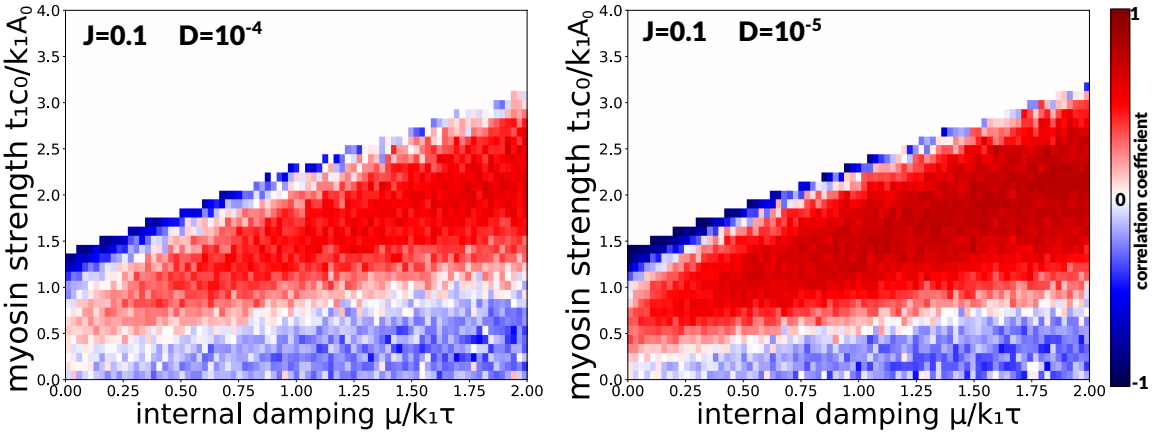

Figure 5.11: Noise strength affects cross-correlation coefficient of the two cell system. White regions in the top-left half are collapsed realizations. To the left, the noise strength $D = 10^{-4}$ is higher compared to the right panel with $D = 10^{-5}$. Higher noise decorrelates the system, leading to smaller positive correlation coefficients. In addition, the parameter region displaying synchronized oscillations is decreased.

White parameter combinations in the top part of the phase plot are collapsed. This does not include white regions between blue and red, where the average correlation coefficient is truly zero. There are still oscillating regions, like before, that are either oscillating synchronized or anti-synchronized. The correlation coefficient shows that there is now a continuous transition between sync and anti-sync region where correlation coefficients turn from negative to zero to positive. In addition, the stable region now also displays anti-synchronization. In this case, however, there is only constant relaxation towards equilibrium after perturbations from the noise. No microscopic pacemaker is producing stable limit cycles.

The left panel is showing greater noise strength D compared to the right panel. For smaller noise strength, correlated parameter combinations are more dominant and coefficients assume higher values in the middle of the synchronized region. The transition from anti-synchronized to synchronized becomes narrower. For smaller values of μ there is a persistent anti-synchronized region. Simulation trials show that by increasing J, the correlated red region grows bigger, overtaking anti-synchrony first for higher values of μ. The anti-synchronized region for small μ is the last to vanish but ultimately does so for high enough J.

Noise vs. coupling strength

To further investigate how noise strength and coupling strength are interacting we compute phase diagrams for fixed values of myosin strength t_1 and internal damping μ. D and J are varied. Those results are shown in Figure 5.12.

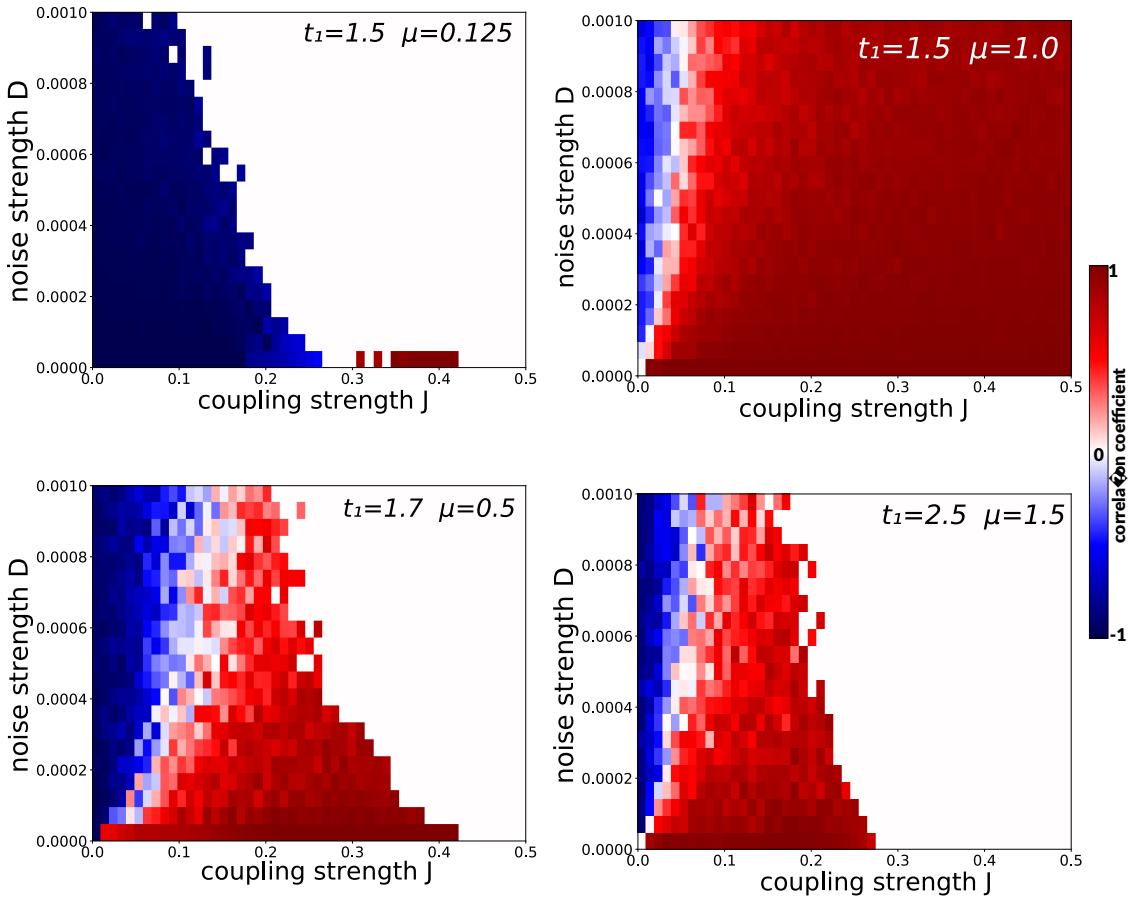

Figure 5.12: Balance between noise D and coupling strength J affects synchronization. The color denotes the cross-correlation coefficient between the cell areas in the two cell model. White regions for larger J are collapsed realizations. Noise decreases the degree of synchronization that is possible. The top left panel shows that for certain parameter combinations increasing the coupling J directly leads to collapse instead of synchronization. For intermediate oscillatory parameter combinations, shown in the bottom two panels, there is a tradeoff between noise and coupling.

The first diagram shows parameters $t_1 = 1.5$ and $\mu = 0.125$. In the original phase diagram we are in an anti-synchronized region near the collapse transition. The large white regions are all collapsed data points, therefore increasing the coupling strength drives the system into collapse without even going into synchronized behavior. Again, white values between red and blue regions are true average correlation coefficients around zero. This shows that for certain parameters there must not be a synchronization at all.

The next parameter combination is $t_1 = 1.5$ and $\mu = 1$, which, in the original phase diagram, lies in the stable region at the border between stable phase and oscillatory phase. For most parameter combinations there is a strong synchronization of area dynamics. No parameter

combinations lead to collapse for the shown parameters, but eventually will if J is increased further. Increasing the noise strength D leads to anti-synchronization if the coupling strength is small enough. This region would normally not display any oscillation and would be stable. The fact that noise can not lead to anti-synchronization if J is high enough, also shows that the new oscillation phase is very stable since otherwise anti-synchronized oscillations are the norm.

The last two combinations $t_1 = 1.7$, $\mu = 0.5$ and $t_1 = 2.5$, $\mu = 1.5$ both are in the original oscillation phase, one for intermediate values of μ and the second for high values. White regions for higher values of J again signify collapsed simulations. Qualitatively, both combinations show similar behavior. However for higher noise strength t_1 and higher damping μ more parameter combinations drive the system into collapse. There is a balance between the noise strength on the one hand and the coupling on the other. Increasing the coupling results in a continuous transition toward synchronization. Noise has the opposite effect and promotes anti-synchronized oscillations.

Both noise strength and high coupling strength can induce collapse in the simulations for certain parameter values. Higher coupling strength results in stronger recruitment of myosin, which effectively drives the system across the critical point between collapse and oscillation phase. The noise increases the volatility of the system and increases the probability that a collapse occurs simply by chance. Either through area fluctuations themselves or by temporarily driving the myosin concentration above a critical threshold, which then leads to diverging tension.

Because of the tradeoff between coupling and noise it is made clear that synchronization studies should take noise into account. Otherwise synchronization can be achieved more easily than would be expected in a noisy environment such as active biological matter.

5.9 Simulations of tissue model

Being equipped with a general understanding of the novel interactions, we can now investigate the model on the hexagonal lattice. Section 5.6 introduced the basic concepts. Simulations are conducted by starting from equilibrium areas for all cells and drawing random myosin concentration from a Gaussian distribution with mean 1 and standard deviation 10^{-5}, which drives the system out of the fixed point even without noise. Before any analysis is done, the simulation is running long enough to let transients decay. A realization of the cells on a hexagonal grid is shown in Figure 5.13

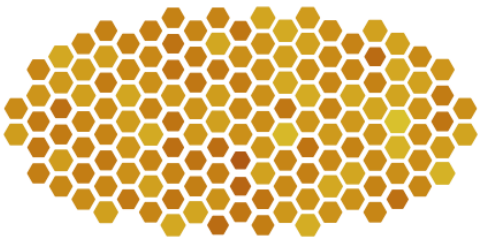

Figure 5.13: Example snapshot of tissue simulation. Cells are depicted as hexagons. Their size and color indicates the current area. Border cells are not shown but are located around the outer layer of cells.

Basic behavior

In the tissue model nothing with the basic equations of the model changed, only the topological configuration is different. Therefore the system still displays stable dynamics, oscillations and collapse. We show examples of the phases for an example cell from the hexagonal lattice in Figure 5.14.

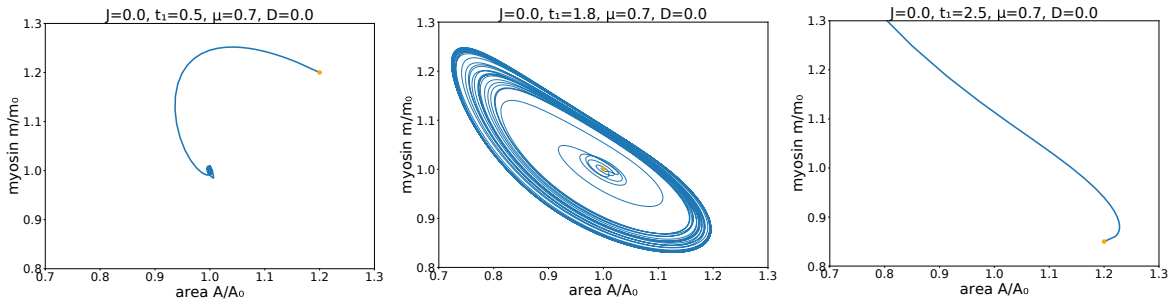

Figure 5.14: Three phases of dynamical behavior, stable dynamics, limit cycle and collapse, were reproduced in the lattice system. Examples for each phase are shown from left to right. The left panel shows stable dynamics, the middle displays a limit cycle and to the right the dynamics is going into collapse. The stable case exhibits fluctuations around the fixed point because the trajectory circles a few times around it, but eventually reaches it and remains there.

To visualize that nearest neighbor coupling still introduces synchronization, we color each cell unit by its current phase. Phases are determined by looking at the zero-crossings of smoothed area trajectories oscillating around an equilibrium area. Between zero crossings the phase is linearly interpolated. This method is one of the most stable phase retraction methods in the presence of noise and can even outperform methods like the Hilbert transform [93]. Significant improvement can only be achieved with more complicated stochastic models, inferring the phase from probability distributions of positions from the stochastic orbit of the limit cycle [318]. This is unnecessary for our needs. Figure 5.15 shows snapshots of the phases of the tissue model for different degrees of coupling strength J.

As can be seen, cells synchronize locally since they assume the same phase of the oscillation. In the presence of noise, cells still synchronize but they do not have to be perfectly in phase for all times.

The exact pattern is dependent on the parameter realization, including λ and k_{ext}, as well as the shape of the ellipse. A full discussion will be provided in a paper that is currently in preparation. Here, we focus on the degree of overall synchronization, not the local spatial structure, in order to compare results from simulations to experimental data. In chapter 7 those results play into the investigation of intercellular synchronization in the amnioserosa of *Drosophila*.

5.10 Model vs Experiment

In chapter 6, we analyze data from *in vivo* recordings of the amnioserosa cell oscillations. This data is supplemented with further experiments and fully discussed in chapter 7, where we find that the mechanosensitive ion channel *Tmc* is necessary for synchronization of neighboring cells. Here we compare the model to this data, perform parameter estimation and conduct simulations that can be compared to the experimental data.

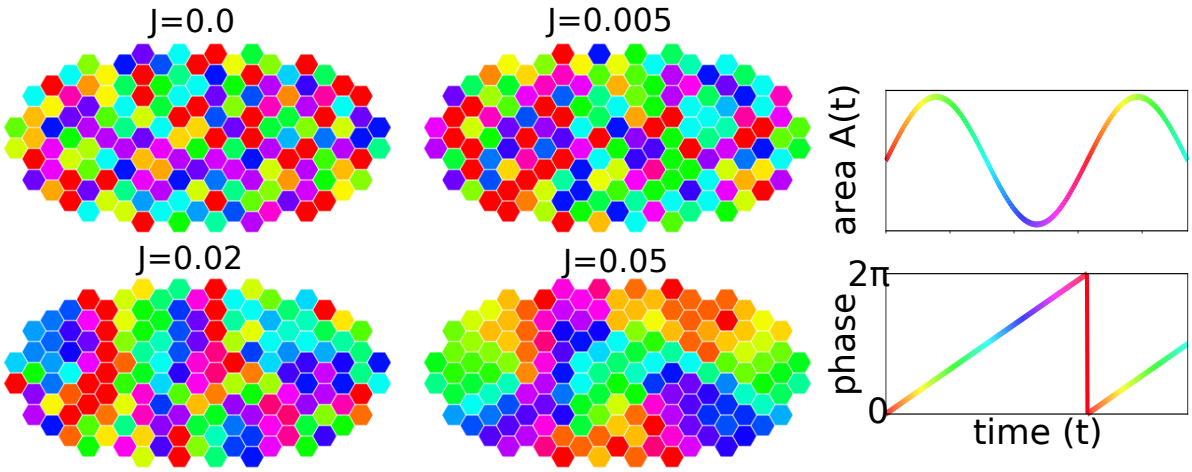

Figure 5.15: Increasing coupling strength promotes the synchronization of neighboring cells in the tissue model. No noise is present in the snapshot from the simulation presented here. The right panel explains the colorcode, which denotes the phase of the oscillation.

We compare the simulations of the model with experimental data by utilizing the distribution of correlation coefficients between neighboring cells as metric for the overall degree of synchronization. This distribution characterizes the to us interesting parts of the tissue dynamics, it is simple enough to retain generality and we have access to it in both experimental data and simulations. In the experiment we have ~ 10 realizations and also use the same number in the simulation. A full discussion on the experimental data is provided in Chapter 6. For this section it is only important to know that we are interested in the comparison of wild type embryos with a *Tmc* mutant, a mechanosensitive ion channel knockout, which impairs the Ca^{2+} dynamics in the amnioserosa.

Since we compare distributions, a cross entropy measure is chosen to evaluate the model likelihood. In particular we use the Jensen-Shannon divergence, a symmetric version of the Kullback-Leibler distance, between the *in vivo* and *in silico* distributions.

The Kullback-Leibler distance is defined as

$$D_{KL}(p^{(\text{simulation})}||q^{(\text{experiment})}) = \sum_i p(x_i) \log \frac{p(x_i)}{q(x_i)} \tag{5.79}$$

The Kullback-Leibler divergence is minimized by the maximum likelihood estimate which can

be swiftly calculated

$$\hat{\theta} = \arg\max_{\theta} \prod_{i=1}^{N} p(x_i|\theta) \tag{5.80}$$

$$= \arg\max_{\theta} \sum_{i=1}^{N} \log p(x_i|\theta) \tag{5.81}$$

$$= \arg\max_{\theta} \frac{1}{N} \sum_{i=1}^{N} \log p(x_i|\theta) - \frac{1}{N} \sum_{i=1}^{N} \log p(x_i|\theta_0) \tag{5.82}$$

$$= \arg\max_{\theta} \frac{1}{N} \sum_{i=1}^{N} \log \frac{p(x_i|\theta)}{p(x_i|\theta_0)} \tag{5.83}$$

$$\underset{N\to\infty}{\to} \arg\min_{\theta} \int \log \frac{p(x|\theta_0)}{p(x|\theta)} p(x|\theta_0) \mathrm{d}x \tag{5.84}$$

This is intuitively clear because minimizing the distance between the 'real' distribution with correct parameters θ_0 and the model distribution with parameters θ ultimately leads to the closest representation of the data that is possible for a given model.

Then we obtain the Jensen divergence in the following way

$$D_{JS}(p||q) = \frac{1}{2} D_{KL}(p||M) + \frac{1}{2} D_{KL}(q||M) \tag{5.85}$$

with

$$M = \frac{1}{2}(p^{(\text{simulation})} + q^{(\text{experiment})}) \tag{5.86}$$

The Jensen divergence is a similar distance metric with the advantage to yield symmetric distances while the Kullback-Leibler divergence is dependent on the order of model and simulation distribution.

Parameter optimization is performed utilizing nested sampling [303], which is a sampling algorithm to optimize the likelihood. The likelihood function is chosen to be the Jensen divergence. Nested sampling was originally developed to efficiently estimate the evidence, but it has also proven to be an excellent algorithm to estimate the likelihood. In short, nested sampling draws uniformly distributed samples from the likelihood and then consecutively replaces the point with the lowest likelihood value by sampling a new one. The parameter space in each step is constrained via multi-ellipsoidal fits to the existing points. In Julia, we use a multiellipsoidal implementation using the package NestedSamplers.jl, which is an implementation of MultiNest [87].

This approach yielded optimal parameters as $t_1 = 1.9$, $\mu = 1.2$, $k_3 = 6$ $D = 0.001$, $\lambda = 0.7$, $k_{ext} = 0.001$, $J = 0.015$, $p = 1$. Using these parameters, we now take a closer look at the likelihood for the model by varying the coupling strength J and occupation probability p. The occupation probability is a number drawn from a uniform distribution between 0 and 1, which gives the fraction of cell pairs that are coupled by the mechano-transduction mechanism. For $p = 0.5$ half of the cell pairs are coupled on average. Results are shown in Figure 5.16 .

First we see that the average correlation coefficient is decreasing when either J or p are decreasing as expected. It makes sense that the average degree of synchronization is determined by both the coupling strength and the number of pairs that exhibit the coupling mechanism. However the width of the distribution, quantified by the standard deviation of the correlation distribution, depends on the combination of coupling strength and occupation probability. The

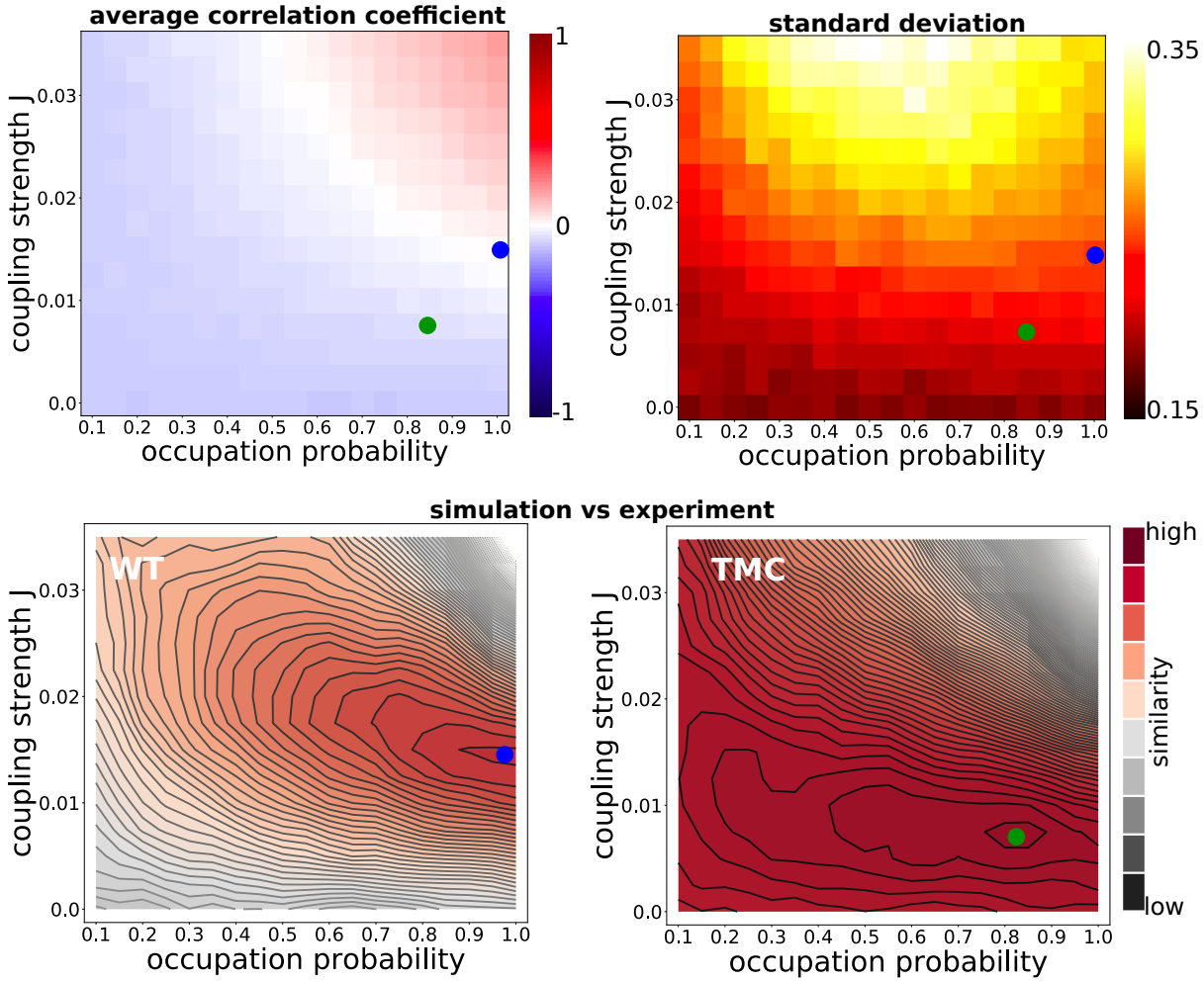

Figure 5.16: Parameter optimization for coupling strength J and occupation probability p leads to an unimodal likelihood for WT and sloppy parameter geometry for *Tmc* . In the top left and right, the mean and standard deviation of the correlation coefficient distribution is depicted. Green and blue dots mark the best matching parameter combinations for wild type and *Tmc* experimental data respectively. In the bottom row, the distance from the model to the experiment is displayed by giving the Jensen divergence value for each parameter combination.

distribution becomes wider for higher coupling values. The reason is that the coupling encourages synchronized oscillations while geometrical constraints still have to be obeyed, which is more difficult the higher the coupling. For the occupation probability the dependency on the width is U-shaped, having smaller values for very low or very high occupation probability and assuming the highest values for intermediate values around $p = 0.5$. The volatility is lowest when either all cells are coupled or none. For intermediate values there is the most room for sample by sample variation.

The second row in the figure depicts the Jensen distance between experimental distribution and simulation outcome. For wild type a clear unimodal peak is visible, meaning that a clear parameter combination exists for which the simulation is closest to the experiment. In the case of *Tmc* many of the parameter combinations, that produce skewed distributions towards negative correlations, are equally likely as they have similar distance. The parameter space in the *Tmc* case is therefore much more sloppy, indicating that more parameters can assume similar behavior as the experiment. As we have stated before, anti-synchronized oscillations are easier to achieve for the system, it is thus not surprising that more realizations lead to a good outcome.

For the best matching parameters we compute "correlation maps", which are studied in section 6.7. In brief, they show the positionally and embryo by embryo averaged correlation. Red colors indicate positive correlation while blue colors indicate negative correlations. Each cell pair is mapped to a position that is the middle between the center of both cells. The correlation coefficient value at that position is spatially and ensemble-wise averaged using kernel density estimation. In Figure 5.17 we show the experimentally achieved correlation maps from wild type and *Tmc* mutants alongside the best matching simulation.

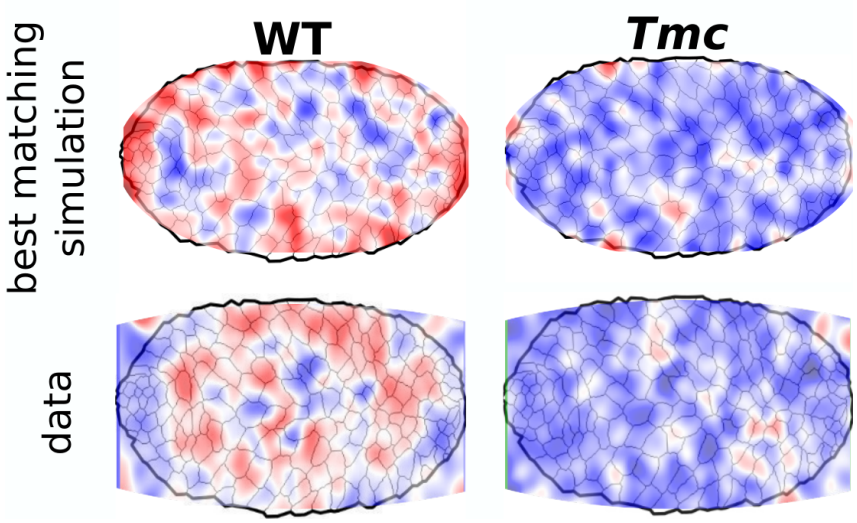

Figure 5.17: Average correlation but not spatial organization is reproduced in the tissue model simulations for WT. In case of *Tmc* the correlation maps from simulation and experiment are statistically indistinguishable. The correlation maps were computed using the positional information of the correlation coefficients, pooled together from all embryos/simulation runs, and averaging them spatially using kernel density estimation with a Gaussian filter kernel.

Colorwise, simulation and experiment look similar, but there is a spatial organization in the wild type data that is not captured by the simulation. We only optimized the simulation compared to the full distribution of correlation coefficients which does not contain information about spatial order. Ellipsoidal topology alone does not seem to be enough to induce spatial

order, however this has to be investigated in greater detail. This result invites speculations about a morphogen controlled patterning system in the amnioserosa, similar to planar cell polarity in the germband. It could be that bulk cells preferentially are equipped with a microscopic coupling mechanism, while cells at the canthi do not express the mechanism or at least less. Spatial patterning might play into the maintenance of topology or might be required for force generation during dorsal closure. However, importantly the difference for *Tmc* mutant and simulation is very close. This suggests that there is not spatial distribution in the arrangement of coupled vs uncoupled cell pairs since it is enough to optimize the model according to the full distribution to achieve similar results.

Calcium uncaging

In chapter 3, we have introduced a novel experimental technique to induce cell contractions *in vivo* by optochemical uncaging of Ca^{2+} , which mediates the activation of myosin. In the simulation we can replicate this experiment by increasing the amount of Ca^{2+} in a cell within the tissue (see Figure 5.18).

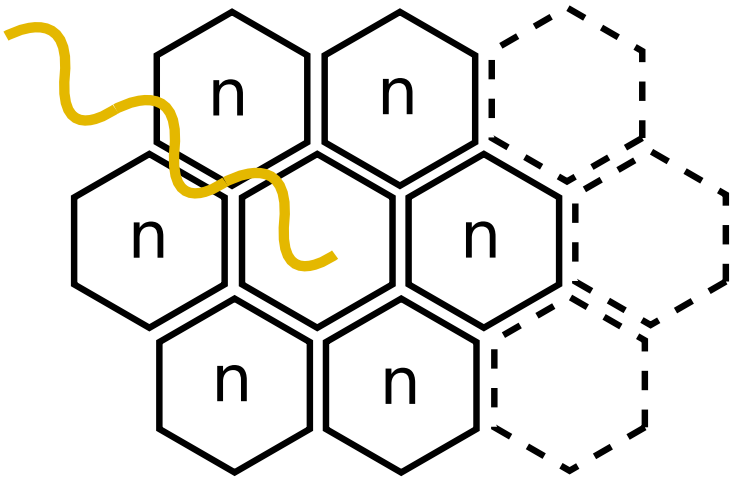

Figure 5.18: Scheme of Ca^{2+} uncaging simulation. Choosing a random cell within the tissue, the amount of Ca^{2+} is considerably increased. Neighbor contraction response is monitored. The target cell and its neighbors are not positioned at the border of the tissue.

We are interested how the neighbors of this target cell are reacting. If cells are utilizing a mechanosensitive coupling mechanism, the neighbors should also decrease, or at least react to the contraction of the neighbor. Without a coupling mechanism we expect that the neighbors will increase their area since the geometrical constraints favor anti-synchronized dynamics.

Simulations are performed for the optimal parameters, only tuning J, and repeated 50 times. After transients have decayed, a random cell within the tissue is selected such that all six neighbors do not lie directly at the border. Then the Ca^{2+} compartment is instantaneously increased by twice the maximum value the cell exhibited during the time of simulation, and the resulting relative area change of the neighbors is measured. When the target cell has reached the minimum of the contraction, neighbor areas right before the uncaging event are compared with the momentary area. The contraction is defined as the negative relative area change.

$$\text{Contr} := \frac{A^n(t_{uc}) - A^n(t_{uc} + t_{\text{target at min}})}{A^n(t_{uc})} \tag{5.87}$$

Results are depicted in Figure 5.19.

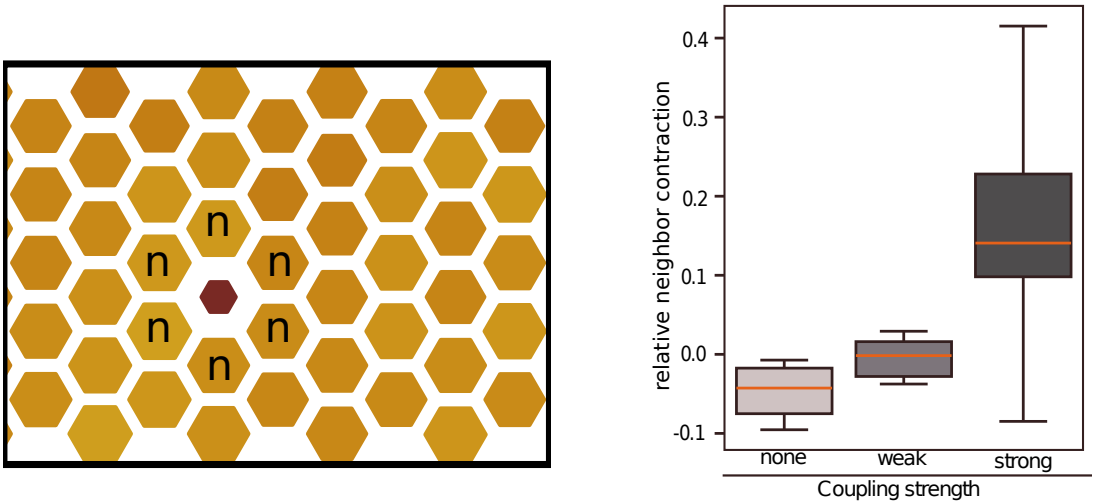

Figure 5.19: Simulations predict that significant neighbor contractions in response to Ca^{2+} release in a target cell requires strong a coupling mechanism. On the left an example snapshot from an uncaging simulation is shown. Color and size of the hexagons is according to the area. While the target cell is noticeably contracting, we evaluate the behavior of the neighbors. To the right the results of the relative neighbor contraction for different coupling strength is displayed. The contraction of the neighbors is shown as the negative relative area change compared to the time right before the uncaging event. Values for the coupling strength are $J = 0, J = 0.015, J = 0.07$.

As we can see, neighbors contract together with the contracting target cell if the coupling strength is high enough. Noticeably the width of the distribution increases with higher coupling strength as well. This effect is due to the geometrical constraints in the hexagonal packing. While neighboring cells follow the dynamics of the target cell, one or two cells are increasing in area to preserve the mechanical constraints on the lattice.

This shows that we expect neighbor dynamics to react to an uncaging experiment by contracting as well if a coupling mechanism is present. It is noteworthy that the high average contraction of the neighbors could only be achieved with very high coupling strength, already close to the collapse of the system, and therefore higher than optimal parameters compared to the experiment. We compare this model prediction to the experiment in chapter 7 (Figure 5) where we find average neighbor contraction in wild type cells of roughly 0.2, like in the strong case here. This might indicate that for the *in vivo* situation, there is an additional mechanisms at play that regulates neighbor dynamics in case of strong perturbations of the tissue, like uncaging induced contraction. Similar responses have been observed for wounding of the tissue where neighboring cells react drastically in order to stabilize the tissue [105]. In this case *Tmc* still plays as role, as we show in chapter 7 (Figure 5), but it might trigger secondary processes to elicit stronger responses and not be the only mechanism at play.

5.11 Summary

We have introduced extensions to an existing viscoelastic model for cell surface are oscillations. Single cell units have been integrated on a hexagonal lattice configuration with ellipsoidal topology surrounded by a stiff border cells. This system is able to faithfully reproduce known results.

Neighboring cells synchronize their dynamics in dependence of the strength of mechanotransduction coupling. This was shown in a two cell model, realized as linear chain, and the full two dimensional triangular lattice configuration.

Optimal parameters in comparison to experimental data were determined, showing that wild type like behavior can is achieved with an unimodal peak in the likelihood for optimal parameters. *Tmc* like solutions were easier to obtain, as was shown by the parameter space geometry which is more sloppy than for wild type. This is consistent with the observation that anti-synchronized oscillations are the natural state of neighboring oscillators with mechanical interactions.

Using these parameters we have conducted Ca^{2+} uncaging simulations to study the direct neighbor response to the contraction of a target cell. We find that neighbors react by contraction if the mechano-chemical coupling between cells is high. For lower coupling strength, neighbors do not contract as strongly and without coupling neighbors areas increase.

Together, the results are indicating that *Tmc* might provide a distinct mechanism for the coordination between neighboring cells during *Drosophila* development. These results are combined with analysis of experimental data and additional experiments in Chapter 7. We find that *Tmc* is a necessary component for the synchronization of cell dynamics in the amnioserosa

5.12 Appendix

Increment covariance of area trajectories

For fluctuations of cell junctions in the germband it has been tested, and confirmed, that noise is additive [188]. Because cell area fluctuations are equivalent to junction fluctuations by Leibniz' rule, this already gives some hints that additive noise is the way to go.

To test this with our real data from amnioserosa cells we follow the same procedure described in [188] and check the increment covariance. The procedure is mainly used in single particle tracking [22] and exploits that the increment autocovariance matrix gives an estimate of the noise strength and the measurement error for a simple diffusion process and for Langevin dynamics to first order.

$$\mathrm{Cov} = \begin{cases} D\Delta\tau - 2\sigma^2_{meas} & \text{for } j = k \\ -(\sigma^2_{meas})_{\max(j,k)}, & \text{for } j = k \pm 1 \\ 0, & \text{otherwise} \end{cases} \qquad + \mathcal{O}(\Delta\tau\sigma^2_{meas}, \Delta\tau^2, \sigma^2_{meas}) \tag{5.88}$$

It is assumed that the measurement error follows a Gaussian distribution with 0 mean and variance σ^2_{meas}.

Since our timeseries exhibit oscillations, and thus are periodic, we employ filtering to remove the oscillation trend before the analysis using a Savitzky-Golay filter [263] with 5 timesteps windowlength ($\approx$ 3 min) and a polynomial of third order. Filtering should be coarse enough to leave fluctuations intact but capture the global oscillatory trend. Subtracting the filtered signal from the original yields timeseries without oscillation. The resulting approximation of the fluctuations around the deterministic mean are used to calculate the increment autocovariance shown in Figure 5.20.

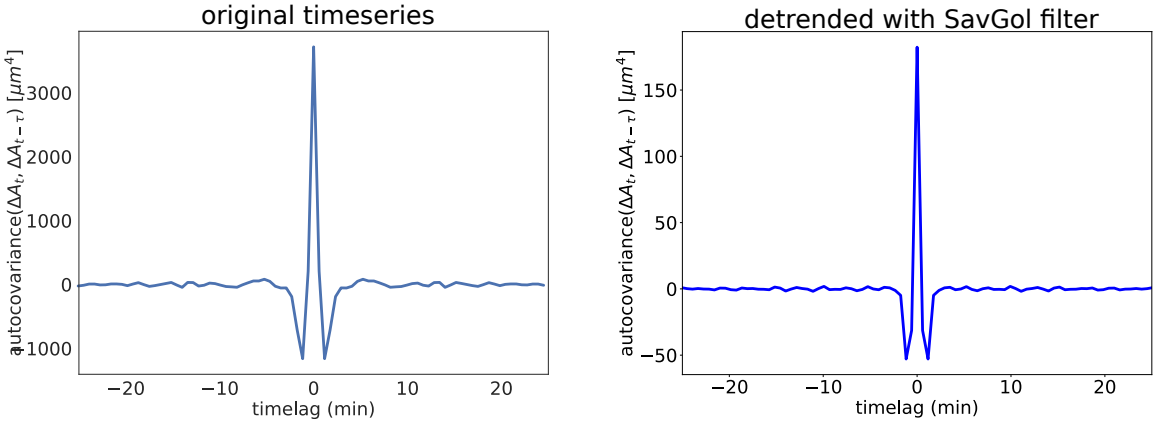

Figure 5.20: No long range correlations in experimental increment autocovariance. Average increment autocovariance of original area timeseries (left) and of deviations from filtered area timeseries (right). Regarding the original timeseries data, no longer ranged correlations are visible except for the expected correlation due to the periodicity of the area oscillation (roughly at 5min). In addition, the peaks are too large to reflect random fluctuations. Therefore, we remove the oscillation trend by filtering the timeseries using a Savitzky-Golay filter. For the filtered timeseries data, there are no long range correlations visible. From this autocovariance we can also estimate measurement noise and intrinsic noise strength.

The analysis was done with surface area timeseries of wild type amnioserosa cells, a dataset that is further described in chapter 6. For original timeseries data, including oscillations, we can already suspect that there are no longer ranged correlations except for the periodicity, having a mean period of roughly 5 min. But the magnitude of the autocovariance is way too high to be noise and reflects the variance imposed by the oscillations. The data from the filtered timeseries shows that the trend was successfully removed and the magnitude is much smaller. There are no long range correlations visible.

This observation makes it very likely that the origin of the noise stems from thermal fluctuations, fluctuations of the actomyosin network, the network of cells in the tissue or from movement of the rest of the embryo which directly translates into area fluctuations. We are not claiming that myosin or calcium dynamics are not noisy as well but we have obtained good indications that the separation of timescales is large enough such that these do not matter for the fluctuations of the cell surface area.

Extended parameters for model comparison

In the main section we showed a smaller window of parameters to focus on the most optimal parameter regions. Here, a broader range of parameters is shown in Figure 5.21

A novelty is the plot that displays collapse probability. Since we repeated simulations 10 times we obtain the frequency of successful simulation runs without collapse. Because our system is stochastic, there is a transition region between parameter combinations that always oscillate or are stable and regions which always collapse. In the deterministic case, the border between collapse and oscillations would be sharp between frequencies 0 and 1. In the other phase diagrams we have blacked out parameter combinations for a collapse probability > 0.3.

Otherwise, the figure does not contain new information, but they show that the system behavior consistently continues as expected for the extended parameter window.

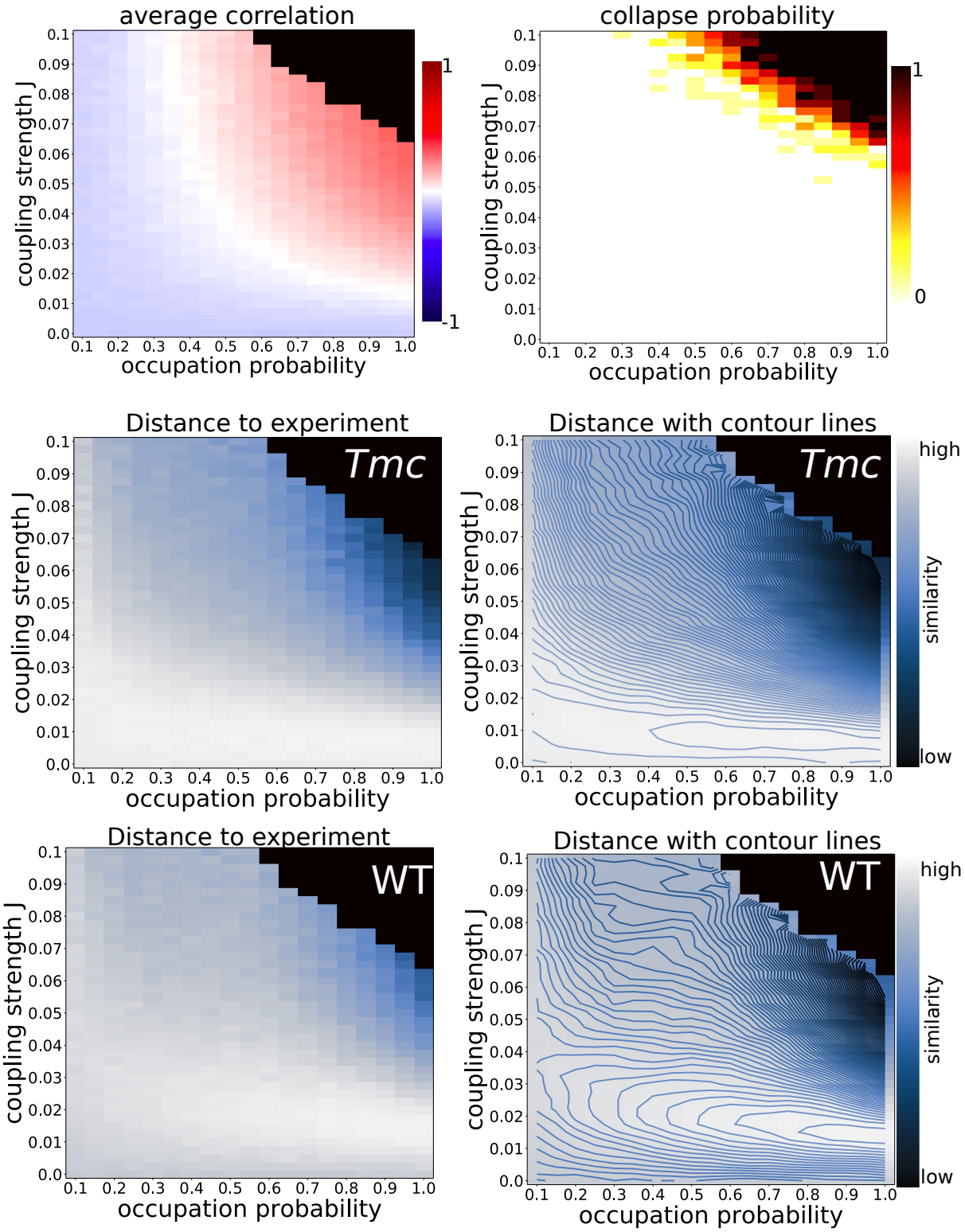

Figure 5.21: Extended parameter window for simulation comparison with the experiment. Expanded parameters are consistent with the smaller fraction we showed before. In the top right the collapse probability is displayed which shows the fraction of collapsed simulation runs.

Chapter 6

Quantitative analysis of ellipsoidal amnioserosa dynamics

"Statistical laws are not necessarily used as a result of our ignorance. Statistical laws can reflect how things really are. There are matters that can only be treated statistically."

James Clerk Maxwell

6.1 Content

In this section I quantitatively describe the amnioserosa of *Drosophila* during the ellipsoidal stage before dorsal closure onset. First, the experimental details and properties of the dataset will be described followed by an analysis of single cell and whole tissue dynamics.

Through the advances in image processing techniques (see chapter 4) it is now possible to record, segment and track cells in epithelial tissues with very high accuracy. I here describe a unique dataset consisting of fully segmented amnioserosa time lapse movies of roughly 10 wild type embryos and a similar number for two mutants *Tmc* and *xit* . For the first time we have access to 1-2 hour long trajectories of thousands of cells in the amnioserosa for the complete tissue. Previous studies only focused on smaller regions of interest and few examples.

Of special interest is the analysis of cell oscillations and cell-cell coordination. Subtle differences between wild type embryos and *xit* and *Tmc* mutants can be resolved using our large scale analysis approach. Synchronization is quantified by the cross-covariance of cell pairs over the whole ellipsoidal phase.

Tmc mutants show a substantial loss of synchronization with their direct neighbors. In addition, the spatial order of synchronous and anti-synchronous regions in the amnioserosa is clearly distinct compared to wild type embryos. *xit* mutants experience loss of synchronization to a lesser extend. Interestingly, the spatial order of correlations is closer to wild type.

Local false discovery rate (FDR) analysis is used to dissect the ensemble of correlations into statistically significant and insignificant correlations. The FDR subsample confirms the result of the global analysis, showing that the detected distribution and spatial organization of wild type embryos is consistent.

Furthermore, observables like cell area or cell anisotropy are described and morphological differences between wild type and the mutants become clear. In general, wild type embryos show less embryo by embryo variation and shorter completion time of the ellipsoidal phase, which indicates higher efficiency in comparison to the mutant embryos. In addition, WT cells

have more isotropic shapes. Considering different spatial regions in the amnioserosa, the analysis reveals that in particular peripheral cells show distinct features from bulk cells, but also anterior/posterior cells from middle cells.

Results in this chapter have been obtained using the segmentation method described in chapter 4. Key results from this chapter are also presented in chapter 7 where they are combined with results from chapter 5 and additional experiments to understand the roles of *Tmc* and *xit* for intercellular coordination.

The experimental data used in this chapter has been recorded by Prachi Richa from the lab of Jörg Großhans, Department of Developmental Biochemistry, University Medicine Göttingen (now University of Marburg (JG) and Cambridge University (PR)).

6.2 Dataset description

The here used dataset consists of time-lapse movies of the amnioserosa pre dorsal closure. For wild type 8 embryos are incorporated into the dataset and respectively 7 embryos for *xit* and *Tmc* , which are mutants that affect E-Cadherin glycolization in the case of *xit* and a mechanosensitive ion channel in the case of *Tmc* .

Movies have been recorded using a Zeiss Observer.Z1, CSU-X1 spinning disc microscope with the objective Plan-Apochromat (25X, NA 0.5oil, mutli-immersion, DIC), recorded via a emCCD evolve 512. The temporal resolution is $35s$/frame and spatial resolution is $0.5333 \cdot 0.5333 \cdot 1\,\mu m$/voxel. Embryos were recorded in a room with 22°C [279].

A second dataset exists with higher spatial and temporal resolution using a 40x objective with 10s/frame recording time. This dataset is not considered for data analysis. However, higher resolution example trajectories from this dataset might be shown, or results may be double checked. It only shows a part of the full amnioserosa and the total recording time is not long enough for full evaluation.

If not declared otherwise, the data that is shown or analyzed will come from the dataset that shows the full amnioserosa for the whole ellipsoidal phase.

Spatial normalization

In this study, different experimental realizations of the same system are compared with each other. One important question is how to align these datasets. In case of spatial alignment the solution is quite simple. The coordinates along the axial direction are normalized such that the position of the anterior most cell has value 0 and the posterior most cell position has value 1. In the same way coordinates in the lateral direction are also normalized between 0 and 1, whereas the bottom most cell position has value 0.

Time course alignment

Another alignment question poses itself when the temporal development of some process is investigated. This question is not trivial because, as we will see in later sections, there is significant temporal variance across the experiments, especially in case of the mutants.
One example is that the manually determined ellipsoidal phase has different durations, as can be seen in Figure 6.3. Since it is interesting and important to investigate how tissue properties evolve over time these datasets have to be aligned to yield a valid time resolved ensemble description.
There are several options how such an alignment can be achieved: (i) alignment to the beginning

of the ellipsoidal phase, (ii) alignment to the end (dorsal closure onset), (iii) aligning the whole time course and interpolating such that all time series are of the same length. Options (iii) and (i) are excluded because (iii) would strongly alter the possibly nonlinear temporal structure of the data and for (i) we actually do not have an exact objective criterion for the onset. Therefore alignment to dorsal closure is left. The greatest advantage here is that we have a relatively clear alignment point. Since dorsal closure onset is associated with the beginning of the zipping process, which roughly begins when both canthi are fully formed, we have an objective criterion for this alignment point which is depicted in Figure 6.1.

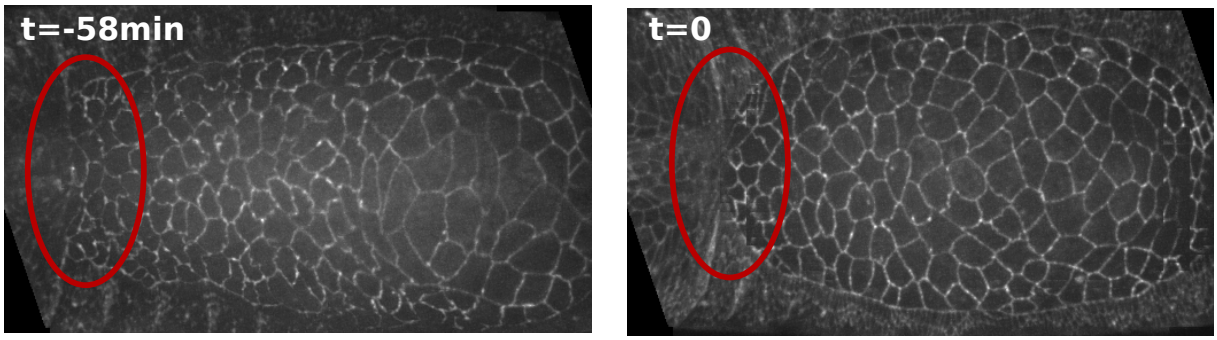

Figure 6.1: Alignment of different experiments by visually determining the time of dorsal closure onset. When the canthi at the anterior end of the tissue has formed the zipping process is initiated or shortly after. This is a singular event with clearly determinable occurrence which can be used as alignment point. We call this alignment point *dorsal closure onset*, although this terminology is not a consensus in the literature because it is not clear when exactly dorsal closure is initiated.

It has to be said that also this criterion is not fully exact. The zipping does not have to start immediately after canthi formation and also the exact point when the canthi is formed has some ambiguity to it. The visual cue is only accurate $\pm 5min$, which is estimated by manually looking over the movies. In addition, the onset of dorsal closure is not very well defined by itself. Scientifically it is important in this section that we have a clear alignment point and that this point does not yet fall into dorsal closure. During dorsal closure different biological processes are at work that would interfere with the statistical stationarity condition we require to analyze timeseries.
There is also the option that a quantitative measure exists, an order parameter like in a phase transition, that abruptly changes at dorsal closure onset and therefore signifies the time point. Such a parameter could not be found during ellipsoidal phase. While there are changes in the dynamics during ellipsoidal phase they are happening continuously and too slowly such that a clear onset point could not be determined quantitatively.

Regions of interest

One question to be investigated is whether all cells within the amnioserosa are completely homogeneous as a population or whether there are spatial differences. The topology of the tissue or anisotropic external forces exerted form the lateral epidermis could result in differences for certain static parameters like cell area or anisotropy as well as dynamical differences. In later sections there will be mainly two types of division of the tissue, which can be seen in Figure 6.2.

First, a distinction is being made between peripheral and interior (or bulk) cells. The behavior of the peripheral cells is biologically different, as described in the introduction, and in

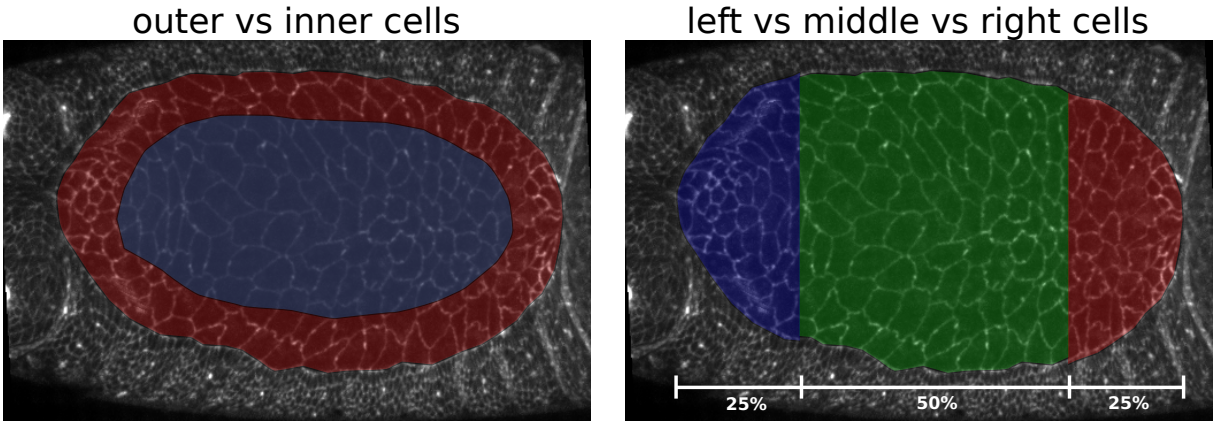

Figure 6.2: Regions of interest within the amnioserosa used in later quantifications. Amnioserosa bulk cells express different proteins than the peripheral most cells, which for example play a role for purse string formation. Cells at the canthi are considered separately from middle cells.

addition the formation of the actin cable around the amnioserosa might cause differences in cell behavior. Secondly, it will be distinguished between anterior, middle and posterior regions. The middle part of the amnioserosa has to counteract the forces from the lateral epidermis the most. Furthermore, the concave topology of the cells near the canthi might provide more stability and thus show different dynamics.
Anterior, posterior and middle cells are defined by the 25% quartiles of the normalized cell positions.

6.3 Basic properties of the amnioserosa

Here, the basic properties of the amnioserosa are presented. First the focus is on static properties and statistics, then the dynamics will be discussed afterwards.

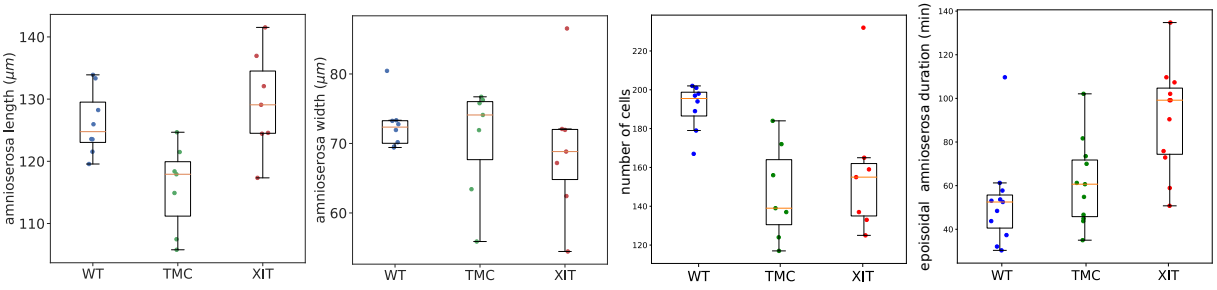

Figure 6.3: Loss of *Tmc* and *xit* disturbs basic properties of amnioserosa cells in the ellipsoidal phase. Single dots represent a single experiment / embryo. The left panel and the one next to it show the length and width of the tissue in agreement with values from the literature [167, 260, 285, 321]. The number of cells matches the literature as well [97, 107, 122, 260]. As stated in the introduction, the definition of the ellipsoidal phase is not unique, therefore there are no values we can compare the duration to.

Figure 6.3 displays amnioserosa width, length, cell count and duration of the ellipsoidal

phase. While the wild type values match the literature [97, 107, 122, 167, 260, 285, 321], already some differences can be seen in the mutants. *Tmc* and *xit* seem to be in reasonable agreement with wild type for the dimensions, however *Tmc* is roughly 10 microns shorter on average. This difference is the width of a typical cell. It can also be seen that *xit* and *Tmc* have fewer cells and the duration of the ellipsoidal phase is longer. It has to be noted here however, that the duration is determined manually by visual inspection of the movies. Dorsal closure onset is defined as the time when the canthi at the anterior end is fully formed. The beginning of the ellipsoidal phase starts when the germband has retracted.

Cell area

Amnioserosa bulk cells display oscillatory behavior. Before this dynamics is investigated more closely, the average properties like the average cell area and their distribution are of interest as well. Areas are computed by counting the pixels per cell, or alternatively via Leibniz' rule during junction labeling. An example of the segmented cells, where they have been color coded by area, is shown in Figure 6.4.

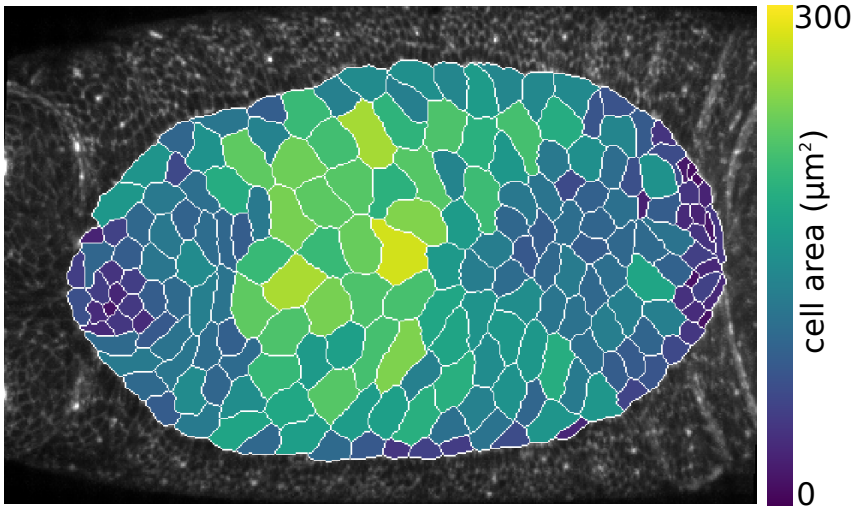

Figure 6.4: Example of area quantification from a wild type embryo. Each cell is colored according to its area.

Figure 6.5 displays histograms for the cell area pooled from all embryos. Comparison of the average area shows only slight differences between the mutants but using the regions of interest and looking at the temporal development reveals distinct phenotypes.

For the temporal development, a histogram for the cell area at four different time points is shown. First at the beginning of the respective movie, which still is situated in the germband retraction phase, second at the initiation of the ellipsoidal phase, then in the middle of the ellipsoidal phase and finally at dorsal closure onset. The measured cell area for WT is in agreement with published data [107, 260, 306]. For *Tmc* and WT there are no clear differences between the distributions. *xit* on the other hand clearly experiences a shift of the distribution towards smaller areas.

While the overall average histogram did not reveal significant differences between areas of the mutants, when we look only at the middle cells and the bulk cells the distributions are different. Compared to *xit* and *Tmc* the WT distribution is significantly shifted toward smaller areas and *xit* even has some bigger cells in those regions than *Tmc* . The distributions in the peripheral region and the anterior/posterior canthi are not significantly different from each other.

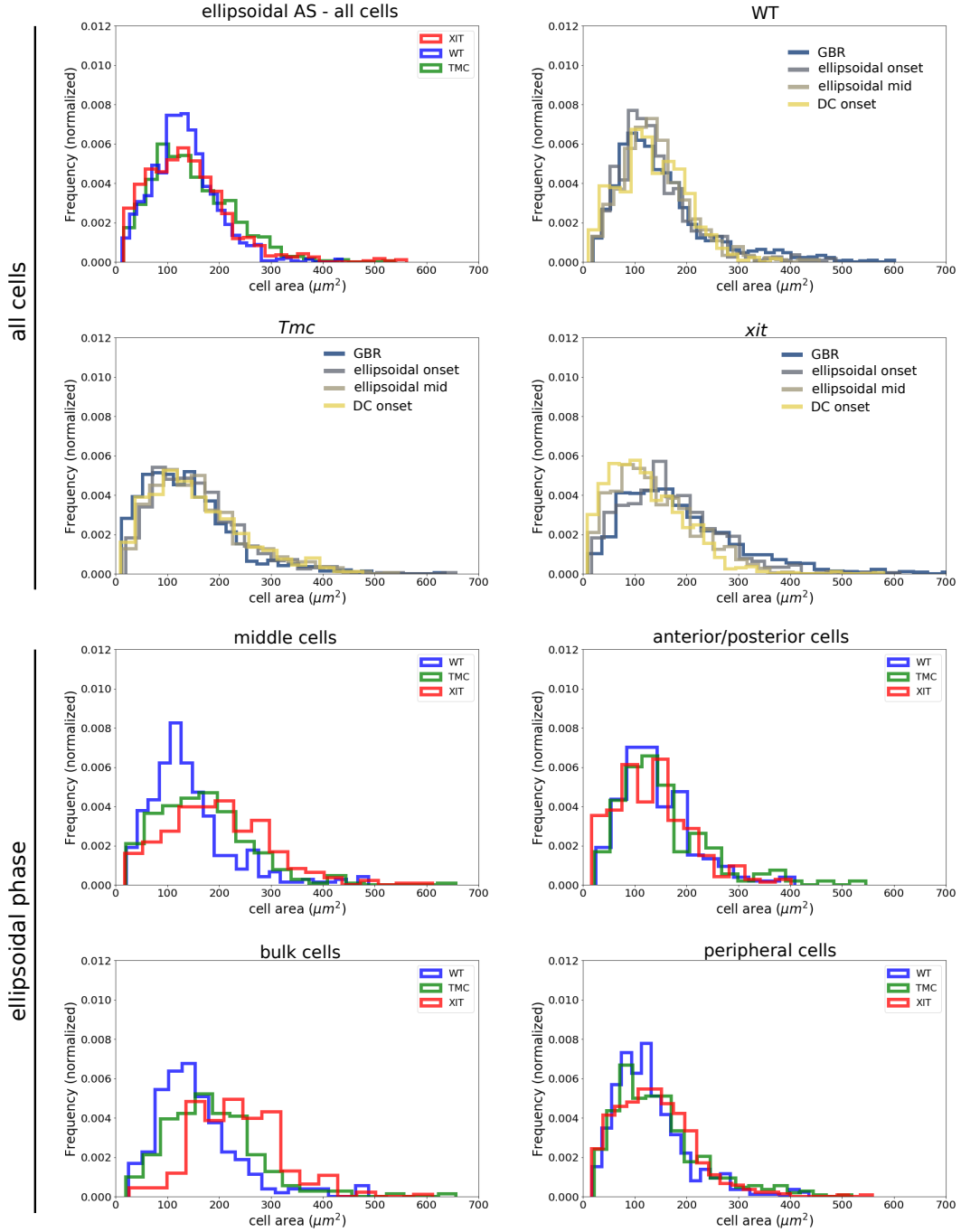

Figure 6.5: *Tmc* and *xit* mutant cell area is increased in bulk cells and for middle cells. Histograms show amnioserosa cell area. Top left shows the average cell area throughout the ellipsoidal amnioserosa phase of WT, *Tmc* and *xit* embryos. The remaining three panels on the top half show the temporal development of the area distribution without spatial restrictions for WT, *Tmc* and *xit* respectively. In the bottom panel, the two graphs on the left are displaying the area distribution in the middle part (top) and the inside part (bottom) as defined in Figure 6.2. In comparison, the histograms on the right display the distribution in the complementary region with respect to the left side. The distribution of anterior cells is not significantly different from the distribution of posterior cells.

Those regions contain more cells because they are smaller which makes the histograms smoother.

Total area is computed by summing the individual cell areas per frame. Time courses of total and average area change is computed frame by frame and then aligned to dorsal closure at $t = 0$. Figure 6.6 displays the corresponding data.

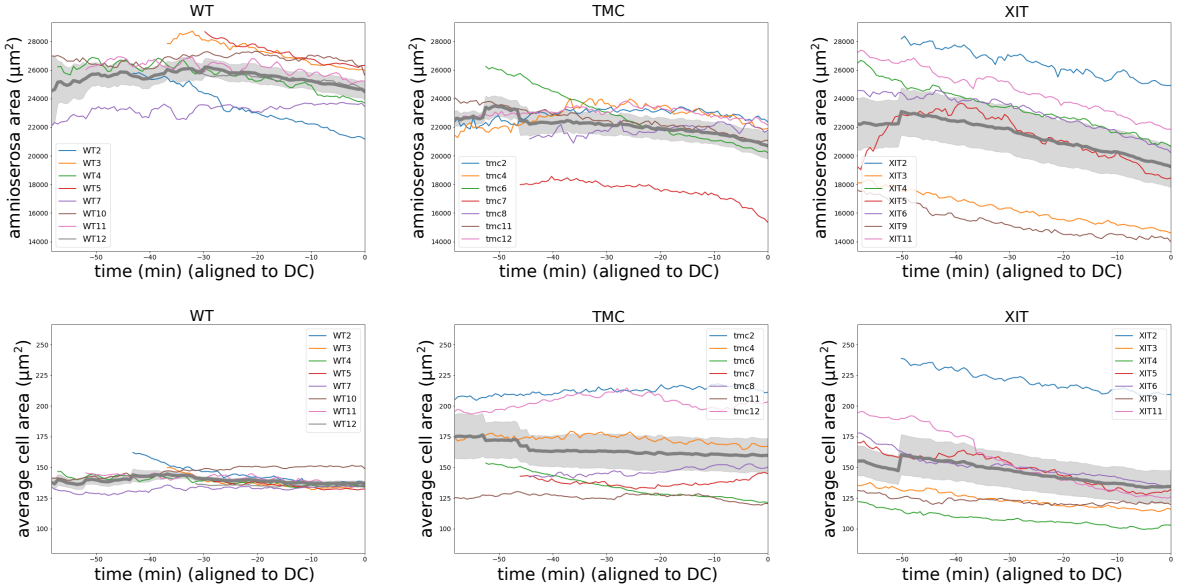

Figure 6.6: Amnioserosa area decreases during ellipsoidal stage. Time courses of complete amnioserosa area and average cell area for WT, *Tmc* and *xit* respectively. The thick gray curve is the ensemble average and the region around it is the standard error of the mean. All time courses have been aligned to the onset of dorsal closure. Especially interesting is the consistency of average cell area in the wild type case. The mutants show much higher variance and especially *xit* displays notable trends.

For all mutants the total area decreases continuously over the ellipsoidal phase. The slope, however, is noticeably increased for *xit* while for *Tmc* and WT there is an acceleration when dorsal closure onset is approaching. In terms of absolute size, the amnioserosa has the largest total area for WT. *xit* in addition, displays a large volatility across experimental realizations.

The average cell area time course curiously is roughly constant for *Tmc* and WT. Therefore some cells have to increase in area while others shrink. Only in case of *xit* there is a consistent decrease in average area as well. Both mutants display a noticeably higher variance in embryo by embryo than WT, which is very consistent.

Cell anisotropy

Another morphological feature that emphasizes the differences between the examined mutant phenotypes is the cell anisotropy, which quantifies its elongation. Anisotropy and cell angle are computed per cell using a nematic order parameter [221], which is described in more detail in section 6.9.

Before the ellipsoidal phase, the germband is retracting and cells in all embryos are very elongated. Over time cells in WT embryos assume a more isotropic shape while this effect is less pronounced in the mutants. Figure 6.7 displays an example of segmented amnioserosa with color coded cells, according to their anisotropy.

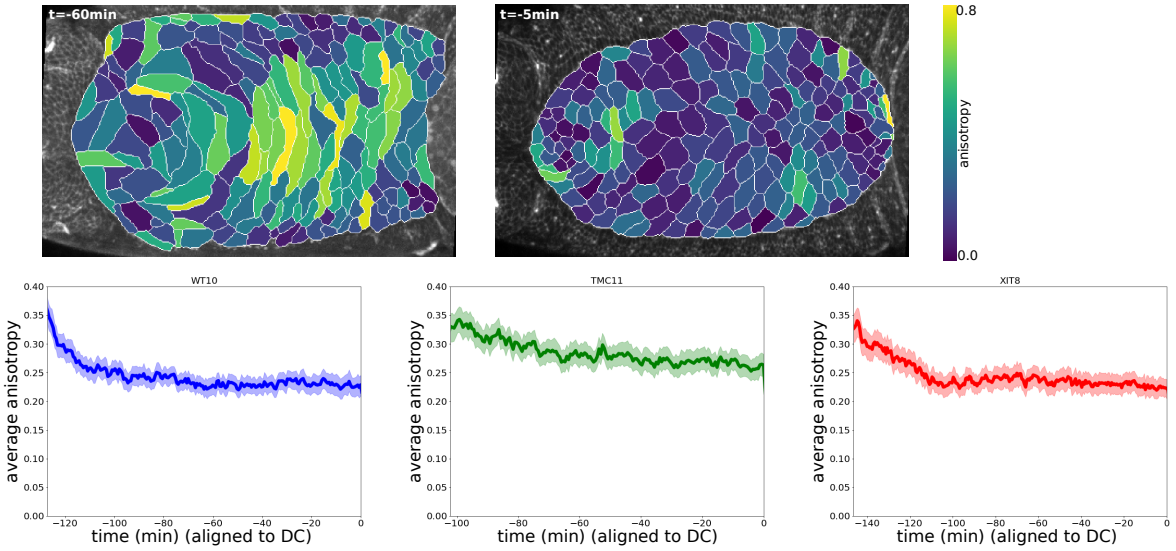

Figure 6.7: Anisotropy decreases after germband retraction until dorsal closure onset. The top row displays a segmented wild type example with anisotropy values being color coded. Higher values reflect more pronounced elongation. Below, one example for each mutant for the whole time course is displayed, including datapoints before the ellipsoidal phase. The examples show average anisotropy across all cells from the tissue with bootstrapped 95% confidence region.

An example from a single embryo for each investigated line shows the average anisotropy over time, aligned to dorsal closure. It can be seen that for WT the average anisotropy decreases and then roughly stays stationary until the onset of dorsal closure. The examples from *xit* and *Tmc* show similar behavior.

In Figure 6.8, histograms of cell anisotropies are displayed. Similar to the area quantification, we look at snapshots from different times and different regions of interest.

The average anisotropy for the full ellipsoidal phase shows a difference for *xit* , but *Tmc* and WT have similar distributions. The snapshot histograms for different times, however, reveal some greater differences. While WT amnioserosa cells clearly develop towards more isotropic cell shapes, the mutants display this effect to a lesser extend.

In addition, for the regions of interest, the middle cells and the bulk cells, anisotropy is higher in *xit* and *Tmc* whereas *xit* cells show overall highest elongation, *Tmc* in the middle and WT having the most isotropic cell shapes. This difference is lost when comparing the peripheral cells and the anterior/posterior cells.

The time course shown in Figure 6.9 was determined the same way as for the area. Additionally, the average angle is displayed, which is the angle between the axial direction and the director of the cell. See Figure 6.28 in section 6.9 for more details. For the angle calculation no difference is being made between cells that point towards the anterior or the posterior end such that the angle takes a value between 0 and 90 degrees.

For WT the average anisotropy during ellipsoidal phase stays fairly constant. For *Tmc* it decreases with a constant slope, whereas at the beginning it assumes a clearly higher value and arrives at a similar level as WT at the onset of dorsal closure. *xit* shows higher variance across embryos and much larger values. The average anisotropy also decreases until dorsal closure onset.

The average cell angle shows similar behavior as the anisotropy. Cells in *xit* are mostly elongated in the lateral direction. For WT and *Tmc* this is more mixed, which is the reason

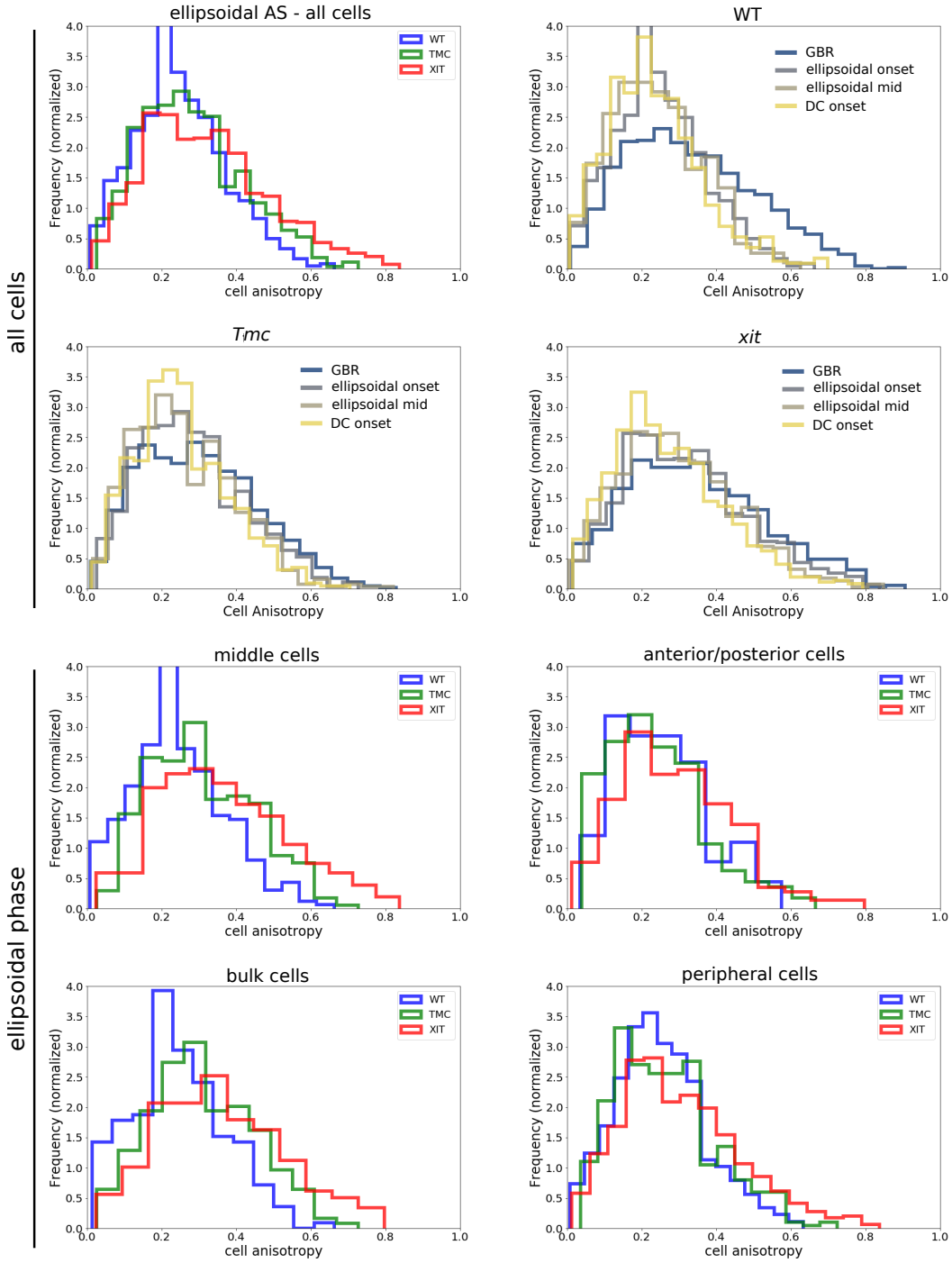

Figure 6.8: Bulk and middle cells in *Tmc* and *xit* mutants have a higher anisotropy than wild type cells. Histograms show amnioserosa cell anisotropy. Top left shows the average anisotropy throughout the ellipsoidal amnioserosa phase of WT, *Tmc* and *xit* embryos. The remaining three panels on the top half show the temporal development of the anisotropy distribution without spatial restrictions for WT, *Tmc* and *xit* respectively. In the bottom panel, the two graphs on the left are displaying the anisotropy distribution in the middle part (top) and the inside part (bottom). In comparison, the histograms on the right display the distribution in the complementary region with respect to the left side. The distribution of anterior cells is not significantly different from the distribution of posterior cells.

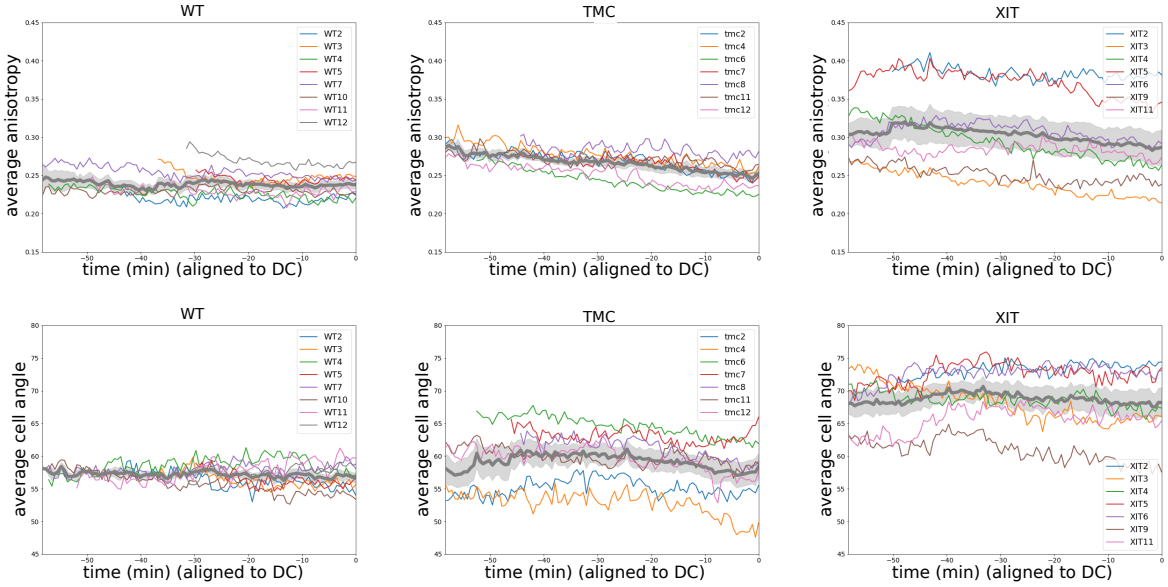

Figure 6.9: Cell shapes in *xit* and *Tmc* are more elongated, show more variance and decrease over time while wild type anisotropy is stable. First row shows the average anisotropy and the second row the average cell angle over time for WT, *Tmc* and *xit* respectively. The thick gray curve is the ensemble average and the region around it is the standard error of the mean. All time courses have been aligned to the onset of dorsal closure. The wild type averages and again is way more consistent than the mutants. The trend in the mutants towards higher anisotropy and laterally oriented cells is also clearly visible.

lower values are displayed. The embryo-to-embryo variance is noticeably higher in the mutants compared to WT.

The analysis of area and anisotropy therefore reveals differences in the phenotypes between WT, *xit* and *Tmc* . Especially the temporal development is different as well as the morphology in the middle part of the amnioserosa, and the bulk part.

6.4 Single cell trajectories

Cells in the amnioserosa are exhibiting area oscillations. In this section we are exploring the basic dynamical features of these cells to get an idea what kinds of behavior the dataset is showing.

Figure 6.10 shows some typical examples of cellular dynamics. Areas are fluctuating around an average value A_0 but as we see in those examples the average is not always remaining constant, but can show drifts that both increase and decrease as well as show mixed behavior of stable fluctuations and drift.

We selected the examples in Figure 6.10 manually by visually inspecting hundreds of examples and determining that most trajectories fall into three classes: (i) stable oscillations around a fixed average area, (ii) cells that show a constant increase or decrease in the average area and (iii) cells that display mixed behavior showing both stable and drifting behavior or alternatively exhibit a change in the drift.

In order to come from this qualitative assessment to a quantitative one the drift is determined

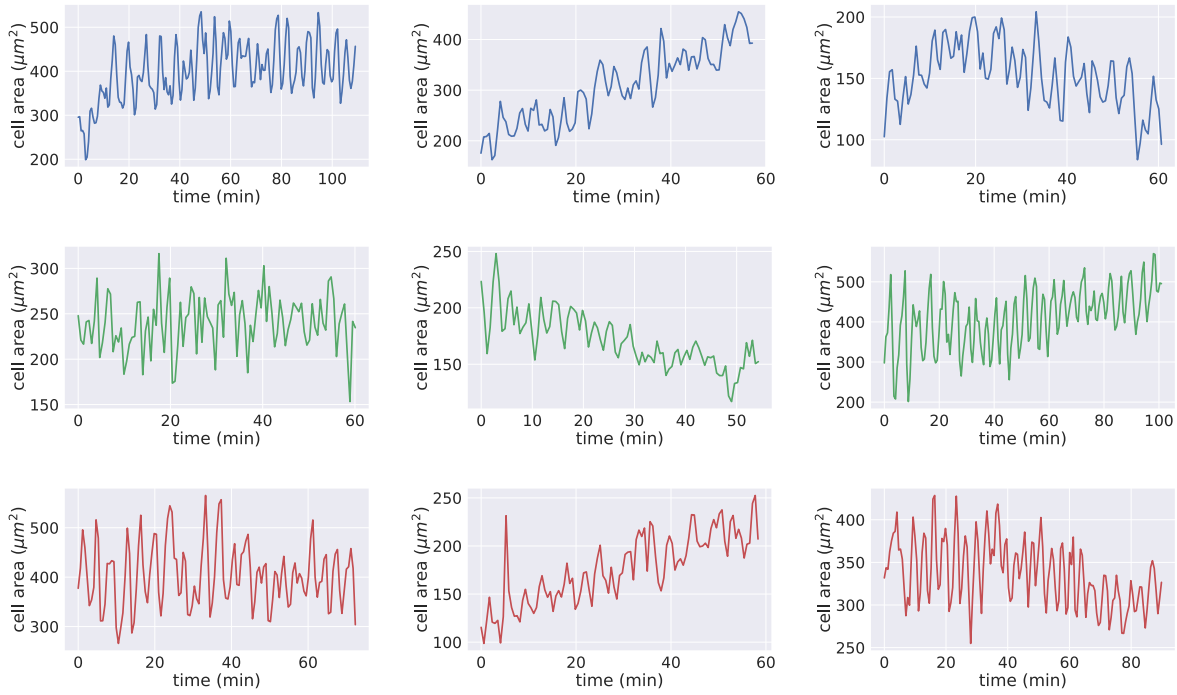

Figure 6.10: In the ellipsoidal phase amnioserosa cells oscillate while maintaining a stable average area, increasing or decreasing their average area or they show a mixed behavior. Examples of single cell area trajectories from WT (blue), *Tmc* (green) and *xit* (red) are shown. In the first column, cells exhibit stable oscillations around an equilibrium area. In the second column cells display a constant systematic drift while retaining oscillations. In the third column, cells exhibit mixed behavior, for example stable in the first half and then shrink in the second half like in the *xit* case.

by piecewise linear fits to the original time series. This will later be used to detrend timeseries in the dataset and analyze oscillation in the amnioserosa. To determine how many pieces should be used (e.g. how many changes in the trajectories will need to be considered) the Bayesian information criterion (BIC) is used, which is explained in more detail in section 6.9. Our algorithm automatically finds the best breaking points between the linear segments.

Because of the qualitative assessment we known that some trajectories change their behavior from for example growing to shrinking (compare Figure 6.10). This can not be investigated if only a single segment is fitted which is why we choose to have at least two piecewise linear segments. The analysis of BIC values shows that adding more than two segments is not improving the overall model goodness. Therefore we will determine trends via piecewise linear fits with 2 segments, but variable breakpoint.

The full dataset is now being analyzed by fitting two piecewise linear segments to the area trajectories. The optimal breakpoint between the segments is determined by choosing the point with the highest overall likelihood of the fit. Figure 6.11 shows the slopes of the segments, the time of the breakpoint and the relative change in area between the beginning and end of the segment. The relative area change serves as a more intuitive measure to understand how strongly average cell areas grow or shrink.

The distribution of slopes reveals a tendency of slightly decreasing cell areas. This tendency is increased in the second linear segment which can be explained by the preparation of the

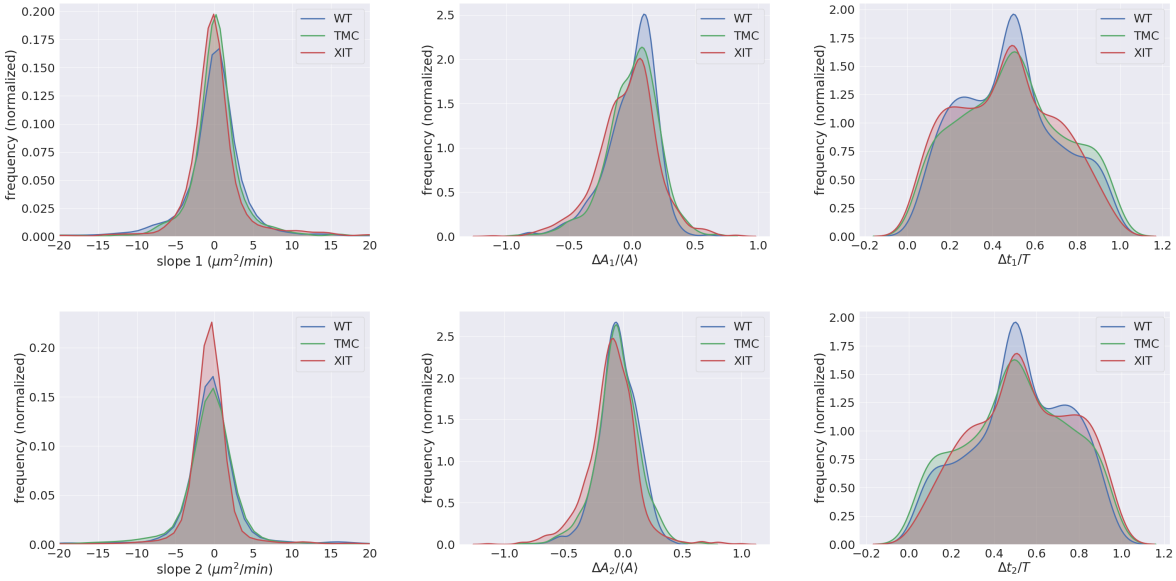

Figure 6.11: In the ellipsoidal phase most amnioserosa cells stay within ±20% of their starting area but slightly decrease their average area with the breakpoint at around half time of the observation. The distributions of the drift on the left show that the drift is relatively slow and roughly centered around zero while having a bias towards negative slopes. In the middle the distributions of the relative area change also shows a tendency towards negative changes since both have more probability mass in the left half. The time of the optimal breakpoint is concentrated around 0.5 but with a very broad distribution. Note that values above 1 and below 0 do not exist. The displayed probability mass in those regions is due to the fit of the distribution.

tissue for the dorsal closure. As we will see later in this section the overall area is also slightly decreasing because the tissue is contracting at the canthi since this is necessary for initiation of the zipping process that guides dorsal closure. As the distribution of the relative area change shows, most of the cells are staying within ±20% of their starting area.

The distribution for the time of the breakpoint is very broad but shows a peak around 0.5. In addition, there is a skew towards smaller values for the first linear segment meaning that the first segment tends to be smaller. This also hints towards the preparation for the dorsal closure that more cells are decreasing in area in the second segment and may have been stationary in the first.

Classes and spatial distribution

The next question is whether the behavior of cells is dependent upon their spatial arrangement or position in the tissue. To this end, cells are being classified as follows: A cell that exhibits increasing or decreasing drift in both linear segments is classified as increasing or decreasing. Cells that do not drift in both segments are classified stable. If one of the segments is either decreasing or increasing and one is stable then the whole trajectory is classified as increasing or decreasing. If one of the segments shows increasing drift and the other decreasing then this is classified as mixed.

Each class is assigned a color as can be seen in Figure 6.12 and the position of the cell in the tissue is normalized between 0 and 1 for both x and y coordinates. Hereby the left-most/lowermost cell position is defined as 0 and the rightmost/uppermost cell position as 1. In

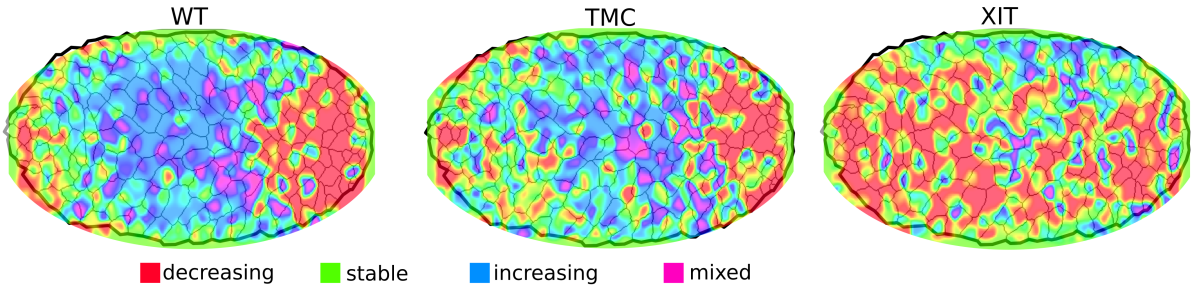

Figure 6.12: Cells which decrease in area are located towards the canthi in wild type and *Tmc* while in *xit* the overall tissue seems to be decreasing in area. Illustration shows spatial arrangement of area drift classes in wild type, *Tmc* and *xit* .

this manner datapoints from all embryos can be gathered and via kernel density estimation [14] an average spatial map of these classes can be computed. This map is projected over a 'typical' amnioserosa sketch to visualize the positions.

The spatially resolved classes show that decreasing area mainly happen at the canthi of the amnioserosa. After germband retraction at the posterior end of the tissue, the cells are constricting to prepare for dorsal closure. A crucial process is the zipping at the canthi [166]. To this end, the parts from the lateral epidermis at the canthi have to be conjoined. In contrast, *xit* seems to promote shrinking cells all over the amnioserosa. This is also consistent with the constant decrease in total tissue area over the whole ellipsoidal phase.

Area variance

Before we take a close look at the oscillations and their properties, the investigation of the variance of the detrended time series already gives some information about their behavior.

In Figure 6.13, we show the variance and the coefficient of variation compared for all embryos. Displayed is the total variation over the whole ellipsoidal phase time period, computed individually for each cell in each embryo.

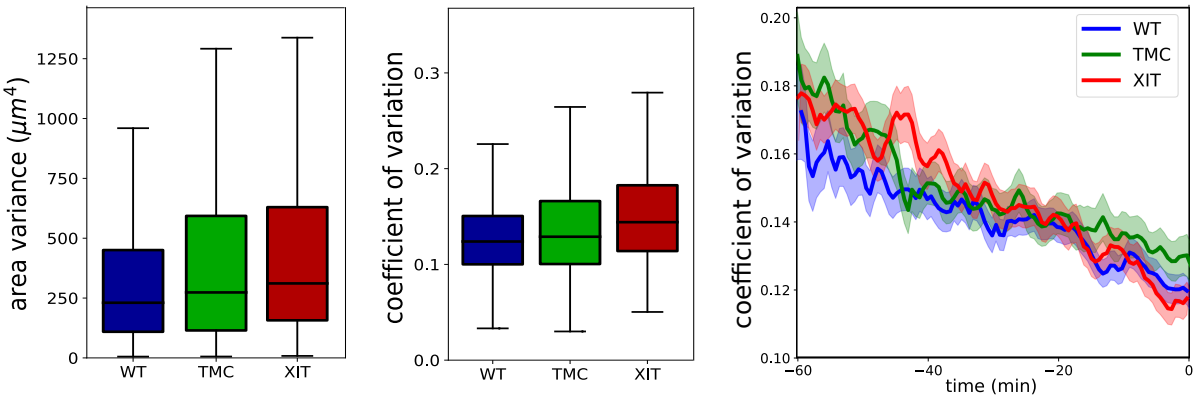

Figure 6.13: Cell area variance decreases over time. Variance and coefficient of variation are displayed in the left and middle panel. To the right, the coefficient of variation is plotted by time resolved windowing (window length 15 min) and aligned to the onset of dorsal closure at $t = 0$.

The variance is slightly enhanced in the mutants but not much. The distribution is very broad, which stems from the distribution of cell areas in the first place. Therefore the coefficient of variation gives a better representation of how strongly areas are fluctuating around their equilibrium area.

Indeed the distributions become narrower, pointing to fluctuations around 10-15% of equilibrium area. We see a slight increase for the mutants. A possible explanation for the slightly higher variation could be the different number of cells in the tissue. In wild type we have more cells on average, see Figure 6.3, therefore individual cell oscillations are more restricted by the packing if the total AS area is roughly preserved.

In addition, Figure 6.13 displays the time-resolved coefficient of variation across all embryos, which is aligned to the onset of dorsal closure. We computed the coefficient of variation in sliding windows of 15 min length. It is compelling, that the variations decrease as time approaches dorsal closure onset. This is consistent with the literature, which states that the tissue is stiffening before DC [166], therefore decreasing oscillation amplitudes.

6.5 Area oscillations

Amnioserosa cells undergo oscillations of cell surface area. Their dynamics tell us much about the mechanics of the tissue during the ellipsoidal phase. In addition, the synchronization of those oscillations is of particular interest in the next section.

For the description of the area oscillations we use autocorrelation function and Fourier spectrum analysis. Original cell area timeseries data is extended by zeropadding to avoid periodic boundary artifacts and help with the visualization by interpolation of the spectrum. As a side effect, the discrete Fourier transform becomes numerically much faster if the length of the signal is a power of 2 $L = 2^N$, with $N \in \mathbb{N}$. We can use the zeropadding to exactly yield such a number of steps in the timeseries.

Autocovariance functions

Some example autocovariance functions from cell area timeseries are displayed in Figure 6.14. Timeseries have been detrended with the piecewise linear segment method.

We empirically find a wide range of oscillation types. However, oscillations are generally very coherent and stable over a long period of time. On the other hand we also find cells that do not exhibit oscillations but rather fluctuate around a mean. In addition, observations show cells that are composed of several harmonics, shorter smaller scale oscillations and longer oscillations with usually higher amplitude. The middle wild type autocovariance example in Figure 6.14 would be an example for such behavior.

Theoretical autocovariance functions are fitted to the timeseries data. The theoretical model consists of a delta function at $t = 0$, an exponential decay and cosine function multiplied with exponentials. The delta peak is denoting noise in the timeseries, the exponential decay reflects decay in the correlation and cosine function is modeling the oscillation. This reads

$$f(t) = a\,\delta(t) + b_1\,\exp(-t/b_2) + \sum_{i=i}^{N} c_i\,\cos(\omega_i t)\,\exp(-t/\tau_i) \tag{6.1}$$

We define 4 model classes. The first class is the model without the sum, so only deltapeak and exponential. Then we consecutively add cosine terms up to $N = 3$. Using the Bayesian information criterion (see 6.9) as evaluation which model fits the data best, we can classify each realization of the autocovariance. In Figure 6.15 the average autocovariance from all area trajectories is shown alongside the distribution of model classes.

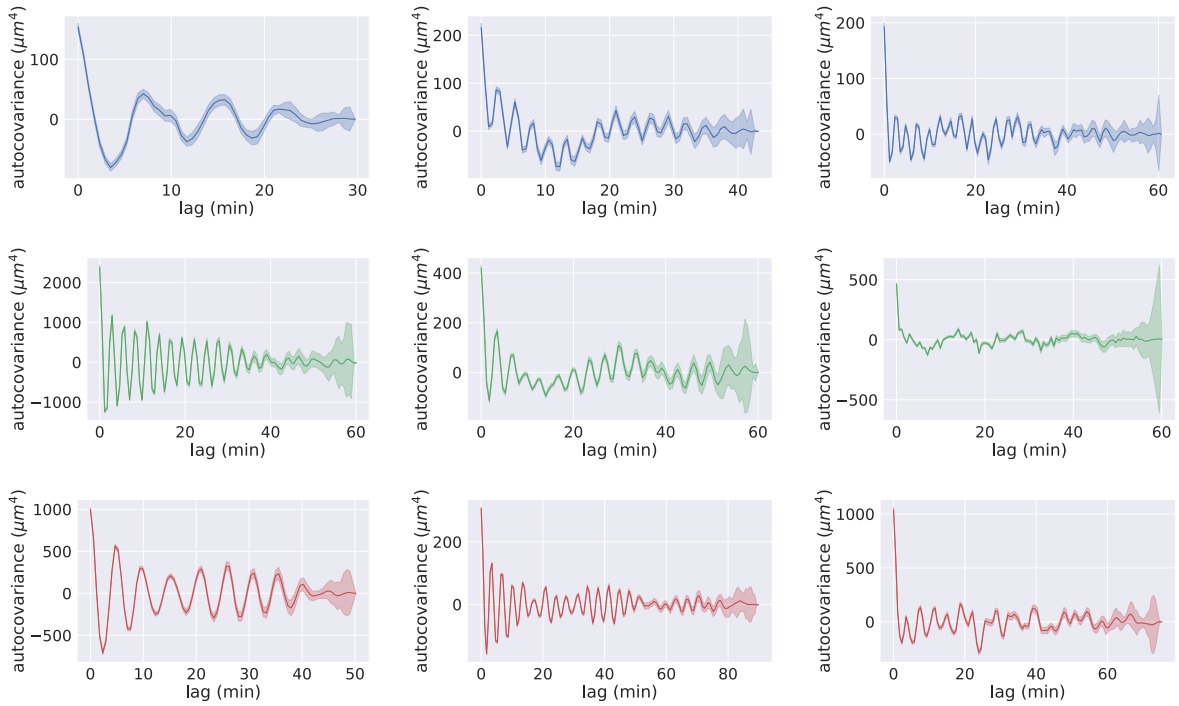

Figure 6.14: Different classes of oscillations, quantified via autocovariance functions, can be found in the amnioserosa ellipsoidal phase. Examples of autocovariance functions from WT (blue), *Tmc* (green) and *xit* (red) cell area timeseries are shown. Error regions show that for larger lags fewer datapoints are available, which increases the uncertainty. For wild type and mutants a wide range of oscillation kinds can be found. The examples here include very stable and robust oscillations, oscillations that include lower harmonics, but also irregularly oscillating cells and different frequencies.

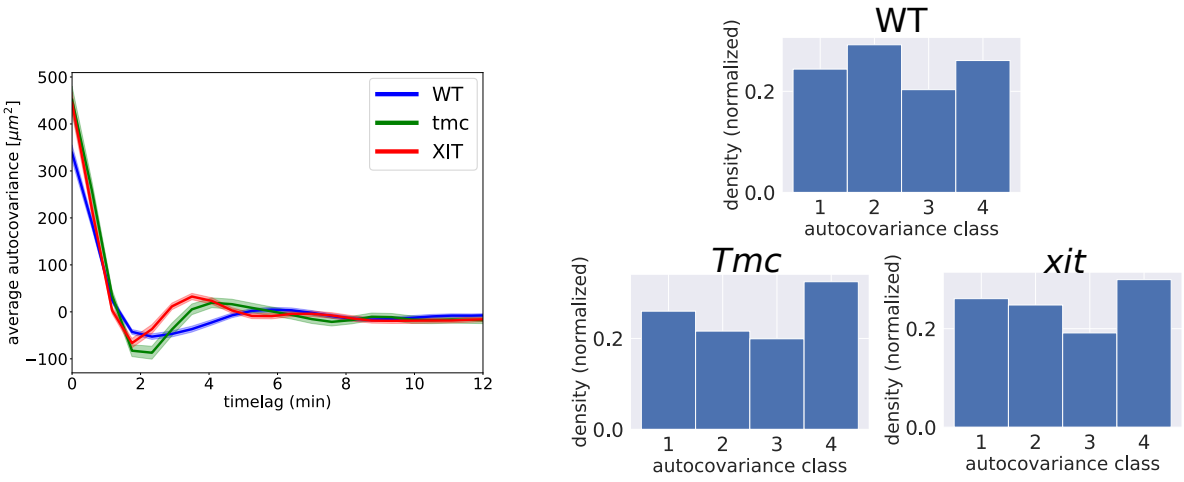

Figure 6.15: Cell area oscillations are faster in *xit* and *Tmc* mutants (left) Averaged autocovariance over all area trajectories of wild type and mutants. (right) Distribution of autocovariance classes. In wild type seems uniform the most but class 2 has most cases which could point towards slightly more coherent oscillations compared to the mutants. For *xit* and *Tmc* class 4 has most cases which is including the most secondary oscillations.

First it has to be noted that the fit of the theoretical model to the data sometimes did not converge. In most such cases autocovariance functions were classified into the first class, which is only the delta peak and an exponential decay. Therefore most of those cases are not smooth exponential decays but rather irregularly fluctuating cases that do not show high goodness of fit in the other classes as well. Similarly, manual evaluation of fits showed that for the highest model order class 4 many cases were irregular enough to benefit from the additional parameters of the higher model order. They were classified in 4 because of dominating slower oscillations. Classes 2 and 3 show the behavior we were mostly expecting beforehand by having one or two oscillations, in case of class 3 usually one faster oscillation and one slower.

In comparison to the mutants, wild type embryos have more cells that are having only one dominant oscillation and are falling into class 2. All three have many cases in class 4 which is probably due to one or two dominant oscillatory modes and irregularities or trends that have not been removed by the piecewise linear fits. Below we make a Fourier spectrum analysis which sometimes finds long scale remaining trends, that are not linear.

Im summary, the class analysis shows that over 75% of area trajectories in the amnioserosa are best represented with oscillatory autocorrelation functions for both mutants and wild type embryos. Only roughly a quarter is too irregular or displays too weak oscillations and thus is classified with only an exponential decay in the autocovariance. Of the oscillatory cases two third, namely classes 2 and 3, show highest likelihood for one or two dominant oscillations. Roughly a third in all cases exhibits additional irregularities or additional harmonics such that the bestfit autocovariance has three oscillatory components.

Fourier analysis and periodicity

For further investigation of cell area oscillation, power spectra are computed to determine main oscillation periods. To this end we compare several methods, see Figure 6.16.

In particular discrete Fourier transformation [10], Welch's method [219], multitaper method [16] and wavelets [256] are used to generate a power spectrum from the timeseries data. Zeropadding is chosen such that the timeseries has a length of 2^N to improve computation time.

A fundamental problem with power spectrum computation is that the Fourier transform is defined as the integral from $-\infty$ to ∞ of the signal. Our timeseries are of course finite, which is equivalent to an infinite timeseries that has been multiplied with a box function. The Fourier algorithm can not discriminate this and therefore harmonics of the boxfunction appear in the signal. In addition, noise in the timeseries can also affect resolution of the spectrum.

To mitigate these problems, window functions are used, for example a Gaussian, that is multiplied with the signal. The Fourier spectrum is computed for each window, sliding over the timeseries. The resulting spectrum is the average of those windows. This procedure is called Welch's method. It is less sensitive to noise, and the particular choice of the window function also reduces artificial harmonics. This comes at the cost of resolution because the single windows are shorter than the overall signal.

Welch's method is particularly dependent on the choice of the window function and has limitations because the windows reduce signal length. Instead of using a single window function, the multitaper technique uses a set of different window functions over the complete signal and does the average over those. So instead of computing an ensemble average, like in Welch's method, multitaper creates independent samples from the whole signal and averages those. The different 'tapers' are orthogonal to each other such that averaging indeed yields independent estimates of the spectrum.

A third method is continuous wavelet transform. The signal is projected on a family of frequency bands represented by the wavelet. Because the projection of the signal depends only on the length of the wavelet, which is quite small, this procedure yields high temporal preci-

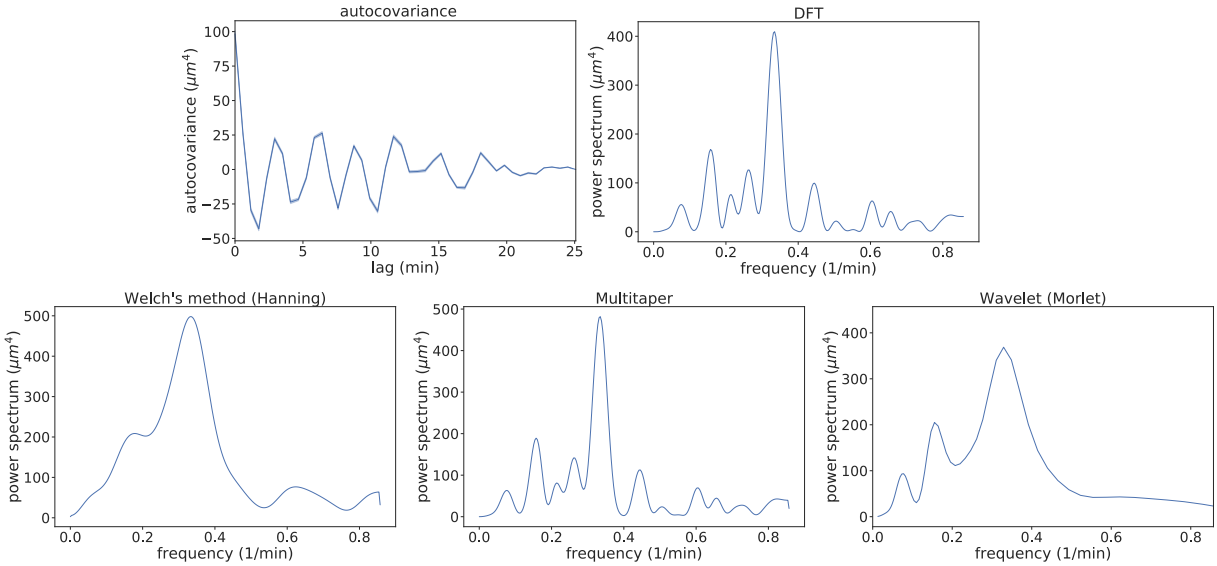

Figure 6.16: Comparison of methods to generate the Fourier spectrum. The first panel in the top left displays the autocovariance of an example timeseries. To the right the discrete Fourier transform (numpy implementation) is shown. In the bottom row, three methods are compared: (left) Welch's method, using a Hanning window, which empirically gave the best results among roughly 10 different tested windows, (middle) multitaper method and (right) wavelet spectrum using a Morlet. It can be seen that all methods reliably find the oscillation frequency at 0.33/min, which corresponds to a period of 3 min. We use the wavelet transform in the following because we have good prior knowledge of the oscillations and it can also provide time resolved information, while the other methods are global.

sion. The disadvantage is that prior knowledge of the frequencies of interest is needed. Fourier transform can be viewed as a special case of wavelet transform with the wavelet e^{-ikt}, difference mainly being that for wavelet transforms, wavelets are used that are localized in time and frequency. We here used the Morlet wavelet.

As can be seen in Figure 6.16, all methods reliably find the correct dominant frequency of the signal at $f = 0.33/$ min. Welch's method and wavelet have comparably lower resolution. In particular the wavelet is not able to detect higher frequency components due to the frequency localization. We will use the wavelet transform for further investigations, because it is the most reliable method if prior knowledge of the oscillation characteristics exist. This is the case here from extensive empirical understanding of the author and also description of amnioserosa oscillations in the literature. In addition, we can exploit the temporal resolution of wavelet transform.

Figure 6.17 shows the wavelet analysis for an example trajectory from a wild type amnioserosa cell. Thereby a realization was picked that still includes a drift, or lower harmonic oscillation, which has not been removed by the piecewise linear detrending procedure. Next to the timeseries, the wavelet spectrum is displayed and time-averaged and scale-averaged power spectra.

Significance has been computed by comparing the spectrum with an estimate of the underlying noise spectrum which was generated via Monte-Carlo subsampling. If a peak in the power spectrum is significantly above the estimated noise level it is significant. The noise distribution thereby is cut off at the 95% quantile.

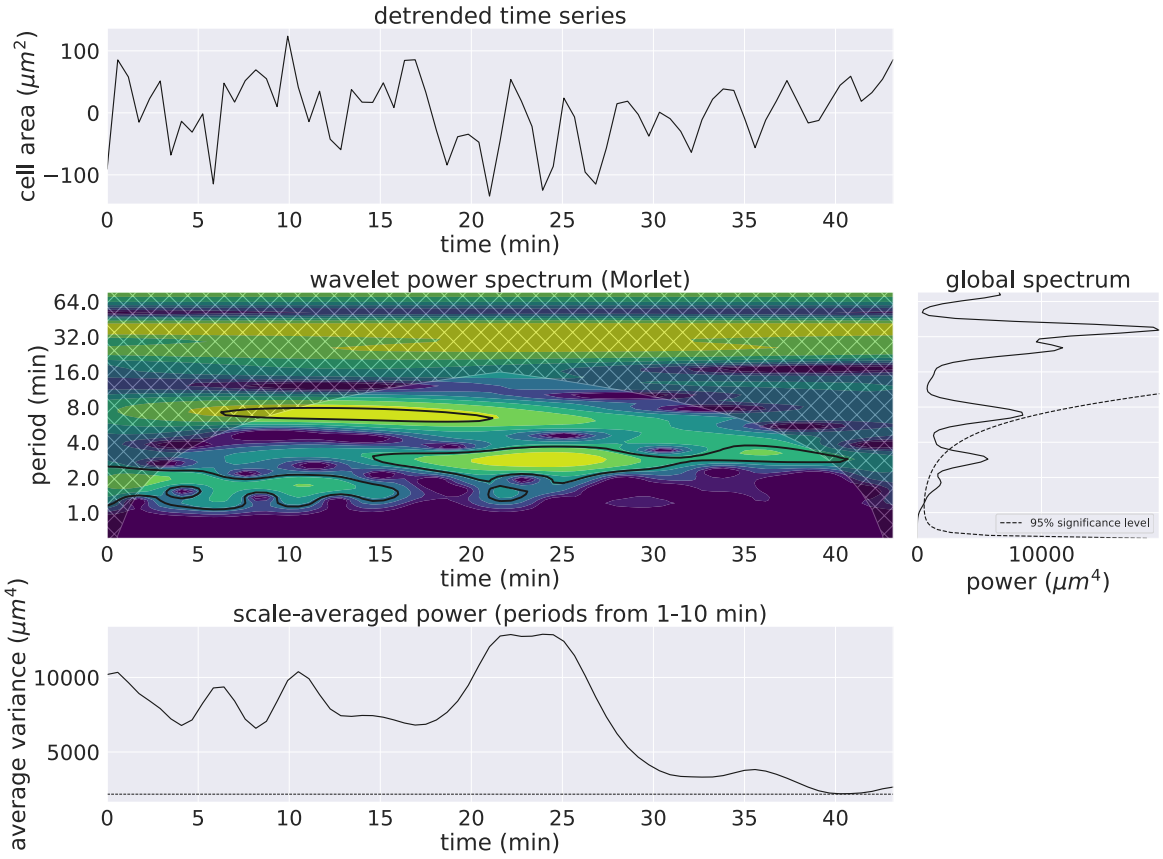

Figure 6.17: Oscillation analysis using Morlet wavelets reveals that oscillation periods can change over time. (top) Example timeseries where the piecewise linear detrend did not remove lower harmonic oscillations and the oscillation is irregular. (middle) The wavelet spectrum. Color denotes the power, significant regions are surrounded by a black contour. (right) Global power spectrum with 95% significance denoted by the dashed line. (bottom) Time-resolved power, which was averaged from periods between 1-10 min. This example shows that wavelet analysis is able to resolve changes in oscillation behavior over time. In the first part of the timeseries the oscillation has a period around 1.5 min, while it changes to ~ 3 min after 20 min. It also picks up the lower harmonic with a period of 8 min in the first half and there also is a trend with a period of 32 min.

In Figure 6.17 significant regions are indicated via a dashed line in the global spectrum and solid black lines in the wavelet spectrum. To determine oscillation periods we compute the global spectrum and take the maximum peak frequency above the significance level as estimate for the average oscillation period.

The spectrum is able to detect higher and lower harmonics in addition to the average frequency. In the example, the first half is comprised of a lower harmonic with a period of roughly 8 min and a higher harmonic with a period of roughly 2 min. Only in the second half an oscillation of about 3-4 min becomes dominant. Thus there is some variability in the oscillations of this cell. In addition, the global trend of the timeseries is picked up by a peak in the spectrum at > 32 min. The ability to resolve all the details is the great advantage of wavelet transform and the reason we chose this procedure.

The scale averaged power gives some information about the strength of the oscillations over time. From the variance analysis in the previous section (see Figure 6.13) we expect that oscillations amplitudes go down on average. The spectrum, in this case, confirms this but also shows a second explanation. While the variance certainly goes down in the second half, which is reflected in the scale-averaged spectrum, it also becomes more regular. We have to be careful here because it can not easily be distinguished whether oscillation amplitudes decrease or they simply become more regular while the tissue approaches the onset of dorsal closure. Heuristic analysis of data, however, has shown that amplitudes really go down in most cases.

Equipped with the wavelet transform, we can now determine the average periods of amnioserosa cell area oscillations. We use the method described above and results are shown in Figure 6.18.

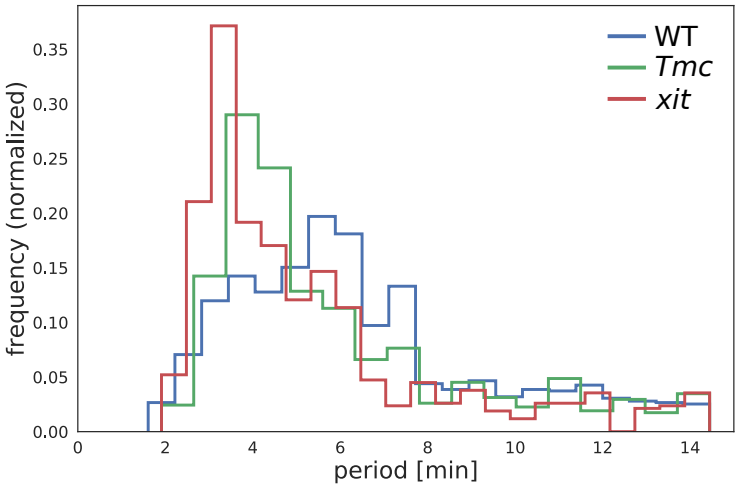

Figure 6.18: Cells in *Tmc* and *xit* oscillate faster than in wild type. Histograms of oscillation periods for WT, *Tmc* and *xit* are shown. Values were determined via wavelet transform.

The histogram of oscillation periods shows that *xit* noticeably oscillates with a faster pace than in *Tmc* and WT. Periods of *Tmc* and WT are only marginally different, but they are slightly faster in *Tmc* .

Faster oscillations can be due to several differences between the mutants and wild type. First, the elastic properties of the tissue might be different. It is known that the amnioserosa is stiffening when dorsal closure approaches [198]. Another possibility is anisotropic tension.

In chapter 7 we show that in the lateral direction junction exhibit higher recoil velocity after junction cuts. Higher tension could therefore influence the oscillations. A third possibility are different chemical properties of the pacemaker, namely the actomyosin dynamics. If *xit* and *Tmc* alter the regulation of myosin this could affect actomyosin oscillations as well which would be observed as differences in area oscillation periods.

Knowing the wavelet power spectrum for each cell in the amnisoerosa enables us to average them and obtain embryowise averaged powerspectra. An example for a wild type embryo is depicted in Figure 6.19.

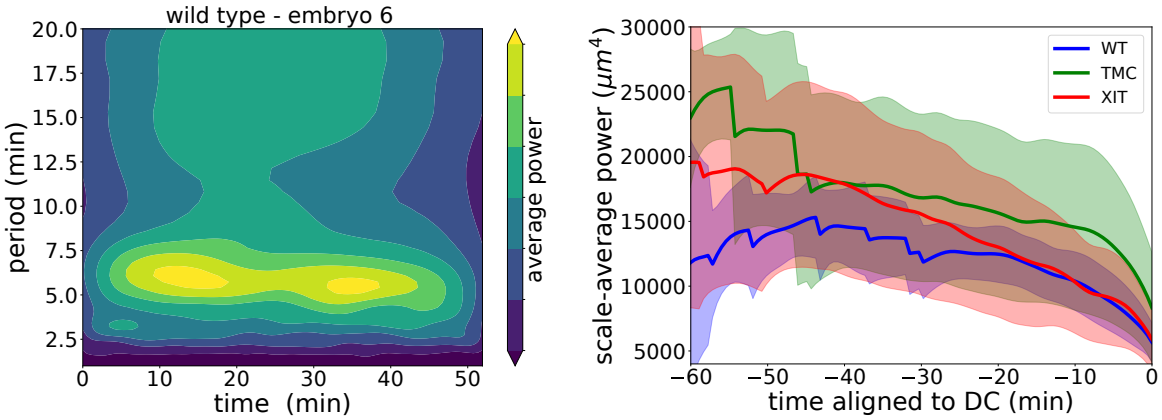

Figure 6.19: Wavelet analysis confirms that power decreases over time. (left) Example of embryo-averaged wavelet spectrum. (right) Scale-averaged power aligned with respect to dorsal closure onset at $t = 0$. The scale averaged power is averaged across all embryos decreases during ellipsoidal phase, which is consistent with the decreasing variance (Figure 6.13).

From the averaging per embryo, we compute the scale-averaged power and obtain time courses for the average oscillation strength. Those are aligned to dorsal closure onset and averaged over the whole ensemble of embryos. Results are also shown in Figure 6.19. The scale average power decreases over the course of the ellipsoidal amnioserosa phase until dorsal closure onset. This is consistent with the decreasing coefficient of variation, observed a few sections ago and summarized in Figure 6.13. The decrease in power seems to accelerate shortly before dorsal closure, but this is partly due to the end of the timeseries and the zeropadding. To better understand the transition to dorsal closure we would have to take data from at least 10 min into dorsal closure into account.

6.6 Synchronization of cell-cell area dynamics

The main question of this thesis is how processes are locally coordinated during morphogenesis. To determine intercellular coordination we use pairwise cross-correlation analysis. Figure 6.20 shows the frequency difference between the cell pairs and the distribution of the lag of extremum of the cross-correlation function.

Both wild type and *Tmc* cell pairs have more similar frequencies compared to randomly selected cell pairs from the whole tissue. *xit* has significantly larger differences for the frequencies. This is already some form of synchronization. Neighboring pairs have more similar frequencies compared to random pairs. The distribution of lags of the extremum of the cross-correlation function is centered around zero, which shows that most cases are either in synchrony with

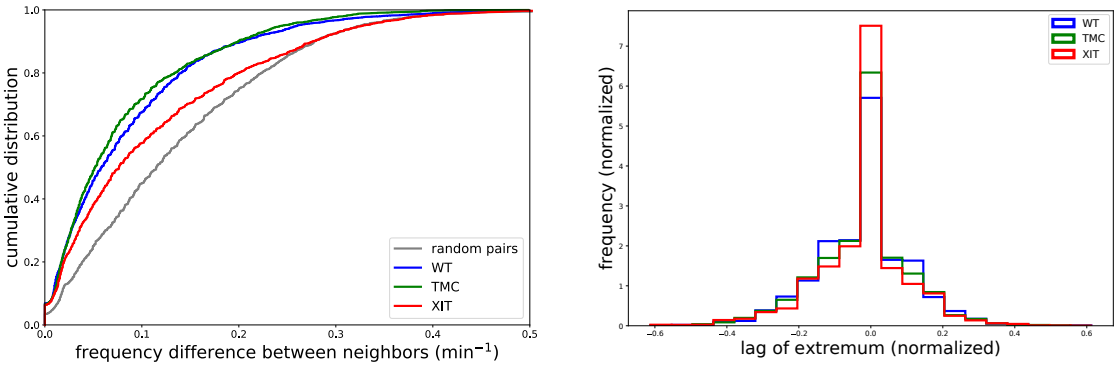

Figure 6.20: Neighboring cells have similar frequencies and mainly are either synchronized or anti-synchronized. (left) Cumulative distribution of frequency differences for neighboring cell oscillations. Cells that are neighbored therefore have more similar frequencies compared to random pairs from the same tissue. (right) Distribution of lags from the extremum of the cross-correlation function. Lags are normalized between -0.5 and +0.5 according to the frequency of the oscillation of the cells. A sharp peak is centered around lag zero, which means that most of the cell pairs are either in sync or anti-sync with each other and there is no delay in the oscillations of the timeseries. The distribution falls off for larger lags.

the neighbor cell or anti-synchrony. The lags have been normalized according to the frequency of the participating cells. Therefore the lag distribution goes to zero when lag -0.5 or +0.5 is approached.

As could be seen in the last section, single cell oscillations can be irregular and change their behavior over time. Our approach is therefore a large scale ensemble method. Correlation coefficients are computed over the whole time course of the ellipsoidal amnioserosa phase for an ensemble of embryos. Across the full distribution, statistical methods are used to determine significance of those correlations. We then analyze their ratio and spatial distribution.

The large scale approach allows to detect systematic differences across mutants despite irregularities. Correlation coefficients are the most simple measure for the synchronization of two signals. Higher order methods involve additional assumptions or prior knowledge.

In addition, we directly compare the ensembles of cell coupling in spatially resolved manner via computing the average correlation in a normalized region of the amnioserosa using Gaussian density kernel estimation. Together, the ensemble average spatial correlation and the statistically significant couplings allow detailed comparison of the mutants.

Statistical analysis

To determine the statistically significantly coupled cell pairs we use two methods: 1) Bayesian large scale testing [78], in particular local false discovery rate analysis [76, 77], and 2) circular block bootstrapping [183]. Methods and results are depicted in Figure 6.21.

For false discovery rate (FDR) analysis, first z values for each correlation coefficient are computed by comparing the value with an empirical null distribution. This empirical null was computed via random cross-embryo subsampling, which means that two area trajectories from different embryos where correlated. Because cells from different embryos can not be interdependent the distribution of correlation coefficients from this data gives a probability for the

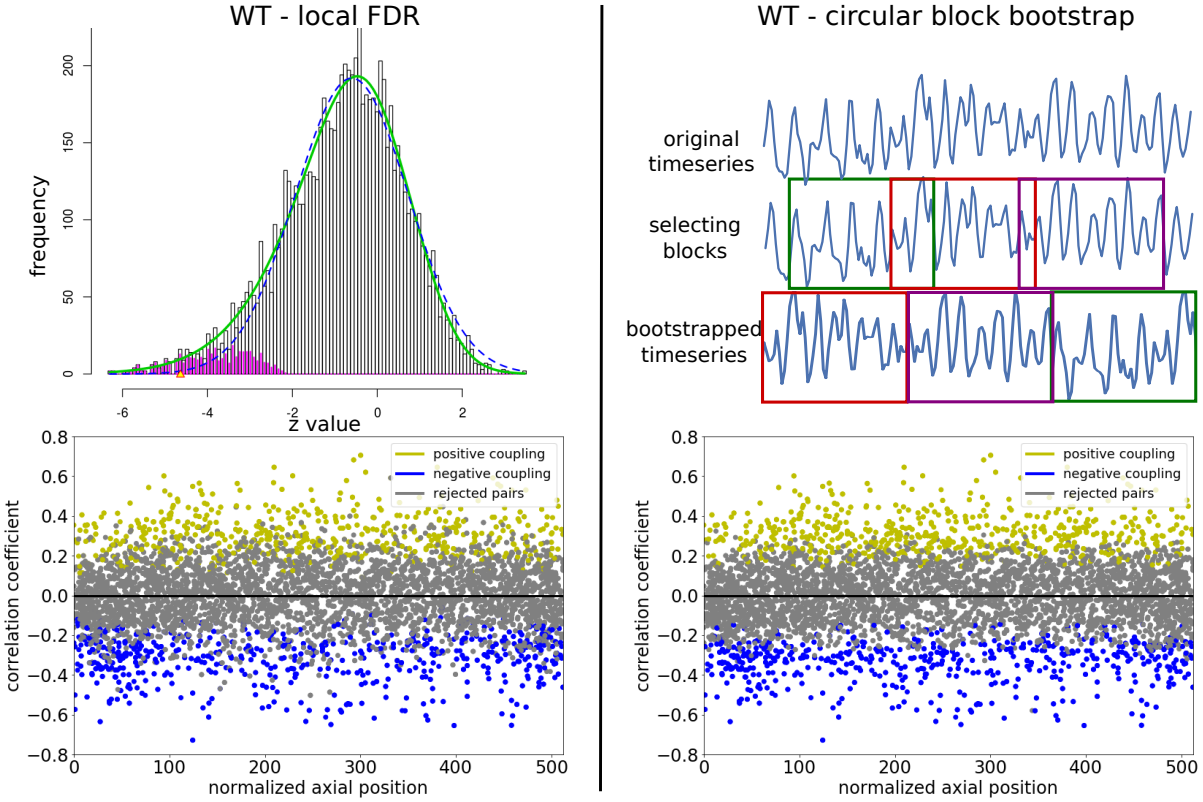

Figure 6.21: Determining the significance of cell-cell coupling via local false discovery rate analysis and the circular block bootstrap yields similar results. (top left) Distribution of z values from cross-correlations in WT. Local FDR determines the null distribution from the data directly, which is the blue curve. The green curve is the fitted mixture density. Deviations show unexpected events. Purple bars indicate significant values. (bottom left) Correlation coefficients for WT plotted over normalized axial direction. The insignificant cases are plotted in gray and the significant in color. (top right) Visualization of the circular block bootstrap. Blocks with fixed size are randomly sampled from the time series, which are conjoined to yield a bootstrap sample of a timeseries. Significance is determined by comparing the bootstrap confidence interval with an empirical null distribution. (bottom right) Correlation coefficients, similar as (bottom left). Both methods yield qualitatively similar results, but there are local differences.

real correlation appearing randomly. This is also called a p value. The corresponding z value statistics is what is used for local FDR.

Local FDR does not rely on theoretical null distribution instead it is estimated directly from the data, in this case we chose 1/4 of the data, the middle quartile around $z = 0$. Justification comes from the fact that a large part of large scale test statistics are insignificant anyway and therefore coincide with a random density. But the method is also able to infer the proportion of the null.

The empirical null is then compared to the mixed density which consists of all values, including the unexpected, and therefore significant, cases. It is simply fitted via a higher order polynomial. Local FDR is called this way because the method is able to decide locally via Bayesian inference to reject a z value or not. This yields a powerfully significance estimation, not depending on theoretical null assumptions and deciding case by case instead of simply putting a p value threshold for example.

We are able to control the false discovery rate with this method and set it to 0.1, therefore 10% of the significant cases are expected to be false discoveries. This corresponds, for Gaussian statistics, to a p value threshold of 0.05. To compute local false discovery rates we use the R implementation *locfdr*.

Because determining the significance of correlation coefficients is crucial for later analysis, we compute it via a second method called circular block bootstrapping [183].

Correlations are supposed to detect temporal interdependencies between two signals. Therefore one can not simply bootstrap samples from data that includes correlations, since the samples are not independent anymore. To circumvent this, blocks are chosen from the signals such that the blocks can be assumed to be independent. Determining the block size is the crucial step which has thus been extensively studied. We refer the interested reader to the literature and here just state that we used the method devised by Politis and White [259].

From sampling random blocks from the combined timeseries of both cell areas (if a block selects a time window for one cell area trajectory, exactly the same window is chosen for the second), a bootstrap sample is computed 2000 times. The resulting distribution is used to calculate 95% confidence intervals. The circular block bootstrap hereby assumes period boundary conditions for the timeseries.

Comparing the results for the statistically significant vs insignificant correlation coefficients from both methods, it can be seen in Figure 6.21 that both yield qualitatively similar results. Locally, however there are differences in the selection of the significant cases. Small deviations are expected because we have used two completely different methods having fundamentally different approaches. Local FDR estimates significance from the distribution of correlation coefficients itself, while circular block bootstrapping determines the significance from the timeseries case by case. That we have achieved such similar results indicates that we can be relatively confident to really have selected correct significantly coupled pairs.

Correlation analysis results

Using the methods for determining statistical significance we can now compare the results for the different mutants. See Figure 6.22.

It can be seen that the total density of correlation coefficients is roughly Gaussian with 0 mean for *xit* and WT. The distribution for *Tmc* is skewed towards negative values. This can also be seen by visual inspection of the data points in the *Tmc* graph. Visually, WT has most positive significant correlations while *Tmc* has the least. The exact values are summarized in

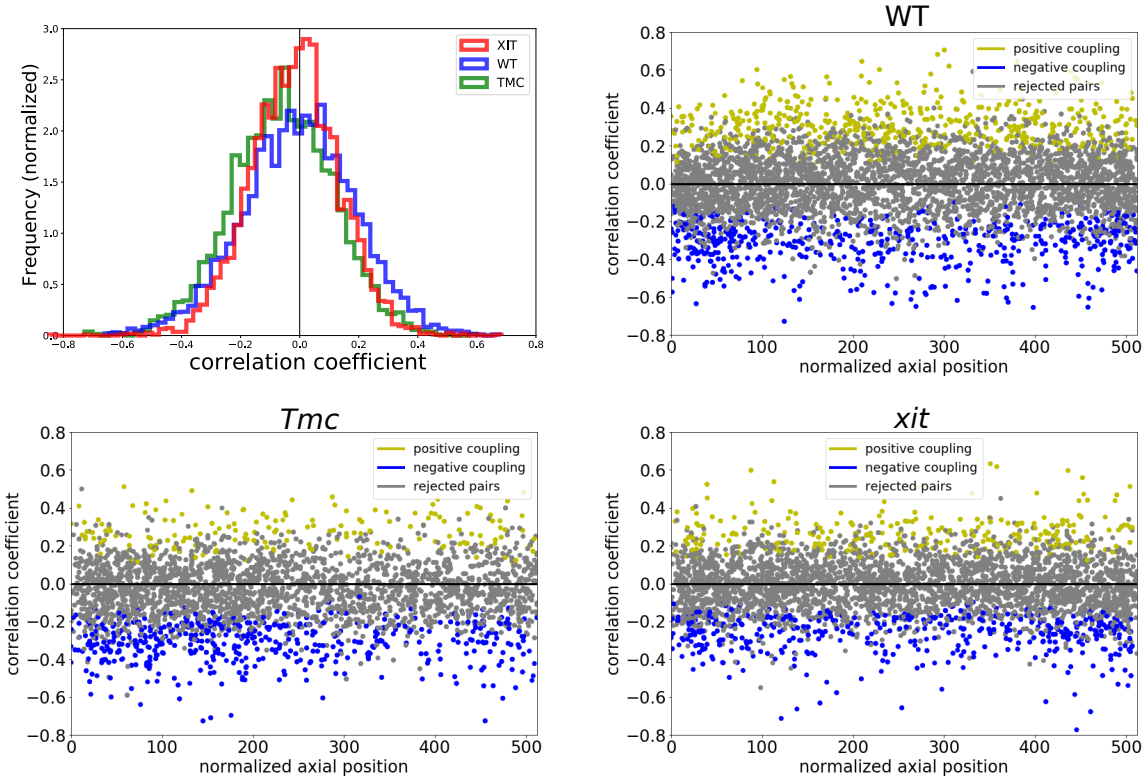

Figure 6.22: Distribution of correlation coefficients is shifted towards negative values in *Tmc* compared to *xit* and wild type. Histogram for all correlation coefficients are shown in the top left panel. The other graphs indicate are the significant positive and negative correlations and in gray the statistically insignificant correlation coefficients plotted over normalized axial position. For both mutants significant correlations are reduced compared to WT.

the following table.

correlation analysis					
type	positive	negative	stat. insig.	pos. / neg.	sig./insig.
WT	795	805	5774	0.99	0.27
Tmc	254	809	3570	0.31	0.29
xit	324	541	3849	0.59	0.31

The ratio of significant to insignificant values is roughly the same for all embryos. However, the ratio comparing significant positive correlations and significant negative ones is dramatically different for WT and the two mutants. In WT the ratio of positive/negative values is almost 1:1. *xit* experience a drop in positive correlations by 40% and *Tmc* even 70% compared to wild type. These ratios are also visualized in Figure 6.23.

The loss of significant positive cell couplings indicates a function for *Tmc* for intercellular coordination. Not only are the significant couplings different, but the whole distribution is shifted towards negative correlations as well, while in *xit* this is still intact compared to WT. However, *xit* also experiences loss of coupling to a lesser extend. Since *xit* affects E-Cadherin complexes at adherens junctions directly, this suggests a function for E-Cadherin as signal transducer. This results is one of the first direct indications that ion channels mediate intercellular coordination

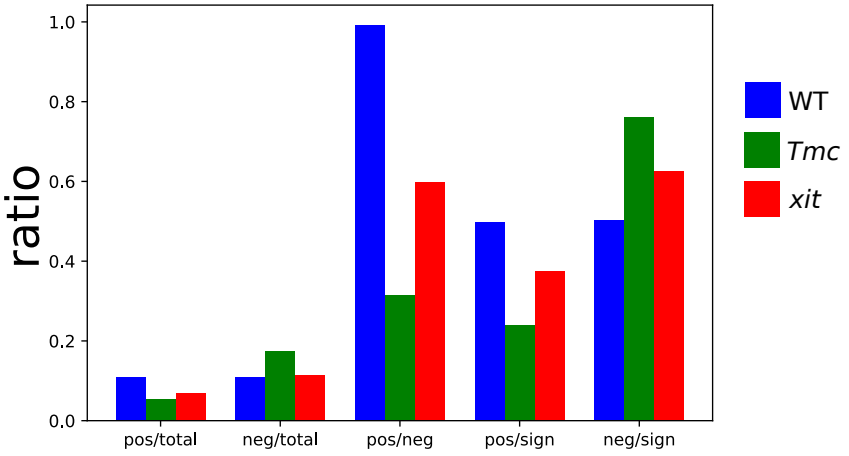

Figure 6.23: *Tmc* and *xit* show a loss of synchronized oscillations compared to wild type. In WT, the ratio of statistically significant positive and negative correlation coefficients is almost 1 to 1, whereas in *Tmc* it is 1:3. Therefore anti-synchronized cell pairs are over-represented in the mutants.

in the amnioserosa during morphogenesis.

6.7 Spatial analysis of synchronization

In the last section it was established that there is a loss of positive cell coupling in the mutants compared to WT. Now the spatial distributions of cell coupling is investigated.

To this end, data of the positions of cell pairs in the amnioserosa is normalized. The position of a cell pair is defined as the average position of the center of mass from both cells. Across the tissue it is then assigned a value between 0 and 1 for axial and lateral direction respectively. Thereby 0 is the leftmost/bottommost cell position and 1 the rightmost/topmost cell position. In this way, positions from different embryos can be pooled together and compared across WT, *Tmc* and *xit* .

Spatial distribution of significant cell couplings

Using the significant cell couplings from last section, their position is plotted on a prototypical amnioserosa image after position normalization. This is depicted in Figure 6.24. In addition, the density profile of negative and positive significant correlation coefficients is plotted against the normalized axial direction.

First, it is again noticeable that in *Tmc* and *xit* there are less positive values compared to WT. In addition, a difference in spatial distribution can be seen. Negative values in wild type and *xit* are concentrated at the canthi of the tissue. In between the distribution is more sparse. In contrast, positive values are more homogeneously distributed. Density profiles confirm this impression, showing a bimodal negative curve and roughly homogeneous positive curve. WT is the only case across mutants where a higher density of positive correlations is present in the middle part of the tissue. For *xit* and *Tmc* there is consistently a higher density of significant negative cell couplings.

Tmc shows a different distribution compared to the other two. Significant negative cell pairs are mainly concentrated towards the anterior end of the amnioserosa. In addition, the difference in the amount of negative vs. positive cell coupling is apparent both visually and in the density

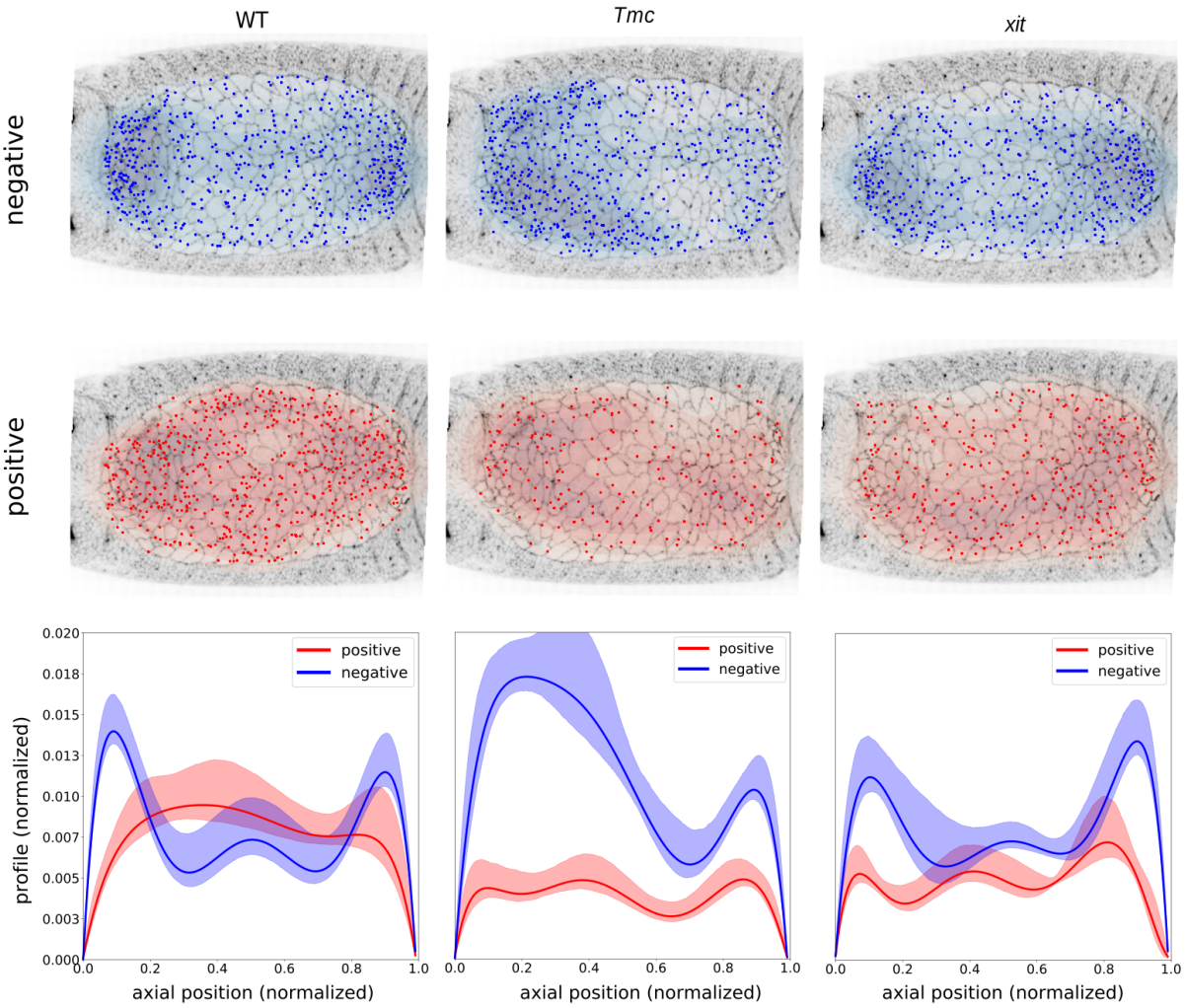

Figure 6.24: Spatial distribution of significant positive and negative correlations is altered in *Tmc* . Significant correlations are plotted on a prototypical image from the amnioserosa according to their normalized positions. Negative coupling in top row, positive in the middle. The bottom row shows normalized density profile along the axial direction, which compares the negative and positive profile directly. Error regions are bootstrapped 95% confidence intervals over the embryos. Only in WT there is a surplus in positive density in the middle part of the tissue. In *Tmc* and *xit* it is consistently below the negative profile. In addition, *Tmc* does not show the bimodal behavior of WT and *xit* where the negative correlations seem to mostly prevalent at the canthi.

profile.

Visual impression are additionally tested using anisotropy metrics on the spatial distribution of negative and positive couplings respectively. First, a nematic anisotropy is computed and secondly the radius of gyration of the point cloud. Both methods are explained in section 6.9. Results are shown in Figure 6.25.

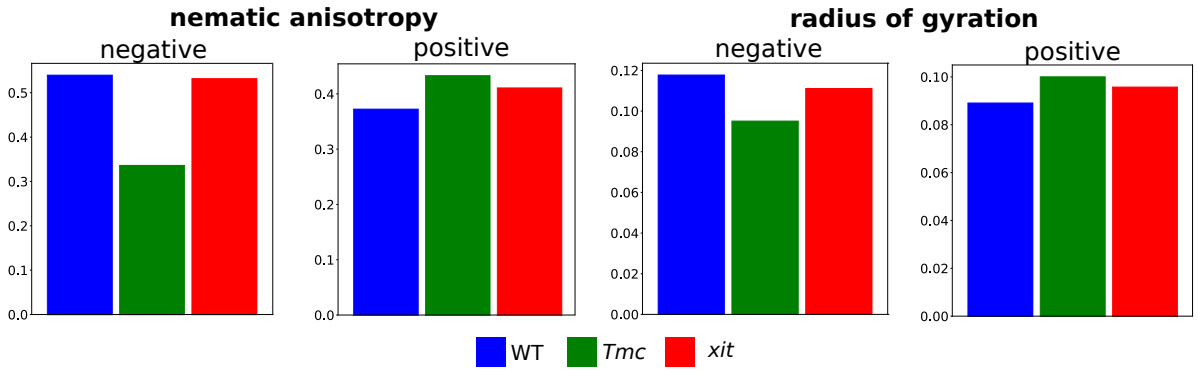

Figure 6.25: Distribution of negative significant correlations is anisotropic in wild type and *xit* but not in *Tmc* . The spatial distribution of significant correlations is measured via nematic anisotropy and radius of gyration. Both measures confirm numerically what can already be seen in Figure 6.24, that the distribution in *Tmc* is less anisotropic and more concentrated toward one end of the tissue.

For the positive coupling positions, both the anisotropy and radius gyration do not show big differences between the mutants. Both values are lower than the negative positions, indicating a more homogeneously distributed spatial order. In case of the negative positions there are larger differences between *Tmc* on the one hand and *xit* and WT on the other. Because of the bimodal spatial distribution, in *xit* and WT there are higher values indicating an imbalance in the spatial order. In *Tmc* this drops dramatically showing that the positions are more concentrated.

Therefore, *Tmc* not only displays a loss in coordination but also has a very different spatial order compared to *xit* and WT. Spatially organized cell coordination could be important for the maintenance of isotropic tension within the tissue or be a crucial component later during dorsal closure.

Correlation maps

In addition to looking at the significant correlations, our large scale data approach enables to detect subtle differences by ensemble averaging. Thus all cell-cell correlations are now taken into account and spatial order is analyzed. Positions are again normalized across all embryos.

Using a Gaussian convolution kernel, correlation values are spatially averaged. To this end an algorithm is used that can interpolate missing NaN values faithfully [13]. The same approach is usually applied in astrophysics [14]. Results for the averaged spatial distribution of correlation values, which we call correlation maps, can be found in Figure 6.26.

In addition to the averaging, randomized maps are generated via random permutations of the positions. This creates an empirical null distribution of randomized correlation maps. Figure 6.26 shows one sample for WT, *Tmc* and *xit* .

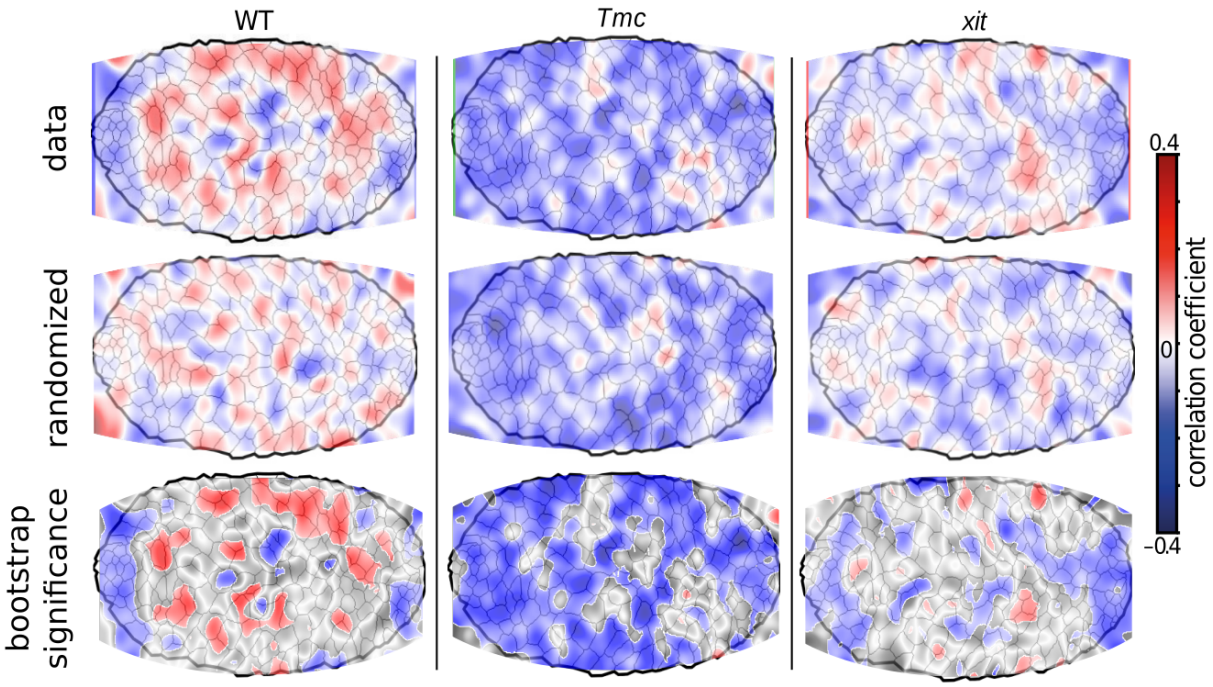

Figure 6.26: Positive correlations for wild type cell pairs are lost in *Tmc* and *xit* mutants and *Tmc* additionally displays a different spatial organization. First row is the original data, computed with kernel density estimation from all cell couplings. Next row is a random sample generated by position permutation. Last row is bootstrap evaluated significant regions

Using bootstrapping over the different embryos, significant regions can be determined in the correlation maps. The bootstrapping is done over the embryos and not positions because there may be spatial correlations in the data. Therefore, bootstrapping over embryos is the safer option. The Bootstrap distribution is used to generate pixelwise confidence intervals that are compared to empirical null distributions. For empirical nulls correlations are drawn from the empirical null of last section, where random cell pairs from different embryos were correlated. In this way significant regions are determined. The interpretation is that those regions would appear only with small probability if correlations are randomly drawn at exactly the same positions.

By visual inspection of the color it becomes immediately clear that there are more positive correlations in the WT data. *Tmc* looses almost all of the red regions and *xit* is in between the two others having less pronounced red but also blue regions.

In addition, it appears that there is a spatial organization in wild type. The red regions almost form a ring like structure while the ends are more colored in blue. In *xit* the ends are also dominantly blue which fits to the results of the spatial distribution of only the significant values. The comparison to the randomized maps, with shuffled positions, makes it clearer that for WT the red regions are stronger localized than expected if correlations would be randomly distributed. In *Tmc* a spatial structure is not to be seen apart from more blue regions to the left of the tissue, which again fits to the distribution of the significant couplings.

Significant regions confirm some of these impressions by selecting the blue regions at the canthi for WT and some of the ringlike organized red regions. For *xit* , also the blue regions at the canthi seem to be significant. For *Tmc* almost all regions are significant, which shows that the whole shift of the correlation coefficient distribution towards negative values is stronger

than expected by a Gaussian distribution around zero.

Numerical evaluation of spatial structure is done using the variogram method, which is often used in geology [206], see also 6.9. Variograms are analytically equivalent to spatial correlation functions but are numerically more robust and easier to implement.

Fitting a theoretical model to the variogram data yields estimates for the length scales of the correlation maps. We used a Gaussian model, which outperformed exponential, spherical and polynomial models in terms of the Goodness of fit. Results are displayed in Figure 6.27.

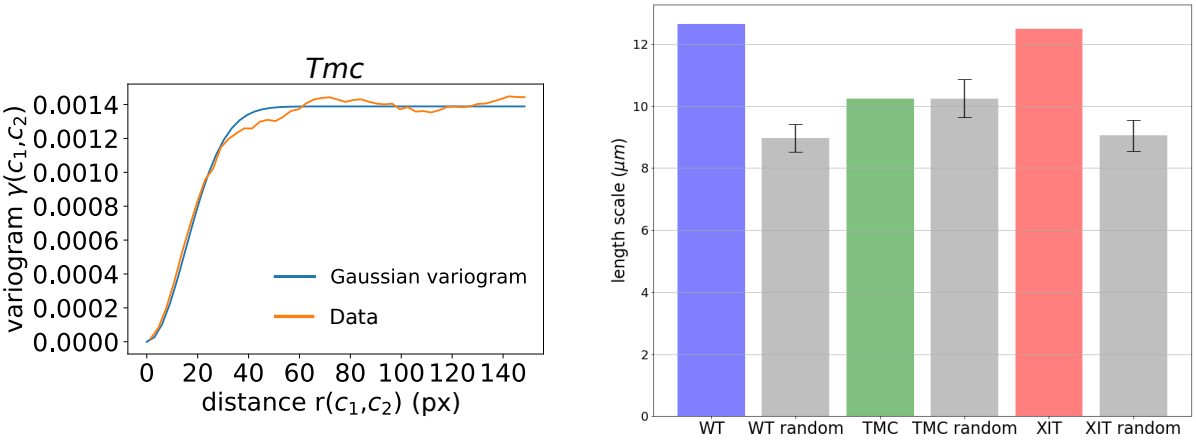

Figure 6.27: Variogram analysis reveals missing structure in correlation maps. (left) Example fit of the empirical variogram, denoted by the orange curve, to the bestfit Gaussian model, shown in blue. (right) Length scales from the variogram fits compared to randomized fields. Shuffling of the correlations has no impact on the *Tmc* length scale, which indicates no structure, while *xit* and WT loose structure when correlations are permuted.

The fitted length scales are an estimate for the structure size in the correlation maps. We compare length scales to maps with random permutations of the correlation coefficients. Calculations for the random maps is repeated 100 times, which yields bootstrapped 95% confidence intervals for the random timescales.

For WT and *xit* there is a significant drop of the length scale which indicates structure. While in WT it is visually obvious, especially for the red regions, in *xit* the blue regions at the canthi contribute to the structure in the correlation map even if it is not that obvious visually. *Tmc* shows no statistically detectable difference between original length scale and randomized length scales. This indicates that there is no spatial organization of the cell couplings in *Tmc* . Both original and randomized length scales are larger compared to the randomized length scales in *xit* and WT. This is due to the skewed distributions of correlation coefficients towards negative values, producing a higher probability for locally similar correlation values.

The spatial analysis of the cell-cell correlations shows that not only do WT cells have overall higher coordination, but in *Tmc* mutants there is a loss in spatial structure as well. How the spatial organization is created remains unclear however. A conceivable option could be a morphogen related organization, like planar cell polarity in the germband. Bulk cells in the amnioserosa have been shown to express different genes than peripheral cells. This could also affect the spatial distribution of a molecular coupling mechanism.

6.8 Summary and additional discussion

In summary, both *Tmc* and *xit* mutants display changes in basic amnioserosa properties, morphology, cell oscillation and cell-cell coordination. Both *Tmc* and *xit* mutants have fewer amnioserosa cells, these cells are bigger, their size is more variable and have a higher anisotropy than in WT.

WT and mutant amnioserosa cells oscillate and their amplitude decays over time, which is consistent with a stiffening of the tissue approaching dorsal closure onset [166, 198]. *xit* and *Tmc* both show increased average oscillation frequency. This could be caused by differences in stiffness of the tissue. Using laser ablation experiments, described in chapter 7, we find higher tension on junctions in the lateral direction for both mutants. Increased tension could result in faster oscillations. Alternatively, the dynamics of a molecular pacemaker, for example the underlying actomyosin dynamics, could be changed. While we have no reason to assume that the on/off rate dynamics is altered, *Tmc* and *xit* are both affecting Ca^{2+} signaling, as shown in chapter 7, which could interfere by regulation of myosin II. The mathematical model, presented in chapter 5, also shows that a Ca^{2+} coupling could in principle change amplitude and frequency of the oscillations.

We find that in wild type embryos cell pairs are synchronized and positive and negative significant correlations are distributed with the ratio 1:1. In contrast, *Tmc* mutant amnioserosa cells loose significant positive cell couplings and in addition display altered spatial distribution of correlations. *xit* mutants similarly show a loss of significantly synchronized cell pairs, but to a lesser degree, and they retain some of the spatial ordering found in wild type, since negatively correlated cell pairs seem to gather preferentially at the canthi of the tissue.

This suggests a role for both *Tmc* and *xit* for intercellular coordination. In case of *Tmc* this indicates a role of mechanosensitive ion channels for coordination during *Drosophila* morphogenesis. It has already been hypothesized that such ion channels are involved in this process [128, 141]. *xit* affects the distribution of E-Cadherin at the adherens junction [355] which could also affect the transduction of mechanical stimuli across neighboring cells. A role for E-Cadherin in mechanotransduction in epithelia has previously been proposed [33, 112]. We continue the investigation of *Tmc* in chapter 7 and *xit* in chapter 8 and study their role in greater detail.

The whole amnioserosa tissue is decreasing slightly over the course of ellipsoidal AS phase, but for *xit* mutants a different spatial arrangement of cell area drifts is displayed. For wild type embryos, mainly cells at the posterior end are contracting while bulk cells are slightly increasing in area. For *xit* mutants overall cells are decreasing in area and there is no spatial ordering. During dorsal closure, an important process is the zipping at the canthi where part of the epidermal most cells are connected on both sides [69, 92, 142, 167]. Cells in wild type embryos could thus prepare the tissue for the zipping by contraction and facilitate it.

xit and *Tmc* mutants are not able to assume isotropic cell shapes during the ellipsoidal AS phase. Using junction cut experiments, described in chapter 7, we find that tension is anisotropically distributed across the tissue for both mutants. The tension decreases substantially if the lateral epidermis is completely separated from the amnioserosa before the junction cut. Therefore tension coming from the epidermal cells could cause the elongated cell shapes and increased junction tension in the mutants. *Tmc* and *xit* therefore could also have a function for efficiently assuming, and maintaining, isotropic cell shapes as well as isotropically distributing tension.

In general, both mutants show higher variance in most observables. This result alone already shows that coordination of processes could be affected. Presumably one of the key reasons for coordination via transmission and feedback of mechanical stimuli is to increase the robustness of developmental processes by collectively counteracting external perturbations [166]. Another aspect could be the efficiency of developmental processes. It can be seen that wild type observables show less variance across most observables and they also have shorter ellipsoidal stages.

After germband retraction, the amnioserosa sets the stage for dorsal closure [166], the purse string formation is happening [142, 167], but also tension is isotropically distributed and the stiffness increases [198]. *Tmc* and *xit* therefore are probably contributing to efficiently prepare the tissue for dorsal closure. Since the epithelium during dorsal is still the same, while some additional processes like zipping and cell ingression are at work, they could have an impact on dorsal closure as well.

6.9 Appendix: Methods

Some of the quantitative methods used in the main text are described here.

Cross-correlation

Correlations are one of the primary tools to understand if and how dynamics of neighboring are coupled. Therefore, we briefly state some basics here, and refer for further information to the literature, for example in [25] chapter A.2.

The cross-correlation function is defined as

$$(f \star g)(\tau) = \int_{-\infty}^{\infty} \overline{f(t)}\, g(t+\tau)\, \mathrm{d}t \tag{6.2}$$

for two continuous time dependent functions $f(t)$ and $g(t)$. $\overline{f(t)}$ denotes the complex conjugate.

The empirical cross-correlation function for two discrete timeseries X_t, Y_t is given by

$$\mathrm{Cov}_{XY}(\tau) = \mathbb{E}((X_t - \mu_X)(Y_{t+\tau} - \mu_Y)) \tag{6.3}$$

with μ, the average of X or Y respectively. As estimator for the expectation the arithmetic mean is used, following the law of large numbers.

The correlation coefficient is defined as the covariance at timelag $\tau = 0$, normalized by the standard deviation σ_X, σ_Y of both timeseries.

$$\mathrm{CorrCoeff}_{XY} = \frac{\mathrm{Cov}_{XY}(0)}{\sigma_X \sigma_Y} \tag{6.4}$$

Nematic anisotropy

In our experiments we are interested in how 'stretched' a cell appears and thus we need some quantitative measure to characterize this property. The elongation of an object can be described with a nematic order parameter. We use the same method presented in [221], which has been used to study the elongation of wingdisc cells in *Drosophila*. The basic principle is depicted in Figure 6.28.
The nematic tensor is defined as follows

$$\begin{pmatrix} \epsilon_{xx} & \epsilon_{xy} \\ \epsilon_{xy} & -\epsilon_{xx} \end{pmatrix} \tag{6.5}$$

whereby we have

$$\epsilon_{xx} = \frac{1}{A_c} \int \cos(2\phi)\, \mathrm{d}A \tag{6.6}$$

$$\epsilon_{xy} = \frac{1}{A_c} \int \sin(2\phi)\, \mathrm{d}A \tag{6.7}$$

Here the integral goes over the whole object (all pixels of a cell) and A_c is the total area of this cell. The angle ϕ is defined by the angle between the vectors pointing from the center of mass to the position of the cell part $|r_c - r|$ and the axial vector defined by the abscissa of the coordinate system.

$$r_c = \frac{1}{A_c} \int r \mathrm{d}A \tag{6.8}$$

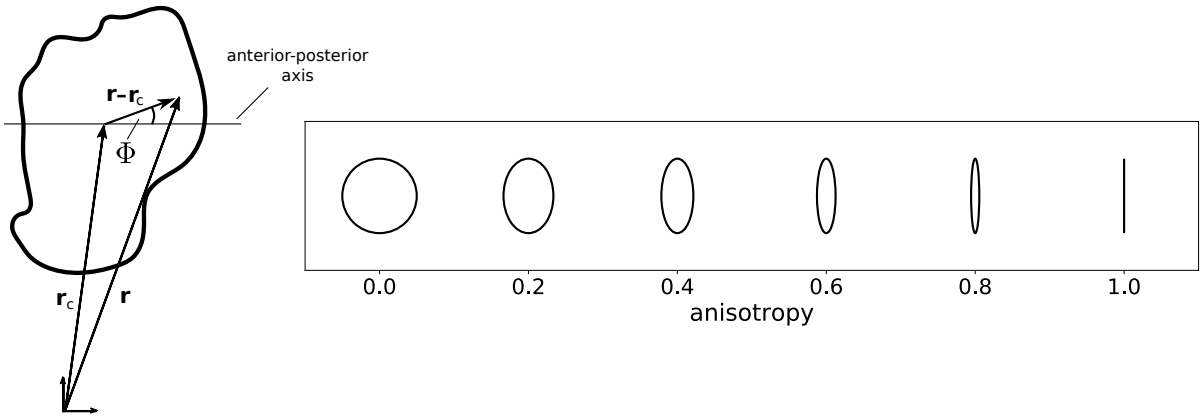

Figure 6.28: A nematic order parameter to characterize cell elongation. The left scheme is displaying an example cell and the vectors pointing to the center of mass and a pixel contained by the cell. The right panel shows how an ellipse would look like for certain values of the nematic elongation.

What we call anisotropy most of the time in this thesis is actually the magnitude of the elongation defined as

$$\epsilon = \sqrt{\epsilon_{xx}^2 + \epsilon_{xy}^2} \tag{6.9}$$

The orientation angle φ of the object can be computed by

$$\cos(2\varphi) = \frac{\epsilon_{xx}}{\epsilon} \tag{6.10}$$

$$\sin(2\varphi) = \frac{\epsilon_{xy}}{\epsilon} \tag{6.11}$$

Note that the magnitude of the elongation is slightly unintuitive because it is a nonlinear measure in the sense that a twofold stretch of an object does not yield a two fold in the anisotropy measure.

Radius of gyration

Under the assumption that a body consists of n particles of equal mass m the radius of gyration of such a rotating body is defined as

$$R_g^2 = \frac{1}{n}\sum_{i=1}^{n} r_i^2 \tag{6.12}$$

whereby the r_n are vectors pointing to the position of the particle perpendicular from the axis of rotation of the body. Therefore the radius of gyration is actually nothing else but the root mean square distance of these particles from the axis of rotation.

The intuition is that if the body has a completely even distribution of particles around the axis R_g^2 would be zero. If it is nonzero R_g^2 points to the position of a body that has the same moment of inertia I if the whole body mass would be concentrated in this point.

We can thus use this concept as another measure of anisotropy with the following alteration. Instead of an axis of rotation we take the mean position as reference point and hence

$$R_g^2 = \frac{1}{n}\sum_{i=1}^{n}(\langle r\rangle - r_i)^2 \tag{6.13}$$

Variogram

A method that is frequently used in geoscience to quantify spatial correlation is the variogram [36, 215] e.g. applied in [47]. the variogram is defined as

$$2\gamma(\mathbf{s}_1, \mathbf{s}_2) = \mathrm{var}\left(Z(\mathbf{s}_1) - Z(\mathbf{s}_2)\right) = E\left[\left((Z(\mathbf{s}_1) - \mu(\mathbf{s}_1)) - (Z(\mathbf{s}_2) - \mu(\mathbf{s}_2))\right)^2\right] \tag{6.14}$$

$\mathbf{s}_1, \mathbf{s}_2$ are locations of points in a random field having the value Z. It is related to the spatial correlation function by

$$2\gamma(\mathbf{s}_1, \mathbf{s}_2) = \mathrm{Cov}(\mathbf{s}_1, \mathbf{s}_1) + \mathrm{Cov}(\mathbf{s}_2, \mathbf{s}_2) - 2\mathrm{Cov}(\mathbf{s}_1, \mathbf{s}_2) \tag{6.15}$$

To estimate the variogram from data we use the estimator

$$\hat{\gamma}(h) = \frac{1}{2N(h)} \sum_{i=1}^{N(h)} [z(x_i) - z(x_i + h)]^2 \tag{6.16}$$

$N(h)$ is the number of elements that are separated by distance h. $z(x_i)$ denotes the value of the random field at position x_i. $N(h)$ is determined by binning the data in a range around the actual distance $|x_i - x_j| = [h - \epsilon, h + \epsilon]$.

Theoretical models are fitted to the variogram, which estimates structural parameters of the underlying random field. For example, in the main text we used a Gaussian model of the form

$$\gamma(h) = c_0 + c_1(1 - e^{-h^2/d^2}) \tag{6.17}$$

c_0 estimates noise strength of the random field, c_1 is called "Sill" but essentially estimates the variance of the structured parts and d is the typical length scale of the structure. Other models, like exponential or polynomial can be used but the Gaussian model was showing the best Goodness of fit for our data.

Statistical methods - the Bootstrap

In general we refer the interested reader to the literature if the used statistical method is unclear. All methods used in this thesis are nicely described in the book "Computer Age Statistical Inference" by Efron and Hastie [78]. This includes methods like the false discovery rate analysis. However one method we use very frequently is the bootstrap which is therefore briefly explained here.

Bootstrapping is a statistical method of estimating confidence intervals via repeated sampling from data [75]. A bootstrap sample is generated by randomly drawing from the original distribution the same number of elements with replacement. A simple example would be if the original data is $D = \{1, 4, 7, 9\}$, then a bootstrap sample could be $\hat{D} = \{1, 7, 7, 4\}$. From repeatedly generated bootstrap samples, a bootstrap distribution of some estimator is created by computing the estimator for each sample and combining them in a distribution. For instance the mean of each sample could be computed and the distribution contains all means of the bootstrap samples. The region containing 95% of the estimators, by putting the thresholds at 2.5% and 97.5% of the sorted distribution of estimators, gives an estimate for the confidence interval of the estimator of interest. This is called the percentile method and constitutes the simplest version of generating confidence intervals from the bootstrap distribution. We usually use bias-corrected and accelerated confidence intervals. This method accounts for possible bias and changing variance of the dataset [78]. There is no disadvantage in using this method, which is slightly more complex and involves jackknife estimation from the data, because in the limit of unbiased estimators, the percentile method is recovered. This is usually the case for Gaussian

distributions. The bootstrap method only relies on the condition that the original data is representative in the sense that the estimator of interest is faithfully represented by the data. Other methods, like the computation of p values, always assume an underlying model, for example a Gaussian. Bootstrapping, however, is model free and can produce for example asymmetric bounds by construction.

Bayesian information criterion

The Bayesian information criterion is a method to compare how well different models fit to data. In general the model with more parameters is able to outperform models with fewer parameters, therefore the BIC punishes the number of parameters as well as deviations of the model to the data. It reads

$$k \ln(n) - 2 \ln(L) \tag{6.18}$$

where L is the optimized likelihood, n the length of the data and k the number of parameters. The likelihood is the probability of the observed datapoints given a certain model M and parameters θ, $L = p(x|M, \theta)$. Models are preferred that yield smaller BIC values.

As likelihood function we usually choose the following empirical likelihood if not specified otherwise.

$$L = \left(\frac{1}{2\pi\sigma_{res}^2} \right)^{n/2} \exp\left(-\frac{1}{2} \frac{(x_{res} - \mu_{res})^2}{\sigma_{res}^2} \right) \tag{6.19}$$

x_{res} are the residuals between the model and the original data. μ_{res} and σ_{res} are the respective mean and standard deviation of those residuals.

Chapter 7

Intercellular coordination is mediated by ion channels

"The life contest is primarily a competition for available energy."

Ludwig Boltzmann

7.1 Content

The amnioserosa of *Drosophila* is a squamous epithelium that has an essential role during dorsal closure (DC). Dorsal closure is an important model system for epithelial morphogenesis and wound healing. It closes the dorsal back of the fly embryo at the end of gastrulation. Amnioserosa bulk cell dynamics plays an important role for force generation during dorsal closure which has to be coordinated to yield non-zero net force on the peripheral cells in direction of the midline. We investigate amnioserosa cell behavior and intercellular coordination shortly before DC, where the tissue assumes an ellipsoidal geometry and bulk cells exhibit statistically stationary oscillations.

In this study, we show that *Tmc*, a mechanosensitive ion channel known for its mechanotransduction function in the auditory sensory organ, has a function for synchronization of neighboring cell oscillations in the amnioserosa. Large scale whole tissue analysis reveals that nearest neighbor coupling is dramatically reduced in *Tmc* mutants which, in addition, display a different spatial order of pairwise-coupled cell hubs. Optically induced cell contraction leads to contraction in neighbors of the target cell only in WT embryos. This effect is inhibited in *Tmc* mutants. These findings suggest that *Tmc* is necessary for the synchronization of amnioserosa cell activity. In addition, *Tmc* contributes to the maintenance of isotropic force distribution and tissue morphology.

Many experimental studies rely on spatio-temporally restricted analysis due to the lack of fully automated data acquisition techniques. Using our deep learning segmentation pipeline, based on cycle-consistent generative adversarial networks, it was possible to acquire a dataset consisting of an ensemble of fully segmented amnioserosa tissues, see chapter 4.

Using this dataset it is shown that *Tmc* has an impact on the amnioserosa morphology during ellipsoidal phase, which is shortly before dorsal closure onset. Cells in WT tissue become more isotropic after germband retraction, which is reduced in *Tmc* . A possible explanation is an anisotropic force distribution across the tissue, resulting from tension exerted by the lateral epidermis.

Laser cutting experiments reveal that, indeed, there is a tension increase across cell junctions in the lateral direction for *Tmc* and *xit* but not in axial direction when comparing the tension to WT embryos. Separating the whole epidermis from the amnioserosa shows a significant drop in junction tension, showing that *Tmc* and *xit* are reducing the ability to isotropically distribute forces coming from the lateral epidermis.

Cross-correlation analysis of neighboring cell pairs indicates that cell-cell coupling is significantly reduced in both mutants. in *Tmc* , the proportion of synchronized to anti-synchronized pairs with significant coupling is reduced by the factor of 2. In addition, the spatial organization of synchronized and anti-synchronized hubs is different for *Tmc* compared to *xit* and WT. *Tmc* therefore not only affects the synchronization of neighboring cell oscillations but also their spatial order.

Modeling intercellular coordination with single cell units on a 2-dimensional hexagonal grid shows that topology alone can not induce the degree of synchronization observed in wild type, see chapter 5. Coordinated behavior is exhibited when a distinct coupling mechanism is switched on, which consists of mechanosensitive activation of Ca^{2+} , which in turn leads to intercellular synchronization. Comparison of simulation results and experiment reveals that *Tmc* might affect the homogeneous distribution of ion channels in the epithelium. Inducing Ca^{2+} increase in a target cell shows that with activated Ca^{2+} coupling, neighboring cells follow the contraction.

This mechanism is tested *in vivo* using UV induced uncaging of Ca^{2+} in single cells during the ellipsoidal phase in the amnioserosa, see chapter 3. Neighboring cells react to the contraction of the target cell by contracting as well. *Tmc* and *xit* neighbors show no significant response.

In summary, our results indicate a novel function for *Tmc* for linking mechanical activity with biochemical signaling during morphogenesis in the amnioserosa. Local coordination might help cells to collectively resist external forces and even comprise a driver of tissue rearrangements.

Results in this chapter have been obtained by applying results from chapters 3 and 4. Furthermore, there is overlap with results of chapters 5 and 6. The manuscript would usually contain a theory supplement that explains the model, however chapter 5 is more detailed and contains all the information of the SI, therefore the SI was omitted here.

7.2 Synchronization of epithelial cells by mechanosensitive Tmc channels

This chapter includes a draft of a manuscript, intended for later publication in a scientific journal.

Original contribution

Jörg Großhans and Fred Wolf conceived the study. Prachi Richa and Deqing Kong planed and conducted experimental strategies and assays. **Matthias Häring** performed segmentation and quantifications. **MH** conceived the mathematical model with FW and **MH** performed analysis and simulations. Materials and expertise about the *Tmc* mutant allele was provided by Martin Göpfert. PR, **MH**, FW and JG analyzed the results. All authors wrote, revised or commented on the manuscript.

Prachi Richa, **Matthias Häring** and Deqing Kong contributed equally.

References

References are included in the manuscript.

Synchronization of epithelial cells by mechanosensitive Tmc channels

Prachi Richa[1, 4, 7], Matthias Häring[2–5, 7], Deqing Kong[1, 7], Martin C. Göpfert[6], Fred Wolf[2–5, 8 *], Jörg Großhans[1, 4, 8 *]

1 Department of Biology, Philipps University, Karl-von-Frisch-Str. 8, 35043 Marburg, Germany
2 Max Planck Institute for Dynamics and Self-Organization, Am Faßberg 17, 37077 Göttingen, Germany
3 Institute for Nonlinear Dynamics, Georg August University, Friedrich Hund Pl. 1, 37077 Göttingen, Germany
4 Göttingen Campus Institute for Dynamics of Biological Networks (CIDBN), Georg August University, Heinrich-Düker-Weg 12, 37073 Göttingen, Germany
5 Max Planck Institute for Experimental Medicine, Hermann Rein St. 3, 37075 Göttingen, Germany
6 Department of Cellular Neurobiology, Georg August University, Julia-Lermontowa-Weg 3, 37077 Göttingen, Germany
7 These authors contributed equally: Prachi Richa, Matthias Häring, Deqing Kong
8 These authors supervised the project: Fred Wolf, Jörg Großhans

Cells sense mechanical signals using force-gated ion channels to detect touch, sound, and noxious mechanical stimuli[1-3]. In developing tissues, internally generated forces and stresses are the signals that travel fastest, and force-gated ion channels can transduce them into intracellular responses virtually instantaneously and with exquisite sensitivity[4]. Here, we show that mechanosensitive *Tmc* channels synchronize contractile cell oscillations in a force-generating epithelium during *Drosophila* morphogenesis. *Tmc*-dependent synchronisation is required for establishing an isotropic tissue morphology and isotropic force balance and mediates the emergence of a ring-like array of synchronously contracting cells. We present a data-driven model for cell synchronisation by *Tmc*-mediated Ca^{2+} signals and confirm the presence and *Tmc*-dependence of Ca^{2+} signals *in vivo*. Force-gated ion channels in this morphogenetically active epithelium thus function to transduce internally generated forces into intracellular Ca^{2+} signals that synchronise cell behaviour. Our results suggest that the evolution of mechanotransduction in metazoans has tailored force-gated ion channels dually for detecting environmental and morphogenetic force.

Animal morphogenesis is a complex process that critically depends on individual cells in the developing embryo initiating specific behaviours at the right time and place[5]. In an embryo, cells undergo an orderly progression through a hierarchy of cell-fate and cell-type decisions that can be used as a meter of developmental time. Some cells move within the embryo and may thus use positional information to tell time. In addition, cells in developing tissues have various molecular clocks such as circadian and segmentation clocks[6]. All these molecular time keeping mechanisms, however, are probably not sufficiently precise to orchestrate cellular activity with minute-by-minute precision. On such fast timescales, cells may determine the appropriate timing for their actions by dynamical mechanisms of 'online' information exchange and coordination with neighbouring cells.

Actively generated mechanical forces and stresses are necessary to drive morphogenetic transformations and, within an embryo, forces and stresses are the type of signal that travels fastest[7-9]. To transduce such mechanical signals into biochemical response variables, force-gated ion channels are among the fastest and temporally most precise molecular devices[2,3.] Intriguingly, recent evidence indicates that force-gated ion channels previously primarily associated with mechano-sensory transduction are expressed in developing tissues[10-14]. We now found that *Tmc*, a mechanosensory transduction channel component implicated in vertebrate hearing[15], *Drosophila* proprioception and food texture sensing[16], and *C. elegans* touch sensation[17], is expressed in epithelia of *Drosophila* embryos. To assess whether *Tmc* is involved in the spatio-temporal orchestration of

cell behaviour, we examined the impact of a *Tmc* loss-of-function mutation on the amnioserosa (AS) dynome, the complete record of morphodynamic activity of AS cells, focusing on the precise timing of mechanical cell activities.

Tmc is expressed and mediates a Ca^{2+} response in the AS.

We focused on the amnioserosa (AS), a squamous epithelium, which is mechanically highly active and exquisitely accessible for comprehensive *in vivo* imaging and optophysiological and mechanical perturbation. From germband retraction (GBR) until the onset of dorsal closure, AS cells change from a highly elongated to isotropic shape, while the AS tissue acquires an elliptical shape (Fig. 1a, g)[18,19]. In this study, we define the elliptical AS stage as the period between the end of the GBR and the onset of dorsal closure at t=0.

Tmc proteins are highly conserved mechanosensitive ion channel subunits[20,21]. *Drosophila Tmc* is expressed and functions in sensory neurons during larval and adult stages[16,22]. *Tmc* is also expressed in embryonic epithelial cells (Fig. 1b). We detected *Tmc* expression in the lateral and apical plasma membrane of amnioserosa cells but not *Tmc* deficiency mutants[16] demonstrating staining specificity. Most *Tmc* mutant embryos were viable, although about 1/6 of the embryos failed to hatch with a variety of cuticle defects, including exoskeletal holes. For comparison we included *xit* mutants in our analysis. *xit* encodes a glucosyltransferase enzyme involved in N-glycosylation. *xit* was previously reported to be involved in E-Cadherin (E-Cad) glycosylation, localisation and functions[23].

Ca^{2+} is the prime candidate for linking mechanical and biochemical signalling. Ca^{2+} has been implicated in activation of actomyosin contractility in epithelial cells in vertebrates and invertebrates[24-27], and we employed a genetically encoded membrane-bound sensor, myristoylated-GCaMP6s[28], to monitor Ca^{2+} signals in the cells. As the weak Ca^{2+} signal in the undisturbed tissue showed neither a specific pattern nor correlated with mechanical cell behaviour (Extended Data Fig. 1a, b), we turned to a wounding assay (Fig. 1c). Following ablation of a single cell by a UV laser, Ca^{2+} concentration strongly increased in the damaged cell and, importantly, also in the neighbours, indicating a mechano-dependent response[29-31]. We recorded the time course of Ca^{2+} levels specifically in the neighbours (Fig. 1d, Supplementary Video 1). The Ca^{2+} signal increased almost two-fold immediately upon wounding and slowly returned to low levels within several minutes (Fig. 1e, f and Extended Data Fig. 1c, Supplementary Video 1). Strikingly, the Ca^{2+} traces remained low in *Tmc* and *xit* mutants (Fig. 1e, f and Extended Data Fig. 1c, Supplementary Video 1), implicating the respective proteins in tissue-scale and fast mechanosensing. Being a mechanotransduction channel component in neurosensory cells, *Tmc* contributes to Ca^{2+} influx in the epithelial AS, effectively sensing force changes within the tissue.

Dynome analysis reveals a function of *Tmc* for isotropic cell morphology.

Based on time lapse recordings of embryos with GFP-labelled cell junctions (E-Cad-GFP) and automated image segmentation, we established the dynome of the AS, i. e. the complete record of morphodynamic activity of every AS cell ≈180 per embryo (Extended Data Fig. 2a) over a period of one hour (Extended Data Fig. 3a, Supplementary Video 2). To assess whether *Tmc* is involved in the spatio-temporal orchestration of AS cell behaviour, we examined the impact of a *Tmc* mutation on the AS dynome. Based on at least 8 embryos each genotype, we compared the AS dynomes of wild type, *Tmc* and *xit* embryos (Extended Data Fig. 3a). The AS tissue acquired its typical elliptical shape, and GBR proceeded comparably to wild type (Extended Data Fig. 3). The total cell count per embryo was slightly reduced in both *Tmc* and *xit* mutants from about 190 to 150 (Extended Data Fig. 2a). The distribution and mean cross sectional area per cell was slightly more variant in mutants than wild type (Extended Data Fig. 2b). The junctions appeared undulated in *Tmc* and *xit* mutants (Extended Data Fig. 2d), and the dominant periods of cell oscillations were faster in *xit* and *Tmc* than in wild type (Extended Data Fig. 2c, e). Importantly, cell shape analysis revealed a difference in

establishing isotropic morphology in *Tmc* and *xit* mutants during the elliptical stage (Fig. 1g-k, Extended Data Fig. 3). Given the distinct behaviour of the peripheral cells at the interface of the lateral epidermis and AS, we omitted them from the analysis (Fig. 1h). We quantified the cell shape by an anisotropy parameter, which is 0 for a circular cell and 1 for a line shape (Fig. 1j-k). The distribution of cell anisotropies shifted towards lower values from the end of germband retraction to onset of dorsal closure (Fig. 1k, Extended Data Fig. 3b-e). In the mutants, the left-shift of cell anisotropies was less pronounced than in wild type and cell anisotropy was generally higher (Fig. 1k, Extended Data Fig. 3b-e). Thus, our data reveals a role of *Tmc* and *xit* in establishing isotropic cell shapes within the AS tissue.

Sync and anti-sync oscillations in the AS

Our dynome data sets contain also the spatial relationships between the cells. To assess coordination between cells, we systematically calculated correlations of area trajectories of all pairs of direct neighbours (≈500 pairs per embryo, at least 8 embryos per genotype) (Fig. 2a, b and Supplementary Video 4, 5). In the case of independent oscillations, periods of positive and negative correlation will be balanced, yielding an averaged correlation close to zero. Cell pairs with stable coupling, either in synchronized (sync) or anti-synchronized (anti-sync) will be identified by a positive or negative correlation, respectively (Fig. 2a–c), if the cross-correlation function peaks at zero time lag. Irrespective of genotypes, we found this condition fulfilled (Extended data Fig. 4a, c, d). We obtained a symmetrical distribution of correlation coefficients (Fig. 2c) which were significantly different from zero for about one third of the pairs, both in wild type and in mutants (Extended Data Fig. 4b).

The symmetrical distribution of correlation coefficients in the wild type (sync/anti-sync = 0.99) was shifted towards more negative coefficients in the mutants (*Tmc* sync/anti-sync =0.31, *xit* sync/anti-sync =0.59) indicating a gain of anti-sync pairs on the expense of sync pairs (Fig. 2c, d and Extended Data Fig. 4b). The proportion of significant coupling pairs remained about the same (Fig. 2c, d and Extended Data Fig. 4b). Our correlation analysis revealed a loss of sync pairs in the mutants, suggesting that *Tmc* and *xit* promote synchronous oscillation between adjacent cells.

Distinct spatial distribution of coupling types within the AS tissue

Next, we analysed the spatial distribution of the sync and anti-sync pairs. We assigned each junction a colour code corresponding to its correlation coefficient, with sync pairs in red and anti-sync pairs in blue (Fig. 2e). We generated correlation maps for each genotype by averaging over multiple embryos. Strikingly we obtained distinct patterns for wild type and mutants, indicating a stereotypic distribution of coupling pairs (Fig. 2f). In wild type, sync pairs accumulate in a ring-like distribution, which was lost in both mutants and after scrambling the positions of the pairs. The correlation map of *Tmc* mutants strikingly revealed the loss of sync pairs and gain of anti-sync pairs. The map for *xit* also shows a reduced number of sync pairs. This spatial organization would not be obvious if only the dynamics of a single embryo were considered (Supplementary Video 3). Using large-scale ensemble analysis, however, it was possible to reveal phenotypes that would otherwise have remained hidden in the embryo-by-embryo variation.

To assess the significance of the observed pattern, we calculated a pixel-wise confidence interval for the correlation maps, using bootstrap subsampling over different embryos. This revealed that the ring-like positive pattern in WT embryos as well as the overrepresentation of anti-sync pairs in *Tmc* mutants were indeed statistically significant (Extended Data Fig. 4e). In addition, we confirmed the spatial coupling configuration by considering only statistically significantly coupled pairs via local false discovery rate subsampling[32] (Fig. 2f). For wild type embryos, the observed spatial pattern reveals an obvious excess of positively correlated pairs while the negatively correlated pairs assemble preferentially at the canthi. To further assess and visualise the spatial pattern, we projected

the two-dimensional data onto the anterior-posterior axis (Fig. 2g). Two peaks of anti-sync pairs marked the poles of the elliptical AS, whereas sync pairs are more abundant in the medial part. In *Tmc* mutants, the anti-sync pairs were dominant throughout. In *xit* embryos the distribution of the anti-sync and sync pairs was comparable to wild type, except for a lower abundance of sync pairs.

In summary the ensemble analysis of wild type and mutant phenotypes revealed a specific pattern of stable sync and anti-sync coupling pairs whose abundance and distribution depended on *Tmc* and *xit*, with both genes synchronizing oscillations between neighbours.

Mechano-transduction coupling in a lattice model of limit cycle oscillators leads to synchronisation.

To assess whether coupling by a mechano-sensitive ion channel can explain the observed pattern of sync and anti-sync oscillations, we designed a computational model scaled to the amnioserosa. We mathematically modelled the dynamics of AS tissue using a two-dimensional sheet of single cell units with hexagonal packing. Cell units are capable of area oscillations, following Dierkes' model (Fig. 3a)[33], and are coupled to their neighbours via mechanical interactions and Ca^{2+} signals triggered by mechano-transduction. We further extended Dierkes' model by adding stochasticity via Gaussian noise to the cell area dynamics and solved the dynamics on a two-dimensional triangular lattice with elliptical topology and an additional mechano-chemical coupling between neighbouring cells. We introduced Ca^{2+} coupling in the following way: If one cell exerts a force on its neighbour, the concentration of Ca^{2+} will increase in the neighbouring cell. Ca^{2+} then activates myosin, triggering an increase in the active myosin concentration and, thus, inducing area contraction (Fig. 3a).

Simulations showed that this mechanotransduction mechanism can lead to the synchronisation of neighbouring cell area oscillations (Fig. 3b, c, Extended data Fig. 5a, Supplementary Video 6), which is visible as a new state in the phase diagram (Fig. 3b). We estimated the model parameters via data-driven inference. To this end, we systematically compared experimental and simulated data via nested sampling[34-36], using the Jensen-Shannon divergence between the distributions of correlation coefficients as a distance metric (Fig. 3d). For wild type all junctions are predicted to contain the Ca^{2+} coupling mechanism (Fig. 3d and Extended Data Fig. 5). For *Tmc* mutants, we inferred that lower synchronization results from a decreased coupling constant, which corresponds to less activation of non-muscle MyoII by the coupling mechanism, and from a sparsified distribution of channels. Decreasing the coupling constant or removing channels from junctions generally resulted in anti-synchronized oscillations (Fig. 3d and Extended Data Fig. 5).

Since the AS is constrained by the lateral epidermis, its total area is roughly preserved during the elliptical stage. Therefore, mechanical interactions naturally promote anti-synchronised cell oscillations. A specialized mechanism, such as mechanotransduction coupling by *Tmc* channels, is thus necessary to obtain synchronised cell oscillations.

Response to mechanical pulling by optically triggered contraction is lost in *Tmc* and *xit* mutants.

If *Tmc* and *xit* indeed promote synchronized contractions, cells will respond to a mechanical stimulus of a neighbour cell. We tested this hypothesis both computationally and experimentally (Fig. 4). In our simulations, we triggered contraction of a single cell by up to 40%, which is slightly above the amplitude of regular oscillations (10–20%) (Fig. 4a, Extended Data Fig. 6a). In case of strong coupling, neighbouring cells contracted by 10–20%. No contraction or even slight expansion was seen with low or without coupling (Fig. 4a). Thus, our computational model predicts synchronized cell contractions in case of triggered contraction. To test this prediction experimentally, we optochemically triggered contraction by Ca^{2+} uncaging in a single cell[24] and recorded the area trajectories before and after uncaging (Fig. 4b, Extended Data Fig. 6a and Supplementary Video 7).

After the target cell contracted by up to 40%, neighbours followed suit and contracted by an average of 10–20% in wild type, but not in *Tmc* or *xit* mutants (Fig. 4b, Extended Data Fig. 6a, b and Supplementary Video 7). These results confirm predictions of the computational model and demonstrate that *Tmc* and *xit* contribute to a coupling mechanism that enables synchronized contractions.

Synchronized cell oscillations distribute tissue-scale tensions.

We next assessed whether *Tmc*-mediated synchronization plays a role in establishing isotropic cell shapes. The lateral epidermis pulls on the AS and may be responsible for the laterally stretched cell shapes during the elliptical stage[37-40]. We therefore incorporated an external pulling force in our model perpendicular to the long axis of the ellipse (Fig. 5a). Our simulations with WT-like synchronization revealed high tension at edge cells and uniformly low tension at central cells (Fig 5a and Extended Data Fig. 7). In contrast, simulations without synchronization predicted high tension at all cells throughout the tissue (Fig 5a and Extended Data Fig. 7). Therefore, simulations predicted a qualitative difference in the distribution of tension in the tissue: isotropic in wild type and anisotropic in mutants lacking synchronization.

We experimentally assayed tension at junctions by UV laser ablation comparing axial junctions (along the anterior-posterior axis) and lateral junctions perpendicular to the embryonic axis (Fig. 5b, c and Extended Data Fig. 8a, b). Initial recoil velocities after ablation are considered to be proportional to the tension at the junction[38]. For *Tmc* and *xit* mutants, tension at lateral junctions was significantly higher compared to axial junctions. In contrast, no difference could be detected among junctions in WT embryos (Fig. 5d, e and Extended Data Fig. 8c). These measurements indicate that *Tmc* and *xit* are necessary to distribute tension isotropically on the tissue scale. On the same data, we applied a viscoelastic model to estimate time scales of velocity decay, which can serve as a proxy of local viscoelasticity[41]. We did not detect any significant difference in the velocity decay between axial and lateral junctions in wild type and *Tmc* mutants (Extended Data Fig. 8d). Junction tension may be due to intrinsic forces generated within a given cell or to extrinsic pulling from the neighbouring cells or tissue[42,40,43]. To distinguish intrinsic and extrinsic contributions to junction tension, we physically separated part of the AS tissue from the lateral epidermis by a UV laser induced tissue-cut and probed membrane tension immediately afterwards (Fig. 5b, c). Initial recoil velocities were strongly reduced to less than 1 µm/s and equalised in both wild type and mutants (Fig. 5d, e and Extended Data Fig. 8c). Our measurements indicate that a large portion of the observed junction tension is due to extrinsic, tissue scale forces likely due to the lateral epidermis.

Taking together computational modelling and experiment, our data link *Tmc* and *xit*-mediated cell synchronization, uniform distribution of tissue scale mechanical tensions and establishment of isotropic cell shapes (Fig. 5f).

Discussion

Previously, Tmc has been implicated in neurosensory transduction mechanisms. Our findings now demonstrate that Tmc also controls epithelial morphodynamics, raising the question of its original function. In fact, force sensing is a near universal capability of cells that predates the evolution of multicellularity and animal life and *Tmc* itself is of ancient origin, appearing near the base of eukaryotes[15,21,44-47]. Consistent with an early function in membrane-based force transduction, *Tmc* orthologs are present in plant and fungal lineages that lack rigid cell walls. *Tmc* underwent a first gene duplication in choanoflagellates, our closest non-animal relatives, and in eumetazoan then multiplied into a superfamily of membrane proteins, at least some of them being mechano-transduction channel components[21]. Our data indicate that force transduction in morphogenesis can confer a substantial evolutionary benefit. While Drosophila embryos and larvae can develop without *Tmc*, the duration of the unproductive elliptical AS stage is substantially prolonged in *Tmc* embryos,

increasing the total metabolic cost of embryonic development. In addition, in a substantial fraction (10%) of embryos the mutation is lethal demonstrating that the reduction in robustness directly impairs the number of viable offspring. Thus, although causing a mild phenotype, *Tmc* loss-of-function is clearly associated with a substantial fitness cost. Force-gated ion channels presumably provide a very fast and temporally most precise modality of developmental mechano-transduction[14,48]. We therefore expect force-gated ion channels to be involved in a multitude of morphogenetic processes. Dissecting the morphogenetic function of force-gated ion channels on an equal footing with their function in hearing and touch should uncover an integrated picture of the mechanism and evolution of animal mechanosensation.

Methods

Fly strains and genetics. *Drosophila* stocks and crosses were raised and maintained at 25°C unless stated otherwise. We employed following stocks: E-Cad-GFP[49], w^{1118}; +/+; $Tmc^{Gal4\ 20}$ and w^{1118}; P{UAS-Tmc.Z}[16,22], *w*; +/+ ;UASt-GCaMP6s-myr[28], *w* $xit^{X\text{-}330}$ *f* Frt [9-2, 18E] Flp122{ry+} /FM7c, *y* w^{a} *sn B*;+/+;+/0+[23]. *xit* germline clones were generated and selected with ovo^{D} Frt^{18E}. Larvae were heat-shocked twice on following days for 30 min at 37°C[23]. The following transgenes are from the Bloomington Drosophila Stock Centre[50] and a Flybase Symbol[51] for each transgene is provided here. AS-Gal4 (Bloomington number 3734, Flybase Symbol, Dmel\P{GawB}c381).

Immunohistochemistry. Embryos were stained using previously established standard protocols[52]. Embryos were fixed in 4% formaldehyde for 20 min and were hand-devitalised. For the blocking step, embryos were incubated in 5% BSA + 0.1% Triton X-100 for 1 h at room temperature. The following primary antibodies were used: rabbit anti-Tmc (1:5000), Phalloidin (1:1000) (ThermoFisher), and Dapi (1:250) (ThermoFisher). Alexa-conjugated secondary antibodies (Life Technologies Carlsbad, USA) were used at a 1:500 dilution. AS tissue in fixed embryos was imaged using a Confocal Microscope LSM 780 (Zeiss AxioObserver.Z1) with x40/1.2 NA, water C-Apochromat objective. Images were acquired using ZEN software and processed using Fiji/ImageJ[53]. *Z*-stacks of the AS cells were acquired at the apical, apical-lateral, and basal levels and were *z*-projected using Fiji plug-in.

Live imaging. Embryos for live imaging were prepared as previously described[24]. In briefly, 0–4 h embryos were collected on apple juice agar plates at room temperature and aged overnight at 18°C until stage 11–12. Following dechorionation with 50% bleach (hypochlorite) for 2 min, washing and desiccation for 3–5 min, embryos were oriented with the dorsal side facing the coverslip. Embryos were covered in a drop of halocarbon oil prior. Time-lapse recordings were taken on an inverted spinning-disk confocal microscope (Zeiss) with emCCD camera (Photometrics, Evolve 512). Dynamic cell-behaviour of complete AS tissue was recorded starting from the end of germband retraction to the initiation of dorsal-closure (~25–30 min for wild-type and *Tmc* embryos and 60–90 min for *xit* embryos). For oscillatory dynamics, time-lapse was recorded with a frame-rate of 35 s with multiple axial stacks, using a Zeiss, 25x/0.8 NA oil Plan-Apochromat objective.

Laser ablation and Ca^{2+} response assay after wounding. Junctional laser ablation and target cell wounding were done using UV laser (DPSL355/14, 355 nm pulsed YAG laser, 70 μJ/pulse) targeted at the single-cell resolution from an epiport of the microscope and was controlled by an independent scanning head. The UV laser was illuminated under the 'Click and Fire' Mode on the 'REO394 SysCon-Zen' platform (Rapp OptoElectronic). The UV laser was targeted at the plane of adherens junction (or at the centre of the target cell for Ca^{2+} response assay after wounding), at a single-cell resolution with 2% of laser power. The exposure time was kept at 1500 ms (around 300 pulses). Images were recorded with the frame-rate of 0.3 s on an inverted spinning disc microscope (Zeiss, 40x/1.3 NA oil Plan-Apochromat objective) with AxioCam MRm CCD camera.

Calcium uncaging. Calcium uncaging were performed as previously described[24]. In briefly, stage 11 embryos expressing E-Cad-GFP were injected with 1 mM NP-EGTA, AM in injection solution (180 mM NaCl, 10 mM HEPES [pH 7.2], 5 mM KCl, 1 mM $MgCl_2$) in the peri-vitelline space. After injection, the embryos were incubated at room temperature in the dark around 10 min. Ca^{2+} uncaging

was performed at a single cell resolution in amnioserosa tissue during the recording using a continuous wave diode laser with 375 nm wavelength and 70 mW power DL-375/70 (Rapp OptoElectronic). This laser is controlled with an independent scan module (Rapp UGA-42 Caliburn) and linked to the microscope via the epiport. Images were recorded with the frame-rate of 1 s, via a spinning disk mounted on the side port (Zeiss ObserverZ1, x100/1.4 NA oil, AxioCam MRm). 10% of laser power, and 200 ms exposure time during the recording mode was used to perform uncaging.

Staging. Movies were aligned to the end of germband retraction and onset of dorsal closure as identified by fusion of leading edges at the anterior front of the embryo[54].

Segmentation and large-scale analysis of complete amnioserosa tissue. Maximal intensity projection from original z-stacks were used to yield a 2D representation of the AS. To acquire analyzable data, we used a custom designed image segmentation pipeline. The core element of this pipeline is the machine learning based skeletonising of the tissue, using so called cycle consistent generative adversarial networks (CycleGAN)[55]. These networks achieve a very high precision of over 95% segmentation accuracy without additional filtering of the original recordings. We manually corrected the predicted segmentation using the Tissue Analyser[56] to achieve a complete segmentation of the AS. A second person controlled the finalised segmentation again. Parsing the data was done via TissueMiner[57], as well as custom written software in python.

Image analysis and quantification.

Cell anisotropy. Anisotropy or cell-elongation was quantified using a *nematic tensor* characterising the magnitude of the elongation[57]. Anisotropy in the AS cells was computed independent of lateral and axial axis orientation of the cells with respect to the anterior–posterior axis of the embryo.

Initial recoil velocity. Initial recoil velocity was calculated from the first 5 s of the displacement trajectory following the UV laser ablation. Displacement of the adjacent 3x vertices of the ablated junction were followed over time by using MTrackJ plugin[58] in Image J. The strain trajectories were fitted to a model for a viscoelastic element (d=v/k * [1-exp(-k*t)]). Here, *v* represents the recoil velocity and *k* is the time-scale.

Oscillation and cross-correlation analysis. Oscillatory cell dynamics was analysed during the elliptical phase of AS. Time series for the cell area have been detrended using piecewise linear fits to each respective trajectory. The period of oscillation in AS cells were directly estimated from a wavelet transformation on the cell area trajectory over time. Intercellular synchronisation of the AS cell-pairs was analysed using cross-correlation between detrended cell area trajectories. Statistical significance of the correlation coefficients has been tested using large scale false discovery rate analysis.

Spatial distribution of coupling types. To calculate the correlation maps cell-pair positions were normalised with respect to the anterior/posterior and dorsal/ventral ends of the tissue for each embryo respectively. These were approximated by taking the position of the anterior-most/posterior-most/... cell positions as end of the tissue. Using a 2D Gaussian filter kernel, correlation coefficient values from all embryos were convolved according to their positions which yields a spatial representation of average correlation coefficient values across the whole ensemble of embryos. Hereby, all values were taken into account. In addition to the correlation maps, we generated subsamples of coupling pairs which were selected according to their local false discovery rate[32], which indicates the statistical significance of the synchronisation. These values are visualised by plotting them according to their normalised position as described above.

Ca^{2+} response assay. Normalised GCaMP6-myr intensity fold increase was measured at the junctions of all directly-linked neighbours to the target cell. Mean fluorescence intensity (I) was normalised to the fluorescence intensity of the background/control junctions 3–4 cells away from the target cell (I_0). Mean fluorescence intensity was measured by manually selecting ROIs every 10 s for up to 300 s using Fiji (I/I_0). Correction for bleaching was done by detrending.

Statistics. Large scale false discovery rate analysis: The analysis of many repeated trials has the drawback that the probability of finding a significant result is proportional to the number of trials.

We utilised local false discovery rates (local FDR), a Bayesian method that makes it possible to assign a false discovery rate to every test statistic (hence local) and therefore accounts for the many trials problem. It does not rely on a theoretical null distribution but instead infers it directly from the data and also works on non-gaussian statistics. Confidence intervals: If not stated otherwise, error regions have been determined by calculating 95% bias-corrected and accelerated bootstrap confidence intervals with 5000 samples. Statistical tests: If not stated otherwise, the *p* values for estimators have been calculated from one- or two-sided t-tests. The *p* values to compare distributions were calculated using Kolmogorov-Smirnov tests.

References

1 Delmas, P. & Coste, B. Mechano-Gated Ion Channels in Sensory Systems. *Cell* **155**, 278-284, doi:https://doi.org/10.1016/j.cell.2013.09.026 (2013).

2 Douguet, D. & Honoré, E. Mammalian Mechanoelectrical Transduction: Structure and Function of Force-Gated Ion Channels. *Cell* **179**, 340-354, doi:10.1016/j.cell.2019.08.049 (2019).

3 Kefauver, J. M., Ward, A. B. & Patapoutian, A. Discoveries in structure and physiology of mechanically activated ion channels. *Nature* **587**, 567-576, doi:10.1038/s41586-020-2933-1 (2020).

4 Jin, P., Jan, L. Y. & Jan, Y. N. Mechanosensitive Ion Channels: Structural Features Relevant to Mechanotransduction Mechanisms. *Annu Rev Neurosci* **43**, 207-229, doi:10.1146/annurev-neuro-070918-050509 (2020).

5 Collinet, C. & Lecuit, T. Programmed and self-organized flow of information during morphogenesis. *Nat Rev Mol Cell Biol* **22**, 245-265, doi:10.1038/s41580-020-00318-6 (2021).

6 Goldbeter, A. Biological rhythms: clocks for all times. *Curr Biol* **18**, R751-r753, doi:10.1016/j.cub.2008.06.044 (2008).

7 Heisenberg, C. P. & Bellaïche, Y. Forces in tissue morphogenesis and patterning. *Cell* **153**, 948-962, doi:10.1016/j.cell.2013.05.008 (2013).

8 Lecuit, T., Lenne, P. F. & Munro, E. Force generation, transmission, and integration during cell and tissue morphogenesis. *Annu Rev Cell Dev Biol* **27**, 157-184, doi:10.1146/annurev-cellbio-100109-104027 (2011).

9 Agarwal, P. & Zaidel-Bar, R. Mechanosensing in embryogenesis. *Current Opinion in Cell Biology* **68**, 1-9, doi:https://doi.org/10.1016/j.ceb.2020.08.007 (2021).

10 Ranade, S. S. *et al.* Piezo1, a mechanically activated ion channel, is required for vascular development in mice. *Proceedings of the National Academy of Sciences* **111**, 10347-10352, doi:10.1073/pnas.1409233111 (2014).

11 He, M. *et al.* Cytoplasmic Cl− couples membrane remodeling to epithelial morphogenesis. *Proceedings of the National Academy of Sciences* **114**, E11161-E11169, doi:10.1073/pnas.1714448115 (2017).

12 Nonomura, K. *et al.* Mechanically activated ion channel PIEZO1 is required for lymphatic valve formation. *Proc Natl Acad Sci U S A* **115**, 12817-12822, doi:10.1073/pnas.1817070115 (2018).

13 George, L. F. *et al.* Ion Channel Contributions to Wing Development in Drosophila melanogaster. *G3 Genes|Genomes|Genetics* **9**, 999-1008, doi:10.1534/g3.119.400028 (2019).

14 Roy Choudhury, A., Großhans, J. & Kong, D. Ion Channels in Epithelial Dynamics and Morphogenesis. *Cells* **10**, doi:10.3390/cells10092280 (2021).

15 Marcovich, I. & Holt, J. R. Evolution and function of Tmc genes in mammalian hearing. *Current Opinion in Physiology* **18**, 11-19, doi:https://doi.org/10.1016/j.cophys.2020.06.011 (2020).

16 Guo, Y. *et al.* Transmembrane channel-like (tmc) gene regulates Drosophila larval locomotion. *Proc Natl Acad Sci U S A* **113**, 7243-7248, doi:10.1073/pnas.1606537113 (2016).
17 Yue, X., Sheng, Y., Kang, L. & Xiao, R. Distinct functions of TMC channels: a comparative overview. *Cell Mol Life Sci* **76**, 4221-4232, doi:10.1007/s00018-019-03214-1 (2019).
18 Sokolow, A., Toyama, Y., Kiehart, Daniel P. & Edwards, Glenn S. Cell Ingression and Apical Shape Oscillations during Dorsal Closure in Drosophila. *Biophysical Journal* **102**, 969-979, doi:https://doi.org/10.1016/j.bpj.2012.01.027 (2012).
19 Pasakarnis, L., Frei, E., Caussinus, E., Affolter, M. & Brunner, D. Amnioserosa cell constriction but not epidermal actin cable tension autonomously drives dorsal closure. *Nat Cell Biol* **18**, 1161-1172, doi:10.1038/ncb3420 (2016).
20 Chatzigeorgiou, M., Bang, S., Hwang, S. W. & Schafer, W. R. tmc-1 encodes a sodium-sensitive channel required for salt chemosensation in C. elegans. *Nature* **494**, 95-99, doi:10.1038/nature11845 (2013).
21 Jia, Y. *et al.* TMC1 and TMC2 Proteins Are Pore-Forming Subunits of Mechanosensitive Ion Channels. *Neuron* **105**, 310-321.e313, doi:10.1016/j.neuron.2019.10.017 (2020).
22 Zhang, Y. V., Aikin, T. J., Li, Z. & Montell, C. The Basis of Food Texture Sensation in Drosophila. *Neuron* **91**, 863-877, doi:https://doi.org/10.1016/j.neuron.2016.07.013 (2016).
23 Zhang, Y. *et al.* The glucosyltransferase Xiantuan of the endoplasmic reticulum specifically affects E-Cadherin expression and is required for gastrulation movements in Drosophila. *Dev Biol* **390**, 208-220, doi:10.1016/j.ydbio.2014.03.007 (2014).
24 Kong, D. *et al.* In vivo optochemical control of cell contractility at single-cell resolution. *EMBO Rep* **20**, e47755, doi:10.15252/embr.201947755 (2019).
25 He, L., Wang, X., Tang, H. L. & Montell, D. J. Tissue elongation requires oscillating contractions of a basal actomyosin network. *Nat Cell Biol* **12**, 1133-1142, doi:10.1038/ncb2124 (2010).
26 Christodoulou, N. & Skourides, P. A. Cell-Autonomous Ca(2+) Flashes Elicit Pulsed Contractions of an Apical Actin Network to Drive Apical Constriction during Neural Tube Closure. *Cell Rep* **13**, 2189-2202, doi:10.1016/j.celrep.2015.11.017 (2015).
27 Kaneuchi, T. *et al.* Calcium waves occur as *Drosophila* oocytes activate. *Proceedings of the National Academy of Sciences* **112**, 791-796, doi:10.1073/pnas.1420589112 (2015).
28 Chen, T. W. *et al.* Ultrasensitive fluorescent proteins for imaging neuronal activity. *Nature* **499**, 295-300, doi:10.1038/nature12354 (2013).
29 Xu, S. & Chisholm, A. D. A Gαq-Ca^{2+} signaling pathway promotes actin-mediated epidermal wound closure in C. elegans. *Curr Biol* **21**, 1960-1967, doi:10.1016/j.cub.2011.10.050 (2011).
30 Razzell, W., Evans, I. R., Martin, P. & Wood, W. Calcium flashes orchestrate the wound inflammatory response through DUOX activation and hydrogen peroxide release. *Curr Biol* **23**, 424-429, doi:10.1016/j.cub.2013.01.058 (2013).
31 Shannon, E. K. *et al.* Multiple Mechanisms Drive Calcium Signal Dynamics around Laser-Induced Epithelial Wounds. *Biophysical Journal* **113**, 1623-1635, doi:https://doi.org/10.1016/j.bpj.2017.07.022 (2017).
32 Efron, B. Correlation and Large-Scale Simultaneous Significance Testing. *Journal of the American Statistical Association* **102**, 93-103 (2007).
33 Dierkes, K., Sumi, A., Solon, J. & Salbreux, G. Spontaneous Oscillations of Elastic Contractile Materials with Turnover. *Physical Review Letters* **113**, 148102, doi:10.1103/PhysRevLett.113.148102 (2014).
34 Skilling, J. Nested sampling for general Bayesian computation. *Bayesian Analysis* **1**, 833-859, 827 (2006).

35 Feroz, F., Hobson, M. P. & Bridges, M. MultiNest: an efficient and robust Bayesian inference tool for cosmology and particle physics. *Monthly Notices of the Royal Astronomical Society* **398**, 1601-1614, doi:10.1111/j.1365-2966.2009.14548.x (2009).
36 Handley, W. J., Hobson, M. P. & Lasenby, A. N. polychord: nested sampling for cosmology. *Monthly Notices of the Royal Astronomical Society: Letters* **450**, L61-L65, doi:10.1093/mnrasl/slv047 (2015).
37 Solon, J., Kaya-Copur, A., Colombelli, J. & Brunner, D. Pulsed forces timed by a ratchet-like mechanism drive directed tissue movement during dorsal closure. *Cell* **137**, 1331-1342, doi:10.1016/j.cell.2009.03.050 (2009).
38 Hutson, M. S. *et al.* Forces for morphogenesis investigated with laser microsurgery and quantitative modeling. *Science* **300**, 145-149, doi:10.1126/science.1079552 (2003).
39 Kiehart, D. P., Galbraith, C. G., Edwards, K. A., Rickoll, W. L. & Montague, R. A. Multiple forces contribute to cell sheet morphogenesis for dorsal closure in Drosophila. *J Cell Biol* **149**, 471-490, doi:10.1083/jcb.149.2.471 (2000).
40 Lv, Z., Zhang, N., Zhang, X., Großhans, J. & Kong, D. The Lateral Epidermis Actively Counteracts Pulling by the Amnioserosa During Dorsal Closure. *Front Cell Dev Biol* **10**, 865397, doi:10.3389/fcell.2022.865397 (2022).
41 Fernandez-Gonzalez, R., Simoes Sde, M., Röper, J. C., Eaton, S. & Zallen, J. A. Myosin II dynamics are regulated by tension in intercalating cells. *Dev Cell* **17**, 736-743, doi:10.1016/j.devcel.2009.09.003 (2009).
42 Paluch, E. & Heisenberg, C. P. Biology and physics of cell shape changes in development. *Curr Biol* **19**, R790-799, doi:10.1016/j.cub.2009.07.029 (2009).
43 Kong, D. & Großhans, J. Planar Cell Polarity and E-Cadherin in Tissue-Scale Shape Changes in Drosophila Embryos. *Front Cell Dev Biol* **8**, 619958, doi:10.3389/fcell.2020.619958 (2020).
44 Kurima, K., Yang, Y., Sorber, K. & Griffith, A. J. Characterization of the transmembrane channel-like (TMC) gene family: functional clues from hearing loss and epidermodysplasia verruciformis. *Genomics* **82**, 300-308, doi:10.1016/s0888-7543(03)00154-x (2003).
45 Pan, B. *et al.* TMC1 and TMC2 are components of the mechanotransduction channel in hair cells of the mammalian inner ear. *Neuron* **79**, 504-515, doi:10.1016/j.neuron.2013.06.019 (2013).
46 Ballesteros, A., Fenollar-Ferrer, C. & Swartz, K. J. Structural relationship between the putative hair cell mechanotransduction channel TMC1 and TMEM16 proteins. *Elife* **7**, doi:10.7554/eLife.38433 (2018).
47 Erives, A. & Fritzsch, B. A Screen for Gene Paralogies Delineating Evolutionary Branching Order of Early Metazoa. *G3 (Bethesda)* **10**, 811-826, doi:10.1534/g3.119.400951 (2020).
48 Hehlert, P., Zhang, W. & Göpfert, M. C. Drosophila Mechanosensory Transduction. *Trends in Neurosciences* **44**, 323-335, doi:https://doi.org/10.1016/j.tins.2020.11.001 (2021).
49 Huang, J., Zhou, W., Dong, W., Watson, A. M. & Hong, Y. From the Cover: Directed, efficient, and versatile modifications of the Drosophila genome by genomic engineering. *Proc Natl Acad Sci U S A* **106**, 8284-8289, doi:10.1073/pnas.0900641106 (2009).
50 Whitworth, C. in *The Biological Resources of Model Organisms* (ed Robert L. Jarret and Kevin McCluskey) Ch. Chapter 8, 145–162 (CRC Press, Taylor & Francis Group, 2019).
51 Thurmond, J. *et al.* FlyBase 2.0: the next generation. *Nucleic Acids Res* **47**, D759-d765, doi:10.1093/nar/gky1003 (2019).
52 Grosshans, J. *et al.* RhoGEF2 and the formin Dia control the formation of the furrow canal by directed actin assembly during Drosophila cellularisation. *Development* **132**, 1009-1020, doi:10.1242/dev.01669 (2005).
53 Schindelin, J. *et al.* Fiji: an open-source platform for biological-image analysis. *Nat Methods* **9**, 676-682, doi:10.1038/nmeth.2019 (2012).

54 Kiehart, D. P., Crawford, J. M., Aristotelous, A., Venakides, S. & Edwards, G. S. Cell Sheet Morphogenesis: Dorsal Closure in Drosophila melanogaster as a Model System. *Annu Rev Cell Dev Biol* **33**, 169-202, doi:10.1146/annurev-cellbio-111315-125357 (2017).
55 Häring, M., Großhans, J., Wolf, F. & Eule, S. Automated Segmentation of Epithelial Tissue Using Cycle-Consistent Generative Adversarial Networks. *bioRxiv*, 311373, doi:10.1101/311373 (2018).
56 Aigouy, B., Umetsu, D. & Eaton, S. Segmentation and Quantitative Analysis of Epithelial Tissues. *Methods Mol Biol* **1478**, 227-239, doi:10.1007/978-1-4939-6371-3_13 (2016).
57 Etournay, R. *et al.* TissueMiner: A multiscale analysis toolkit to quantify how cellular processes create tissue dynamics. *eLife* **5**, e14334, doi:10.7554/eLife.14334 (2016).
58 Meijering, E., Dzyubachyk, O. & Smal, I. Methods for cell and particle tracking. *Methods Enzymol* **504**, 183-200, doi:10.1016/b978-0-12-391857-4.00009-4 (2012).

Acknowledgements
We are grateful to Christine Rostosky for help with the manual correction of the segmentation. Stocks obtained from the Bloomington Drosophila Stock Centre (NIH P40OD018537) were used in this study. This work was in part supported by and the Deutsche Forschungsgemeinschaft (DFG FOR1756, GR1945/8-2, GR1945/10-1/2, WO/1 , SFB 889, A1 and C8), equipment grant INST1525/16-1 FUGG), and the Cluster of Excellence Multiscale Bioimaging (MBExC).

Author contributions
J.G. and F.W. conceived the study. P.R. and D.K. planed and conducted experimental strategies and assays. M.H. performed segmentation and quantifications. M.H. conceived the mathematical model with F.W. and M.H. performed analysis and simulations. P.R., M.H., F.W. and J.G. analysed the results. Materials and expertise about the Tmc mutant allele was provided by M. G.. All authors wrote, revised or commented on the manuscript.

Conflict of interest
The authors declare that they have no conflict of interest.

Materials & Correspondence
Jörg Großhans (grosshan@uni-marburg.de)
Fred Wolf (fred.wolf@ds.mpg.de)

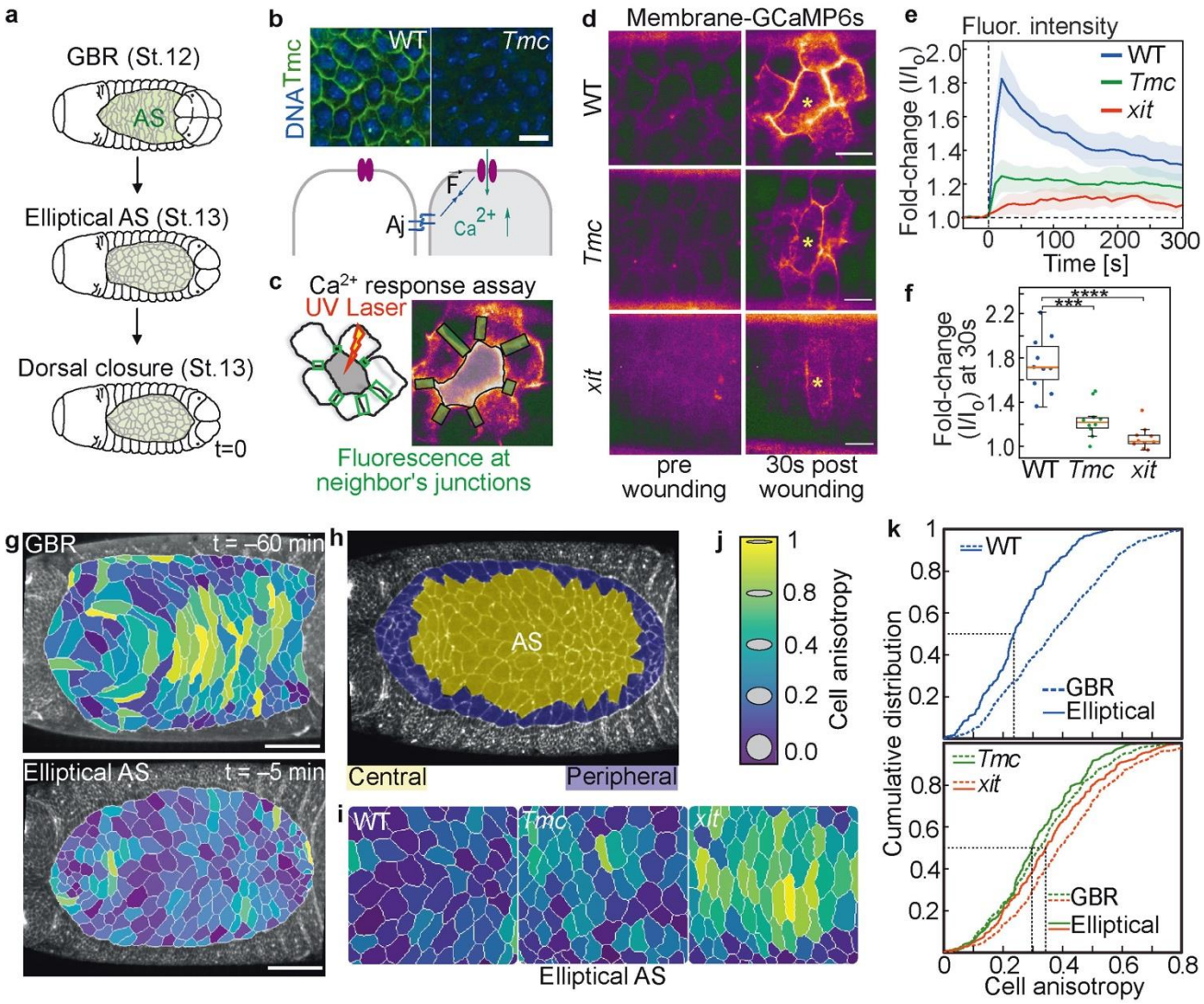

Fig. 1 *Tmc* promotes isotropic cell morphology of the amnioserosa. a, Morphology of AS tissue (green) changes during germband retraction and elliptical stage. **b**, Staining and scheme of hypothesized mechanism of Tmc in amnioserosa cells. Fixed wild type and *Tmc* embryos (stage 13, elliptical stage) stained for DNA (blue) and Tmc (green). Scale bar 10 µm. **c**, Experimental scheme of the Ca^{2+} response assay. Fluorescence of membrane bound Ca^{2+} sensor (myr-GCaMP6s) was measured at the junctions between the next neighbours (rectangle in green) before and following ablation of the target cell (grey). Next to it, image from time lapse recordings of the Ca^{2+} sensor 30 s after wounding. Mean intensity was measured at all neighbour cell junctions (green) adjacent to the wounded cell (target-cell in grey). **d**, Time-lapse imaging of neighbour cell dependent Ca^{2+} response 10 s before and 30 s after wound induction in the marked target cell in embryos of indicated genotypes. **e**, Time course of normalized fluorescence of Ca^{2+} sensor with mean (solid line) and 95% bootstrapped confidence interval (band). Wounding at t=0. N=10 embryos per genotype. **f**, Normalized fluorescence of Ca^{2+} sensor 30 s after wounding. Statistical significance by student T test. P values (WT vs *Tmc*) = 3.3×10^{-5}; (WT vs *xit*) = 3.6×10^{-7}. Scale bars 10 µm. **g**, Anisotropy colour coded according to scale in panel j during GBR and elliptical AS stage. Scale bar 50 µm. **h**, Morphodynamics analysis included the central cells (yellow) but not the peripheral cells at the boundary to the epidermis (blue). **i**, Representative AS tissue from time-lapse recording of WT, *Tmc*, and *xit* embryos during the elliptical AS stage. Cells coloured coded as in g. **j**, Colour coding for cell anisotropy. **k**, Cumulative distributions of cell anisotropy in WT, *xit* and *Tmc* during germband retraction and elliptical stages.

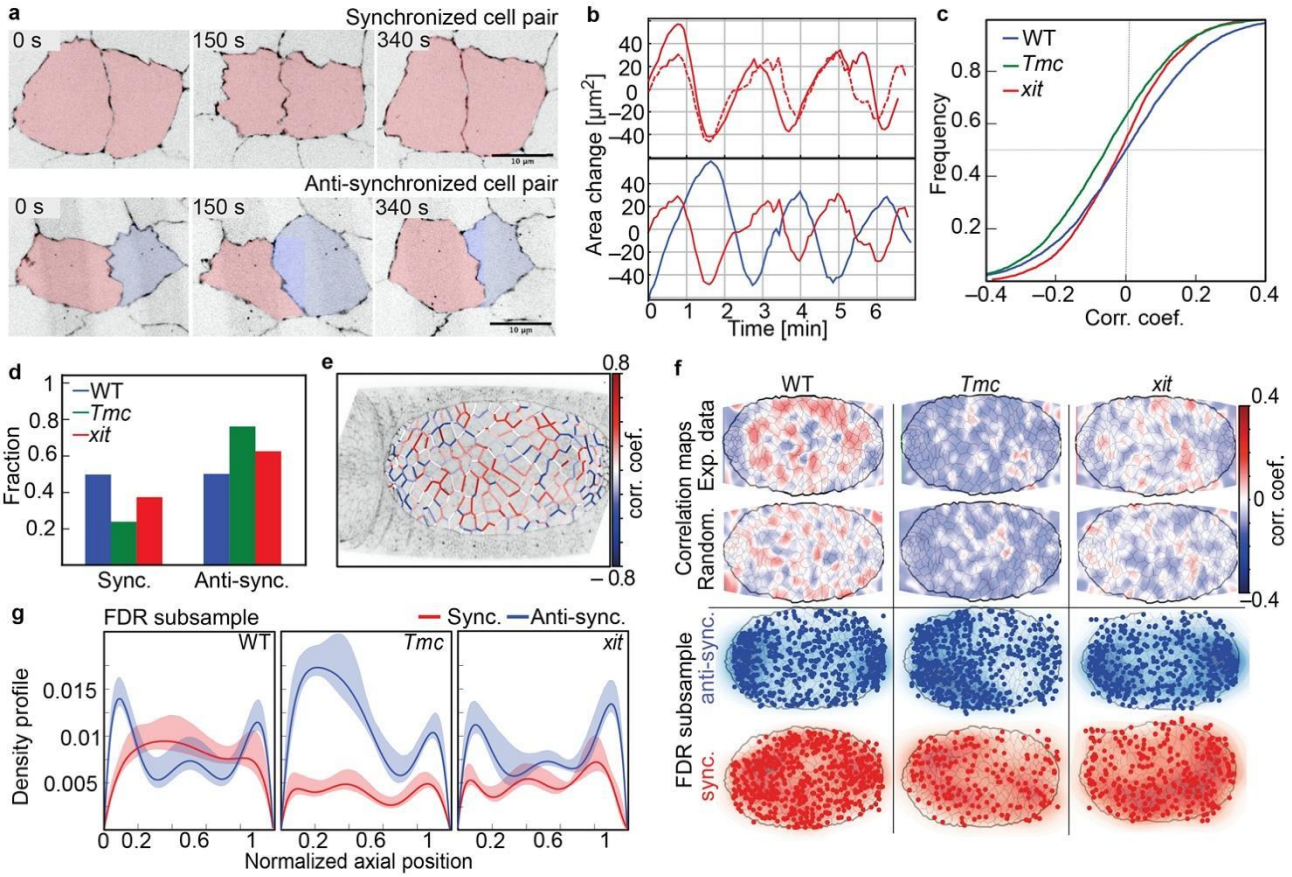

537 **Fig. 2 Synchronization of cell oscillations is impaired in *Tmc* and *xit* mutants**. **a**, Cell pairs with
538 synchronous (red-red) and anti-synchronous (red-blue) oscillation in cell area. Images from time-
539 lapse recordings. Scale bars 10 μm. **b**, Area trajectories of sync and anti-sync cell pairs in **(a). c**,
540 Cumulative distribution of correlation coefficients of all cell pairs computed over the complete
541 elliptical stage. **d**, Proportion of sync and anti-sync cell pairs among cell pairs with statistically
542 significant coupling. Wild type, 8 embryos 7370 pairs with 795 sync, 801 anti-sync significant
543 coupling, *Tmc*, 7 embryos, 4633 pairs with 254 sync, 809 anti-sync significant coupling, *xit*, 7
544 embryos with 4714 pairs with 324 sync, 541 anti-sync significant coupling. **e**, AS tissue with colour
545 coded junctions according to the average correlation coefficient. **f**, Maps with all correlation
546 coefficients averaged over each respective genotype. Colour coding represents average correlation.
547 To assess the specificity of the pattern, coefficients were averaged after scrambling the positions. A
548 sample is shown in the second row. A subsample of pairs was selected via controlling the local false
549 discovery rate (FDR subsample). Those pairs were plotted on a normalized AS separately for sync
550 and anti-sync pairs. **g**, Spatial density profile of FDR subsampled pairs. Confidence bands were
551 computed via bootstrapping over embryos.

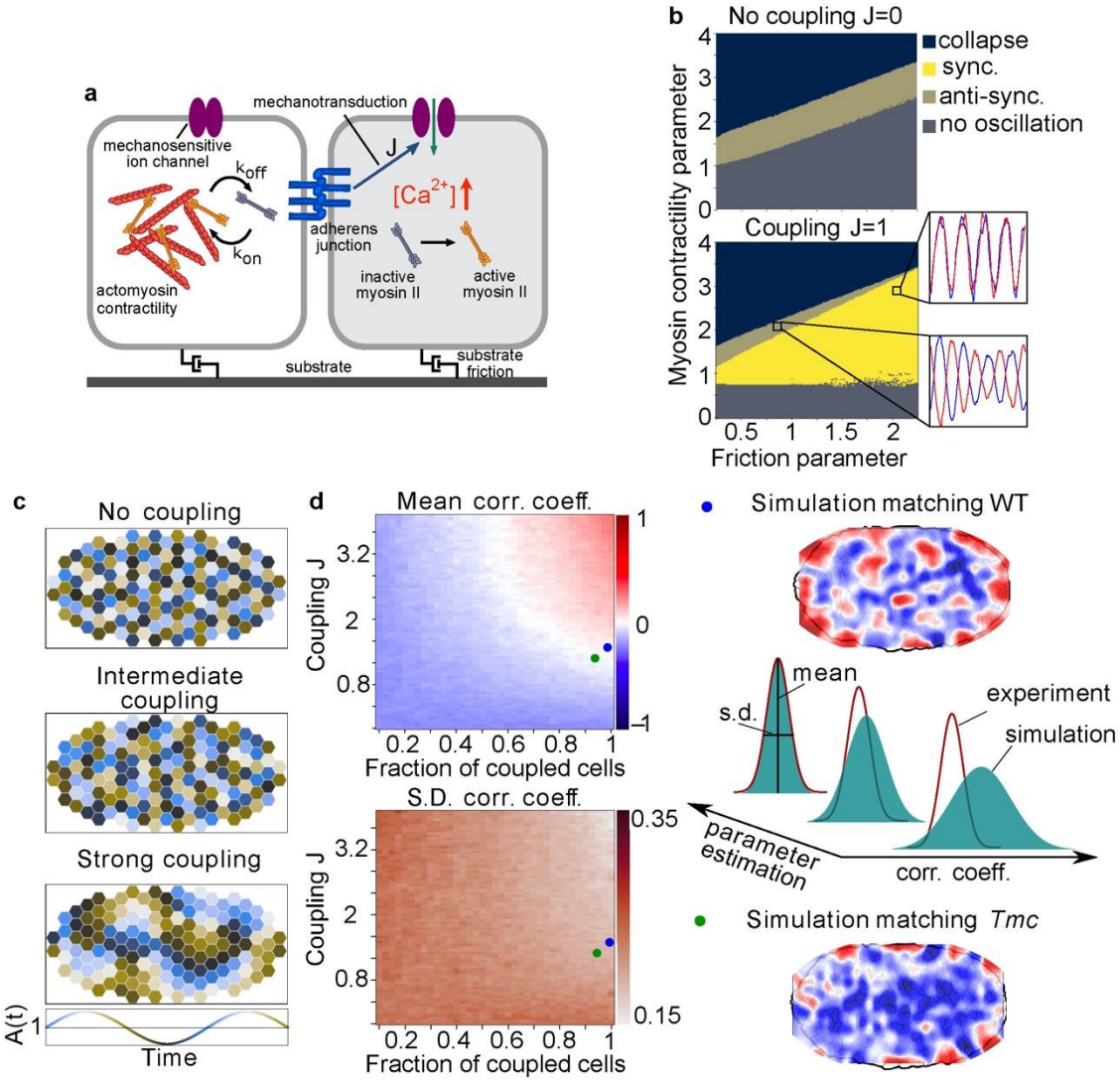

Fig. 3 Ca^{2+} coupling leads to intercellular synchronization in a biophysical model. a, Schematical depiction of coupling mechanism based on mechanosensitive ion channels. Mechanical tension at the cell-cell interface results in ion channel activation and influx of Ca^{2+} which leads to activation of myosin. Cell units experience friction due to the motion of the cells over a substrate. The model for a single cell unit consists of dynamical equations for the cell area, myosin concentration and Ca^{2+}. **b**, Phase diagram for two coupled cells. The phase diagram without coupling reproduces shows that the system undergoes a Hopf bifurcation when critical parameter values are exceeded, leading to area oscillations. In addition, the phase diagram features a collapse and a stable phase without oscillations. When Ca^{2+} coupling is included, a new dynamical phase appears in which both cells oscillate in synchrony. Without the coupling mechanism, neighbours oscillate in anti-sync. **c**, Snapshots of model simulations with roughly 150 cells and hexagonal packing. The colour code indicates the phase of each oscillator. Similar to (**b**), Ca^{2+} coupling induces synchronization of neighbouring oscillators, whereas cell pairs remain unsynchronized without coupling. **d**, Results of simulations with varying coupling strength and fraction of coupled cells. For fraction of coupled cells = 1, every cell pair in the tissue is coupled. Simulations are repeated 20 times for each parameter combination and the average mean and standard deviation of the correlation coefficient distribution were plotted. Parameters were optimized for matching the experimental distribution of correlation coefficients. Samples of correlation maps for best matching parameters are shown.

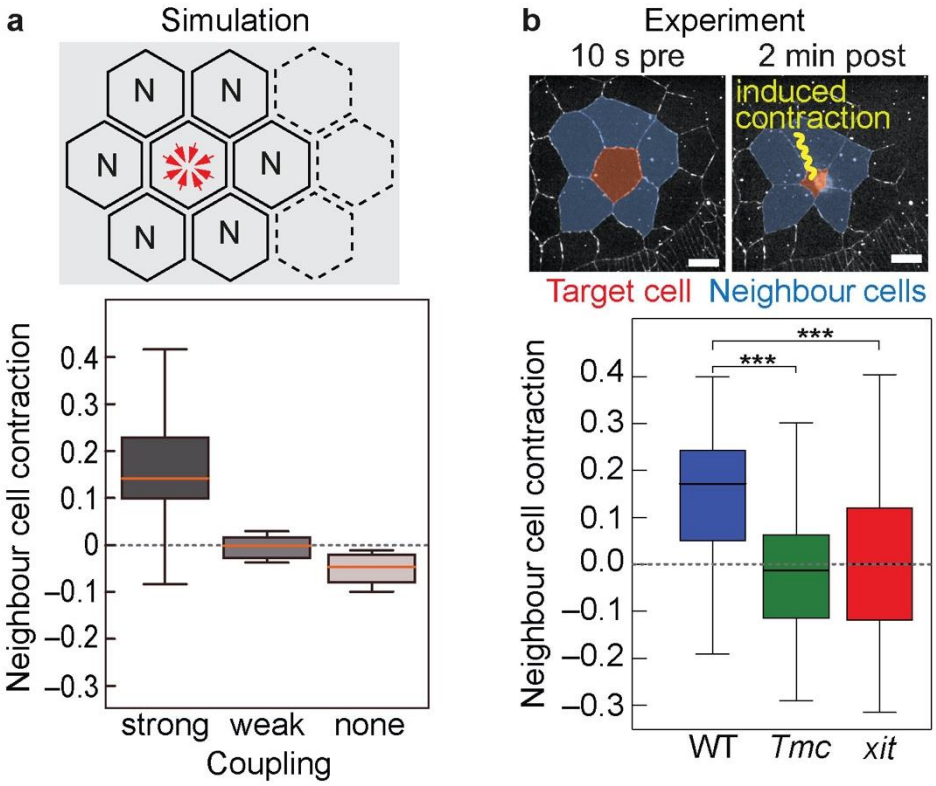

570 **Fig. 4 Mechanically triggered neighbour response depends on *Tmc* mediated coupling. a**,
571 Neighbour cell contraction from 50 simulations for varying coupling strength *J* (7.0, 1.5, 0.0). In the
572 simulation, a random cell was triggered to contract and the response of the neighbours was recorded.
573 **b**, Experimental scheme for triggered contraction of the target cell (red) by Ca^{2+} uncaging. Area
574 trajectories for the next neighbours (blue) were recorded. Experimentally measured area changes in
575 next neighbours in wild type, *Tmc* and *xit* mutants. P values were calculated via *Mann-Whitney-*
576 *Wilcoxon test*, ***: 1.0e-04 < p <= 1.0e-03. WT-*Tmc* p= 1.3e-04, WT-*xit* p= 4.9e-04. N_{WT}=48,
577 N_{Tmc}=28, N_{xit}=34.

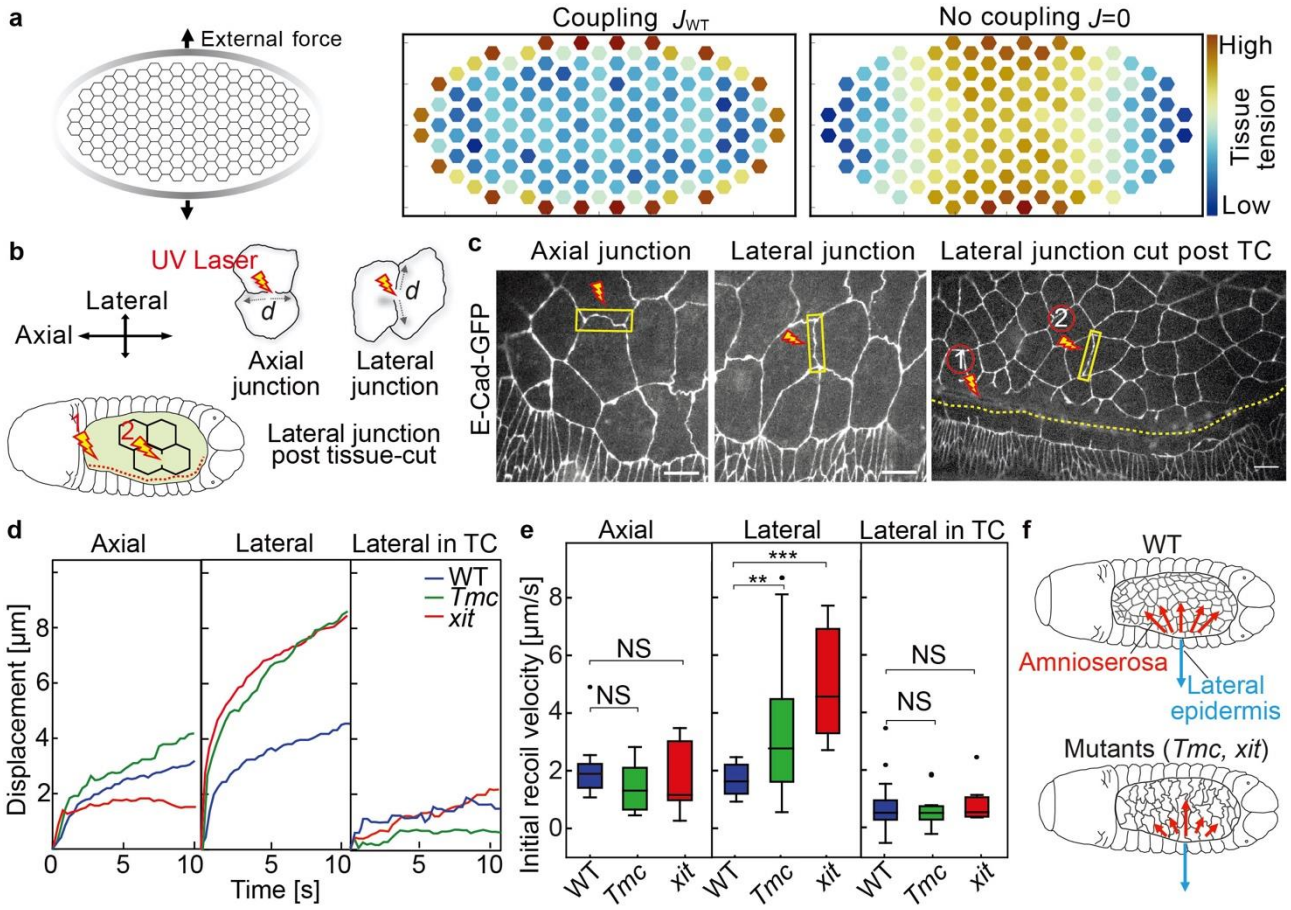

578 **Fig. 5: Prediction and experimental detection of isotropic force distribution by Tmc-mediated**
579 **coupling. a**, In simulations, external tension was applied perpendicular to the AS in order to mimic
580 pulling by the lateral epidermis, as depicted in **(f)**. The strength of the external tension is indicated by
581 the shading of the grey ellipse. Next to it, cells are coloured according to the averaged tension they
582 experienced in simulations after application an external force to the AS. **b**, In experiments, junction
583 tension was assayed by UV laser cuts and recoil was measured at junctions of axial or lateral
584 orientation. The impact of tissue scale tension was assessed by junction ablation following a cut
585 separating AS and epidermis. **c**, Exemplary images from cutting experiments. Scale bars, 10 µm. **d**,
586 Representative displacement curves following junction cuts. **e**, Initial recoil velocities. Each laser cut
587 experiment was performed in a single embryo. n=10 embryos for each genotype and condition.
588 Statistical significance by *Student's T-test*. **p<0.05, ***p<0.0001. **f**, Model for force balance
589 between the lateral epidermis (blue arrow) and AS (red arrow). Pulling force is uniformly spread in
590 wild type leading to an isotropic junction tension in the AS. Force spreading is uneven in *Tmc* and *xit*
591 mutants leading to higher tension in lateral than in axial junctions.

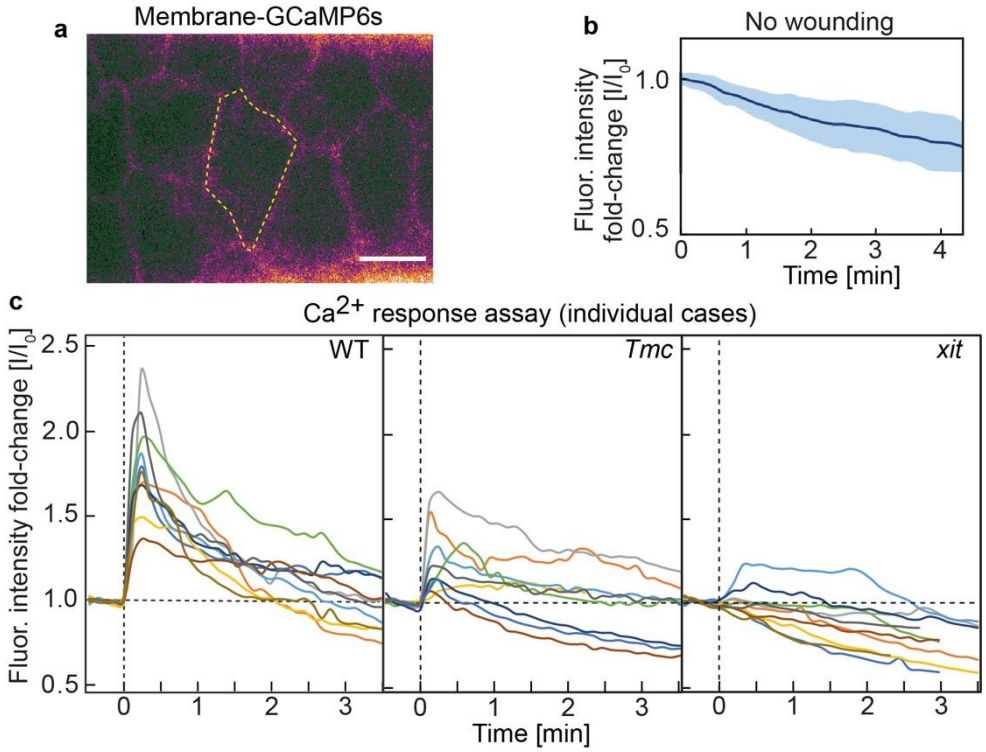

Extended Data Fig. 1 Ca^{2+} response assay. **a**, Image from living embryo expressing the Ca^{2+} sensor (GCaMP6s). Scale bar 10 µm. **b**, Fluorescence trace of Ca^{2+} sensor without wounding indicating the degree of bleaching of the sensor. **c**, Individual traces of normalized Ca^{2+} sensor fluorescence at junctions of neighbours in wounding experiments. Laser induced wounding at T=0.

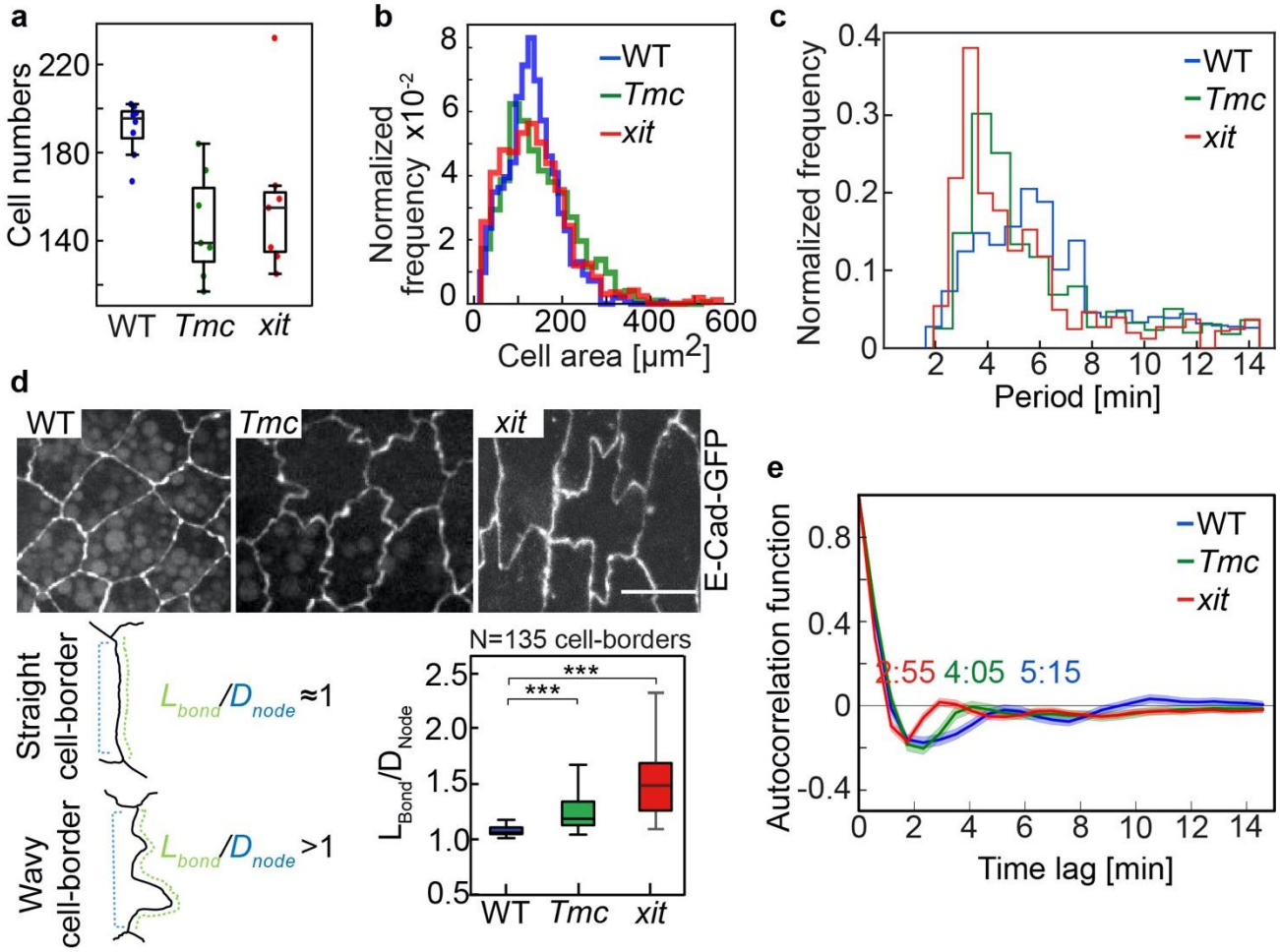

Extended Data Fig. 2 Parameters of cellular morphology and dynamics during the elliptical stage. a, Cell numbers of the AS. **b**, Distribution of apical cross-section area. **c**, Distributions of cell oscillation periods determined via wavelet transform. **d**, Representative live images of AS cells in embryos expressing E-Cad-GFP. Junction straightness parameters calculated as indicated in the scheme and shown by boxplots. Statistical significance by *Student's t test*. n=135 junctions for each genotype. Scale bar 10 µm. **e**, Autocorrelation functions of the area trajectories. Average with confidence band. Numbers indicate the major periods of the oscillations.

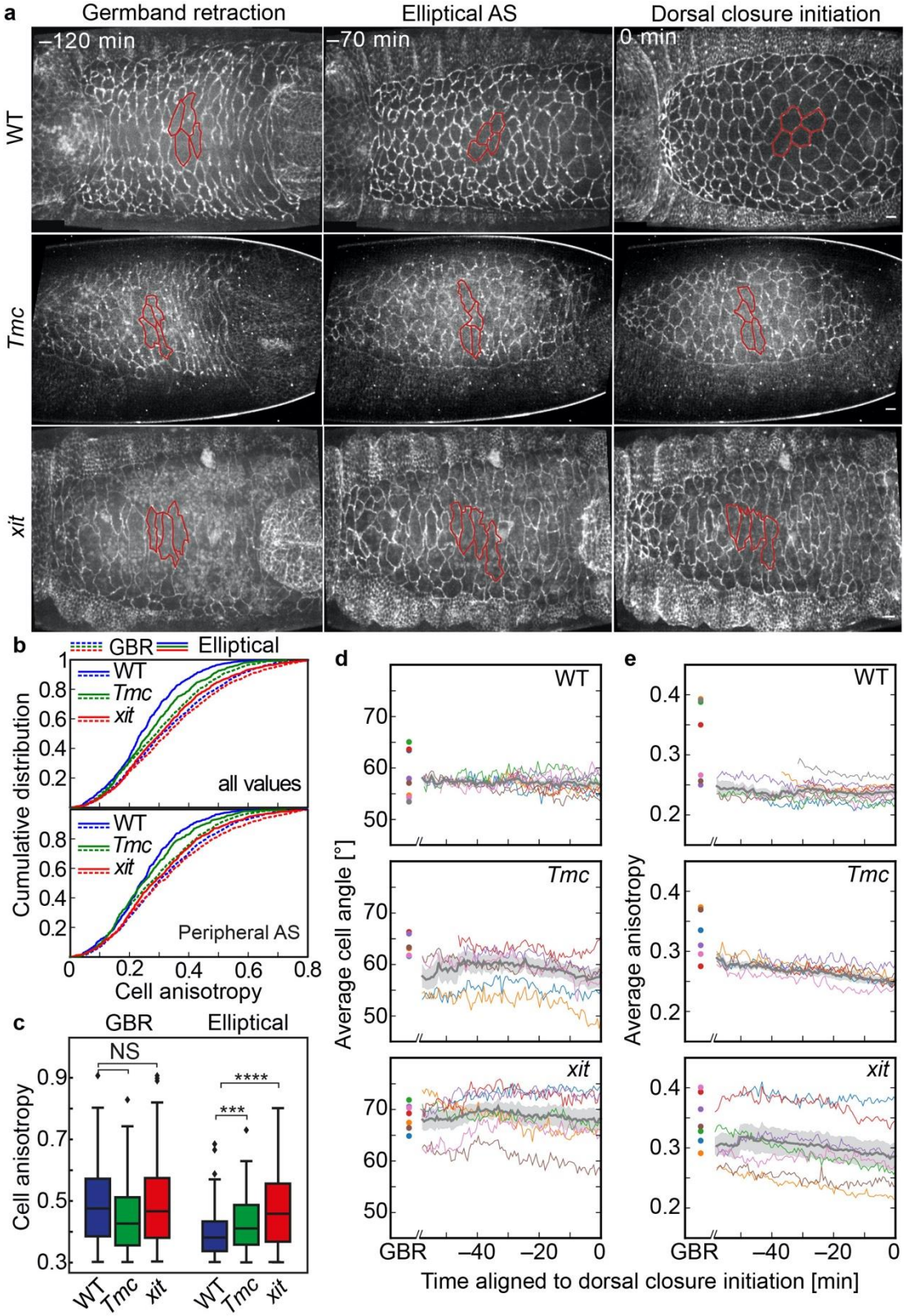

Extended Data Fig. 3 Cell shape changes during germband retraction and elliptical stage. **a**, Images from time lapse recordings of wild type, *Tmc* and *xit* mutants. Dorsal view, axial projections. Junction labelled by E-Cad-GFP. A few cells are outlined in red. **b**, Cumulative distributions of cell anisotropy separately for all values and peripheral cells during indicated stages. **c**, Distribution of cell shapes with an anisotropy larger than 0.3 indicated by boxplots in wild-type, *Tmc*, and *xit* embryos. Statistical significance: p-value (WT vs *Tmc)* = 5.4×10^{-2} and p-value (WT vs *xit)*

609 = 8.3×10^{-8}; two-sided *Mann–Whitney test*. WT, n=8 embryos, 436 cells; *Tmc*, n=7 embryos, 317
610 cells; *xit*, n=7 embryos, 238 cells. **d**, Time course for the average orientation of AS cells for each
611 embryo. Mean and standard deviation averaged over embryos are indicated by grey line and band.
612 Angle is normalized between axial axis and lateral axis. Dots indicate average values during
613 germband retraction. **e**, Time course of the average shape anisotropy for each embryo. Mean and
614 standard deviation averaged over embryos are indicated by grey line and band. Dots indicate average
615 values during germband retraction.

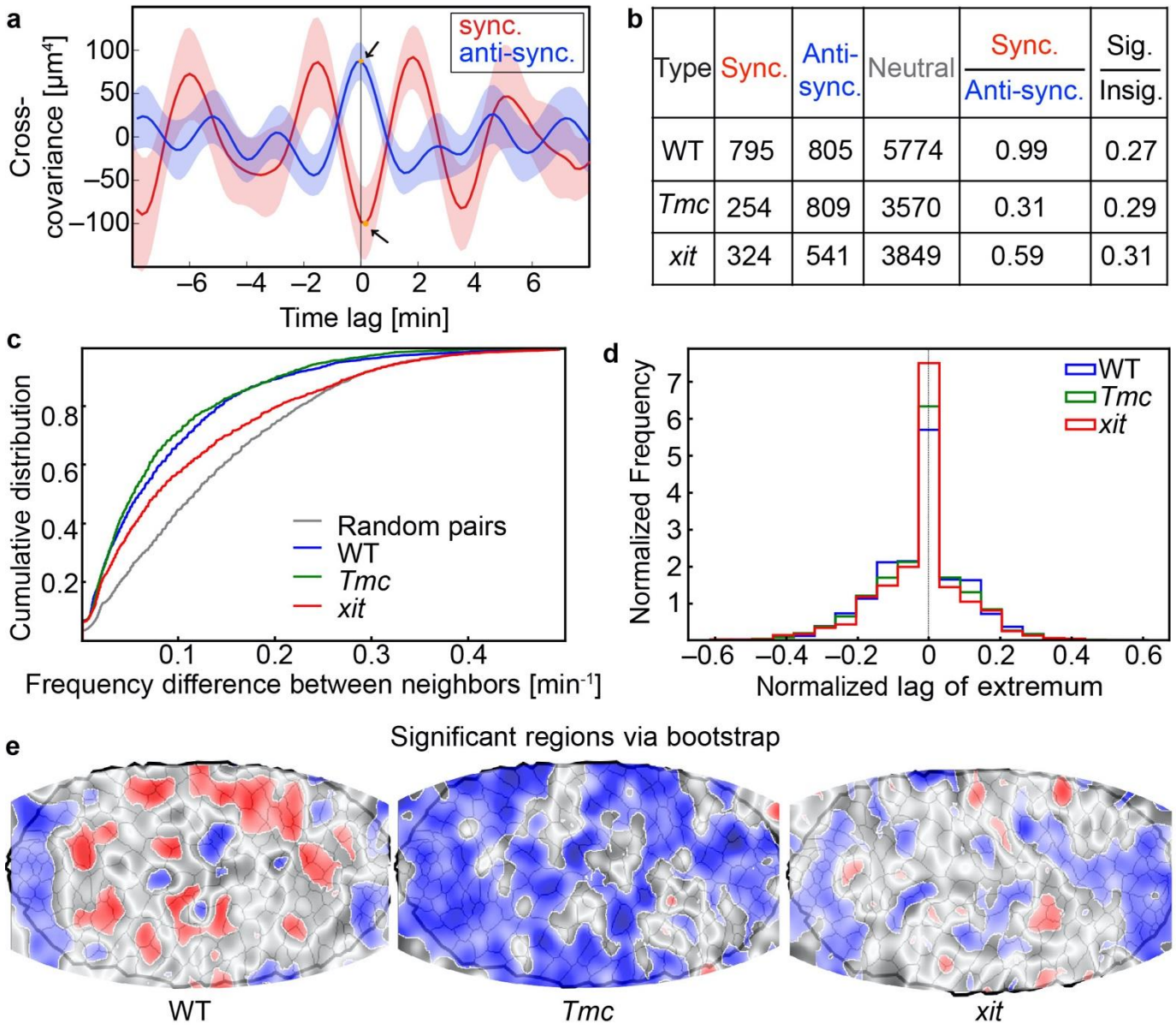

Type	Sync.	Anti-sync.	Neutral	Sync. / Anti-sync.	Sig. / Insig.
WT	795	805	5774	0.99	0.27
Tmc	254	809	3570	0.31	0.29
xit	324	541	3849	0.59	0.31

Extended Data Fig. 4 Synchronization and subsampling analysis. a, Exemplary cross-covariance of a synchronised cell pair (red) and an anti-synchronised cell pair (blue). Time lag for both coupling types marked with an arrow. **b**, Numbers of cell pairs for correlation analysis from the complete data set. Neutral cases have a local false discovery rate>0.1. **c**, Difference in oscillation frequency in cell pairs shown by cumulative distribution. **d**, Time lag of the extremum in the cross-correlation functions between neighbouring cells. Distribution plotted as histogram. **e**, Significant regions of the correlation maps determined via bootstrapping over the embryos.

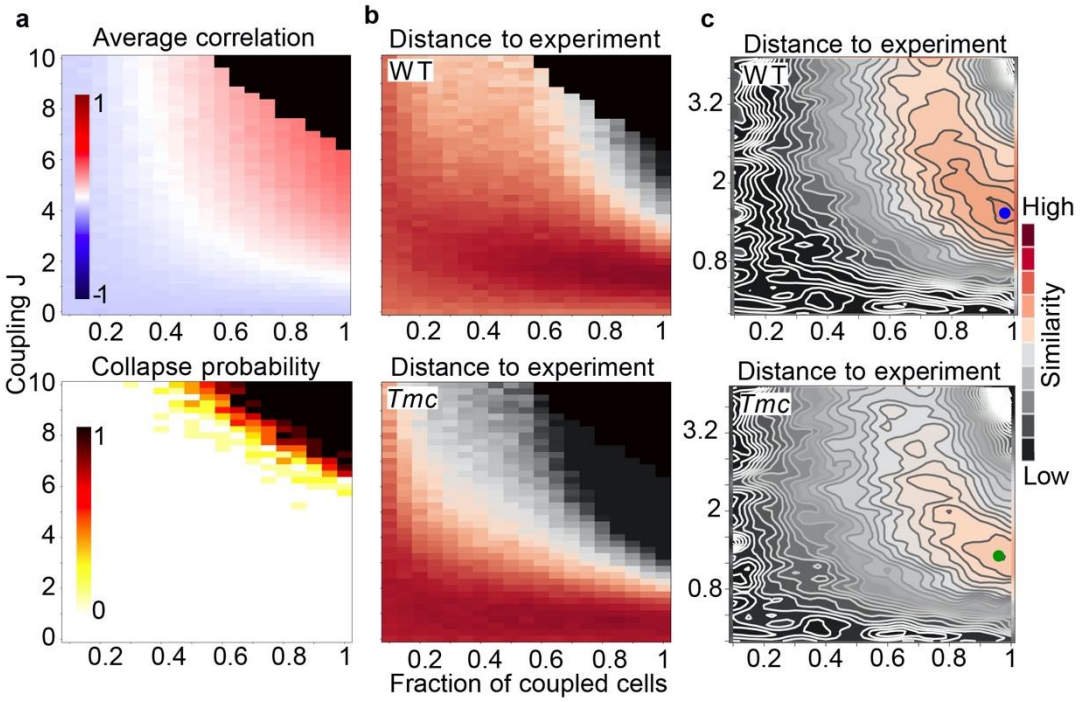

Extended Data Fig. 5 Quantification of similarity between simulations and experiment. a, Same plots as in main Fig. 3d, here with extended parameter range for coupling strength J. Blacked regions are collapsed simulations in more than 30% of simulations. In addition, the collapse probability is shown. **b**, Distance between model and experiment quantified by the Jensen divergence between the distribution of correlation coefficients. **c**, Same as (b) but showing relevant parameter region and additional contour lines for clarity. Blue and green dots mark maximum *a posteriori* estimates of model parameters obtained by nested sampling.

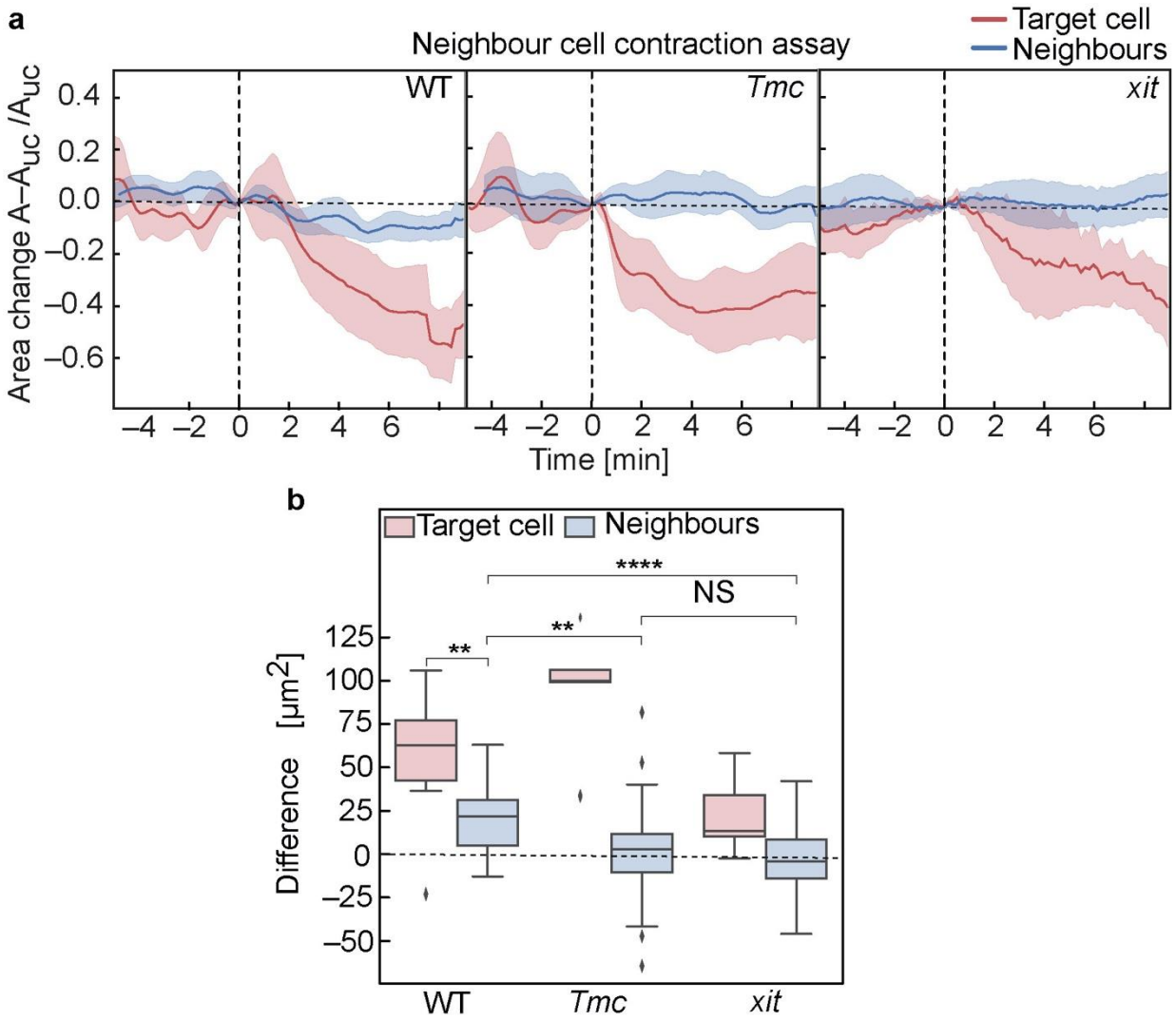

630 **Extended Data Fig. 6. Response of neighbours to triggered contraction of target cell. a**, Area
631 trajectories of target cells (red) and next neighbours (blue) after triggered contraction in the target
632 cell by Ca^{2+} uncaging at T=0. Solid lines indicate average, bands the 95% bootstrap confidence
633 interval. **b**, Area difference of target cell and neighbours between time of uncaging and 6 min
634 thereafter.

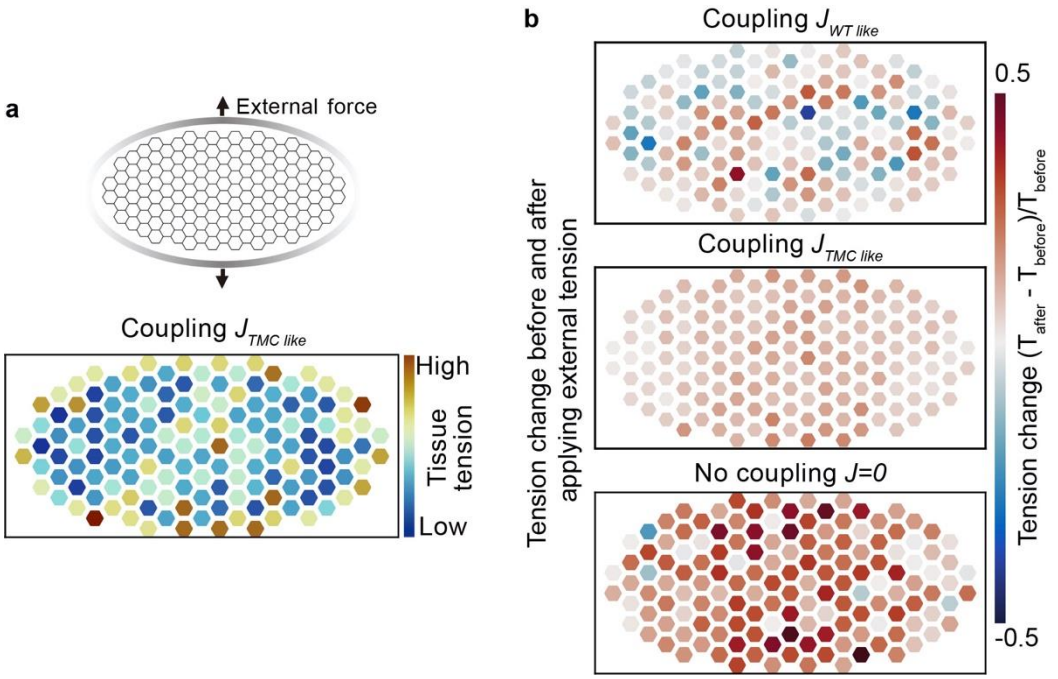

635 **Extended Data Fig. 7 Simulation of tissue-scale tension distribution in response to epidermal**
636 **pulling force. a,** External tension was applied perpendicular to the AS in order to mimic pulling by
637 the lateral epidermis as described in Fig 5a. Below: similar scheme like in Fig 5a but for *Tmc* like
638 parameters, showing tension in individual cells. **b,** Tension changes in cells in AS simulation. First,
639 the simulation ran long enough to equilibrate without external force, then external force was applied
640 and simulation ran again until equilibration. Colours denote the change in tension before and after
641 applying the external force.

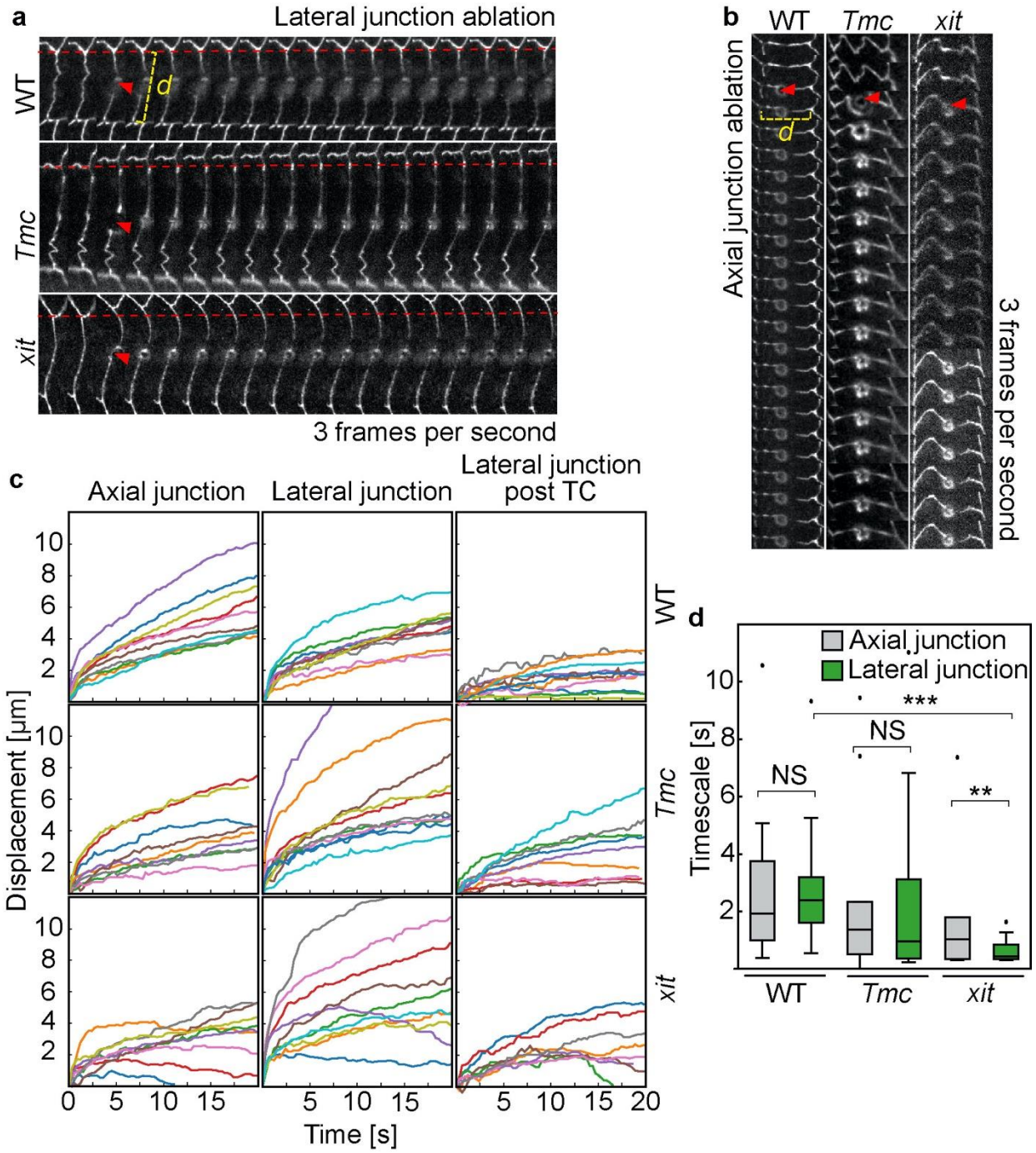

642 **Extended Data Fig. 8 Experimental measurement of junction tension by junction**
643 **microdissection. a**, **b**, Kymographs of representative experiments with junctions in lateral **(a)** or
644 axial **(b)** orientations. Arrow head in red points to position of laser application. Displacement d is the
645 change in the distance between the adjacent 3x vertices indicated by dashed line in yellow. **c**,
646 Individual displacement traces. **d**, Time scales calculated by fitting of a viscoelastic element to the
647 displacement traces. Statistical significance by *Student's t-test* **p<0.01, ***p<0.0001.

Supplementary information

This file contains the details of the modelling of amnioserosa dynamics.

Supplementary Videos

Video 1. Ca^{2+} response assay after wounding. Time-lapse recordings of amnioserosa cells at elliptical stage from the wild type (top panel), *Tmc* (middle panel), and *xit* (bottom panel) embryos expressing a membrane-bound, myristoylated variant of GCaMP6s. A wound was induced in the centre cells as in Fig. 1d by a 355 nm UV laser during recording.

Video 2. Overlay of original and segmented images of the amnioserosa in time-lapse recordings from germband retraction until dorsal closure in wild type (top panel) and *Tmc* (bottom panel) embryos expressing E-Cad-GFP. Scale bar 50 μm. The colour code represents the size of the cells from large, yellow to small, blue.

Video 3. Time lapse recording of WT and *Tmc* amnioserosa at elliptical phase. Cells are coloured according to the phase of the oscillation, each colour uniquely representing a phase angle between 0 and 2pi. The phase has been extracted from the original cell area time series using a Hilbert transform.

Video 4. Cell pairs with synchronous oscillation in the cell area. Time-lapse recording of amnioserosa cells (top panel) at elliptical stage in wild type embryos expressing E-Cad-GFP. Cell area trajectories of cross-sections over time from the synchronous cell pairs (bottom panel). The blue and yellow curves are the cell cross-sectional area of the blue and yellow cells on the top panel.

Video 5. Cell pairs with anti-synchronous oscillation in the cell area. Time-lapse recording of amnioserosa cells (top panel) at elliptical stage in wild type embryos expressing E-Cad-GFP. Cell area trajectories of cross-sections over time from the synchronous cell pairs (bottom panel). The blue and yellow curves are the cell cross-sectional area of the blue and yellow cells on the top panel.

Video 6. Model simulations with roughly 150 cells in a hexagonal packing. The colour code represents the phase of each oscillator. Intermediate Ca^{2+} coupling (middle panel), or strong Ca^{2+} coupling (bottom panel) induces spatial synchronization of neighbouring oscillators. In top panel, cell pairs remain unsynchronized without any coupling.

Video 7. Neighbouring cells respond to optochemically induced rapid cell contraction. Time lapse recordings of amnioserosa cells at elliptical phase from the wild type (top panel) and *Tmc* (bottom panel) embryos expressing E-Cad-GFP. Rapid cell contraction in the centre cell (indicated with red dot) was induced optochemically via Ca^{2+} during recoding as in Fig. 4b. The colour code represents the size of the cells from large, yellow to small, blue.

Code availability

The custom codes used to process images analyse data, and run simulations are available upon reasonable request.

Chapter 8

Synchronization of cell quadruplets drive efficient T1 transitions

"One is not struck by the truth until prompted quite accidentally by some external event."

Kazuo Ishiguro

8.1 Content

Epithelial morphogenesis is driven by active local processes which have to be orchestrated to yield global robust tissue rearrangements. One of these processes are T1 transitions, which are local neighbor exchanges that collectively drive germband convergent extension during gastrulation.

In this study, we show that cell quadruplet synchronization drives efficient cell intercalation. The identified coordination mechanism is dependent on *xit*, a mutant that affects E-Cadherin glycolization in adherens junctions, which suggests an essential function for E-Cadherin as mechanosensitive signal transducer to orchestrate directed neighbor exchanges. Experimental findings were possible due to automated large-scale data acquisition and analysis of >1000 T1 transitions. Results from experiments are supplemented by a mathematical study.

Analysis of morphogenetic tissue rearrangements has largely relied on the analysis of single cell behavior so far. We developed large-scale experimental and analytical methods to gain the statistical power needed to interpret T1 dynamics as a directed stochastic process. In addition, we applied Ca^{2+} uncaging as an optochemical tool to induce cell contractions and directly interfere with neighbor exchanges. We can induce the formation of new cell contacts *in vivo* by triggering contraction in the participating anterior and posterior cells. This cell contact formation is dependent on *xit*.

We further investigate the cell junction formation using our large *in vivo* data set and find that the formation of a new junction is exhibiting a stochastic attempt phase, which is flanked by contact collapse before the transition and junction elongation afterwards. Attempt phase durations vary widely, but are consistent with a constant probability of extension phase initiation. The transit time of the attempt is significantly shorter in wild type compared to *xit* mutants.

For consistent interpretation of the experimental findings it was crucial to develop a mathematical theory of the stochastic coordination and its topological constraints. It is shown that

correlation coefficients are bounded because of conservation constraints, which are stronger in hexagonal topologies compared to square packing. Simulations of T1 transitions predict time-dependent intercellular correlations even for constant intercellular coupling. A strong enhancement of simultaneous contraction probability can be achieved by constriction of A-P cells during the attempt phase.

Ensemble analysis of the experimental data shows the existence of phase-dependent and maintained differential contraction of quadruplet cells entering the attempt phase. Hereby, *xit* quadruplet cells fail to maintain differential contraction states. Correlation analysis of contractions reveals stage-dependent cell-by-cell coordination in WT but not in *xit*. Hereby, average WT correlations are negative and near the theoretical limit for short-range correlations whereas *xit* shows a strong influence of mean correlations which are specifically enhanced during T1 transitions.

Time resolved phase-dependent correlation analysis reveals that coordinated contractions are reduced and phase-insensitive both in *xit* and with E-Cadherin knock-down respectively. Irrespective of the specific genotype, successful cell contact extension are always triggered by a peak in the anti-correlation of next neighbor cells (AP and DV). The coordinated cell area fluctuations indicate a time-dependent switching of intracellular coupling.

In this chapter we present first direct evidence that contractions of cells during T1 transitions are coordinated and that this coordination is mediated by *xit*. Cells are linked via E-Cadherin complexes at the cell-cell junction that also have mechanosensory function. *xit* mutants show loss of efficiency and are unable to regulate coordination in a time dependent manner. E-Cadherin therefore constitutes an essential component for a molecular coordination mechanism regulating active stresses during morphogenesis.

The Ca^{2+} uncaging method CaLM, developed in chapter 3, is applied in this investigation.

8.2 Cell quadruplets synchronize on the fly to drive efficient cell intercalation

This chapter includes a draft of a manuscript, intended for later publication in a scientific journal.

Original contribution

Jörg Großhans and Fred Wolf conceived the study. Deqing Kong conducted the experiments. Lars Reichel and **Matthias Häring** performed the quantitative analysis. Lars Reichel implemented the data acquisition pipeline. Stephan Eule and FW developed the analytical theory of intercellular coordination with input from **MH** and Jacob Metzger. JM performed numerical simulations. DK, **MH**, FW and JG analyzed the results. DK, **MH**, FW and JG wrote the manuscript with comments from all authors.

Deqing Kong and **Matthias Häring** contributed equally.

References

References are included in the manuscript.

Cell quadruplets synchronize *on the fly* to drive efficient cell intercalation

Deqing Kong[1, 7], Matthias Häring[2–5, 7], Lars Reichl[2], Jakob Metzger[6], Stefan Eule[2], Fred Wolf[2–5, 8 *], Jörg Großhans[1, 4, 8 *]

1 Department of Biology, Philipps University, Karl-von-Frisch-Str. 8, 35043 Marburg, Germany
2 Max Planck Institute for Dynamics and Self-Organization, Am Faßberg 17, 37077 Göttingen, Germany
3 Institute for Dynamics of Complex Systems, Georg August University, Friedrich Hund Pl. 1, 37077 Göttingen, Germany
4 Göttingen Campus Institute for Dynamics of Biological Networks, Georg August University, Hermann Rein Str. 3, 37075 Göttingen, Germany
5 Max Planck Institute for Experimental Medicine, Hermann Rein St. 3, 37075 Göttingen, Germany
6 Max Delbrück Center for Molecular Medicine in the Helmholtz Association (MDC), Berlin Institute for Medical Systems Biology (BIMSB), Hannoversche Str. 28, 10115 Berlin, Germany
7 These authors contributed equally: Deqing Kong, Matthias Häring
8 These authors supervised the project: Fred Wolf, Jörg Großhans

Summary

Synchronized contractility enhances the effective force[1] within tissues and might be critical for the effectiveness and economic deployment of cellular force generators in animal morphogenesis[2–4]. In dynamic tissues of developing embryos, however, no global synchronizing signal exists and cell contacts that may support local synchronization are continuously lost, formed, and remodelled; existing perhaps too fleetingly to mediate synchronizing interactions. Here we demonstrate that exactly in the act of breaking and making new contacts, cell quadruplets in Drosophila embryos synchronize their contractile activity to enhance the speed and efficiency of embryo axis elongation. We show that synchronized contraction and expansion of cells within cell quadruplets is an actively coordinated process, which initiates successful cell contact elongation and strongly increases the success rate of stochastic elongation attempts. Using a novel theory of stochastic epithelial cell synchronization, large-scale analysis and computational modelling we uncover that cell quadruplets activate fast and specific signal transduction pathways in a precisely timed manner to achieve synchronization only when needed. Thus, epithelial cells actively synchronize their contractile activity *on the fly*, acting as a smart collective in morphogenetic force generation.

On all levels of biological organization, from animal groups (1) to organs (2) and tissues (3), synchronization of single cell activities can enhance the efficiency of biological function. Prominently, in systems of excitable cells, such as muscles or neural circuits, synchronized action across groups of cells enables the generation of forces (4) and information streams (5) that individual cells could not achieve.

In animal embryos, many morphogenetic transformations are driven by populations of force generating epithelial cells (6,7,8), which - in contrast to e.g. myocytes with their ordered arrangement of contractile fibres - are not designed for maximal force generation (9). Synchronization of individual cells may thus substantially expand the dynamic range of morphogenetic forces. Given the softness of embryonic tissue components (10) mild levels of synchronization may already be of substantial impact. We thus examined the occurrence, strength, type, and impact of morphodynamic synchronization in a prototypical example of embryonic tissue remodelling, i.e. germband extension driven by cell intercalation and T1-type neighbour exchanges in cell quadruplets in Drosophila embryos.

Pulsed contractions have been implicated in intercalation (11) but their coordination and relative timing has not been investigated (Fig. 1a). We thus interrogated intercalation dynamics by optochemically induced synchronization of cell contractions (12) and harvested large samples of T1 transitions by live-imaging to examine intrinsically generated patterns of cell synchronization.

Intercellular synchronization promotes new junction formation.

We optochemically induced contraction in one or two cells within quadruplets undergoing intercalation at the 4x vertex stage by Ca^{2+} uncaging[21] (Fig. 1b–d, Extended Data Fig. 1, Video1–4). Comparisons of area trajectories and junction dynamics showed that induced contraction in A and P cells did not interfere with the resolution of the 4x vertices and formation of a new junction[18,19]. First, we tested the impact of synchronous cell contractions of 4x vertex resolution by inducing contraction in opposing cell pairs. 4x vertices were resolved only when the contraction was synchronously induced in opposing cell pairs (A+P or D+V) (Fig. 1c, Extended Data Fig. 1a–c, Video 2) but not when we induced contraction of the second cell with a delay (Fig. 1c, Extended Data Fig. 1a–c, Video 3). Consistent with a synchronicity condition, induced contraction in only one of the two new neighbours (D, V) often arrested 4x vertex resolution (Fig. 1c, Extended Data Fig. 1a–c, Video 4). Our data thus demonstrate that 4x vertex resolution and subsequent neighbour exchange in cell quadruplets can be promoted by synchronous cell contractions in opposing cell pairs. Simultaneous to the contraction of old neighbours, new neighbours must not contract (Fig. 1c, Extended Data Fig. 1a–c, Video 4), suggesting a need for coordination between contracting old neighbours and not-contracting new neighbours.

xiantuan (*xit*) is required for germband extension[22] which encodes a glucosyl-transferase in the N-glycosylation pathway leading to hypo-N-glycosylation of E-Cadherin (E-Cad) and possibly other membrane proteins[22]. We induced contraction in one or two cells of T1 quadruplets and tested the resolution of 4x vertices in *xit* embryos. In contrast to wild type, we found that neither synchronous nor single induced cell contractions promoted junction formation and 4x vertex resolution (Fig. 1d, Extended Data Fig. 1d–f). Despite the successfully induced contraction in the AP neighbour cells, no new junction was established between the DV cells. Thus, the induction of a force dipole by simultaneous contraction of opposing cells per se is not sufficient to drive new junction formation. Among the conceivable functions compromised in *xit* embryos is coordination by signal transduction between cells in the quadruplet.

To assess such coordination mechanisms, we used two more assays. Firstly, next neighbours responded to induced contraction of a target cell by increased fluctuations (area variance) in wild type but not *xit* embryos (Fig. 1e, Extended Data Fig. 2a). Further distant cells in the same tissue served as control. The increased area variance points to an active response, which is not simply due to area conservation, since we did not detect a similar response in *xit* mutant embryos (Fig. 1e, Extended Data Fig. 2a, b). Secondly, we recorded cell oscillations in the amnioserosa as a sensitive readout of cell behaviour[23,24]. As previously reported, cell oscillations were dampened after junction cut or cell ablation in the neighbourhood[23,24]. As expected we observed a drop in area variance from 250 to 50 μm^4 in wild type (Fig. 1f, Extended Data Fig. 2c, Video 5). In contrast, oscillations persisted in *xit* embryos, as indicated by a weak drop in area variance from about 200 to 150 μm^4 (Fig. 1f, Extended Data Fig. 2c, Video 5). Xit is thus required for morphodynamic neighbour cell responses.

In summary, the above observations show that AP cell synchronization is a strong but strictly *xit*-dependent driver for the completion of intercalation by new junction formation. It is unclear, however, whether and when synchronization is in fact deployed during the physiological intercalation.

Stochastic resolution of 4x vertices

To address this question, we next examined the kinetics of germband extension and neighbour exchange in large ensembles of WT and *xit* embryos. Germband extension has been associated with a solid-fluid transition, which can be assessed by simple geometric parameters. Since germband extension is impaired in *xit* embryos, we first assessed whether this fluidization transition was affected. Surprisingly, we found that germband tissue appears as fluidized in *xit* as in WT (Extended Data Fig. 3).

We next assessed the detailed kinetics of neighbour exchanges and junctions dynamics. For this we specifically harvested hundreds of quadruplets in T1 transitions (Extended Data Fig. 4) from wild type (N=630) and *xit* mutant embryos (N=981). We found a striking diversity in the behaviour of quadruplets (Fig. 2a, b and Video 6). Beside textbook-like T1 transitions with prompt resolution of the 4x vertex by junction elongation, many T1 transitions exhibited meta-stable 4x vertices, which resolved only after several minutes in some cases. The meta-stable cases exhibited fluctuations with short junctions temporarily forming in both directions (Fig. 2a, b, and Extended Data Fig. 5a). We also observed non-productive cases when the 4x vertex resolved in the reverse direction (Fig. 2a, Video 6).

For quantification of the dynamics, we defined two points of reference: the time of the first as well as the last 4x vertex (Fig. 2a, b). The „attempt“ phase is defined as the period between the first and last 4x vertex, following the collapse phase and preceding the elongation phase (Fig. 2b). The trace during the attempt phase is plotted twice, following the first 4x and prior to the last 4x vertex. We then analysed junction dynamics in detail (Fig. 2c, Extended Data Fig. 5d, e). The kinetics of collapse, as well as elongation, were comparable in shape and extent between wild type and *xit* embryos. Junctions collapsed with a speed of about 1 µm / min and elongated comparably in forward and reverse cases. The length of the other four junctions within the quadruplet did change much less in both wild type and *xit* embryos (Extended Data Fig. 5e). During the attempt phase, the 4x vertex transiently resolved with junction lengths fluctuating up to ≈1 µm (Fig. 2c, Extended Data Fig. 5d).

We calculated the exit rates from attempt phase by fitting an exponential distribution to the histogram of attempt durations. The distributions for wild type and xit both collapse by rescaling, which indicates that both follow the same process but with different rates. The attempt phases in *xit* mutants are longer, with an average attempt length of 4.6 min, than in wild type, where the attempt phase takes 2.8 min on average (Fig. 2d, e, Extended Data Fig. 5f). The transition from attempt to elongation phase is therefore consistent with a stochastic process with a constant rate of completion (Fig. 2e, Extended Data Fig. 5f). The proportion of reversed vertex resolutions, which completes the attempt with a junction between A and P cells, was also higher in *xit* than in wild type (27% in *xit* versus 12% in wild type embryos, see Fig. 2e). In contrast, collapse and elongation proceed with similar speed for both genotypes. Thus, the *xit* mutant specifically affected exit rates of the attempt phase and proportion of successful junction elongation events. We therefore hypothesized that there is a *xit*-dependent and phase-specific synchronization mechanisms that promotes a fast initiation of junction elongation.

Modelling collective cell area fluctuations in dynamic epithelia

Any pattern of synchronized contractions, whether spontaneous or induced by physiological interactions will be superimposed on a background of other cell shape fluctuations. In addition, the potentially fleeting nature of synchronization and the ongoing topological remodelling of intercalating cell quadruplets enhances the complexity of measuring and detecting intercellular synchronization. We thus first used mathematical models to examine the expected magnitude of statistical correlations between cells, to assess whether changing topology by itself may induce phase-specific synchronization and to explore how the frequency of synchronized AP contractions could be physiologically controlled.

We modelled fluctuations in cell cross-sectional area as a multivariate statistical process (Fig. 3a). Assuming fluctuations of different cells to be statistically similar, we allowed for distinct statistical dependencies between cells that could range from anti-correlation, such that contraction of one cell is systematically associated with the expansion of another, to statistical independence to positive correlations, indicating synchronization of contractions in different cells. As a readout of between-cell coordination, we analysed correlations between arbitrary cell pairs in an extended epithelium and nearest-neighbour and next-nearest-neighbour correlations between pairs of cells in quadruplets.

In principle, correlation coefficients between pairs of dynamical variables can assume any value between –1 (complete anti-correlation) and 1 (total synchrony). In stochastic systems with many dynamical elements and spatial organization, however, correlation coefficients are additionally constrained by collective effects and self-consistency requirements. Next-nearest-neighbour correlations, for instance, must be consistent with nearest-neighbour correlations and even nearest-neighbour correlations cannot assume arbitrary values if a cell has multiple neighbours. With total area conservation, we find that the law of total variance implies average pairwise correlations to be negative and very small (Fig. 3b). If correlation coefficients are negligible beyond local m-cell clusters, the average correlation coefficient cannot be more negative than –(m–1)-1. With substantial correlations confined to nearest neighbours the magnitude of correlations, 0.16, is thus predicted to be small in a generic or hexagonal epithelium (m = 6). If correlations in fact are of such low magnitude, low noise measurements and large ensembles of observations are strictly required to detect and characterize coordinated behaviour (Extended Data Fig. 6).

Topologically induced and specific patterns of synchronization

In local groups of cells, such as an intercalating quadruplet, total area is not a strictly conserved quantity. We thus next examined bounds on nearest- and next-nearest-neighbour correlations in the main topologies (hexagonal and square) through which intercalation progresses. We find that in both topologies admissible correlations are substantially constrained by the requirement that the covariance matrix is positive definite. Reflecting geometric frustration at threefold vertices, hexagonal epithelia are more strongly constrained than square topologies (Fig. 3c). Assuming a single dominant timescale for the relaxation of cross-sectional area fluctuations and uniform next-neighbour physiological coupling, in a model of interacting cells, we find next-nearest-neighbour correlations to be generally positive (Fig. 3d). Except for very weak coupling, correlations generally differ between topologies for identical coupling strengths.

As intercalation involves a transition from hexagonal to square to hexagonal topology, AP pairs turn from nearest-neighbour into next-nearest neighbour. A transition from AP anti-correlation to AP synchronization with the onset of the attempt phase is expected to happen for topological reasons (Fig. 3e). For a weak overall magnitude of correlations, the resulting rise in the rate of simultaneous contractions is relatively modest. It can, however, be boosted by phase-dependent additional couplings or synchronized contraction during the attempt phase overall (Fig. 3f).

***xit*- and phase-dependent synchronization in T1 quadruplets**

Having considered constraints imposed by topology, we analysed the recorded area dynamics of quadruplets in detail. Averaged area trajectories of old (A, P) and new (D, V) neighbours strikingly diverged (Fig. 4a, Extended Data Fig. 7a). While new neighbours expanded during the last two minutes of the collapse phase, old neighbours maintained their size. A small but pronounced dip was observed for old neighbours at the time of the first 4x vertex. During attempt phase, the difference between old and new neighbours persisted. Area trajectories were more similar in *xit* embryos, especially during attempt phase (Fig. 4a). At the onset of elongation phase, old neighbours contracted by about 2.5%, while new neighbours further expanded. A contraction of old neighbours is also seen in *xit* embryos albeit less pronounced. We detected similar relationships for the cell

perimeters (Extended Data Fig. 7b). The less pronounced changes in the averaged area in *xit* embryos (about 5% versus 10% in wild type during collapse phase) may be due to weaker cell activity in *xit* embryos or to a less synchronized individual behaviour. We quantified the total area changes by the auto-covariance of the quadruplets (Extended Data Fig. 7c). Our data point to a loss of synchronization in *xit* embryos, as we detected a comparable degree of cellular activities in wild type and *xit* embryos. The auto-covariance was even slightly higher in *xit* embryos than in wild type. Our data is consistent with the notion, that coordination is impaired between the four cells of a quadruplet in *xit* embryos. In summary, we provided support for the coordination hypothesis. The analysis of average area dynamics revealed stereotypic patterns with divergent areas of old and new neighbours as the most prominent feature. The difference between wild type and *xit* embryos indicates that *xit* promotes and maintains a divergence of area trajectories during collapse and attempt phase despite a similar degree of area fluctuations.

Having analysed averaged trajectories, we systematically compared the four individual area trajectories within quadruplets to each other. We calculated cross-covariance functions of area changes for all six pairwise combinations (Fig. 4b, Extended Data Fig. 7d). AP and DV pairs represent next-nearest neighbours, at least for some part of the T1 transition, whereas the other pairs represent next neighbours for the complete T1 transition. We found negative correlations in four pairs and positive correlations in two pairs during collapse, attempt and extension phases (Fig. 4b, c and Extended Data Fig. 7d). We also detected a positive correlation of the DV pair during the collapse phase, when they were not in contact with each other. This may be due to coupling of two anti-correlated neighbours (DA and AV). The new junction during the elongation phase did not show any significant coupling behaviour between the D and V cells, indicating an insensitivity of this new junction. For all six pairs, the peaks of the cross-covariance were at $\tau=0$, indicating that cells are linked without a measurable time lag. These features were less pronounced in *xit* than in wild type embryos (Extended Data Fig. 7d). This analysis suggests that cell junctions mediate anti-correlated behaviour except for a T1 specific behaviour of the collapsing AP and newly forming DV junctions.

We averaged area correlations of negatively coupled maintained neighbour pairs over three minutes after the first 4x in comparison to random cell pairs (Extended Data Fig. 7d). We obtained a correlation of $c_1(t) = -0.14$, which was significantly higher than in *xit* embryos –0.06 and in random cell pairs –0.04 (Fig. 4d). In contrast to correlations between area changes, a stronger correlation was detected between changes in the area and junction length, which was not *xit*-dependent, however, and may be due to geometrical constraints (Extended Data Fig. 7e). In summary, our correlation analysis within individual quadruplets identified a T1 specific and *xit*-dependent coordination between area fluctuations.

Next, we separately averaged maintained neighbours and opposite pairs and applied time-resolved ensemble statistics by correlating the ensembles of trajectories of old and new neighbours (Fig. 4e, f). The resulting correlation maps uncovered negative correlations along the diagonal for the maintained pairs (Fig. 4f). This indicates that the strongest correlations of area changes are observed without a time lag. Conversely, positive correlations were detected for the AP and DV pairs elongation phases. The degree of both positive and negative correlation was *xit* dependent since they were both strongly reduced in *xit* embryos (Fig. 4f).

We further analysed the weak negative correlation in area fluctuations within random cell pairs. This correlation may be a simple consequence of area preservation or reflect an active response to a contracting neighbour. According to the first option, we would expect no dependence on the junction orientation of the neighbours. Plotting the correlation of area fluctuations against the junction angle revealed a dependence on orientation (Extended Data Fig. 7f). Random cell pairs with an AP junction anti-correlate stronger than duplets with a DV junction. Such a bias was not detected in *xit* embryos. Similarly, correlations at AP and DV junctions were not different in *eve* RNAi embryos,

which are largely devoid of planar polarization [11,25,26]. This finding indicates that also in random cell duplets a *xit*-dependent mechanism exists that coordinates area fluctuations in a manner dependent on planar polarity.

Phase-dependent coordination depends on E-Cad and dynamically switching intercellular coupling

To uncover stage-specific coordination behaviour, we extracted time courses of area cross-correlation with a lag time $\tau = 0$ (Fig 5a, the diagonals of correlation maps in Fig. 4f). The correlation traces clearly diverged between maintained and opposite pairs. During collapse phase, correlation of maintained next neighbour pairs showed a significant valley by the end of junction collapse (t=0, first 4x). During attempt phase the negative correlation of the maintained pairs was almost lost, while the positive correlation of the opposite pairs persisted. During elongation, the positive correlation of next-nearest neighbours decreased, while the correlation of maintained next neighbour pairs had a significant valley at the last 4x with $c_1 \approx -0.15$. In *xit* embryos, both correlation traces remained flat and close to zero except for a statistically significant valley ($c_1 \approx -0.1$) at the onset of elongation. This valley indicates that opposing area changes (contraction versus relaxation) initiate elongation also in *xit* mutants. Our data suggest that *xit*-dependent mechanisms mediate stage-dependent coordinated area changes in T1 quadruplets, divergent changes in maintained next neighbour pairs and synchronized area changes in opposite pairs.

We also calculated correlation functions for perimeters (sum of junction lengths) and for the junctions next to collapsing (AP) and elongating (DV) (Extended Data Fig. 8). We found *xit*-dependent traces with peaks and corresponding valleys for both positively and negatively coupled pairs, respectively for correlations with cell perimeters (Extended Data Fig. 8a). In contrast, the correlations of junction lengths are similar for both wild type and *xit* mutants (Extended Data Fig. 8b).

The molecular nature of *xit*-dependent coordination is unknown. We have previously identified E-Cad as a target of *xit*, since E-Cad is hypo-N-glycosylated and less restricted to the subapical domain in *xit* mutants[22]. E-Cad has previously been shown to be involved in cell intercalation[17,22]. As a complete loss would impair oogenesis[29] and result in a mesenchymal tissue[30], we partially depleted E-Cad by injection of dsRNA[17,22]. In *E-Cad* RNAi embryos, we detected impaired coordination within T1 quadruplets reminiscent to *xit* (Fig. 5b, Extended Data Fig. 9). The probability distribution of attempt phase duration fell between the distributions of wild type and *xit* with a clear fraction of T1 transitions with long attempt phases (Extended Data Fig. 5c, 9a). Similar to *xit*, we found a high proportion (28%) of reversed T1 transitions. Although the averaged areas of old and new neighbours diverged (Extended data Fig. 9b), the correlations were strongly reduced similar to *xit* embryos (Fig. 5a).

We aimed to computationally simulate phase dependent switching of cell coupling by tuning the coupling constant. We achieved phase dependent correlations of the participating cells only with phase-specific coupling between the cell pairs (Fig. 5b, c). A topology-only simulation with constant coupling generated a flat trace comparable to the *xit* and *E-Cad* RNAi data except for the peak at the onset of elongation phase. Therefore, a mere change in topology from hexagonal to square to hexagonal topology is not sufficient to explain the phase-dependent coordination of cell pairs during T1 transition. This shows that *xit* and E-Cad promote phase-specific cell coupling.

Discussion

Our study uncovers an unanticipated degree of flexibility and context-dependence in the active mechanical behaviour of early ectodermal cells. The T1 attempt phase represents an important bottleneck in the dynamics of intercalation. Nearly all quadruplets are unable to directly progress through the 4x vertex state, although it is topologically unstable, and the germband epithelium in a

fluidized state. The metastable dynamics during the attempt phase thus suggests the existence of an additional barrier that needs to be overcome to initiate productive contact elongation. Quadruplet morphodynamic synchronization is specifically activated when this barrier needs to be overcome and strongly accelerates the initiation of productive contact elongation. From a theoretical perspective, this strategic, rapid and transient deployment of synchronization mechanisms precludes the application of most computational methods for the analysis of synchronization such as phase-response curves, stroboscopic maps or cyclo-stationary statistics. The stage resolved, non-stationary ensemble analysis introduced here, should thus provide a versatile framework to quantify and dissect transient synchronization mechanisms in a morphodynamic systems in general.

Most studies so far focused on how myosin contractility contributes to cell intercalation. The planar polarised junctional myosin with pulsatile medial myosin flow along the AP axis is crucial for junction collapse. Pulsed contractions of medial myosin in A and P cells contribute to the growth of new junctions. Our experiments demonstrate that merely contractions in A and/or P cells are insufficient for quadruplets through the 4x vertex state. Rather they are most effective if the contractions are synchronized. The loss of synchronisation and impaired intercalation in *xit* mutants likely result from a specific loss of signalling functions mediated by adherens junctions. Notably, *xit* also disrupts ion-channel mediated synchronisation in the amnioserosa. Morphodynamic synchronisation may thus more generally serve as a sensitive and specific readout of E-Cad's signalling functions. Germband extension is associated with a transition to more fluid-like tissue behaviour emerging from the cell contractility and oriented stress release along tissue extension direction via posterior midgut invagination. Our results show that fluid is only necessary but not sufficient to determine the speed. We propose that phase-dependent synchronisation is an essential element in satisfying rapid morphogenetic events.

Most embryos must complete morphogenesis on a fixed, maternally provided energy budget. Cellular physiology spends this energy budget essentially at a constant rate. Thus, in morphogenesis, speed equals energy efficiency. As embryonic cells harbour a diversity of mechano-transduction mechanisms and apparently are capable of deploying them rapidly and flexibly to coordinate, we expect that developmental systems may generally be under selective pressure to recruit synchronisation mechanisms to increase the efficiency and speed of morphogenetic transformations.

Methods

Fly stocks and genetics. Genetic markers and annotations are described in Flybase[40]. *Drosophila* melanogaster stocks were obtained from the Bloomington stock centre[41], if not otherwise noted in Supplementary Table 1. Flies were crossed at 25°C. Experiments were performed at room temperature (~22°C). *xit* germline clones were generated with a cross of the chromosome *xit* FrtX [9-2] hs-Flp[122] with ovo[D2] FrtX [9-2] and 2X40 min, 37°C heat shocks of larvae(24–72h).

RNAi interference. Double-stranded RNAs (dsRNAs) for the *shotgun (shg)* and *even skipped (eve)* was transcribed from PCR-generated templates containing T7 promoters on both ends. The dsRNA template was amplified by the following primer pairs which were preceded by a T7 promoter sequence (5'-taatacgactcactataggg-3'): *shg* (5'-gagtctctttgataatggcgagc-3', 5'-ggtttccatcgttctggtgaatc-3') [17]; *eve* (5'-ctcgagctgtgaccgccg-3', 5'- tttgtacaatctttgggg-3')[42]. 0–30 min embryos were collected at 25°C and dechorionated, dried in a desiccation chamber for ~8 min, covered with halocarbon oil and injected dorsally with dsRNA (c≈3.5 µg/µl) at room temperature (22°C). After injection, the embryos were aged in a wet chamber for two hours at 25°C. After that, imaging was carried out at room temperature (22°C).

Live imaging. Embryos were mounted as previously described[43]. Briefly, 2.5–3.5 hours' embryos carried multiple copies of GFP markers (2xresilleGFP, 2xspiderGFP, in case of *xit* embryos: 2xresilleGFP, 1xspiderGFP) were dechorionated with 50% hypochloride bleach for 90 s, aligned on a piece of apple-juice agar, transferred to a coated coverslip and covered with halocarbon oil. Time-

lapse image series were recorded with an inverted spinning disc microscope (40x/oil NA 1.3 or 63x/oil NA 1.4, 5 s/frame) with 108x108 μm of the field of view at the lateral range, cephalic furrow as the reference point. As these markers are expressed along the lateral membrane, the projected images contained the averaged position of cell junctions along the apical 5–6 μm.

Laser ablation. E-Cad-GFP or the germline clone of *xit;* E-Cad-GFP flies were used to collect 0–2 h embryos, and the embryos were aged for 15 h at 20°C to yield populations of dorsal closure staged embryos. Dechorionated embryos were aligned on agar block and transferred to a cover slide and dried in a desiccation chamber for 2 min, covered with halocarbon oil. The UV laser (DPSL355/14, 355 nm, 70 μJ/pulse, Rapp Optoelectronic) was introduced from the epi-port of the microscope and was controlled by an independent scanning head (Rapp Optoelectronic)[21,44]. An ablation was carried out at the plane of adherence junction with the 10% of laser power, and the exposure time was 200 milliseconds (around 40 pulses) during recording mode on an inverted spinning disc microscope (Zeiss, 40x/oil, NA1.3) with a CCD camera (Zeiss). After cutting around 30 image stacks with 1 μm Z-interval were recording by a spinning disc microscope (Zeiss, 100x/oil, NA1.4) with an emCCD camera (Photometrics, Evolve 512). The recording started in 1 min after the ablation was done. The image stacks were processed with ImageJ/Fiji[45] by Z-Projection with "Max Intensity" projection.

Ca^{2+} uncaging. Uncaging was conducted as previously described[21]. Briefly, NP-EGTA, AM (2 mM, Invitrogen, in 180 mM NaCl, 10 mM Hepes [pH 7.2], 5 mM KCl, 1 mM $MgCl_2$)[46] was injected into embryos in late cellularization about 10–20 min prior to the uncaging experiment and kept in the dark at 25°C. Ca^{2+} was released by a 355 nm pulsed YAG laser (DPSL-355/14, Rapp OptoElectonic) under the 'Click and Fire' Mode, while a movie was recorded on a spinning disc microscope (Zeiss, 100x/oil, NA1.4). The intensity of the uncaging laser was adjusted so that no morphological changes were induced in 1x injection solution injected embryos. The laser was exposed 1500 milliseconds (around 300 pulses) per cell with 2.5% laser power (~0.5 mJ/cell). The release of Ca^{2+} was controlled with a GCaMP6 sensor protein[47].

Cell junction dynamics in cell quadruplets following Ca^{2+} uncaging. E-Cad-GFP embryos were performed with Ca^{2+} uncaging at the 4X vertices stage, afterwards, 3-4 image stacks with 0.5 μm z-interval were recording by an inverted spinning disc microscope (Zeiss, 100x/oil, NA 1.4, 10 s/frame) with an emCCD camera (Photometrics, Evolve 512). The recording started in 0.5 min after Ca^{2+} uncaging was done. The image stacks were processed with ImageJ/Fiji by Z-Projection with "Max Intensity" projection type. Embryos from the *xit;* E-Cad-GFP germline clone females were performed with Ca^{2+} uncaging at the 4X vertices stage while the images were recording by an inverted spinning disc microscope (Zeiss, 100x/oil, NA1.4, 5 s/frame) with a section at cell junctions. Cell junctions were measured manually with ImageJ/Fiji.

Individual cell area tracking. Images from the Ca^{2+} uncaging and laser ablation experiments were segmented with "Tissue Analyzer"[48] in ImageJ/Fiji, cell area measurements were carried out with ImageJ/Fiji. E-Cad-GFP embryos and embryos from the *xit;* E-Cad-GFP germ line clone females were performed with Ca^{2+} uncaging at single cell while the images were recorded by an inverted spinning disc microscope (Zeiss, 100X/oil, NA 1.4, 5 s/frame) with a section at cell junctions.

Area variance analysis. Images from the Ca^{2+} uncaging and laser ablation experiments were segmented and manual corrected and the cell areas were measured with Embryo Development Geometry Explorer (EDGE)[49]. E-Cad-GFP embryos and embryos from the *xit;* E-Cad-GFP germ line clone females were performed with Ca^{2+} uncaging at single cell while the images were recorded by an inverted spinning disc microscope (Zeiss, 100x/oil, NA 1.4, 5 s/frame) with a section at cell junctions. Control cells for Ca^{2+} uncaging experiments were at least 5 cells away from the target cell in the same embryos being recording. Control cells for laser ablation experiments were from the embryos without laser ablation. Box plot with mean (red horizontal line) and second and third quartile. Black horizontal dash line with whisker, 95% bootstrap confidence intervals.

Quantitative analysis of cell intercalation.

Segmentation of GFP images. Time-lapse images were processed using the Embryo Development Geometry Explorer (EDGE)[49] (http://code.google.com/p/embryo-development-geometry-explorer) and ilastik . Using EDGE, a bandpass filter with typical values 0.1 μm (low pass) and 12 μm (high pass) was applied. Using ilastik, the discrimination between border and background was obtained. In a second step, the prediction maps from ilastik were further processed using particular routines of EDGE that we customized to our needs. Our data acquisition pipeline is fully automated and without manual correction. Instead several custom error correction routines were applied and afterwards still faulty data was disregarded. Identified polygons were tracked over time. Polygons in adjacent images were associated if their centroids differed by less than 4.5 μm and their fractional overlap was larger than 60%, and each polygon contained the centroid of the other. If this criterion failed, up to four subsequent images were examined. Vertices closer than a threshold distance of 0.2 μm were merged into a single vertex. Polygons with area less than 5 μm^2 were removed from the automated segmentation. For some of the analysis we needed the full information of all cells in the tissue. In those cases, we used a custom written automated segmentation pipeline based on deep neural networks and corrected segmentation errors manually using the Tissue Analyzer.

4x vertex life time. The 4x vertex lifetime of a given transition was defined as the shortest time interval in which 4x vertices were identified for the corresponding four cells. From the obtained set of polygons we identified the 4x vertices as the set of vertices that were part of four different edges. In addition, we considered a 4x vertex to be present at timestep *t* if there is a DV (AP) border with length above threshold at timestep $t - 1$ while there is an AP (DV) border with length above threshold at timestep *t* (since a 4x vertex must have existed between these times). We defined the time $t = 0$ by the first occurrence of a 4x vertex in a transition. Time series of the constricting DV edge lengths, the extending AP edge lengths, and the involved cells areas were calculated based on the identified polygons.

Correlation of cells area to border length. The time series of cells area *A* and the new border length *L* were analysed starting from the onset of junction expansion and ending at the saturation of the new border length. For mutants and embryos with tissue cut, cases with extended life time of 4x vertices were selected. Time series were smoothed using a Gaussian filter kernel with width $\sigma_t = 15$ s. For the smoothed time series we calculated the approximate temporal derivatives $\dot{A}$ and $\dot{L}$. For each transition *i* we calculated the cross-covariance

$$\Phi_{AL}^{(i)}(\tau) = 1/(\sigma_{\dot{A}}^{(i)}\sigma_{\dot{L}}^{(i)}N_t)\sum_{t=0}^{N_t-\tau-1}\left(\dot{A}^{(i)}(t+\tau) - \langle\dot{A}^{(i)}\rangle_t\right)\left(\dot{L}^{(i)}(t) - \langle\dot{L}^{(i)}\rangle_t\right),$$

and the auto-covariance

$$\Phi_{AA}^{(i)}(\tau) = 1/N_t\sum_{t=0}^{N_t-\tau-1}\left(\dot{A}^{(i)}(t+\tau) - \langle\dot{A}^{(i)}\rangle_t\right)\left(\dot{A}^{(i)}(t) - \langle\dot{A}^{(i)}\rangle_t\right)$$

at time lag τ and the correlation coefficient $c^{(i)} = \Phi_{AL}^{(i)}(0)$, where

$$\sigma_{\dot{A}}^{(i)} = \sqrt{\frac{1}{N_t}\sum_{t=0}^{N_t-1}\left(\dot{A}^{(i)}(t) - \langle\dot{A}^{(i)}\rangle_t\right)^2},$$

$$\sigma_{\dot{L}}^{(i)} = \sqrt{\frac{1}{N_t}\sum_{t=0}^{N_t-1}\left(\dot{L}^{(i)}(t) - \langle\dot{L}^{(i)}\rangle_t\right)^2},$$

denotes the standard deviation of $\dot{A}^{(i)}$ and $\dot{L}^{(i)}$, $\langle\rangle_t$ denotes the mean over the time interval, and N_t is the number of timesteps. We averaged the cross-covariance and auto-covariance over the number of T1 transitions N_{T1}

$$\Phi_{AL}(\tau) = \frac{1}{N_{T1}}\sum_{i=1}^{N_{T1}}\Phi_{AL}^{(i)}(\tau).$$

$$\Phi_{AA}(\tau) = \frac{1}{N_{T1}} \sum_{i=1}^{N_{T1}} \Phi_{AA}^{(i)}(\tau),$$

In order to obtain the cross-covariance peak position we fitted a parabola to $\Phi_{AL}(\tau)$ in the time interval $\tau = [-0.25, 0.25]$ min. Confidence intervals of the peak position were calculated by bootstrapping over the set of T1 transitions.

Fluidization analysis

We used a method presented in *Wang X., et al., PNAS, (2020)* to explore solid-like and fluid-like states of the germband in both WT and *xit* embryos. Fluidization of the tissue can be assessed via the geometrical quantifiers P and Q. The cell shape index reads P = p/sqrt(A), where p is the perimeter of the cell polygon and A the cell polygon area. Using the average vertex coordination number z, the corrected cell shape index is obtained by P_corr = P - (z-3)/B, where B=3.85. Averaging over all cells per frame yields the data used in the Extended Fig. 3. Cell shape alignment Q is computed using the triangle method described in *Merkel M, et al., Phys Rev E, (2017).* The prediction of the solid-like to fluid-like transition is P_crit = 3.818 + 4bQ^2. Further details can be found in *Wang X., et al., PNAS, (2020).* We processed the data from time-lapse movies via custom written python software. For the extraction of Q we are gratefully acknowledging code published in https://github.com/mmerkel/triangles-segga, which was extended to fit into our analysis pipeline.

Stochastic models for the inter-cellular coordination of contractile activity. We used the theory of stochastic dynamics to model the coordinated contractile activity of epithelial cells and assess signatures of mechano-transduction-mediated and mechanical interactions in intracellular correlations of contractile behaviour. Details of models and calculations are presented in Appendix 1. In brief, the contractile activity of every cell was described by a dynamical variable representing the cell's cross-sectional area

$$a_i(t) = \bar{a}_i + x_i(t)$$

decomposed into average area plus dynamical fluctuations. The dynamics of individual cells was modelled as a stochastic process influence by interactions with neighbouring cells.

To assess general bounds on and the expected magnitude of inter-cellular correlations we determined a universal bound on mean intercellular correlations implied by the law of total variance

$$\overline{\langle x_m(t) x_n(t) \rangle} \geq -\frac{1}{N-1}.$$

Assuming that correlations beyond next neighbours are negligible the average size of next neighbour correlations is bounded by

$$\bar{c}_1^{(K)} \geq -\frac{1}{K\sigma^2}$$

where *K* denotes the number of next-neighbours (coordination number).
If the total area of the tissue is conserved

$$\left\langle \left(\sum_m x_m(t)\right)^2 \right\rangle = 0$$

the above bounds become equalities.

To assess how distinct epithelial topologies may impact inter-cellular correlations, we inferred general bounds on the maximal strength of inter-cellular correlations between next- and next-nearest-neighbours from the property that covariance matrices are positive-definite in general. For square lattices of cell we obtain

$$-1 \leq -\frac{1+c_2}{2} \leq c_1 \leq \frac{1+c_2}{2} \leq 1$$

were c_1 and c_2 denote next- and next-nearest-neighbour correlations. For hexagonal lattices we obtain a set of 5 linear and 2 non-linear bounds that together define the range of admissible inter-cellular correlations (see Appendix 1).

We assessed how changing the coupling strength of intercellular coordination mechanisms impacts on the magnitude of intercellular coordination we assumed that the dynamics of fluctuations in contractile state are captured by a system of first order linear stochastic differential equations

$$\dot{x}_m(t) = \sum_{n=1}^{N^2} W_{m,n}(t) x_n(t) + \eta_m(t)\,,$$

that define a multidimensional Ornstein Uhlenbeck process. With time-dependent interaction strength $W_{m,n}(t)$ this framework allows to model both the effect of changing topology as well as the transient activation of stage-specific interactions. Assuming a fixed topology of the epithelium

$$\begin{aligned}\dot{x}_{m,n}(t) = &-\beta x_{m,n} + \eta_{m,n}(t) \\ &J\left(x_{m+1,n} + x_{m-1,n} + x_{m,n+1} + x_{m,n-1}\right)\end{aligned}$$

for a square lattice and

$$\begin{aligned}\dot{x}_{m,n}(t) = &-\beta x_{m,n} + \eta_{m,n}(t) \\ &+ J\left(x_{m+1,n} + x_{m-1,n} + x_{m,n+1} + x_{m,n-1} + x_{m-1,n+1} + x_{m+1,n-1}\right)\,.\end{aligned} \tag{40}$$

for a hexagonal lattice, we obtained all correlation functions in the model analytically via the spectral decomposition of the model's lattice Green's function. Formulas for dependence of correlations and correlation functions on the inter-cellular coupling constant J are given in Appendix 1.

Numerical simulations. The large number of equations to be simulated require an efficient and reliable implementation. We use a highly efficient strong stochastic Runge-Kutta method of order 1.0[50] which provides fast and accurate simulations of the of the set of coupled stochastic differential equations above. The core of the code is written in C++, which is wrapped by a thin python layer for ease of use. The implementation can easily handle on the order of 100 coupled SDEs on a normal desktop computer. Square and hexagonal as well as the combined lattice, are implemented, as are periodic and non-periodic boundary conditions. The explicit time dependent factors $\alpha(t)$ and $\kappa(t)$ can be naturally included in the stochastic Runge-Kutta scheme. Simulations are then performed with parameters as described in the main text, with lattices of size 10 by 10 and a step size of $\Delta t = 0.01$. Both increasing the lattice and reducing the step size did not significantly affect the results. For big enough lattices such as the ones used here, the effect of the boundary conditions (periodic vs. non-periodic) was found to be negligible. As a check, we first simulated the hexagonal and squared lattices, for which we have calculated the analytical solutions above, and found perfect agreement. We then proceeded to simulate the case of time-dependent transitions that captures important features of the experimentally observed dynamics. For this, we let the system equilibrate from $t = -3$ to $t = 0$, and then simulated a contraction, intermediate and expanding phase as follows. At four different times $t_i = \{2.5,3,7,8\}$, the couplings between different neighbours are updated according to the values $J_1 = \{-0.2,-0.01,-0.2,-0.01\}$ and $J_2 = \{0.2,0.2,0.15,0.01\}$ from their initial values of $J_1 = -0.1$ and $J_2 = 0.1$.

The simulated equation is given by

$$\dot{x}_{m,n}(t) = -\beta x_{m,n} + J_1(t)(x_m+1,n + x_m-1,n + x_{m,n}+1 + x_{m,n}-1) + J_2(t)J(x_m-1,n+1 + x_m+1,n-1) + \eta_{m,n}(t) \tag{1}$$

with $\beta = 1$. For the case of an additional shift in the mean of the cell area, we add a sigmoid to the cell area described by

$$\bar{a}(t) = \frac{\nu\,\eta}{1 + e^{-k(t-t_0)}} \qquad (2)$$

where $v = 1$ for DV and $v = -1$ for AP cells, k=1, $t_0 = 3$ and η is the magnitude of the sigmoid.

References

1 Koenderink, G. H. & Paluch, E. K. Architecture shapes contractility in actomyosin networks. *Curr Opin Cell Biol* **50**, 79-85, doi:https://doi.org/10.1016/j.ceb.2018.01.015 (2018).

2 Solnica-Krezel, L. & Sepich, D. S. Gastrulation: making and shaping germ layers. *Annu Rev Cell Dev Biol* **28**, 687-717, doi:10.1146/annurev-cellbio-092910-154043 (2012).

3 Kasza, K. E. & Zallen, J. A. Dynamics and regulation of contractile actin-myosin networks in morphogenesis. *Curr Opin Cell Biol* **23**, 30-38, doi:10.1016/j.ceb.2010.10.014 (2011).

4 Munjal, A. & Lecuit, T. Actomyosin networks and tissue morphogenesis. *Development* **141**, 1789-1793, doi:10.1242/dev.091645 (2014).

5 Collinet, C. & Lecuit, T. Programmed and self-organized flow of information during morphogenesis. *Nat Rev Mol Cell Biol* **22**, 245-265, doi:10.1038/s41580-020-00318-6 (2021).

6 Murrell, M., Oakes, P. W., Lenz, M. & Gardel, M. L. Forcing cells into shape: the mechanics of actomyosin contractility. *Nat Rev Mol Cell Biol* **16**, 486-498, doi:10.1038/nrm4012 (2015).

7 Clarke, D. N. & Martin, A. C. Actin-based force generation and cell adhesion in tissue morphogenesis. *Curr Biol* **31**, R667-R680, doi:https://doi.org/10.1016/j.cub.2021.03.031 (2021).

8 Lecuit, T., Lenne, P. F. & Munro, E. Force generation, transmission, and integration during cell and tissue morphogenesis. *Annu Rev Cell Dev Biol* **27**, 157-184, doi:10.1146/annurev-cellbio-100109-104027 (2011).

9 Heisenberg, C. P. & Bellaïche, Y. Forces in tissue morphogenesis and patterning. *Cell* **153**, 948-962, doi:10.1016/j.cell.2013.05.008 (2013).

10 Walck-Shannon, E. & Hardin, J. Cell intercalation from top to bottom. *Nat Rev Mol Cell Biol* **15**, 34-48, doi:10.1038/nrm3723 (2014).

11 Irvine, K. D. & Wieschaus, E. Cell intercalation during Drosophila germband extension and its regulation by pair-rule segmentation genes. *Development* **120**, 827-841 (1994).

12 Bertet, C., Sulak, L. & Lecuit, T. Myosin-dependent junction remodelling controls planar cell intercalation and axis elongation. *Nature* **429**, 667-671, doi:10.1038/nature02590 (2004).

13 Blankenship, J. T., Backovic, S. T., Sanny, J. S., Weitz, O. & Zallen, J. A. Multicellular rosette formation links planar cell polarity to tissue morphogenesis. *Dev cell* **11**, 459-470 (2006).

14 Kong, D., Wolf, F. & Grosshans, J. Forces directing germ-band extension in Drosophila embryos. *Mech Dev* **144**, 11-22, doi:10.1016/j.mod.2016.12.001 (2017).

15 Paré, A. C. & Zallen, J. A. Cellular, molecular, and biophysical control of epithelial cell intercalation. *Curr Top Dev Biol* **136**, 167-193, doi:10.1016/bs.ctdb.2019.11.014 (2020).

16 Kong, D. & Großhans, J. Planar Cell Polarity and E-Cadherin in Tissue-Scale Shape Changes in Drosophila Embryos. *Front Cell Dev Biol* **8**, 619958, doi:10.3389/fcell.2020.619958 (2020).

17 Rauzi, M., Lenne, P. F. & Lecuit, T. Planar polarized actomyosin contractile flows control epithelial junction remodelling. *Nature* **468**, 1110-1114, doi:10.1038/nature09566 (2010).

18 Collinet, C., Rauzi, M., Lenne, P.-F. & Lecuit, T. Local and tissue-scale forces drive oriented junction growth during tissue extension. *Nat Cell Biol* **17**, 1247-1258, doi:10.1038/ncb3226 (2015).
19 Yu, J. C. & Fernandez-Gonzalez, R. Local mechanical forces promote polarized junctional assembly and axis elongation in Drosophila. *Elife* **5**, doi:10.7554/eLife.10757 (2016).
20 Stern, T., Streichan, S. J., Shvartsman, S. Y. & Wieschaus, E. F. Deconstructing Gastrulation at the Single Cell Level. *bioRxiv*, 2021.2009.2016.460711, doi:10.1101/2021.09.16.460711 (2021).
21 Kong, D. *et al.* In vivo optochemical control of cell contractility at single-cell resolution. *EMBO Rep* **20**, e47755, doi:10.15252/embr.201947755 (2019).
22 Zhang, Y. *et al.* The glucosyltransferase Xiantuan of the endoplasmic reticulum specifically affects E-Cadherin expression and is required for gastrulation movements in Drosophila. *Dev Biol* **390**, 208-220, doi:10.1016/j.ydbio.2014.03.007 (2014).
23 Solon, J., Kaya-Copur, A., Colombelli, J. & Brunner, D. Pulsed forces timed by a ratchet-like mechanism drive directed tissue movement during dorsal closure. *Cell* **137**, 1331-1342, doi:10.1016/j.cell.2009.03.050 (2009).
24 Jayasinghe, A. K., Crews, S. M., Mashburn, D. N. & Hutson, M. S. Apical oscillations in amnioserosa cells: basolateral coupling and mechanical autonomy. *Biophys J* **105**, 255-265, doi:10.1016/j.bpj.2013.05.027 (2013).
25 Bertet, C. & Lecuit, T. Planar polarity and short-range polarization in Drosophila embryos. *Semin Cell Dev Biol* **20**, 1006-1013, doi:10.1016/j.semcdb.2009.05.004 (2009).
26 Zallen, J. A. & Wieschaus, E. Patterned gene expression directs bipolar planar polarity in Drosophila. *Dev Cell* **6**, 343-355, doi:10.1016/s1534-5807(04)00060-7 (2004).
27 Martin, A. C., Kaschube, M. & Wieschaus, E. F. Pulsed contractions of an actin–myosin network drive apical constriction. *Nature* **457**, 495-499 (2009).
28 Garcia De Las Bayonas, A., Philippe, J. M., Lellouch, A. C. & Lecuit, T. Distinct RhoGEFs Activate Apical and Junctional Contractility under Control of G Proteins during Epithelial Morphogenesis. *Curr Biol* **29**, 3370-3385.e3377, doi:10.1016/j.cub.2019.08.017 (2019).
29 Niewiadomska, P., Godt, D. & Tepass, U. DE-Cadherin is required for intercellular motility during Drosophila oogenesis. *J Cell Biol* **144**, 533-547, doi:10.1083/jcb.144.3.533 (1999).
30 Knust, E. & Leptin, M. Adherens junctions in the Drosophila embryo: the role of E-cadherin in their establishment and morphogenetic function. *Bioessays* **18**, 609-612, doi:10.1002/bies.950180802 (1996).
31 Stephens, D. J. & Allan, V. J. Light Microscopy Techniques for Live Cell Imaging. *Science* **300**, 82-86, doi:doi:10.1126/science.1082160 (2003).
32 Stelzer, E. H. K. *et al.* Light sheet fluorescence microscopy. *Nat Rev Met Pri* **1**, 73, doi:10.1038/s43586-021-00069-4 (2021).
33 Keller, P. J. Imaging morphogenesis: technological advances and biological insights. *Science* **340**, 1234168, doi:10.1126/science.1234168 (2013).
34 McDole, K. *et al.* In Toto Imaging and Reconstruction of Post-Implantation Mouse Development at the Single-Cell Level. *Cell* **175**, 859-876.e833, doi:10.1016/j.cell.2018.09.031 (2018).
35 Wan, Y., McDole, K. & Keller, P. J. Light-Sheet Microscopy and Its Potential for Understanding Developmental Processes. *Annu Rev Cell Dev Biol* **35**, 655-681, doi:10.1146/annurev-cellbio-100818-125311 (2019).
36 Häring, M., Großhans, J., Wolf, F. & Eule, S. Automated Segmentation of Epithelial Tissue Using Cycle-Consistent Generative Adversarial Networks. *bioRxiv*, 311373, doi:10.1101/311373 (2018).

37 Lugagne, J.-B., Lin, H. & Dunlop, M. J. DeLTA: Automated cell segmentation, tracking, and lineage reconstruction using deep learning. *PLOS Comp Biol* **16**, e1007673, doi:10.1371/journal.pcbi.1007673 (2020).
38 Stern, T., Shvartsman, S. Y. & Wieschaus, E. F. Template-based mapping of dynamic motifs in tissue morphogenesis. *PLOS Comp Biol* **16**, doi:10.1371/journal.pcbi.1008049 (2020).
39 Stegmaier, J. *et al.* Real-Time Three-Dimensional Cell Segmentation in Large-Scale Microscopy Data of Developing Embryos. *Dev Cell* **36**, 225-240, doi:10.1016/j.devcel.2015.12.028 (2016).
40 Thurmond, J. *et al.* FlyBase 2.0: the next generation. *Nucleic Acids Res* **47**, D759-d765, doi:10.1093/nar/gky1003 (2019).
41 Whitworth, C. in *The Biological Resources of Model Organisms* (ed Robert L. Jarret and Kevin McCluskey) Ch. Chapter 8, 145–162 (CRC Press, Taylor & Francis Group, 2019).
42 Sen, J., Goltz, J. S., Stevens, L. & Stein, D. Spatially restricted expression of pipe in the Drosophila egg chamber defines embryonic dorsal-ventral polarity. *Cell* **95**, 471-481, doi:10.1016/s0092-8674(00)81615-3 (1998).
43 Wenzl, C., Yan, S., Laupsien, P. & Grosshans, J. Localization of RhoGEF2 during Drosophila cellularization is developmentally controlled by Slam. *Mech Dev* **127**, 371-384, doi:10.1016/j.mod.2010.01.001 (2010).
44 Lv, Z. *et al.* The Emergent Yo-yo Movement of Nuclei Driven by Cytoskeletal Remodeling in Pseudo-synchronous Mitotic Cycles. *Curr Biol* **30**, 2564-2573.e2565, doi:10.1016/j.cub.2020.04.078 (2020).
45 Schindelin, J. *et al.* Fiji: an open-source platform for biological-image analysis. *Nat Methods* **9**, 676-682, doi:10.1038/nmeth.2019 (2012).
46 Hunter, G. L., Crawford, J. M., Genkins, J. Z. & Kiehart, D. P. Ion channels contribute to the regulation of cell sheet forces during Drosophila dorsal closure. *Development* **141**, 325-334, doi:10.1242/dev.097097 (2014).
47 Chen, T. W. *et al.* Ultrasensitive fluorescent proteins for imaging neuronal activity. *Nature* **499**, 295-300, doi:10.1038/nature12354 (2013).
48 Aigouy, B., Collinet, C., Merkel, M. & Sagner, A. in *Cell Polarity and Morphogenesis* Vol. 139 *Methods in Cell Biol* (ed T. Lecuit) 121-+ (2017).
49 Gelbart, M. A. *et al.* Volume conservation principle involved in cell lengthening and nucleus movement during tissue morphogenesis. *Proc Natl Acad Sci U S A* **109**, 19298-19303, doi:10.1073/pnas.1205258109 (2012).
50 Rößler, A. Runge–Kutta Methods for the Strong Approximation of Solutions of Stochastic Differential Equations. *SIAM Journal on Numerical Analysis* **48**, 922-952, doi:10.1137/09076636x (2010).
51 Huang, J., Zhou, W., Dong, W., Watson, A. M. & Hong, Y. From the Cover: Directed, efficient, and versatile modifications of the Drosophila genome by genomic engineering. *Proc Natl Acad Sci U S A* **106**, 8284-8289, doi:10.1073/pnas.0900641106 (2009).
52 Chou, T. B. & Perrimon, N. Use of a yeast site-specific recombinase to produce female germline chimeras in Drosophila. *Genetics* **131**, 643-653 (1992).
53 Vogt, N., Koch, I., Schwarz, H., Schnorrer, F. & Nüsslein-Volhard, C. The γTuRC components Grip75 and Grip128 have an essential microtubule-anchoring function in the Drosophila germline. *Development* **133**, 3963-3972 (2006).

Achnowlegements

We are grateful F Schnorrer, Y Hong, T Lecuit, M Silles ……. for materials. We acknowledge service support from the Bloomington Drosophila Stock Center (supported by NIH P40OD018537). This work was in part supported by and the Deutsche Forschungsgemeinschaft (DFG FOR1756, GR1945/8-2, GR1945/10-1/2 and WO/ 1, equipment grant INST 160/718-1, INST1525/16-1

FUGG).

Author contributions

JG and FW conceived the study. DK conducted the experiments. MH and LR performed the quantitative analysis. LR implemented the data acquisition pipeline. SE and FW developed the analytical theory of intercellular coordination with input from MH and JM. JM performed numerical simulations. DK, MH, FW and JG analyzed the results. DK, MH, FW and JG wrote the manuscript with comments from all authors.

Conflict of interest

The authors declare that they have no conflict of interest.

Materials & Correspondence

Jörg Großhans (grosshan@uni-marburg.de)
Fred Wolf (fred.wolf@ds.mpg.de)

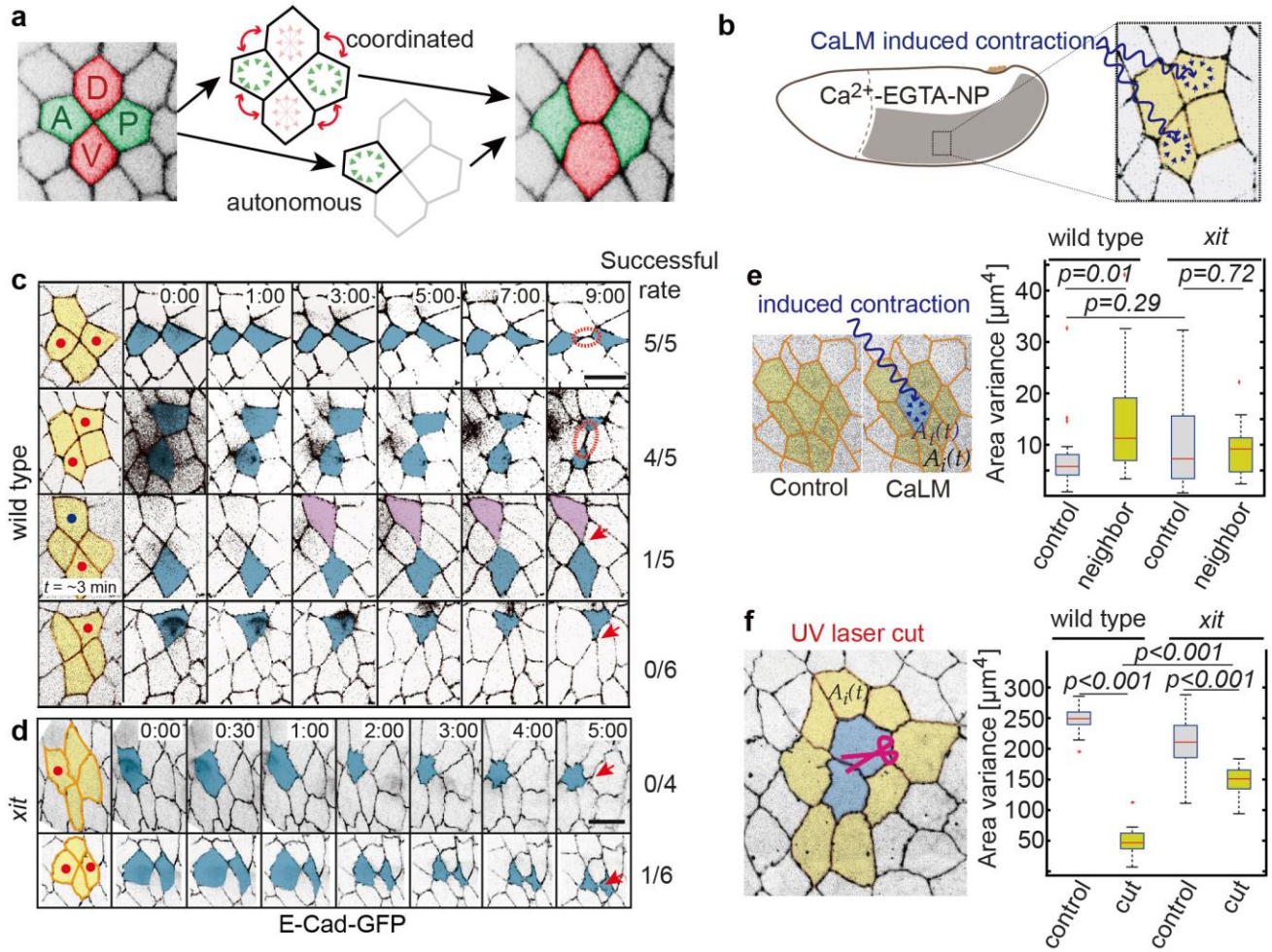

664 **Fig. 1 Intercellular synchronization promotes formation of cell contacts. a,** Autonomous or
665 coordinated cellular contractility resolves a 4x vertex in an epithelial cell. Old neighbours (A, P,
666 green), new neighbours (D, V, red). **b**, Optically triggered contractility in selected individual cells by
667 Ca^{2+} uncaging. EGTA-nitrophenol, cage. **c**, **d,** Triggered cell contraction during neighbour
668 exchanges in wild type (c) and *xit* (d) embryos. Triggered contractions in single and pairwise
669 (synchronous, asynchronous, 3 min time lag) cells of a quadruplet. Red dots indicate the target cells.
670 Blue dot indicates second laser pulse delayed by 3 min in purple cell. Arrow in red points to
671 elongating junction. The number of cases with an elongating junction is indicated by success rate. **e**,
672 Response of next neighbours (yellow) to cell with triggered contractility (blue) in wild type and *xit*
673 embryos. **f,** Response of next neighbours (yellow) to junction ablation (blue) in the amnioserosa of
674 wild type and *xit* embryos. **e, f**, Area variance of next neighbours and further distant control cells.
675 The *p* values were estimated by a two-sided *t*-test. Number of cells: **(e)**, control 28, neighbour 24
676 from 3 wild type embryos and control 20, neighbour 15 from 3 *xit* embryos; **(f)** control 100,
677 neighbour 106 from 15 wild type embryos and control 100, neighbour 75 from 15 *xit* embryos. Cell
678 junctions in embryos labelled with E-Cadherin-GFP. Scale bars: 10 µm.

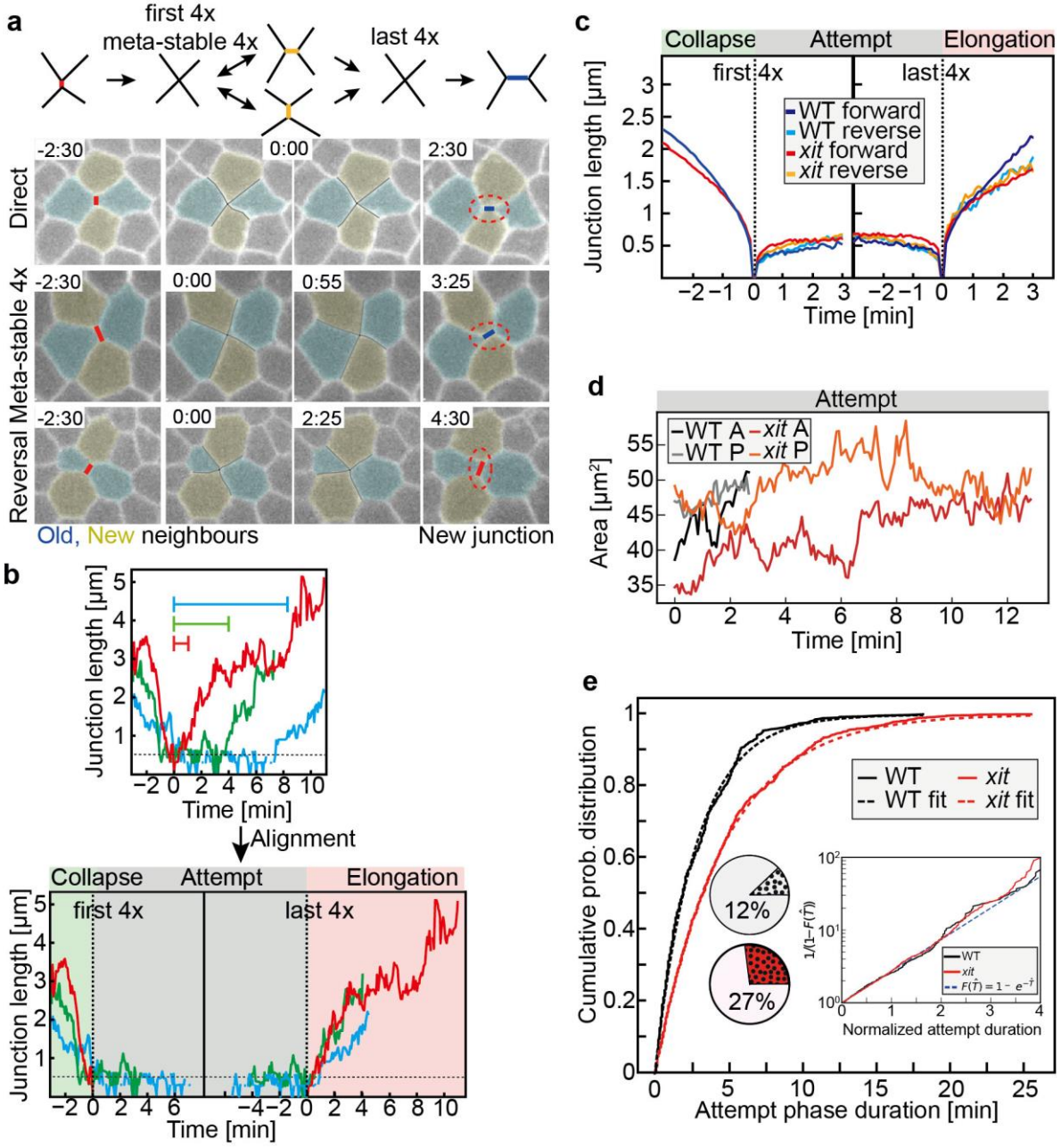

Fig.2 T1 transitions exhibit an attempt phase with a stochastic and *xit*-dependent exit. a, Varying path of T1 transitions. Images from time-lapse recordings of wild type embryos expressing GFP tagged membrane proteins. Old and new neighbours are marked in blue and yellow, respectively. The new junction is marked by a circle in red. Time in min:s. Scale bar 10 µm. **b,** Temporal alignment of three exemplary T1 transitions to the time of the first and last 4x vertex. Definition of collapse, attempt and elongation phases. Junction length during collapse and extension phase are plotted on the same axis. **c**, Averaged junction length (solid) with shaded confidence intervals in wild type (red) and *xit* (blue) embryos for forward and reversal cases. **d**, Two examples of fluctuating areas of indicated cells during attempt phase. **e,** Cumulative distribution of attempt phase duration of successful T1 transitions in wild type (black) and *xit* (red) embryos . Solid lines are the data, and dotted lines are the fitted exponentials (λ_{WT} = 0.360 min^{-1}, R^2_{WT} = 0.992; λ_{xit} = 0.217 min^{-1}, R^2_{xit} = 0.999; $\Delta\lambda$ ~ 1e-4). Distributions collapse when we rescale the abscissa with the fitted exponential rate, which is displayed as log-linear plot in the inset. Pie graphs show the proportion of reversal cases.

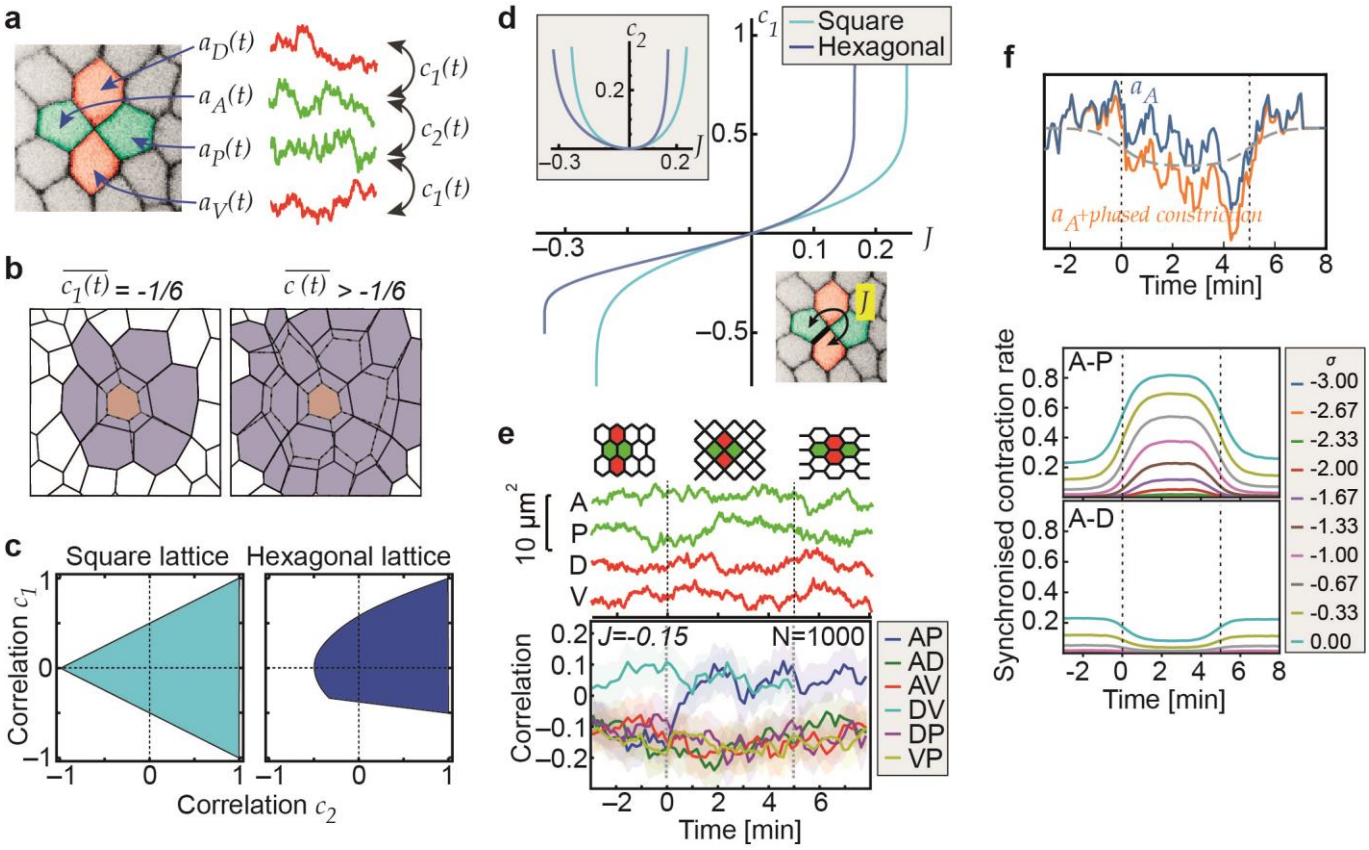

Fig. 3 Theory of the stochastic coordination and its topological constraints in dynamic epithelia. a, Quadruplet with old neighbours (green) and new neighbours (red) with corresponding traces of area fluctuations. Indicated are the next-neighbour correlation $c_1(t)$ and next-next neighbour correlation $c_2(t)$. **b,** Mechanical interactions in epithelia can be constraint to direct neighbours or be longer ranged. These scenarios have a direct impact on the expected average correlation. **c,** Correlations have model-independent bounds due to area conservation. Possible correlation values are indicated by the coloured regions. White regions are inaccessible. Bounds depend on the specific topology, here square and hexagonal packing. **d**, Comparison of average correlation in square and hexagonal packing for varying neighbour coupling strength J. **e**, Stochastic simulations of T1 transitions by changing from hexagonal to square packing and back with a constant coupling strength. Changes in the correlations are only due to changes in the topology. **f,** To mimick the attempt phase, area contractions are induced using a simple sigmoid function. Phased contraction of A-P cells results in a strong enhancement of the simultaneous contraction probability. Increasing the stochasticity by upregulating the noise level (σ) mitigates this effect.

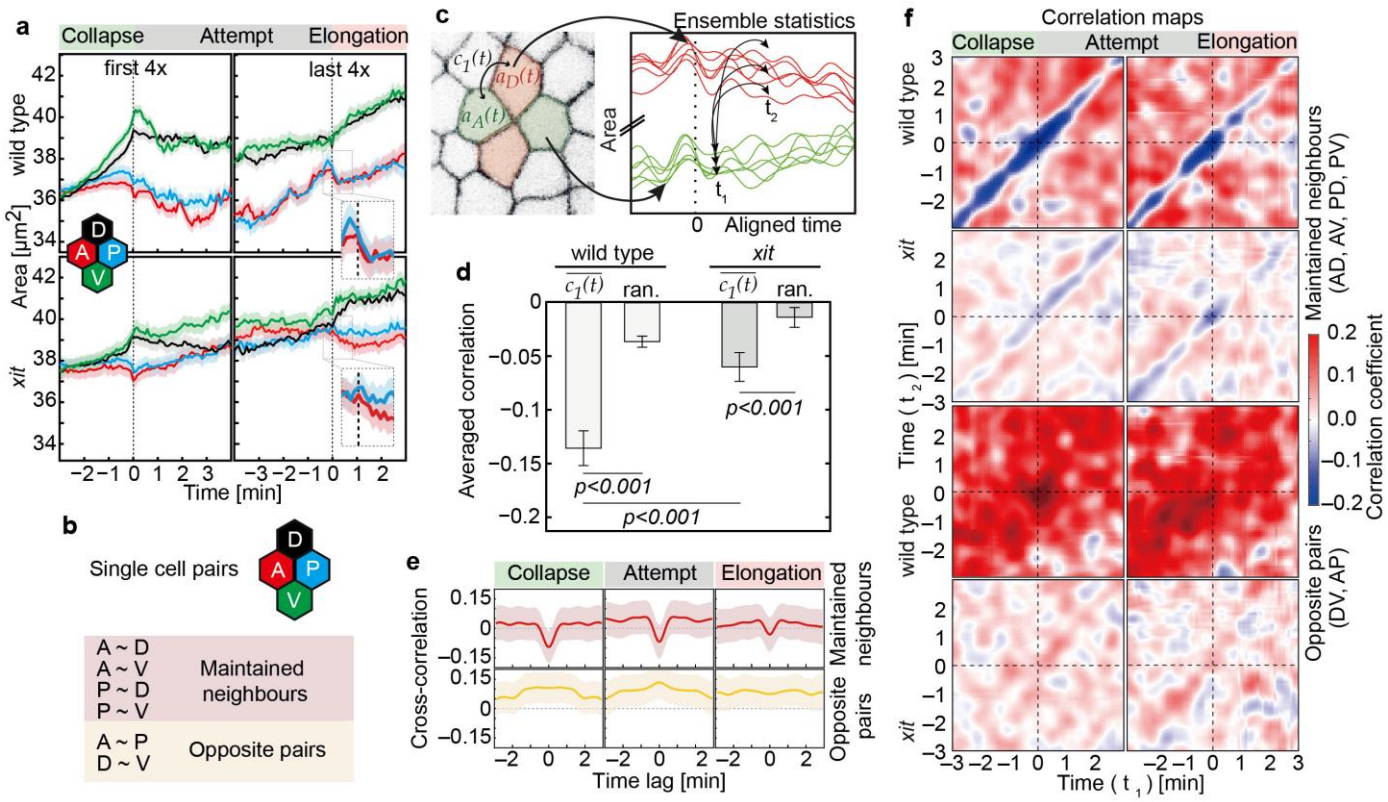

Fig.4 *xit*-dependent coordination of T1 quadruplets during the attempt phase. a, Averaged cross-sectional areas with shaded confidence intervals of cells in quadruplets. **b,** Classification of the six pairwise combinations into two groups. **c**, Time resolved ensemble statistics during the intercalation process normalized to the first and last 4x vertex. Schematic drawing of area trajectories of old (green) and new (red) neighbours. **d**, Correlation coefficients of area fluctuations of next neighbour pairs in quadruplets and random cell duplets in wild type (c_1 = –0.1388, c_1(random) = –0.0358) and *xit* (c_1 = –0.0591, c_1(random) = –0.0133) embryos averaged over three minutes after the first 4x vertex. The error bars indicate 95% confidence intervals. Sample sizes for random cell pairs from wild type and *xit* embryos are 21271 and 9227 respectively. The *p* values were estimated by a two-sided *t*-test. **e,** Cross-covariance of area fluctuations of two cell pairs (AP, AD) within a quadruplet during the three phases of intercalation. Average with shaded confidence intervals. **f**, Correlation maps for wild type and *xit* embryos averaged over the two classes of cell pairs. Degree of correlation is colour coded from blue (anti-correlation) to red (correlation).

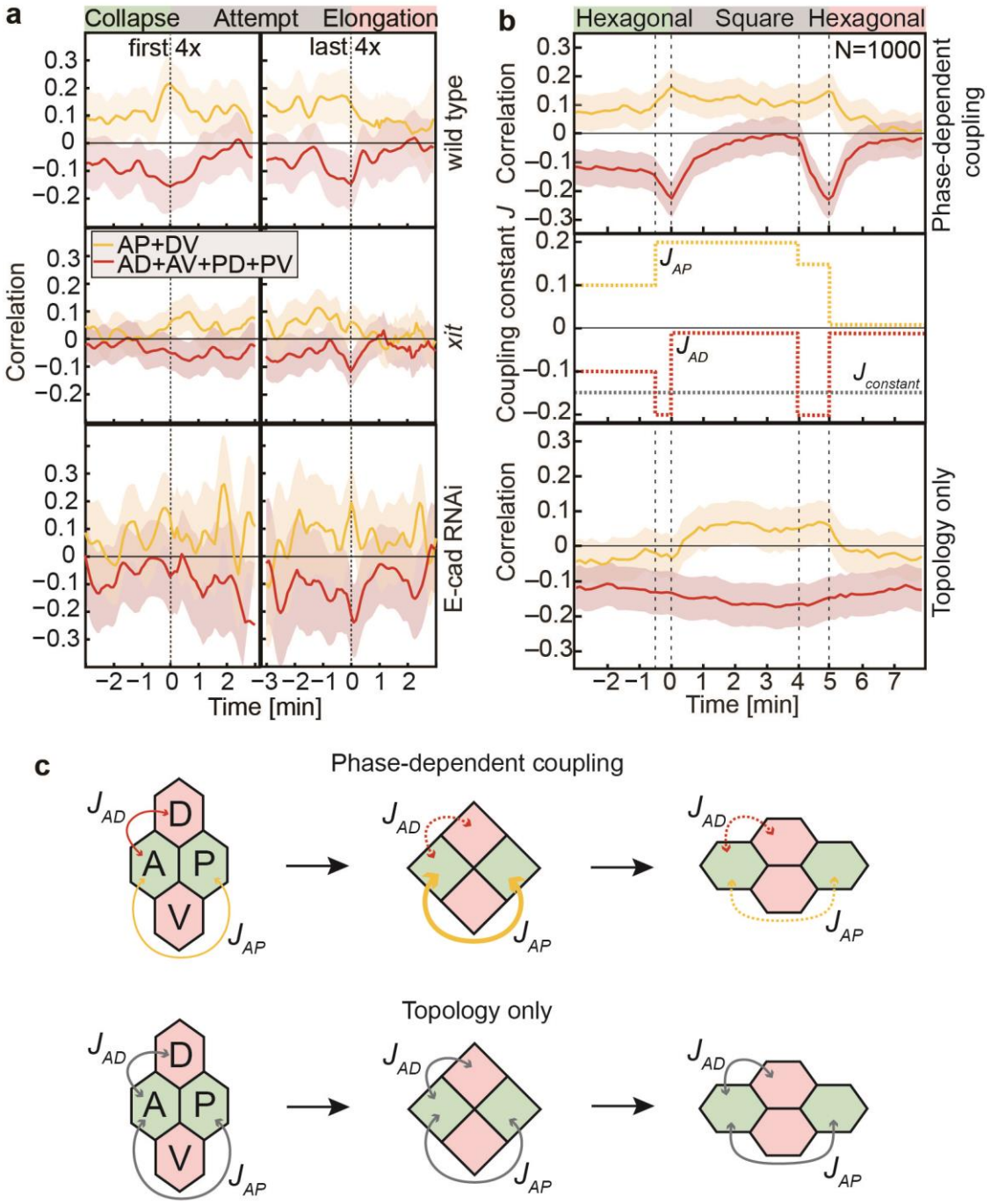

Fig.5 Phase-dependent coordination depends on E-Cad and dynamically switching intercellular coupling. **a,** Time-resolved correlation of area fluctuations with shaded confidence intervals calculated separately for the two groups of cell pairs in wild type, *xit*, and E-Cad RNAi embryos (diagonal from the correlation maps in Fig. 4f). **b,** Time-resolved correlation of area fluctuations from simulations with phase-dependent coupling and constant cell coupling (topology only). Protocol for phase dependent coupling constants is shown in the middle panel. **c**, Schematic drawing of intercalation with or without phase-dependent coupling.

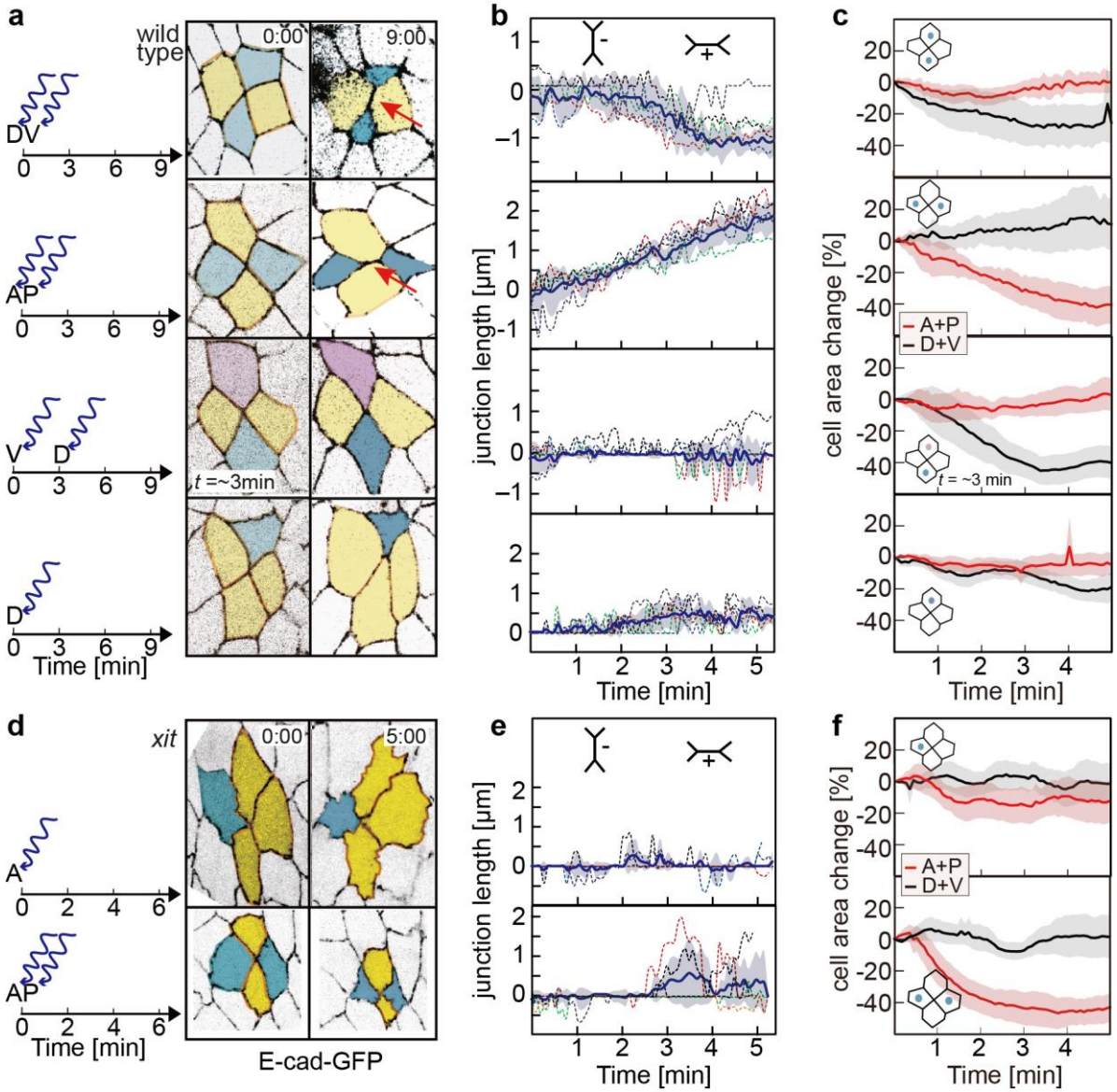

Extended Data Fig. 1 Triggered cell contraction during neighbour exchanges in wild type and *xit* embryos. a, d, Triggered cell contraction during neighbour exchanges in wild type **(a)** and *xit* **(d)** embryos. Single and pairwise (synchronous, asynchronous, 3 min time lag) contractions by Ca^{2+} uncaging in cell quadruplets. The target cells are indicated with blue and purple. Arrow in red points to extending junction. The number of cases with extending junction is indicated. Cell junctions in embryos labelled with E-Cadherin-GFP. Scale bars: 10 µm. **b**, **e,** Cell junction lengths during neighbour exchanges in dorsal-ventral orientation (AP junction) with a positive value, and anterior-posterior orientation (DV junction) with a negative value. Mean (bold line) with a standard deviation of the mean (ribbon band). Dotted lines indicate representative traces of length of cell junctions in dorsal-ventral orientation (AP junction) positive value, and anterior-posterior orientation (DV junction) negative value during neighbour exchanges. **(b)** wild type, **(e)** *xit*. **d,** Cell area changes (red and black) over time in cell quadruplets following Ca^{2+} uncaging in wild type **(c)** and *xit* **(f)** embryos. Mean (bold line) with standard deviation of the mean (ribbon band).

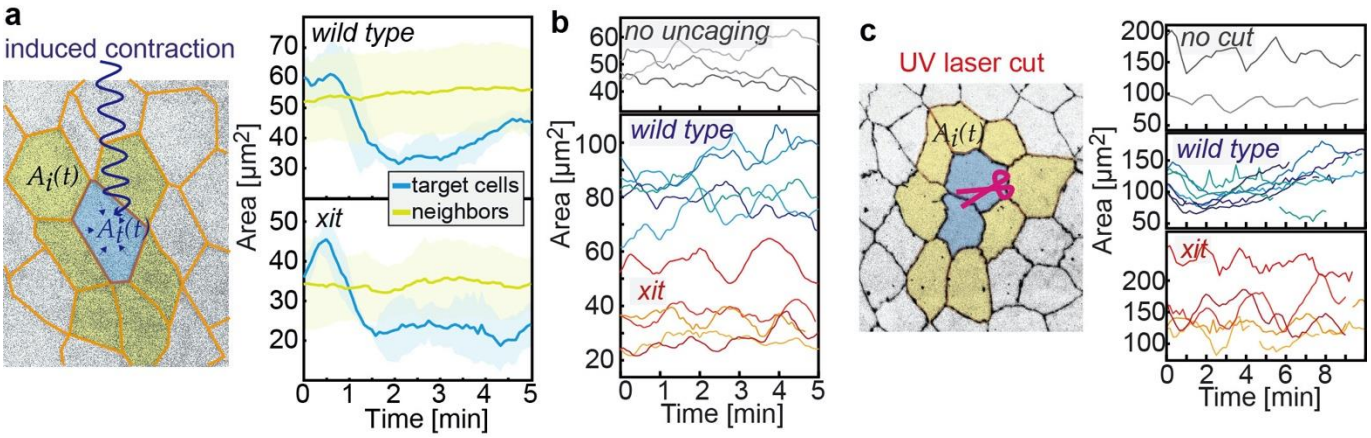

740 **Extended Data Fig. 2 Neighbour cell response to local mechanical stimulation is *xit*-dependent.**
741 **a,** Triggered cell contraction via Ca^{2+} uncaging. Area dynamics following Ca^{2+} uncaging in wild type
742 and *xit* embryos. Target cells (blue), next neighbours (yellow). The standard deviation of the mean is
743 marked by the shaded area. **b,** Representative traces of cell area. **c,** Response of next neighbours
744 (yellow) to junction ablation (blue) in the amnioserosa of wild type and *xit* embryos. The
745 amnioserosa is characterized by regular cell oscillations. Area traces were from next neighbours
746 (yellow).

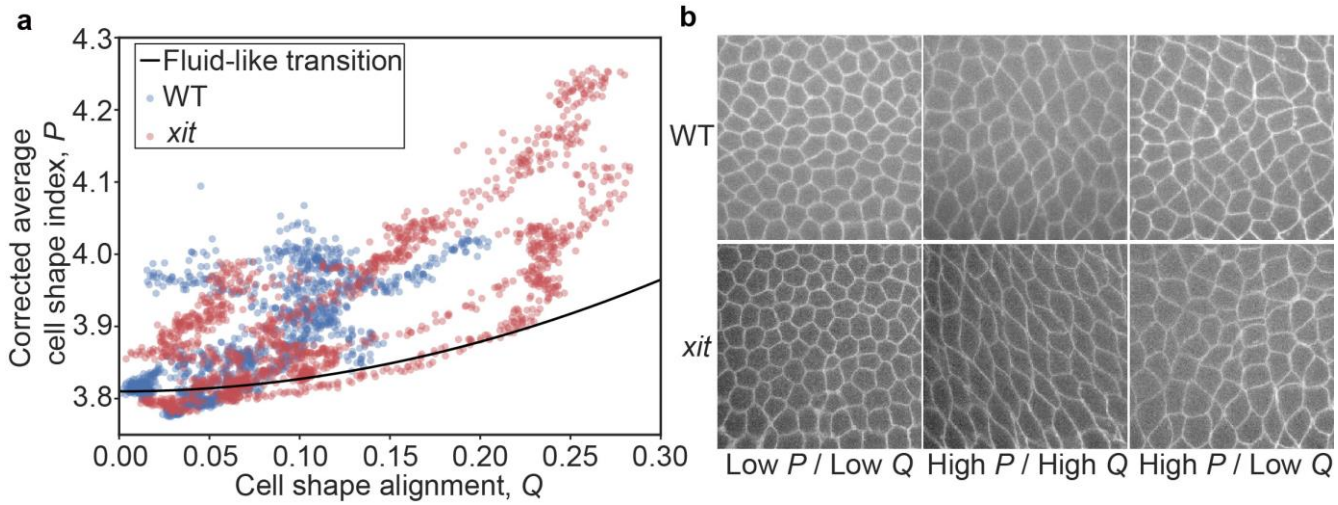

747 **Extended Data Fig. 3 Geometrical indicators of fluidization show that both wild type and *xit***
748 **tissue are fluid-like during germband extension. a,** Phase diagram of tissue states using cell shape
749 alignment *Q* and the corrected average cell shape index *P* as geometrical quantifiers. Each dot
750 represents a single frame from a single embryo of germband time-lapse recordings. Black curve is
751 the theoretical parameter free prediction of solid-like (below the curve) to fluid-like (above the
752 curve) transition derived by Wang et al., PNAS, (2020). **b,** Snapshots from time-lapse recordings
753 during germband extension as examples for the tissue states shown in (**a)**.

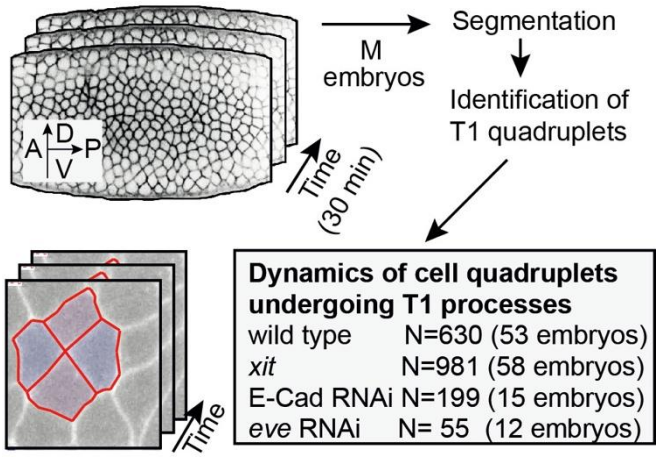

754 **Extended Data Fig. 4 Workflow of automated image analysis and computational extraction of**
755 **T1 transitions.** Genotypes and the number of quadruplets are indicated.

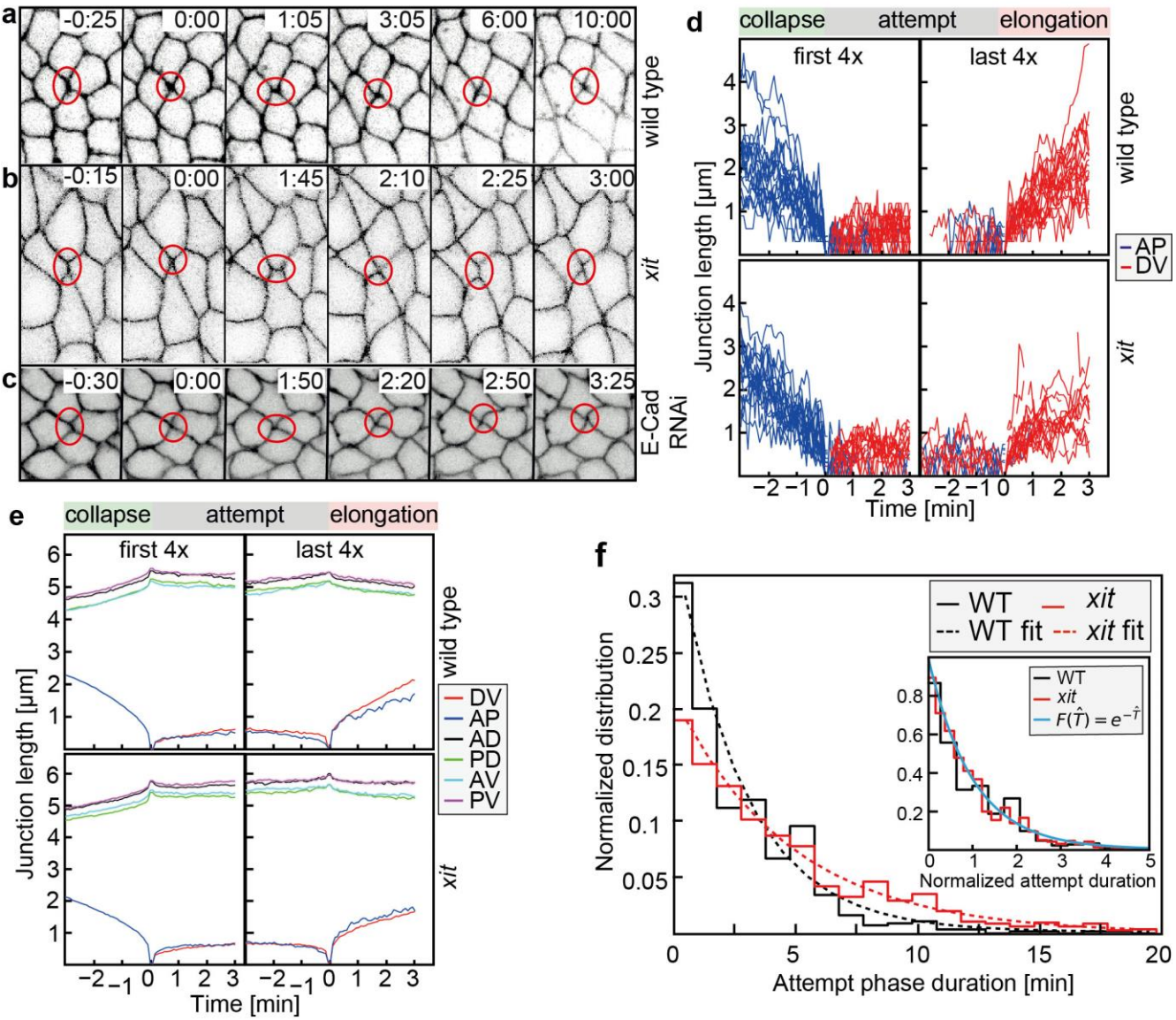

Extended Data Fig. 5 Junction dynamics during T1 transitions in wild type and mutants. A–c, Examples of a metastable 4x vertex**.** Images from a time-lapse recording of wild type **(a)**, *xit* **(b)** and E-cadherin RNAi **(c)** embryos expressing GFP tagged membrane marker. Circles in red mark the dynamical 4x vertex. **d,** Traces of randomly chosen quadruplets (10 per genotype). Colour coding according to the orientation of the junction (blue, AP junction, red, DV junction). **e,** Averaged junction lengths with a shaded confidence interval of the six different junctions within a quadruplet. **f,** Normalized histograms of attempt phase duration wild type (black) and *xit* (red) embryos. Solid lines are the data and dotted lines are the fitted exponentials ($\lambda_{WT} = 0.36$ min^{-1}, $R^2_{WT} = 0.97$, $\lambda_{xit} = 0.21$ min^{-1}, $R^2_{xit} = 0.98$). Distributions collapse when we rescale the abscissa with the fitted exponential rate, which is displayed in the inset.

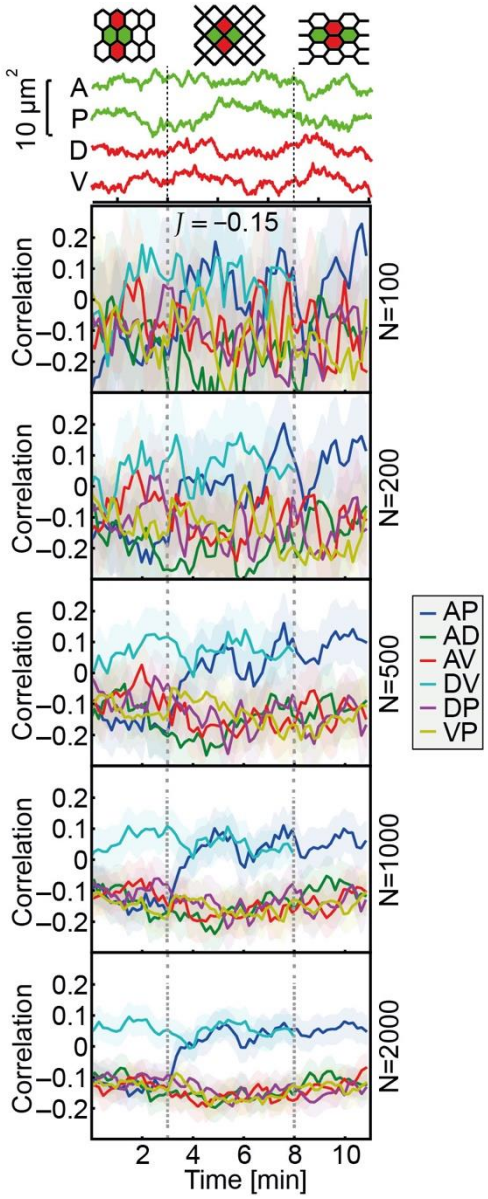

766 **Extended Data Fig. 6 Stochastic simulations of T1 transitions**. Stochastic simulations of T1
767 transitions with increasing sample size and changing topology (from hexagonal to square and back).
768 Changes in the correlations are only due to changes in the topology.

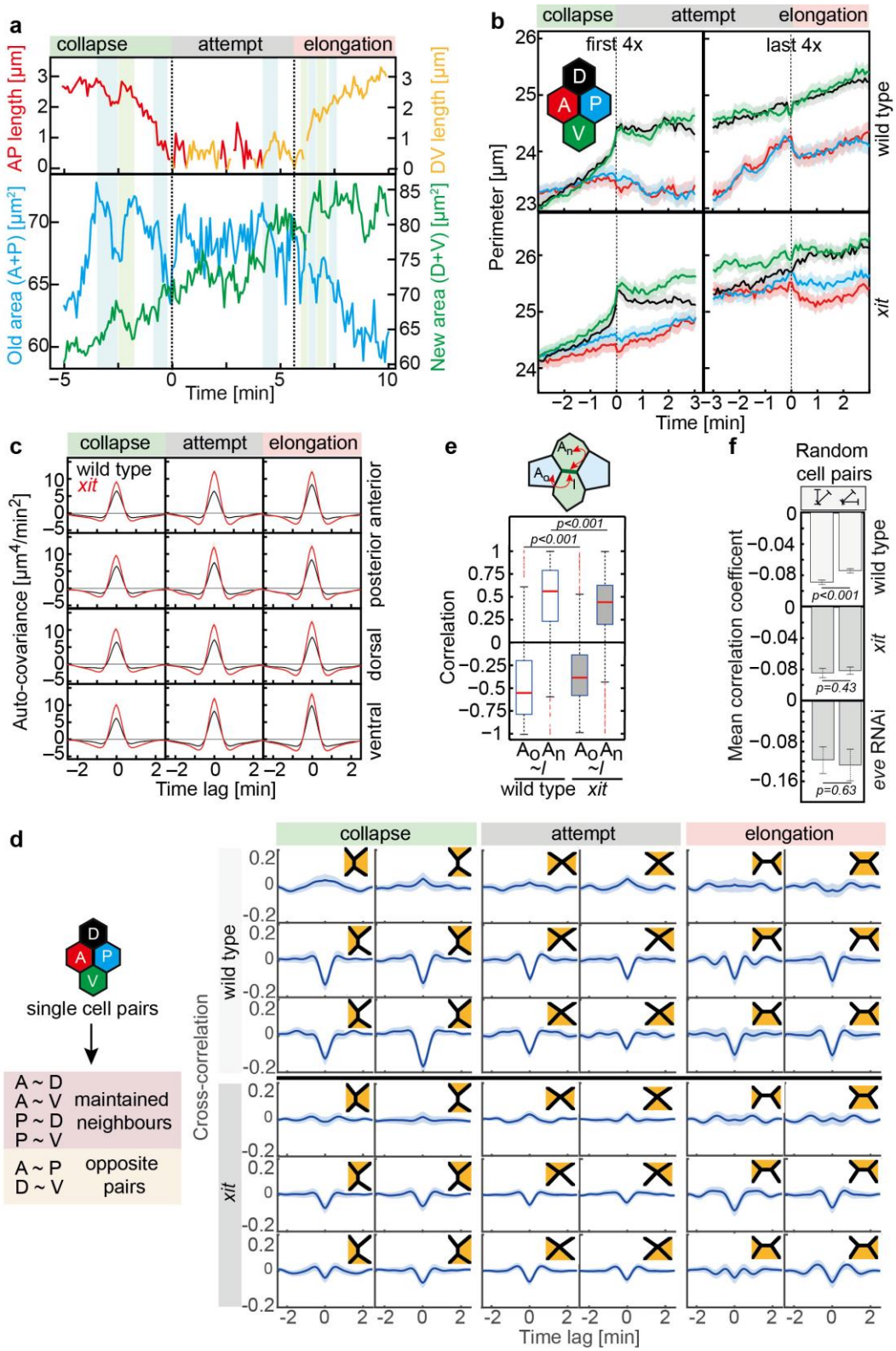

Extended Data Fig. 7 Area fluctuations, perimeter dynamics and pair-wise correlations during T1 transitions. a, Exemplary time course of junction length and cell areas from a wild type embryo. **b,** Averaged perimeter dynamics with a shaded confidence interval of the four cells during T1 transitions in wild type and *xit* mutants**. c,** Auto-covariance with shaded confidence intervals for the cell area in quadruplets. **d,** Cross-correlation of area fluctuations for all six pair-wise combinations within quadruplets in wild type and *xit* embryos separately for collapse, attempt and extension phase. Averaged correlation with shaded confidence intervals over three minutes. **e,** Averaged correlation

776 coefficient for area fluctuations versus length of the new junction in wild type and *xit* embryos
777 averaged over three minutes after the first 4x vertex. *p* values were estimated by Mann-Whitney-
778 Wilcoxon two-sided test. **f,** Dependence of area correlations (mean) in random cell duplets on
779 junction orientation in wild type (N=21272), *xit* (N=9227) and *eve* (N=4681). Error bars indicate
780 95% bootstrap confidence intervals. The *p* values are estimated by a two-sided *t-test*.

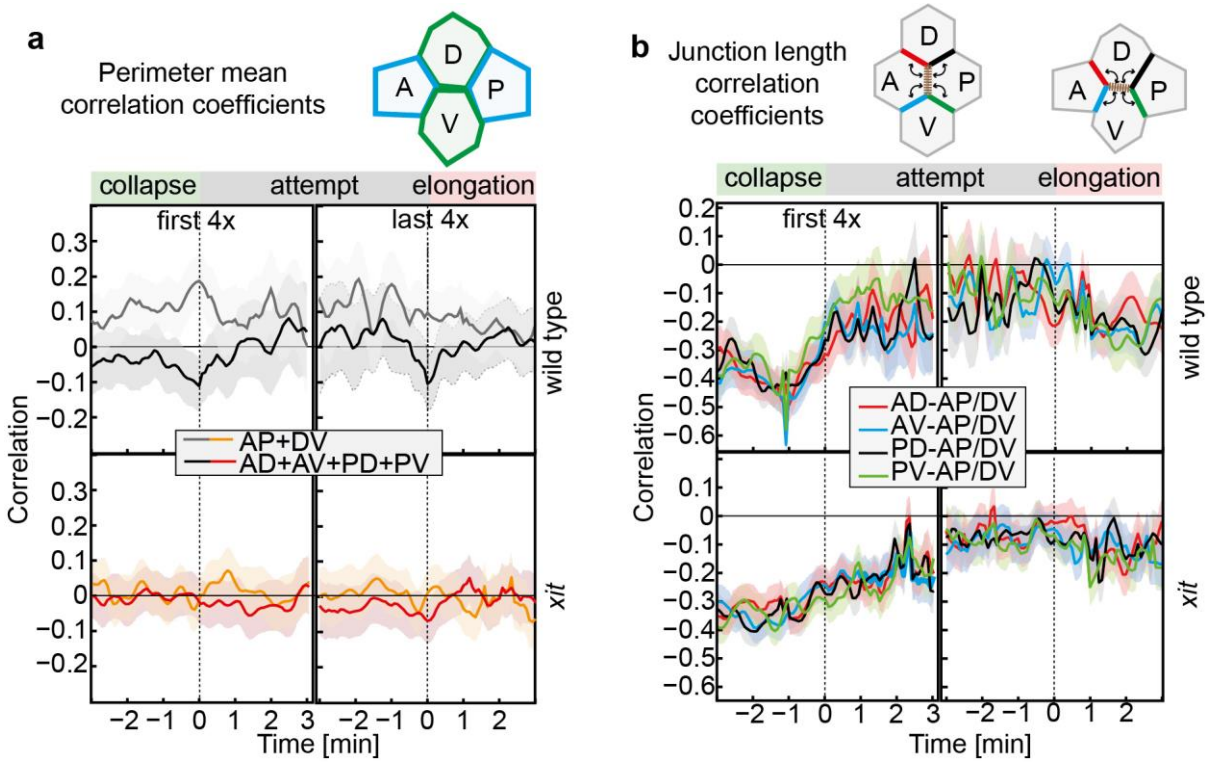

781 **Extended Data Fig. 8 Time-resolved correlations of perimeters and junction lengths**. **a,** Time
782 course of averaged perimeter correlations in the indicated pairs of cells. **b,** Time course of correlation
783 between indicated junction lengths.

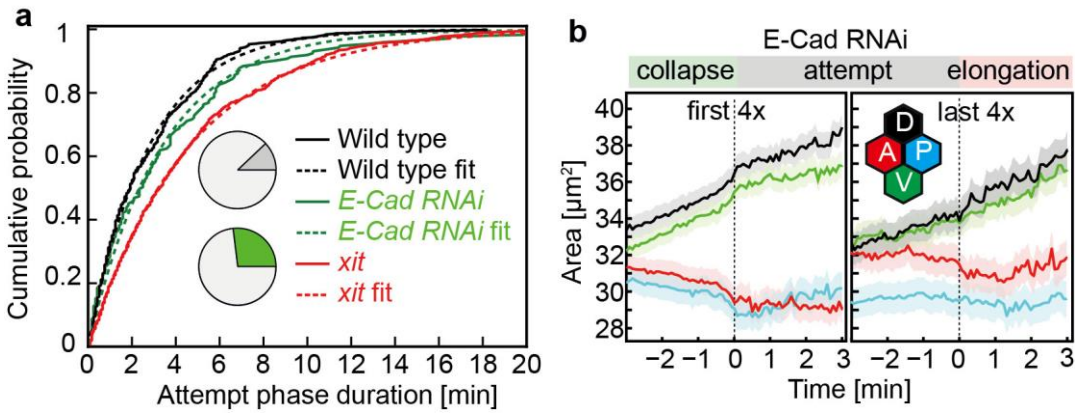

784 **Extended Data Fig. 9 Phase-dependent coordination depends on E-Cad. a,** Distribution of
785 attempt phase durations in embryos depleted of E-Cad by RNAi injection. Pie graphs show the
786 proportion of reversal cases. **b,** Dynamics of the averaged cross sectional areas in quadruplets in
787 embryos depleted of E-Cad.

Supplementary information

This file contains the details of the theory of the stochastic coordination and its topological constraints in dynamic epithelia.

Supplementary Table 1: Fly stocks

Name	Genotype	Source
117GFP	w; Resille-GFP; +/+; +/+	P{PTT-un}CG8668[1117-2] better Morin 2001, Blankenship et al.,
E-Cad-GFP	w; DE-Cadherin-GFP[k-in]; +/+; +/+	Huang et al., 2009 [51]
mat67, 15	w; tub-Gal4-VP16{w+} [67]; tub-Gal4-VP16{w+} [15]; +/+	St. Johnston /Cambridge
ovo18	ovo[D2] v [24] FrtX [9-2] {w+}/C (1) D X, y, w, f; +/+; +/+; +/+	Chou and Perrimon, 1992 [52]
GFP-Spider	w; +/+; GFP95-1 (GFP-Spider) {w+}; +/+	Spider-GFP (P{PTT-GB}gish, Bloomington #59025 Blankenship et al., 2006 [13]
GCaMP6m	w [1118]; +/+;UASp-GCaMP6-myr; +/+	Chen et al., 2013 [47]
xit	w xit[X-330] f Frt [9-2, 18E] Flp122{ry+} /FM7c, y w[a] sn B; +/+; +/+; +/+	Vogt et al., 2006 [53] and Zhang et al., 2014 [22]
4XGFP	w; GFP-Resille{w+}; GFP-Spider{w+}; +/+	generated in this study
xit; 4XGFP	w xit[X-330] f Frt [9-2, 18E] Flp122{ry+} /FM7c; GFP-Resille (117GFP); Spider-GFP; +/+	generated in this study
ovo18X; 117GFP	ovo[D2] v [24] FrtX [9-2] {w+} / C (1) DX, y, w, f; GFP-Resille (117GFP); +/+; +/+	generated in this study
xit; E-Cad-GFP	w xit[X-330] f Frt [9-2, 18E] Flp122{ry+} /FM7c; DE-Cadherin-GFP[k-in]; +/+; +/+	generated in this study
ovo18X; E-Cad-GFP	ovo[D2] v [24] FrtX [9-2] {w+} / C (1) DX, y, w, f; DE-Cadherin-GFP[k-in]; +/+; +/+	generated in this study

Supplementary Videos

Video1. Embryo expressing a GFP tagged membrane protein and loaded with caged Ca^{2+}. Scale bar 10 µm.

Video 2–4. Embryos expressing E-Cadherin-GFP and loaded with a caged Ca^{2+}. Specified cells of a quadruplet engaged in a T1 transition were targeted for uncaging as indicated with a red dot.

Video 2. D and V cells contraction synchronously.

Video 3. D and V cells contraction asynchronously with a time lag of 3 min.

Video 4. D cell contraction.

Video 5. Time-lapse recordings of amnioserosa in wild type and *xit* embryos expressing E-Cadherin-GFP. *xit* genotype: zygotically heterozygous embryos from females with *xit* germline clones. Junction ablation was induced with a pulsed UV laser. Target cells are labelled in yellow, immediate neighbours in blue. Scale bar 10 µm.

Video 6. Time-lapse recordings of cells during germband extension in wild type embryos expressing

a GFP-tagged membrane protein. The 4x vertex is resolved promptly (top panel), meta-stable (middle panel) or in reversed direction (bottom panel).

Data availability

The original image data will be made available prior to publication in a public repository of the Göttingen eResearch alliance (https://data.goettingen-research-online.de/) as specified in the following.

Raw Data. Raw data from the germband experiments is provided as two-dimensional z-projected ".tiff" images, containing gray values of cell junction label intensity.
The paths to the raw data are
"./rawdata/genotype/embryo"
for example
"./rawdata/WildType/Embryo_0045"
The naming convention for respective frames of a movie is given by
"Embryo_embryonumber_z01_tframenumber.tif"
for example
"Embryo_0045_z01_t008.tif"
Each "./rawdata/mutant" directory contains a .pdf file, specifying exact genotype and recording date for each embryo. Furthermore, the accompanying .xlsx file contains information regarding imaging techniques and recording parameters, for example time interval between consecutive frames, microscope objective or exposure time.
Time Series Data. We also provide time series data for several dynamical variables that are involved in the T1 transition. This data was extracted from the raw data via our acquisition pipeline as described by the methods section of the paper.
All data is stored in ".dat" matlab files. For each mutant there exist the following files
"MvalsT2All.dat"
"MvalsT3All.dat"
"MvalsT4All.dat"
and accompanying files "I2.dat", "I3.dat", "I4.dat".
"MvalsAll" contains the raw time series (no further filtering) and "I" contains the time vector. T2, T3 and T4 specify the time interval:

- T2/I2 is aligned to the first 4x
- T3/I3 is aligned to the last 4x
- T4/I4 is only the time interval between the first and the last 4x

All of these variables have the following structure: MvalsT2All{u}(t) where u is the variable, v is the number of the variable (number of the T1 transition), and t is the time.

- u=1,...,7 are the length of the borders that are involved in the T1 transition
- u=8,...,15 are areas of the 4 cells and compound areas
- u=16-19 contain cell perimeters
- u=20-23 contain cell anisotropies
- u=24 is the angle of the AP border

In detail, the variables are

u	name	description	unit
1	L_DV	length of edge separating cells D and V	μm
2	L AP	length of edge separating cells A and P	μm
3	L-	L DV - L AP	μm
4	L AD	length of edge separating cells A and D	μm
5	L PD	length of edge separating cells P and D	μm
6	L AV	length of edge separating cells A and V	μm

7	L PV	length of edge separating cells P and V	μm
8	Area A	area of cell A	μm^2
9	Area P	area of cell P	μm^2
10	Area D	area of cell D	μm^2
11	Area V	area of cell V	μm^2
12	Area Old	Area A + Area P	μm^2
13	Area New	Area D + Area V	μm^2
14	Area Sum	Area Old + Area New	μm^2
15	Area Diff	Area Old - Area New	μm^2
16	Perimeter A	perimeter of cell A	μm
17	Perimeter P	perimeter of cell P	μm
18	Perimeter D	perimeter of cell D	μm
19	Perimeter V	perimeter of cell V	μm
20	Anisotropy A	anisotropy of cell A	$\in [0,1]$
21	Anisotropy P	anisotropy of cell P	$\in [0,1]$
22	Anisotropy D	anisotropy of cell D	$\in [0,1]$
23	Anisotropy V	anisotropy of cell V	$\in [0,1]$
24	Angle	angle of L AP edge	$\in [0,1]$
25		empty	
...			
36			
I2/3/4	t	time vector	frames

A (anterior), P (posterior), D (dorsal), V (ventral) denote the cells that participate in the T1 transition. The angle of the AP border contains values between 0 and 1, where 0 is a horizontal edge and 1 denotes vertical edges.

Usually the data file only contains 24 cells but in some cases there may also be cells 25-36. These are a remainder from a different study and do not contain any data.

The time vector only has alignment purposes and its unit is given in frames. The usual timestep is 5s, therefore I*.dat has to be divided by 12 to obtain the time in minutes. The actual timestep is always given in the datasheet (*.xlsx) with the original raw movies.

Note that the time series all have the same length. A time series was filled with NaNs if it was shorter than the specified time interval. Evaluations of the data must therefore take NaN values into account and require some care when dealing with cross-correlations for example.

Code availability

The custom codes used to process images analyse data, and run simulations are available upon reasonable request.

Theory supplement - Epithelial Cell Coordination Dynamics

I. INTRODUCTION

We consider the dynamics of a tissue consisting of N cells. Each cell is described by its cross sectional area $a_m(t)$ where the index m labels the cell and t is the time. We are interested in the intercellular correlations $C_{i,j}(t,t') = \langle a_i(t)a_j(t')\rangle$ in the tissue and focus mainly on the behavior of nearest neighbor and next-nearest neighbor correlations. In the following we

1. derive general, model-independent bounds for the correlation function $C_{i,j}(t,t')$, in particular for hexagonal and quadratic arrangements of cells

2. quantify $C_{i,j}(t,t')$ in a linearized model for the dynamics of the corss sectional areas in a hexagonal and quadratic arrangement of cells.

3. quantify the influence of a time-dependent topology on the correlation function that the mimics the rearrangement of cells during the T1 transition

II. MODEL INDEPENDENT BOUNDS FOR THE CORRELATION FUNCTION

Complex systems far from equilibrium such as the dynamics of coupled epithelial cells are notoriously difficult to describe analytically due to their inherent randomness and non-linearity. An interesting idea is to approach the problem analytically is to drop the demand to get exact results in the form of equations and consider universal inequalities instead. For example, irrespective of the specific dynamics, the normalized covariance matrix of the cross sectional areas must always be positive semidefinite with non-negative eigenvalues. Inequalities of this kind can be used to find universal bounds for covariances, correlations, etc. . Such bounds are are extremely useful for at least two reasons: i.) They can be used to asses the typical range of observed values of a complex system; and ii.) they can be used to reject models if they lead to observations that are outside of the allowed range of values.

In the following we derive bounds for the average and the maximal anti-correlation between the cell's cross sectional area for different cell arrangements. These bounds are independent of the specific model and follow from the general properties of the covariance matrix. If we assume that the cell areas fluctuate around a typical mean value $\bar{a}$, we can write $a_i(t) = \bar{a}_i + x_i(t)$, where $x_i(t)$ describes the fluctuations around the average.

A very general lower bound for the average anti-correlation between all cells follows from the non-negativity of the variance of the sum of all cell-size fluctuations, i.e.

$$\left\langle \left(\sum_m x_m(t) \right)^2 \right\rangle = \sum_m \langle x_m^2(t)\rangle + 2\sum_{n>m} \langle x_m(t)x_n(t)\rangle \geq 0 \tag{1}$$

For a tissue consisting of N identical cells with $\langle x_m^2(t)\rangle = \sigma^2$, it follows that

$$\frac{2}{N}\sum_{n>m} \frac{\langle x_m(t)a_n(t)\rangle}{\sigma^2} \geq -1\,. \tag{2}$$

Hence, the *average cross correlation* defined by

$$\overline{\langle x_m(t)x_n(t)\rangle} = \frac{2}{N(N-1)}\sum_{n>m} \frac{\langle x_m(t)x_n(t)\rangle}{\sigma^2} \tag{3}$$

has a lower bound that increases with the lattice size

$$\overline{\langle x_m(t)x_n(t)\rangle} \geq -\frac{1}{N-1} \tag{4}$$

In particular, we see that for all to all coupled cells where all correlations coincide with $\langle x_m(t)x_n(t)\rangle = c\sigma^2$ that $c \geq \frac{1}{N-1}$.

Assuming that correlations between cells that are not nearest neighbours are vanishingly small we obtain from Eq.(2) for the average nearest neighbor correlation $\bar{c}_1^{(K)}$ in a tissue with coordination number K

$$\bar{c}_1^{(K)} \geq -\frac{1}{K\sigma^2} \tag{5}$$

and in particular for a hexagonal lattice $\bar{c}_1^{(hex)} \geq -\frac{1}{6\sigma^2}$ and a square lattice $\bar{c}_1^{(sq)} \geq -\frac{1}{4\sigma^2}$. Given that the variability of the nearest neighbor correlations is not too hight, these values provide good estimates for the typical size correlations in such cell arrangements.

Note that if the tissue size is constant, i.e. $\left\langle \left(\sum_m x_m(t)\right)^2 \right\rangle = 0$ the equality holds strictly in all of the above equations.

Such bounds can be refined if more information about the system is included into the formulation of the inequalities, for example by making assumption about the structure of the tissue. In the following, we consider isotropic tissues that are arranged in form of a hexagonal and square lattice. Let us start with a four cells arranged in a square lattice. Denoting the nearest neighbor correlations c_1 and the next-nearest neighbor correlations c_2 the covariance matrix of the four cells is of Toeplitz type and proportional to

$$C_{sq} = \begin{bmatrix} 1 & c_1 & c_2 & c_1 \\ c_1 & 1 & c_1 & c_2 \\ c_2 & c_1 & 1 & c_1 \\ c_1 & c_2 & c_1 & 1 \end{bmatrix}\,, \tag{6}$$

Since the eigenvalues λ_i of a covariance matrix represent the variance along the respective eigenvector directions they have to be non-negative. This condition leads to a set of inequalities

$$\lambda_{1,2} = 1 - c_2 \geq 0 \quad \lambda_3 = 1 - 2c_1 + c_2 \geq 0 \quad \lambda_4 = 1 + 2c_1 + c_2 \geq 0 \tag{7}$$

which can be straightforwardly reduced to the condition

$$-1 \leq -\frac{1+c_2}{2} \leq c_1 \leq \frac{1+c_2}{2} \leq 1 \tag{8}$$

Thus the region of possible (c_1, c_2) value pairs is confined, e.g. for next nearest neighbors to be perfectly correlated ($c_2 = 1$), nearest neighbors need to be either perfectly correlated (c_1=1) or perfectly anti-correlated ($c_1 = -1$), see Fig.1. But notice that no single value of c_1 or c_2 is forbidden.

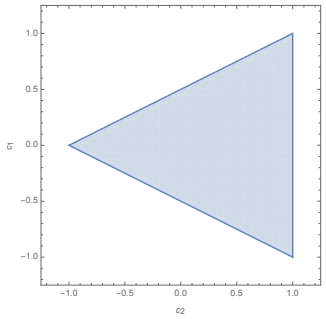

FIG. 1. Allowed range of (c_1, c_2) value pairs in the square lattice

This changes when we look at the correlations of three neighboring cells in a hexagonal lattice. Due to isotropy the cross-correlations between these cells have to be identical c_1 and the normalized covariance matrix C_{tri} of these three cells reads

$$C_{tri} = \begin{bmatrix} 1 & c_1 & c_1 \\ c_1 & 1 & c_1 \\ c_1 & c_1 & 1 \end{bmatrix} . \tag{9}$$

Since the eigenvalues of a covariance matrix represent the variance along the respective eigenvector directions they have to be non-negative. This condition leads to a set of inequalities

$$\lambda_1 = 1 + 2c_1 \geq 0 \tag{10}$$
$$\lambda_{2,3} = 1 - c_1 \geq 0\,, \tag{11}$$

which can be simplified to

$$-1/2 \leq c_1 \leq 1\,. \tag{12}$$

That means, while neighboring cells in a hexagonal lattice can be perfectly correlated their maximal anti-correlation is bounded by $-\frac{1}{2}$. This can be intuitively understood; if cells A and B were perfectly anti-correlated, cell C cannot be perfectly anti-correlated to both, A and B. A similar phenomenon is well-known in statistical physics, where spin systems show a similar type of geometric frustration on anti-ferromagnetic triangular spin lattices. Here, the geometry induced frustration leads to a highly degenerate ground state with non-zero entropy since not all spins can perfectly anti-align.

The above idea can be extended to a patch of cells that consists of a center cell and its six neighboring cells in a hexagonal lattice. Denoting c_1, c_2 and c_3 the different possible correlations, see Fig.2, the covariance matrix reads

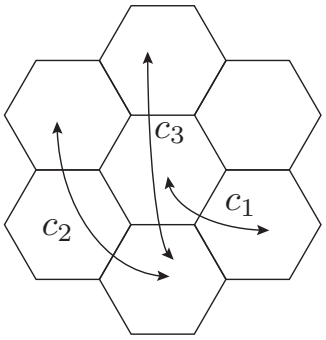

FIG. 2. The possible correlations in the hexagonal arrangement of seven cels with one center cell. c_1 denotes the nearest neighbor correlations, whereas c_2 and c_3 denote the two different types of next-nearest neighbor correlations.

$$C_{hex} = \begin{bmatrix} 1 & c_1 & c_1 & c_1 & c_1 & c_1 & c_1 \\ c_1 & 1 & c_1 & c_2 & c_3 & c_2 & c_1 \\ c_1 & c_1 & 1 & c_1 & c_2 & c_3 & c_2 \\ c_1 & c_2 & c_1 & 1 & c_1 & c_2 & c_3 \\ c_1 & c_3 & c_2 & c_1 & 1 & c_1 & c_2 \\ c_1 & c_2 & c_3 & c_2 & c_1 & 1 & c_1 \\ c_1 & c_1 & c_2 & c_3 & c_2 & c_1 & 1 \end{bmatrix} . \tag{13}$$

Here, the first row accounts for the correlations of center cell and the second to last row account for the correlations of surrounding cells. While the center cells has only direct neighbors, each surrounding cell has three direct neighbors with correlation c_1, two next nearest neighbors with correlation c_2 and one next nearest neighbor with

correlation c_3, see Fig.2. The Eigenvalues of C_{hex} are

$$\lambda_1 = 1 + c_1 - c_2 - c_3 \tag{14}$$
$$\lambda_2 = 1 + c_1 - c_2 - c_3 \tag{15}$$
$$\lambda_3 = 1 - 2c_1 + 2c_2 - c_3 \tag{16}$$
$$\lambda_4 = 1 - c_1 - c_2 + c_3 \tag{17}$$
$$\lambda_5 = 1 - c_1 - c_2 + c_3 \tag{18}$$
$$\lambda_6 = \frac{1}{2}\Big(2 + c_1 + 2c_2 + c_3 - \sqrt{28c_1^2 + 8c_1 d + 4c_1 c_3 + 4c_2^2 + 4c_2 c_3 + c_3^2}\Big) \tag{19}$$
$$\lambda_7 = \frac{1}{2}\Big(2 + c_1 + 2c_2 + c_3 + \sqrt{28c_1^2 + 8c_1 d + 4c_1 c_3 + 4c_2^2 + 4c_2 c_3 + c_3^2}\Big) \tag{20}$$

The condition $\lambda_i \geq 0$ for $i = 1, ..., 7$ restricts the values for (c_1, c_2, c_3). The allowed range of correlation combinations in (c_1, c_2, c_3)-space is depicted in Fig.3 In particular

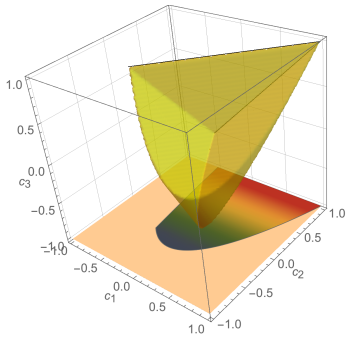

FIG. 3. Allowed range of (c_1, c_2, c_3) values for the hexagonal arrangement of seven cells.

the allowed range of (c_1, c_2) values is of interest (Why??), see Figure 2B in the main paper and the projection in Fig.3

III. CORRELATION FUNCTIONS IN A LINEAR MODEL

After these general considerations on bounds for the anti-correlation, we now proceed to discuss a concrete model that describes the time-evolution of cell-sizes $a(t) = \bar{a} + x(t)$ in the tissue. Assuming that the tissue has an extension of $N \times N$ cells, we analyze a general linear model defined by

$$\dot{x}_m(t) = \sum_{n=1}^{N^2} W_{m,n}(t) x_n(t) + \eta_m(t)\,, \tag{21}$$

where $\eta_m(t)$ is an additive Gaussian white noise that captures the random size fluctuations with $\langle \eta_m(t) \rangle = 0$ and $\langle \eta_m(t)\eta_n(t') \rangle = q_{m,n}\delta(t-t')$. An essential feature of this tissue model is that Eq.(21) is linear and that the fluctuations are additive. For a time-independent coupling matrix $W_{m,n}(t) \equiv W_{m,n}$ the solution of the noise-less equation can be written as

$$x_m(t) = \sum_n G_{m,n}(t) x_n(0)\,, \tag{22}$$

where the Green's function has to solve

$$\dot{G}_{m,n}(t) = \sum_j W_{m,j} G_{j,n}(t) \tag{23}$$

with the initial condition $G_{m,n}(0) = \delta_{m,n}$. The mean and the variance can be obtained in terms of the Green's function according to

$$\langle x_m(t) \rangle = \sum_n G_{m,n}(t) x_n(0) \tag{24}$$
$$\sigma_{m,n}(t) = \langle [x_m(t) - \langle x_m(t) \rangle][x_n(t) - \langle x_n(t) \rangle] \rangle \tag{25}$$
$$= \sum_{i,j} q_{i,j} \int_0^t G_{m,i}(\tau) G_{n,j}(\tau)\, d\tau \tag{26}$$

If the coupling is symmetric a complete bi-orthogonal set of the coupling matrix exists, and the spectral decomposition of $W_{m,k}$ reads

$$W_{n,m} = \sum_{k=1}^{N^2} \gamma(k) u_m^{(k)} v_n^{(k)}\,, \tag{27}$$

where $\gamma(k)$ are the N^2 eigenvalues and u and v denote the right- and left-eigenvectors of the coupling matrix, respectively. Using the spectral decomposition, we can solve Eq.23

$$G_{m,n}(t) = \sum_k e^{\gamma(k)t} u_m^{(k)} v_n^{(k)} \tag{28}$$

We see that the system is stable if all eigenvalues are negative. Then the system reaches a stationary state after time T where $T \gg -\gamma_{max}^{-1}$ with γ_{max} being the largest eigenvalue of the $W_{m,n}$. In the stationary state, i.e. for $t > T$, we obviously have

$$\langle x_m(t) \rangle^{(s)} = 0 \tag{29}$$
$$\sigma_{m,n}^{(s)}(t) = \langle x_m(t) x_n(t) \rangle \tag{30}$$

and the time-covariance function can be obtained as

$$\langle x_m(t+\tau) x_n(t) \rangle^{(s)} = \sum_j G_{m,j}(\tau) \sigma_{j,n}^{(s)}(t) \tag{31}$$

Thus, from Eqs.(27), (28) and (31), we can obtain any time-covariance function for the model Eq.(21).

Before we present the explicit solutions for the quadratic and hexagonal lattice, let us first discuss as a

pedagogical example, how the solution of a linear chain of length N with constant nearest neighbor couplings, independent Gaussian noises and periodic boundary condition can be obtained. The equation of motion for this model reads

$$\dot{x}_n(t) = -\beta x_n + J(x_{n+1} + x_{n-1}) + \eta_n(t)\,, \tag{32}$$

where $\eta_n(t)$ is a Gaussian white noise with zero mean $\langle \eta_n(t) \rangle = 0$ and variance $\langle \eta_n(t)\eta_m(t') \rangle = q\delta_{n,m}\delta(t-t')$ and $x_{n+N} = x_n$. Using the recipe introduced above we can calculate the left and right-eigenvectors of the coupling matrix. Noting that the coupling matrix is circulant the eigenvectors read $u_m^{(k)} = \exp[m\frac{2\pi ik}{N}]$ and $v_n^{(k)} = \exp[-n\frac{2\pi ik}{N}]$ and the eigenvalues are given by

$$\begin{aligned}\gamma(k) &= -\beta + Ju_1^{(k)} + Ju_{N-1}^{(k)} = -\beta + J\left(e^{\frac{2i\pi k}{N}} + e^{-\frac{2i\pi k}{N}}\right) \\ &= -\beta + 2J\cos\left(\frac{2\pi k}{N}\right)\end{aligned} \tag{33}$$

The system is stable for $-\frac{\beta}{2} \leq J \leq \frac{\beta}{2}$.The solution of the inhomogeneous system given by Eq.(32) accordingly reads

$$\begin{aligned}x_n(t) = &\sum_{k=1}^{N} \hat{x}_k(0) e^{n\frac{2i\pi k}{N}} e^{-[\beta - 2J\cos\left(\frac{2\pi k}{N}\right)]t} \\ &+ \int_0^t \sum_{k=1}^{N} e^{n\frac{2i\pi k}{N}} e^{-[\beta - 2J\cos\left(\frac{2\pi k}{N}\right)](t-t')} \hat{\eta}_k(t') dt'\,,\end{aligned} \tag{34}$$

where $\hat{x}_k(0) = \sum_{n=1}^{N} e^{-k\frac{2\pi in}{N}} x_n(0)$ and $\hat{\eta}_k(t') = \sum_{n=1}^{N} e^{-k\frac{2\pi in}{N}} \eta_n(t')$ can be interpreted as the Fourier-coefficients of the initial condition and the Gaussian white noise respectively. Note, that $\langle \hat{\eta}_k(t)\hat{\eta}_{k'}(t') \rangle = q\delta_{k,k'}\delta(t-t')$. The correlation function $\langle x_n(t_1)x_m(t_2) \rangle$ is given by

$$\begin{aligned}&\langle x_n(t_1)x_m(t_2) \rangle = \\ &\sum_{k=1}^{N} \hat{x}_k^2(0) e^{(n-m)\frac{2i\pi k}{N}\gamma(k)(t_1+t_2)} \\ &+q\int_0^{\min(t_1,t_2)} dt' \sum_{k=1}^{N} e^{(n-m)\frac{2i\pi k}{N}} e^{\gamma(k)(t_1+t_2-2t')} \\ &= \sum_{k=1}^{N} \hat{x}_k^2(0) e^{(n-m)\frac{2i\pi k}{N} + \gamma(k)(t_1+t_2)} \\ &+q\sum_{k=1}^{N} e^{(n-m)\frac{2i\pi k}{N}} \frac{-1}{2\gamma(k)} \left(e^{\gamma(k)|t_1-t_2|} - e^{\gamma(k)(t_1+t_2)}\right)\end{aligned} \tag{35}$$

In the stationary state, i.e. where both t_1 and t_2 are much larger than $|\gamma(k)|^{-1} = |(-\beta+2|J|)|^{-1}$, one obtains

$$\langle x_n(t_1)x_m(t_2) \rangle_s = \sum_{k=0}^{N-1} e^{(n-m)\frac{2i\pi k}{N}} \frac{-q}{2\gamma(k)} e^{\gamma(k)|t_1-t_2|}\,. \tag{36}$$

For two-dimensional cell arrangements it is convenient to label the cell with two indices (m,n). In the square lattice each cell has four neighbors and the cell at (m,n) at $(m+1,n),(m-1,n),(m,n+1),(m,n-1)$. For constant and isotropic nearest neighbor couplings, Eq.(21) simplifies significantly. Assuming again periodic boundary conditions and that the diagonal elements of the coupling matrix are constant $-\beta$ one obtains for the square lattice

$$\begin{aligned}\dot{x}_{m,n}(t) = &-\beta x_{m,n} + \eta_{m,n}(t) \\ &J\left(x_{m+1,n} + x_{m-1,n} + x_{m,n+1} + x_{m,n-1}\right)\,.\end{aligned} \tag{37}$$

Following the same logic as for the one-dimensional problem, we first obtain the eigenvalues of the coupling matrix

$$\begin{aligned}\gamma_{sq}(k_x,k_y) &= -\beta + J\left(e^{\frac{2i\pi k_x}{N}} + e^{-\frac{2i\pi k_x}{N}} + e^{\frac{2i\pi k_y}{N}} + e^{-\frac{2i\pi k_y}{N}}\right) \\ &= -\beta + 2J\left[\cos\left(\frac{2\pi k_x}{N}\right) + \cos\left(\frac{2\pi k_y}{N}\right)\right]\,.\end{aligned} \tag{38}$$

The system is now stable for $-\frac{\beta}{4} \leq J \leq \frac{\beta}{4}$. The homogeneous solution of Eq.(37) reads

$$x_{m,n}^h(t) = \sum_{k_x=0}^{N-1}\sum_{k_y=0}^{N-1} e^{m\frac{2i\pi k_x}{N} + n\frac{2i\pi k_y}{N}} e^{\gamma_{sq}(k_x,k_y)t} \hat{x}_{k_x,k_y}(0)\,, \tag{39}$$

where $\hat{x}_{k_x,k_y}(0)$ can again be interpreted as the Fourier coefficients of the initial conditions and the covariance function in the stationary state is given by

$$\begin{aligned}&\langle x_{m,n}(t_1)x_{j,l}(t_2) \rangle_s^{(sq)} = \\ &\sum_{k_x=1}^{N}\sum_{k_y=1}^{N} e^{(m-j)\frac{2i\pi k_x}{N}} e^{(n-l)\frac{2i\pi k_y}{N}} \frac{-q}{2\gamma_{sq}(k_x,k_y)} e^{\gamma_{sq}(k_x,k_y)|t_1-t_2|}\,.\end{aligned} \tag{40}$$

For the the hexagonal cell arrangement the situation is slightly more difficult. Let us consider a cell at a position $\mathbf{R}$. In a hexagonal arrangement this cell has six neighboring sites at $\mathbf{R}+\mathbf{a}_1$, $\mathbf{R}-\mathbf{a}_1$, $\mathbf{R}+\mathbf{a}_2$, $\mathbf{R}-\mathbf{a}_2$, $\mathbf{R}+\mathbf{a}_1-\mathbf{a}_2$ and $\mathbf{R}-\mathbf{a}_1+\mathbf{a}_2$, with $\mathbf{a}_1 = (-\frac{1}{2}, \frac{\sqrt{3}}{2})^T$ and $\mathbf{a}_2 = (\frac{1}{2}, \frac{\sqrt{3}}{2})^T$. Each cell location can be written as $\mathbf{R} = m\mathbf{a}_1 + n\mathbf{a}_2$ and we can label each cell by $x_{m,n}$. The equation of motion of our tissue model then reads

$$\begin{aligned}\dot{x}_{m,n}(t) = &-\beta x_{m,n} + \eta_{m,n}(t) \\ &+ J\big(x_{m+1,n} + x_{m-1,n} + x_{m,n+1} \\ &+ x_{m,n-1} + x_{m-1,n+1} + x_{m+1,n-1}\big)\,.\end{aligned} \tag{41}$$

The eigenvalues are given by

$$\begin{aligned}\gamma_{hex}(k_1,k_2) = &-\beta + 2J\Big[\cos\big(\frac{2\pi k_1}{N}\big) \\ &+ \cos\big(\frac{2\pi k_2}{N}\big) + \cos\big(\frac{2\pi(k_1-k_2)}{N}\big)\Big]\,,\end{aligned} \tag{42}$$

implying that the system is stable for $-\frac{\beta}{3} < J < \frac{\beta}{6}$. The geometry of the hexagonal coupling thus introduces non-symmetric bounds for the allowed range of coupling values, allowing for larger absolute values for anti-coupling between cells. Repeating the same steps as before, we arrive at the stationary state covariance function

$$\langle x_{m,n}(t_1)x_{j,l}(t_2)\rangle_s^{(hex)} = \sum_{k_1=1}^{N}\sum_{k_2=1}^{N} e^{(m-j)\frac{2i\pi k_1}{N}} e^{(n-l)\frac{2i\pi k_2}{N}} \frac{-q}{2\gamma(k_1,k_2)} e^{\gamma_{hex}(k_1,k_2)|t_1-t_2|} \quad (43)$$

To model the T1-transition we need to introduce time-dependent coupling strength. Consider the following equation

$$\begin{aligned}\dot{x}_{m,n}(t) = &-\beta x_{m,n} \\ &+ J(x_{m+1,n} + x_{m-1,n} + x_{m,n+1} + x_{m,n-1}) \\ &+ \alpha(t)J(x_{m-1,n+1} + x_{m+1,n-1}) \\ &+ \kappa(t)J(x_{m+1,n+1} + x_{m-1,n-1}) \\ &+ \eta_{m,n}(t) \end{aligned} \quad (44)$$

For $\alpha(t) = 1$ and $\kappa(t) = 0$ this equation reduces to Eq.(41) while for $\alpha(t) = 0$ and $\kappa(t) = 0$ it describes the dynamics on the quadratic lattice. Thus for $\alpha(t) = L(t)/L_0$, where $L(t)$ is the length of the constricting boundary, and $\kappa(t) = 0$ it describes the constriction phase of the T1-transition. For $\kappa(t) = D(t)/D_0$, where $D(t)$ is the length of the newly established boundary, and $\alpha(t) = 0$ it describes the expansion phase of the T1-transition. Note that due to the transition the topology of the periodic boundaries changes, making their interpretation difficult. Furthermore, due to the introduction of a time-dependent coupling it is no longer possible to find an analytical solution of Eq.(44). We thus need to study Eq.(44) numerically.

IV. NUMERICAL SIMULATIONS

The large number of equations to be simulated require an efficient and reliable implementation. We use a highly efficient strong stochastic Runge-Kutta method or order 1.0 17 which provides fast and accurate simulations of the set of coupled stochastic differential equations . The core of the code is written in C++, which is wrapped by a thin python layer for ease of use. The implementation can easily handle on the order of 100 coupled SDEs on a normal desktop computer. Square and hexagonal as well as the combined lattice, are implemented, as are periodic and non-periodic boundary conditions. The explicit time dependent factors $\alpha(t)$ and $\kappa(t)$ can be naturally included in the stochastic Runge-Kutta scheme. Simulations are then performed with parameters as described in the main text, with lattices of size 10 by 10 and a step size of $\Delta t = 0.01$. Both increasing the lattice and reducing the step size did not significantly affect the results. For big enough lattices such as the ones used here, the effect of the boundary conditions (periodic vs. non-periodic) was found to be negligible. As a check, we first simulated the hexagonal and squared lattices, for which we have calculated the analytical solutions above, and found perfect agreement. We then proceeded to simulate the case of time-dependent transitions that captures important features of the experimentally observed dynamics. For this, we let the system equilibrate from $t = 3$ to $t = 0$, and then simulated a contraction, intermediate and expanding phase as follows. At four different times $t_i = \{2.5,3,7,8\}$, the couplings between different neighbors are updated according to the values $J_1 = \{0.2,0.01,0.2,0.01\}$ and $J_2 = \{0.2,0.2,0.15,0.01\}$ from their initial values of $J_1 = 0.1$ and $J_2 = 0.1$.

The simulated equation is given by

$$\begin{aligned}\dot{x}_{m,n}(t) = &-\beta x_{m,n} \\ &+ J_1(t)(x_{m+1,n} + x_{m-1,n} + x_{m,n+1} + x_{m,n-1}) \\ &+ J_2(t)(x_{m-1,n+1} + x_{m+1,n-1}) \\ &+ \eta_{m,n}(t) \end{aligned} \quad (45)$$

with $\beta = 1$.

For the case of an additional shift in the mean of the cell area, we add a sigmoid to the cell area described by

$$\bar{a}(t) = \frac{\nu\eta}{1 + e^{-k(t-t_0)}} \quad (46)$$

where $\nu = 1$ for DV and $\nu = 1$ for AP cells, k=1, $t_0 = 3$ and η is the magnitude of the sigmoid.

Chapter 9

Conclusions

In this thesis, the coordination of epithelial cells during *Drosophila* embryo development was investigated. I contributed to the field by developing novel experimental and quantitative methods, performing quantitative large scale analysis of epithelial tissue dynamics, mathematical modeling of intercellular coordination and combining all of these aspects to investigate concrete biological questions during *Drosophila* development.

9.1 Main results

Epithelial cells can receive and respond to mechanical stimuli transmitted at the cell-cell junction. This has been shown by others before, for instance by mechanically or genetically perturbing the system, and therefore by experimental intervention [33, 43, 204, 247]. However, for the first time, it was possible to find quantitative evidence of intercellular coordination during morphogenesis by means of large-scale data analysis in living embryos. Investigating the resulting ensemble, subtle phenotypical differences between wild type and mutant embryos could be resolved that would otherwise not have been detected by inspection of a few examples or single embryos or by focusing only on certain parts of a tissue. To this end, data from several experimental trials have to be aligned to biologically well defined target states. Examples are dorsal closure onset at the end of gastrulation or the 4x vertex points of T1 processes. Because biological processes have a function the alignment procedure to these functionally important target states allows us to study the average dynamics that drives the system towards these states by means of statistical ensemble analysis. Deterministic signals and cues can be separated from noise that would normally hide the important dynamics. Gaining better quantitative understanding about such processes allows the inference of qualitative underlying principles from the data and ultimately helps us understand how biology achieves such a fascinating thing as developing a new organism.

Tmc is necessary for synchronization of cell oscillations

We have gathered evidence that the ion channel *Tmc* has a function for synchronization of cell oscillations in the amnioserosa, a squamous epithelium at the dorsal side of the embryo, which is involved in dorsal closure. It is one of the first studies that directly shows the importance of a mechanosensitive mechanism for intercellular coordination from the analysis of an ensemble of embryos.

Synchronization was directly measured via cross-correlation analysis of neighboring cells from data of fully segmented amnioserosa tissue during the ellipsoidal phase, which is beginning after germband retraction and lasts until dorsal closure onset. Using a mathematical model,

introduced in chapter 5, we have shown that a mechanosensitive coupling mechanism, like *Tmc* , indeed leads to synchronization of local cell dynamics. Simulations were conducted to perturb single cells in the tissue by inducing contractions and revealing that neighboring dynamics is dependent on the strength of the modeled coupling mechanism. Experimentally, we tested this by induced cell contractions in a target cell (using the method from chapter 3) and found that neighbors of that cell do not contract in *Tmc* mutants while wild type cells contract simultaneously with the target, which confirms the simulation result. From the literature it is already known that loss of *Tmc* causes a decrease in the Ca^{2+} response of peripheral sensory neurons upon bending of larvae [113]. To directly show that *Tmc* has an effect on the Ca^{2+} dynamics in the amnioserosa as well, the tissue has been challenged via wounding experiments. Here we could show that the resulting Ca^{2+} signal at neighboring junctions was significantly lower for *Tmc* mutants, which therefore presents direct evidence that *Tmc* has an effect on Ca^{2+} signaling in the amnioserosa.

In addition, *Tmc* mutants show morphological differences to the wild type, which was presented in chapter 6. AS bulk cells assume isotropic shapes to a significantly lesser degree compared to wild type embryos. The elongated cell shapes are pointing preferentially in the lateral direction, which could be caused by anisotropic tension. Using laser ablation experiments we estimated tension at axial and lateral junction via observations of the recoil velocity. Lateral junctions in *Tmc* mutants showed a significantly higher tension compared to axial junction, while wild type embryos display no difference and therefore isotropically distributed tension in the epithelium. Separating the lateral epidermis from the amnioserosa shortly before junction ablation shows a dramatic decrease in recoil velocity, indicating that the tension is due to forces from the epidermal cells.

The fact that *Tmc* affects both synchronization of local cell dynamics and force distribution in the tissue hints towards a function of intercellular synchronization for orchestrating internal cellular forces on the tissue level. It is well known that dorsal closure is a complex orchestra of forces, originating from several different sources, which operate together to shrink the amnioserosa towards the midline and close the back of the fly, e.g. reviewed in [123, 166]. While certainly different processes are at work during closure than in the ellipsoidal phase, which precedes it, the stage for dorsal closure is already being set from germband retraction onwards. This includes isotropic distribution of tension, stiffening of the tissue and the formation of the actin purse string around the amnioserosa. During dorsal closure, several redundant processes contribute the force to shrink the tissue [72, 92, 142, 166, 321], however one of the main force contributions is coming from the amnioserosa bulk cells [166]. Since *Tmc* impairs isotropic force distribution during ellipsoidal phase, it is conceivable that it also assists in the coordination of forces during dorsal closure.

While the focus here was on *Tmc* we also investigated data from *xit* which is affecting the distribution of E-Cadherin at the adherens junction [355]. Some similarities of both mutants are mainly for the morphological differences to wild type which also for *xit* include anisotropic tension and elongated cell shape, even displaying a stronger phenotype in this regard. Mechanical stimuli are transmitted at the adherens junction, where E-Cadherin essentially connects the cytoskeleton of two neighboring cells as described in the introduction section 2.10. *xit* affects the E-Cadherin clustering at the junction, therefore direct interference with the signal transmitting capability at the adherens junction also results in the described phenotypical differences. Interestingly, while we observe a drop in overall synchronization in *xit* it is not so strong as for *Tmc* and in addition the spatial arrangement of cell couplings is preserved. This points toward distinct mechanisms of *Tmc* and *xit* . It is still conceivable that *Tmc* is colocalized with E-Cadherin and both are part of the same molecular mechano-transduction mechanism at the cell-cell junction, but the distinct results indicate that there are other processes for which both

components are important.

E-Cadherin affects efficiency of T1 transitions

E-Cadherin is also the focus of investigation in the next study where we looked at T1 transitions in the germband. Using optochemical uncaging we succeed in the initiation of a T1 process and triggering the formation of a new junction by simultaneously contracting the participating cells in a directed manner. This indicates that synchronization of the participating cells could enhance the efficiency of T1 transitions and lead to new junction formation.

This is further studied in an ensemble of >1000 T1 processes where we indeed find that synchronization of the participating cells enhances T1 rate and that *xit* is necessary for the coordination of participating cells. T1 processes do not always result in neighbor exchange and formation of a new junction. Data analysis shows that the process is stochastic and exhibits an exponential exit rate for the formation of a junction between the new neighbors. There is a non-vanishing probability for the reverse transition, resulting in failure for novel junction formation. Both, the exit rate and the fraction of reverse transitions are dependent on *xit* whereas *xit* mutant embryos display smaller rates and a higher reverse probability.

In wild type embryos, the synchronization of the participating cells is significantly higher than in the mutants. Therefore the efficiency of the T1 process could be directly related to the coordination capability of the cells.

A mathematical theory supplements the findings by showing that the degree of synchronization is very high compared to the theoretical limit that was calculated for hexagonal packing. In addition, comparison of simulation and experiment shows that a time-dependent protocol is necessary to achieve the observed phase-dependent correlation between the cells.

As already mentioned, *xit* affects the E-Cadherin distribution at the adherens junction which suggests a role for E-Cadherin as signal transducer for the coordination of the participating cells. *xit* is necessary for the efficiency of T1 processes. As others have shown, speed of a T1 process has direct implications for the rheological features of the tissue. According to vertex simulations done in [81], slow T1 transitions result in elastic properties, while the plasticity needed for the germband to elongate can only be achieved with sufficiently high transition rate of the T1. It is fitting that germband elongation is impaired in *xit* , taking longer and displaying a higher failure rate.

According to this result, E-Cadherin mediated coordination of active stresses during T1 processes might be one of the main components needed for successful convergent extension of epithelial tissues. Our findings constitute compelling evidence for how mechanical regulation on the fly drives morphogenesis.

Quantitative analysis of amnioserosa

While the main aim of the thesis was to investigate the above noted biological questions, as a "side effect" the large scale analysis of the amnioserosa provides a unique dataset that allows to accurately quantify the ellipsoidal phase before dorsal closure onset. Most of the research field is more concerned with dorsal closure itself, while the phase preceding it is less studied. This phase, which we termed the ellipsoidal phase, due to its geometry, denotes the time when germband is almost retracted and before the zipping at the canthi of the amnioserosa begins. Cells and tissue are preparing for dorsal closure, for instance the purse string formation is happening [166].

We quantified static and kinematic properties of the amnioserosa and its cells and made a comparison between *xit* and *Tmc* mutants and the wild type. Most striking morphological differences are the elongated cells in *xit* and *Tmc* mutants which we quantified in terms of a nematic order parameter. The direction of elongation is mostly towards the lateral epidermis,

which suggests anisotropic tension due to forces from the epidermal cells. This was confirmed by laser ablation experiments analyzed in chapter 7.

In general, it is remarkable that the variance of nearly all observables is higher in the mutants. Wild type embryos are significantly more robust and display less sample by sample variation. This points toward essential function of *xit* and *Tmc* for the maintenance of robustness during epithelial morphogenesis. As also shown in the above noted studies we suspect that *xit* and *Tmc* are mediating intercellular coordination. A loss of those molecular components would lead to less coordination and therefore higher variation and less robustness.

Synchronization was studied in large scale ensemble analysis of neighboring cell oscillations. First, we have quantified the oscillations themselves, determining mean periods and their time dependent behavior. Probably due to ongoing stiffening in the amnioserosa in preparation for dorsal closure, the amplitudes of those oscillations decrease. Some embryos also display a shift towards faster oscillations on average.

Using cross-correlation analysis, neighboring cell area synchronization is quantified. Large scale statistical testing reveals differences of composition and spatial order of significantly coupled cell pairs. This result is confirmed by spatial ensemble analysis of the complete correlation coefficient distribution. In chapter 7 we have discussed implications and a possible molecular mechanism that could cause the observed results.

Mathematical model of intercellular coordination

We have modeled epithelial tissue dynamics via a cell-based hexagonal lattice model. The aim of this model is to investigate the impact of a mechanotransduction coupling mechanism between the contraction of neighboring cells and the regulation of Ca^{2+} which in turn upregulates tension via myosin II [212, 315]. It is shown that such a mechanism indeed leads to synchronization between neighboring cells. The mathematical theory makes it clear that anti-synchronized behavior is favorable due to geometric constraints of the cell packing and dissipation of energy at the cell borders.

Comparison of model and experiment was done via optimizing the Jensen divergence between the distribution of correlation coefficients of the cell pairs. For *Tmc* a much broader parameter range is able to produce similar results as found in the experiment. In particular the model suggests that both a loss in coupling strength and a loss in the frequency of cell pairs that are equipped with the coupling mechanism can lead to the shift towards anti-synchronized neighbor dynamics.

To test how neighbors react to the contraction of a target cell we increase Ca^{2+} in a random cell. If the coupling strength is high enough, neighbors do contract as well. The needed coupling is higher than the determined optimal parameter in comparison to the experiment. It might be the case that in such extreme cases, such as the Ca^{2+} uncaging and sudden contraction, a secondary cell machinery is triggered in response. This would explain the high coupling strength. Similar effects are known from wound healing where in response to laser wounding high amounts of Ca^{2+} are recruited and the neighboring cells react with oscillation arrest and contraction to stabilize the tissue [9, 296].

Novel methods for investigation of *Drosophila* morphogenesis

Our approach was to study tissue dynamics systemically by observing thousands of trajectories from several embryos. This became feasible by the development of a segmentation pipeline that utilizes deep neural networks, in particular generative adversarial networks. Our method greatly outperforms traditional rule based methods and enables full segmentation of amnioserosa tissue even despite challenging artifacts due to noise or autofluorescence of secondary structures.

In comparison to other deep learning architectures, our method can be trained even in absence of image-mask ground truth data and still provides similar accuracy. GANs can show better performance in the inference of hardly visible features.

Neural networks are embedded in a semi-automated segmentation pipeline that allows manual correction. If 100% segmentation accuracy is not needed, the pipeline can be operated in fully automated fashion. Segmentation errors are often repeated in specific region of the tissue, for example for very small cells, or due to secondary structures. This leads to the expectation that long, error free, trajectories can still be recorded even without manual correction. The modularized structure of the pipeline makes it easy to replace single components if new technology becomes available. In addition, integration into existing frameworks is simple.

We transferred knowledge from the neuroscience field by exploiting the Ca^{2+} mediated activation of myosin to induce cell contraction *in vivo*. Ca^{2+} is released optochemically by microinjection of Ca^{2+} cages into the living embryo and using a laser to cleave away the bond, which releases Ca^{2+} into the cell. The method is able to induce contraction with single cell resolution and temporally on dynamically relevant timescales.

The functionality of this methods demonstrates that Ca^{2+} is able to regulate myosin II dynamics during *Drosophila* morphogenesis. It was applied in studies in chapter 8 in the germband and chapter 7 in the amnioserosa. The above noted coupling mechanism utilizing mechanosensitive ion channels for the regulation of Ca^{2+} could therefore microscopically work as hypothesized. In addition, the results indicate that Ca^{2+} release could trigger secondary recruitment of Ca^{2+} via opening of membrane channels and leading to influx of extracellular Ca^{2+} or similarly Ca^{2+} from the ER.

9.2 Outlook

One of the main questions that arise from our studies is how *Tmc* is microscopically involved in the mechanotransduction machinery of the cells. Is it colocalized with E-Cadherin at the adherens junctions? How does the recruitment of Ca^{2+} happen? For instance it could be that *Tmc* triggers the opening of further Ca^{2+} ion channels which lead to an influx of Ca^{2+} from the extracellular region. Alternatively Ca^{2+} could also come from the endoplasmatic reticulum. It is difficult to image Ca^{2+} dynamics directly in the amnioserosa, at least with high enough signal to noise ratio which is able to resolve the spatio-temporal dynamics on relevant scales, which would tremendously help to uncover the actual microscopic dynamics.

To link coordination of local cell hubs with force transmission on the tissue level more quantitative analysis is necessary that investigates how the dynamics of the whole amnioserosa plays into coordination. Furthermore, the role of bulk cell oscillations has been subject to many speculations. A dominant hypothesis is that they achieve ratchet-like shrinking of the amnioserosa by subsequently decreasing the area and stiffening of the surround purse string, which is augmented by the zipping process. Evidence for those interactions might be found in the data of the ellipsoidal phase.

To further investigate ion channel function during development studies are planned and already underway that investigate other channels, namely *nompC* and *piezo*, in the amnioserosa in a similar way as we have investigated *Tmc* mutants. Understanding the different impact of distinct channels will help to uncover the full coordination pathway and discriminate between different functions of the channels.

Our mathematical model should be further investigated in particular to understand the impact of local coordination on the morphology and force distribution within the tissue. This can

be achieved by finding the morphology that exerts a constant force on the boundary cells. For different coupling strengths distinct geometrical shapes of the whole tissue should be favorable.

Segmentation using deep learning has already become state of the art during the time this thesis has been worked on. However, the application of GANs is still underutilized for the segmentation of biomedical images where classifiers, like the U-Net are more common. We have preliminary data showing further improvement of segmentation accuracy by incorporation of temporal consistency in the learning objective of the networks. This means, that because we record movies, subsequent frames also contain information about the current one, leading to higher accuracy if this information is incorporated. This is especially true for the amnioserosa where a cell typically stays at roughly the same position throughout the recording.

In addition, neural networks could be used for segmentation in a real-time microscopy setup. Once the networks are trained the inference of features from the image is very fast. This allows to analyze data during the experiment and give the experimentalists cues to further investigate interesting cells or automatically trigger experimental procedures, e.g. automated laser ablation at an exact time point and position.

Bibliography

[1] DS Adams, R Keller, and MA Koehl. "The mechanics of notochord elongation, straightening and stiffening in the embryo of Xenopus laevis". In: *Development* **110** (1990).

[2] K Afshar, B Stuart, and SA Wasserman. "Functional analysis of the Drosophila Diaphanous FH protein in early embryonic development". In: *Development* **127** (2000).

[3] B Aigouy, D Umetsu, and S Eaton. "Segmentation and Quantitative Analysis of Epithelial Tissues." In: *Methods in molecular biology (Clifton, N.J.)* **1478** (2016), pp. 227–239.

[4] B Aigouy et al. "Cell Flow Reorients the Axis of Planar Polarity in the Wing Epithelium of Drosophila". In: *Cell* **142** (2010), pp. 773–786.

[5] B Aigouy et al. "EPySeg: a coding-free solution for automated segmentation of epithelia using deep learning". In: *Development (Cambridge, England)* **147** (2020), pp. 1–4.

[6] JW Alford, RD Vanderneut, and VJ Zaleckas. "Laser Scanning Microscopy". In: *Proceedings of the IEEE* **70** (1982).

[7] S Alt, P Ganguly, and G Salbreux. "Vertex models: from cell mechanics to tissue morphogenesis." In: *Philosophical transactions of the Royal Society of London. Series B, Biological sciences* **372** (2017).

[8] F Amat et al. "Efficient processing and analysis of large-scale light-sheet microscopy data". In: *Nature Protocols* **10** (2015).

[9] M Antunes et al. "Coordinated waves of actomyosin flow and apical cell constriction immediately after wounding". In: *Journal of Cell Biology* **202** (2013).

[10] T Arens et al. *Mathematik*. Springer Berlin Heidelberg, 2015. ISBN: 9783642449192.

[11] M Arjovsky, S Chintala, and L Bottou. "Wasserstein GAN". In: *arXiv e-prints* (2017), arXiv:1701.07875. arXiv: `1701.07875 [stat.ML]`.

[12] J Árnadóttir and M Chalfie. "Eukaryotic mechanosensitive channels". In: *Annual Review of Biophysics* **39** (2010).

[13] Astropy Collaboration et al. "Astropy: A community Python package for astronomy". In: *\aap* **558** (2013), A33. arXiv: `1307.6212 [astro-ph.IM]`.

[14] Astropy Collaboration et al. "The Astropy Project: Building an Open-science Project and Status of the v2.0 Core Package". In: *\aj* **156** (2018), p. 123. arXiv: `1801.02634 [astro-ph.IM]`.

[15] D Azevedo et al. "DRhoGEF2 regulates cellular tension and cell pulsations in the amnioserosa during drosophila dorsal closure". In: *PLoS ONE* (2011).

[16] B Babadi and EN Brown. "A review of multitaper spectral analysis." eng. In: *IEEE transactions on bio-medical engineering* **61** (2014), pp. 1555–1564.

[17] HT Banks, S Hu, and ZR Kenz. "A brief review of elasticity and viscoelasticity for solids". In: *Advances in Applied Mathematics and Mechanics* **3** (2011), pp. 1–51.

[18] K Barrett, M Leptin, and J Settleman. "The Rho GTPase and a putative RhoGEF mediate a signaling pathway for the cell shape changes in Drosophila gastrulation". In: *Cell* **91** (1997).

[19] M Basan et al. "Dissipative particle dynamics simulations for biological tissues: rheology and competition." In: *Physical biology* **8** (2011), p. 26014.

[20] C Batters et al. "Calcium can mobilize and activate myosin-VI". In: *Proceedings of the National Academy of Sciences of the United States of America* **113** (2016).

[21] A Berezhkovskii and A Szabo. "Time scale separation leads to position-dependent diffusion along a slow coordinate". In: *The Journal of Chemical Physics* **135** (2011), p. 74108.

[22] AJ Berglund. "Statistics of camera-based single-particle tracking". In: *Phys. Rev. E* **82** (2010), p. 11917.

[23] M Beurg et al. "Localization of inner hair cell mechanotransducer channels using high-speed calcium imaging". In: *Nature Neuroscience* **12** (2009).

[24] M Beurg et al. "Subunit determination of the conductance of hair-cell mechanotransducer channels". In: *Proceedings of the National Academy of Sciences of the United States of America* **112** (2015).

[25] WS Bialek. *Biophysics : searching for principles*. English. 2012. ISBN: 9780691138916 0691138915.

[26] D Bilder and KD Irvine. "Taking Stock of the Drosophila Research Ecosystem". In: *Genetics* **206** (2017), pp. 1227–1236.

[27] T Bittig et al. "Dynamics of anisotropic tissue growth". In: *New Journal of Physics* **10** (2008), p. 63001.

[28] GB Blanchard and RJ Adams. "Measuring the multi-scale integration of mechanical forces during morphogenesis". In: *Current Opinion in Genetics and Development* **21** (2011).

[29] GB Blanchard, J Étienne, and N Gorfinkiel. "From pulsatile apicomedial contractility to effective epithelial mechanics". In: *Current Opinion in Genetics and Development* (2018).

[30] GB Blanchard, AG Fletcher, and LJ Schumacher. "The devil is in the mesoscale: Mechanical and behavioural heterogeneity in collective cell movement". In: *Seminars in Cell and Developmental Biology* (2019).

[31] GB Blanchard et al. "Cytoskeletal dynamics and supracellular organisation of cell shape fluctuations during dorsal closure". In: *Development* (2010).

[32] DK Blumenthal and JT Stull. "Activation of Skeletal Muscle Myosin Light Chain Kinase by Calcium(2+) and Calmodulin". In: *Biochemistry* **19** (1980).

[33] N Borghi et al. "E-cadherin is under constitutive actomyosin-generated tension that is increased at cell-cell contacts upon externally applied stretch". In: *Proceedings of the National Academy of Sciences of the United States of America* (2012).

[34] TO Buchholz et al. "DenoiSeg: Joint Denoising and Segmentation". In: *arXiv* (2020).

[35] H Byrne and D Drasdo. "Individual-based and continuum models of growing cell populations: a comparison." In: *Journal of mathematical biology* **58** (2009), pp. 657–687.

[36] CA Calder and N Cressie. “Kriging and Variogram Models”. In: ed. by R Kitchin and NBTIEoHG Thrift. Oxford: Elsevier, 2009, pp. 49–55. ISBN: 978-0-08-044910-4.

[37] JA Campos-Ortega and V Hartenstein. “Stages of Drosophila Embryogenesis”. In: *The Embryonic Development of Drosophila melanogaster*. Springer Berlin Heidelberg, 1997, pp. 9–102.

[38] J Canny. “A Computational Approach to Edge Detection”. In: *IEEE Transactions on Pattern Analysis and Machine Intelligence* **PAMI-8** (1986), pp. 679–698.

[39] E Caussinus, O Kanca, and M Affolter. “Fluorescent fusion protein knockout mediated by anti-GFP nanobody”. In: *Nature Structural and Molecular Biology* (2012).

[40] M Cavey et al. “A two-tiered mechanism for stabilization and immobilization of E-cadherin”. In: *Nature* (2008).

[41] L von Chamier et al. “ZeroCostDL4Mic: an open platform to simplify access and use of Deep-Learning in Microscopy”. In: *bioRxiv* (2020).

[42] S Chanet and AC Martin. “Mechanical force sensing in tissues”. In: *Progress in Molecular Biology and Translational Science*. Vol. 126. 2014.

[43] G Charras and AS Yap. “Tensile Forces and Mechanotransduction at Cell-Cell Junctions”. In: *Current Biology* **28** (2018).

[44] B Chauhan et al. “Epithelial morphogenesis: The mouse eye as a model system”. In: *Current Topics in Developmental Biology* **111** (2015), pp. 375–399.

[45] BC Chen et al. “Lattice light-sheet microscopy: Imaging molecules to embryos at high spatiotemporal resolution”. In: *Science* (2014).

[46] HY Chen. “Internal States of Active Inclusions and the Dynamics of an Active Membrane”. In: *Phys. Rev. Lett.* **92** (2004), p. 168101.

[47] L Chen et al. “Quantifying the scale effect in geospatial big data using semi-variograms”. In: *PLOS ONE* **14** (2019), e0225139.

[48] TW Chen et al. “Ultrasensitive fluorescent proteins for imaging neuronal activity”. In: *Nature* **499** (2013).

[49] X Chen et al. “InfoGAN: Interpretable Representation Learning by Information Maximizing Generative Adversarial Nets”. In: *arXiv e-prints* (2016), arXiv:1606.03657. arXiv: `1606.03657 [cs.LG]`.

[50] LE Cheng et al. “The Role of the TRP Channel NompC in Drosophila Larval and Adult Locomotion”. In: *Neuron* **67** (2010).

[51] AP Christensen and DP Corey. “TRP channels in mechanosensation: Direct or indirect activation?” In: *Nature Reviews Neuroscience* **8** (2007).

[52] M Chu et al. “Learning Temporal Coherence via Self-Supervision for GAN-based Video Generation”. In: *arXiv e-prints* (2018), arXiv:1811.09393. arXiv: `1811.09393 [cs.CV]`.

[53] R Cilla et al. “Segmentation and tracking of adherens junctions in 3D for the analysis of epithelial tissue morphogenesis”. In: *PLoS Computational Biology* **11** (2015).

[54] AG Clark et al. “Integration of Single and Multicellular Wound Responses”. In: *Current Biology* **19** (2009).

[55] K Clark, J Middelbeek, and FN van Leeuwen. “Interplay between TRP channels and the cytoskeleton in health and disease”. In: *European Journal of Cell Biology* **87** (2008).

[56] S Cohen-Addad and R Höhler. “Rheology of foams and highly concentrated emulsions”. In: *Current Opinion in Colloid & Interface Science* **19** (2014), pp. 536–548.

[57] C Collinet and T Lecuit. “Programmed and self-organized flow of information during morphogenesis.” eng. In: *Nature reviews. Molecular cell biology* **22** (2021), pp. 245–265.

[58] B Coste et al. “Piezo proteins are pore-forming subunits of mechanically activated channels”. In: *Nature* **483** (2012).

[59] CD Cox, N Bavi, and B Martinac. “Biophysical Principles of Ion-Channel-Mediated Mechanosensory Transduction”. In: *Cell Reports* **29** (2019).

[60] A Dance. “The secret forces that squeeze and pull life into shape”. In: *Nature* **589** (2021), pp. 186–188.

[61] DJ David, A Tishkina, and TJ Harris. “The PAR complex regulates pulsed actomyosin contractions during amnioserosa apical constriction in Drosophila”. In: *Development* (2010).

[62] D Devenport. “Tissue morphodynamics: Translating planar polarity cues into polarized cell behaviors”. In: *Seminars in Cell and Developmental Biology* **55** (2016).

[63] M Dicko et al. “Geometry can provide long-range mechanical guidance for embryogenesis”. In: *PLoS Computational Biology* (2017).

[64] K Dierkes et al. “Spontaneous oscillations of elastic contractile materials with turnover”. In: *Physical Review Letters* **113** (2014).

[65] A Diz-Muñoz, DA Fletcher, and OD Weiner. “Use the force: Membrane tension as an organizer of cell shape and motility”. In: *Trends in Cell Biology* (2013).

[66] D Drasdo and S Höhme. “A single-cell-based model of tumor growthin vitro: monolayers and spheroids”. In: *Physical Biology* **2** (2005), pp. 133–147.

[67] H Driesch. “Entwicklungsmechanische Studien: I. Der Werthe der beiden ersten Furchungszellen in der Echinogdermenentwicklung. Experimentelle Erzeugung von Theil- und Doppelbildungen. II. Über die Beziehungen des Lichtez zur ersten Etappe der thierischen Formbildung”. In: *Zeitschrift für wissenschaftliche Zoologie* **53** (1891), pp. 160–184.

[68] W Driever and C Nüsslein-Volhard. “The bicoid protein determines position in the Drosophila embryo in a concentration-dependent manner”. In: *Cell* **54** (1988).

[69] A Ducuing and S Vincent. “The actin cable is dispensable in directing dorsal closure dynamics but neutralizes mechanical stress to prevent scarring in the Drosophila embryo”. In: *Nature Cell Biology* (2016).

[70] A Ducuing et al. “A DPP-mediated feed-forward loop canalizes morphogenesis during Drosophila dorsal closure”. In: *Journal of Cell Biology* (2015).

[71] S Dunst and P Tomancak. “Imaging flies by fluorescence microscopy: Principles, technologies, and applications”. In: *Genetics* **211** (2019).

[72] J Duque and N Gorfinkiel. “Integration of actomyosin contractility with cell-cell adhesion during dorsal closure”. In: *Development (Cambridge)* (2016).

[73] KA Edwards et al. “GFP-moesin illuminates actin cytoskeleton dynamics in living tissue and demonstrates cell shape changes during morphogenesis in Drosophila”. In: *Developmental Biology* (1997).

[74] T Effertz, R Wiek, and MC Göpfert. “NompC TRP channel is essential for Drosophila sound receptor function”. In: *Current Biology* **21** (2011).

[75] B Efron. “Bootstrap Methods: Another Look at the Jackknife”. In: *The Annals of Statistics* **7** (1979), pp. 1–26.

[76] B Efron. “Large-scale simultaneous hypothesis testing: The choice of a null hypothesis”. In: *Journal of the American Statistical Association* **99** (2004), pp. 96–104.

[77] B Efron. “Local False Discovery Rates”. In: *Large-Scale Inference* (2013), pp. 70–88.

[78] B Efron and T Hastie. *Computer Age Statistical Inference*. 2016. ISBN: 9781107149892.

[79] GT Eisenhoffer et al. “Crowding induces live cell extrusion to maintain homeostatic cell numbers in epithelia”. In: *Nature* **484** (2012).

[80] B Enyedi and P Niethammer. “Mechanisms of epithelial wound detection”. In: *Trends in Cell Biology* **25** (2015).

[81] G Erdemci-Tandogan and ML Manning. “Effect of cellular rearrangement time delays on the rheology of vertex models for confluent tissues”. In: *bioRxiv* (2021).

[82] T Erickson et al. “Integration of Tmc1/2 into the mechanotransduction complex in zebrafish hair cells is regulated by transmembrane o-methyltransferase (Tomt)”. In: *eLife* **6** (2017).

[83] R Etournay et al. “TissueMiner: A multiscale analysis toolkit to quantify how cellular processes create tissue dynamics”. In: *eLife* **5** (2016).

[84] R Farhadifar et al. “The influence of cell mechanics, cell-cell interactions, and proliferation on epithelial packing.” In: *Current biology : CB* **17** (2007), pp. 2095–2104.

[85] DL Farrell et al. “SEGGA: a toolset for rapid automated analysis of epithelial cell polarity and dynamics”. In: *Development* (2017), pp. 1725–1734.

[86] R Fernandez-Gonzalez et al. “Myosin II Dynamics Are Regulated by Tension in Intercalating Cells”. In: *Developmental Cell* **17** (2009).

[87] F Feroz, MP Hobson, and M Bridges. “MultiNest: an efficient and robust Bayesian inference tool for cosmology and particle physics”. In: *Monthly Notices of the Royal Astronomical Society* **398** (2009), pp. 1601–1614.

[88] R Fettiplace. “Is TMC1 the Hair Cell Mechanotransducer Channel?” In: *Biophysical Journal* **111** (2016).

[89] SC Fischer et al. “Contractile and mechanical properties of epithelia with perturbed actomyosin dynamics”. In: *PLoS ONE* (2014).

[90] AG Fletcher, F Cooper, and RE Baker. “Mechanocellular models of epithelial morphogenesis”. In: *Philosophical Transactions of the Royal Society B: Biological Sciences* **372** (2017).

[91] AG Fletcher et al. “Vertex models of epithelial morphogenesis.” In: *Biophysical journal* **106** (2014), pp. 2291–2304.

[92] JD Franke, RA Montague, and DP Kiehart. “Nonmuscle myosin II generates forces that transmit tension and drive contraction in multiple tissues during dorsal closure”. In: *Current Biology* **15** (2005).

[93] JA Freund, L Schimansky-Geier, and P Hänggi. “Frequency and phase synchronization in stochastic systems”. In: *Chaos: An Interdisciplinary Journal of Nonlinear Science* **13** (2003), pp. 225–238.

[94] J Galle et al. “Individual cell-based models of the spatial-temporal organization of multicellular systems - achievements and limitations.” In: *Cytometry. Part A : the journal of the International Society for Analytical Cytology* **69** (2006), pp. 704–710.

[95] J Gates and M Peifer. “Can 1000 reviews be wrong? Actin, α-catenin, and adherens junctions”. In: *Cell* **123** (2005).

[96] LA Gatys, AS Ecker, and M Bethge. "A Neural Algorithm of Artistic Style". In: *arXiv e-prints* (2015), arXiv:1508.06576. arXiv: 1508.06576 [cs.CV].

[97] J Gavin-Smyth et al. "A genetic network conferring canalization to a bistable patterning system in Drosophila". In: *Current Biology* **23** (2013).

[98] J Ge et al. "Architecture of the mammalian mechanosensitive Piezo1 channel". In: *Nature* **527** (2015).

[99] MC Gibson et al. "The emergence of geometric order in proliferating metazoan epithelia". In: *Nature* **442** (2006), pp. 1038–1041.

[100] D Gilmour, M Rembold, and M Leptin. "From morphogen to morphogenesis and back". In: *Nature* (2017).

[101] G Gompper et al. "The 2020 motile active matter roadmap". In: *Journal of Physics Condensed Matter* **32** (2020). arXiv: 1912.06710.

[102] IJ Goodfellow et al. "Generative Adversarial Networks". In: *arXiv e-prints* (2014), arXiv:1406.2661. arXiv: 1406.2661 [stat.ML].

[103] I Goodfellow. "Tutorial: Generative Adversarial Netoworks". In: (2016). arXiv: arXiv:1701.00160v4.

[104] MC Göpfert et al. "Specification of auditory sensitivity by Drosophila TRP channels". In: *Nature Neuroscience* **9** (2006).

[105] N Gorfinkiel. "From actomyosin oscillations to tissue-level deformations". In: *Developmental Dynamics* (2016).

[106] N Gorfinkiel and GB Blanchard. "Dynamics of actomyosin contractile activity during epithelial morphogenesis". In: *Current Opinion in Cell Biology* **23** (2011).

[107] N Gorfinkiel et al. "Mechanical control of global cell behaviour during dorsal closure in Drosophila". In: *Development* (2009).

[108] R Gräf, J Rietdorf, and T Zimmermann. "Live cell spinning disk microscopy". In: *Advances in Biochemical Engineering/Biotechnology* **95** (2005).

[109] SA Gudipaty et al. "Mechanical stretch triggers rapid epithelial cell division through Piezo1". In: *Nature* **543** (2017).

[110] I Guerrero. *http://guerreroslab.cbm.uam.es/wp/*. 2021.

[111] J Gui et al. "A Review on Generative Adversarial Networks : Algorithms , Theory , and Applications". In: *Journal of Latex Class Files* **14** (2015), pp. 1–28. arXiv: arXiv:2001.06937v1.

[112] C Guillot and T Lecuit. "Mechanics of epithelial tissue homeostasis and morphogenesis". In: *Science* (2013).

[113] Y Guo et al. "Transmembrane channel-like (tmc) gene regulates Drosophila larval locomotion". In: *Proceedings of the National Academy of Sciences of the United States of America* (2016).

[114] U Häcker and N Perrimon. "DRhoGEF2 encodes a member of the Dbl family of oncogenes and controls cell shape changes during gastrulation in Drosophila". In: *Genes and Development* **12** (1998).

[115] P Haffter et al. "The identification of genes with unique and essential functions in the development of the zebrafish, Danio rerio". In: *Development* **123** (1996), pp. 1–36.

[116] JM Halbleib and WJ Nelson. "Cadherins in development: Cell adhesion, sorting, and tissue morphogenesis". In: *Genes and Development* **20** (2006).

[117] KG Hales et al. “Genetics on the fly: A primer on the drosophila model system”. In: *Genetics* **201** (2015), pp. 815–842.

[118] Y Hara, M Shagirov, and Y Toyama. “Cell Boundary Elongation by Non-autonomous Contractility in Cell Oscillation”. In: *Current Biology* **26** (2016).

[119] N Harden et al. “Drac1 and crumbs participate in amnioserosa morphogenesis during dorsal closure in Drosophila”. In: *Journal of Cell Science* **115** (2002).

[120] M Häring et al. “Automated Segmentation of Epithelial Tissue Using Cycle-Consistent Generative Adversarial Networks”. In: *bioRxiv* (2018).

[121] V Hartenstein. *Atlas of Drosophila development*. Vol. 328. Cold Spring Harbor Laboratory Press, 1993.

[122] V Hartenstein, GM Technau, and JA Campos-Ortega. “Fate-mapping in wild-type Drosophila melanogaster”. In: *Wilhelm Roux’s Archives of Developmental Biology* **194** (1985).

[123] P Hayes and J Solon. “Drosophila dorsal closure: An orchestra of forces to zip shut the embryo”. In: *Mechanisms of Development* (2017).

[124] K He et al. “Deep Residual Learning for Image Recognition”. In: *arXiv e-prints* (2015), arXiv:1512.03385. arXiv: `1512.03385 [cs.CV]`.

[125] L He et al. “Mechanical regulation of stem-cell differentiation by the stretch-activated Piezo channel”. In: *Nature* **555** (2018).

[126] L He et al. “Tissue elongation requires oscillating contractions of a basal actomyosin network”. In: *Nature Cell Biology* **12** (2010).

[127] NC Heer et al. “Actomyosin-based tissue folding requires a multicellular myosin gradient”. In: *Development (Cambridge, England)* **144** (2017), pp. 1876–1886.

[128] P Hehlert, W Zhang, and MC Göpfert. “Drosophila Mechanosensory Transduction.” eng. In: *Trends in neurosciences* **44** (2021), pp. 323–335.

[129] CP Heisenberg. “Dorsal closure in Drosophila: Cells cannot get out of the tight spot”. In: *BioEssays* (2009).

[130] CP Heisenberg and Y Bellaïche. “Forces in tissue morphogenesis and patterning”. In: *Cell* **153** (2013), p. 948.

[131] W Helfrich. “Elastic properties of lipid bilayers: theory and possible experiments.” In: *Zeitschrift fur Naturforschung. Teil C: Biochemie, Biophysik, Biologie, Virologie* **28** (1973), pp. 693–703.

[132] D Heller et al. “EpiTools: An Open-Source Image Analysis Toolkit for Quantifying Epithelial Growth Dynamics Technology”. In: *Developmental Cell* **36** (2016), pp. 103–116.

[133] A Hilfinger and J Paulsson. “Separating intrinsic from extrinsic fluctuations in dynamic biological systems.” eng. In: *Proceedings of the National Academy of Sciences of the United States of America* **108** (2011), pp. 12167–12172.

[134] GE Hinton and RR Salakhutdinov. “Reducing the Dimensionality of Data with Neural Networks”. In: *Science* **313** (2006), pp. 504–507.

[135] H Huang et al. “UNet 3+: A Full-Scale Connected UNet for Medical Image Segmentation”. In: *arXiv e-prints* (2020), arXiv:2004.08790. arXiv: `2004.08790 [eess.IV]`.

[136] J Huang et al. “Directed, efficient, and versatile modifications of the Drosophila genome by genomic engineering”. In: *Proceedings of the National Academy of Sciences of the United States of America* **106** (2009).

[137] RJ Huebner and JB Wallingford. "Coming to Consensus: A Unifying Model Emerges for Convergent Extension". In: *Developmental cell* **46** (2018), pp. 389–396.

[138] L Hufnagel et al. "On the mechanism of wing size determination in fly development". In: *Proceedings of the National Academy of Sciences* **104** (2007), pp. 3835–3840.

[139] J Huisken and DY Stainier. "Selective plane illumination microscopy techniques in developmental biology". In: *Development* **136** (2009).

[140] J Huisken et al. "Optical sectioning deep inside live embryos by selective plane illumination microscopy". In: *Science* **305** (2004).

[141] GL Hunter et al. "Ion channels contribute to the regulation of cell sheet forces during Drosophila dorsal closure". In: *Development (Cambridge)* (2014).

[142] MS Hutson et al. "Forces for morphogenesis investigated with laser microsurgery and quantitative modeling". In: *Science* (2003).

[143] Ian Goodfellow and Yoshua Bengio and Aaron Courville. *Deep Learning*. MIT Press, 2016. ISBN: 978-0262035613.

[144] R Iino, I Koyama, and A Kusumi. "Single molecule imaging of green fluorescent proteins in living cells: E-cadherin forms oligomers on the free cell surface". In: *Biophysical Journal* **80** (2001).

[145] T Isokawa, H Nishimura, and N Matsui. "Quaternionic Multilayer Perceptron with Local Analyticity". In: *Information* **3** (2012), pp. 756–770.

[146] P Isola et al. "Image-to-Image Translation with Conditional Adversarial Networks". In: *arXiv e-prints* (2016), arXiv:1611.07004. arXiv: `1611.07004 [cs.CV]`.

[147] A Jacinto, S Woolner, and P Martin. "Dynamic Analysis of Dorsal Closure in Drosophila: From Genetics to Cell Biology". In: *Developmental Cell* **3** (2002), pp. 9–19.

[148] A Jacinto et al. "Dynamic actin-based epithelial adhesion and cell matching during Drosophila dorsal closure". In: *Current Biology* (2000).

[149] F Jankovics and D Brunner. "Transiently reorganized microtubules are essential for zippering during dorsal closure in Drosophila melanogaster." In: *Developmental cell* **11** (2006), pp. 375–385.

[150] AK Jayasinghe et al. "Apical oscillations in amnioserosa cells: Basolateral coupling and mechanical autonomy". In: *Biophysical Journal* (2013).

[151] Y Jia et al. "TMC1 and TMC2 Proteins Are Pore-Forming Subunits of Mechanosensitive Ion Channels". In: *Neuron* **105** (2020), 310–321.e3.

[152] F Jug et al. "Bioimage Informatics in the context of Drosophila research". In: *Methods* **68** (2014).

[153] F Jülicher and J Prost. "Cooperative Molecular Motors". In: *Phys. Rev. Lett.* **75** (1995), pp. 2618–2621.

[154] F Jülicher and J Prost. "Spontaneous Oscillations of Collective Molecular Motors". In: *Phys. Rev. Lett.* **78** (1997), pp. 4510–4513.

[155] J Jurado, J de Navascués, and N Gorfinkiel. "α-Catenin stabilises Cadherin-Catenin complexes and modulates actomyosin dynamics to allow pulsatile apical contraction". In: *Journal of Cell Science* (2016).

[156] A Kamikouchi et al. "The neural basis of Drosophila gravity-sensing and hearing". In: *Nature* **458** (2009).

[157] T Kaneuchi et al. “Calcium waves occur as Drosophila oocytes activate”. In: *Proceedings of the National Academy of Sciences of the United States of America* **112** (2015).

[158] K Kaouri et al. “A simple mechanochemical model for calcium signalling in embryonic epithelial cells”. In: *Journal of Mathematical Biology* **78** (2019), pp. 2059–2092. arXiv: 1901.07016.

[159] T Karras, S Laine, and T Aila. “A Style-Based Generator Architecture for Generative Adversarial Networks”. In: *arXiv e-prints* (2018), arXiv:1812.04948. arXiv: 1812.04948 [cs.NE].

[160] M Kaschube et al. “Universality in the Evolution of Orientation Columns in the Visual Cortex”. In: *Science* **330** (2010), pp. 1113–1116.

[161] KE Kasza, DL Farrell, and JA Zallen. “Spatiotemporal control of epithelial remodeling by regulated myosin phosphorylation”. In: *Proceedings of the National Academy of Sciences of the United States of America* **111** (2014).

[162] Y Kawashima et al. “Mechanotransduction in mouse inner ear hair cells requires transmembrane channel-like genes”. In: *Journal of Clinical Investigation* **121** (2011).

[163] PJ Keller. “Imaging morphogenesis: Technological advances and biological insights”. In: *Science* (2013).

[164] R Keller. “Physical biology returns to morphogenesis”. In: *Science* **338** (2012).

[165] G Keresztes, H Mutai, and S Heller. “TMC and EVER genes belong to a larger novel family, the TMC gene family encoding transmembrane proteins”. In: *BMC Genomics* **4** (2003).

[166] DP Kiehart et al. “Cell Sheet Morphogenesis: Dorsal Closure in Drosophila melanogaster as a Model System”. In: *Annual Review of Cell and Developmental Biology* **33** (2017), pp. 169–202.

[167] DP Kiehart et al. “Multiple forces contribute to cell sheet morphogenesis for dorsal closure in Drosophila”. In: *Journal of Cell Biology* (2000).

[168] KX Kim and R Fettiplace. “Developmental changes in the cochlear hair cell mechanotransducer channel and their regulation by transmembrane channel-like proteins”. In: *Journal of General Physiology* (2013).

[169] T Kim et al. “Learning to Discover Cross-Domain Relations with Generative Adversarial Networks”. In: *arXiv e-prints* (2017), arXiv:1703.05192. arXiv: 1703.05192 [cs.CV].

[170] DP Kingma and JL Ba. “A : a m s o”. In: (2015), pp. 1–15. arXiv: arXiv:1412.6980v9.

[171] V Kölsch et al. “Control of drosophila gastrulation by apical localization of adherens junctions and RhoGEF2”. In: *Science* (2007).

[172] D Kong, F Wolf, and J Großhans. “Forces directing germ-band extension in Drosophila embryos”. In: *Mechanisms of Development* (2017).

[173] D Kong et al. “In vivo optochemical control of cell contractility at single-cell resolution”. In: *EMBO reports* **20** (2019).

[174] S Koride et al. “Mechanochemical regulation of oscillatory follicle cell dynamics in the developing Drosophila egg chamber”. In: *Molecular Biology of the Cell* **25** (2014).

[175] M Kosloff et al. “Regulation of light-dependent Gqα translocation and morphological changes in fly photoreceptors”. In: *EMBO Journal* (2003).

[176] K Kruse et al. “Generic theory of active polar gels: a paradigm for cytoskeletal dynamics.” In: *The European physical journal. E, Soft matter* **16** (2005), pp. 5–16.

[177] K Kruse and F Jülicher. “Oscillations in cell biology”. In: *Current Opinion in Cell Biology* **17** (2005).

[178] U Krzic et al. “Multiview light-sheet microscope for rapid in toto imaging.” In: *Nature methods* **9** (2012), pp. 730–733.

[179] K Kurima et al. “Characterization of the transmembrane channel-like (TMC) gene family: Functional clues from hearing loss and epidermodysplasia verruciformis”. In: *Genomics* (2003).

[180] K Kurima et al. “Dominant and recessive deafness caused by mutations of a novel gene, TMC1, required for cochlear hair-cell function”. In: *Nature Genetics* (2002).

[181] K Kurima et al. “TMC1 and TMC2 Localize at the Site of Mechanotransduction in Mammalian Inner Ear Hair Cell Stereocilia”. In: *Cell Reports* **12** (2015).

[182] ME Lacy and MS Hutson. “Amnioserosa development and function in Drosophila embryogenesis: Critical mechanical roles for an extraembryonic tissue”. In: *Developmental Dynamics* (2016).

[183] SN Lahiri. “Theoretical comparisons of block bootstrap methods”. In: *Annals of Statistics* **27** (1999), pp. 386–404.

[184] T Lecuit. *Cell Polarity and Morphogenesis*. Academic Press, 2017.

[185] T Lecuit, PF Lenne, and E Munro. “Force generation, transmission, and integration during cell and tissue morphogenesis”. In: *Annual Review of Cell and Developmental Biology* **27** (2011).

[186] T Lecuit and AS Yap. “E-cadherin junctions as active mechanical integrators in tissue dynamics”. In: *Nature Cell Biology* **17** (2015).

[187] HC Lee and N Auersperg. “Calcium in epithelial cell contraction”. In: *Journal of Cell Biology* (1980).

[188] NW Lenner. “Reverse-time Inference of Biological Dynamics”. PhD thesis. Göttingen: Georg-August-Universität Göttingen, 2020.

[189] I Lestas, G Vinnicombe, and J Paulsson. “Fundamental limits on the suppression of molecular fluctuations”. eng. In: *Nature* **467** (2010), pp. 174–178.

[190] X Liang and J Howard. “Structural Biology: Piezo Senses Tension through Curvature”. In: *Current Biology* **28** (2018).

[191] SY Lin and DP Corey. “TRP channels in mechanosensation”. In: *Current Opinion in Neurobiology* **15** (2005), pp. 350–357.

[192] J Lippincott-Schwartz and GH Patterson. “Development and use of fluorescent protein markers in living cells”. In: *Science* **300** (2003).

[193] WC Lo et al. “Unified biophysical mechanism for cell-shape oscillations and cell ingression”. In: *Phys. Rev. E* **97** (2018), p. 62414.

[194] H Lu et al. “Quantifying dorsal closure in three dimensions”. In: *Molecular Biology of the Cell* **27** (2016).

[195] H Lu et al. “Remodeling Tissue Interfaces and the Thermodynamics of Zipping during Dorsal Closure in Drosophila”. In: *Biophysical Journal* (2015).

[196] AM Lucas et al. “Open-source deep-learning software for bioimage segmentation”. In: *Molecular Biology of the Cell* **32** (2021).

[197] HE Lynch et al. “Cellular mechanics of germ band retraction in Drosophila”. In: *Developmental Biology* (2013).

[198] X Ma et al. “Probing embryonic tissue mechanics with laser hole drilling”. In: *Physical Biology* **6** (2009).

[199] PF Machado et al. “Cytoskeletal turnover and Myosin contractility drive cell autonomous oscillations in a model of Drosophila Dorsal Closure”. In: *European Physical Journal: Special Topics* (2014). arXiv: 1402.5258.

[200] PF Machado et al. “Emergent material properties of developing epithelial tissues”. In: *BMC Biology* (2015).

[201] R Maeda et al. “Functional analysis of the transmembrane and cytoplasmic domains of Pcdh15a in zebrafish hair cells”. In: *Journal of Neuroscience* **37** (2017).

[202] R Maeda et al. “Tip-link protein protocadherin 15 interacts with transmembrane channel-like proteins TMC1 and TMC2”. In: *Proceedings of the National Academy of Sciences of the United States of America* **111** (2014).

[203] AA Mahmud et al. “Loss of the proprioception and touch sensation channel PIEZO2 in siblings with a progressive form of contractures”. In: *Clinical Genetics* **91** (2017).

[204] JL Maître and CP Heisenberg. “Three functions of cadherins in cell adhesion”. In: *Current Biology* (2013).

[205] JL Maître et al. “Pulsatile cell-autonomous contractility drives compaction in the mouse embryo”. In: *Nature Cell Biology* **17** (2015).

[206] M Maleki, X Emery, and N Mery. “Indicator variograms as an aid for geological interpretation and modeling of ore deposits”. In: *Minerals* **7** (2017).

[207] WA Malik et al. “On the Modeling of the Viscoelastic Response of Embryonic Tissues”. In: *Mathematics and Mechanics of Solids* **13** (2007), pp. 81–91.

[208] Y Mao and B Baum. “Tug of war-The influence of opposing physical forces on epithelial cell morphology”. In: *Developmental Biology* **401** (2015).

[209] Y Mao et al. “Differential proliferation rates generate patterns of mechanical tension that orient tissue growth”. In: *EMBO Journal* **32** (2013).

[210] Y Mao et al. “Planar polarization of the atypical myosin Dachs orients cell divisions in Drosophila.” In: *Genes & development* **25** (2011), pp. 131–136.

[211] MC Marchetti et al. “Hydrodynamics of soft active matter”. In: *Rev. Mod. Phys.* **85** (2013), pp. 1143–1189.

[212] O Markova, S Senatore, and PF Lenne. “Spatiotemporal dynamics of calcium transients during embryogenesis of Drosophila melanogaster”. In: *bioRxiv* (2019), p. 540070.

[213] AC Martin and B Goldstein. “Apical constriction: Themes and variations on a cellular mechanism driving morphogenesis”. In: *Development (Cambridge)* (2014).

[214] AC Martin, M Kaschube, and EF Wieschaus. “Pulsed contractions of an actin-myosin network drive apical constriction”. In: *Nature* **457** (2009).

[215] G Matheron. “Principles of geostatistics”. In: *Economic Geology* **58** (1963), pp. 1246–1266.

[216] M Mathieu, C Couprie, and Y LeCun. “Deep multi-scale video prediction beyond mean square error”. In: 2016.

[217] K Matsuzawa et al. “α-Catenin Controls the Anisotropy of Force Distribution at Cell-Cell Junctions during Collective Cell Migration”. In: *Cell Reports* **23** (2018).

[218] P Matula et al. “Cell Tracking Accuracy Measurement Based on Comparison of Acyclic Oriented Graphs”. In: *PLOS ONE* **10** (2015), e0144959.

[219] DR Mehra. "Power Spectrum Estimation using Welch method for various Window techniques". In: *International Journal of Scientific Research Engineering & Technology* **2** (2013), pp. 389–392.

[220] C Mellon and UC Berkeley. "Tutorial on Variational Autoencoders". In: (2016), pp. 1–23. arXiv: `arXiv:1606.05908v2`.

[221] M Merkel et al. "TissueMiner: A multiscale analysis toolkit to quantify how cellular processes create tissue dynamics". In: *eLife* (2016), pp. 1–28.

[222] L Mescheder, S Nowozin, and A Geiger. "Adversarial variational bayes: Unifying variational autoencoders and generative adversarial networks". In: *34th International Conference on Machine Learning, ICML 2017* **5** (2017), pp. 3694–3707. arXiv: `1701.04722`.

[223] M Mirza and S Osindero. "Conditional Generative Adversarial Nets". In: *arXiv e-prints* (2014), arXiv:1411.1784. arXiv: `1411.1784 [cs.LG]`.

[224] Y Mizuno et al. "Myosin light chain kinase activation and calcium sensitization in smooth muscle in vivo". In: *American Journal of Physiology - Cell Physiology* **295** (2008).

[225] TH Morgan. "Sex limited inheritance in Drosophila". In: *Science* **32** (1910), 120 LP –122.

[226] TH Morgan. "Half-embryos and whole-embryos from one of the first two blastomeres of the frog's egg". In: *Anat. Anz.* **10** (1895), pp. 623–628.

[227] S Mulinari and U Häcker. "Rho-guanine nucleotide exchange factors during development: Force is nothing without control". In: *Small GTPases* **1** (2010).

[228] S Muliyil, P Krishnakumar, and M Narasimha. "Spatial, temporal and molecular hierarchies in the link between death, delamination and dorsal closure". In: *Development* (2011).

[229] A Munjal and T Lecuit. "Actomyosin networks and tissue morphogenesis". In: *Development (Cambridge)* **141** (2014).

[230] A Munjal et al. "A self-organized biomechanical network drives shape changes during tissue morphogenesis". In: *Nature* **524** (2015).

[231] G Myers. "Why bioimage informatics matters". In: *Nature Methods* **9** (2012).

[232] M Narasimha and NH Brown. "Novel Functions for Integrins in Epithelial Morphogenesis". In: *Current Biology* **14** (2004), pp. 381–385.

[233] J Nash. "Non-Cooperative Games". In: *Annals of Mathematics* **54** (1951), pp. 286–295.

[234] CM Niessen and CJ Gottardi. "Molecular components of the adherens junction". In: *Biochimica et Biophysica Acta - Biomembranes* **1778** (2008).

[235] CM Niessen, D Leckband, and AS Yap. "Tissue organization by cadherin adhesion molecules: Dynamic Molecular and Cellular Mechanisms of Morphogenetic Regulation". In: *Physiological Reviews* **91** (2011).

[236] T Nishimura and M Takeichi. "Chapter 2 Remodeling of the Adherens Junctions During Morphogenesis". In: *Current Topics in Developmental Biology* **89** (2009).

[237] N Noll, SJ Streichan, and BI Shraiman. "Variational Method for Image-Based Inference of Internal Stress in Epithelial Tissues". In: *Phys. Rev. X* **10** (2020), p. 11072.

[238] S Nowozin, B Cseke, and R Tomioka. "f-GAN: Training Generative Neural Samplers using Variational Divergence Minimization". In: *arXiv e-prints* (2016), arXiv:1606.00709. arXiv: `1606.00709 [stat.ML]`.

[239] C Nüsslein-Vollhard and E Wieschaus. "Mutations affecting segment number and polarity in drosophila". In: *Nature* **287** (1980).

[240] PW Oakes et al. “Optogenetic control of RhoA reveals zyxin-mediated elasticity of stress fibres”. In: *Nature Communications* **8** (2017), p. 15817.

[241] B Obara et al. “Contrast-Independent Curvilinear Structure Detection in Biomedical Images”. In: **21** (2012), pp. 2572–2581.

[242] M Oezkaja, Nihat; Nordin. *Fundamentals of Biomechanics*. second edi. Springer US, 1999. ISBN: 9781441931160.

[243] S Okuda, Y Inoue, and T Adachi. “Three-dimensional vertex model for simulating multicellular morphogenesis.” In: *Biophysics and physicobiology* **12** (2015), pp. 13–20.

[244] C Ong et al. “Drosophila melanogaster as a model organism to study nanotoxicity”. In: *Nanotoxicology* **9** (2015), pp. 396–403.

[245] A van den Oord, N Kalchbrenner, and K Kavukcuoglu. “Pixel Recurrent Neural Networks”. In: *arXiv e-prints* (2016), arXiv:1601.06759. arXiv: 1601.06759 [cs.CV].

[246] J Oreopoulos, R Berman, and M Browne. “Chapter 9 - Spinning-disk confocal microscopy: present technology and future trends”. In: *Quantitative Imaging in Cell Biology*. Ed. by JC Waters and TBTMiCB Wittman. Vol. 123. Academic Press, 2014, pp. 153–175. ISBN: 0091-679X.

[247] AW Orr et al. “Mechanisms of mechanotransduction”. In: *Developmental Cell* (2006).

[248] SW Paddock. “Confocal laser scanning microscopy”. In: *BioTechniques* **27** (1999).

[249] B Pan et al. “TMC1 Forms the Pore of Mechanosensory Transduction Channels in Vertebrate Inner Ear Hair Cells”. In: *Neuron* **99** (2018).

[250] B Pan et al. “TMC1 and TMC2 are components of the mechanotransduction channel in hair cells of the mammalian inner ear”. In: *Neuron* **79** (2013).

[251] KA Panfilio and S Roth. “Development: Getting into the groove, or evolving off the rails?” In: *Current Biology* **23** (2013).

[252] L Pasakarnis et al. “Amnioserosa cell constriction but not epidermal actin cable tension autonomously drives dorsal closure”. In: *Nature Cell Biology* (2016).

[253] D Pathak et al. “Context Encoders: Feature Learning by Inpainting”. In: *Proceedings of the IEEE Computer Society Conference on Computer Vision and Pattern Recognition* **2016-Decem** (2016), pp. 2536–2544. arXiv: 1604.07379.

[254] XG Peralta et al. “Emergent properties during dorsal closure in Drosophila morphogenesis”. In: *Physical Biology* (2008).

[255] XG Peralta et al. “Upregulation of forces and morphogenic asymmetries in dorsal closure during Drosophila development”. In: *Biophysical Journal* (2007).

[256] V Perrier, T Philipovitch, and C Basdevant. “Wavelet spectra compared to Fourier spectra”. In: *Journal of Mathematical Physics* **36** (1995), pp. 1506–1519.

[257] MD Petkova et al. “Optimal Decoding of Cellular Identities in a Genetic Network”. In: *Cell* **176** (2019), 844–855.e15.

[258] D Pinheiro and Y Bellaïche. “Mechanical Force-Driven Adherens Junction Remodeling and Epithelial Dynamics”. In: *Developmental Cell* **47** (2018).

[259] DN Politis and H White. “Automatic Block-Length Selection for the Dependent Bootstrap”. In: *Econometric Reviews* **23** (2004), pp. 53–70.

[260] KL Pope and TJ Harris. “Control of cell flattening and junctional remodeling during squamous epithelial morphogenesis in Drosophila”. In: *Development* **135** (2008), pp. 2227–2238.

[261] DMW Powers. “Evaluation : From Precision , Recall and F-Factor to ROC , Informedness , Markedness & Correlation”. In: (2007).

[262] J Pradel and RA White. “From selectors to realizators”. In: *International Journal of Developmental Biology* **42** (1998).

[263] WH Press and SA Teukolsky. “Savitzky-Golay Smoothing Filters”. In: *Computers in Physics* **4** (1990), p. 669.

[264] L Preziosi, D Ambrosi, and C Verdier. “An elasto-visco-plastic model of cell aggregates.” In: *Journal of theoretical biology* **262** (2010), pp. 35–47.

[265] J Prost, F Jülicher, and JF Joanny. “Active gel physics”. In: *Nature Physics* **11** (2015), pp. 111–117.

[266] M Purves et al. “Life: The Science of Biology 7th Edition”. In: *McGraw Hill* **7** (2004).

[267] C Rackauckas and Q Nie. “DifferentialEquations.jl – A Performant and Feature-Rich Ecosystem for Solving Differential Equations in Julia”. In: *Journal of Open Research Software* **5** (2017).

[268] A Radford, L Metz, and S Chintala. “Unsupervised Representation Learning with Deep Convolutional Generative Adversarial Networks”. In: *arXiv e-prints* (2015), arXiv:1511.06434. arXiv: 1511.06434 [cs.LG].

[269] KR Rajagopal and AR Srinivasa. “Mechanics of the inelastic behavior of materials-part 1, theoretical underpinnings”. In: *International Journal of Plasticity* **14** (1998), pp. 945–967.

[270] S Ramaswamy, J Toner, and J Prost. “Nonequilibrium Fluctuations, Traveling Waves, and Instabilities in Active Membranes”. In: *Phys. Rev. Lett.* **84** (2000), pp. 3494–3497.

[271] SS Ranade et al. “Piezo1, a mechanically activated ion channel, is required for vascular development in mice”. In: *Proceedings of the National Academy of Sciences of the United States of America* **111** (2014).

[272] J Ranft et al. “Fluidization of tissues by cell division and apoptosis.” In: *Proceedings of the National Academy of Sciences of the United States of America* **107** (2010), pp. 20863–20868.

[273] C Raokauokas and Q Nie. “Adaptive methods for stochastic differential equations via natural embeddings and rejection sampling with memory”. In: *Discrete and Continuous Dynamical Systems - Series B* **22** (2017), pp. 2731–2761.

[274] M Rauzi, PF Lenne, and T Lecuit. “Planar polarized actomyosin contractile flows control epithelial junction remodelling”. In: *Nature* **468** (2010).

[275] M Rauzi et al. “Nature and anisotropy of cortical forces orienting Drosophila tissue morphogenesis.” In: *Nature cell biology* **10** (2008), pp. 1401–1410.

[276] BH Reed et al. “Integrin-Dependent Apposition of Drosophila Extraembryonic Membranes Promotes Morphogenesis and Prevents Anoikis”. In: *Current Biology* **14** (2004), pp. 372–380.

[277] S Restrepo and K Basler. “Drosophila wing imaginal discs respond to mechanical injury via slow InsP 3 R-mediated intercellular calcium waves”. In: *Nature Communications* **7** (2016).

[278] N Rezaei and A Saghazadeh. “The role of PIEZO2 in human mechanosensation”. In: *Acta Medica Iranica* **55** (2017).

[279] P Richa. "Role of mechanosensitive ion channels in coordinated epithelial cell dynamics in Drosophila". PhD thesis. Göttingen: Georg-August University Göttingen, 2019.

[280] A Rodriguez-Diaz et al. "Actomyosin purse strings: Renewable resources that make morphogenesis robust and resilient". In: *HFSP Journal* **2** (2008).

[281] O Ronneberger, P Fischer, and T Brox. "U-Net: Convolutional Networks for Biomedical Image Segmentation". In: *arXiv e-prints* (2015), arXiv:1505.04597. arXiv: `1505.04597 [cs.CV]`.

[282] W Roux. "Beiträge zur Entwickelungsmechanik des Embryo - Ueber die künstliche Hervorbringung halber Embryonen durch Zerstörung einer der beiden ersten Furchungskugeln, sowie über die Nachentwickelung (Postgeneration) der fehlenden Körperhälfte". In: *Archiv für Pathologische Anatomie und Physiologie und für Klinische Medicin* **114** (1888).

[283] S Ruder. "An overview of gradient descent optimization algorithms". In: *arXiv e-prints* (2016), arXiv:1609.04747. arXiv: `1609.04747 [cs.LG]`.

[284] SK Sadanandan et al. "Automated Training of Deep Convolutional Neural Networks for Cell Segmentation". In: *Scientific Reports* (2017), pp. 1–7.

[285] L Saias et al. "Decrease in Cell Volume Generates Contractile Forces Driving Dorsal Closure". In: *Developmental Cell* (2015).

[286] G Salbreux, G Charras, and E Paluch. "Actin cortex mechanics and cellular morphogenesis". In: *Trends in Cell Biology* **22** (2012).

[287] G Salbreux and F Jülicher. "Mechanics of active surfaces". In: *Phys. Rev. E* **96** (2017), p. 32404.

[288] G Salbreux et al. "Coupling mechanical deformations and planar cell polarity to create regular patterns in the zebrafish retina." In: *PLoS computational biology* **8** (2012), e1002618.

[289] K Saotome et al. "Structure of the mechanically activated ion channel Piezo1". In: *Nature* **554** (2018).

[290] Y Sasaki. "The truth of the F-measure". In: (2007), pp. 1–5.

[291] J Schindelin et al. "Fiji: an open-source platform for biological-image analysis". In: *Nature Methods* **9** (2012), pp. 676–682.

[292] J Schindelin et al. "The ImageJ ecosystem: An open platform for biomedical image analysis". In: *Molecular Reproduction and Development* **82** (2015), pp. 518–529.

[293] CA Schneider, WS Rasband, and KW Eliceiri. "NIH Image to ImageJ: 25 years of image analysis". In: *Nature Methods* **9** (2012).

[294] J Sedzinski et al. "Polar actomyosin contractility destabilizes the position of the cytokinetic furrow." In: *Nature* **476** (2011), pp. 462–466.

[295] K Sethi, EJ Cram, and R Zaidel-Bar. "Stretch-induced actomyosin contraction in epithelial tubes: Mechanotransduction pathways for tubular homeostasis". In: *Seminars in Cell and Developmental Biology* **71** (2017).

[296] EK Shannon et al. "Multiple Mechanisms Drive Calcium Signal Dynamics around Laser-Induced Epithelial Wounds". In: *Biophysical Journal* (2017).

[297] A Shindo. "Models of convergent extension during morphogenesis". In: *Wiley Interdisciplinary Reviews: Developmental Biology* **7** (2018).

[298] PC Shivakumar and PF Lenne. "Laser Ablation to Probe the Epithelial Mechanics in Drosophila." In: *Methods in molecular biology (Clifton, N.J.)* **1478** (2016), pp. 241–251.

[299] BI Shraiman. "Mechanical feedback as a possible regulator of tissue growth". In: *Proceedings of the National Academy of Sciences of the United States of America* **102** (2005), pp. 3318–3323.

[300] LC Siang, R Fernandez-Gonzalez, and JJ Feng. "Modeling cell intercalation during Drosophila germband extension". In: *Physical Biology* **15** (2018), p. 66008.

[301] H Siedentopf and R Zsigmondy. "Uber Sichtbarmachung und Größenbestimmung ultramikoskopischer Teilchen, mit besonderer Anwendung auf Goldrubingläser". In: *Annalen der Physik* **315** (1902).

[302] H Singh. *Practical Machine Learning and Image Processing*. Springer, 2019.

[303] J Skilling. "Nested sampling for general Bayesian computation". In: *Bayesian Analysis* **1** (2006), pp. 833–859.

[304] P Skoglund et al. "Convergence and extension at gastrulation require a myosin IIB-dependent cortical actin network". In: *Development* **135** (2008).

[305] A Sokolow et al. "Cell ingression and apical shape oscillations during dorsal closure in Drosophila". In: *Biophysical Journal* (2012).

[306] J Solon et al. "Pulsed Forces Timed by a Ratchet-like Mechanism Drive Directed Tissue Movement during Dorsal Closure". In: *Cell* (2009).

[307] C Sommer et al. "Ilastik: Interactive learning and segmentation toolkit". In: *Proceedings - International Symposium on Biomedical Imaging*. 2011.

[308] EA Specht, E Braselmann, and AE Palmer. "A Critical and Comparative Review of Fluorescent Tools for Live-Cell Imaging". In: *Annual Review of Physiology* **79** (2017).

[309] J Stegmaier et al. "Real-Time Three-Dimensional Cell Segmentation in Large-Scale Microscopy Data of Developing Embryos". In: *Developmental Cell* (2016).

[310] DJ Stephens and VJ Allan. "Light microscopy techniques for live cell imaging". In: *Science* **300** (2003).

[311] SJ Streichan et al. "Global morphogenetic flow is accurately predicted by the spatial distribution of myosin motors". In: *eLife* **7** (2018). Ed. by F Jülicher, e27454.

[312] C Stringer et al. "Cellpose: a generalist algorithm for cellular segmentation". In: *Nature Methods* **18** (2021), pp. 100–106.

[313] JT Stull, KE Kamm, and R Vandenboom. "Myosin light chain kinase and the role of myosin light chain phosphorylation in skeletal muscle". In: *Archives of Biochemistry and Biophysics* **510** (2011).

[314] A Sutherland and A Lesko. "Pulsed actomyosin contractions in morphogenesis". In: *F1000Research* **9** (2020).

[315] M Suzuki et al. "Distinct intracellular Ca2+ dynamics regulate apical constriction and differentially contribute to neural tube closure". In: *Development (Cambridge)* (2017).

[316] JR Swedlow, IG Goldberg, and KW Eliceiri. "Bioimage informatics for experimental biology". In: *Annual Review of Biophysics* **38** (2009).

[317] YQ Tang et al. "Ankyrin Is An Intracellular Tether for TMC Mechanotransduction Channels". In: *Neuron* **107** (2020).

[318] PJ Thomas and B Lindner. "Phase descriptions of a multidimensional Ornstein-Uhlenbeck process". In: *Phys. Rev. E* **99** (2019), p. 62221.

[319] G Tkačik and T Gregor. "The many bits of positional information". In: *Development* **148** (2021).

[320] G Tkačik et al. "Positional information, positional error, and readout precision in morphogenesis: a mathematical framework." eng. In: *Genetics* **199** (2015), pp. 39–59.

[321] Y Toyama et al. "Apoptotic force and tissue dynamics during Drosophila embryogenesis". In: *Science* (2008).

[322] A Turing. "The chemical basis of morphogenesis". In: *Philosophical Transactions of the Royal Society B: Biological Sciences* (1952), pp. 37–72.

[323] F Twiss et al. "Vinculin-dependent Cadherin mechanosensing regulates efficient epithelial barrier formation". In: *Biology Open* **1** (2012).

[324] V Ulman et al. "An objective comparison of cell-tracking algorithms". In: *Nature Methods* **14** (2017).

[325] L Valon et al. "Optogenetic control of cellular forces and mechanotransduction". In: *Nature Communications* **8** (2017), p. 14396.

[326] CG Vasquez, M Tworoger, and AC Martin. "Dynamic myosin phosphorylation regulates contractile pulses and tissue integrity during epithelial morphogenesis". In: *Journal of Cell Biology* (2014).

[327] M Vicente-Manzanares et al. "Non-muscle myosin II takes centre stage in cell adhesion and migration". In: *Nature Reviews Molecular Cell Biology* **10** (2009).

[328] N Vogt et al. "The γTuRC components Grip75 and Grip128 have an essential microtubule-anchoring function in the Drosophila germline". In: *Development* **133** (2006).

[329] AH Voie, DH Burns, and FA Spelman. "Orthogonal-plane fluorescence optical sectioning: Three-dimensional imaging of macroscopic biological specimens". In: *Journal of Microscopy* **170** (1993).

[330] TTK Vuong-Brender, X Yang, and M Labouesse. "Chapter Thirty-Five - C. elegans Embryonic Morphogenesis". In: *Essays on Developmental Biology, Part A*. Ed. by PMBTC-TiDB Wassarman. Vol. 116. Academic Press, 2016, pp. 597–616. ISBN: 0070-2153.

[331] CH Waddington. "The strategy of the genes. A discussion of some aspects of theoretical biology. With an appendix by H. Kacser." In: *The strategy of the genes A discussion of some ...* **8** (1957).

[332] RG Walker, AT Willingham, and CS Zuker. "A Drosophila mechanosensory transduction channel". In: *Science* **287** (2000).

[333] Q Wang, JJ Feng, and LM Pismen. "A cell-level biomechanical model of Drosophila dorsal closure". In: *Biophysical Journal* **103** (2012).

[334] TC Wang et al. "Video-to-Video Synthesis". In: *arXiv e-prints* (2018), arXiv:1808.06601. arXiv: `1808.06601 [cs.CV]`.

[335] Y Wang, JY Shyy, and S Chien. "Fluorescence proteins, live-cell imaging, and mechanobiology: Seeing is believing". In: *Annual Review of Biomedical Engineering* **10** (2008).

[336] Z Wang, E Wang, and Y Zhu. "Image segmentation evaluation: a survey of methods". In: *Artificial Intelligence Review* **53** (2020), pp. 5637–5674.

[337] AS Warkman and PA Krieg. "Xenopus as a model system for vertebrate heart development." In: *Seminars in cell & developmental biology* **18** (2007), pp. 46–53.

[338] "Watershed of a continuous function". In: *Signal Processing* **38** (1994), pp. 99–112.

[339] AR Wells et al. "Complete canthi removal reveals that forces from the amnioserosa alone are sufficient to drive dorsal closure in Drosophila". In: *Molecular Biology of the Cell* **25** (2014).

[340] C Wenzl et al. "Localization of RhoGEF2 during Drosophila cellularization is developmentally controlled by slam". In: *Mechanisms of Development* **127** (2010).

[341] F Wolf. "Symmetry, Multistability, and Long-Range Interactions in Brain Development". In: *Phys. Rev. Lett.* **95** (2005), p. 208701.

[342] LL Wolpert. *Principles of development*. eng. Ed. by C Tickle and A Martinez Arias. Sixth edit. Oxford, United Kingdom: Oxford University Press, 2019. ISBN: 9780198800569.

[343] L Wolpert. "Positional information and the spatial pattern of cellular differentiation". In: *Journal of Theoretical Biology* **25** (1969), pp. 1–47.

[344] W Wood. "Wound healing: Calcium flashes illuminate early events". In: *Current Biology* **22** (2012).

[345] W Wood et al. "Wound healing recapitulates morphogenesis in Drosophila embryos". In: *Nature Cell Biology* **4** (2002).

[346] S Xie and AC Martin. "Intracellular signalling and intercellular coupling coordinate heterogeneous contractile events to facilitate tissue folding". In: *Nature Communications* **6** (2015).

[347] S Yamada et al. "Deconstructing the cadherin-catenin-actin complex". In: *Cell* **123** (2005).

[348] Z Yan et al. "Drosophila NOMPC is a mechanotransduction channel subunit for gentle-touch sensation". In: *Nature* **493** (2013).

[349] S Yonemura et al. "α-Catenin as a tension transducer that induces adherens junction development". In: *Nature Cell Biology* **12** (2010).

[350] JA Zallen and JT Blankenship. "Multicellular dynamics during epithelial elongation." In: *Seminars in cell & developmental biology* **19** (2008), pp. 263–270.

[351] JA Zallen and E Wieschaus. "Patterned gene expression directs bipolar planar polarity in Drosophila." In: *Developmental cell* **6** (2004), pp. 343–355.

[352] H Zhang et al. "A tension-induced mechanotransduction pathway promotes epithelial morphogenesis". In: *Nature* **471** (2011).

[353] W Zhang et al. "Ankyrin Repeats Convey Force to Gate the NOMPC Mechanotransduction Channel". In: *Cell* **162** (2015).

[354] YV Zhang et al. "The Basis of Food Texture Sensation in Drosophila". In: *Neuron* **91** (2016).

[355] Y Zhang et al. "The glucosyltransferase Xiantuan of the endoplasmic reticulum specifically affects E-Cadherin expression and is required for gastrulation movements in Drosophila". In: *Developmental Biology* (2014).

[356] Z Zhou et al. "UNet++: A Nested U-Net Architecture for Medical Image Segmentation". In: *arXiv e-prints* (2018), arXiv:1807.10165. arXiv: `1807.10165 [cs.CV]`.

[357] JY Zhu et al. "Unpaired Image-to-Image Translation using Cycle-Consistent Adversarial Networks". In: *arXiv e-prints* (2017), arXiv:1703.10593. arXiv: `1703.10593 [cs.CV]`.

[358] Y Zhu et al. "A finite viscoelastic-plastic model for describing the uniaxial ratchetting of soft biological tissues". In: *Journal of Biomechanics* **47** (2014), pp. 996–1003.

[359] R Zwanzig. "Memory Effects in Irreversible Thermodynamics". In: *Phys. Rev.* **124** (1961), pp. 983–992.

Acknowledgements

Acknowledgements

A dissertation is a team effort. I might be the composer, but without orchestrator, conductor, musicians, audio technicians and mastering engineer there can not be a finished record.

Most importantly, I thank my fantastic wife, Christine, who supports me throughout my life and without whom I couldn't have done this PhD. For being patient and encouraging and providing a home one wants to return to after a long days work. But also for direct contributions by helping with manual correction of the segmentation, taking the position as editor in chief for this thesis and being one of my first sources for feedback.

I am truly in debt to Fred Wolf for giving me this position and putting a lot of faith in me and trust in my abilities. I would like to thank you for giving me the freedom to pursue all my scientific interests, even when they are not related to my thesis work, and supporting me throughout the PhD. Without your input, guidance, training and expertise this work would not have been possible.

Similarly, I am grateful to Jörg Großhans for his supervision and constant encouragement, patiently explaining biology to a naive physicist, being a very reliable collaborator and being someone who is never in a bad mood, always spreading his enthusiasm about the flies. In addition, for helpful comments on the initial draft of this thesis.

I owe much to Stephan Eule for a fantastic start into my PhD project by doing the machine learning segmentation project together. It resulted from a discussion over a coffee, without hesitation and great motivation we worked on it and were quickly rewarded. The obtained results later became the cornerstone for the rest of my work.

Next, I thank Ulrich Parlitz for taking part in my advisory committee who always was the pragmatic voice and helped me to focus on the important questions.

Prachi Richa, who is the best experimental coworker a theoretician can wish for. Knowledgeable and willing to share that knowledge, being reliable and fun to work with.

I also thank Deqing Kong, for another fruitful collaboration, being very dependable and willing to work a lot for the completion of the manuscripts.

I thank Lars Reichl whos work I took partially over and who answered many initial questions of mine. Likewise, I want to thank all collaborators who contributed to the published work that have formed a part of this thesis.

Many thanks go out to Nicolas Lenner, great office mate and person, who always motivated me to learn more and try out things I haven't thought of yet. Thanks for the many discussions and always giving a first critical input to fresh ideas. For our many activities including setting up a challenging seminar, or re-initiation of our program retreats, among others. In addition for reading and providing great help to streamline the thesis.

Similarly, I am indepted to Steffen Mühle for always being available to discuss problems and providing a secondary view, for many years of fun scientific and unscientific conversations and for thorough and detailed comments on the thesis manuscript. Thanks to you and Liz, the quarantine crew, who made sure my time was not only filled with work and prevented me from going crazy.

Erik Schultheis, for sharing his expertise about machine learning and coding and contributing to the segmentation pipeline, showing me how to program properly, managing our IT requirements during founding of the new institute and many helpful project related comments.

Andreas Neef, one of the most enthusiastic scientist I know, for discussions about statistical methods, data analysis and many comments in group meetings.

Theo Geisel, for providing a stimulating annual winter seminar and setting up the whole department and a great working environment at the MPI DS.

I also thank my other beta readers Michael Sternbach and Julian Vogel for providing feedback for the manuscript and many discussions throughout the PhD. In addition, for many good memories of the work at the institute and out of work activities. Also thanks for watering my plants!

I thank the GGNB, and my graduate program PTCN, for their administrative and financial support and all the organizers and participants of our retreats for many scientifically interesting experiences. Arriba!

I thank my whole group who are ever helpful and gave much input in group meetings and providing a great working atmosphere, especially during challenging times of corona.

Scientific work is not possible without the people in the background, managing and administrating the institute. I am especially grateful to Christina von Behren who worked like crazy and was always available in the stressful times of setting up a new founded institute. For the same reasons I am very thankful for Yvonne Reimann and Rebecca Jürgens, who instantly helped me in case of administrative problems and making retreats and conferences possible. I thank Bernhard Bandow, for quickly providing help with the cluster when I needed it. At the MPI DS I thank Ayse Bolik, Vika Novak and Yorck Beensen for all the administrative support.

I am also very grateful for my immediate and extended family, who are always supportive and provide stability in good times and build up in bad times. Its a great privilege to not have to worry about life and being able to study freely.

Last but not least, I would like to thank all the fruit flies, who gave their life for science.